

# **ESTIMATION OF SUSPENDED SEDIMENT CONCENTRATION BY DEVELOPING INTEGRATED SURFACE REFLECTANCE FUNCTION**

by

**Janhavi Kishor Joshi**

(Reg. No. 2019/03)

A Thesis submitted to the  
**MAHATMA PHULE KRISHI VIDYAPEETH,  
RAHURI - 413 722, DIST-AHMEDNAGAR,  
MAHARASHTRA, INDIA.**

In partial fulfilment of the requirements for the degree of

**DOCTOR OF PHILOSOPHY (AGRICULTURAL ENGINEERING)**

in

**SOIL AND WATER CONSERVATION ENGINEERING**



**DEPARTMENT OF SOIL AND WATER CONSERVATION  
ENGINEERING**

**DR. ANNASAHEB SHINDE COLLEGE OF AGRICULTURAL ENGINEERING AND  
TECHNOLOGY**

**MAHATMA PHULE KRISHI VIDYAPEETH, RAHURI – 413722,  
DIST-AHMEDNAGAR, MAHARASHTRA, INDIA**

**ESTIMATION OF SUSPENDED SEDIMENT CONCENTRATION BY  
DEVELOPING INTEGRATED SURFACE REFLECTANCE FUNCTION**

by

**Janhavi Kishor Joshi**

(Reg. No. 2019/03)

A Thesis submitted to the  
**MAHATMA PHULE KRISHI VIDYAPEETH,  
RAHURI - 413 722, DIST-AHMEDNAGAR,  
MAHARASHTRA, INDIA.**

In partial fulfilment of the requirements for the degree of

**DOCTOR OF PHILOSOPHY (AGRICULTURAL ENGINEERING)**

in

**SOIL AND WATER CONSERVATION ENGINEERING**

APPROVED BY

**Dr. A. A. Atre**

(Chairman and Research Guide)

**Dr. S. B. Nandgude**

(Committee Member)

**Dr. M. G. Shinde**

(Committee Member)

**Dr. A. G. Durgude**

(Committee Member)

**Dr. S. D. Gorantiwar**

(Committee Member)

**Dr. M. R. Patil**

(Committee Member)

**DEPARTMENT OF SOIL AND WATER CONSERVATION  
ENGINEERING**

**DR. ANNASAHEB SHINDE COLLEGE OF AGRICULTURAL ENGINEERING AND  
TECHNOLOGY**

**MAHATMA PHULE KRISHI VIDYAPEETH, RAHURI – 413722,  
DIST-AHMEDNAGAR, MAHARASHTRA, INDIA**

2024

## ***Dedication***

*Dedicated wholeheartedly to Mother nature,  
water resource development and farming community and  
my beloved teachers*

*..... Janhavi Kishor Joshi*



Mahatma Phule Krishi Vidyapeeth - Rahuri

**Certificate of Plagiarism Check for Thesis**

<b>Author Name</b>	Janhavi Kishor Joshi
<b>Course of Study</b>	Ph.D.
<b>Name of Guide</b>	Dr. A. A. Atre
<b>Department</b>	Soil and Water Conservation Engineering
<b>Acceptable Maximum Limit</b>	10 %
<b>Submitted By</b>	headswcerahuri@gmail.com
<b>Paper Title</b>	Integration of Suspended Sediment Concentration by Developing Integrated Surface Reflectance Function
<b>Similarity</b>	7 %
<b>Paper ID</b>	1282032
<b>Submission Date</b>	2023-12-27 10:51:09

Signature of Student

Signature of Guide

Head  
Deptt. of SWCE  
Dr. ASCAE&T, MPKV,  
Rahuri

University Librarian

Associate Dean  
Dr. ASCAE&T, Rahuri

\* This report has been generated by DrillBit Anti-Plagiarism Software

## CANDIDATE'S DECLARATION

I hereby declare that,  
this thesis or part of this thesis has not been submitted by me or any other person  
to any other University or Institute for a Degree or Diploma

Place: MPKV, Rahuri

Date:     /     /

**(Janhavi Kishor Joshi)**

**Dr. Atul Arvind Atre**

Chairman, Student Advisory Committee

Professor,

Department of Soil and Water Conservation Engineering,

Dr. Annasaheb Shinde College of Agricultural Engineering and Technology

Mahatma Phule Krishi Vidyapeeth,

Rahuri – 413 722

District – Ahmednagar, Maharashtra (India)

## **CERTIFICATE**

This is to certify that the thesis entitled “**Estimation of Suspended Sediment Concentration by Developing Integrated Surface Reflectance Function**” submitted to the Faculty of Agricultural Engineering, Mahatma Phule Krishi Vidyapeeth, Rahuri, Dist. Ahmednagar (Maharashtra) in partial fulfilment of the requirements for the award of the degree of **DOCTOR OF PHILOSOPHY (AGRICULTURAL ENGINEERING)** in **SOIL AND WATER CONSERVATION ENGINEERING**, embodies the results of a piece of bonafide research work carried out by **MISS JANHAVI KISHOR JOSHI** under my guidance and supervision and that no part of this thesis have been submitted for any other degree or diploma.

The assistance and help received during the course of this investigation has been duly acknowledged.

Place: MPKV, Rahuri

Date:     /     /

**(A. A. Atre)**

**Dr. S. B. Nandgude**

Professor and Head,

Department of Soil and Water Conservation Engineering,

Dr. Annasaheb Shinde College of Agricultural Engineering and Technology

Mahatma Phule Krishi Vidyapeeth,

Rahuri – 413 722

District – Ahmednagar, Maharashtra (India)

## **CERTIFICATE**

This is to certify that the thesis entitled “**Estimation of Suspended Sediment Concentration by Developing Integrated Surface Reflectance Function**” submitted to the Faculty of Agricultural Engineering, Mahatma Phule Krishi Vidyapeeth, Rahuri, Dist. Ahmednagar (Maharashtra) in partial fulfilment of the requirements for the award of the degree of **DOCTOR OF PHILOSOPHY (AGRICULTURAL ENGINEERING)** in **SOIL AND WATER CONSERVATION ENGINEERING**, embodies the results of a piece of bonafide research work carried out by **MISS JANHAVI KISHOR JOSHI** and that no part of this thesis have been submitted for any other degree or diploma.

Place: MPKV, Rahuri

Date:     /     /

**(S. B. Nandgude)**

**Dean,**  
Faculty of Agricultural Engineering,  
Mahatma Phule Krishi Vidyapeeth,  
Rahuri – 413 722  
District – Ahmednagar, Maharashtra (India)

## **CERTIFICATE**

This is to certify that the thesis entitled “**Estimation of Suspended Sediment Concentration by Developing Integrated Surface Reflectance Function**” submitted to the Faculty of Agricultural Engineering, Mahatma Phule Krishi Vidyapeeth, Rahuri, Dist. Ahmednagar (Maharashtra) in partial fulfilment of the requirements for the award of the degree of **DOCTOR OF PHILOSOPHY (AGRICULTURAL ENGINEERING)** in **SOIL AND WATER CONSERVATION ENGINEERING**, embodies the results of a piece of bonafide research work carried out by **MISS JANHAVI KISHOR JOSHI** under the guidance and supervision of **Dr. A. A. Atre**, Professor and Head, Department of Soil and Water Conservation Engineering and that no part of this thesis have been submitted for any other degree or diploma.

Place: MPKV, Rahuri

Date:    /    /

Dean,  
Faculty of Agricultural Engineering  
Mahatma Phule Krishi Vidyapeeth

## ACKNOWLEDGEMENTS

Today, I am on the verge of a new beginning, a testament to the unwavering support and endless encouragement I have received. Words often fall short in expressing the depths of our gratitude. My heartfelt appreciation stretches far beyond the confines of language, but in the absence of grand gestures, I offer these words as a humble token of my profound gratitude.

I extend my heartfelt gratitude to my research guide, Dr. A. A. Atre, Chairman, Student Advisory Committee and Professor, Department of Soil and Water Conservation Engineering, Dr. Annasaheb Shinde College of Agricultural Engineering and Technology, Mahatma Phule Krishi Vidyapeeth (MPKV), Rahuri for his invaluable mentorship and guidance throughout this project. His expertise, insightful feedback, and unconditional support were instrumental in successful completion of my doctoral research. He provided me with clear objectives, a detailed roadmap, and constructive criticism on my proposal, methodology, and results. His constant availability and encouragement fostered my creativity, critical thinking, and research skills. I am particularly grateful for his support during this challenging work, motivating me to persevere and achieve my goals.

I am thankful to Dr. D. D. Pawar, Dean, Faculty of Agricultural Engineering and Associate Dean, Dr. Annasaheb Shinde College of Agricultural Engineering and Technology, Mahatma Phule Krishi Vidyapeeth, Rahuri for constant encouragement for completing the research and providing necessary facilities required during my research work.

I am also grateful to Dr. S. B. Nandgude, Member, Advisory Committee and Professor and Head, Department of SWCE, Dr. ASCAET, MPKV, Rahuri for his valuable suggestions and guidance during my doctoral research and course work.

I can't thank enough Dr. S. D. Gorantiwar, Member, Advisory Committee, Director of Research, MPKV, Rahuri, Head, Department of Agricultural Engineering, and Principal Investigator, CAAST-CSAWM Project, MPKV, Rahuri and Dr. M. G. Shinde, Member, Advisory Committee and Professor of SWCE, Department of Agricultural Engineering, and Co-Principal Investigator, CAAST-CSAWM Project, MPKV, Rahuri for guiding me throughout the research and ensuring access to all necessary facilities under the CAAST-CSAWM Project.

I am especially thankful to Dr. A. G. Durgude, Member, Advisory Committee and Analytical Chemist, Micronutrient Research Scheme, Department of Soil Science and Agricultural Chemistry, Post Graduate Institute, MKPV, Rahuri and Dr. M. R. Patil, Member, Advisory Committee and Assistant Professor of Statistics, Department of Statistics, Post Graduate Institute, MPKV, Rahuri for their valuable insights, suggestions and timely help at every stage of the study.

I am thankful to Dr. V. N. Barai, Professor of SWCE, Dr. B. K. Gavit, Associate Professor of SWCE, Dr. Mrs. S. S. Shinde, Assistant Professor of SWCE and Dr. Himalaya Ganachari, Assistant Professor of SWCE, for technical support and guidance during my research work. I am also thankful to Dr. S. K. Upadhye, Professor of SWCE, ZARS, Solapur, MPKV for building up my morale and inspiring me throughout my doctoral studies.

I am very much thankful to Dr. S. A. Kadam, Associate Professor of IDE and Member, CAAST-CSAWM Project, MPKV, Rahuri for making me acquainted with operating instruments, data analysis and technical guidance required for the research.

I extend my special thanks to all staff members of Department of SWCE for their timely cooperation and help I am thankful to Mr. S. S. Salunkhe, Mr. M. G. Kamble, Mr. Nikhil Pawar, Mrs. Panmalkar and Smt. Kachole.

Many thanks to Dr. Mangesh Baviskar, former Research Associate, CAAST-CSAWM Project, Er. Mohasin Tamboli, Research Associate, CAAST-CSAWM Project and Dr. Neelam Kondvilkar, former research Associate, CAAST-CSAWM Project for facilitating me to conduct my research work and encouragement.

I am also thankful to Er. Sanglikar Sir, Er. Nilkanth More, Central Workshop, MPKV, Rahuri for their help for my work.

I express my gratitude to the Superintending Engineer of the Irrigation Division in Ahmednagar for granting me permission to carry out data acquisition campaigns in the Mula Dam reservoir for the purpose of collecting samples and obtaining various readings.

I express my gratitude to Mr. Bhimraj Bare for his assistance during the conduct of my research experiments. I am very much obliged to thank Lambe Mama, Karake Mama, Chavan Mama and Ughade Mama for helping me during actual experimentation. I am also thankful to Mr. Sagar Mane for his cooperation during my work.

I am thankful to the members of Samarth Udyog, Mulanagar for providing necessary facilities during data collection required for my research work.

I shall be failing in my duty if I do not acknowledge the sincere contribution of my friends, seniors and juniors. I would like to be thankful to Dr. Ujjwala, Dr. Vaibhav, Dr. Sachin, Dr. Rahul, Dr. Mayavati, Vaishali, Dr. Kiran, Ashok, Sandesh, Dr. Pranav, Dnyaneshwar, Komal, Vishal, Prasanna, Prajakta, Rutuja, Sushma, Swamini, Dhanashree and Pranoti.

I extend my sincere appreciation to my brother, Smitesh, whose moral support and encouragement have been instrumental throughout my doctoral journey. I am also thankful to my cousin, Mrs. Swanandi and brother-in-law Mr. Ajay for being there for me as local guardian during earlier period of my work.

I would like to express my deepest gratitude to my parents, Mrs. Shubhada Joshi and Mr. Kishor Joshi, for their support, encouragement, and sacrifices throughout the journey. I am profoundly thankful for the countless sacrifices they made to ensure my education and well-being. Their wisdom, guidance, and encouragement have been invaluable, shaping not only my academic endeavours but also my personal and professional growth. I dedicate this achievement to them with heartfelt appreciation for being my greatest supporters, mentors, and role models.

Last but not the least, I am grateful to all the authorities of university, all teaching and non-teaching staff and everyone else who has been an integral part of my journey who helped me either directly or indirectly.

**Place: MPKV, Rahuri**

**Date:     /     /2024**

**(Janhavi Kishor Joshi)**

## CONTENTS

Chapter No.	Title	Page No.
	CANDIDATE'S DECLARATION	i
	CERTIFICATE OF RESEARCH GUIDE	ii
	CERTIFICATE OF HEAD OF THE DEPARTMENT	iii
	CERTIFICATE OF DEAN	iv
	ACKNOWLEDGEMENTS	v
	LIST OF TABLES	xiii
	LIST OF FIGURES	xiv
	LIST OF PLATES	xvii
	LIST OF ABBREVIATIONS AND SYMBOLS	xviii
	ABSTRACT	xx
<b>I</b>	<b>INTRODUCTION</b>	<b>1-4</b>
<b>II</b>	<b>REVIEW OF LITERATURE</b>	<b>5-32</b>
	2.1 Historical Developments in Assessment of Suspended Sediment	5
	2.2 Need and Significance of Suspended Sediment Concentration Estimation	6
	2.3 Methods of Suspended Sediment Concentration Estimation	6
	2.3.1 Various Methods of Suspended Sediment Concentration Estimation	6
	2.3.2 Remote Sensing Reflectance Methods	8
	2.3.2.1 Handheld Spectroradiometer	10
	2.3.2.2 Unmanned Aerial Vehicle (UAV)	13
	2.3.2.3 Satellite Remote Sensing	13
	2.3.2.4 Studies on Spectral Integration Approach	21
	2.4 Summary and Critique on Reviewed Literature	25
<b>III</b>	<b>MATERIALS AND METHODS</b>	<b>35-57</b>
	3.1 Details of the Study Area	35
	3.2 Data Collection of in-situ Suspended Sediment Concentration and surface reflectance	36
	3.2.1 Collection of Water Samples	38

---

3.2.2	Determination of Suspended Sediment Concentration in Laboratory	39
3.2.3	In-situ Surface reflectance acquisition using Spectroradiometer	39
3.2.4	Recording coordinates of sampling site	43
3.2.5	Satellite Data Acquisition	44
3.2.6	Identification of Mula dam reservoir in Satellite Imagery	46
3.3	Development of Spectral Response using Spectroradiometer and Sentinel-2 images	46
3.3.1	Spectral Signature using Spectroradiometer	46
3.3.2	Spectral Signature using Sentinel-2 images	47
3.3.3	Comparison of Spectral Signature captured using Sentinel-2 (BOA) and Spectroradiometer	48
3.4	Selection of spectral bands indices and band combinations for estimation of SSC	48
3.4.1	Selection of Spectral Indices	48
3.4.2	Selection of Band Combinations	50
3.5	Bifurcation of Data set Into Calibration and Validation Data Set	51
3.6	Development of Relationships between Spectroradiometer and Satellite Indices, Band Functions and Observed Suspended Sediment Concentration using Calibration Data Set	52
3.6.1	Relationship between Various Spectroradiometer Indices, Band Combinations and Observed Suspended Sediment Concentration	52
3.6.2	Relationship between Spectroradiometer Indices, Band Functions and Satellite Indices, Band Functions	53
3.7	Validation and Performance Evaluation	53
3.7.1	Graphical Method or Visual Interpretation	54
3.7.2	Slope and y-intercept	54
3.7.3	Performance Evaluation using Significance tests	55
3.7.3.1	t-test for testing the Coefficients of Linear Equation	55

---

	3.7.3.2	Student's t-test for Testing the Difference of Mean	55
	3.7.4	Performance Evaluation using Statistical Indicators	55
	3.7.4.1	Coefficient of Determination ( $R^2$ )	55
	3.7.4.2	Root Mean Square Error (RMSE)	56
	3.7.4.3	Mean Absolute Percentage Error (MAPE)	56
	3.7.4.4	Nash Sutcliffe Model efficiency coefficient (NSE)	56
	3.7.4.5	Index of Agreement (d)	57
	3.8	Historic Mapping of Estimated SSC	57
<b>IV</b>	<b>RESULTS AND DISCUSSION</b>		<b>59-100</b>
	4.1	Distribution of sampling locations and observed SSC in Mula dam reservoir	59
	4.1.1	Statistical Analysis of Suspended Sediment Concentration	61
	4.2	Analysis of Spectral Signature	62
	4.2.1	Spectral Signature using spectral responses captured by Spectroradiometer SVC-1024i	62
	4.2.2	Relationship between observed SSC and band values obtained from Spectroradiometer SVC-1024i	63
	4.2.3	Comparison of Spectral Signature obtained from Spectroradiometer SVC – 1024i and Sentinel – 2 Satellite	67
	4.3	Development of Relationship between SSC and Band Indices and Band Ratios/ Combinations derived from Spectroradiometer SVC – 1024i	71
	4.3.1	Relationship between Spectroradiometer derived index and SSC	71
	4.3.1.1	Relationship between NDSSI – Spectro and SSC	71
	4.3.1.2	Relationship between NSMI – Spectro and SSC	71
	4.3.1.3	Relationship between M-NDSSI – Spectro and SSC	71
	4.3.1.4	Relationship between R-NDSSI – Spectro and SSC	72

4.3.2	Relationship between Spectroradiometer derived band ratio/ combination and SSC	73
4.3.2.1	Relationship between Band Combination (Red + Green)/2 and SSC	73
4.3.2.2	Relationship between Band Combination (Red + RE1 + Green)/3 and SSC	74
4.3.2.3	Relationship between Band Combination (Green – Red Edge 1) and SSC	75
4.3.2.4	Relationship between Band Ratio (Green × Red Edge 1)/ Red and SSC	76
4.4	Development of relationships between different band indices derived from Sentinel – 2 Satellite imagery and Spectroradiometer SVC – 1024i	79
4.4.1	Development of Relationship Between Band Indices Derived from Sentinel – 2 Satellite Imagery and Spectroradiometer SVC – 1024i	79
4.4.2	Development of Relationship Between Band Combinations/ Ratios Derived from Sentinel – 2 Satellite Imagery and Spectroradiometer SVC – 1024i	80
4.5	Estimation of SSC using Validation Data Set	83
4.6	Validation of Integrated Relationships of Band Index/ Ratio / Combination used for Estimation of SSC	87
4.6.1	Visual Interpretation, Slope and y-intercept	87
4.6.2	Performance Evaluation using tests of Significance	91
4.6.3	Performance Evaluation using Statistical Indicators	92
4.7	Mapping of Suspended Sediment Concentration in Mula dam Reservoir	94
<b>V</b>	<b>SUMMARY AND CONCLUSION</b>	<b>101-106</b>
<b>VI</b>	<b>REFERENCES</b>	<b>107-116</b>
<b>VII</b>	<b>APPENDICES</b>	<b>117-237</b>
	Appendix – A: Procedure for Determination of Suspended Sediment Concentration and Observations	117

Appendix – B:	Operating procedure for Capturing Spectral Response using Spectroradiometer SVC HR - 1024i	125
Appendix – C:	False Colour Composites of Sentinel-2 (BOA) Satellite Imageries	133
Appendix – D:	Spectral signatures captured by using Spectroradiometer SVC HR - 1024i	137
Appendix – E:	Band Values Obtained from Spectroradiometer SVC – 1024i & Sentinel – 2 Satellite Imagery	179
Appendix – F:	Comparison of Spectral Signatures obtained by Spectroradiometer SVC HR – 1024i and Sentinel - 2 Satellite data	185
Appendix – G:	Values of band indices/ ratio/ combinations obtained from Spectroradiometer SVC - HR 1024i and Sentinel 2 Satellite data	227
Appendix – H:	Procedure for Applying t-test for testing linear regression coefficients and Student t-test	233
Appendix – I:	Publications based on this research work	237
<b>VIII</b>	<b>VITAE</b>	<b>239</b>

## LIST OF TABLES

<b>Table No.</b>	<b>Description</b>	<b>Page No.</b>
2.1	Operating principle, advantages and limitations of various methods of SSC estimation	9
2.2	Summary of review of literature	25
3.1	Data collection calendar	38
3.2	List of instruments/material carried to field along with its purpose	38
3.3	Specifications of SVC HR 1024i Spectroradiometer	45
3.4	Sentinel 2 Bands with their wavelength region, central wavelength and spatial resolution	47
3.5	Various band combinations used to correlate with SSC in Mula dam reservoir	51
4.1	Statistical characteristic of overall, calibration and validation dataset	62
4.2	Various relationships between band indices (x) and observed SSC in mg/L (y)	77
4.3	Various relationships between band ratio/ combination (x) and observed SSC in mg/L (y)	78
4.4	Relation between different indices derived by Sentinel 2 (Bottom-of-the-Atmosphere) satellite imagery and Spectroradiometer	83
4.5	Relation between different band combinations/ ratios derived by Sentinel 2-BOA satellite imagery and Spectroradiometer	84
4.6	Integrated relationships of band index/ ratio / combination used for estimation of SSC (mg/L)	85
4.7	Estimated values of SSC against observed SSC using band indices	86
4.8	Estimated values of SSC against observed SSC using band ratio/ combinations	87
4.9	Test statistics for Linear Regression t-tests and Student t-tests	93
4.10	Values of various Statistical Indicators for Spectral Integration Functions	94

## LIST OF FIGURES

<b>Fig. No.</b>	<b>Description</b>	<b>Page No.</b>
2.1	Remote Spectral Reflectance of Sediment Particles in Water	8
3.1	Schematic representation of 25° Field of View (FOV) for lens attached to Optical fibre	43
4.1	Distribution of 121 sampling locations with dates of the data collection over Mula dam reservoir	62
4.2	Distribution of SSC in Mula Dam reservoir during October 2021 to February 2022	63
4.3	Surface reflectance spectrum for representative samples covering the given range of SSC (mg/L)	64
4.4 (a)	Linear relation between SSC and average reflectance in Blue band (458-523 nm)	64
4.4 (b)	Linear relation between SSC and average reflectance in Green band (543-578 nm)	64
4.4 (c)	Linear relation between SSC and average reflectance in Red band (650-680 nm)	65
4.4 (d)	Linear relation between SSC and average reflectance in Red Edge 1 band (698-713 nm)	65
4.4 (e)	Linear relation between SSC and average reflectance in Red Edge 2 band (733-748 nm)	65
4.4 (f)	Linear relation between SSC and average reflectance in Red Edge 3 band (773-793 nm)	66
4.4 (g)	Linear relation between SSC and average reflectance in NIR band (785-900 nm)	66
4.4 (h)	Linear relation between SSC and average reflectance in Red Edge 4 band (855-875 nm)	66
4.5 (i)	(a) Spectral Signatures obtained from band values Spectroradiometer SVC 1024i & Sentinel-2 BOA Image and (b) linear relation between band values for sample 7 having SSC of 23.52 mg/L.	68
4.5 (ii)	(a) Spectral Signatures obtained from band values Spectroradiometer SVC-1024i & Sentinel-2 BOA Image and (b) linear relation between band values for sample 14 having SSC of 16.85 mg/L.	68

<b>Fig. No.</b>	<b>Description</b>	<b>Page No.</b>
4.5 (iii)	(a) Spectral Signatures obtained from Spectroradiometer SVC-1024i & Sentinel-2 BOA Image and (b) linear relation between band values for sample 27 having SSC of 52.33 mg/L.	68
4.5 (iv)	(a) Spectral Signatures obtained from band values Spectroradiometer SVC-1024i & Sentinel-2 BOA Image and (b) linear relation between band values for sample 44 having SSC of 62.36 mg/L.	69
4.5 (v)	(a) Spectral Signatures obtained from band values Spectroradiometer SVC-1024i & Sentinel-2 BOA Image and (b) linear relation between band values for sample 95 having SSC of 77.55 mg/L.	69
4.5 (vi)	(a) Spectral Signatures obtained from Spectroradiometer SVC-1024i & Sentinel-2 BOA Image and (b) linear relation between band values for sample 101 having SSC of 118.95 mg/L.	69
4.6	Relationship between NDSSI – Spectro and observed SSC (mg/L)	72
4.7	Relationships between NSMI – Spectro and observed SSC (mg/L)	72
4.8	Relationships between M-NDSSI – Spectro and observed SSC (mg/L)	73
4.9	Relationships between R-NDSSI – Spectro and observed SSC (mg/L)	73
4.10	Relationships between (Red + Green)/2 – Spectro and SSC (mg/L)	74
4.11	Relationships between (Red + Green + Red Edge 1)/3 – Spectro and SSC (mg/L)	75
4.12	Relationships between (Green – Red Edge 1) – Spectro and SSC (mg/L)	75
4.13	Relationship between [(Green × Red Edge 1)/ Red] and SSC (mg/L)	76
4.14	Relationship between NSMI derived from Sentinel – 2 Satellite imagery and Spectroradiometer SVC – 1024i along with developed relations.	80
4.15	Relationship between M-NDSSI derived from Sentinel – 2 Satellite imagery and Spectroradiometer SVC – 1024i along with developed relations.	80
4.16	Relationship between R-NDSSI derived from Sentinel – 2 Satellite imagery and Spectroradiometer SVC – 1024i along with developed relations.	80

<b>Fig. No.</b>	<b>Description</b>	<b>Page No.</b>
4.17	Relationship between $(\text{Red} + \text{Green}) / 2$ derived from Sentinel – 2 Satellite imagery and Spectroradiometer SVC – 1024i	80
4.18	Relationship between $(\text{Red} + \text{Green} + \text{Red Edge 1}) / 3$ derived from Sentinel – 2 Satellite imagery and Spectroradiometer SVC – 1024i	80
4.19	Relationship between $(\text{Green} - \text{Red})$ derived from Sentinel – 2 Satellite imagery and Spectroradiometer SVC – 1024i	82
4.20	Relationship between $(\text{Green} \times \text{Red Edge 1}) / \text{Red}$ derived from Sentinel – 2 Satellite imagery and Spectroradiometer SVC – 1024i	82
4.21	Comparison of observed and estimated SSC using Spectral Integration of NSMI using a) line graph and b) linear regression	89
4.22	Comparison of observed and estimated SSC using Spectral Integration of M-NDSSI using a) line graph and b) linear regression	89
4.23	Comparison of observed and estimated SSC using Spectral Integration of R-NDSSI using a) line graph and b) linear regression	89
4.24	Comparison of observed and estimated SSC using Spectral Integration of $(\text{Red} + \text{Green})/2$ using a) line graph and b) linear regression	90
4.25	Comparison of observed and estimated SSC using Spectral Integration of $(\text{Red} + \text{Green} + \text{Red Edge 1})/3$ using a) line graph and b) linear regression	90
4.26	Comparison of observed and estimated SSC using Spectral Integration of $(\text{Green} - \text{Red Edge 1})$ using a) line graph and b) linear regression	90
4.27	Comparison of observed and estimated SSC using Spectral Integration of $(\text{Green} \times \text{Red Edge 1})/\text{Red}$ using a) line graph and b) linear regression	91
4.28	Distribution of SSC in surface waters of Mula dam reservoir on a) 17 <sup>th</sup> October, 2019 and b) 16 <sup>th</sup> October, 2020	96
4.29	Distribution of SSC in surface waters of Mula dam reservoir on a) 11 <sup>th</sup> November, 2019 and b) 10 <sup>th</sup> November, 2020	97
4.30	Distribution of SSC in surface waters of Mula dam reservoir on a) 16 <sup>th</sup> December, 2019 and b) 20 <sup>th</sup> December, 2020	98
4.31	Distribution of SSC in surface waters of Mula dam reservoir on a) 15 <sup>th</sup> January, 2020 and b) 14 <sup>th</sup> January, 2021	99
4.32	Distribution of SSC in surface waters of Mula dam reservoir on a) 14 <sup>th</sup> February, 2020 and b) 13 <sup>th</sup> February, 2021	100
5.1	Flowchart of methodology used in the research	102

## LIST OF PLATES

<b>Plate No.</b>	<b>Description</b>	<b>Page No.</b>
3.1	Location map of the Mula Dam Reservoir	37
3.2	Boat used for collection of in-situ SSC samples and spectral data	37
3.3	Sampler for lifting water sample	38
3.4	Water sample collected from Mula dam reservoir kept for filtration	40
3.5	Traces of suspended sediment filtered by Whatman paper after oven drying	40
3.6	SVC (Spectra Vista Corporation) HR-1024i (High Resolution) portable field Spectroradiometer with optical fibre attached.	42
3.7	Spectrolon or reference panel, along with the PDA	42
3.8	Capturing spectral response of reference/ Spectrolon panel	42
3.9	Capturing spectral response from the surface of Mula Dam reservoir	44

## LIST OF ABBREVIATIONS AND SYMBOLS

%	:	Per cent
@	:	At the rate
µm	:	micrometre
ASD	:	Analytical Spectral Devices
BOA	:	Bottom-Of Atmosphere
CSPM	:	suspended particulate matter concentration
CV	:	Coefficient of Variation
d	:	Index of Agreement
et al	:	and others
FOV	:	Field of View
GPS	:	Global Positioning System
LISST	:	Laser In-Situ Scattering and Transmissometry
MAPE	:	Mean Absolute Percentage Error
mg/L	:	Milligram per Litre
ml	:	millilitre
mm	:	Millimetre
MODIS	:	Moderate Resolution Imaging Spectroradiometer
MPKV	:	Mahatma Phule Krishi Vidyapeeth
MSI	:	Multispectral Imager
MSS	:	Multispectral Scanner
NDSSI	:	Normalized Difference Suspended Sediment Index
NDTI	:	Normalized Difference Turbidity Index
NDVI	:	Normalized Difference Vegetation Index
NDWI	:	Normalized Difference Water Index
NIR	:	Near Infra-Red
nm	:	Nano meter
NSE	:	Nash Sutcliff Model efficiency coefficient
NSMI	:	Normalized Suspended Material Index
OCM	:	Ocean Colour Mapper
PDA	:	Personal Digital Assistants
R <sup>2</sup>	:	Coefficient of Determination
RMSE	:	Root Mean Square Error
SD	:	Standard Deviation
SPM	:	suspended particulate matter

sq.km	:	square kilometers
SRS	:	Simple Random Sampling
SSC	:	Suspended Sediment Concentration
SVC	:	Spectra Vista Corporation
SWIR	:	Short Wave Infra-Red
TM/ ETM	:	Thematic Mapper/ Enhances Thematic Mapper
TOA	:	Top-of-atmosphere
TSM	:	total suspended matter
TSS	:	total suspended sediments
UAV	:	Unmanned Aerial Vehicle
UV	:	Ultra Violet

**ABSTRACT**

---

**ESTIMATION OF SUSPENDED SEDIMENT CONCENTRATION BY  
DEVELOPING INTEGRATED SURFACE REFLECTANCE FUNCTION**

---

by

**MISS JANHAVI KISHOR JOSHI**

A candidate for the Degree of

**Ph.D. (AGRICULTURAL ENGINEERING)**

in

**SOIL AND WATER CONSERVATION ENGINEERING****MAHATMA PHULE KRISHI VIDYAPEETH, RAHURI -413 722****2024**

---

**Research Guide : Dr. A. A. Atre****Department : Soil and Water Conservation Engineering**

---

This study, conducted at the Mula dam reservoir near M. P. K. V., Rahuri, focuses on estimating suspended sediment concentration using integrated spectroscopy. It aims to capture spectral responses from both Spectroradiometer and satellite imagery, establish relationships between surface reflectance and suspended sediment concentration, develop integrated surface reflectance functions and methodology, and validate the accuracy of these methods.

For this study, suspended sediment samples were collected and spectral signatures at sampling locations were captured using a Spectroradiometer. Simultaneously, the GPS was used to record the precise locations of the sampling sites, synchronized with the Sentinel-2 satellite passes over the Mula dam reservoir during five different campaigns from October, 2021 to February, 2022. Suspended sediment concentration (SSC) in the Mula dam reservoir, ranged between 15.62 to 137.65 mg/L, with an average of 61.43 mg/L. 85% of the data points indicated SSC values below 100 mg/L, underscoring low concentration of suspended sediment in Mula dam during period under consideration.

Spectral analysis using a Spectroradiometer showed distinct patterns in surface reflectance, with strong positive correlations between SSC and Green, Red Edge 1, and Red bands. Comparison with Sentinel-2 satellite imagery indicated parallel spectral behaviour, with Sentinel-2 consistently displaying higher reflectance values.

Various indices and band ratios were explored for SSC estimation, to develop their relationship with observed SSC in Mula dam Reservoir. Following the establishment of relationships between different band indices, ratios, and combinations with observed SSC (mg/L), an effort was made to establish a relation between these spectral parameters derived from the Spectroradiometer and those obtained from Sentinel-2 satellite imagery. The established relationships were validated as 'spectral integration functions' using validation data set and were subjected to the t-test for testing the hypothesis of  $a = 1$  and  $b = 0$  for linear relationship ' $y = ax + b$ ' and difference between mean of observed and mean of estimated SSC, to be zero were carried out to find suitable estimator of SSC. The results revealed the suitability of 'spectral integration functions' of  $(\text{Green} \times \text{Red Edge 1})/\text{Red}$ ,  $(\text{Red} + \text{Green} + \text{Red Edge 1})/3$  and Revised - NDSSI (RE1) to estimate SSC.

These spectral integration functions were compared using performance evaluation criteria, where "Spectral Integration of  $(\text{Green} \times \text{Red Edge 1})/\text{Red}$ " emerged as the most accurate estimator. It displayed the highest  $R^2$  (0.80), lowest RMSE (8.58 mg/L), and lowest MAPE (19.41%). This function was applied to create spatio-temporal maps of SSC in the Mula Dam reservoir using historical Sentinel-2 satellite imagery from October 2019 to February 2021. These maps showed a consistent seasonal pattern, with higher SSC in October and November, indicative of intensified sediment runoff, and lower values in January and February due to reduced sediment transport. Year-on-year comparisons highlighted increased sediment concentrations in 2020, particularly in October and November.

In conclusion, the study successfully characterized the in-situ reflectance spectra obtained from the Spectroradiometer in the Mula dam reservoir, revealing a consistent and distinctive pattern indicative of lower concentrations of suspended sediment in surface waters. The investigation highlighted the efficacy of band indices and combinations involving the Green, Red, and Red Edge 1 bands from both the Spectroradiometer and Sentinel-2 imagery, showcasing strong correlations with Suspended Sediment Concentration (SSC) during calibration and validation. Among the developed functions, the 'Spectral Integration Function of  $(\text{Green} \times \text{Red Edge 1})/\text{Red}$ ' demonstrated superior performance in estimating SSC, supported by various statistical indices, followed by the 'Spectral Integration Function of  $(\text{Red} + \text{Green} + \text{Red Edge 1})/3$ ' and 'Spectral Integration function of R-NDSSI.' The contribution of the study lies in the promising applicability of the Spectral Integration Methodology for synoptic retrieval of spatially variable SSC using medium-resolution Sentinel-2 (BOA) L2A imagery. This methodology holds great potential as a valuable source of information for managers, researchers, and stakeholders engaged in the assessment and sustainable use of surface water resources or large water bodies.

## I. INTRODUCTION

Sediment particle can be defined as fragmented material that is transported by, suspended in water or air and finally get deposited. When the sediment particles are carried in suspension, it is referred to as suspended sediment. Suspended sediment primarily consists of fine inorganic particles such as clay and silt, which are usually smaller than 0.063 mm. Additionally, it may include fine sand and particulate organic matter that remains suspended in the water column. One important characteristic of suspended sediment is its ability to be dispersed throughout the vertical column of fluid due to turbulence, setting it apart from bed load sediment.

Que (2014) used the term 'suspended sediment concentration' (SSC) to describe the solid-phase material that is suspended within a water-sediment mixture. In river systems, sediment particles are transported downstream as either suspended sediment (consisting of fine particles like clays, silts, and fine sands) or bed load sediments (comprising coarser particles like gravels and coarse sands). Among these transport modes, suspended sediments dominate, accounting for approximately 70% of the annual sediment reaching coastal areas (Vercruyssen *et al.*, 2017).

Reservoir sedimentation stems from excessive sediment inflow, surpassing the reservoir's capacity. This process involves three phases: sediment origin, stream transport, and reservoir deposition. Rainfall breaks soil into grains, and wind and slope determine particle movement. Overland flow carries particles to channels, eroding surfaces. Sediment accumulates, forming channels or gullies. Some sediment gets transported to main channels. In natural rivers, sediment balance is maintained, with occasional flow events moving sediment downstream. Long-term dynamics include aggradation (sediment increase) and degradation (streambed reduction). A dam alters this balance, creating a pool with low velocity, efficiently trapping sediment.

Wide range of problems, including storage loss, delta deposition, navigation hindrance, increased possibility of earthquake hazard, abrasion, energy loss, and blocking or clogging of intakes and low-level outlets can be due to trapping of sediment upstream of dam reservoir. Sediment accumulation in lakes and reservoirs with high suspended sediment concentrations accelerates the siltation process, shortening their useful life and efficiency (Lodhi *et al.*, 1998). An increase in suspended sediment can have significant environmental impacts downstream of dam reservoir. These effects encompass altered flow patterns, disruptions in nutrient cycling, fluctuations in water temperature, all of which collectively intensify the ecological consequences.

Clear water downstream of the dam can lead to streambed scouring, causing it to coarsen, degrade, and become armored, making it unsuitable as an ecological habitat and spawning location for native and introduced species. This channel degradation can also cause increased scour at downstream bridges, lower water levels at intakes, reduced navigational depth in critical locations, and lower groundwater tables in riparian areas, negatively impacting wetlands and agricultural areas. Dams can significantly alter the mobility of organic material, nutrients, and pollutants, as they are connected with fine sediments. The trapping of silt by the dam also has substantial

engineering effects downstream, dramatically impacting stream morphology by reducing the supply of bed material sediment (Lodhi *et al.*, 1998).

For several decades, suspended sediment has been a significant environmental concern in freshwater systems, primarily due to its status as one of the most common pollutants in terms of both weight and volume (Que, 2014). As sediment moves within water bodies, it can act as a carrier and reservoir for various pollutants, including adsorbed phosphorus, nitrogen, pesticides, and industrial chemicals like polychlorinated biphenyls (Stow *et al.*, 2015). The increased concentration of suspended sediment (SSCs) in water bodies can have detrimental effects on aquatic ecosystems, disrupting their proper functioning.

High suspended sediment concentrations (SSCs) pose a critical concern, causing benthic smothering as excess sediment settles, suffocating organisms on riverbeds or lake bottoms. This disrupts habitats, impacting benthic species and ecological balance. Elevated sediment loads alter water chemistry, affecting temperature and dissolved oxygen, stressing aquatic life's growth, reproduction, and survival. Sediment-laden water limits light penetration, reducing photosynthesis for plants and algae, decreasing aquatic productivity and biodiversity. Sediment particles can carry pollutants, endangering aquatic and human health. Addressing suspended sediment entails comprehensive strategies: implementing erosion prevention in agriculture and construction, managing storm water to reduce sediment influx. Mitigating sediment levels safeguards aquatic ecosystems, preserving their health, integrity, and vital functions.

Converting sedimenting reservoirs into enduring resources necessitates substantial design and operational adjustments. The traditional notion of limited reservoir life due to sedimentation must give way to a holistic management approach addressing both water and sediment for sustained performance. Sustainable use involves various sediment control methods: reducing inflow through erosion control or upstream trapping, sediment routing via drawdown and bypass, removal by flushing and dredging, providing extra storage for sediment compensation, and strategic sediment placement for easier removal. Tailored strategies are crucial, considering unique sedimentation challenges at each site. Vital suspended sediment measurement assesses load, concentration, and size gradation in water bodies, aiding water resources development. Various techniques like acoustic, reflectance, and optical methods accurately gather sediment data. Implementing these approaches ensures effective sediment management, securing reservoir longevity, and safeguarding aquatic ecosystems and water quality.

Estimating suspended sediment concentration (SSC) through in-situ sampling over vast water areas is a time-consuming, costly, and often imprecise process. River systems' large size, challenging weather conditions, and remote rural locations further complicate data acquisition, adding to the expenses. SSC can fluctuate rapidly due to tide changes, winds, and river discharge, resulting in significant spatial variability. Collecting shipboard data for monitoring and modelling

purposes under such variable conditions becomes exceedingly expensive and logistically complex (Stumph, 1989). To address these challenges, researchers and scientists have been exploring remote sensing techniques as a more efficient and cost-effective alternative for estimating SSC over large water bodies. Remote sensing technologies, such as satellite or airborne sensors, offer the advantage of wide spatial coverage, providing valuable information on suspended sediment dynamics over different water areas. These methods can enhance our understanding of sediment transport processes and aid in developing more effective sediment management strategies.

The quantitative retrieval of Surface Suspended Sediment Concentration (SSC) from water's spectral reflectance using remote sensing has gained increasing attention as a response to environmental challenges. Satellite sensors can measure spectral reflectance, offering a synoptic, rapid, and cost-effective approach to assess SSC in reservoirs, lakes, and rivers. Suspended sediments in the water can alter the spectral response by absorbing and scattering light, making satellite remote sensing highly effective in retrieving SSC data due to its wide spatial coverage and frequent revisits (Wang and Lu, 2010).

Remote sensing technologies, such as multispectral or hyperspectral imaging, enable us to capture the unique spectral signatures of water bodies affected by suspended sediments. The electromagnetic radiation that reaches the water from the Sun comprises direct solar irradiance and diffuse irradiance. This irradiance falls with a zenith angle onto the water surface where it is specularly reflected and also transmitted into the water. The specularly reflected flux undergoes polarisation and the transmitted flux is either absorbed or scattered. The upwelling radiance is usually expressed as the spectral radiance and its ratio against irradiance the spectral reflectance. The upwelling radiance measured by a sensor above the water which depends on wavelength, atmospheric transmission, reflectance at the water surface, and reflectance from a 100% diffuse reflector. Remote sensing is vital for estimating Suspended Sediment Concentration (SSC) by analysing water's spectral reflectance, informing sediment dynamics and water quality. Algorithms analyse spectral signatures, guiding sediment management for ecosystem health. This enables extensive aquatic area monitoring, aiding informed decisions in water resource sustainability.

Mathematical models such as the empirical, semi-empirical, and theoretical have been successfully employed to estimate surface SSC by using remotely sensed data. Techniques used for SSC retrieval can be categorized into four general groups: simple regression, which correlates single-band remote sensing data with in-situ measurements; spectral unmixing techniques; band ratio technique using two or more bands; and multiple regressions. Each of these methods contributes to a better understanding of sediment dynamics and water quality variations, improving the overall management of aquatic environments (Wang and Lu, 2010)

Ground-based Spectroradiometers play a vital role in enhancing sediment concentration estimation from remote sensing data. They validate spectral reflectance values, ensuring data

consistency, refining regression models, and spectral un-mixing techniques for SSC retrieval. These instruments can collect site-specific spectral signatures, accounting for sediment variations and environmental conditions in water bodies, elevating monitoring precision. High spatial resolution enables detailed sediment dynamics capture, while real-time monitoring aids short-term variation understanding. The use of Spectroradiometer can validate remote sensing algorithm accuracy, ensuring dependable sediment concentration estimates. Integrating ground-based Spectroradiometers with remote sensing bolsters our capacity to assess and manage aquatic sediment dynamics effectively.

The quantification of suspended sediment load in reservoirs or water bodies holds significant importance as it directly address the management of hydro- and eco-systems, as well as morphological issues in watersheds (Margareta and Ulf, 2000). Monitoring Suspended Sediment Concentration (SSC) in water bodies like lakes and reservoirs is crucial for various applications related to inland water resource management, especially for domestic and agricultural water supply. Understanding the dynamics of SSC is essential to optimize human interventions and enhance the sustainability of ecosystems.

Given the significance of estimating SSC using integrated spectroscopy and the scope of the research, this study titled '**Estimation of Suspended Sediment Concentration by Developing Integrated Surface Reflectance Function**' was undertaken on Mula dam reservoir near M. P. K. V., Rahuri with following specific objectives:

1. To capture spectral response of suspended sediment concentration in large reservoir (Mula Dam) using Spectroradiometer and from satellite imagery.
2. To develop relationships between surfaces' reflectance obtained from Spectroradiometer and satellite imagery and measured suspended sediment concentration.
3. To develop the integrated surface reflectance functions and methodology for estimating the suspended sediment concentration in large water body.
4. To validate the developed functions and methodology for estimation of suspended sediment concentration in large water body.

## II. REVIEW OF LITERATURE

The measurement of suspended sediment in river stretches, coastal regions, and water bodies has garnered significant attention in numerous studies across the globe. Various techniques, including acoustic, optical, and spectral reflectance methods, have been employed to capture suspended sediment data accurately. Additionally, different platforms such as boats, drones, and satellites have been utilized to cover diverse water environments. Furthermore, researchers have developed models based on surface spectral reflectance to estimate suspended sediment concentrations, enhancing our ability to assess and manage sediment dynamics effectively. This chapter, through its various sections, comprehensively reviews the significance of assessing suspended sediment, historical advancements, various techniques, platforms, and model development for SSC estimation based on surface spectral reflectance.

### 2.1 Historical Developments in Assessment of Suspended Sediment

The historical development of sediment transportation studies, which initially focused on coarse material carried as bed load with little attention to suspended sediment, was highlighted by **Vanoni (2006)**. Efforts were directed towards understanding the suspension phase of sedimentation since approximately 1925. While suspended-load discharge was better understood than bed load transport, predicting both types of discharge remained challenging due to their interdependence on fluid forces at the bed.

In 1970s, **Ritchie *et al.* (1976)** initiated the use of satellite remote sensing for monitoring suspended sediment based on spectral reflectance data. **Ritchie and Schiebe (2000)** further emphasized the application of remote sensing in studying suspended sediments. The early focus was on discovering connections between suspended sediments and spectral reflectance, leading to the development of empirical methods. The increased spectral reflectance in the visible and near-infrared region of the electromagnetic spectrum was attributed to higher levels of suspended sediment, which caused backscattering in the water column.

In 1988, **Edwards and Glysson** discussed the most commonly used method for sediment observation, involving in situ sampling and laboratory analysis. This approach entailed various steps, including site selection, water sampling, transportation of samples, laboratory processing, and post-analysis. Despite this method required substantial effort and resources, it has widespread use.

Recent scientific advances led to the development of systems that monitored suspended sediment in rivers and lakes remotely. **Marinho *et al.* (2021)** highlighted how institutions worldwide utilized remote sensing alongside in-situ monitoring for suspended sediment. With the availability of high-frequency data and various orbital platforms, remote water sensing became more efficient and accessible for studying sediment dynamics in water bodies.

## 2.2 Need and Significance of SSC Estimation

**Ritchie *et al.* (1987)** stated that ‘the technique needs to be developed which can be used to quickly survey the landscape and locate those aquatic ecosystems with significant suspended sediment problems so that soil conservation efforts can be concentrated in those watersheds with the most serious erosion and sediment yield problems’.

According to **Bejestan and Rezania (2010)**, a wide range of hydrological and environmental activities, such as upstream erosion and topsoil loss, sediment and water transit, nutrient and toxic loading, and pollutant accumulation, are indicated by changes in the spatial distribution of suspended sediment in riverine systems. One of the main considerations in the design of hydraulic systems like canals, valves, and dam turbines is the amount of silt and particle matter present along with flowing water.

**Sheela *et al.* (2014)** stated that suspended sediments act like a transporting source to carry a variety of materials and mix them into the water column of lakes, estuaries, and coastal environments, controlling growth and productivity of aquatic ecosystems. From other perspectives, such as preserving the quality of the soil in agricultural regions, environmental concerns, and the use of water resources for drinking and industries, this issue is very significant.

Suspended sediment can have a substantial effect on water quality in rivers. Suspended sediment can serve as a transport medium for pollutants like phosphorus (**House *et al.* 1998**) and bacteria (**Badgley *et al.* 2011**).

**Gupta (2015)** presented a detailed analysis of suspended sediment concentration (SSC) in the Gulf of Kachchh, Arabian Sea, and using data from OCEANSAT-1 OCM and MIKE 21 simulations. The study focused on understanding the impact of tidal and monsoonal changes on sediment dynamics in the region. Both temporal and spatial variations of SSC, bathymetry, and tidal current speed and direction were examined through tidal harmonic analysis. Results showed that OCM-derived SSC and MIKE 21 simulations provided valuable insights into suspended sediment behavior, with sequential high temporal resolution OCM-derived SSC images proving to be an ideal tool for monitoring changes. The study highlighted the influence of spring tide and bathymetry on sediment dynamics at Okha and Navlakhi ports, and the impact of deficient monsoon in 2004 on SSC variations. The findings contribute to a better understanding of sediment transport in the Gulf of Kachchh and can be useful for future management strategies.

## 2.3 Methods of SSC Estimation

### 2.3.1 Various Methods of Suspended Sediment Concentration Estimation

**Ritchie and Cooper (2003)** and **Gholizadeh *et al.* (2016)** discussed the limitations of in-situ data collection for water quality assessment, emphasizing challenges in capturing spatial and temporal variations in large water bodies. These methods are labor-intensive, time-consuming, and

costly, hindering large-scale or continuous monitoring. The vastness of large water bodies makes it nearly impossible to investigate spatial and temporal variations using conventional methods. The accuracy and precision of in-situ data are also questioned due to field-sampling and laboratory errors, impacting decision-making and management strategies.

Acoustic methods utilize high-frequency sound to measure suspended sediment concentration (SSC). **Yong et al. (2004)** presented a methodology based on the modified sonar equation, emphasizing accuracy in estimating SSC when sediment is predominantly sand. **Meral et al. (2010)** validated the acoustic method for soil sediment concentration under various conditions. **Xavier et al. (2014)** used Acoustic Doppler Velocimeter to estimate SSC, particularly for coarse sediment concentrations below 1000 mg/L. **Gruber et al. (2016)** confirmed the effectiveness of single-frequency acoustic methods in field studies, measuring SSC up to 15 mg/L of mainly medium silt. **Oliveira et al. (2021)** explored the use of Acoustic Doppler current profilers as an alternative method, demonstrating a satisfactory correlation between measured and estimated sediment concentrations in the Amazon basin.

Bottle sampling involves extracting water samples manually, and **Interagency Committee (1963)** describes point and depth integrating samplers. This method is reliable and well-documented but has poor temporal resolution. Bottle sampling serves as a standard for calibrating other types of samplers, providing sediment concentration and size distribution data through laboratory analysis (**Guy, 1965**).

Focused beam reflectance measurement uses a rotating laser beam to encounter particles, determining their chord length and calculating volume. **Phillips and Walling (1995)** and **Law et al. (1997)** report successful field studies with this method. The instrument has a wide measuring range and is easily portable but may produce poor readings for non-spherical particle shapes.

LASER diffraction involves directing a LASER beam into the sample volume, measuring scattered light to determine particle size. **Agrawal and Pottsmith (1996)** demonstrate accurate particle size and concentration determination using a commercially available LASER backscatter instrument. **Gartner et al. (2001)** highlight the accuracy of the LISST-100 in measuring sediment concentration and particle size distribution at lower concentrations.

**McHenry et al. (1967)** utilize nuclear techniques relying on the attenuation of X or gamma rays by sediment particles. Nuclear instruments are well-suited for continuous monitoring, covering a wide range of sediment concentrations, and are not affected by water color or suspended organic matter.

OBS sensing uses light to determine sediment concentration. **Green and Boon (1993)** and **Black and Rosenberg (1994)** reported nearly linear responses to varying sediment concentrations. OBS instruments offer good spatial and temporal resolution, and their readings are not affected by the refractive index of particles.

In optical transmission sensing, light is directed into the sample volume, and sediment concentration is determined by the degree of light attenuation. **Baker and Lavelle (1984)** note nonlinear responses to increasing particle concentrations but highlight the instruments' sensitivity to low particle concentrations.

Various sediment concentration measurement methods offer a range of advantages and limitations. **Wren *et al.*, (2000)** provided a detailed review on the field techniques for suspended-sediment measurement with emphasis on new technologies for SSC measurement including acoustic method, pumping sampling, laser diffraction method, nuclear method, and methods based on focused beam reflectance, optical backscattering, optical transmission, and spectral reflectance. The operating principles, advantages, and limitations of different techniques are described in table 2.1.

### 2.3.2 Remote Sensing Reflectance Methods

Spectral reflectance measurement of suspended-sediment concentration is based on the relationship between the amount of radiation, generally in the visible or infrared range, reflected from a body of water and the properties of that water (Fig. 2.1). The radiation is measured by a handheld, airborne, or satellite based spectrometer. The correlation between concentration of suspended sediment and the reflected radiation has been observed and validated by several researchers. This relationship is dependent on many parameters such as the optical properties of the sediment type, sensor observation angle, solar zenith angle, and the spatial resolution of the measurements (**Wren *et al.*, 2000**).

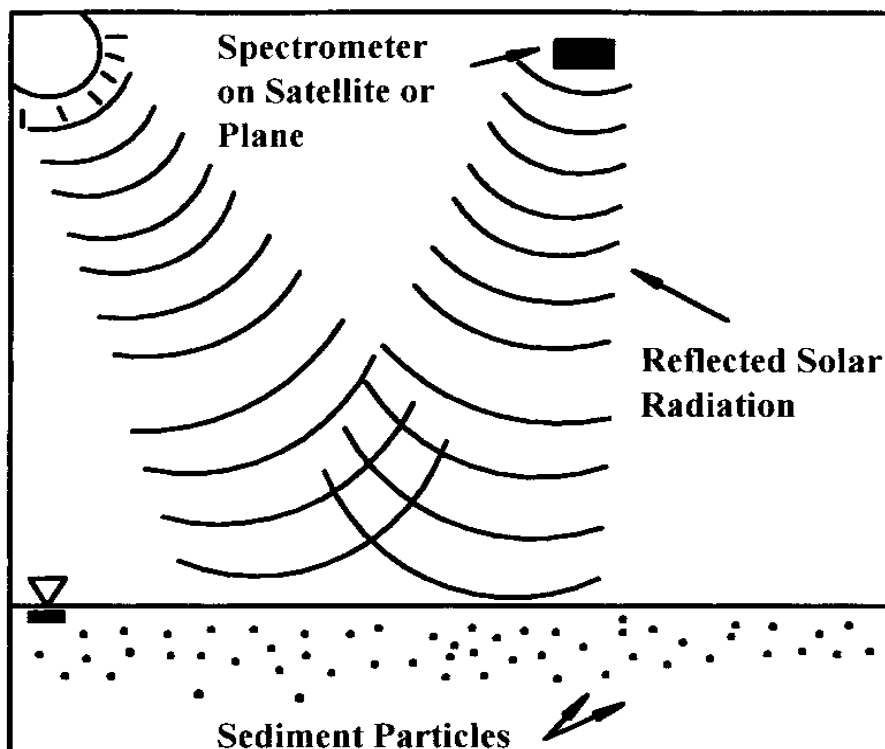


**Fig. 2.1 Remote Spectral Reflectance of Sediment Particles in Water (Wren *et al.*, 2000)**

**Table: 2.1 Operating principle, advantages and limitations of various methods of SSC estimation (Wren *et al.*, 2000)**

Sr. No	Technology	Operating Principle	Advantages	Limitations
1	Acoustic	Sound backscattered from sediment determines size distribution.	Good spatial & temporal resolution	Difficult to translate backscattered signal, signal attenuation at high particle concentration
2	Bottle Sampling	Water-sediment sample collected in container for analysis.	Accepted, time-tested, determines concentration & size distribution	Poor temporal resolution, flow intrusive, requires lab analysis, on-site personnel needed
3	Pump Sampling	Water-sediment sample pumped and analyzed.	Accepted, determines concentration & size distribution	Poor temporal resolution, flow intrusive, requires lab analysis, not isokinetic
4	Focused Beam Reflectance	Laser measures reflection time on sediment particles.	No particle size dependency, wide measuring range	Expensive, flow intrusive, limited to point measurements
5	Laser Diffraction	Laser measures refraction angle on sediment particles.	No particle-size dependency	Unreliable, expensive, flow intrusive, limited to point measurements
6	Nuclear	Gamma or X-rays backscatter/transmission measured on samples.	Low power consumption, wide measuring range	Low sensitivity, radioactive decay, regulations, flow intrusive, limited to point measurements
7	Optical	Visible or infrared light backscatter/transmission measured.	Simple, good temporal resolution, remote deployment	Strong particle-size dependency, flow intrusive, limited to point measurements, instrument fouling
8	Remote Spectral Reflectance	Light reflection/scattering from water measured remotely.	Measures over broad areas	Limitation on spatial resolution, limited applicability in fluvial environment, particle-size dependency

### 2.3.2.1 Handheld Spectroradiometer

**Ritchie *et al.* (1976)** used a portable ISCO (Instrument Specialties Company) Model SR Spectroradiometer equipped with a 2.95 m fiber optic conduit to measure reflected solar radiation at 25 nm interval from 400 to 750 nm, and at 50-nm intervals from 750 to 1550 nm on cloud free days within 2 hours of solar noon in six study reservoirs in northern Mississippi, USA. They observed that solar radiation reflected from water surfaces varied with the amount of suspended sediment and wavelength. They found that the reflected solar radiation between 450 to 900 nm increased as the concentration of suspended sediment increased. The region of maximum reflected solar radiation shifted from about 550 nm at low sediment concentration to above 600 nm at higher sediment concentrations. Between 700 and 800 nm, the change in reflected solar radiation with change in suspended sediment exhibited a more regular pattern than that seen between 400 and 700 nm. They concluded that the Linear regression analyses show the best fit for the relationship between reflected solar radiation, or reflectance, and suspended sediment concentration of surface water between 700 and 800 nm. Their study suggested that quantitative estimates of suspended sediment concentration of surface water could be made using reflected solar radiation.

**Milton (1987)** described the importance of field spectroscopy as an important technique of fundamental importance in remote sensing, both at the level of primary research and in operational applications in his review article. He also stated that the technique of field spectroscopy was basically developed for increasing precision and accuracy in response to improvements in the technology available to disperse incident light energy into its constituent wavelengths and then detect and analyze this energy. He also concluded that the field spectroscopy provides a bridge between the theoretical understanding gained in the artificial environment of the laboratory and the largely qualitative skills of the image interpreter.

**Chen *et al.* (1991)** conducted a laboratory study to determine the form of relationship between the suspended sediment concentration (SSC) and the spectral reflectance. The data were recorded in 875 wavebands from 350 to 2500 nm for eighteen sediment type/grain size samples, each at up to thirty SSC concentrations over a range of 0 to 1300 mg/L using Daedalus 1268 multispectral scanner. They found the strong relationship between SSC and spectral reflectance, log-linear for wavelengths from 450 to 700 nm and linear from 700 to 1050 nm and recommended that, where a limited number of SSC measurements are available for the calibration of the SSC-Spectral Reflectance relationship, a log-linear relationship in the visible wavebands and linear relationship in the near infrared wavebands would be assumed.

**Chen *et al.* (1992)** measured spectral reflectance, derivative spectral reflectance (change in reflectance per unit wavelength) and SSC in the laboratory, where the effects of environmental variability were small and at sea where the effects of environmental variability were large. There was a strong correlation between SSC and derivative spectral reflectance both in the laboratory

(max  $R^2 = -0.98$ ) and at sea (max  $R^2 = -0.83$ ) and derivative spectral reflectance was used to estimate SSC in the laboratory to an error of less than 8 % of the mean SSC. The correlation between spectral reflectance and SSC was weaker at sea (max  $R^2 = 0.46$ ) than in the laboratory (max  $R^2 = 0.96$ ). This difference was attributed to the presence of large and spectrally variable environmental effects. Authors recommended the use of derivative spectra for the estimation of SSC when continuous spectra are available.

**Han (1997)** conducted a study to characterize the relationship between suspended sediment concentration (SSC) and reflectance in clear water. A controlled experiment was conducted outdoors in a 7510 litre water tank using natural sunlight. A red loam soil was added and suspended in the tank filled with clear water. A total of 20 levels of SSC (from 25 to 500 mg/L) were created. Reflectance was recorded using an ASD Spectroradiometer, and the bi-directional reflectance factor was computed and analyzed. The same amount of suspended sediment generated higher reflectance between 400 and 700 nm. The linearity in the SSC-Reflectance relationship increased with wavelength between 400 and 900 nm. A near-linear relationship between SSC and reflectance was found between 720 and 900 nm. The best wavelengths for a first-order regression model to estimate SSC using reflectance were 827, 830, and 847 nm.

**Ritchie *et al.* (1976)** using in-situ studies concluded that the wavelengths between 700 nm and 800 nm were most useful for determining suspended sediment in surface waters. It was observed that the Red and NIR wavelength (700-900 nm) is a useful range for determining the suspended sediment. If the range of suspended sediments is between 0 and 50 mg/l, reflectance from almost any wavelength will be significantly related to suspended sediment concentrations (Ritchie, 2000). As the range of suspended sediments increases to 200 mg/l or higher, curvilinear relationships have to be developed with reflectance in the longer wavelength.

In the Tamar Estuary located in the southwest UK, investigations were conducted by **Doxaran *et al.* (2005)** to assess the concentrations of colored dissolved organic matter and suspended matter (total, organic, and inorganic) by establishing their connection with in-situ hyperspectral remote-sensing reflectance (Rrs) measurements. To mitigate surface reflection effects, a straightforward approach was employed to extract the reflectance signal from underwater optical measurements. Consistent with findings in other estuaries, a strong correlation was identified between the ratio  $Rrs(850 \text{ nm})/Rrs(550 \text{ nm})$  and the total suspended matter concentration, extending similarly to the inorganic suspended matter concentration. They concluded that, utilizing airborne remote sensing data, these relationships could potentially be employed to map the tidal turbidity movements within the estuary.

**Bhatti (2006)** developed band ratio model to investigate the relationship between suspended sediment and reflectance received by hyper spectral Field SpecPro FR Spectroradiometer. The relationship is based on a simple reflectance ratio between NIR and visible

wavelength and strong correlation was observed between these two bands. The polynomial function with coefficient of determination 0.98 allowed an accurate estimation of SSC from reflectance measurement. Similar results were obtained when multispectral remotely sensed data (Landsat TM) were used for estimation.

**Bhatti *et al.* (2008)** used a hyperspectral Field SpecPro FR Spectroradiometer to measure reflectance from the water in the electromagnetic spectrum region of 400 nm to 900 nm. Reflectance of water with varying concentration of clayey red soil ranging from 50 to 1000 mg/L was measured. Significant change in reflectance was observed for the same suspended sediment concentration (SSC) with time. The near- infrared (NIR) wavelength was found to be optimum range for assessment of suspended sediment concentration in surface water.

**Raut and Gavit (2015)** developed spectral signature for different SSC ranging between 1000 mg/L to 10000 mg/L for various soil series in a controlled experiment conducted in outdoors condition with a 40 L water tank having natural sunlight condition. Reflectance was recorded using SVC HR 1024i Spectroradiometer. The linearity in the SSC-reflectance relationship increased with wavelength between 400 and 900 nm. For relationship between suspended sediment concentration and reflectance data four different functions, viz., exponential, linear, logarithmic, and power were tried. The power was found to be the best fit.

**Zhang and Wang (2015)** using data sets of observed in-situ data for the slightly turbid water of the Xin'anjiang Reservoir developed a semi-analytical algorithm to estimate the total suspended matter (TSM) concentration ranging between 0.67 to 5.66 mg/L. Using ASD field spectrometer, they observed that the reflectance in the green region was higher than that of blue region and reflectance in red region dropped immediately with increase in the wavelength. The reflectance in NIR region was consistently lower than the reflectance in Blue, Green and Red region. They found significantly positive correlation between TSM concentrations with highest coefficient of determination ( $R^2$ ) greater than 0.9 at 542 nm (in the green region).

**Zhan *et al.* (2017)** reproduced SSC conditions in laboratory at increasing concentrations within a range common to field observations of Yellow River and south-eastern Laizhou Bay. They captured spectrum measurements of various surface SSCs ranging from 1 to 5700 mg/L using AvaField – 3 Spectrometer. They found that there exists a good correlation between water SSC and spectral reflectance in the spectral range of 726–900 nm. At surface SSC greater than 2700 mg/L, the 740–900 nm spectral range was less susceptible to the effects of spectral reflectance saturation and more suitable for retrieval of high sediment concentrations. The best correlations were obtained for the reflectance ratio of 820 nm to 490 nm. They developed a novel cubic model with coefficient of determination equal to 0.992, which used the ratio of a near-infrared (NIR) band (740–900 nm) to a visible band (400–600 nm) and provided robust quantification of high surface SSC water samples.

### 2.3.2.2 Unmanned Aerial Vehicle (UAV)

**Larson *et al.* (2018)** used MicaSense Sequoia sensor with four bands [green, red, red edge, and near-infrared (NIR)] mounted on-board a fixed-wing UAV to map SSC within the Maumee River in Ohio, USA, at multiple depth intervals (15, 61, 91, and 182 cm). The simple linear and stepwise regression models show the advantage of multiple bands and band ratios over single bands in mapping SSC. The findings show a limited performance of the Sequoia sensor when compared to field Spectroradiometer measurements. They concluded that UAVs can be a practical but somewhat limited tool to monitor SSC in small- to medium-sized rivers.

**Khairi (2021)** compared the spectral response of suspended sediment concentration in a water body in Maheshgad Watershed, MPKV, Rahuri. Water surface spectral reflectance reading at 21 locations in the water body were taken using Spectroradiometer and as well as drone with onboard hyperspectral sensor. Revised NDSSI was found to be the best index for mapping SSC using both Spectroradiometer and Drone. Modified NDSSI performed better when the values of index from UAV mounted sensor were converted to the index of Spectroradiometer.

### 2.3.9.3 Satellite Remote Sensing

In this study **Schiebe *et al.* (1992)** delved into the relationship between suspended sediment concentration and radiance/reflectance values for Lake Chicot, Arkansas, utilizing Landsat-MSS satellite data and corresponding water quality measurements. By evaluating various models, the research aimed to unlock the potential of remote sensing in uncovering this connection. The investigation, involving 310 observations, concluded that longer wavelengths exhibited improved average maximum signal-to-noise ratios for Landsat-MSS bands. The study favoured the Landsat MSS band 3 (6) (700-800 nm) due to its balanced blend of signal-to-noise ratio and predictive accuracy. The research demonstrated that an exponential curve, derived theoretically, was the optimal fit for characterizing the relationship between reflectance and suspended sediment concentration. This study significantly contributes to advancing the understanding of satellite-derived data's potential in assessing suspended sediment concentration, thereby offering improved insights for water body monitoring and management.

In this study, **Reddy (1993)** aimed to use Landsat-MSS digital data for the mapping of suspended sediments (SS) in the Krishna Bay Estuary. The author quantified the relationship between Landsat-MSS radiance values for all four bands and measured values of suspended solid concentrations at 13 locations through simple linear and multiple regression equations. Based on the percentage error of estimation, Chi' values, and model simplicity, the author chose an optimum and best-fitted equation. This equations was based on the radiance values computed from all four bands (B4:500-600 nm, B5:600-700 nm, B6:700-800 nm and B7:800-1100 nm) of Landsat MSS. This calibrated regression model was then applied to map the SS (mg/l) concentration for the entire study area. The study showed the successful use of Landsat-MSS data in quantifying suspended

sediment concentrations in this geographical area, and potentially in other regions with similar environmental and climatic conditions, given the testing of the regression equation using an independent data set.

In their study in 1997, **Lodhi *et al.*** explored the application of remote sensing technology for analysing suspended loess soils in surface waters. The researchers identified the visible spectral range of 580 to 690 nm as informative for distinguishing sediment types, while the NIR range of 714 to 880 nm provided the most accurate estimates of sediment concentration. These findings offer valuable insights for precise sediment analysis using remote sensing data, benefiting environmental monitoring and management. Further investigations are necessary to evaluate the spectral ranges' adaptability to different environmental conditions and sediment compositions.

The study by **Myint and Walker (2002)** aimed to accurately quantify suspended sediment concentrations using satellite data over both time and space. Data acquired from the NOAA Advanced Very High Resolution Radiometer (AVHRR) and the Orbview-2 Sea-viewing wide field-of-view (SeaWiFS) ocean color sensor, along with field measurements, were used to develop statistical models for estimating near-surface suspended sediments and suspended solids. 'Ground truth' water samples were collected through helicopter, small boat, and automatic water sampler within a few hours of satellite overpasses. The NOAA AVHRR atmospheric correction was modified to account for the high turbidity levels along the Louisiana coast. Models were developed based on the field measurements and reflectance/radiance measurements in the visible and near-infrared Channels of NOAA-14 and Orbview-2 SeaWiFS. The best models for predicting surface suspended sediment concentrations were obtained with a NOAA AVHRR Channel 1 (580–680 nm) cubic model, Channel 2 (725–1100 nm) linear model, and SeaWiFS Channel 6 (660–680 nm) power model.

In 2003, **Liew *et al.*** aimed to develop algorithms for estimating total suspended sediment concentration (TSS) from water reflectance spectra in the highly turbid inland lower Jinsha River, China. They discovered that the empirical method using a band ratio could only effectively estimate TSS at lower concentration levels, up to 400 g/m<sup>3</sup>, which fell significantly below the median and average concentrations of about 800 and 1,900 g/m<sup>3</sup> in the region. However, the spectral fitting method showed promising results, allowing TSS retrieval across the entire range of concentrations, including extremely high levels of up to 13,000 g/m<sup>3</sup>. By fitting the entire spectrum to a water reflectance model, the method successfully retrieved the backscatter coefficient of sediment particles at 550 nm, enabling accurate TSS concentration calculation using the regression relationship between field-measured TSS concentration and reflectance at 550 nm. This research presents a robust approach for estimating TSS in highly turbid river environments and contributes valuable insights for effective sediment concentration assessment.

The study conducted by **Miller and McKee (2004)** focused on the significance of high concentrations of suspended particulate matter in coastal waters and its influence on various water column and benthic processes. The utility of MODIS 250 m data was assessed in the Northern Gulf of Mexico, where a robust linear relationship was established between band 1 (620–670 nm) MODIS Terra 250 m data and in-situ measurements of Total Suspended Matter. The findings emphasize the potential of MODIS 250 m data in analysing complex coastal waters, particularly in smaller bodies of water like bays and estuaries, to examine material transport and fate effectively.

In **2007, Bhatti *et al.*** conducted a study to analyze the impact of suspended sediment concentration (SSC) on remote sensing reflectance using both the Hyperspectral Field SpecPro FR Spectroradiometer and quantum sensor. Indoor spectral reflectance was measured at a height of 1m above the water surface. The research revealed that reflectance generally increased with an increase in SSC, with some minor exceptions. At low SSC levels, peak reflectance occurred at short visible wavelengths, while at high SSC levels, the peak reflectance shifted towards longer wavelengths. Below 400 mg/L of SSC, reflectance centred around 575 nm with minor differences. However, above 400 mg/L, the peak reflectance shifted to 675 nm and slightly increased with sediment load. The study observed maximum reflectance in the visible domain, with high absorption in the NIR. The researchers concluded that reflectance between 700 to 900 nm (NIR) exhibited a more uniform increase with SSC, and the first derivative (rate of change of reflectance with respect to wavelength) proved effective for estimating SSC. This research provides valuable insights into the relationship between SSC and remote sensing reflectance, offering potential applications in water quality assessments and environmental monitoring.

In **2005, Wang and Lu** used time series satellite data from high-resolution Terra MODIS to estimate suspended sediment concentration (SSC). They discovered that differences in water reflectance between Band 2 and Band 5 could provide relatively accurate SSC estimation, even when in-situ atmospheric conditions were unknown. Cross-validation of their empirical relationship resulted in relatively low mean absolute relative error (ARE) and relative root mean square error (RRMSE) values (25.5% and 36.5%, respectively). This research highlights the promise of satellite data for SSC estimation, offering valuable insights for water quality assessments and environmental monitoring in turbid river systems.

The research conducted by **Wang *et al.* (2009)** assessed Suspended Sediments Concentration (SSC) in surface water, a crucial indicator of coastal water quality, particularly in high-energy coastal regions. An Artificial Neural Network (ANN) model was employed to establish a connection between SSC and satellite-received radiances. In situ SSC measurements from Hangzhou Bay and MODIS 250 m daily products were utilized, revealing significant correlations between in-situ data and MODIS band 1–2 (wavelength) reflectance values. The ANN

model with one hidden layer outperformed regression analysis ( $R^2 = 0.98$ ;  $n = 25$ ), exhibiting superior simulation performance with an RMSE of less than 10% compared to the regression analysis's RMSE of more than 25%. The research demonstrated the utility of MODIS 250 m daily products and the ANN model in monitoring surface SSC dynamics in high-energy coastal water environments.

In 2010, **Hossain *et al.*** conducted an observation on Landsat TM/ETM imagery, noting that Band 1 (Blue band/~ 450-515 nm) and Band 4 (Near-infrared/~ 750 - 900 nm) are highly sensitive to water and its transparency (turbidity). Band 1 consistently yielded the highest reflectance values for water, while Band 4 showed the lowest values. These characteristics were observed across various levels of water turbidity. The researchers calculated the Normalized Difference Suspended Sediment Index (NDSSI) using Landsat 7 ETM+ imagery with Bands 1 and 4. They utilized this index to determine the spatial distribution of relative variations in suspended sediment concentration in river/lake water. By correlating NDSSI values to near real-time in-situ measurements of suspended sediment concentration (SS), the researchers successfully quantitatively estimated the suspended sediment concentration. This study offers valuable insights into utilizing remote sensing data for accurate estimation of suspended sediment concentration, contributing to enhanced environmental monitoring and water quality assessments in rivers and lakes.

In 2011, **Bhatti *et al.*** utilized band 3 (610 nm to 690 nm) and band 4 (760 nm to 890 nm) from remotely sensed data-ALOS/AVNIR-2 to create a monitoring system for suspended sediment in surface water. The collected hyper spectral reflectance spectra were integrated into ALOS/AVNIR-2 bandwidth for field application. Through a series of experiments, the researcher developed a reflectance model  $(B4 + B3) / (B4 / B3)$  that proved to be the best predictor of suspended sediment concentration (SSC) in the Tarbela Dam on the Indus River in Pakistan. This study showcases the potential of remote sensing data in establishing effective monitoring systems for sediment concentration in water bodies, aiding in water resource management and environmental assessments.

**Kazemzadeh *et al.*, 2013** studied temporal and spatial variations of suspended sediment concentration in Bahmanshir Estuary, Iran using MODIS remote sensing data in concurrence with five field campaigns. They performed simple regression analysis for different curve fitting methods with different multiplicative, additive and subtractive band combinations and compared the results with ANN models. This study demonstrated ANN model and MODIS MOD09GQ products are appropriate tools for monitoring surface SSC dynamics within coastal water environments such as Bahmanshir Estuary.

The study by **Long and Pavelsky (2013)** utilized daily 250-m MODIS imagery in band 1 (620–670 nm) and band 2 (841–876 nm) to monitor suspended sediment transport and hydrologic

recharge in the Peace–Athabasca Delta, Canada. The aim was to maintain ecological diversity and hydrologic connectivity in freshwater delta systems by observing regular floodplain recharge with river water. A highly predictive suspended sediment concentration (SSC)-reflectance model (Spearman's  $\rho=0.95$ ) was identified through comparisons of 31 published empirical equations using a field dataset containing 147 observations of SSC and in situ spectral reflectance. The model fulfilled the criteria of using a near-infrared band in combination with at least one visible band, being developed based on SSCs similar to those in the observed region, and having a nonlinear form. With this model, a twelve-year time series of SSC was established in the westernmost end of Lake Athabasca, revealing the timing and sources of major sediment flux events.

In 2013, **Sravanthi et al.** established an empirical relationship between suspended sediment concentrations (SSCs) and radiometer remote sensing reflectance values in the coastal waters of Kerala. The study found a significant correlation ( $R^2=0.84$ ; linear regression) between the remote sensing reflectance ( $R_{rs}$ ) values derived from specific band combinations (490, 555, and 620 nm) and in-situ SSCs. The researchers further tested the algorithm's suitability for satellite data by implementing it for SSC retrieval from Oceansat-2 OCM sensor data and validating the results. The regional algorithm demonstrated good performance with a correlation ( $R^2=0.62$ ) between in situ SSCs and retrieved SSCs from satellite data. Concentrations of suspended sediments ranged from 1 to 40 mg/L in the coastal waters off Cochin, southwest India, with higher concentrations closer to the shore and lower values in the offshore areas.

In 2015, **Robert et al.** conducted a study in which they applied various algorithms and indices proposed in the literature for inland waters on MODIS series data from 2005 to 2015 over the Barge reservoir. The acquired data and algorithms were evaluated using field measurements of suspended sediment concentration (SSC) ranging from 18 to 926.67 mg/L, turbidity, and field radiometry. The researchers observed that the reflectance in the red band increased at low concentrations of SSC, up to 350 mg/L. They suggested using the power function of NIR/RED band ratio for SSC estimation in the considered range using both MODIS and field spectroscopy data. However, they noted that SSC retrieval from satellite measurements could be less precise for small values of SSC, with overestimation occurring for SSC values less than 200 mg/l. To improve spatial variability analysis of SSC in water bodies, the researchers recommended conducting SSC analysis using Sentinel-2 images with 5-day temporal and 10 m spatial resolution. This study highlights the potential and challenges of using remote sensing data for SSC estimation, offering valuable insights for water quality monitoring and environmental assessment in inland water bodies.

The study by **Novoa et al. 2017** addresses challenges posed by atmospheric correction (AC) complexities near land and high suspended particulate matter-induced reflectance, leading to saturation effects. A novel switching method is introduced to select the most sensitive

relationship between SPM and water reflectance ( $\rho_w$ ), effectively avoiding saturation issues. High-resolution satellite imagery and in-situ SPM and  $\rho_w$  data were utilized to validate the approach. The method was applied to medium-high spatial resolution sensors such as Landsat-8/Operational Land Imager, National Polar-Orbiting Partnership/Visible Infrared Imaging Radiometer Suite, and Aqua/Moderate Resolution Imaging Spectrometer, yielding consistent results. Despite minor discrepancies in  $\rho_w$  retrieval, reliable SPM estimation was achieved across sensors. The success of this approach paves the way for its application with Sentinel2/MSI and Sentinel3/OLCI sensors, promising enhanced SPM dynamics study in coastal oceans with higher resolutions.

In 2018, **Shahzad *et al.*** conducted a study to explore the potential of Landsat's Enhanced Thematic Mapper Plus (ETM+) sensor for remote sensing-based quantification of suspended sediment concentration (SSC) in the turbid Indus Delta Region (IDR) of Pakistan. They developed an empirical model using in-situ SSC measurements (ranging from 9.4 to 761.4 mg/L) collected during several data collection campaigns coinciding with satellite overpasses (within an 11-day window). The researchers found that by utilizing Landsat-7 ETM+ bands 1 (Blue: 450 to 520 nm), 2 (Green: 520 to 600 nm), 3 (Red: 630 to 690 nm), and 5 (Shortwave infrared: 1550 to 1750 nm), along with the Normalized Difference Suspended Sediment Index (NDSSI), they could achieve precise and accurate estimation of SSC. The developed model exhibited a relatively small Root Mean Square Error of 67.24 mg/L, Mean Absolute Error of 54.75 mg/L, and a coefficient of determination of 0.88. Moreover, the study indicated that the residuals did not increase with an increasing time window (0 – 11 days) between the satellite overpass and in situ data collection. Based on these findings, the researchers concluded that the established algorithm has the potential for frequent (after 8 days) synoptic mapping of SSC in the IDR and similar estuarine environments. This research provides valuable insights into the effective use of remote sensing data for monitoring suspended sediment in turbid coastal regions, contributing to improved water quality assessments and environmental management.

**Li *et al.* (2018)** conducted a study for evaluation of Sentinel-2A surface reflectance derived using Sen2Cor for water quality monitoring and suggested the use of Sen2Cor surface reflectance of bands except B01, B02, and B09 for the quantitative applications to avoid the strong aerosol scattering and water vapour absorption.

In their research, **Munir *et al.* (2019)** explored the applicability of Sentinel-2A imagery for mapping the dynamics of Total Suspended Sediment (TSS) at the river mouth of Padang City. The study involved the use of various image transformations, including Normalized Difference Suspended Sediment Index (NDSSI), Normalized Suspended Material Index (NSMI), and Band Ratio, utilizing the green, red, and blue band channels to establish correlations with observed TSS levels ranging from 0.98 to 4.56 mg/L. The key conclusion was that Sentinel-2A imagery

demonstrated a promising capability for mapping TSS in Padang City, achieving an accuracy of 80.51% when employing the band ratio (Green/Blue) image transformation method. This finding highlights the potential utility of Sentinel-2A data for monitoring and understanding sediment dynamics in river environments, which can be valuable for environmental management and decision-making processes.

In 2019, **Pereira *et al.*** conducted a comprehensive evaluation of multi-temporal high-resolution satellite imagery (RapidEye) to assess the suspended sediment concentration (SSC) in the Jaguaribe River, Brazil, over a 5-year period. They investigated 15 one-, two-, and three-band indices specifically derived for SSC estimation based on RapidEye spectral bands, along with nine indices proposed in previous studies for other optical sensors. The comparison of these indices with in-situ concentration data, ranging from 67 mg per litre to 230 mg per litre, served as the validation process. Their analysis revealed that the near-infrared band performed most effectively in representing SSC. Particularly, when combined with the green band, its performance improved significantly. This finding aligns with previous literature results across various sedimentological contexts. Overall, the study demonstrated the potential of RapidEye imagery for accurately assessing suspended sediment concentration in the Jaguaribe River, contributing valuable insights for future monitoring and management of sediment dynamics in similar environments.

This study by **Pitchaikani *et al.* (2019)** presented a regional algorithm to estimate suspended sediment concentration (SSC) using remote sensing reflectance (Rrs) and field observations in the Hooghly Estuary and coastal waters of West Bengal. The aim was to understand SSC variations and their environmental implications for erosion and deposition. Cloud-free water samples were collected along the Hooghly Estuary and the open coast. Field synchronous Ocean Colour Monitor (OCM) data underwent geometric corrections, enabling retrieval of pixel-level remote sensing reflectance. The SSC varied from 35 to 75 mg/L in coastal waters and 24 to 270 mg/L in the Hooghly Estuary. Notably, a strong correlation was found between SSC and the summation of reflectance at 555 and 620 nm, exhibiting an exponential relationship with an  $R^2$  value of around 0.74. Intriguingly, the algorithm displayed higher correlations in the Hooghly Estuary, particularly for clay sediment, compared to coastal waters with sand sediment. This regional algorithm demonstrates its potential for SSC estimation and environmental assessment in West Bengal's coastal areas.

In 2020, **Garg *et al.*** conducted an analysis using Sentinel-2 multispectral remote sensing data to study water quality, specifically turbidity, along different stretches of the Ganges River, including Haridwar, Kanpur, Prayagraj, and Varanasi. The study focused on examining changes in water reflectance in the visible region before and after the nationwide lockdown. To ensure consistency in atmospheric correction, the Level-1C product of Sentinel-2A/B, which provides radiometrically and geometrically corrected top of atmosphere reflectance, was utilized. Their

investigation revealed that the Near-Infrared (NIR) and Red bands were particularly sensitive to turbidity variations. Interestingly, they observed a reduction in turbidity during the lockdown period. To validate their findings, the researchers employed the Normalized Difference Turbidity Index (NDTI) band ratio technique. The study demonstrated the usefulness of remote sensing in quantitatively estimating turbidity, especially in optically deep water areas, without the need for extensive field observations. This approach using Sentinel-2 data and the NDTI index holds great potential for monitoring water quality and environmental changes in river ecosystems more efficiently and accurately.

In 2020, **Sutari *et al.*** proposed a novel method for quantifying Suspended Sediment Concentration (SSC) using Landsat imagery and corresponding SSC data from the International Commission for the Protection of the Rhine (IKSR) and Dutch Rijkswaterstaat spanning the years 1995 to 2016. The researchers developed a model based on the ratio of logarithmic transformations of the red/green band and SSC, derived from in-situ sampling measurements. The SSC estimation model demonstrated good performance, particularly for values below 20 mg/L, showing satisfactory accuracy. However, for values exceeding 20 mg/L, the model's precision diminished, consistently underestimating the higher concentration levels. It was observed that around 84% of SSC values were below 20 mg/L, while the remaining 16% exceeded this threshold. One significant challenge encountered with the model was its tendency to saturate predicted values at higher SSC concentrations, resulting from limited data points for higher SSC values and significant variations between the maximum and minimum SSC values. These variations in the extreme ends of the SSC range contributed to the saturation effect, which could hinder the model's accuracy at higher concentrations. Considering these findings, the researchers emphasized that a wider range of data covering both high and low SSC values is crucial to improving the model's performance at higher concentrations. Addressing the issue of model saturation requires careful consideration of processing limitations and handling extreme variations in SSC values. Despite this limitation, their approach offers a promising framework for estimating SSC in river environments using remote sensing data.

In their 2021's study, **Womber *et al.*** aimed to characterize the spatial and temporal distribution of suspended sediment in Lake Tana using both in situ measurements and remote sensing applications. They developed a relationship between in situ and remote sensing observations to retrieve suspended sediment concentration (SSC) and map its spatial distribution. By collecting 20 samples during four sampling campaigns, they calibrated regression models using data from the first three campaigns. The study found that MODIS-Terra reflectance in the Near-Infrared (NIR) band was strongly correlated with SSC ( $R^2 = 0.81$ ) and turbidity ( $R^2 = 0.85$ ). The developed models were validated, estimating a 10-year time series of SSC from 2008–2017 and revealing an increasing trend during this period. The research highlights the potential of using

satellite data to monitor and obtain past SSC records, aiding in the implementation of management practices to reduce sediment inflow and promote better water quality in the lake.

This study by **Dehkordi *et al.*, (2021)** focussed on the estimation of Suspended Sediment Concentration (SSC), a vital parameter influencing hydrological and ecological dynamics, using Sentinel-2 (S2) Level-2A (L2A) imagery along the Missouri River. Leveraging supervised machine learning-based regression models, particularly Support Vector Regression (SVR) and Random Forests (RF), the research aims to predict SSC values for water pixels based on reflectance values from different spectral bands. By employing less than 1% cloud coverage S2 L2A images, the study capitalizes on Google Earth Engine (GEE) for processing, eliminating the need for data downloads. Through training and validation with time-series ground measurements from three stations, the RF model emerges as superior, boasting a Root Mean Square Error (RMSE) and Mean Absolute Error (MAE) of 59.521 and 46.493 mg/L, respectively. Notably, the RF model showcases a stronger correlation between actual and predicted SSC values ( $R^2 = 0.79$ , Pearson's  $r = 0.877$ ), underlining its efficacy. Furthermore, the study identifies the significance of short-wave infrared (SWIR) and red bands in SSC estimation using S2 L2A imagery, underscoring their pivotal role in remote sensing applications for water quality assessment. Overall, these findings offer valuable insights into the utilization of satellite imagery and machine learning techniques for SSC estimation, contributing to improved understanding and monitoring of water quality dynamics in riverine ecosystems.

In their 2022 study, **Zhang *et al.*** conducted in-situ spectral measurements within 12 hours of corresponding Sentinel-2 derived spectral reflectance. They investigated the spectral response to Suspended Sediment Concentration (SSC) and found that the Red and Green bands were most sensitive when SSC was low. However, as SSC increased, the sensitivity shifted towards the Near-Infrared (NIR) spectral region. To classify water as clear or turbid, they used the Forel-Ule index (FUI) and developed optimal SSC retrieval models accordingly. For FUI values  $\leq 14$ , the spectral indices based on the Green and Red bands were employed. Conversely, for FUI values  $> 14$ , the spectral indices based on the Red and NIR bands were used. The study demonstrated that the estimated SSC in turbid water (FUI  $> 14$ ) showed strong agreement with in-situ measurements, with a root mean squared error (RMSE) of 24.87 mg/L and a mean relative error (MRE) of 51.91%. These results indicate the potential of the developed models for accurately estimating SSC in turbid waters using remote sensing data from Sentinel-2 imagery.

The study by **Kavan *et al.* in 2022** explores the application of the Normalized Difference Suspended Sediment Index (NDSSI) derived from multi-temporal Sentinel-2 images to assess sediment flux in fjords and coastal waters over a five-year period. Through their analysis, the researchers established a correlation ( $R^2 = 0.45$ ) between NDSSI and suspended sediment in glacial lake fjords. This finding suggests the potential of remote sensing-derived suspended sediment

indexes as a valuable tool for quantifying sediment flux in large-scale fjord and coastal environments. However, the study emphasizes the importance of proper in-situ calibration to improve accuracy. The research sheds light on the advantages of remote sensing techniques for monitoring sediment dynamics in ecologically sensitive aquatic ecosystems. This work offers valuable insights and paves the way for further advancements in using remote sensing data to understand and manage sediment transport in coastal regions. With appropriate calibration and refinement, remote sensing can play a crucial role in monitoring sediment movement and its impact on the environment in these critical areas.

In this study, **Yu *et al.*, (2022)** investigated the potential of using satellite remote sensing, specifically the Ocean and Land Color Instrument (OLCI) on Sentinel-3A, to assess water quality in estuarine regions, focusing on suspended sediment concentration (SSC) in Hangzhou Bay. They emphasize SSC's significance as an indicator of water quality, correlating directly with optical properties like transparency, turbidity, and colour. Despite challenges related to atmospheric correction uncertainties, the authors leverage OLCI imagery to develop an SSC retrieval model, validated with Geostationary Ocean Colour Imager (GOCI) data. Key findings highlight the efficacy of an ultraviolet-based atmospheric correction algorithm, the superiority of a multi-band index model using specific OLCI spectral bands, and the spatial complexity of SSC distribution in Hangzhou Bay. Notably, OLCI estimates generally outperform GOCI data, especially in areas with higher SSC levels, underscoring the potential of OLCI for enhancing SSC estimation and understanding water quality dynamics in estuarine environments. Overall, the developed SSC retrieval models offer a promising tool for evaluating water quality in Hangzhou Bay's coastal estuary, contributing to the advancement of satellite remote sensing techniques for monitoring suspended sediment and other water quality parameters in similar settings.

**Paulista *et al.*, (2023)** used Sentinel-2 A and B satellite imagery to estimate Suspended Sediment Concentration (SSC) along the Teles Pires River within the Brazilian Amazon. They synchronized sensor images with field sampling dates. Utilizing Google Earth Engine (GEE), a versatile tool known for its efficiency, they processed the data. Their access to diverse data sources and the robustness of their processing demonstrate GEE's capability to precisely estimate water quality parameters through remote sensing. The most effective estimator for SSC was found to be the reflectance of the B4 band, corresponding to the red portion of the visible spectrum. The exponential model displayed the highest level of fit and accuracy.

#### **2.3.2.4 Studies on Spectral Integration Approach**

A study by **Lodhi *et al.* (1998)** focused on estimating suspended sediment concentration (SSC) using high-resolution Spectroradiometer data integrated into Landsat-TM 4 bands. The study developed regression models to establish the relationship between reflectance values and SSC levels. The use of the NIR range in Landsat-TM 4 bands and a second-order regression model

proved to be the most effective for SSC estimation. This approach bridged the gap between ground-based measurements and satellite data, advancing remote sensing technologies for environmental monitoring. By using high-resolution Spectroradiometer data and integrating it with Landsat-TM 4 bands, the research offers valuable insights for monitoring SSC levels in water bodies remotely. The second-order regression model's success in the NIR range highlights its importance for precise SSC estimation. In conclusion, this research contributed to the development of effective tools for managing sediment dynamics in aquatic environments through remote sensing technologies. The findings, particularly the optimal use of the NIR range and the second-order regression model, have practical implications for water quality assessment and environmental monitoring.

**Doxaran *et al.* in 2002**, presented an experimental method for determining water composition from "ocean color" satellite data, specifically in visible and near-infrared (NIR) wavelengths, applied to highly turbid waters in the Gironde estuary. The researchers conducted numerous Spectroradiometric measurements to establish empirical relationships between remote-sensing reflectance (Rrs) in SPOT-HRV bands and suspended particulate matter (SPM) concentration. The study observed that Rrs increased with SPM concentration, and the SPOT bands saturated at the highest turbidities. The reflectance values between 500–590 nm, 610–680 nm, and 790–890 nm were weighed by sensitivity to obtain Rrs (XS1), Rrs (XS2), and Rrs (XS3), respectively. The best correlations were found for the NIR band XS3 (790–890 nm) and reflectance ratios  $Rrs(XS3)/Rrs(XS1)$  and  $Rrs(XS3)/Rrs(XS2)$ . The algorithm allowed estimation of SPM concentrations up to 2000 mg/L with an accuracy better than  $\pm 35\%$ . The research successfully applied the algorithm to a SPOT scene, retrieving the horizontal distribution of SPM and revealing detailed sedimentary flows. The high spatial resolution HRV-SPOT sensor provided valuable insights, particularly in the visible XS1 and XS2 spectral bands. The study significantly contributed to the advancement of remote sensing methods for studying water composition and understanding sediment dynamics in turbid estuarine environments.

**Saenz *et al.*** conducted a study in 2015, presenting a local algorithm for monitoring total suspended sediments (TSS) in the micro-watershed of the Teusacá River, Colombia, using drone-based remote sensing applications. The research involved comparing reflectance values with in-situ data measurements of SSCs from the river's surface layer during two campaigns. By establishing an empirical relationship between reflectance values and TSS concentration, they identified strong correlations with Near IR, Green, and Red bands. The study achieved a coefficient of determination of 0.8781, validating the efficacy of the remote sensing methodology. This drone-based approach proves valuable for monitoring water quality in vulnerable and challenging-to-access micro-watersheds, offering promising insights for enhancing water quality assessment and management in such environments.

This study by **Robert *et al.* (2016)** investigated the applicability of Moderate Resolution Imaging Spectroradiometer data (MODIS), specifically the MOD09Q1 and MYD09Q1 products with red (R) and near-infrared (NIR) bands, to monitor turbidity and Surface Suspended Sediment Concentration (SSC) in Burkina Faso's Bagre Reservoir. Utilizing field measurements encompassing turbidity, SSC, and radiometry, various radiometric indices were evaluated. Field Spectroradiometric measurements by TriOs were convolved to match the MODIS radio-metric bands to test different radiometric indices. The research identified the NIR/Red ratio as the optimal method for estimating SSSC and turbidity, successfully adaptable to both in-situ Spectroradiometer measurements and satellite reflectance data from MODIS.

In this study, the applicability of Sentinel 2 Multispectral Imager (MSI) images for retrieving suspended particulate matter concentration (CSPM) in Poyang Lake, China, was investigated by **Liu *et al.* (2017)**. Through the utilization of in-situ spectral and CSPM measurements alongside Sentinel 2 MSI images, CSPM retrieval models were developed and CSPM values were estimated. The study calibrated the models using thirty-four samples and validated them with the remaining data. The results indicated that the Sentinel 2 MSI B4–B8b (Red, Red Edge 1, 2, 3 and NIR) models exhibited favourable fitting accuracies, explaining 81–93% of CSPM variation. The estimated CSPM values showed strong correlation with measured CSPM, with a mean absolute percentage error ranging from 36.87% to 21.54%. Notably, the B7-based (NIR) model demonstrated the highest accuracy. The findings underlined the potential of Sentinel 2 MSI for CSPM retrieval in Poyang Lake, with specific B4 and B7 bands recommended for distinct SPM loadings.

The study conducted by **Kwon *et al.* 2021** presents a significant advancement in the field of suspended sediment concentration (SSC) estimation. By utilizing a UAV-based hyperspectral measurement system, the researchers addressed the limitations of traditional point-based measurements, enabling remote and comprehensive SSC analysis. The construction of intrinsic hyper spectral datasets for different sediment characteristics through laboratory and field experiments allowed for the development of a global SSC estimation model. Notably, Optimal Band Ratio Analysis (OBRA) and Recursive Feature Elimination (RFE) were employed to select the most relevant spectral bands for SSC estimation, ensuring the model's accuracy. Using Support Vector Regression (SVR) with the optimal spectral bands, the developed model demonstrated improved performance, providing more accurate estimations of SSC in rivers. This approach, taking into account sediment types and grain size, shows promising potential for enhancing the understanding and monitoring of sediment dynamics in aquatic environments. The study's outcomes contribute significantly to the field of remote sensing-based sediment analysis and have practical implications for better managing water resources and environmental conservation efforts.

**Marinho *et al.* (2021)** used remote sensing reflectance from in-situ measurements and Sentinel-2 Multi-Spectral Instrument (MSI) images to estimate the suspended sediment concentration (SSC) in the largest black-water river of the Amazon basin. They measured in-situ spectral reflectance using TriOS RAMSES Spectroradiometer operating in the spectral range of 350 – 950 nm. They analysed this in-situ in terms of shape and magnitude. The magnitudes of water reflectance in the Sentinel-2 MSI Red band were consistent with in situ spectral reflectance measurements, indicating the large spatial variability of the lower SSC values (0 to 15 mg/L) in a complex anabranching reach of the Negro River. They obtained better results for Sentinel-2 MSI Red band (Band 4 at 665 nm) in order to estimate the SSC. They found that the models with the best were obtained while using Band 3 (Green @ 560 nm) and Band 4 (Red @ 665 nm) with an  $R^2$  value greater than 0.85 and an error less than 20% and good results were obtained with Band 5 (Red Edge 1 @ 705 nm). They suggested that the radiometric characteristics of sensors, like sentinel-2 MSI, are suitable for monitoring the suspended sediment concentration in large tropical black-water rivers. They concluded that the in-situ reflectance dataset from this study contributed to the knowledge of the apparent optical properties in Amazonian rivers.

#### 2.4 Summary and Critique on Reviewed Literature

The literature review presented above underscores the crucial significance of evaluating and measuring suspended sediment, given its profound implications for water quality, ecosystem health, and sediment transport behaviour. The evolution of suspended sediment measurement methodologies has transitioned from traditional manual methods to advanced remote sensing technologies, enabling more efficient and extensive data collection. The synthesis of the literature review outcomes is succinctly captured in Table 2.2, followed by a subsequent in-depth critique of its contents.

**Table 2.2 Summary of review of literature**

Salient feature of the study	Author (Year)
Developed a band ratio model for SSC estimation using hyperspectral data, showing a strong correlation between NIR and visible wavelength bands.	Bhatti (2006)
Monitoring system for SSC developed using band ratio index $(B4 + B3) / (B4 / B3)$ from ALOS/AVNIR-2 data.	Bhatti (2011)
Reflectance increased with SSC, peak shifted from visible to NIR, NIR exhibited uniform increase with SSC. First derivative effective for SSC estimation.	Bhatti A. M. <i>et al.</i> , (2007)
Used hyperspectral data to observe significant changes in reflectance for varying SSC levels, highlighting NIR as an optimum range for assessing suspended sediment concentration.	Bhatti <i>et al.</i> , (2008)

Found a strong relationship between SSC and spectral reflectance, with log-linear behaviour between 450 to 700 nm and linear behavior from 700 to 1050 nm. They recommended assuming log-linear relationships in visible and linear relationships in near-infrared wavebands for SSC estimation.	Chen <i>et al.</i> , (1991)
Established a strong correlation between SSC and derivative spectral reflectance both in laboratory and at sea, with derivative spectral reflectance used for SSC estimation with less than 8% error in the laboratory.	Chen <i>et al.</i> , (1992)
Developed an algorithm based on SPOT-HRV bands to estimate suspended particulate matter (SPM) concentration in highly turbid waters, with best correlations found in the NIR band XS3.	Doxaran <i>et al.</i> , (2002)
Spectral signature with peak approximately at 560 (Green) and 650 (Red) nm with concentration of suspended particulate material of 45 mg/litre in Tamar estuary.	Doxaran <i>et al.</i> , (2005)
Identified a strong correlation between the ratio $R_{rs}(850\text{ nm})/R_{rs}(550\text{ nm})$ and total suspended matter concentration in the Tamar Estuary, suggesting potential for mapping tidal turbidity using remote sensing data.	Doxaran <i>et al.</i> , (2005)
Sentinel-2 data used to estimate turbidity. Reduction observed during lockdown. Potential for water quality assessment demonstrated.	Garg <i>et al.</i> , (2020)
There is increase in the reflectance of visible region specifically red region with increase in sediments or turbidity in water and it is also noticed that peak shifts from green to red region of spectrum with increase in inorganic material.	Gholizadeh <i>et al.</i> , (2016).
Band ratio method used to estimate SSC using Landsat imagery. Spatial distribution of SSC revealed.	Hossain <i>et al.</i> , (2010)
Correlation between NDSSI and suspended sediment established. Potential tool for quantifying sediment flux in fjords and coastal waters suggested.	Kavan <i>et al.</i> , (2022)
Developed a comprehensive model for suspended sediment concentration (SSC) estimation using UAV-based hyperspectral data and optimal band selection techniques.	Kwon and Seo (2022)
Identified that higher SSC levels generated increased reflectance between 400 and 700 nm, with linearity in the SSC-Reflectance relationship improving between 400 and 900 nm, and a near-linear relationship between 720 and 900 nm. Best wavelengths for first-order regression to estimate SSC were 827, 830, and 847 nm.	Han (1997)

Demonstrated the advantage of using multiple bands and band ratios from Mica Sense Sequoia sensor on a UAV for mapping SSC within the Maumee River, emphasizing the practical but somewhat limited utility of UAVs in monitoring SSC.	Larsen <i>et al.</i> , (2018)
Found visible range (580-690 nm) informative for sediment types, NIR range (714-880 nm) accurate for sediment concentration estimates.	Lodhi <i>et al.</i> , (1997)
Used of the NIR range in Landsat-TM 4 bands and a second-order regression model is effective for estimating suspended sediment concentration (SSC).	Lodhi <i>et al.</i> , (1998)
Highly predictive SSC-reflectance model established using MODIS data. Time series mapped SSC, revealed sediment flux events.	Long and Pavelsky (2012)
Suitability of Sentinel-2 MSI bands, especially Band 4 (665 nm) and Band 3 (560 nm), for estimating suspended sediment concentration (SSC) in the Amazon River.	Marinho <i>et al.</i> , (2021)
Established linear relationship between MODIS band 1 (620–670 nm) data and Total Suspended Matter (TSM) measurements.	Miller and McKee (2004)
Emphasized field spectroscopy as vital for remote sensing, bridging theoretical understanding and image interpretation, aiding precision, and building a spectral data knowledge base for future use.	Milton (1987)
Stressed the need for a new paradigm in field spectroscopy, focusing on simultaneous measurements of directional radiance and irradiance.	Milton <i>et al.</i> , (2006)
Potential of Sentinel-2A data for mapping TSS in coastal waters demonstrated. Effective band ratios for estimating TSS identified.	Munir <i>et al.</i> , (2019)
Developed statistical models for suspended sediment estimation using satellite data. Different bands exhibited varied SSC estimation performance.	Myint and Walker (2002)
Developed optimal regression model using radiance values from all four Landsat MSS bands (B4, B5, B6, B7) for SSC estimation. Successfully mapped SSC concentrations.	Novoa (1993)
RapidEye imagery effective for SSC estimation. NIR band particularly useful for representing SSC.	Pereira <i>et al.</i> , (2019)
The spectral band that best represented SSC was the near infrared, whose performance improved when associated with the green band when RapidEye satellite imagery was used to assess the SSC ranging between 67 to 230 mg/L in Jaguaribe River, Brazil, during a 5-year period.	Pereira <i>et al.</i> , (2019)

Found that suspended sediment concentration (SSC) ranged from 35 to 75 mg/l in coastal waters and 24 to 270 mg/l in the Hooghly Estuary, and a significant correlation existed between SSC and the sum of reflectance at 555 and 620 nm, following an exponential relationship with an R2 value of approximately 0.74.	Pitchaikani <i>et al.</i> , (2019)
Typical reflectance spectra have three distinct peaks in 400 – 1000 nm region. The first peak is centred at 590 nm (Green), the second at 700 nm (Red Edge 1), and the third at 810 nm (NIR). At lower SSC (< 1000 ppm), the spectra have a characteristic plateau in 590 – 690 nm window i.e. around Green and Red region.	Radhakrishna (2013)
Established a spectral signature for SSC ranging from 1000 to 10000 mg/L, with the best-fit model being a power function for SSC-reflectance relationship.	Raut and Gavit (2015)
If the range of suspended sediments is between 0 and 50 mg/l, reflectance from almost any wavelength will be significantly related to suspended sediment concentrations.	Ritchie (2000)
Found that solar radiation reflected from water surfaces varied with suspended sediment, with maximum reflection shifting from 550 nm to above 600 nm at higher sediment concentrations, and the best fit for SSC estimation was between 700 and 800 nm.	Ritchie <i>et al.</i> , (1976)
Concluded that wavelengths between 700 and 800 nm were most useful for determining suspended sediment in surface waters.	Ritchie <i>et al.</i> , (1976)
The reflectance in the red band increases at low concentration of surface SSC up to 350 mg/l and suggested the use of power function of NIR/RED band ratio for surface SSC estimation in the considered range using MODIS and field spectroscopy data.	Robert <i>et al.</i> , (2015)
Explored algorithms for SSC estimation using MODIS data, potential and challenges of satellite-derived SSC estimates highlighted.	Robert <i>et al.</i> , (2015)
Identified the NIR/Red ratio as the optimal method for estimating Surface Suspended Sediment Concentration (SSSC) using MODIS data from Burkina Faso's Bagre Reservoir.	Robert <i>et al.</i> , (2016)
Band ratio method effective at lower TSS concentrations, spectral fitting method successful at entire range (including high TSS concentrations).	S. C. Liew <i>et al.</i> , (2003)

Demonstrated strong correlations between reflectance values and total suspended sediments (TSS) in the Teusacá River micro-watershed using drone-based remote sensing.	Saenz <i>et al.</i> , (2015)
Identified Landsat MSS band 3 (700-800nm) as optimal for SSC estimation using an exponential curve model. Longer wavelengths exhibited improved signal-to-noise ratios.	Schiebe <i>et al.</i> , (1992)
Empirical model for SSC estimation using Landsat-7 ETM+ data developed. Potential for synoptic mapping in turbid coastal regions demonstrated.	Shahzad <i>et al.</i> , (2018)
Highlighted the increasing use of UAVs for mapping and monitoring water quality and quantity, with a focus on chlorophyll content and turbidity, but noted limited research attention towards open water reservoirs supplying smallholder farms. They also discussed challenges related to costs, skills, regulations, and the need for further research in this area.	Sibanda <i>et al.</i> , (2021)
A linear regression having good correlation with $R^2 = 0.84$ was obtained between the reflectance values derived from band combinations of 490 (Blue), 555 (Green) and 620 (Red) nm and in situ SSCs ranging between 1 to 40 mg/L in coastal waters of Kerala.	Sravasthi <i>et al.</i> , (2013)
SSC estimation model developed using Landsat data. Challenges with saturation effect at high SSC concentrations noted.	Sutari <i>et al.</i> , (2020)
Band 2 and Band 5 reflectance relationship used for SSC estimation using Terra MODIS data.	Wang and Lu (2009)
Developed ANN model using MODIS data for SSC estimation, outperformed regression analysis.	Wang <i>et al.</i> , (2008)
Correlation between MODIS-Terra NIR band and SSC established. Time series mapped SSC, increasing trend over time observed.	Womber <i>et al.</i> , (2021)
Suggested use of Sen2Cor surface reflectance for quantitative applications, excluding specific bands for accurate results.	Yingjie Li <i>et al.</i> , (2018)
Identified a good correlation between water SSC and spectral reflectance in the range of 726–900 nm, recommending a novel cubic model for robust quantification of high surface SSC water samples.	Zhan <i>et al.</i> , (2017)
Developed a semi-analytical algorithm for TSM estimation using in situ data, finding strong positive correlation between TSM concentrations and reflectance in the Green region (542 nm).	Zhang <i>et al.</i> , (2016)

On examination of the spectral responses of SSC it was discovered that, when the SSC was less than 50 mg/L, the red and green bands showed the most sensitive response. The spectral signal in the VIS band became saturated as the SSC increased, and the sensitive band switched to the NIR spectral region.	Zhang <i>et al.</i> , (2022)
Spectral response to SSC identified. Developed SSC retrieval models for clear and turbid waters based on spectral sensitivity.	Zhang <i>et al.</i> , (2022)
It was observed that when SSC was low, the Red and Green bands produced most sensitive response and as the SSC increased, sensitive band shifted towards the NIR spectral region.	Zhang <i>et al.</i> , (2022)

The assessment of suspended sediment concentration (SSC) is of paramount importance for various hydrological and environmental studies, providing insights into sediment transport, water quality, and ecosystem health in aquatic environments (Bejestan and Rezania, 2010; Gupta, 2015; Sheela *et al.*, 2014). This information is vital for identifying erosion-prone areas and implementing effective soil conservation strategies (Ritchie *et al.*, 1987). However, traditional in-situ sampling methods have limitations in terms of spatial coverage, temporal resolution, and cost-effectiveness (Edwards and Glysson, 1988; Ritchie *et al.*, 2003). To address these challenges, innovative remote sensing techniques have gained prominence, offering comprehensive and efficient SSC monitoring solutions (Marinho *et al.*, 2021). Acoustic methods, bottle sampling, pump sampling, and optical methods are some of the options available for SSC measurement (Yong and George, 2003; Meral *et al.*, 2010; Xavier *et al.*, 2014). Nonetheless, remote sensing methods, such as spectral reflectance techniques, have demonstrated their potential by leveraging spectral information to estimate SSC remotely (Wren *et al.*, 2000). These methods hold promise for overcoming the limitations of traditional techniques and enabling informed decision-making in the management of water resources and aquatic ecosystems.

The presented compilation of studies offers a valuable overview of the methodologies employed for estimating Suspended Sediment Concentration (SSC) through remote sensing techniques. Each study contributes distinct insights into the spectral characteristics and bands utilized for SSC estimation across various water bodies and sediment concentrations. However, it's important to critically assess the methodologies employed and identify potential strengths, limitations, and trends.

Handheld Spectroradiometer-based studies have demonstrated the potential of spectral reflectance measurements for assessing suspended sediment concentration (SSC) in water bodies. Researchers like Ritchie *et al.* (1976) have utilized portable Spectroradiometer to measure reflected solar radiation at different wavelengths and observed correlations between spectral

reflectance and SSC. Chen *et al.* (1991, 1992) conducted laboratory and field studies, highlighting the strong relationships between SSC and derivative spectral reflectance, particularly in the visible and near-infrared wavelengths. Han (1997) emphasized the effectiveness of spectral reflectance in estimating SSC, with optimal wavelengths identified for regression models. Recent studies by Zhang *et al.* (2016) and Zhan *et al.* (2017) used Spectroradiometer data to develop algorithms for estimating suspended matter concentration in water bodies, showcasing the continued relevance of spectral reflectance techniques for accurate SSC assessment. While the studies by Larsen *et al.* (2018) and Sibanda *et al.* (2021) showcase the potential of drones for assessing water quality and suspended sediment, they also emphasized the challenges in regulatory barriers that hinder widespread adoption and comprehensive monitoring.

The assessment of Suspended Sediment Concentration (SSC) using various satellite systems has significantly advanced our understanding of sediment dynamics in aquatic environments. Among these satellites, Sentinel-2 has emerged as a valuable tool for SSC estimation due to its high-resolution multispectral capabilities and frequent revisit times. Sentinel-2's red and near-infrared bands are particularly useful in capturing sediment content variations, enabling the development of robust algorithms for SSC retrieval. Studies like Schiebe *et al.* (1992) have explored the relationship between SSC and satellite-derived reflectance values using Landsat-MSS data. Additionally, researchers like Reddy (1993) and Lodhi *et al.* (1997) have utilized Landsat-MSS data to develop empirical models linking radiance values to measured SSC. Myint and Walker (2002) extended their analysis to incorporate NOAA AVHRR and Orbview-2 SeaWiFS ocean color sensors, aiming to estimate near-surface suspended sediments and solids. Another example is the work of S. C. Liew *et al.* (2003), which focused on utilizing multiple wavelength bands for accurate SSC estimation in the Jinsha River, China. Notably, the success of satellite systems like MODIS, ALOS/AVNIR-2, Oceansat-2 OCM, and RapidEye in mapping SSC and turbidity confirms the broad applicability of satellite remote sensing for sediment assessment. Sentinel-2, with its enhanced spectral and spatial resolution, offers a promising avenue for accurate SSC estimation, demonstrated in studies by Wang *et al.* (2018) and Garg *et al.* (2020). Its ability to capture variations in SSC, as shown by Womber *et al.* (2021), showcases its potential for monitoring sediment distribution and changes in water bodies. Sentinel-2's role in sediment assessment is further validated by research such as that of Zhang *et al.*, (2022), which highlights its sensitivity to different spectral bands for SSC estimation in varying turbidity conditions. These studies collectively emphasize the critical role of satellite data, especially from Sentinel-2, in advancing our capacity to monitor and manage sediment concentrations in aquatic ecosystems, leading to improved water quality assessments and environmental management strategies.

The collective findings from the studies conducted by Lodhi (1998), Doxaran *et al.*, (2002), Robert *et al.* (2016), Liu *et al.* (2017), Marinho *et al.* (2021), and Kwon and Seo (2022) highlight

the value of conjunctive use of satellite-based remote sensing and field spectrometry techniques in assessing suspended sediment concentration (SSC) in aquatic environments. These studies have demonstrated the effectiveness of integrating high-resolution Spectroradiometer data with satellite imagery from sensors like Landsat-TM, SPOT-HRV, MODIS, and Sentinel-2 MSI. By correlating reflectance values obtained from both in-situ spectrometric measurements and satellite data, researchers have established robust relationships between spectral bands and SSC levels. The integration of near-infrared (NIR) and visible bands, coupled with advanced algorithms and models, has enabled accurate estimation of SSC, turbidity, and suspended particulate matter (SPM) concentrations. This conjunctive approach has bridged the gap between ground-based measurements and satellite observations, contributing to a deeper understanding of sediment dynamics and water quality. By effectively leveraging the strengths of both field and satellite technologies, these studies have paved the way for improved management strategies and environmental conservation efforts (Lodhi, 1998; Doxaran *et al.*, 2002; Robert *et al.*, 2016; Liu *et al.*, 2017; Marinho *et al.*, 2021; Kwon *et al.*, 2022).

A common thread throughout the studies is the reliance on spectral reflectance data, which forms the basis for deriving SSC estimates. This approach is well-founded, as the interaction between solar radiation and suspended particles imparts a unique spectral signature to water bodies, thus making reflectance a crucial indicator. For instance, Ritchie *et al.* (1976) observed that higher sediment concentrations lead to a shift in maximum reflection towards longer wavelengths, with a key estimation range between 700 and 800 nm. This shift is attributed to the scattering and absorption properties of suspended particles, showcasing the importance of spectral analysis.

Moreover, various authors emphasize the significance of specific wavelength bands, often in conjunction with spectral ratios, to enhance SSC estimation accuracy. Lodhi *et al.* (1997) note that the visible range (580-690 nm) provides valuable information for distinguishing sediment types, while the near-infrared (NIR) range (714-880 nm) proves accurate for sediment concentration estimation. This underscores the methodological precision required for effective SSC estimation and the careful selection of relevant spectral bands.

The studies also exhibit a trend toward using advanced techniques, such as machine learning algorithms and hyperspectral data, to enhance SSC estimation accuracy. For instance, Zhang *et al.* (2022) explore the correlation between the Normalized Difference Suspended Sediment Index (NDSSI) and suspended sediment, indicating its potential as a tool for quantifying sediment flux. The use of Artificial Neural Networks (ANN) in the work by Wang *et al.* (2008) and the comprehensive model developed by Kwon *et al.* (2022) showcase the integration of cutting-edge computational techniques.

However, methodological challenges and limitations are also evident across the studies. One recurring challenge is the potential saturation effect at higher SSC concentrations, which can hinder accurate SSC estimation in certain spectral bands. Sutari *et al.* (2020) explicitly highlight this challenge and emphasize the need for careful consideration of such issues in methodology development. Additionally, the studies often focus on specific regions or water bodies, raising questions about the generalizability of their findings to diverse environments.

Calibration and validation of the developed models emerge as pivotal aspects in remote sensing-based SSC estimation. While numerous studies highlight the strong correlations between reflectance values and SSC, limited attention is given to the accuracy of these correlations across varying conditions. Ensuring the reliability of the models through rigorous validation against ground truth data remains essential to establish the credibility of the proposed methodologies.

In conclusion, the compiled studies collectively highlight the significance of spectral reflectance data for remote sensing-based SSC estimation. The methodologies presented reflect a spectrum of techniques ranging from simple spectral ratio approaches to sophisticated machine learning algorithms. However, challenges such as saturation effects, limited generalizability, and the need for robust calibration and validation strategies warrant further attention. Addressing these methodological limitations will enhance the accuracy and reliability of SSC estimation methods, thereby supporting more informed water resource management decisions. As the field advances, the integration of various approaches and the exploration of hybrid methods could potentially lead to more accurate and versatile SSC estimation techniques.

### III. MATERIALS AND METHODS

The present research work primarily focuses on development of methodology for estimating suspended sediment concentration (SSC) over the surface of large water body. This chapter explains the details on data collection and methodology used to develop best fit model to estimate SSC in selected study area i.e. Mula Dam reservoir and further to spatial and temporal mapping of estimated SSC throughout the considered period.

#### 3.1 Details of the Study Area

Mula Dam, also known as Dnyaneshwar Sagar Reservoir, is a dam constructed on the Mula River at Baragaon Nandur in the Rahuri tahsil of Ahmednagar district in Maharashtra State, India. The Mula River originates from the eastern slopes of the Sahyadri mountain range in the Western Ghats, situated between Ratangad and Harishchandragad. This river is a tributary of the Pravara River, which, in turn, is one of the tributaries of the Godavari River, a major east-flowing river in India. The Mula Dam is located at latitude 19°20' to 19°35' N and longitude 74°25' to 74°36' E, as shown in Plate 3.1. Average annual stream flow of Mula River at Mula dam is 825.92 Mcum (Titkare, 2009). When the reservoir is at full supply level (FSL), its surface area covers 55 sq.km. The catchment area that feeds into the reservoir has an elongated leaf-like shape, encompassing a total area of about 2,275 sq. km. When the reservoir is at full supply level (FSL), its surface area covers 55 sq.km. The catchment area that feeds into the reservoir has an elongated leaf-like shape, encompassing a total area of about 2,275 sq. km.

The dam has a gross water storage capacity of 735.8 Mcum whereas live storage capacity is 608.45 Mcum and remaining 127.35 Mcum is dead storage capacity at the time of construction of Mula dam in 1972. In 2015, design live storage capacity is 540.073 Mcum and 486.020 Mcum is revised live storage capacity according to survey. Loss in capacity since impounding is 55.053 Mcum i.e. 10 per cent. Observed rate of siltation is 0.563 mm/ year (Anonymous, 2020).

The Mula Dam is a type of earthen dam that stretches over a length of 2857m. It has the Mula Right Bank Canal, which covers a distance of 58 km, and the Mula Left Bank Canal, which extends over 18 km. Together, these canals provide irrigation water to a total net Cultivable Command Area (CCA) of 808 sq.km; 707 sq.km for the right bank canal and 101 sq.km for the left bank canal. The Mula command area plays a critical role in meeting the domestic and irrigation requirements of several tehsils, including Rahuri, Newasa, Pathardi, and Shevgaon, within the Ahmednagar district.

At the bottom of the reservoir, there is a layer of detritus-mud in the littoral zone. The water from this dam is used for both drinking and irrigation purposes by the residents of Ahmednagar city and the surrounding villages, as reported by Anonymous (2009) and Anonymous (1976). Additionally, the reservoir is home to a diverse range of fish species, including economically significant and cultivable fish, as well as ornamental fish. Mula dam reservoir accommodates 19 fish species belonging to 10 families and 6 orders. Commonly found fish are Indian major carp, Striped

Snakehead, Indian Major Head, Common Carp, Labio, Tilapia, Rohu etc (Aher and Sonawane, 2015), which are generally used for human diet.

Assessing suspended sediment levels in the Mula Dam reservoir will be vital for multiple reasons. It will enable effective management of the dam's capacity, essential for maintenance planning. Monitoring sediment levels will ensure water quality for domestic and agricultural use while preserving the delicate ecosystem. Additionally, it will support adapted water treatment for drinking water and efficient irrigation practices, preventing clogs and sustaining soil health. Sustainable fisheries and the functionality of engineering structures will also rely on this assessment, ultimately benefiting both the community and the environment.

### **3.2 Data Collection of in-situ Suspended Sediment Concentration and Surface Reflectance**

Field surveys were conducted at the Mula Dam Reservoir on five clear sunny days using a sampling boat (shown in Plate 3.2) between October 2021 and February 2022. The primary objective of these surveys was to collect on-site spectral data and water samples for subsequent laboratory measurements of Suspended Sediment Concentration (SSC). A detailed record of the dates for collecting spectral response data and water samples is provided in Table 3.1.

The data collection dates were deliberately synchronized with the orbits of the Sentinel 2-A and -B satellites as they passed over the Mula Dam Reservoir. This alignment of field data collection with satellite passes is a critical aspect of the research methodology. The Sentinel 2 satellite acquisition plans available on the European Space Agency's website (<https://sentinels.copernicus.eu/web/sentinel/missions/sentinel-2/acquisition-plans>) were studied to decide the dates of data acquisition campaigns.

This practice of collecting field data in close proximity to satellite passes is a widely adopted approach in environmental monitoring research using RS and GIS. For instance, in a 2014 study by Montanher *et al.*, a similar method was employed. They maintained a time difference of four to nine days when selecting Landsat 5/TM satellite images to develop empirical models for estimating Suspended Sediment Concentration (SSC) in Amazonian rivers. This approach aimed to ensure the accuracy and quality of their research outcomes.

Furthermore, to enhance the quality and precision of their study results, Gare *et al.* in 2021 synchronized their field data collection dates with Sentinel 2 satellite passage over the study area. They took into consideration factors such as clear days and significant storm events, as these could significantly impact the research findings.

The data acquisition campaigns involved the use of various instruments, each serving a specific purpose. A summary of these instruments and their respective roles are given in Table 3.2.

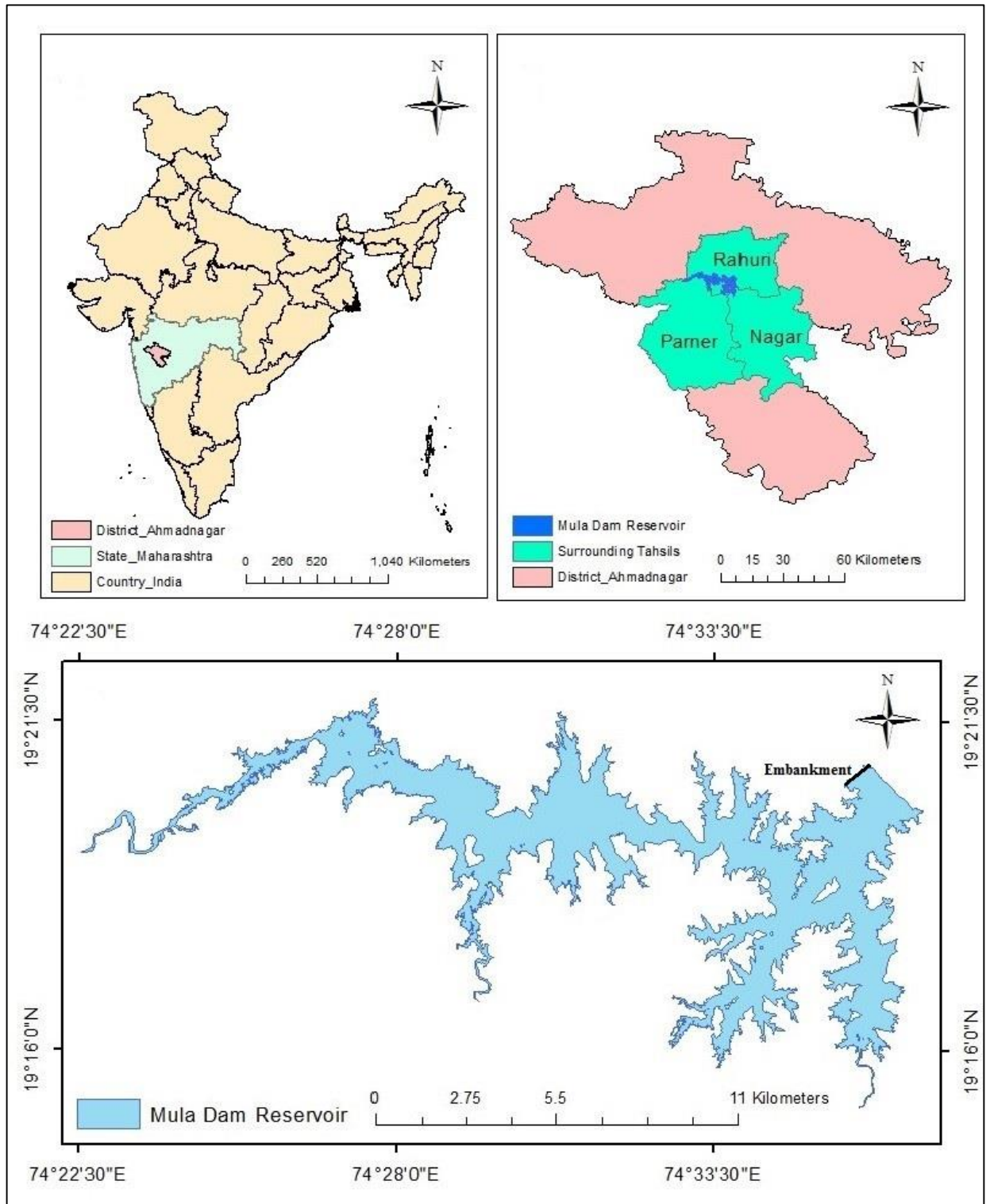


**Plate 3.1 Location map of the Mula Dam Reservoir**



**Plate 3.2: Boat used for collection of in-situ SSC samples and spectral data**

**Table 3.1 Data collection calendar**

<b>Data Acquisition Campaign</b>	<b>Date</b>	<b>Approx. distance traversed by boat (Kms.)</b>
1	31 <sup>st</sup> , October 2021	34
2	20 <sup>th</sup> , December 2021	30
3	04 <sup>th</sup> , January, 2022	32
4	03 <sup>rd</sup> , February 2022	48
5	18 <sup>th</sup> , February 2022	64

**Table 3.2 List of instruments/material carried to field along with its purpose**

<b>Sr. No.</b>	<b>Name of instrument or material</b>	<b>Purpose</b>
1.	One litre Sampler	To lift the water sample from water surface
2.	Plastic Container	To store collected water sample
3.	GPS – Montana 680	To capture location of sampling site.
4.	Spectroradiometer SVC HR – 1024i (with accessories)	To capture spectral response at sampling location.
5.	Cement block tied with rope	To measure the depth of reservoir at sampling location

### 3.2.1 Collection of Water Samples

A total of 121 water samples, using Simple Random Sampling (SRS) method, were collected from the surface layer (0-20 cm) of the Mula dam reservoir. To ensure precision in sampling depth, a 1-liter sampler (Plate 3.3) was used. This sampler, crafted in the Central Workshop at MPKV Rahuri, featured markings at the 20 cm depth to ensure that the samples were consistently collected at a depth not exceeding 20 cm. This is in alignment with research approach employed by previous researchers, *viz.* Womber *et al.* (2021), and Pitchaikani *et al.* (2020), who also conducted similar water sampling at a depth of 20 cm in both inland water bodies and coastal regions to

**Plate 3.3 Sampler for lifting water sample**

establish correlations between Suspended Sediment Concentration (SSC) and remote sensing reflectance.

Each sample was then carefully transferred into a plastic container, which was assigned a unique identification number synchronized with the corresponding GPS location number. This meticulous record-keeping ensured the traceability and organization of the collected samples for further analysis.

### 3.2.2 Determination of Suspended Sediment Concentration in Laboratory

Upon transporting the collected water samples to the laboratory, a preventative measure was taken to inhibit microbial growth by adding 2-3 drops of toluene to each sample. Subsequently, the water samples underwent a filtration process to isolate the suspended sediments present within them. This separation was achieved using Whatman Grade-1 cellulose filter paper, which had a pore size of 11  $\mu\text{m}$  and was pre-dried and pre-weighed, measuring 150 mm in diameter.

The procedure and calculations employed for determining Suspended Sediment Concentration (SSC) are provided in Appendix-A for reference. The SSC value for each water sample was determined through gravimetric analysis, and the sediment content was expressed as a proportion of the original sample in milligram per litre (mg/L), which is equivalent to parts per million (ppm). The concentration of suspended sediments was calculated using the following formula:

$$SSC = \frac{X_2 - X_1}{Y} \times 10^6 \quad \dots(3.1)$$

Where,

$X_2$  = Mass of sample paper and filter paper after oven drying (g)

$X_1$  = Dry weight of blank filter (g)

$Y$  = Volume of water sample (ml)

Photograph captured while filtering water sample containing suspended sediment, is shown in Plate 3.4 and traces of filtered SSC after oven drying in plate 3.5. Following the assessment of Surface Suspended Sediment Concentration (SSC) in Mula Reservoir, several fundamental statistical characteristics were computed utilizing standard formulae. These statistical measures included the Mean, Coefficient of Variation (CV), and Standard Deviation (SD) to provide a comprehensive understanding of the distribution and variability.

### 3.2.3 In-situ Surface Reflectance Acquisition using Spectroradiometer

Quantitative measurement of radiance, irradiance, reflectance or transmission generally termed as field spectroscopy. It acts as a bridge between in-situ or laboratory measurements of spectral reflectance of targeted object and is thus useful in the calibration of airborne or satellite sensors. It is useful in prediction of optimum spectral band and viewing its configuration. It acts

as a tool for the development, refinement and testing of models or functions relating biophysical attributes to remote sensing.



**Plate 3.4: Water sample collected from Mula dam reservoir kept for filtration**



**Plate 3.5: Traces of suspended sediment filtered by Whatman paper after oven drying**

The SVC HR-1024i Spectroradiometer, showcased in Plate 3.6, is a compact and high-performance field instrument. Covering wavelengths from 350 nm to 2500 nm across the UV, visible, near-infrared, and short-wave infrared regions, this device incorporates linear array technology and cooled detectors, ensuring exceptional wavelength and radiometric stability. With an internal memory capable of storing 500 scans and 1024 channels, it utilizes a diffraction grating with a silicon diode for precise wavelength stability, while 256 thermostatically controlled detectors and 256 extended detectors provide radiometric stability. Boasting the ability to read 1024 spectral bands, this instrument is impressively fast, acquiring spectra in just 1 millisecond.

The SVC HR-1024i offers standalone operation through its serial port, providing real-time spectral display and hard disk data transfer options. It comes with two versions of SVC's

software - one compatible with desktop or laptop computers running Windows XP and the other supporting Personal Digital Assistants (PDAs) using Windows Mobile Software for Pocket PC. The DAP Technologies Microflex 2240X PDA, included with the SVC HR-1024i, is rugged, reliable, and lightweight. Its sunlight-readable color display allows real-time viewing of spectral data, and it features Bluetooth wireless communication and embedded GPS functionality. The lens barrel options include standard 4°, 8°, or 14° Field of View (FOV) or a 25° optional armored fiber optic version. Figure 3.1 illustrates a schematic representation of the 25° FOV lens attached to the optical fiber. Data are stored in ASCII format for easy transfer to other software. All the specifications of SVC HR 1024i Spectroradiometer are given in the table 3.3.

The SVC HR 1024i Spectroradiometer is equipped with a "Labsphere" compressed "Spectrolon" white panel, which serves as a reference for the Spectroradiometer. These "Spectrolon" white panels offer several advantages for field applications and remote sensing data collection such as durability and washability, high reflectance values, approximately 95% to 99%, and spectral flatness across the UV- Vis-NIR spectrum, resilience to harsh environmental conditions and chemical inertness.

Reflectance measurements involve scanning a reference (Spectrolon white panel) and calculating the ratio between the target scan and the reference. To minimize errors caused by changes in atmospheric conditions, measurements over the Spectrolon panel and the target were taken with minimal time lag. The spectral data were converted into reflectance, representing the ratio of energy reflected off the target to the energy incident on the target, with reference to the Spectrolon panel before and immediately after each measurement.

This calibration method effectively eliminates all parameters these are multiplicative in nature, such as spectral irradiance of the illumination source and optical properties of the Spectroradiometer, which are present in both the spectral response of a reference sample and the target material. This approach minimizes potential noise from external factors like illumination.

Photographs of the Spectrolon or reference panel, along with the PDA, are shown in Plate 3.7, while Plate 3.8 displays an image captured during the spectral response measurement of the Spectrolon panel. The procedure used for capturing spectral response from the targeted object is given in Appendix – B.

In order to ensure the accuracy and reliability of spectral data collection for satellite analysis, several precautions were meticulously employed throughout this research. One of the foremost challenges in remote sensing lies in preventing spectral interference between the land and the water body under scrutiny. To address this, spectral responses were systematically captured at sampling locations positioned a minimum of 20 m away from the reservoir's shoreline, effectively reducing any potential contamination from the land's spectral characteristics.



**Plate 3.6: SVC (Spectra Vista Corporation) HR-1024i (High Resolution) portable field Spectroradiometer with optical fibre attached.**



**Plate 3.7: Spectrolon or reference panel, along with the PDA**



**Plate 3.8 Capturing spectral response of reference/ Spectrolon panel**

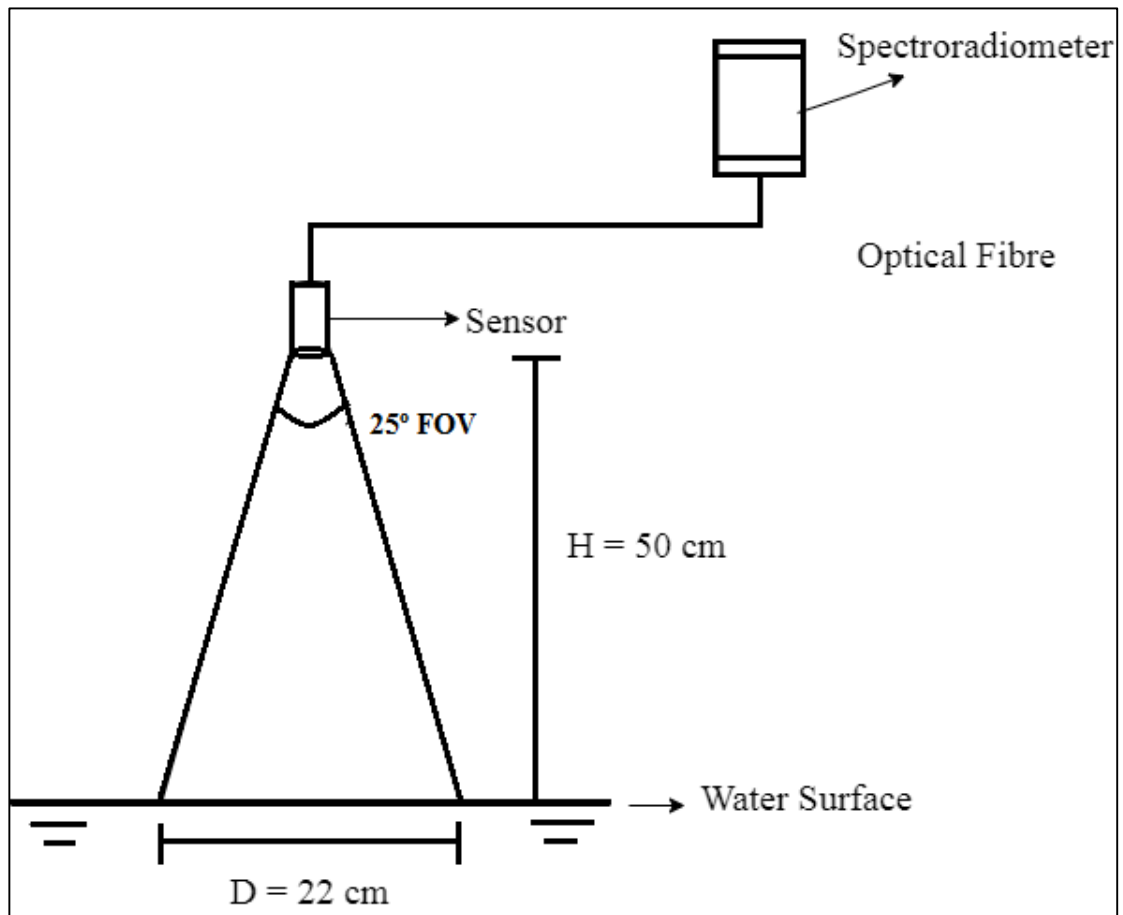


**Figure 3.1 Schematic representation of  $25^\circ$  Field of View (FOV) for lens attached to Optical fibre**

To avoid effects low intensity solar radiation on the experiment, spectral responses were captured between 11 am to 3 pm. Moreover, to minimize turbulence and disturbances on the water surface, the boat's engine was deliberately powered off during data collection, ensuring that measurements were conducted under tranquil water conditions. Specific side of the boat devoid of shadows was chosen for measurements to maintain consistent lighting conditions. To eliminate the influence of bottom reflectance, points having water depth greater than 2 m were chosen.

The research methodology adopted in this study for capturing the spectral response of the target object drew upon previous works, the research conducted by Kadam (2014) and Khaire (2020), providing valuable insights for data collection. The spectral responses obtained from each water sample were rigorously analysed to identify the optimal wavelength range representing Suspended Sediment Concentration (SSC), which was found to be between 350 to 900 nm. Plate 3.9 features photograph taken during the spectral response data collection process from the surface of Mula dam reservoir.

### 3.2.4 Recording Coordinates of Sampling Sites

A GPS Montana 680, available in the Department of Soil and Water Conservation Engineering, was used for precise location tracking during the data collection process. This advanced device offers a comprehensive set of features, including a 3-axis tilt-compensated

compass, a barometric altimeter, and access to both GPS and GLONASS satellite systems, enhancing the accuracy of positioning. It provides users with the capability to create waypoints, record tracks and routes, and even locate geocaches. Moreover, the device boasts a dual battery system, allowing users to choose between a lithium-ion pack or traditional AA batteries, providing flexibility and extended usage in the field.

The recorded sampling point locations, each corresponding to a unique sample number, were stored within the GPS device. Subsequently, these location data were exported to Google Earth Pro, a popular geospatial software, and saved with the '.kml' file extension. To integrate this geographical information into the study, these '.kml' files were then converted into a layer using the conversion tool within ArcMap, a prominent geographic information system (GIS) software. Finally, these layers were overlaid onto the shapefile representing the boundaries of the Mula dam reservoir, facilitating a comprehensive spatial analysis and visualization of the collected data.



**Plate 3.9: Capturing spectral response from the surface of Mula Dam reservoir.**

### 3.2.5 Satellite Data Acquisition

Sentinel 2 Multispectral Imager (MSI), a constellation of two satellites (A and B) in sun-synchronous polar orbit, targets the land and coastal zone monitoring by providing high spatial resolution (10 – 60 m) and temporal resolution of 5 days. MSI has 13 bands from visible to shortwave infrared (SWIR) spectral regions, providing appropriate data source to document concentration of suspended particulate material to variations in coastal and inland waters.

In order to ensure the accuracy and reliability of spectral data collection for satellite analysis, several precautions were meticulously employed throughout this research. One of the foremost challenges in remote sensing lies in preventing spectral interference between the land and the water body under scrutiny. To address this, spectral responses were systematically captured at sampling locations positioned a minimum of 20 m away from the reservoir's shoreline, effectively reducing any potential contamination from the land's spectral characteristics.

**Table 3.3: Specifications of SVC HR 1024i Spectroradiometer**

Sr. No.	Particular	Details
1.	Spectral Range	350 nm – 2500 nm
2.	Internal Memory	1000 Scans
3.	Channels	1024
4.	Bandwidth	$\leq 1.5$ nm, 350 – 1000 nm
5.	Wavelength reproducibility	0.1 nm
6.	Internal Digital Camera	Yes
7.	Internal GPS	Yes
8.	Reference Material	Spectrolon (Dimension 12.5 cm $\times$ 12.5 cm)
9.	Software for spectral analysis	SVC HR-1024i
10.	FOV (Optical Fibre)	25°
11.	Diameter of Scene	44 cm for height 1m above surface
12.	Height of Spectral measurement	50 cm ( Scene Dia. – 22 cm)

Sentinel 2 (A/B) level-1C (Top-of-atmosphere) and level-2A (Bottom-of-atmosphere) are available for users. The level-2A processing of Sentinel 2 MSI includes a scene classification and an atmospheric correction applied to Top-of-atmosphere (TOA) level-1C orthoimage products. Level-2A products are generated by Payload Data Ground Segment (PDGS) using Sen2Cor processor. Sen2Cor is a processor for Sentinel 2 level-2A product generation and formatting; it performs the atmospheric, terrain and cirrus correction of TOA level-1C input data. Sen2Cor creates Bottom-of-atmosphere, optionally terrain and cirrus corrected reflectance images which are freely available for downloading at website provided by European Space Agency (<http://scihub.copernicus.eu/dhus/>).

The present research aims at development of equation for synoptic and quick retrieval of suspended sediment concentration therefore, readily available Bottom-Of Atmosphere (BOA) Level 2A (L2A) corrected reflectance images were used to conduct this research. The details of each band and wavelength regions are given in table 3.4. Pre-processed (Radiometrically, Geometrically and Atmospherically corrected) Level-2A image products of Sentinel 2 satellite images of the required dates given in table 3.1 (during 31<sup>st</sup> October, 2021 and 18th February, 2022) were downloaded. Further processing of downloaded satellite images was performed in ArcGIS. False Colour Composites (FCC) of the downloaded satellite images are shown in Appendix – C.

Information on band values was extracted from the BOA reflectance (in fraction) values with a factor of 10000. To obtain band values, values of band indices and band combinations calculated using ‘raster calculator’ at desired locations, recorded by GPS locations were

superimposed on Sentinel 2's band image and 'extract values to table' feature of Geostatistical tool of ArcMap was used.

Recent studies have harnessed Sentinel-2 data for various purposes. Garg *et al*, 2020 used the Sentinel-2 multispectral remote sensing data directly at Haridwar, Kanpur, Prayagraj, and Varanasi stretches of the Ganga River for detection of turbidity changes. Li *et al*, 2018, evaluated of Sentinel-2A surface reflectance derived Using Sen2Cor in North America and suggested the use of Sen2Cor surface reflectance of bands except B01, B02, and B09 for the quantitative applications. In this study, Sen2Cor surface reflectance of bands B03, B04, B05, B08, B8A are used which are free from aerosol scattering and WV absorption according to Li *et al*, 2018. The Sen2cor performs the atmospheric correction of Top-Of Atmosphere Level 1C (L1C) product to produce Bottom-Of Atmosphere (BOA) Level 2A (L2A) corrected reflectance images (Muller *et al*. 2013). Gare *et al*, 2021 used Bottom-Of Atmosphere (BOA) Level 2A (L2A) corrected reflectance images because it was more readily available and confirmed its suitability for water quality analysis.

### 3.2.6 Identification of Mula Dam Reservoir in Satellite Imagery

The Normalized Difference Water Index (NDWI), as defined by McFeeters in 1996 through equation (3.2), was used in delineating the boundaries of the Mula Dam reservoir and identifying water pixels on various dates.

$$NDWI = \frac{Green - NIR}{Green + NIR} \quad \dots(3.2)$$

Here, 'Green' and 'NIR' represent reflectance values in the green and near-infrared (NIR) bands, respectively. The choice of these specific wavelength regions was grounded in the fact that water exhibits the highest reflectance in the visible (green) region while absorbing all energy in the NIR region of the electromagnetic spectrum. NDWI values range from -1 to +1, with values exceeding 0 signifying water in the NDWI raster. Leveraging NDWI allowed for precise measurement of the surface area coverage of the Mula Dam reservoir. Furthermore, NDWI layers for each date were transformed into shape files, enabling the extraction of the study area on different bands of the Sentinel-2 (Bottom-of-Atmosphere) images corresponding to each date.

## 3.3 Development of Spectral Response using Spectroradiometer and Sentinel-2 images

### 3.3.1 Spectral Signature using Spectroradiometer

The spectral responses, obtained through three replications, were transferred from the PDA (Personal Digital Assistant) to the SVC (Spectral Vision and Classification) software. Within the SVC software, these responses were processed through merging, overlapping, and resampling techniques. Spectral reflectance values at each sampling location were then calculated across the entire spectral range, utilizing 1 nm intervals, as per Equation (3.3). Subsequently, line graphs depicting reflectance values against wavelength were generated for each sampling location using

MS-Excel. These line graphs essentially represent the spectral signatures of each sample, offering insights into the composition and characteristics of the suspended sediments present in the samples. Spectral Signatures captured by using SVC – 1024i Spectroradiometer are given in Appendix D.

$$R(\%) = \frac{SI_{\text{target}}}{SI_{\text{reference}}} \times 100 \quad \dots(3.3)$$

Where,

R = Spectral reflectance of target in per cent,

$SI_{\text{target}}$  = Spectral Irradiance of *target*

$SI_{\text{reference}}$  = Spectral Irradiance of reference panel

**Table 3.4: Sentinel 2 Bands with their wavelength region, central wavelength and spatial resolution**

(Source: [https://developers.google.com/earthengine/datasets/catalog/COPERNICUS\\_S2](https://developers.google.com/earthengine/datasets/catalog/COPERNICUS_S2) )

Band	Wavelength region	Central Wavelength (nm)	Spatial resolution	Wavelength Range (nm)
Band - 1	Coastal Aerosol	443	60	433-453
Band - 2	Blue	490	10	458-523
Band - 3	Green	560	10	543-578
Band - 4	Red	665	10	650-680
Band - 5	Red Edge 1	705	20	698-713
Band - 6	Red Edge 2	740	20	733-748
Band - 7	Red Edge 3	783	20	773-793
Band - 8	NIR	842	10	785-900
Band - 8A	Red Edge 4	865	20	855-875
Band - 9	Water Vapour	945	60	935-955
Band - 10	SWIR – Cirrus	1135	60	1360-1390
Band - 11	SWIR	1690	20	1565-1655
Band - 12	SWIR	2190	20	2100-2280

### 3.3.2 Spectral Signature using Sentinel-2 Images

The Sentinel-2 satellite provides spectral data in the form of band images where each pixel contains a digital number scaled by a factor of 10,000. Reflectance values for specific bands (Blue, Green, Red, Red Edge 1, Red Edge 2, Red Edge 3, NIR, and Red Edge 4), covering wavelengths ranging from 350 to 900 nm, were extracted for each pixel in which sampling location lies. These extracted reflectance values for these bands were then graphically represented by plotting them against the central wavelength for each band, as given in table 3.4.

### 3.3.3 Comparison of Spectral Signature captured using Sentinel-2 (BOA) and Spectroradiometer

To facilitate a comparison between the spectral responses captured by the Spectroradiometer and Sentinel-2 (Bottom-of-Atmosphere), the spectral reflectance obtained from the Spectroradiometer, with measurements at 1 nm intervals, was transformed into band values. This transformation was achieved by averaging the spectral response within the specific wavelength range corresponding to each band discussed earlier. The spectral range considered for each band is as given in table 3.4.

Subsequently, the spectral responses were graphically represented by plotting them against the central wavelength of each band. This comparative analysis was carried out using MS-Excel, where one line on the graph represents the spectral response from Sentinel-2, and another line represents the spectral response obtained from the Spectroradiometer. These line graphs effectively illustrate the similarities and differences between the two datasets, aiding in the assessment of the spectral consistency and accuracy between the two measurement methods. Values of eight bands used for plotting the line graph for comparing the spectral response obtained by Spectroradiometer and Sentinel – 2 Multispectral Imager are given in Appendix – E. These graphs comparing spectral response obtained by Spectroradiometer and Sentinel – 2 Multispectral Imager are given in Appendix – F.

## 3.4 Selection of Spectral Bands Indices and Band Combinations for Estimation of SSC

The practice of using multiband combinations and spectral ratios/ indices in empirical models through regression analyses has been well-established in the literature, as demonstrated by studies such as Pereira *et al.* (2017), and Wang *et al.* (2018). Utilizing band ratios offers a significant advantage by helping to mitigate the influence of atmospheric conditions and bidirectional reflectance distribution function effects, including Sun glint on the surface of water, as captured in the spectral response (Doxaran *et al.*, 2002; Sokoletsky *et al.*, 2016). This approach effectively reduces the impact of data noise, enhancing the clarity and reliability of the spectral information related to water properties (Larson *et al.*, 2018). In essence, employing spectral ratios and indices in empirical models represents a valuable strategy for improving the accuracy and robustness of water quality assessments and related analyses.

### 3.4.1. Selection of Spectral Indices

The selection of spectral indices is a crucial step in correlating with suspended sediment concentration in water bodies and lakes. In this study, various indices taken from the literature such as the Normalized Difference Suspended Sediment Index, Normalized Suspended Material Index, Modified Normalized Difference Suspended Sediment Index, and Revised Normalized Difference Suspended Sediment Index were employed. These indices were calculated using two datasets:

- i) Spectral readings recorded at the surface of the Mula reservoir using the Spectroradiometer SVC 1024i using Microsoft Excel.
- ii) Corresponding bands of Sentinel-2 images, utilizing the raster calculator tool in ArcMap.

Reflectance values from Sentinel-2 data are originally obtained as digital numbers, and to convert them into reflectance, these are divided by 10,000, as specified by Munir *et al.* (2019), through the raster calculator in ArcMap. Since these reflectance values are in fraction form, they are further converted into percentages by multiplying them by 100. This conversion ensures consistency with spectral reflectance values obtained from the Spectroradiometer, allowing for meaningful and consistent comparisons between the two datasets.

#### 3.4.1.1 Normalized Difference Suspended Sediment Index (NDSSI)

Hossain *et al.* (2010) observed that the Blue band (450 – 515 nm) and NIR band (750 – 900 nm) from Landsat imagery were particularly sensitive to water and water transparency (turbidity). In the case of Sentinel-2 data, the wavelength range of the Blue and NIR bands is quite similar, spanning from 458 to 523 nm and 785 to 900 nm, respectively, which closely aligns with the Landsat bands (Blue: 450 nm to 520 nm and NIR: 760 nm to 900 nm).

To assess water quality and sediment concentration, Equation 3.4, known as the Normalized Difference Suspended Sediment Index (NDSSI) and developed by Hossain *et al.* (2010), was used. NDSSI is conceptually similar to NDVI (Normalized Difference Vegetation Index) but tailored for water quality assessment. Like NDVI, NDSSI values also fall within the range of -1 to 1. A higher NDSSI value indicates lower suspended sediment concentration, indicating clearer and less turbid water, while a lower NDSSI value suggests higher sediment concentration, signifying more turbid water.

$$\text{NDSSI} = \frac{\text{Blue} - \text{NIR}}{\text{Blue} + \text{NIR}} \quad \dots(3.4)$$

#### 3.4.1.2 Normalized Suspended Material Index (NSMI)

Much like the Normalized Difference Suspended Sediment Index (NDSSI), Arisanty and Saputra (2017) introduced another index known as the Normalized Suspended Material Index (NSMI) to quantify Suspended Sediment Concentration (SSC). NSMI is calculated by using Red (650-680 nm), Green (543-578 nm), and Blue (458-523 nm) bands in a manner similar to NDSSI.

The NSMI, as determined by Equation 3.5, offers a transforming index where higher values correspond to higher SSC. In other words, as the NSMI value increases, it indicates a higher concentration of suspended sediment in the water. This index, like NDSSI, can provide a valuable means of quantifying and assessing the levels of suspended sediment in aquatic environments.

$$\text{NSMI} = \frac{(\text{Red} + \text{Green}) - \text{Blue}}{\text{Red} + \text{Green} + \text{Blue}} \quad \dots(3.5)$$

### 3.4.1.3 Modified Normalized Difference Suspended Sediment Index (Modified NDSSI)

The Modified Normalized Difference Suspended Sediment Index (Modified NDSSI) is an index introduced by Khaire (2020) for the quantification of suspended sediment concentration. It incorporates additional spectral bands compared to the original NDSSI, specifically the Red region (650-680 nm), which is then summed with the Near-Infrared (NIR) region (785-900 nm).

Similar to the NDSSI and other related indices, the Modified NDSSI (Eqn. 3.6) follows the same principle: higher index values indicate lower suspended sediment concentration in the water, and lower values suggest higher levels of suspended sediment.

$$\text{Modified NDSSI} = \frac{\text{Blue} - (\text{Red} + \text{NIR})}{\text{Blue} + (\text{Red} + \text{NIR})} \quad \dots(3.6)$$

### 3.4.1.4 Revised Normalized Difference Suspended Sediment Index (Revised NDSSI)

The study conducted by Khaire (2020) introduced a revision to the Normalized Difference Suspended Sediment Index (NDSSI) by incorporating reflectance data from the narrower wavelength region known as the Red Edge (670 – 830 nm) (Eqn. 3.7).

$$\text{RNDSSI} = \frac{\text{Blue} - \text{Red Edge}}{\text{Blue} + \text{Red Edge}} \quad \dots(3.7)$$

However, in this study instead of Red Edge region, Sentinel-2 imagery offers four narrower bands within this region: Red Edge 1 (698-713 nm), Red Edge 2 (733-748 nm), Red Edge 3 (773-793 nm), and Red Edge 4 (855-875 nm). The subdivision of the Red Edge region prompted the calculation of the Revised NDSSI (RE1) as given in equation 3.8, with a specific focus on the Red Edge 1 band. This modification allows for a more targeted and precise assessment of suspended sediment concentration based on the unique spectral characteristics observed in the Red Edge 1 band.

$$\text{Revised NDSSI (RE1)} = \frac{\text{Blue} - \text{Red Edge 1}}{\text{Blue} + \text{Red Edge 1}} \quad \dots(3.8)$$

Values of all the indices derived from the spectral response received by Spectroradiometer and Sentinel – 2 MSI are given in the Appendix – G.

## 3.4.2 Selection of Band Combinations

The present study builds upon a body of research that has established correlations between various combinations of spectral bands and suspended sediment concentration (SSC) in water bodies, rivers, or oceans. These correlations are based on the spectral responses captured by diverse sensors mounted on different platforms, as discussed in Review of Literature.

In this study, a range of band combinations was used to establish relationships with SSC. During the calibration phase, certain band ratios or combinations exhibited strong performance. These selected band ratios or combinations were subsequently tested for validation purposes, where they were used to estimate SSC using a separate validation dataset.

The performance of these chosen band ratios or combinations was rigorously evaluated using various statistical methods, as explained in upcoming sections. The specific band ratios or combinations that demonstrated noteworthy performance are summarized in Table 3.5. This meticulous process ensures the reliability and accuracy of the selected spectral indices for estimating SSC, contributing to a deeper understanding of sediment dynamics and water quality in the study area. Computed values of these band combinations are given in Appendix – F.

**Table 3.5: Various band combinations used to correlate with SSC in Mula dam reservoir**

Sr. No	Band Ratio/ Combination	Reference/ Inference
1.	$(\text{Red} + \text{Green}) / 2$	Sutari <i>et al.</i> , 2020
2.	$(\text{Red} + \text{Green} + \text{Red Edge 1}) / 3$	Inspired by Sutari <i>et al.</i> , 2020
3.	$\text{Green} - \text{Red Edge 1}$	Through observation
4.	$(\text{Green} \times \text{Red edge 1}) / \text{Red}$	Based on multiplicative approach attempted by Kazemzadeh <i>et al.</i> , 2023

### 3.5 Bifurcation of Data Set into Calibration and Validation Data Set

In this study, a total of 121 samples were collected from the surface of the Mula Dam reservoir during five field campaigns. These samples were numbered sequentially, with the first sample being labelled as 1 and the last as 121. However, 16 of these samples were rejected due to manual errors during the recording of their spectral responses.

Out of the remaining 105 samples, 84 samples (approximately 80%) were designated for use in establishing the relationship between band indices/ combinations and their corresponding Suspended Sediment Concentration (SSC). The remaining 21 samples (around 20%) were set aside to validate the developed relationship. This calibration-validation split of 80:20 is a common practice and follows the approach used by Zhan *et al.* (2017) in their study.

To select the specific calibration dataset of 84 samples and the validation dataset of 21 samples, a random number table was used. This randomization process helpful to ensure that the datasets are representative and unbiased, enhancing the reliability and robustness of the relationships established between the spectral indices/ combinations and SSC.

### **3.6 Development of Relationships Between Spectroradiometer and Satellite Indices, Band Functions and Observed SSC using Calibration Data Set**

To build a model or function which can estimate suspended sediment with greater accuracy, it is necessary to develop interrelationship between the set of variables prepared from collected data i.e. observed values of suspended sediment concentration of 84 samples separated for calibration and corresponding values of Spectroradiometer and/ or Sentinel 2 satellite derived band indices/ combinations.

The concept behind developing these interrelationships is based on ‘transitive relations’. Transitive relations are binary relations in discrete mathematics represented on a set such that if the first element is linked to the second element and the second component is associated with the third element of the given set then the first element must be correlated to the third element. A relation exhibits transitivity if and only if the relation between X and Y, coupled with the connection between Y and Z, inevitably implies a connection between X and Z (Arstila, 2012).

Thus, to better understand the application of this theory of ‘transitive relation’ in the present research let us consider that,

x = observed values of suspended sediment concentration

y = values of band indices or combination obtained from Spectroradiometer

z = values of band indices or combination obtained from Sentinel – 2 satellite image

The detail procedure followed to set up such relations between the set of variables prepared from collected data is discussed in the following sections.

#### **3.6.1 Relationship Between Various Spectroradiometer Indices, Band Combinations and Observed SSC**

Various indices and band combinations, as discussed in section 3.4, were calculated from the spectral data captured by the Spectroradiometer SVC - 1024i at each location where samples for determining Suspended Sediment Concentration (SSC) were collected. The next step was to find the most suitable coefficients for estimating SSC in the Mula Dam reservoir using these band indices/ band combinations. The procedure involved plotting the obtained values of these indices against the corresponding SSC values from the calibration dataset.

To establish the relationship between the correlated band indices/ band combinations and in-situ SSC measurements, different regression equations were tried. These equations included linear, exponential, logarithmic, polynomial, and power functions. The coefficients associated with the equation that achieved a high Coefficient of Determination ( $R^2$ ) value were considered suitable for estimating SSC in the Mula Dam reservoir. This method is akin to the approach used by Hossain *et al.* (2010), who correlated NDSSI with observed SSC to develop a relationship having power equation for estimating SSC in the Mississippi River in the USA.

In this process, the observed SSC was treated as the independent variable (x), while the corresponding band index/ band combination value was treated as the dependent variable (y). This methodology allows for the establishment of a quantitative relationship that can be used to estimate SSC based on spectral data, contributing to the understanding of sediment dynamics and water quality in the study area.

### **3.6.2 Relationship between Spectroradiometer Indices, Band Functions and Satellite Indices, Band Functions**

In the next step of the study, the aim was to establish a relationship between spectral data obtained from the Spectroradiometer SVC - 1024i and Sentinel-2's Bottom of the Atmosphere (BOA) satellite image. The objective was to find a suitable equation that could effectively convert satellite-derived band indices/ band combinations (represented as "y") to their corresponding values derived using the Spectroradiometer (represented as "x"). To achieve this, the values of the satellite-derived band indices/ band combinations were plotted against their corresponding values derived using the Spectroradiometer. This graphical analysis allowed for the examination of the relationship between the two sets of data and served as the basis for determining the appropriate equation for converting satellite-derived data to Spectroradiometer-derived data.

The set of two calibrated equations obtained through the methods discussed in sections 3.6.1 and 3.6.2 are collectively referred to as 'spectral integration' for a specific band index/ band combination. These spectral integrations are calibrated using 80 percent of the data points. This means that 80 percent of the data are used to establish the relationships between the Spectroradiometer-derived and Sentinel-2 satellite-derived band indices/ combinations. Once these spectral integrations are calibrated, they are capable of estimating band indices/combinations in line with the Spectroradiometer when Sentinel-2 satellite-derived band indices/combinations are substituted into the equations obtained from the methodology discussed in section 3.6.2. Subsequently, these estimated values are further substituted into the equations obtained from the methodology discussed above. This iterative process ultimately allows for the prediction of suspended sediment concentration for the remaining 20 percent of data points that were set aside for validation.

### **3.7 Validation and Performance Evaluation**

Moriasi et al. (2007) recommended the use of both graphical techniques and quantitative statistics for model evaluation, to assess the accuracy of simulated data when compared to measured data and constituent values. The methodology for validating and evaluating the performance of the developed equations involved comparing observed SSC with estimated SSC. This process allowed for an assessment of how well the equations performed in estimating SSC in the Mula Dam reservoir, providing a comprehensive understanding of the accuracy and reliability of the model's predictions.

### 3.7.1 Graphical Method or Visual Interpretation

During the validation process, the best-fit equations that achieved higher values of the Coefficient of Determination ( $R^2$ ) from the calibration phase were employed to estimate Suspended Sediment Concentration (SSC) using the 20 percent of data points that were set aside for validation. The observed SSC values were then compared with the estimated SSC values. To facilitate this comparison, a line graph was plotted to visually interpret and analyse the relationship between observed and estimated SSC.

This graphical technique, as described by ASCE in 1993, enables a visual comparison between the simulated and measured constituent data. It offers an initial overview of the model's performance and is an essential component of appropriate model evaluation, as highlighted by Legates and McCabe in 1999. Pitchaikani *et al.* (2019) also utilized this method for visually interpreting the association between observed and estimated SSC in the Hooghly estuary and West Bengal coastal waters, underscoring its importance in model evaluation and validation processes.

### 3.7.2 Slope and y-intercept

The slope and y-intercept of the best-fit regression line play a crucial role in assessing how well simulated data align with measured data. These parameters provide valuable insights into the relationship between simulated and measured values. The slope of the regression line indicates the relative relationship between simulated and measured values. A slope of 1 implies that the model perfectly reproduces the magnitudes of measured data, while a slope different from 1 suggests a scaling factor. The y-intercept of the regression line indicates whether there is a lag or lead between model predictions and measured data. A y-intercept of 0 would suggest that the data sets are perfectly aligned, while a non-zero y-intercept suggests a time offset or misalignment between the two datasets.

Typically, the slope and y-intercept are examined under the assumption that the relationship between measured and simulated values is linear. This assumption implies that all error variance is contained in the simulated values, assuming that measured data are error-free.

To assess how well estimated Suspended Sediment Concentration (SSC) matches with observed SSC, a linear trend line was added to the scatter plot of observed SSC (y) and estimated SSC (x). The linear equation in the form of  $y = a + b x$  was used, where 'a' and 'b' are coefficients. For a perfect linear relationship between 'x' and 'y,' the coefficients 'a' and 'b' should ideally have values of '0' and '1,' respectively. Analysing the relationship in this manner allows for a direct comparison of results obtained from different equations developed to estimate SSC, providing insights into the model's performance and alignment with observed data.

### 3.7.3 Performance Evaluation using Significance tests

#### 3.7.3.1 't-test' for testing the Coefficients of Linear Equation

The linearity of the linear relationship can be determined by calculating the t-test statistic. The t-statistic helps to determine how linear, or nonlinear, this relationship is. The hypothesis formulation in relation to determining the relationship between dependent and independent variables and how the value that coefficients ('a' and 'b') take to quantify the relationship is presented below.

The observed and estimated SSC values were treated as dependent (y) and independent (x) variables respectively for linear regression,

$$y = a + b x \quad \dots(3.9)$$

Null hypothesis,  $H_0$ :  $a = 0$  and  $b = 1$

Alternate hypothesis:  $a \neq 0$  and  $b \neq 1$

Hypothesis test: t (a) and t (b) for (n-2) degrees of freedom at 5 % level of Significance (LOS)

$$t (a) = | a / SE (a) | \quad \dots(3.10)$$

$$t (b) = | (b-1) / SE (b) | \quad \dots(3.11)$$

If,

$t (a) < t$ - table value of 2.18 at 5 % LOS then 'a' is insignificant

$t (b) > t$ - table value of 2.18 at 5 % LOS then 'b' is insignificant

and the hypothesis is accepted.

#### 3.7.3.2 Student's t-test for Testing the Difference of Mean

The mean of observed and estimated SSC values were compared using student's t-test (Eqn. 3.12) for (n-2) degrees of freedom at 5% level of significance. If the  $t_{cal}$  is less than t-table value for 19 degrees of freedom at 5% level of significance indicates the difference between means of observed and estimated is insignificant.

$$t_{cal} = \frac{|\bar{E} - O|}{\sqrt{S^2 EO/n}} \quad \dots(3.12)$$

The detail procedure of applying Linear Regression t-test and Student's t-test presented in Appendix - H along with illustration.

### 3.7.4 Performance Evaluation using Statistical Indicators

#### 3.7.4.1 Coefficient of Determination ( $R^2$ )

The coefficient of determination, given by equation 3.13, is the square of the correlation coefficient (r). The correlation coefficient, is an index of the degree of dependency between observed and simulated data. If  $r = 0$ , no linear relationship exists. If  $r = 1$  or  $-1$ , a perfect positive or negative linear relationship exists. Similarly,  $R^2$  describes the proportion of the variance in measured data explained by the model.  $R^2$  ranges from 0 to 1, with higher values indicating less

error variance, and typically values greater than 0.5 are considered acceptable (Santhi *et al.*, 2001, Liew *et al.*, 2003). Although  $R^2$  has been widely used for model evaluation, these statistics are oversensitive to high extreme values (outliers) and insensitive to additive and proportional differences between model predictions and measured data (Legates and McCabe, 1999).

$$R^2 = \left( \frac{\sum_{i=1}^n (O_i - \bar{O})(E_i - \bar{E})}{\sqrt{\sum_{i=1}^n (O_i - \bar{O})^2} \sqrt{\sum_{i=1}^n (E_i - \bar{E})^2}} \right)^2 \quad \dots(3.13)$$

#### 3.7.4.2 Root Mean Square Error (RMSE)

The Root Mean Square Error (RMSE) is a measure of the difference between values predicted by a model and the values actually observed from the environment that is being modelled. These individual differences are also called residuals, and the Root Mean Square Error serves to aggregate them into a single measure of predictive power. RMSE calculate by Equation 3.14, measure how much error there is between two data sets. RMSE is one of the commonly used error index statistics (Singh *et al.*, 2004). It is commonly accepted that the lower the RMSE the better the model performance.

$$RMSE = \sqrt{\frac{\sum_{i=1}^n (O_i - E_i)^2}{n}} \quad \dots (3.14)$$

#### 3.4.7.3 Mean Absolute Percentage Error (MAPE)

The mean absolute percentage error (MAPE) given by Equation 3.15, is one of the most popular measures of the forecast accuracy. This approach is useful when the size of a prediction variable is significant in evaluating the accuracy of a prediction (Khair *et al.*, 2017). MAPE indicates how much error in predicting compared with the real value. The MAPE (Mean Absolute Percent Error) measures the size of the error in percentage terms.

$$MAPE = 100 \times \frac{1}{n} \times \sum_{i=1}^n \left| \frac{O_i - E_i}{O_i} \right| \quad \dots(3.15)$$

#### 3.4.7.4 Nash Sutcliffe Model efficiency coefficient (NSE)

The Nash-Sutcliffe efficiency (NSE) given by Equation 3.16, is a normalized statistic that determines the relative magnitude of the residual variance compared to the measured data variance (Nash and Sutcliffe, 1970). Nash-Sutcliffe efficiency indicates how well the plot of observed versus simulated data fits the 1:1 line.  $NSE = 1$ , corresponds to a perfect match of the model to the observed data. Values between 0.0 and 1.0 are generally viewed as acceptable levels of performance,  $NSE = 0$ , indicates that the model predictions are as accurate as the mean of the

observed data,  $-\infty < NSE < 0$ , indicates that the observed mean is a better predictor than the model. NSE was recommended for two major reasons: (i) it is recommended for use by ASCE (1993) and Legates and McCabe (1999), and (ii) it is very commonly used indicator, which provides extensive information on reported values.

$$NSE = 1 - \frac{\sum_{i=1}^n (O_i - E_i)^2}{\sum_{i=1}^n (O_i - \bar{O})^2} \quad \dots(3.16)$$

#### 3.7.4.5 Index of Agreement (d)

The index of agreement (d) was developed by Willmott (1981) (Eqn. 17) as a standardized measure of the degree of model prediction error and varies between 0 and 1. A computed value of 1 indicates a perfect agreement between the measured and predicted values, and 0 indicates no agreement at all. The index of agreement represents the ratio between the “mean square error” and the “potential error”. The author defined potential error as the sum of the squared absolute values of the distances from the predicted values to the mean observed value and distances from the observed values to the mean observed value. The index of agreement can detect additive and proportional differences in the observed and simulated means and variances; however, ‘d’ is overly sensitive to extreme values due to the squared differences (Legates and McCabe, 1999).

$$d = 1 - \frac{\sum_{i=1}^n (O_i - E_i)^2}{\sum_{i=1}^n (|E_i - \bar{O}| + |O_i - \bar{O}|)^2} \quad \dots(3.17)$$

### 3.8. Historic Mapping of Estimated SSC

Following linear regression, t-tests, Student's t-tests, and chi-square tests, equations showing insignificant differences between predicted and observed SSC underwent performance analysis using indicators from section 3.7.4. The best-performing spectral integration function was then utilized to assess historical SSC in the Mula Dam reservoir from October to February in 2019-2020 and 2020-2021. Historic SSC mapping in the reservoir was conducted using ArcMap software, commonly used for GIS and spatial analysis tasks. This allowed visualization of spatial data, including SSC distribution over time, offering valuable insights into sediment dynamics within the reservoir and contributing to a better understanding of sediment dynamics in the area.

## IV. RESULTS AND DISCUSSION

The study focuses on developing an integrated reflectance function for estimating suspended sediment concentration (SSC) in the Mula Dam reservoir. Efforts were made to achieve this by establishing calibrated relationship between observed SSC and various band indices, ratios, and combinations derived from spectral responses derived from Spectroradiometer. These spectral parameters were then related with corresponding values from Sentinel-2 satellite images. The resultant relationships were integrated to estimate SSC using Sentinel-2 data for validation. The estimated SSC was further subjected to statistical analysis to identify the most suitable spectral integration function for estimating SSC in the Mula Dam reservoir's surface waters. This chapter presents a detailed analysis of results discussion.

### 4.1 Distribution of sampling locations and observed SSC in Mula dam reservoir

Field works of sample collection was carried on 31<sup>st</sup> October, 2021; 20<sup>th</sup> December, 2021; 4<sup>th</sup> January 2022; 3<sup>rd</sup> February, 2022 and 18<sup>th</sup> February, 2022, wherein 121 samples located all over the reservoir at about 700 to 1000 m apart from each other were collected. Figure 4.1 shows the distribution of 121 sampling locations in Mula dam reservoir.

Field data collection was divided in five different campaigns. First data collection was conducted on 31<sup>st</sup> October 2021, immediately after monsoon season. Prior to 31<sup>st</sup> October 2021, the Mula dam reservoir posed challenging conditions that hindered the execution of sampling and in-situ spectral data collection. The reservoir experiences heavy inflow, resulting in elevated water levels and increased turbulence during monsoon season. The turbulent conditions made it difficult and potentially hazardous for researchers to venture into the dam for data collection purposes. Additionally, persistent cloud cover further complicated the situation, inhibiting the collection of accurate in-situ spectral data. These adverse weather and hydrological conditions necessitated delaying the fieldwork until after 31<sup>st</sup> October 2021, when the conditions became more favourable for safe and effective data collection activities.

The Mula dam reservoir covered a substantial surface area, ranging from approximately 55.32 km<sup>2</sup> (at Full supply level immediately after the monsoon season) on 31<sup>st</sup> October, 2021 to about 46.48 km<sup>2</sup> on 18<sup>th</sup> February, 2022. The extensive surface area posed challenges in gathering data in a single campaign, especially with the requirement of 4 hours (between 1100 hrs. and 1500 hrs.) of bright sunshine to capture accurate in-situ spectral data.

Figure 4.1 depicts the area covered in the Mula dam reservoir during five different data collection campaign. On 31<sup>st</sup> October 2021, the data collected from 25 sampling locations revealed that the SSC ranged from 15.62 mg/L to 78.261 mg/L. For this campaign, the majority of the samples were collected from the central portion adjacent to the reservoir embankment.

During the second data collection campaign, conducted on 20<sup>th</sup> December, 2021, a total of 30 samples were collected from the dendrite portion of the dam, as illustrated in Figure 4.1. The SSC in this portion ranged from 45.85 mg/L to 65.65 mg/L during the campaign. Additionally, it

was observed that a few small streams were contributing to this dendrite portion of the reservoir from the surrounding area.

On 4<sup>th</sup> January, 2022, 26 samples were collected from another dendrite portion of the reservoir, as in the same figure. The concentration of suspended sediment in this particular area ranged from 33 mg/L to 70 mg/L. A few small streams also contributed in this particular portion of the reservoir.

On 3<sup>rd</sup> February 2022, the subsequent sampling was done, focusing on the section of the reservoir at quite large distance from the embankment as shown in in Figure 4.1. This specific area serves as the entry point for the Mula River into the reservoir. During this sampling, a slightly higher SSC was observed, ranging from 60.60 mg/L to 92.30 mg/L, based on data collected from 19 different locations.

During the final campaign on 18<sup>th</sup> February 2022, a total of 21 samples were collected from an 8 km long river stretch, just before its entry into the reservoir. The width of this river stretch was substantial enough to encompass two to three pixels of the Sentinel-2 image. The samples were collected from the central portion of the Mula River. In this section, the SSC were notably higher, ranging from over 100 mg/L up to 137.65 mg/L. This increase in SSC can likely be attributed to the high turbulence caused by the flowing river and the observed stream bank erosion along the stream.

Figure 4.2 provides a visual representation of the spatio-temporal distribution of suspended sediment concentrations (SSCs) in the Mula dam reservoir over the period from 31<sup>st</sup> October, 2021 to 18<sup>th</sup> February, 2022. The map is generated using the Kriging method, an interpolation technique used to estimate values at unobserved locations based on nearby observed data points. The map clearly shows that the SSC is not uniformly distributed across the reservoir. The portion of the reservoir where rivers or streams enter exhibits relatively higher concentrations of suspended sediment compared to the central portion. This observation aligns with the phenomenon of higher turbulence caused by the incoming flow of water from rivers and streams. The turbulence keeps the sediment particles in suspension, leading to higher SSC values in these areas. In contrast, the central portion of the reservoir experiences lower velocity and reduced turbulence, allowing the silt and sediment to settle and get deposited. This settling process may have resulted in lower SSC values in the central portion of reservoir. The observed data points on the map indicate that SSC in the Mula dam reservoir ranged from 15.62 to 137.65 mg/L, with an average SSC of 61.43 mg/L.

This wide range of values underscores the spatial heterogeneity of suspended sediment concentrations in the reservoir. The spatio-temporal distribution depicted in Figure 4.2 is crucial for understanding sediment dynamics in the reservoir. It helps to identify areas prone to higher sediment transport, erosion, and potential impacts on water quality.

The literature lacks a standardized threshold for categorizing high and low suspended sediment concentrations (SSC), leading to varying values used in different studies. For instance, Robert et al. (2016) used 360 mg/L, Zhang et al. (2022) used 50 mg/L, and Pinet et al. (2017) used 100 mg/L as thresholds to differentiate between lower and higher SSC in their respective study areas.

In this research, during the considered period, 85 percent of the data points recorded SSC values below 100 mg/L, while the remaining 15 percent of data points exhibited SSC higher than 100 mg/L. The higher SSC values were predominantly observed in the river stretch of Mula, suggesting that this area experienced relatively higher suspended sediment concentrations compared to other parts in the Mula dam reservoir. Based on the threshold of 100 mg/L, it can be inferred that the Mula dam reservoir encountered a lower range of SSC levels throughout the investigation period. This highlights the importance of establishing context-specific SSC thresholds for environmental assessments, as different water bodies and reservoirs may exhibit varying sediment dynamics.

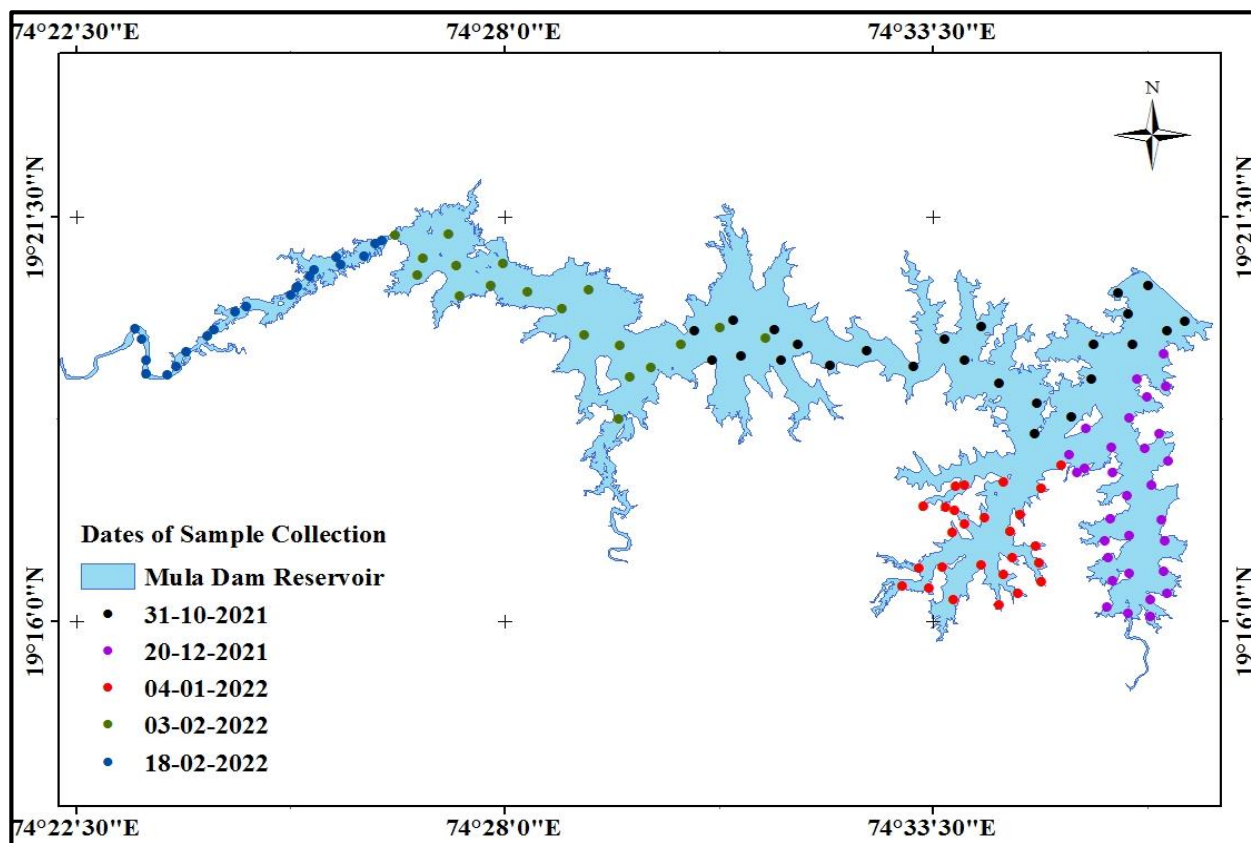
#### **4.1.1 Statistical Analysis of Suspended Sediment Concentration**

During the research conducted on the Mula dam reservoir, a total of 121 water samples, each with an approximate volume of 1 litre, were collected over five different data collection campaigns. However, due to errors during spectral data collection, sixteen samples were rejected, leaving 105 valid samples for further analysis. Out of these valid samples, 84 were utilized for calibration purposes, while the remaining 21 were reserved for validation. The average suspended sediment concentration (SSC) values were calculated for all datasets. The overall average SSC for all samples was found to be 61.43 mg/L. When focusing on the calibration dataset, the average SSC was slightly higher at 62.65 mg/L, while the validation dataset showed a slightly lower average of 57.04 mg/L. The observed SSC values ranged from 15.62 to 137.65 mg/L across all datasets.

Statistical characteristics, represented by the standard deviation (SD) and coefficient of variation (CV), were computed to assess the variability within the datasets. For the combined datasets, the SD was calculated as 32.59 mg/L, with a CV of 53.05%. Both the calibration dataset (SD = 32.87 mg/L, CV = 52.57%) and the validation dataset (SD = 31.78 mg/L, CV = 55.72%) exhibited similar statistical properties to the overall dataset, as shown in Table 4.1. A coefficient of variation (CV) greater than 50% indicates that the standard deviation of the dataset is relatively high compared to the mean value. This can be attributed to the diverse spatial and temporal contexts in which samples are collected, reflecting variations in suspended sediment concentration across different areas of the dam and at different points in time. Statistical characteristics describes the variability of suspended sediment concentrations in the Mula dam reservoir across different datasets, allowing to calibrate and validate their sediment estimation functions effectively.

**Table 4.1. Statistical characteristic of overall, calibration and validation dataset.**

Dataset	No. of Samples	Minimum SSC (mg/L)	Maximum SSC (mg/L)	Average SSC (mg/L)	SD (mg/L)	CV (%)
Overall	105	15.62	137.65	61.43	32.59	53.05
Calibration (80 %)	84	15.91	137.65	62.53	32.87	52.57
Validation (20 %)	21	15.62	121.43	57.04	31.78	55.72

**Figure 4.1 Distribution of 121 sampling locations with dates of the data collection over Mula dam reservoir.**

## 4.2 Analysis of Spectral Signature

### 4.2.1 Spectral Signature using Spectral Responses Captured by Spectroradiometer SVC-1024i

The in-situ surface reflectance spectra (Figure 4.3) consistently exhibit a uniform shape and amplitude. As suspended sediment concentration increases, almost parallel increase in surface reflectance is observed, and vice versa. There is a distinct peak in the Red region (650 to 680 nm), accompanied by an emerging peak in the Red Edge 1 region (698 to 713 nm) and a flat peak in the Green region (543 to 578 nm). These distinct features suggest the presence of suspended sediment at lower concentrations.

These spectral findings align with a peak at 550 nm in the Green spectrum, associated with suspended sediment concentrations ranging from 5.4 to 29.5 mg/L as observed by Sravanthi *et al.*, 2013. Additionally, Wright *et al.* (2018) noted comparable spectral signatures featuring these

characteristic patterns, further validating identification of peaks around 560 and 650 nm, correlating with suspended particulate concentrations of an average of 45 mg/litre in the Tamar estuary by Doxaran *et al.*, (2005).

These consistent findings reinforce the importance of judiciously selecting wavelength bands for accurate SSC estimation. Figure 4.3 provides a comprehensive overview of SSC spectra across the Mula dam reservoir, while Appendix - C shows spectral signatures for all 121 sampling points.

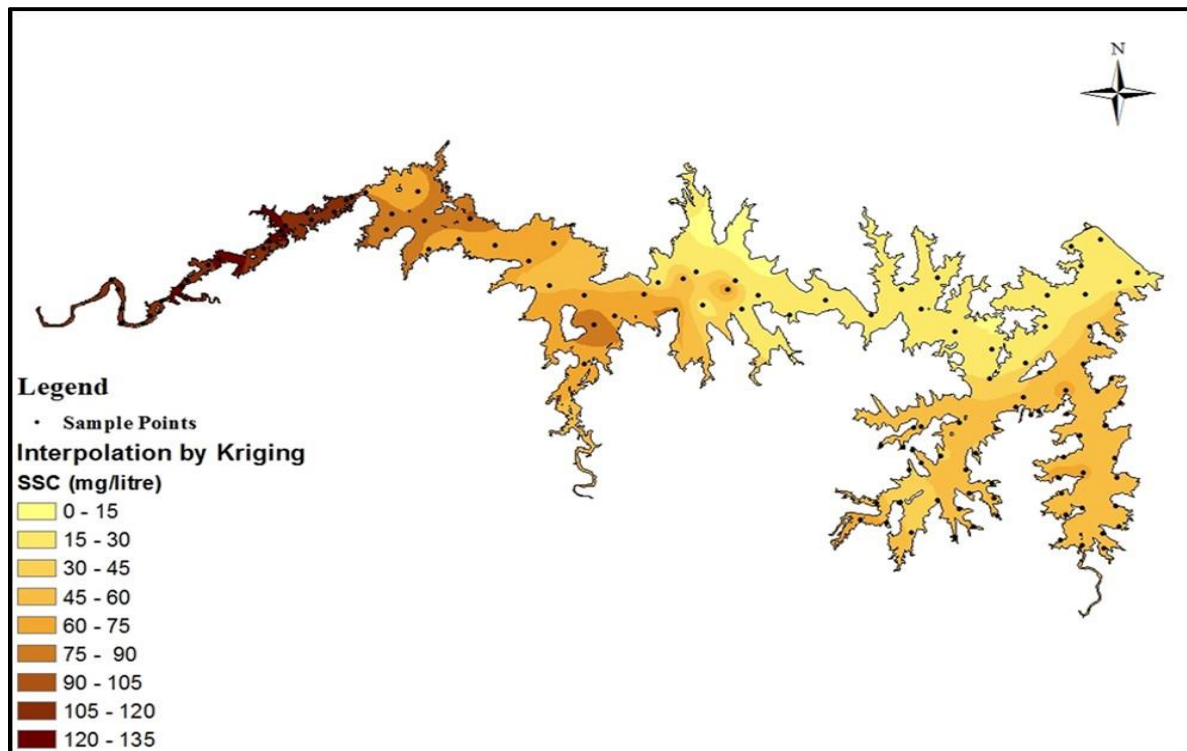


**Figure 4.2: Distribution of SSC in Mula Dam reservoir during October 2021 to February 2022**

#### **4.2.2 Relationship between Observed SSC and Band Values Obtained from Spectroradiometer SVC-1024i**

The spectral reflectance values obtained from the Spectroradiometer across various sampling locations were plotted against the corresponding wavelength ranges and correlated with the observed Suspended Sediment Concentration (SSC). Existing literature has emphasized the significance of wavelengths ranging from 350 nm to 900 nm for evaluating SSC (Chen *et al.*, 1991 and Ramakrishnan *et al.*, 2013). The lower concentration of suspended matter can be well correlated with Sentinel-2 bands viz. Blue, Green, Red, Red Edge 1 (Premkumar *et al.*, 2021). As a result, the relationship between SSC and reflectance within the spectral bands covering this wavelength range was investigated in this study. The average values of Blue, Green, Red, Red Edge 1, 2, 3, and 4, as well as NIR band, were subjected to correlation analysis with SSC in milligrams per litre (mg/L). Average band values at different sampling locations are provided in

the Appendix - E. Figure 4.4 (a to h) shows the recorded reflectance values for observed Suspended Sediment Concentration (SSC) in Mula Dam Reservoir in different bands respectively.

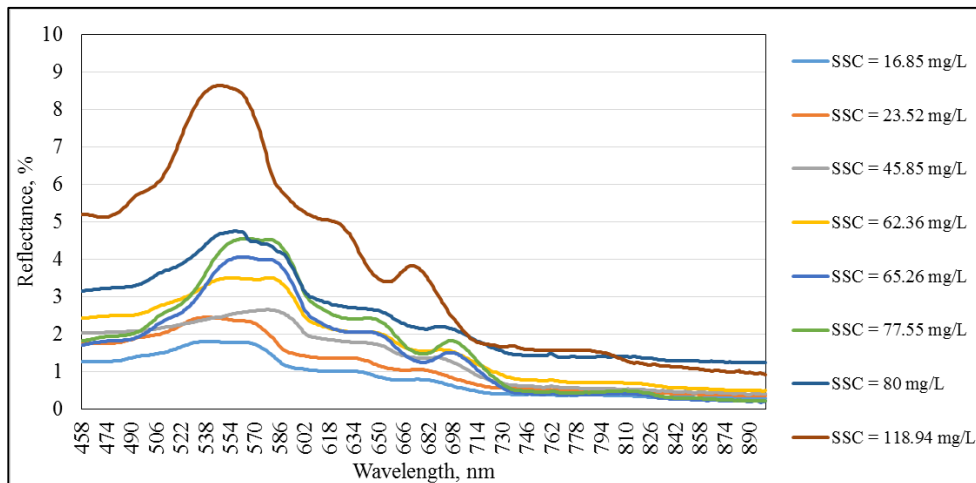


**Fig. 4.3: Surface reflectance spectrum for representative samples covering the given range of SSC (mg/L)**

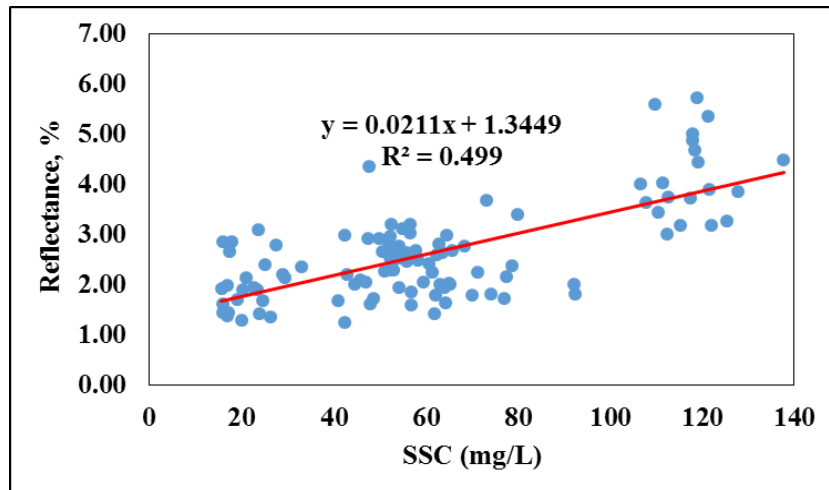


**Fig. 4.4 (a): Linear relation between SSC and average reflectance in Blue band (458-523 nm)**

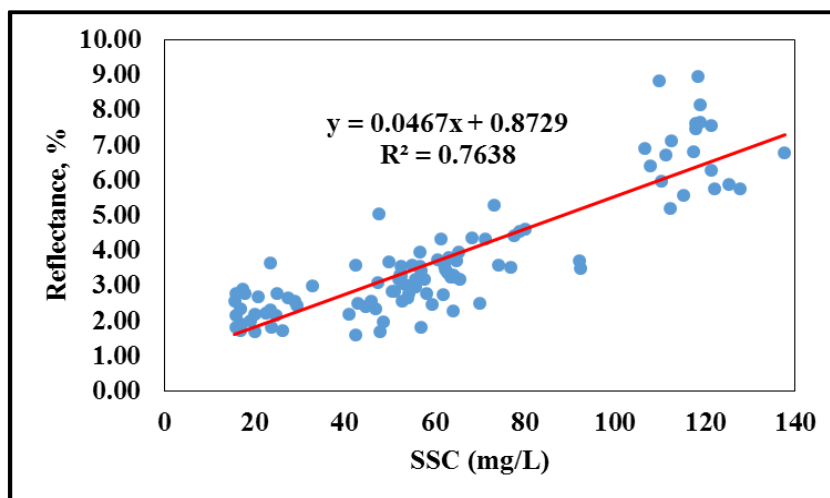


**Fig. 4.4 (b): Linear relation between SSC and average reflectance in Green band (543-578 nm)**

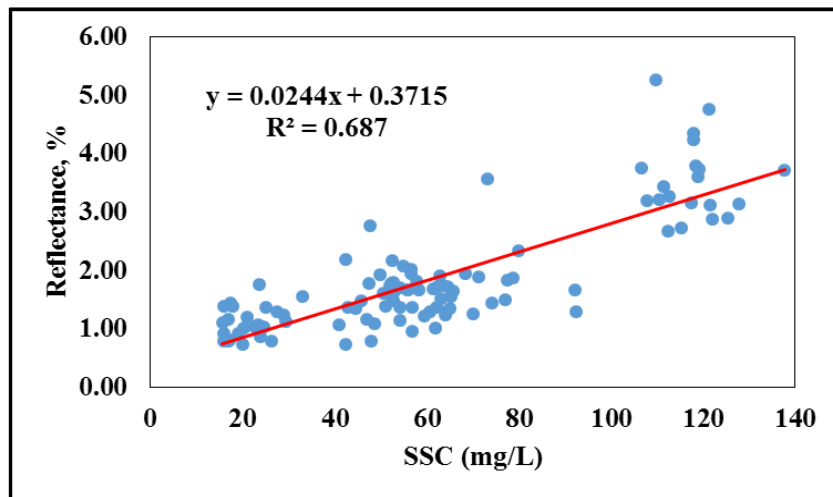


**Fig. 4.4 (c):** Linear relation between SSC and average reflectance in Red band (650-680 nm)

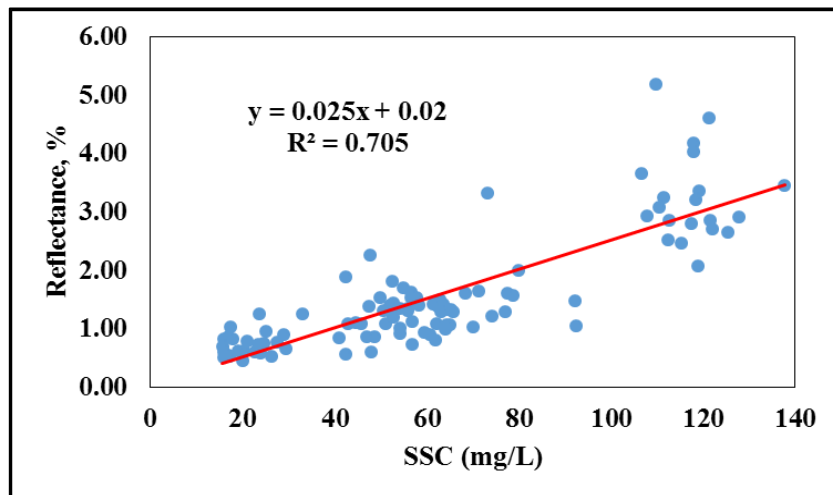


**Fig. 4.4 (d):** Linear relation between SSC and average reflectance in Red Edge 1 band (698-713 nm)

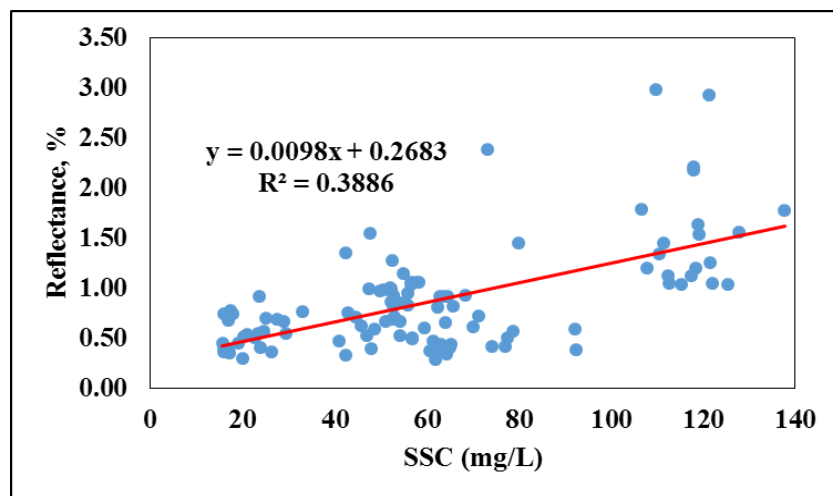


**Fig. 4.4 (e):** Linear relation between SSC and average reflectance in Red Edge 2 band (733-748 nm)

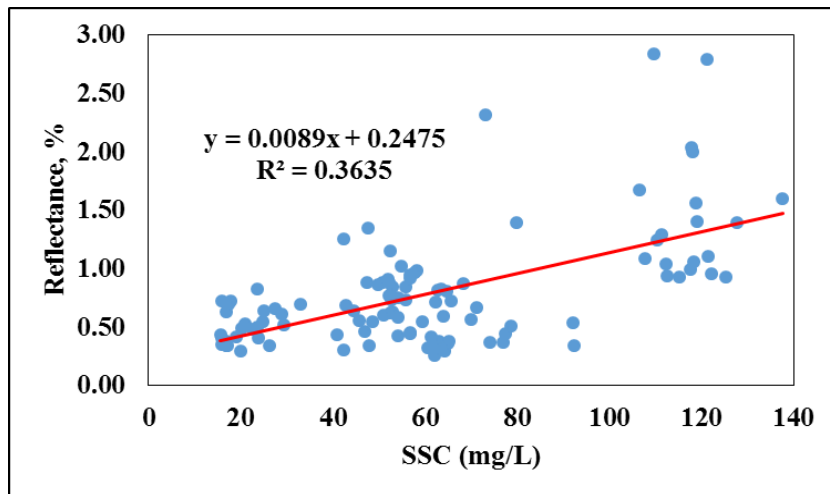


**Fig. 4.4 (f): Linear relation between SSC and average reflectance in Red Edge 3 band (773-793 nm)**

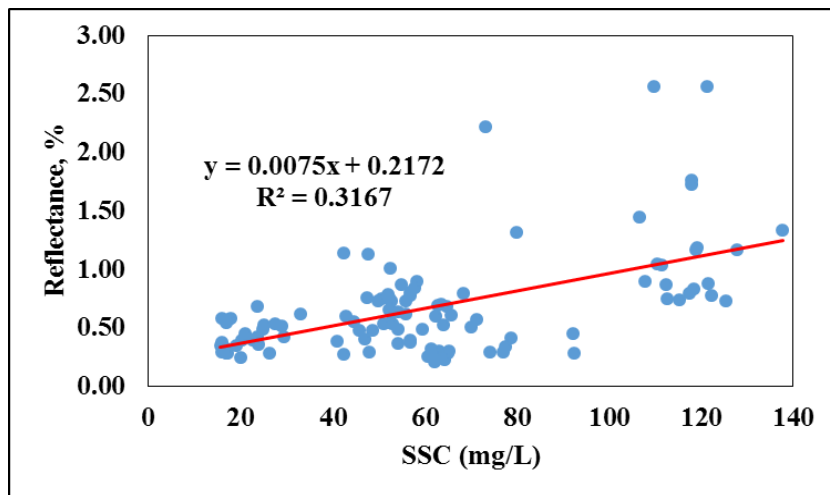


**Fig. 4.4 (g): Linear relation between SSC and average reflectance in NIR band (785-900 nm)**

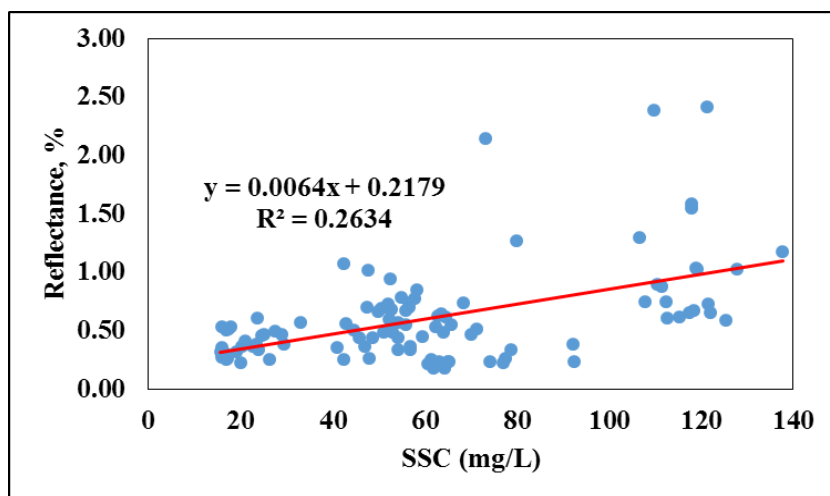


**Fig. 4.4 (h): Linear relation between SSC and average reflectance in Red Edge 4 band (855-875 nm)**

The analysis of Figure 4.4 (a to h) demonstrates a notable and positive correlation between the observed Suspended Sediment Concentration (SSC) and the average reflectance within the Green band (543-578 nm), exhibiting an  $R^2$  of 0.76. This trend is followed by the Red Edge 1 (698-713 nm) band ( $R^2 = 0.71$ ), the Red band (650-680 nm) with  $R^2 = 0.68$ , and the Blue band (458-523 nm) with  $R^2 = 0.50$ , acquired from the Spectroradiometer SVC – 1024i. Conversely, weaker correlations are evident between SSC and the average reflectance within the Red Edge 2, 3, and 4 bands, as well as the NIR band, with coefficients of determination of 0.39, 0.36, 0.26, and 0.32 respectively.

The positive correlation between observed SSC and average reflectance in the Green band highlights its potential suitability for estimating SSC levels. The relatively high R-squared value of 0.76 indicates a meaningful association between SSC and reflectance in this range. Similarly, the positive correlations witnessed in the Red Edge 1 and Red bands, with R-squared values of 0.71 and 0.69 respectively, further highlight their viability as SSC indicators. However, the relatively weaker correlations evident in the Blue band ( $R^2 = 0.50$ ), along with the Red Edge 2, 3, and 4 bands, as well as the NIR band, imply that these wavelengths may offer limited accuracy in predicting SSC levels effectively. Concurring with multiple researchers, including Doxaran *et al.* (2005), Sravanthi *et al.* (2013), Pereira *et al.* (2019), Zhang *et al.* (2022), and Gholizadeh *et al.* (2022), discussions have highlighted the sensitivity and applicability of Green and Red bands for SSC assessment. Additionally, Premkumar *et al.* (2021) have discussed the unique attributes of the Red Edge 1 band. These results pave the way for exploring various band ratios, combinations, or indices utilizing the Green, Red, and Red Edge 1 bands, as recommended in existing literature, or devising new ratios, combinations, or indices involving these bands for precise SSC estimation.

#### **4.2.3 Comparison of Spectral Signature obtained from Spectroradiometer SVC – 1024i and Sentinel – 2 Satellite.**

For the range of 400 to 900 nm on the electromagnetic spectrum, the average band values encompassing Blue, Green, Red, Red Edge 1, 2, 3, and 4, as well as the NIR band were computed using reflectance data collected by the Spectroradiometer SVC-1024i. In parallel, reflectance values from the corresponding sample locations were extracted from Sentinel-2 images of the same date, through the application of a ‘Geostatistical tool’ in ArcMap. A comparison of these reflectance values is graphically shown in Figure 4.5. This figure (i to vi) illustrates a) Spectral Signatures derived from band values of the Spectroradiometer SVC-1024i and Sentinel-2 BOA image, and b) the linear relationship between band values for selected samples, encompassing the entire range of observed SSC in the Mula Dam reservoir during this study.

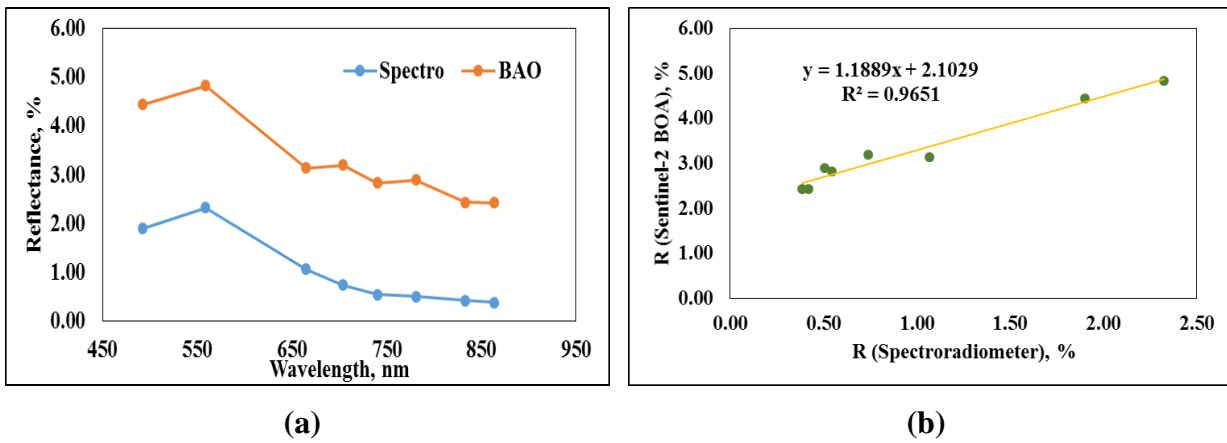


**Fig. 4.5 (i): (a) Spectral Signatures Obtained from band values Spectroradiometer SVC 1024i & Sentinel-2 BOA Image and (b) linear relation between band values for sample 7 having SSC of 23.52 mg/L.**

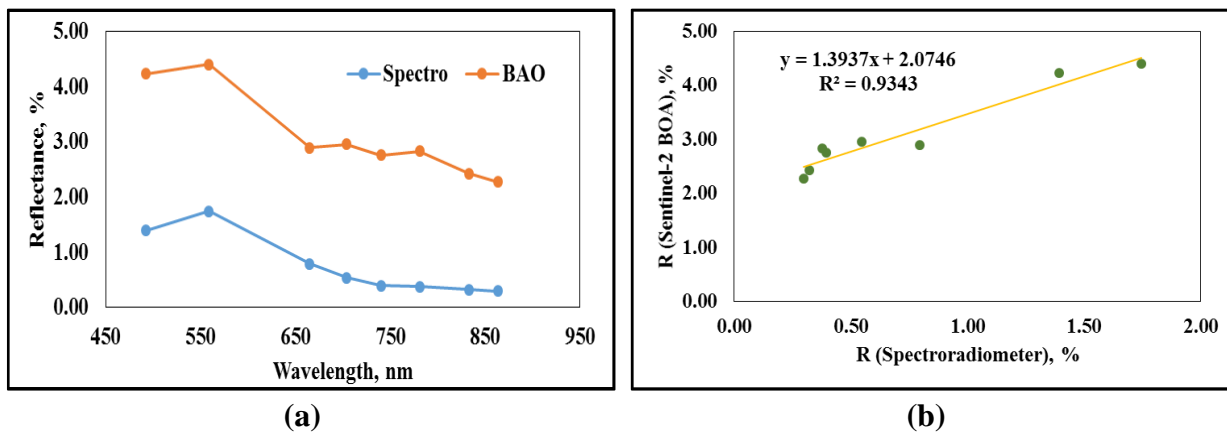


**Fig. 4.5 (ii): (a) Spectral Signatures Obtained from band values Spectroradiometer SVC-1024i & Sentinel-2 BOA Image and (b) linear relation between band values for sample 14 having SSC of 16.85 mg/L.**

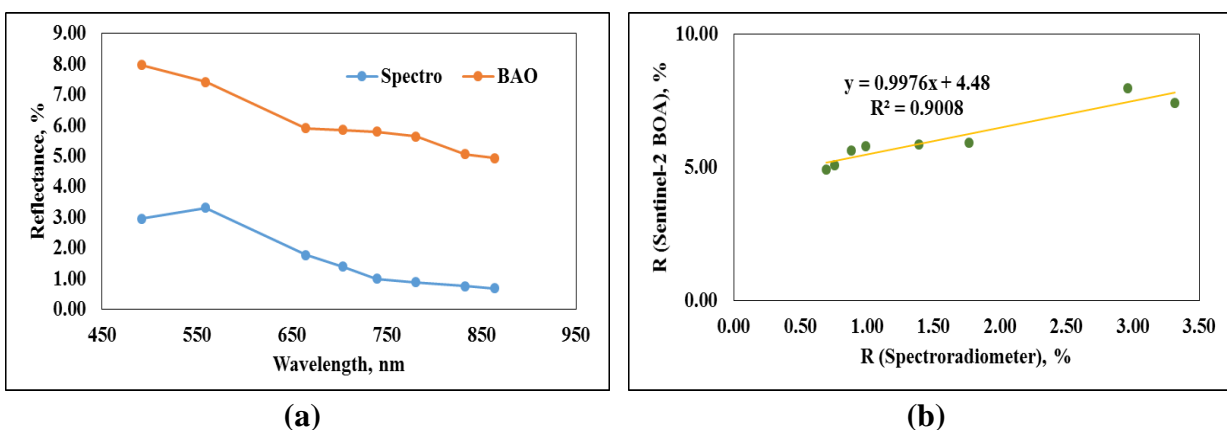


**Fig. 4.5 (iii): (a) Spectral Signatures Obtained from Spectroradiometer SVC-1024i & Sentinel-2 BOA Image and (b) linear relation between band values for sample 27 having SSC of 52.33 mg/L.**

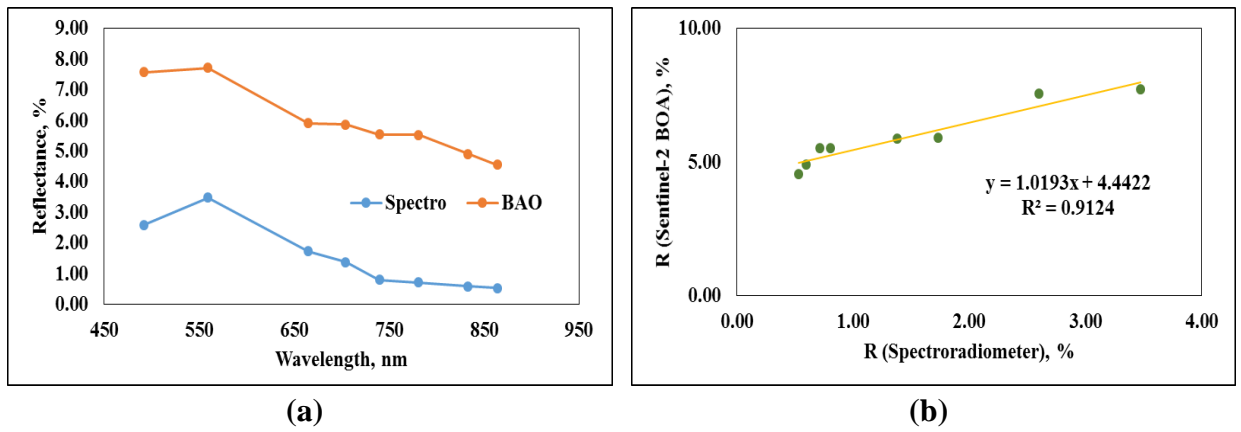


**Fig. 4.5 (iv): (a) Spectral Signatures Obtained from band values Spectroradiometer SVC-1024i & Sentinel-2 BOA Image and (b) linear relation between band values for sample 44 having SSC of 62.36 mg/L.**

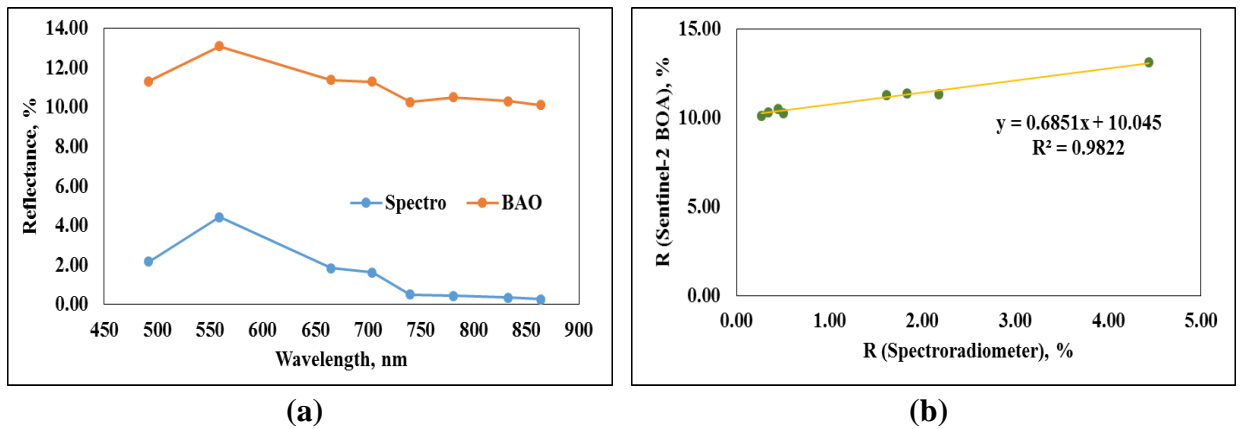


**Fig. 4.5 (v): (a) Spectral Signatures Obtained from band values Spectroradiometer SVC-1024i & Sentinel-2 BOA Image and (b) linear relation between band values for sample 95 having SSC of 77.55 mg/L.**

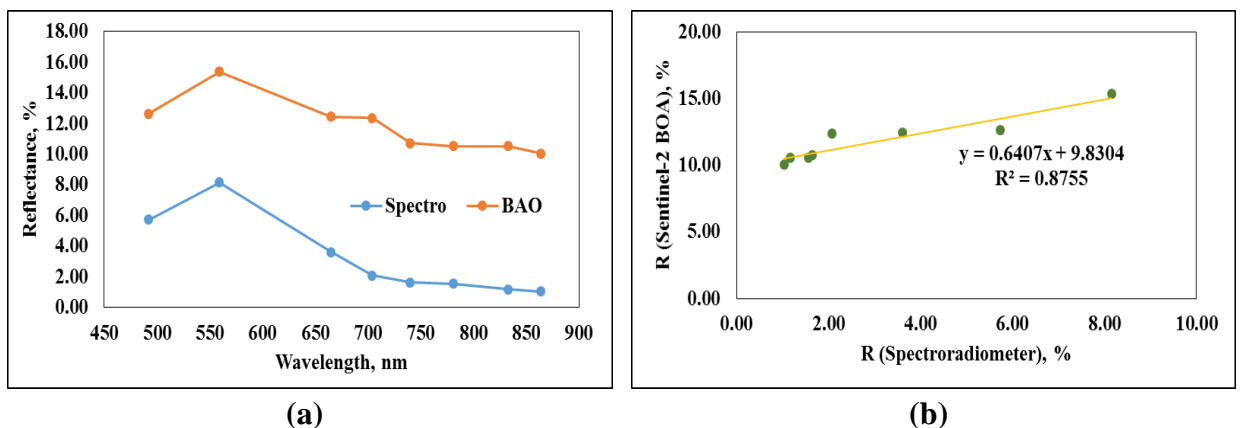


**Fig. 4.6 (vi): (a) Spectral Signatures Obtained from Spectroradiometer SVC-1024i & Sentinel-2 BOA Image and (b) linear relation between band values for sample 101 having SSC of 118.95 mg/L.**

Spectral Signatures derived from band values of the Spectroradiometer SVC-1024i and Sentinel-2 BOA image, almost exhibit the parallel nature as seen from figure 4.5 [ i to vi (a)]. Spectral signature nearly followed a similar pattern of spectral behaviour, although Sentinel – 2 derived spectral signature showed higher reflectance values at all wavelengths from 400 – 900 nm. Satellite sensors have a consistent and controlled viewing geometry, often looking down directly on the Earth's surface. This controlled geometry minimizes the influence of factors such as surface roughness and orientation that can affect ground-based measurements, possibly leading to higher reflectance in satellite images.

Figure 4.5 [i to vi (b)] illustrates a strong correlation between the reflectance values obtained from the Spectroradiometer SVC HR-1024i and the Sentinel-2 BOA image for the chosen samples. Approximately eighty percent of the samples showed a similar correlation, characterized by a Coefficient of Determination ( $R^2$ ) exceeding 0.8. All Spectral Signatures and linear relationships band values of the Spectroradiometer SVC-1024i and Sentinel-2 BOA image are given in Appendix - F. This correlation is consistent across all 121 samples, with a few exceptions exhibiting negative correlation and/ or very low Coefficient of Determination. Specifically, 16 samples (numbered 22, 29, 31, 45, 48, 52, 55, 57, 60, 62, 64, 66, 74, 75, 80, 114) located within 20 meters from the reservoir's bank exhibited this behaviour. This is likely due to spectral mixing with adjacent land and vegetation features, when mapped on the Mula dam reservoir. Exclusion of these sixteen samples was deemed necessary to ensure the integrity of the spectral function to be developed for precise estimation of Suspended Sediment Concentration (SSC), as their presence has the potential to introduce errors in the analysis.

The strong correlation observed between the reflectance values obtained from the ground-based Spectroradiometer and Sentinel-2 satellite imagery highlights the flexibility and usefulness of both in-situ Spectroradiometer measurements and satellite reflectance data. The in-situ reflectance dataset generated can be used for enhanced understanding of the apparent optical properties of Mula Dam waters. Therefore, an integrated approach is needed to comprehensively explore the inherent optical properties through multispectral and hyperspectral approaches, thereby fully utilizing the information present in the measured spectra. Several studies have used a spectral integration approach to estimate suspended sediment concentration (SSC) using remote sensing data. Lodhi *et al.* (1998) used high-resolution Spectroradiometer data integrated into Landsat-TM 4 bands to establish regression models relating reflectance values to SSC. Robert *et al.* (2016) investigated the suitability of Moderate Resolution Imaging Spectroradiometer (MODIS) data, employing radiometric indices for SSC and turbidity estimation. Liu *et al.* (2017) used Sentinel-2 Multispectral Imager (MSI) images along with in-situ spectral measurements to develop SSC retrieval models for estimating suspended particulate material concentration by optimized selection of bands based on varying sediment loads. These studies highlight the effectiveness of spectral integration in bridging ground-based and satellite data for accurate SSC estimation.

### **4.3 Development of Relationship between SSC and Band Indices and Band Ratios/Combinations derived from Spectroradiometer SVC – 1024i**

Multiple indices and band ratios/combinations proposed in existing literature were computed, and various efforts were undertaken to establish connections between these indices and band ratios/combinations and the observed SSC values in Mula dam reservoir, as elaborated in the Chapter 3. The outcomes of these attempts are detailed in the forthcoming sections.

#### **4.3.1 Relationship between Spectroradiometer Derived Indices and SSC**

In this section, a range of indices sourced from the literature such as NDSSI, NSMI, M-NDSSI, and R-NDSSI were computed, and their correlation with observed SSC values is thoroughly examined.

##### **4.3.1.1 Relationship between NDSSI – Spectro and SSC**

In Figure 4.6, the plotted values of observed SSC (mg/L) were correlated against the NDSSI derived from the Spectroradiometer SVC – 1024i. The resulting scatter plot showed a dispersed arrangement of points without any discernible trend or pattern. The correlation between these two variables was found to be minimal with  $R^2 = 0.07$ , indicating a very weak relationship or association between them. This observation indicates that the NDSSI is not effective in accurately estimating Suspended Sediment Concentration (SSC) in the Mula dam reservoir due to very low reflectance in NIR band.

##### **4.3.1.2 Relationship between NSMI – Spectro and SSC**

When the observed SSC (mg/L) values were plotted against NSMI-Spectro, a noticeable positive correlation observed. To establish a connection between these variables, a range of mathematical functions such as exponential, linear, logarithmic, polynomial, and power functions were experimented with. The scatter plot showed in Figure 4.7 visualizes the relationship between Observed SSC (mg/L) and NSMI-Spectro, highlighting the resultant relationships. All these relationships demonstrated the values of coefficient of determination approximately close to 0.5. Generally, values exceeding 0.5 are deemed acceptable, as discussed by Santhi *et al.* (2001) and Liew *et al.* (2003).

##### **4.3.1.3 Relationship between M-NDSSI – Spectro and SSC**

Figure 4.8 displays the scatter plot illustrating the relation between Observed SSC (mg/L) and M-NDSSI-Spectro. The plot showcases the established linear, exponential, and second-order polynomial relationships. The M-NDSSI-Spectro values, ranging from -0.167 to 0.223 as depicted in the figure, exhibited a strong negative correlation with the SSC values. All three types of relationships exhibited coefficient of determination values greater than 0.5. The second-order polynomial equation provided the best fit, yielding an  $R^2$  value of 0.6.

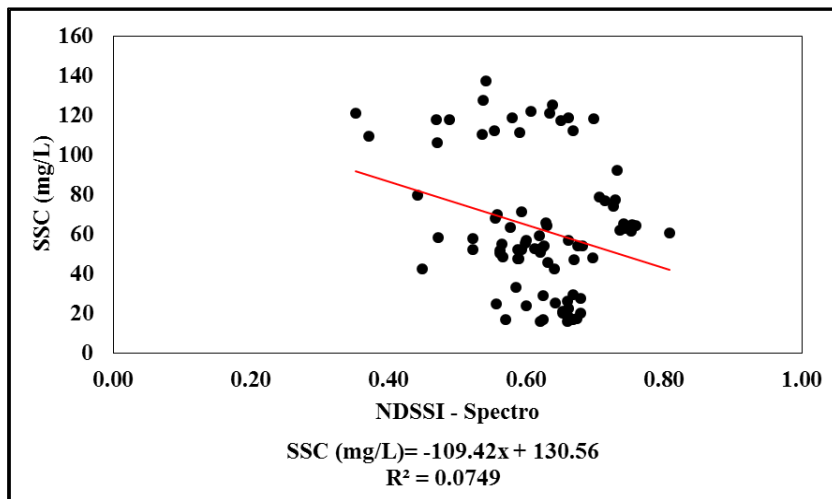


**Fig. 4.6: Relationship between NDSSI – Spectro and observed SSC (mg/L)**

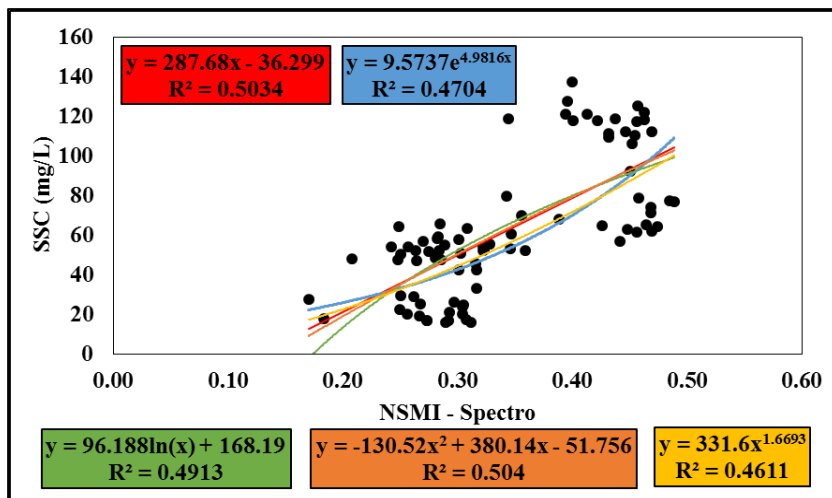


**Fig. 4.7: Relationships between NSMI – Spectro and observed SSC (mg/L)**

#### 4.3.1.4 Relationship between R-NDSSI – Spectro and SSC

By substituting the NIR band with the Red Edge 1 band in the original NDSSI, R-NDSSI was derived and showed notable improvements. The scatter plot showcasing R-NDSSI-Spectro plotted against observed SSC in Mula dam reservoir displayed a robust negative correlation as shown in the Figure 4.9. Different mathematical functions, including exponential, linear and polynomial, functions exhibited  $R^2$  values exceeding 0.7. The most accurate fit was achieved using a second-order polynomial equation with an  $R^2$  value of 0.78, followed by a linear relationship between NDSSI-Spectro and observed SSC with an  $R^2$  value of 0.75.

The analysis of various indices in relation to observed Suspended Sediment Concentration (SSC) provided valuable insights. NDSSI exhibited a weak correlation with SSC, indicating its limited effectiveness for precise estimation. Positive correlations were observed between SSC and NSMI, while experimentation with mathematical functions revealed moderate correlations ( $R^2$  around 0.5) for SSC estimation. Strong negative correlations emerged between SSC and both M-NDSSI and R-NDSSI as seen in figures 4.8 and 4.9, suggesting their potential inaccuracy.

R-NDSSI models, particularly the second-order polynomial equation, showed  $R^2$  values surpassing 0.7, indicating accuracy to estimate SSC. All these relations, range of band indices used to calibrate these relations along with their coefficient of determination are given in table 4.2.

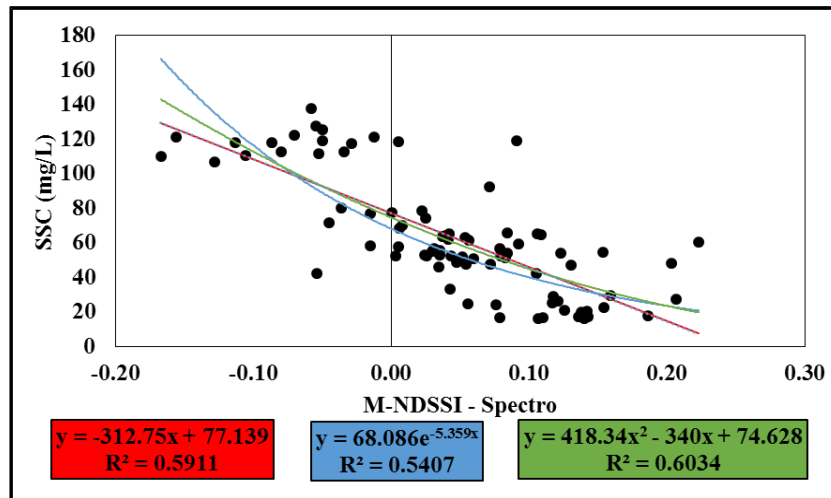


**Fig. 4.8: Relationships between M-NDSSI – Spectro and observed SSC (mg/L)**

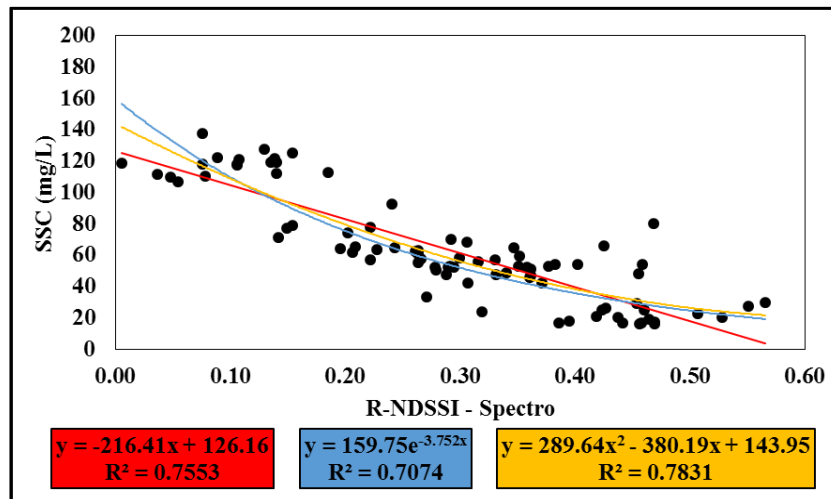


**Fig. 4.9: Relationships between R-NDSSI – Spectro and observed SSC (mg/L)**

#### 4.3.2 Relationship between Spectroradiometer Derived Band Ratio/ Combination and SSC

In this section, different relationship between various band ratio/ combination and suspended sediment concentration in Mula dam were developed. These ratios were derived from or inspired by literature and were identified by observing spectral signatures associated with different levels of Suspended Sediment Concentration (SSC). These ratios resulted from different attempts aimed at establishing links between band ratios or combinations and SSC values. The subsequent analysis explored the outcomes of these efforts, with detailed discussions provided in this section.

##### 4.3.2.1 Relationship between Band Combination (Red + Green)/2 and SSC

In their study, Sutari *et al.* (2020) used the average reflectance from the Red and Green spectral bands to estimate suspended sediment levels. This technique was adapted to the context

of this study, exploring on notable reflectance values within these bands. An attempt was made to calibrate this band combination to establish a relationship with observed suspended sediment concentration (SSC) in the Mula Dam reservoir. A scatter plot (Figure 4.10) revealed a good positive correlation between observed SSC and the calculated  $(\text{Red} + \text{Green})/2$  average reflectance. Various mathematical models yielded  $R^2$  values from 0.5 to 0.7, indicating strong explanatory power. Ultimately, a second-order polynomial equation proved the most fitting, best representing the data when calibrating  $(\text{Red} + \text{Green})/2$  for SSC estimation.

#### 4.3.2.2 Relationship between Band Combination (Red + RE1 + Green)/3 and SSC

Inspired by the approach of averaging reflectance in the Red and Green bands as explored by Sutari *et al.* (2022), an idea emerged to extend this concept by incorporating the Red Edge 1 band as well. The new approach involved calculating the average of three bands—Red, Green, and Red Edge 1 and subsequently establishing a relationship with observed suspended sediment concentration (SSC). The inclusion of the Red Edge 1 band yielded noticeable improvements in the results. Notably, the scatter plot displayed in Figure 4.11 demonstrated a more favourable and positive correlation between the calculated average reflectance,  $(\text{Red} + \text{Green} + \text{Red Edge 1})/3$ , and SSC (mg/L), in comparison to the previously utilized approach suggested by Sutari *et al.* (2020).

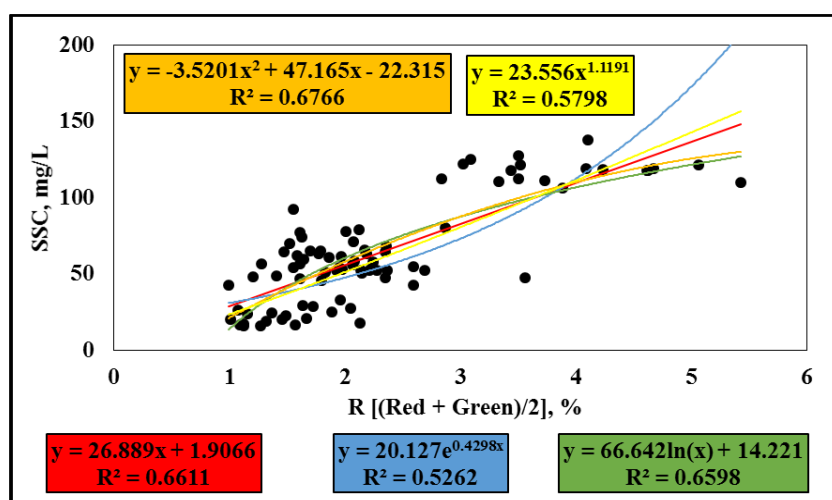


**Fig. 4.10: Relationships between  $(\text{Red} + \text{Green})/2$  – Spectro and SSC (mg/L)**

Various mathematical relationships, encompassing exponential, power, linear, and logarithmic equations, were explored to quantify the connection between the averaged reflectance and SSC. Notably, these equations yielded corresponding  $R$ -squared ( $R^2$ ) values of 0.62, 0.72, 0.78, and 0.80 respectively. The most striking result was achieved with a second-order polynomial equation, which exhibited the highest  $R^2$  value of 0.82. This indicates that the second-order polynomial equation offered the best fit for describing the relationship between the averaged reflectance of  $(\text{Red} + \text{Green} + \text{Red Edge 1})/3$  and SSC. This enhancement underscores the potential effectiveness of incorporating the Red Edge 1 band in the spectroscopy approach for estimating suspended sediment concentration.

#### 4.3.2.3 Relationship between Band Combination (Green – Red Edge 1) and SSC

By analysing the spectral signatures obtained for varying Suspended Sediment Concentration (SSC) levels, distinctive patterns emerged, notably a prominent peak within the Green region and a narrower peak in the Red Edge 1 region. These peaks exhibited varying magnitudes of reflectance corresponding to different SSC levels. This observation sparked the idea of establishing a relationship between the difference in reflectance values within the Green and Red Edge 1 regions and the observed SSC. A scatter plot depicting the relationship between (Green – Red Edge 1) reflectance difference and observed SSC demonstrated a positive correlation, as highlighted in Figure 4.12. This figure not only illustrates the correlation but also presents various mathematical equations that quantify the association between SSC and the reflectance difference between the Green and Red Edge 1 regions of the electromagnetic spectrum. These relations resulted in  $R^2$  values ranging from 0.5 to 0.7 for exponential, power, linear, and logarithmic equations. A second-order polynomial equation outperformed the other relations with an  $R^2$  value of 0.71, signifying its superior fitting to the data. This approach demonstrates the potential of utilizing the reflectance difference between the Green and Red Edge 1 regions as an indicator for estimating SSC, with the second-order polynomial equation.

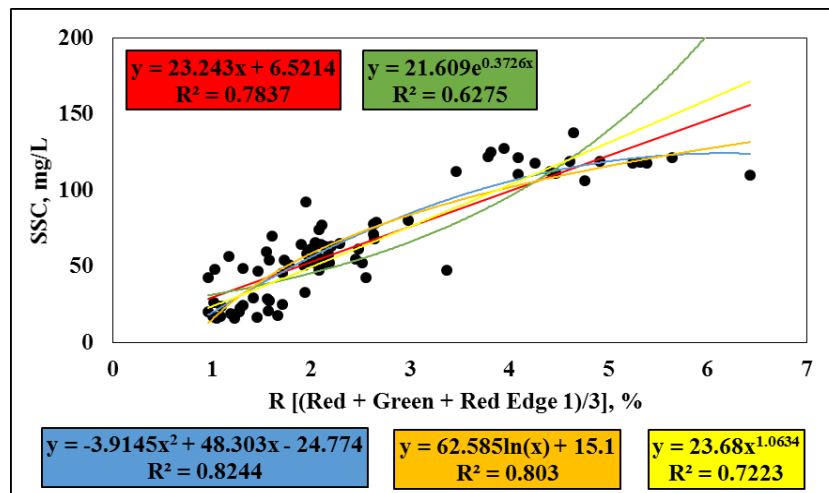


Fig. 4.11: Relationships between (Red + Green + Red Edge 1)/3 – Spectro and SSC (mg/L)

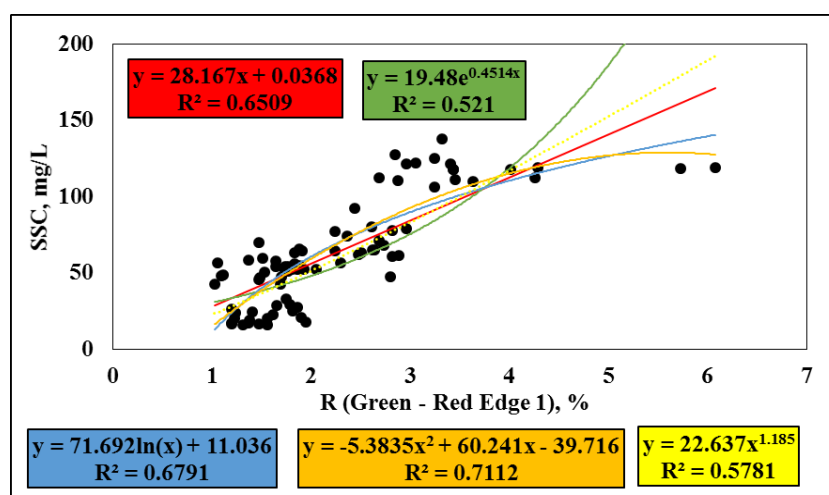
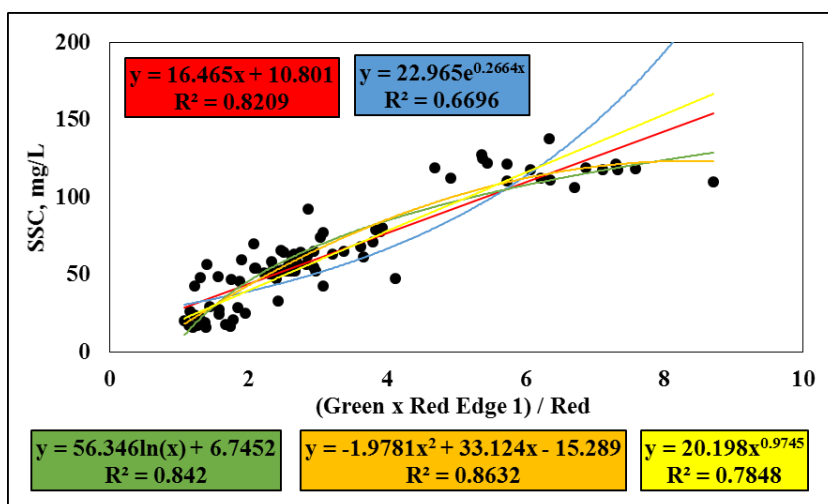


Fig. 4.12: Relationships between (Green – Red Edge 1) – Spectro and SSC (mg/L)



**Fig. 4.13: Relationship between [(Green × Red Edge 1)/ Red] and SSC (mg/L)**

#### 4.3.2.4 Relationship between Band Ratio (Green × Red Edge 1)/ Red and SSC

The primary objective of this study is to identify a suitable index or band ratio that can accurately estimate Suspended Sediment Concentration (SSC) in a large water body, in this case Mula Dam reservoir. Through extensive experimentation with different band ratios and combinations, a promising one emerged: the band ratio (Green × Red Edge 1) / Red. Such multiplicative approach is used by Kazemzadeh *et al.*, 2013. This particular ratio exhibited significant potential for SSC estimation. The scatter plot depicting the relationship between this ratio and SSC values displayed a robust positive correlation, as shown in Figure 4.13.

. The plot also showcases the various mathematical relationships established between these two variables. Linear, logarithmic, and power functions displayed calibration coefficient of determination values of 0.82, 0.84, and 0.78 respectively. Conversely, the exponential function yielded a relatively lower  $R^2$  value of 0.67. An impressive enhancement was observed with the second-order polynomial equation, yielding an  $R^2$  value of 0.86 during calibration. This notable improvement underscores the effectiveness of the polynomial equation for accurately estimating SSC using the (Green × Red Edge 1) / Red band ratio.

**Table 4.2: Various relationships between band indices (x) and observed SSC in mg/L (y)**

<b>Band Index (x)</b>	<b>Range of x</b>	<b>Type of Relation</b>	<b>Equation</b>	<b>R<sup>2</sup></b>	<b>Eqn. No.</b>
NSMI	0.170 to 489	Linear	$y = 287.68x - 36.299$	<b>0.50</b>	<b>4.1</b>
		Logarithmic	$y = 96.188\ln(x) + 168.19$	0.49	4.2
		Exponential	$y = 9.5737e^{4.9816x}$	0.47	4.3
		Polynomial	$y = -130.52x^2 + 380.14x - 51.756$	<b>0.50</b>	<b>4.4</b>
		Power	$y = 331.6x^{1.6693}$	0.46	4.5
M-NDSSI*	-0.167 to 0.223	Linear	$y = -312.75x + 77.139$	0.59	4.6
		Exponential	$y = 68.086e^{-5.359x}$	0.54	4.7
		<b>Polynomial</b>	$y = 418.34x^2 - 340x + 74.628$	<b>0.60</b>	<b>4.8</b>
R-NDDSI*	0.006 to 0.566	Linear	$y = -216.41x + 126.16$	0.75	4.9
		Exponential	$y = 159.75e^{-3.752x}$	0.70	4.10
		<b>Polynomial</b>	$y = 289.64x^2 - 380.19x + 143.95$	<b>0.78</b>	<b>4.11</b>

\*Given that these indices range between -1 and +1, power and logarithmic functions were not applicable for modelling these two indices.

**Table 4.3: Various relationships between band ratio/ combination (x) and observed SSC in mg/L (y)**

Band Ratio/ Combination (x)	Range of x	Type of Relation	Equation	R <sup>2</sup>	Eqn. No.
(Red + Green) / 2	0.997 to 5.427	Linear	$y = 26.889x + 1.9066$	0.66	4.12
		Logarithmic	$y = 66.642\ln(x) + 14.221$	0.65	4.13
		Exponential	$y = 20.127e^{0.4298x}$	0.52	4.14
		<b>Polynomial</b>	<b><math>y = -3.5201x^2 + 47.165x - 22.315</math></b>	<b>0.67</b>	<b>4.15</b>
		Power	$y = 23.556x^{1.1191}$	0.52	4.16
(Red + Green + Red Edge 1) / 3	0.963 to 6.428	Linear	$y = 23.243x + 6.5214$	0.78	4.17
		Logarithmic	$y = 62.585\ln(x) + 15.1$	0.8	<b>4.18</b>
		Exponential	$y = 21.609e^{0.3726x}$	0.62	4.19
		<b>Polynomial</b>	<b><math>y = -3.9145x^2 + 48.303x - 24.774</math></b>	<b>0.82</b>	4.20
		Power	$y = 23.68x^{1.0634}$	0.72	4.21
Green - Red Edge 1	1.024 to 6.078	Linear	$y = 28.167x + 0.0368$	0.65	4.22
		Logarithmic	$y = 71.692\ln(x) + 11.036$	0.68	<b>4.23</b>
		Exponential	$y = 19.48e^{0.4514x}$	0.52	4.24
		<b>Polynomial</b>	<b><math>y = -5.3835x^2 + 60.241x - 39.716</math></b>	<b>0.71</b>	4.25
		Power	$y = 22.637x^{1.185}$	0.57	4.26
(Green x Red Edge 1) / Red	1.078 to 8.714	Linear	$y = 16.465x + 10.801$	0.82	4.27
		Logarithmic	$y = 56.346\ln(x) + 6.7452$	0.84	<b>4.28</b>
		Exponential	$y = 22.965e^{0.2664x}$	0.67	4.29
		<b>Polynomial</b>	<b><math>y = -1.9781x^2 + 33.124x - 15.289</math></b>	<b>0.86</b>	4.30
		Power	$y = 20.198x^{0.9745}$	0.78	4.31

#### **4.4 Development of Relationships between Different Band Indices/ Combinations/ Ratios Derived from Sentinel – 2 Satellite Imagery and Spectroradiometer SVC – 1024i**

One of the objective of this study is to develop a correlation between the spectral responses acquired from two different platforms: the Ground-based Spectroradiometer and the Sentinel-2 satellite sensor. This approach aims to bridge hyper spectral and multispectral remote sensing data. To examine the interrelation between the spectral responses captured by these platforms, it is essential to explore this connection using diverse band indices, combinations and ratios that have been calibrated for suspended sediment estimation, as discussed in section 4.3. Relationship between Sentinel 2-BOA derived band indices and band combinations/ ratios are discussed in this section. To eliminate the influence of extreme values on the relation, some outliers were removed after visualizing scatter plot between considered variables, while developing these relationships.

##### **4.4.1 Development of Relationship Between Band Indices Derived from Sentinel – 2 Satellite Imagery and Spectroradiometer SVC – 1024i**

The scatter plotted between NSMI, M-NDSSI and R-NDSSI derived from Sentinel 2 – BOA Satellite imagery and Spectroradiometer SVC – 1024i is shown in the figure 4.14, 4.15 and 4.16 respectively. The figures reveal that there is good positive correlation between the considered variables in all three cases. The investigation has taken into account a range of mathematical relationships, including exponential, logarithmic, linear, polynomial, and power equations, to model the relation between the indices Sentinel 2 – BOA Satellite imagery and the Spectroradiometer measurements.

Among the three indices, R-NDSSI and NSMI exhibit a stronger correlation with the Spectroradiometer measurements as compared to M-NDSSI. This implies that R-NDSSI and NSMI might be better indicators for estimating Spectroradiometer values in this specific context. All the developed relationships, regardless of the index considered, display R-squared ( $R^2$ ) values exceeding 0.5 during the calibration process. This suggests that over 50% of the variability in Spectroradiometer measurements can be accounted for by the developed relationships.

The highest  $R^2$  value, reaching 0.8 for R-NDSSI, indicates a substantial degree of explanatory power, implying that the relationship between R-NDSSI derived from satellite and Spectroradiometer measurements is particularly well-modelled. Remarkably, across all three cases (NSMI, M-NDSSI and R-NDSSI), the second-order polynomial equation emerged as the most suitable model for forecasting Spectroradiometer measurements. This observation underscores the capacity of the polynomial equation to achieve the highest degree of precision in predicting the relationships between the Sentinel-derived indices and Spectroradiometer measurements. This finding suggests that the curvature introduced by the quadratic term in the polynomial equation can effectively capture the fine patterns present in the data, resulting in improved predictive performance.

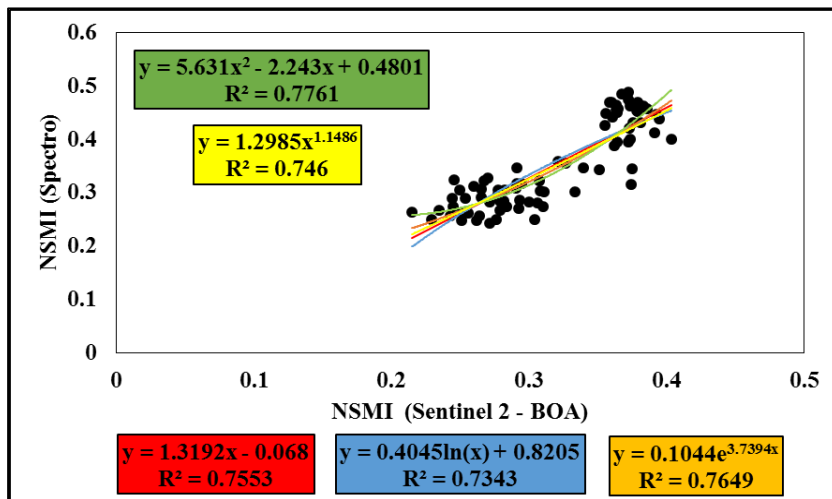


**Fig. 4.14: Relationship between NSMI derived from Sentinel – 2 Satellite imagery and Spectroradiometer SVC – 1024i along with developed relations.**

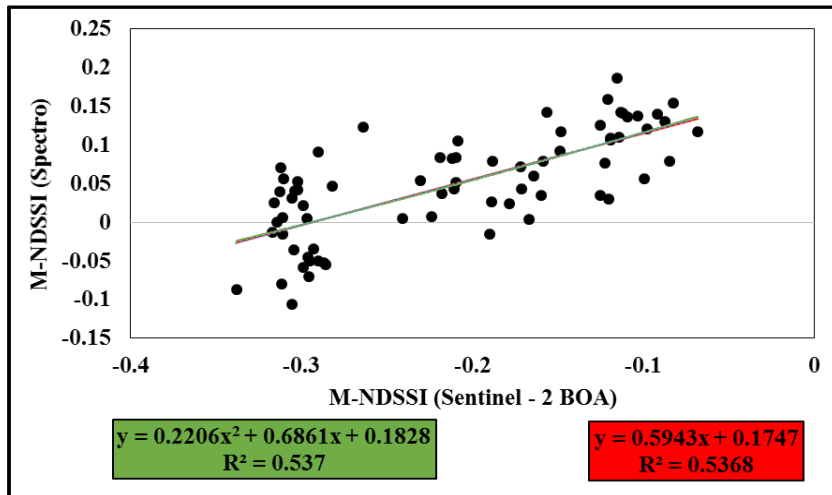


**Fig. 4.15: Relationship between M-NDSSI derived from Sentinel – 2 Satellite imagery and Spectroradiometer SVC – 1024i along with developed relations.**

#### 4.4.2 Development of Relationship between Band Combinations/ Ratios Derived from Sentinel – 2 Satellite Imagery and Spectroradiometer SVC – 1024i

Similarly, scatter plots were generated to visualize the relationships among various band combinations or ratios, specifically: i)  $(\text{Red} + \text{Green})/2$ , ii)  $(\text{Red} + \text{Green} + \text{Red Edge 1}) / 3$ , iii)  $(\text{Green} - \text{Red Edge 1})$ , and iv)  $(\text{Green} \times \text{Red Edge 1}) / \text{Red}$ . These combinations were derived from Sentinel 2 – BOA Satellite imagery and Spectroradiometer SVC – 1024i, and the corresponding scatter plots are shown in figures 4.17, 4.18, 4.19, and 4.20.

The figure 4.17 shows that, as obvious, there is good positive correlation between the considered variables in all the cases. The averaging effect of Red and Green band has achieved  $R^2$  ranging from 0.75 to 0.79 for exponential, logarithmic, linear, polynomial, and power equations. Results are improved when averaging effect of three bands i.e. Red, Green and Red Edge 1 derived from Sentinel 2 – BOA Satellite imagery and Spectroradiometer was related with each other (figure 4.18). All the developed mathematical relations have coefficient of determination greater than 0.8 with best fitting second order polynomial equation having  $R^2 = 0.87$ .

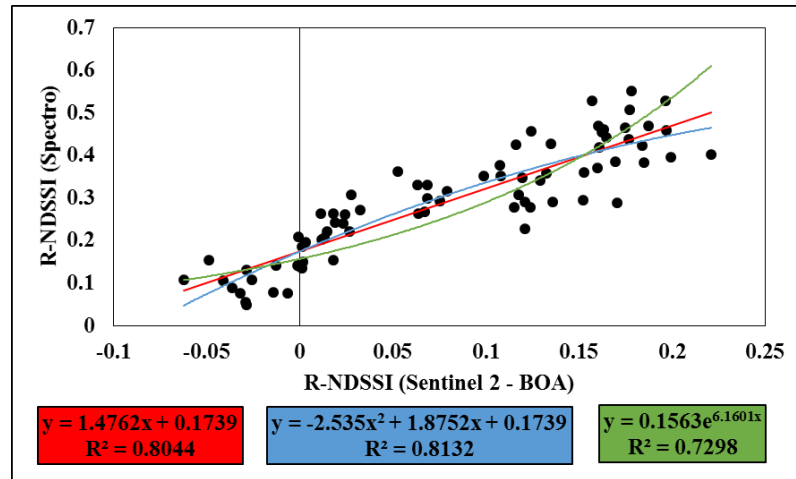


**Fig. 4.16: Relationship between R-NDSSI derived from Sentinel – 2 Satellite imagery and Spectroradiometer SVC – 1024i along with developed relations.**

The (Green - Red Edge 1) combination derived from Sentinel 2 – BOA Satellite imagery and Spectroradiometer exhibited comparatively weaker correlation, demonstrating R-squared values between 0.45 and 0.65, and the most accurate predictive model was found to be a second-order polynomial equation for this band combination (figure 4.19).

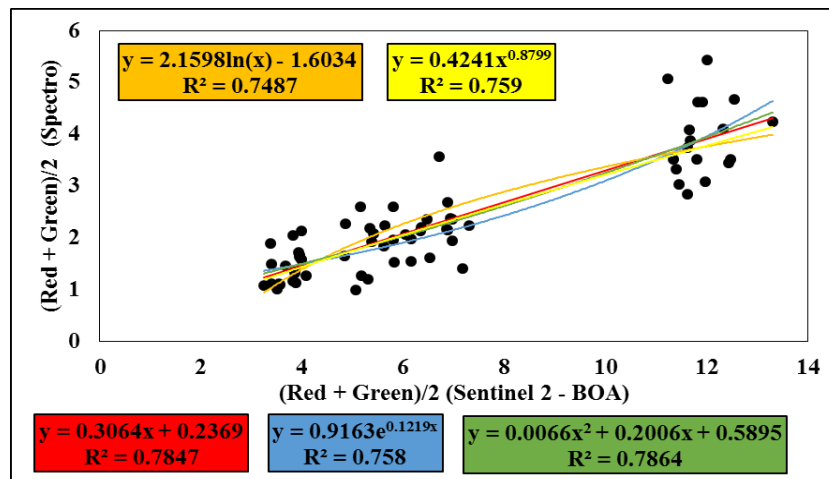


**Fig. 4.17: Relationship between  $(Red + Green) / 2$  derived from Sentinel – 2 Satellite imagery and Spectroradiometer SVC – 1024i**

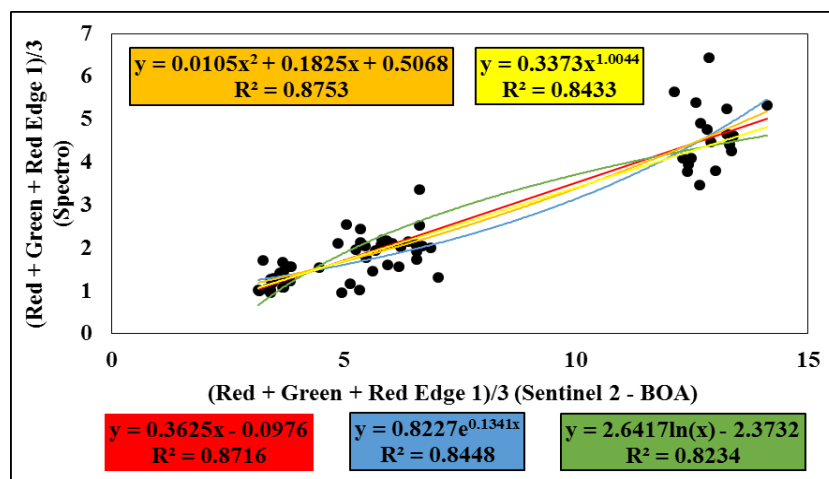


**Fig. 4.18: Relationship between  $(Red + Green + Red Edge 1) / 3$  derived from Sentinel – 2 Satellite imagery and Spectroradiometer SVC – 1024i**

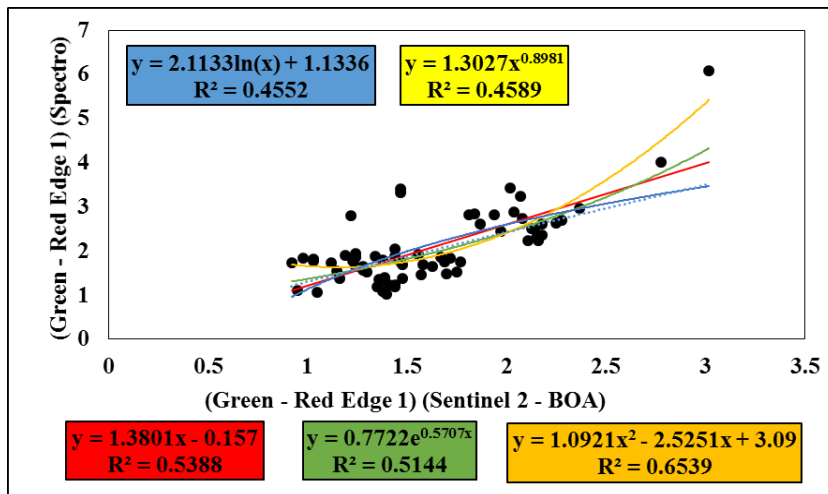


**Fig. 4.19: Relationship between (Green – Red) derived from Sentinel – 2 Satellite imagery and Spectroradiometer SVC – 1024i**

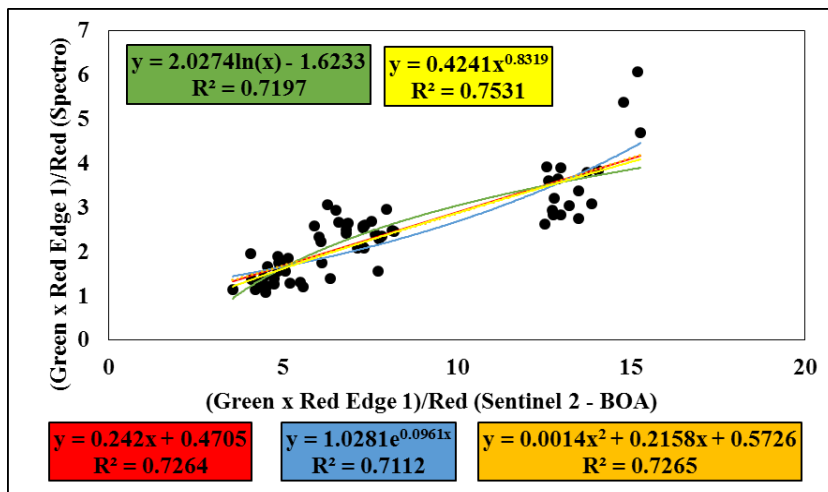


**Fig. 4.20: Relationship between (Green × Red Edge 1) / Red derived from Sentinel – 2 Satellite imagery and Spectroradiometer SVC – 1024i**

The scatter plot in Figure 4.20, depicting the band ratio (Green × Red Edge 1)/ Red derived from Sentinel 2 – BOA Satellite imagery and Spectroradiometer, indicates a strong positive correlation between the variables. Diverse mathematical relationships were established between these variables, yielding  $R^2$  values ranging from 0.7 to 0.75. Unlike prior observations, the most suitable fit was represented by a power equation, as evidenced by the higher  $R^2$  value.

In Section 4.3, Tables 4.2 and 4.3 presented various relationships between different band indices and or combinations/ratios with the observed suspended sediment concentration (mg/L) in the Mula dam reservoir. These relationships were established through calibration using 80 percent of the dataset. In Section 4.4, relationships between different band indices and combinations/ ratios derived from Sentinel 2 – BOA satellite imagery and ground-based Spectroradiometer were developed and detailed in Tables 4.4 and 4.5. To determine the most suitable predictive relationship for SSC in the Mula dam reservoir, validation and performance evaluation were necessary. This involved utilizing the remaining 20 percent (21 samples) of the dataset, which had been set aside for validation purposes.

**Table 4.4: Relation between different indices derived by Sentinel 2-BOA satellite imagery and Spectroradiometer.**

Sr. No	Variables	Type of relation	Equation	R <sup>2</sup>	Eqn. No.
1	x = M-NDSSI Satellite	<b>Linear</b>	<b>y = 0.5943x + 0.1747</b>	<b>0.53</b>	<b>4.32</b>
2	y = M-NDSSI Spectro	Polynomial	y = 0.2206x <sup>2</sup> + 0.6861x + 0.1828	0.53	4.33
3	x = NSMI Satellite y = NSMI Spectro	Linear	y = 1.3192x - 0.068	0.75	4.34
4		Logarithmic	y = 0.4045ln(x) + 0.8205	0.73	4.35
5		Exponential	y = 0.1044e <sup>3.7394x</sup>	0.76	4.36
6		<b>Polynomial</b>	<b>y = 5.631x<sup>2</sup> - 2.243x + 0.4801</b>	<b>0.77</b>	<b>4.37</b>
7		Power	y = 1.2985x <sup>1.1486</sup>	0.74	4.38
8	x = R-NDSSI Satellite	Linear	y = 1.4762x + 0.1739	0.80	4.39
9	y = R-NDSSI Spectro	Exponential	y = 0.1563e <sup>6.1601x</sup>	0.72	4.40
10		<b>Polynomial</b>	<b>y = -2.535x<sup>2</sup> + 1.8752x + 0.1739</b>	<b>0.81</b>	<b>4.41</b>

#### 4.5. Estimation of SSC using Validation Data Set

To estimate Suspended Sediment Concentration (SSC) using various band indices, band combinations, or ratio-based equations, the integrated relationships provided in Table 4.6 are used. These relationships involve the best-fit regression equations that establish the best relation between band indices/ ratios/ combinations derived from Sentinel – 2 BOA with similar indices/ ratios/ combinations derived from Spectroradiometer and a relation between SSC and the band indices, ratios, or combinations obtained from the Spectroradiometer. Thus, estimation of SSC using band indices/ ratios/ combinations developed from observations taken by Sentinel – 2 can be accomplished for 21 samples set aside for validation.

The table 4.7 and 4.8 show the estimated values of SSC against observed SSC using band indices and band ratio/ combination, respectively.

To determine the most suitable band indices, ratios, or combinations the set of observed SSC and estimated SSC were further subjected to visual interpretation, linear regression t-test, student t-test as discussed in the next section.

**Table 4.5: Relation between different band combinations/ ratios derived by Sentinel 2-BOA satellite imagery and Spectroradiometer.**

Sr. No	Variables	Type of relation	Equation	R <sup>2</sup>	Eqn. No.
1	x = (Red + Green)/2 Satellite y = (Red + Green)/2 Spectro	Linear	<b>y = 0.3064x + 0.2369</b>	<b>0.78</b>	4.42
2		Logarithmic	y = 2.1598ln(x) - 1.6034	0.74	4.43
3		Exponential	y = 0.9163e <sup>0.1219x</sup>	0.75	4.44
4		Polynomial	y = 0.0066x <sup>2</sup> + 0.2006x + 0.5895	0.79	4.45
5		Power	y = 0.4241x <sup>0.8799</sup>	0.76	4.46
6	x = (Red + Green + Red Edge 1)/3 Satellite y = (Red + Green + Red Edge 1)/3 Spectro	Linear	y = 0.3625x - 0.0976	0.87	4.47
7		Logarithmic	y = 2.6417ln(x) - 2.3732	0.82	4.48
8		Exponential	y = 0.8227e <sup>0.1341x</sup>	0.82	4.49
9		<b>Polynomial</b>	<b>y = 0.0105x<sup>2</sup> + 0.1825x + 0.5068</b>	<b>0.87</b>	<b>4.50</b>
10		Power	y = 0.3373x <sup>1.0044</sup>	0.84	4.51
11	x = (Green - Red Edge 1) Satellite y = (Green - Red Edge 1) Spectro	Linear	y = 1.5493x - 0.3108	0.55	4.52
12		Logarithmic	y = 2.4807ln(x) + 1.0981	0.48	4.53
13		Exponential	y = 0.7662e <sup>0.6041x</sup>	0.53	4.54
14		<b>Polynomial</b>	<b>y = 1.0052x<sup>2</sup> - 2.1435x + 2.8302</b>	<b>0.62</b>	<b>4.55</b>
15		Power	y = 1.3122x <sup>0.9912</sup>	0.48	4.56
16	x = (Green × Red Edge 1)/Red Satellite y = (Green × Red Edge 1)/Red Spectro	Linear	y = 0.242x + 0.4705	0.73	4.57
17		Logarithmic	y = 2.0274ln(x) - 1.6233	0.72	4.58
18		Exponential	y = 1.0281e <sup>0.0961x</sup>	0.71	4.59
19		Polynomial	y = 0.0014x <sup>2</sup> + 0.2158x + 0.5726	0.73	4.60
20		<b>Power</b>	<b>y = 0.4241x<sup>0.8319</sup></b>	<b>0.75</b>	<b>4.61</b>

**Table 4.6: Integrated relationships of band index/ ratio / combination used for estimation of SSC (mg/L)**

	Relationships	x	y	R <sup>2</sup>
Spectral Integration of NSMI	$y = 5.631x^2 - 2.243x + 0.4801$	NSMI <sub>Sentinel - 2</sub>	Estimated NSMI <sub>Spectro</sub>	0.77
	$y = -130.52x^2 + 380.14x - 51.756$	Estimated NSMI <sub>Spectro</sub>	Estimated SSC (mg/L)	0.50
Spectral Integration of M-NDSSI	$y = 0.2206x^2 + 0.6861x + 0.1828$	M-NDSSI <sub>Sentinel - 2</sub>	Estimated M-NDSSI <sub>Spectro</sub>	0.53
	$y = 418.34x^2 - 340x + 74.628$	Estimated M-NDSSI <sub>Spectro</sub>	Estimated SSC (mg/L)	0.60
Spectral Integration of R-NDSSI	$y = -2.535x^2 + 1.8752x + 0.1739$	R-NDSSI <sub>Sentinel - 2</sub>	Estimated R-NDSSI <sub>Spectro</sub>	0.81
	$y = 289.64x^2 - 380.19x + 143.95$	Estimated R-NDSSI <sub>Spectro</sub>	Estimated SSC (mg/L)	0.78
Spectral Integration of (Red + Green)/2	$y = 0.3064x + 0.2369$	(Red + Green)/2 <sub>Sentinel - 2</sub>	Estimated (Red + Green)/2 <sub>Spectro</sub>	0.78
	$y = -3.5201x^2 + 47.165x - 22.315$	Estimated (Red + Green)/2 <sub>Spectro</sub>	Estimated SSC (mg/L)	0.67
Spectral Integration of (Red + Green + Red Edge 1)/3	$y = 0.0105x^2 + 0.1825x + 0.5068$	(Red + Green + Red Edge 1)/3 <sub>Sentinel - 2</sub>	Estimated (Red + Green + Red Edge 1)/3 <sub>Spectro</sub>	0.87
	$y = -3.9145x^2 + 48.303x - 24.774$	Estimated (Red + Green + Red Edge 1)/3 <sub>Spectro</sub>	Estimated SSC (mg/L)	0.82
Spectral Integration of Green – Red Edge 1	$y = 1.0052x^2 - 2.1435x + 2.8302$	(Green – Red Edge 1) <sub>Sentinel - 2</sub>	Green – Red Edge 1 <sub>Spectro</sub>	0.62
	$y = -5.3835x^2 + 60.241x - 39.716$	Green – Red Edge 1 <sub>Spectro</sub>	Estimated SSC (mg/L)	0.71
Spectral Integration of (Green × Red Edge 1)/Red	$y = 0.4241x^{0.8319}$	[(Green × Red Edge 1)/Red] <sub>Sentinel - 2</sub>	(Green × Red Edge 1)/Red <sub>Spectro</sub>	0.75
	$y = -1.9781x^2 + 33.124x - 15.289$	(Green × Red Edge 1)/Red <sub>Spectro</sub>	Estimated SSC (mg/L)	0.86

**Table 4.7: Estimated values of SSC against observed SSC using band indices**

<b>Observed SSC (mg/L)</b>	<b>Estimated SSC (mg/L) using Spectral Integration of</b>		
	<b>NSMI</b>	<b>M-NDSSI</b>	<b>R-NDSSI</b>
15.96	40.99	43.13	34.30
23.53	49.84	42.89	36.55
17.39	44.13	38.52	34.34
23.66	49.78	42.73	37.64
15.62	45.14	39.08	34.23
52.84	41.85	48.50	37.98
55.83	44.82	55.15	41.73
56.70	51.96	55.84	47.73
49.76	44.42	47.40	40.36
62.37	50.25	53.32	42.84
62.89	41.07	41.72	34.43
56.70	42.97	49.62	40.09
42.93	49.28	56.81	44.89
64.00	57.38	61.58	52.45
44.64	50.83	52.24	38.99
41.00	66.51	76.84	93.34
62.00	81.28	77.17	77.15
73.08	86.14	78.50	82.68
92.23	73.68	75.68	76.07
115.31	82.10	69.04	81.95
107.84	86.81	74.41	93.57

**Table 4.8: Estimated values of SSC against observed SSC using band ratio/ combinations**

Observed SSC (mg/L)	Estimated SSC (mg/L) by Spectral Integration of			
	(Red + Green)/2	(Red + Green + Red Edge 1)/3	Green - Red Edge 1	(Green x Red Edge 1)/Red
15.96	37.94	32.32	47.88	29.99
23.53	38.97	32.62	59.50	32.56
17.39	32.47	27.58	49.31	27.19
23.66	35.77	30.19	49.31	27.72
15.62	35.66	29.99	49.31	26.78
52.84	65.94	58.58	54.73	47.89
55.83	75.52	68.80	65.19	56.29
56.70	59.56	52.44	55.46	47.09
49.76	59.66	52.37	61.30	48.11
62.37	68.32	60.56	70.54	50.65
62.89	62.83	54.74	72.23	47.13
56.70	60.31	53.22	48.53	43.98
42.93	54.09	47.14	47.74	39.91
64.00	53.52	46.70	47.48	40.07
44.64	53.52	45.49	63.20	39.05
41.00	59.96	55.68	73.52	46.92
62.00	109.49	107.73	90.70	77.46
73.08	113.71	112.47	104.63	81.80
92.23	109.58	108.62	62.72	78.01
115.31	117.27	116.53	114.96	87.70
107.84	112.43	111.98	69.98	82.24

#### **4.6 Validation of Integrated Relationships of Band Index/ Ratio / Combination used for Estimation of SSC**

##### **4.6.1. Visual Interpretation, Slope and y-intercept**

The study used a comprehensive analysis of band indices, ratios, and combinations, calibrated to estimate Suspended Sediment Concentration (SSC). These include spectral integration functions of NSMI, M-NDSSI, R-NDSSI, (Red + Green)/2, (Red + Green + Red Edge 1)/3, (Green - Red Edge 1), and (Green x Red Edge 1)/Red. The data were visually interpreted through line graphs, revealing distinctive patterns and associations between the observed SSC and the SSC estimates.

When spectral integration functions such as NSMI, M-NDSSI, R-NDSSI, and Green - Red Edge 1 were employed (as shown in figures 4.21(a), 4.22 (a), 4.23(a), and 4.26 (a)), visual differences in the magnitude of observed and estimated SSC were seen. Moreover, these functions yielded line graphs with a more intricate and zigzag pattern, suggesting less reliable SSC estimations. Among the three indices M-NDSSI showed a more close association between observed SSC and estimated SSC in visual interpretation.

It is evident that certain spectral integration functions, specifically of  $(\text{Red} + \text{Green})/2$ ,  $(\text{Red} + \text{Green} + \text{Red Edge 1})/3$ , and  $(\text{Green} \times \text{Red Edge 1})/\text{Red}$  (as demonstrated in figures 4.24 (a), 4.25 (a), and 4.27 (a)), exhibited a close and noteworthy association between the observed and estimated SSC. The arrangement of line graphs in these cases displayed somewhat parallel nature, underlining the potential utility of these functions in estimating SSC accurately.

This method of visual interpretation provided a synoptic view of the performance of the considered band functions. However, to substantiate these visual findings, a more rigorous quantitative approach linear regression was used. Graphs along with linear equation in the figure 4.21 (b) to 4.27 (b) shows correlation between estimated and observed SSC with and without  $y -$  intercept for integrated band functions considered in the study.

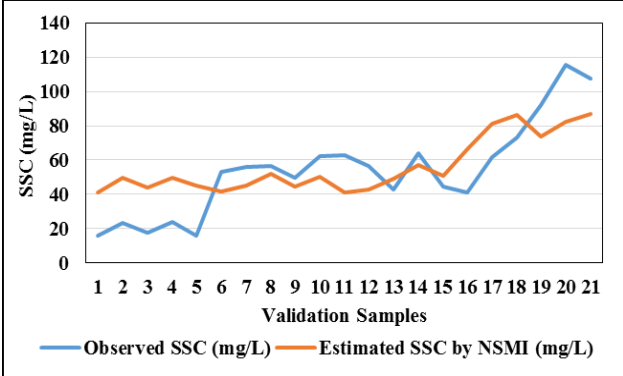
The spectral integration functions of NSMI and M-NDSSI exhibited  $R^2$  almost equal to 0.5 with  $y -$  intercept. Without  $y -$  intercept both of them exhibited negative  $R^2$  (-0.429) and -1.009 respectively. This is often referred to as a "zero-intercept" or "forced-origin" regression. When the regression line is constrained to pass through the origin (0, 0), it has the potential to distort the fit, particularly if the actual intercept is not zero. The distortion introduced by enforcing the regression line to pass through the origin may lead to negative R-squared values. Negative R-squared values signify that the model's explained variation is less than the total variation, indicating a poor fit.

The performance of R-NDSSI as an estimator for SSC was slightly better, with an  $R^2$  of 0.212 (without  $y -$  intercept). While this is an improvement compared to NSMI and M-NDSSI, it is still not sufficient to consider R-NDSSI as an effective estimator for SSC as  $R^2$  does not exceed 0.5 with  $y -$  intercept.

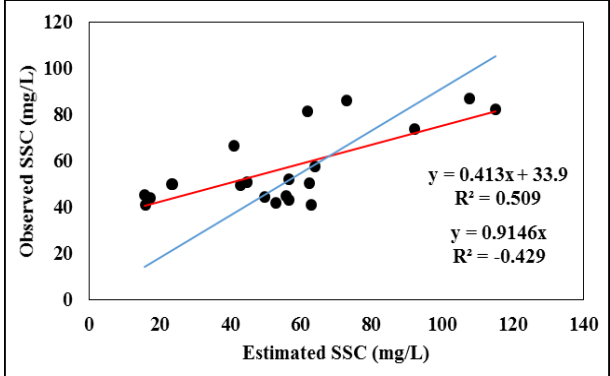
The spectral integration function of (Green - Red Edge 1) performed poorly compared to other band ratios and combinations, as it exhibited an R-squared ( $R^2$ ) value of 0.41 in both cases (with and without a  $y$ -intercept). This  $R^2$  value indicate a weaker linear relationship and less accurate predictive power.

Spectral integration functions of  $(\text{Red} + \text{Green})/2$ ,  $(\text{Red} + \text{Green} + \text{Red Edge 1})/3$ , and  $(\text{Green} \times \text{Red Edge 1})/\text{Red}$  performed well in terms of linear regression analysis between observed and estimated SSC. All of them exhibited  $R^2$  greater than 0.75 in both the cases, with and without  $y -$  intercept.  $R^2$  values greater than 0.75 in linear regression indicate a strong and reliable linear relationship between the independent (estimated SSC) and dependent (observed SSC) variables, with over 75% of the variance in the dependent variable being explained by the independent variable.

On the other hand, Spectral integration functions of R-NDSSI and (Green – Red Edge 1) though slightly more effective with an R<sup>2</sup> of 0.212 and 0.41 respectively, does not meet the desired level of performance. In contrast, (Red + Green)/2, (Red + Green + Red Edge 1)/3, and (Green x Red Edge 1)/Red demonstrated strong and reliable linear relationships with R<sup>2</sup> values exceeding 0.75 in the three cases.

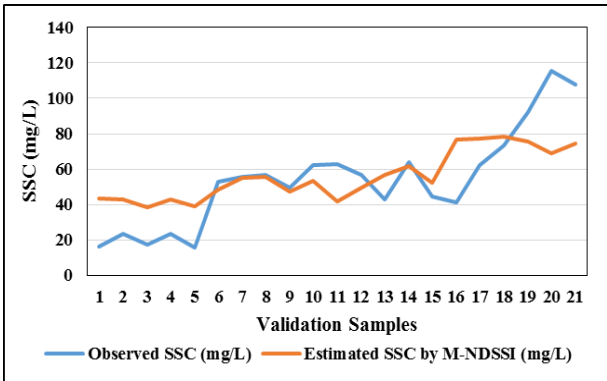


(a)

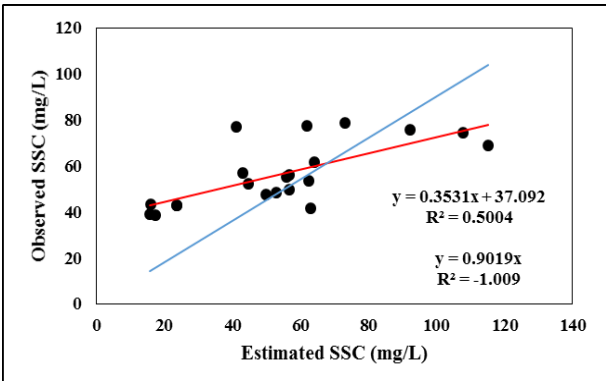


(b)

**Figure 4.21: Comparison of observed and estimated SSC using Spectral Integration of NSMI using a) line graph and b) linear regression**

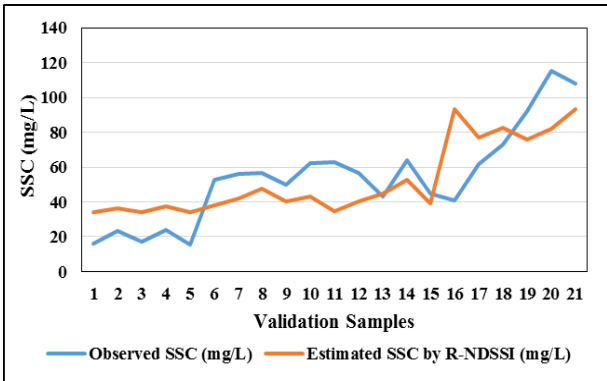


(a)

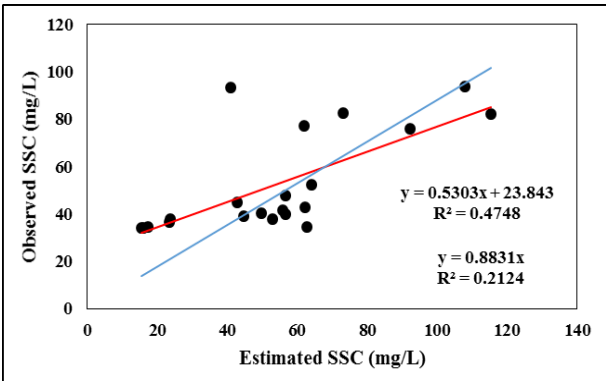


(b)

**Figure 4.22: Comparison of observed and estimated SSC using Spectral Integration of M-NDSSI using a) line graph and b) linear regression**

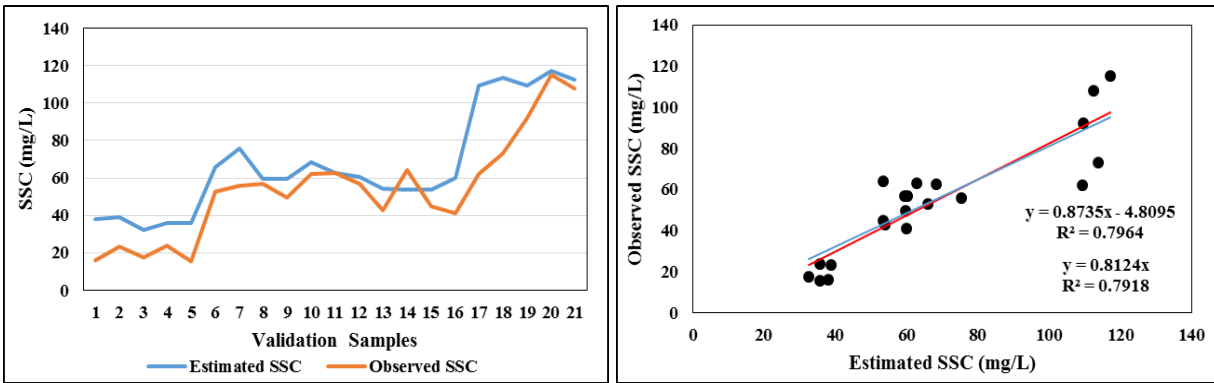


(a)



(b)

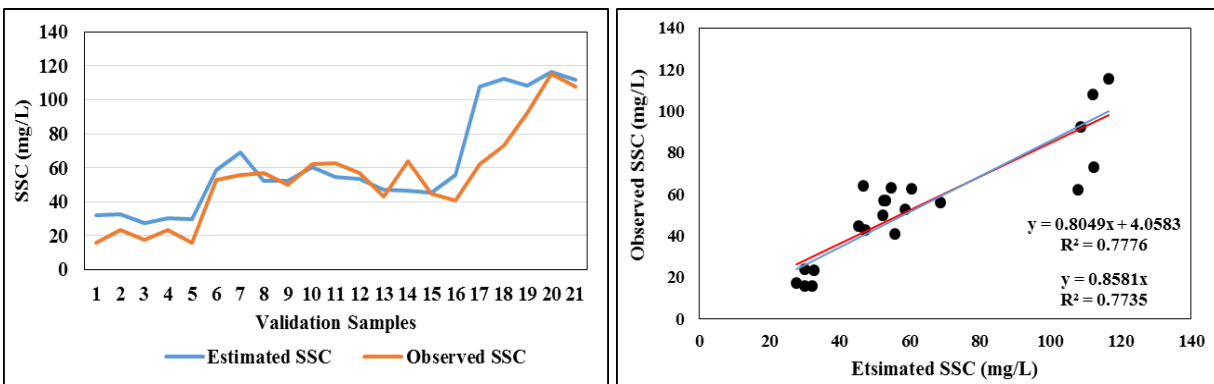
**Figure 4.23: Comparison of observed and estimated SSC using Spectral Integration of R-NDSSI using a) line graph and b) linear regression**



(a)

(b)

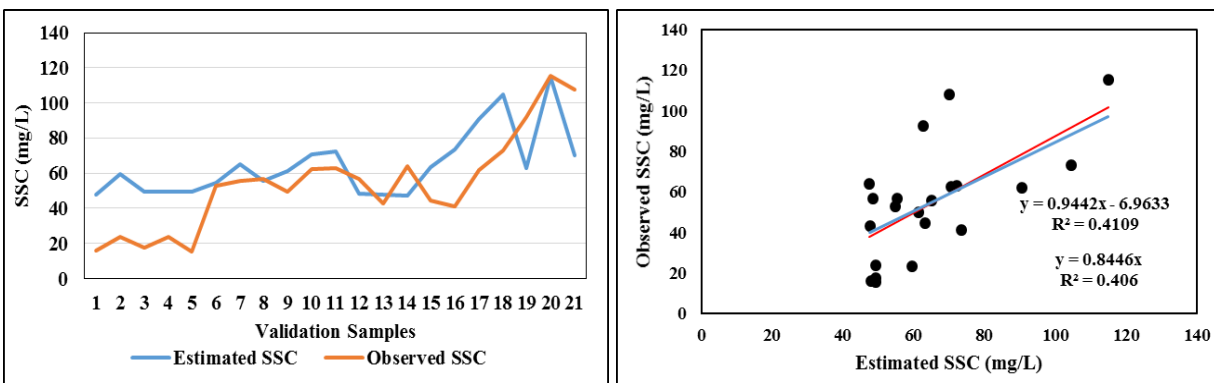
**Figure 4.24: Comparison of observed and estimated SSC using Spectral Integration of (Red + Green)/2 using a) line graph and b) linear regression**



(a)

(b)

**Figure 4.25: Comparison of observed and estimated SSC using Spectral Integration of (Red + Green + Red Edge 1)/3 using a) line graph and b) linear regression**



(a)

(b)

**Figure 4.26: Comparison of observed and estimated SSC using Spectral Integration of (Green - Red Edge 1) using a) line graph and b) linear regression**

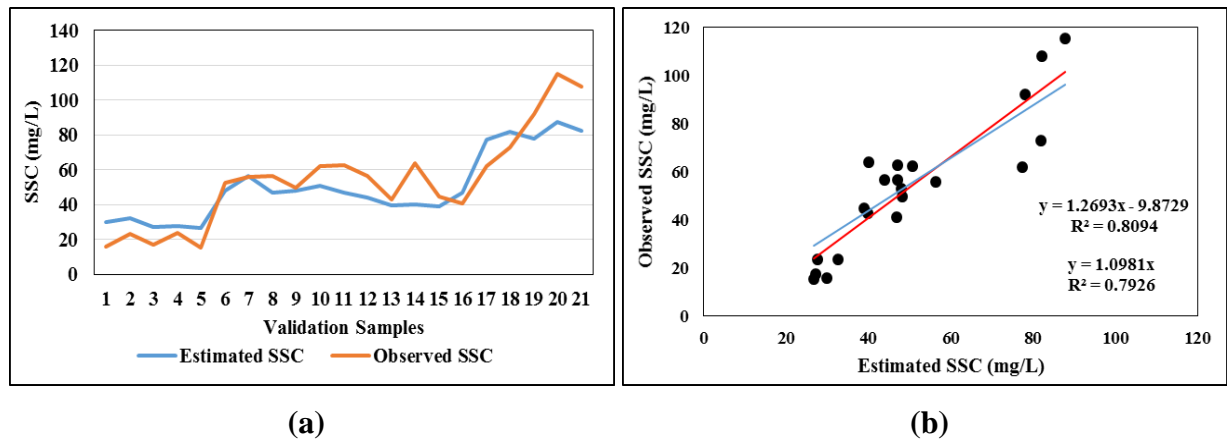


**Figure 4.27: Comparison of observed and estimated SSC using Spectral Integration of (Green x Red Edge 1)/Red using a) line graph and b) linear regression**

#### 4.6.2. Performance Evaluation using tests of Significance

In the light of  $R^2$  values obtained from the analysis of spectral integration functions for estimating SSC, NSMI and M-NDSSI displayed relatively weak linear relationships with  $R^2$  values of 0.5 and even negative  $R^2$  values when the y-intercept was excluded. As a result, t-test for testing the hypothesis of  $a = 0$  and  $b = 1$  for linear relationship ' $y = ax + b$ ' and difference between mean of observed and mean of estimated SSC to be zero, were not carried out.

On the other hand, Spectral integration functions of R-NDSSI and (Green – Red Edge 1) with  $R^2$  of 0.212 and 0.41 respectively, does not meet the desired level of performance. In contrast, the band functions of (Red + Green)/2, (Red + Green + Red Edge 1)/3, and (Green × Red Edge 1)/Red demonstrated strong and reliable linear relationships with  $R^2$  values exceeding 0.75 in all the three cases. Consequently, the t-test for testing the hypothesis of  $a = 0$  and  $b = 1$  for linear relationship ' $y = ax + b$ ' and difference between mean of observed and mean of estimated SSC, to be zero were carried out to find suitable estimator of SSC.

The calculated values of t statistic for a, b and difference of means along with table values of student t-test at 5 per cent level of significance and inference based on these values are shown in table 4.9.

In the preliminary evaluation using linear regression at a 5% level of significance with 19 degrees of freedom, all considered functions were found to be statistically insignificant. This means that the null hypothesis ( $H_0: a = 0$  and  $b = 1$ ) was accepted for all cases.

To further evaluate the differences between the mean values of estimated and observed Suspended Sediment Concentration (SSC), a secondary analysis was conducted using Student t-test. In this analysis, it was found that the test statistic ( $t_{cal}$ ) has a magnitude greater than the critical  $t_{table}$  value (2.093) at 5% level of significance, with 19 degrees of freedom for the Spectral integration functions of (Red + Green)/2 and Spectral Integration of (Green – Red Edge 1).

The mean SSC for the observed values was determined to be 54.10 mg/L. However, the Spectral integration functions of (Red + Green)/2 and Spectral Integration of (Green – Red Edge 1) both overestimated the SSC, with mean values of 67.45 mg/L and 64.67 mg/L, respectively. The absolute difference between these estimated means and the observed mean exceeded 10 mg/L in both cases. As a result of this statistically significant difference between the mean values of estimated and observed SSC, it was decided to reject these two Spectral integration functions of (Red + Green)/2 and (Green – Red Edge 1) in the further analysis.

Spectral Integration Functions of R-NDSSI, [(Red + Green + Red Edge 1)/3], and (Green x Red Edge 1)/Red were found statistically insignificant with test statistic ( $t_{cal}$ ) less than  $t_{table}$  value having 19 degrees of freedom at 5 per cent level of significance with mean of estimated SSC as observed to be 52.53 mg/L, 62.17 mg/L and 50.40 mg/L respectively against mean of observed SSC equal to 54.10 mg/L.

#### 4.6.3. Performance Evaluation using Statistical Indicators

To find the most suitable relationship for estimation of SSC, further performance evaluation was carried out using various statistical indicators, such as Root Mean Square Error (RMSE), Mean Absolute Percentage Error (MAPE), Nash-Sutcliffe Efficiency (NSE), and the Index of Agreement. These indicators are commonly used to assess the accuracy and reliability of estimators and models.

The table 4.10 presents a comprehensive analysis of three spectral integration functions used to estimate Suspended Sediment Concentration (SSC). These functions are evaluated based on various performance metrics. First, the Coefficient of Determination ( $R^2$ ) of linear regression offers insights into the goodness of fit between the estimated SSC and the observed values. "Spectral Integration of (Green × Red Edge 1)/Red" demonstrates the highest  $R^2$  value of 0.80, indicating the best fit between estimated and the observed SSC data, followed by "Spectral Integration of (Red + Green + Red Edge 1)/3" having  $R^2$  of 0.77 and "Spectral Integration of R-NDSSI"  $R^2$  of 0.47.

The Root Mean Square Error (RMSE) measures the average error between the estimated and observed SSC values. Here, "Spectral Integration of (Green × Red Edge 1)/Red" outperforms the others with an RMSE of 8.58 mg/L, suggesting the smallest overall deviation from the observed SSC. "Spectral Integration of (Red + Green + Red Edge 1)/3" follows with an RMSE of 11.86 mg/L, while "Spectral Integration of R-NDSSI" has the highest RMSE at 12.30 mg/L.

The Mean Absolute Percentage Error (MAPE) (Khair *et al.*, 2017) quantifies the percentage difference between the estimated SSC from observed SSC. Lower MAPE values indicate more accurate estimates. "Spectral Integration of (Green × Red Edge 1)/Red" excels in this regard, with a MAPE of 19.41%, followed by "Spectral Integration of R-NDSSI" at 21.58% and "Spectral Integration of (Red + Green + Red Edge 1)/3" with the highest MAPE at 26.93%.

**Table 4.9: Test statistics for Linear Regression t-tests and Student t-tests**

Function	Test	Test statistic	Value	Status w.r.t. to table value @ 5 % LOS	Remark
<b>Spectral Integration of R-NDSSI</b>	Linear Regression t-test	t(a)	0.03	< t <sub>table</sub> = 2.093	Non-significant
		t(b)	0.51	< t <sub>table</sub> = 2.093	Non-significant
	Student t-test	t <sub>cal</sub>	0.36	< t <sub>table</sub> = 2.093	Non-significant
<b>Spectral Integration of (Red + Green)/2</b>	Linear Regression t-test	t(a)	0.01	< t <sub>table</sub> = 2.093	Non-significant
		t(b)	0.63	< t <sub>table</sub> = 2.093	Non-significant
	Student t-test	t <sub>cal</sub>	<b>2.41</b>	<b>&gt; t<sub>table</sub> = 2.093</b>	<b>Significant</b>
<b>Spectral Integration of (Red + Green + Red Edge 1)/3</b>	Linear Regression t-test	t(a)	0.01	< t <sub>table</sub> = 2.093	Non-significant
		t(b)	1.05	< t <sub>table</sub> = 2.093	Non-significant
	Student t-test	t <sub>cal</sub>	1.47	< t <sub>table</sub> = 2.093	Non-significant
<b>Spectral Integration of Green – Red Edge 1</b>	Linear Regression t-test	t(a)	0.02	< t <sub>table</sub> = 2.093	Non-significant
		t(b)	0.25	< t <sub>table</sub> = 2.093	Non-significant
	Student t-test	t <sub>cal</sub>	<b>2.66</b>	<b>&gt; t<sub>table</sub> = 2.093</b>	<b>Significant</b>
<b>Spectral Integration of (Green × Red Edge 1)/Red</b>	Linear Regression t-test	t(a)	0.02	< t <sub>table</sub> = 2.093	Non-significant
		t(b)	0.92	< t <sub>table</sub> = 2.093	Non-significant
	Student t-test	t <sub>cal</sub>	0.66	< t <sub>table</sub> = 2.093	Non-significant

The Nash-Sutcliffe Efficiency (NSE) (Nash and Sutcliffe, 1970) evaluates the predictive performance relative to the mean of observed values. "Spectral Integration of (Green × Red Edge 1)/Red" and "Spectral Integration of (Red + Green + Red Edge 1)/3" both demonstrate relatively high NSE values of 0.76 and 0.80, respectively, while "Spectral Integration of R-NDSSI" is slightly lower at 0.76.

Lastly, the Index of Agreement (d) (Willmott, 1981) measures the agreement between estimated and observed SSC values. "Spectral Integration of (Green × Red Edge 1)/Red" again leads with the highest d value of 0.85, indicating the best agreement. "Spectral Integration of R-NDSSI" follows closely with a d value of 0.79, and "Spectral Integration of (Red + Green + Red Edge 1)/3" has the lowest d at 0.76.

Thus, "Spectral Integration of (Green × Red Edge 1)/Red" emerges as the most accurate and reliable estimator for SSC, outperforming the other two functions across various performance metrics. "Spectral Integration of (Red + Green + Red Edge 1)/3" also performs well but exhibits slightly higher errors. As indicated by lower R<sup>2</sup>, higher RMSE, and higher MAPE, the "Spectral Integration of R-NDSSI" resulted in poor performance than other two functions.

**Table 4.10: Values of various Statistical Indicators for Spectral Integration Functions**

Function	R <sup>2</sup>	RMSE (mg/L)	MAPE (per cent)	NSE	d
Spectral Integration of R-NDSSI	0.47	12.30	21.58	0.76	0.79
Spectral Integration of (Red + Green + Red Edge 1)/3	0.77	11.86	26.93	0.80	0.76
Spectral Integration of (Green × Red Edge 1)/Red	0.80	8.58	19.41	0.76	0.85

#### 4.7. Mapping of Suspended Sediment Concentration in Mula Dam Reservoir

Utilizing "Spectral Integration of (Green × Red Edge 1)/Red" as the most precise estimator for Suspended Sediment Concentration (SSC), spatio-temporal maps of SSC within the surface waters of the Mula Dam reservoir were created. Historical imagery from the Sentinel-2 (BOA) satellite were used to check the suitability of best-fitting function in mapping SSC across varying time frames, specifically spanning from October 2019 to February 2020 and from October 2020 to February 2021.

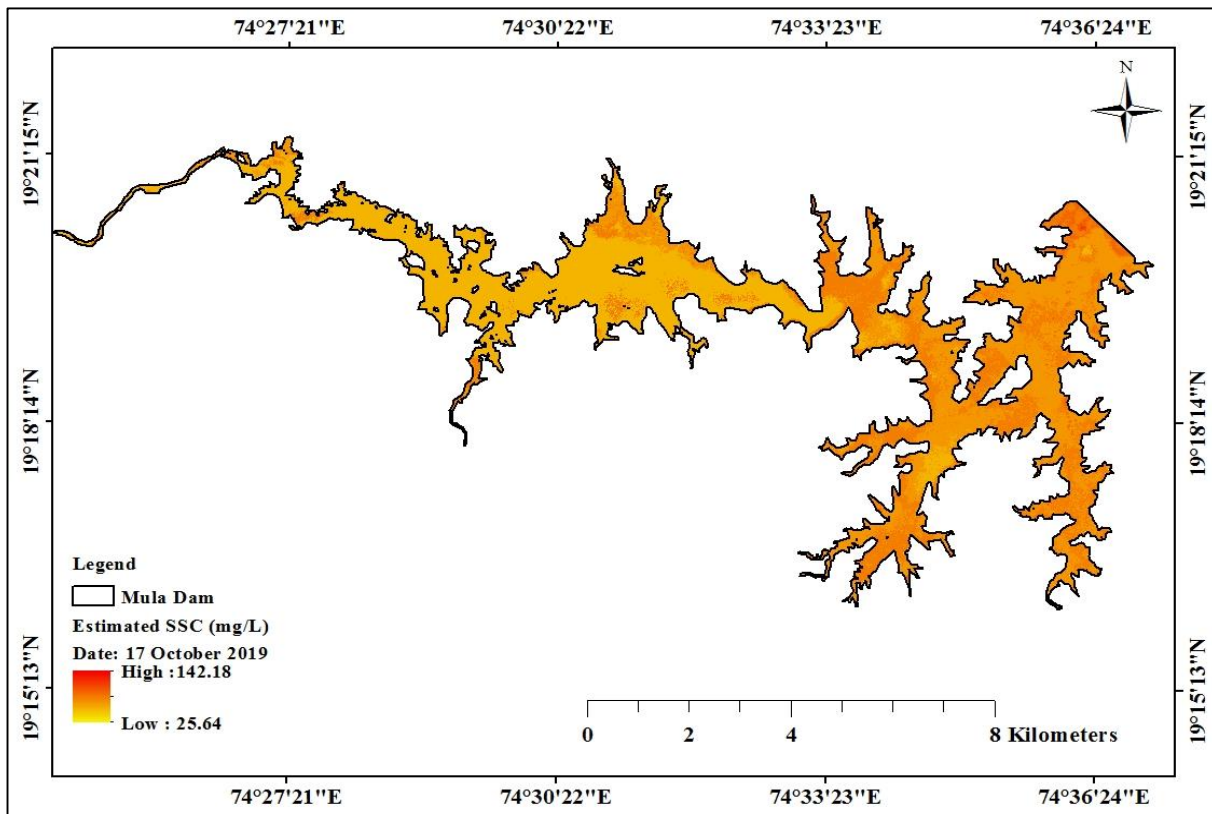
Figures 4.28 to 4.32 depict the spatial mapping of Suspended Sediment Concentration (SSC) in Mula dam reservoir on specific dates: October 17, 2019, and October 16, 2020; November 11, 2019; December 16, 2019, and December 20, 2020 (the image on December 15, 2020, was obscured by cloud cover over the Mula dam reservoir); January 15, 2020, and January 14, 2021; and February 14, 2020, and February 13, 2019. This approach facilitated a synoptic and rapid assessment of the spatio-temporal distribution of SSC in the surface water of the Mula dam reservoir.

The mapping of suspended sediment concentration (SSC) in Mula Dam reservoir from October 2019 to February 2020 and October 2020 to February 2021 provides a few insights into the reservoir's sediment dynamics and seasonal trends. In both years, there's a seasonal pattern, with higher SSC levels consistently observed in October and November, indicative of intensified sediment runoff as compared to December, January and February. For instance, in October 2019, SSC ranged from 25.64 mg/L to 142.18 mg/L, reflecting substantial sediment inflow. This trend continued into November 2019, with SSC ranging from 18.70 mg/L to 117.89 mg/L in 2019 and 28.58 mg/L to 124.25 mg/L in November, 2020. Conversely, January and February consistently displayed lower SSC values, likely due to reduced sediment transport during drier periods. In January 2021, the dataset registered the lowest SSC values, with a range of 8.57 mg/L to 115.23 mg/L. Moreover, a year-on-year comparison reveals increased sediment concentrations in October and November of 2020 compared to 2019, with October 2020 ranging from 36.42 mg/L to 133.49

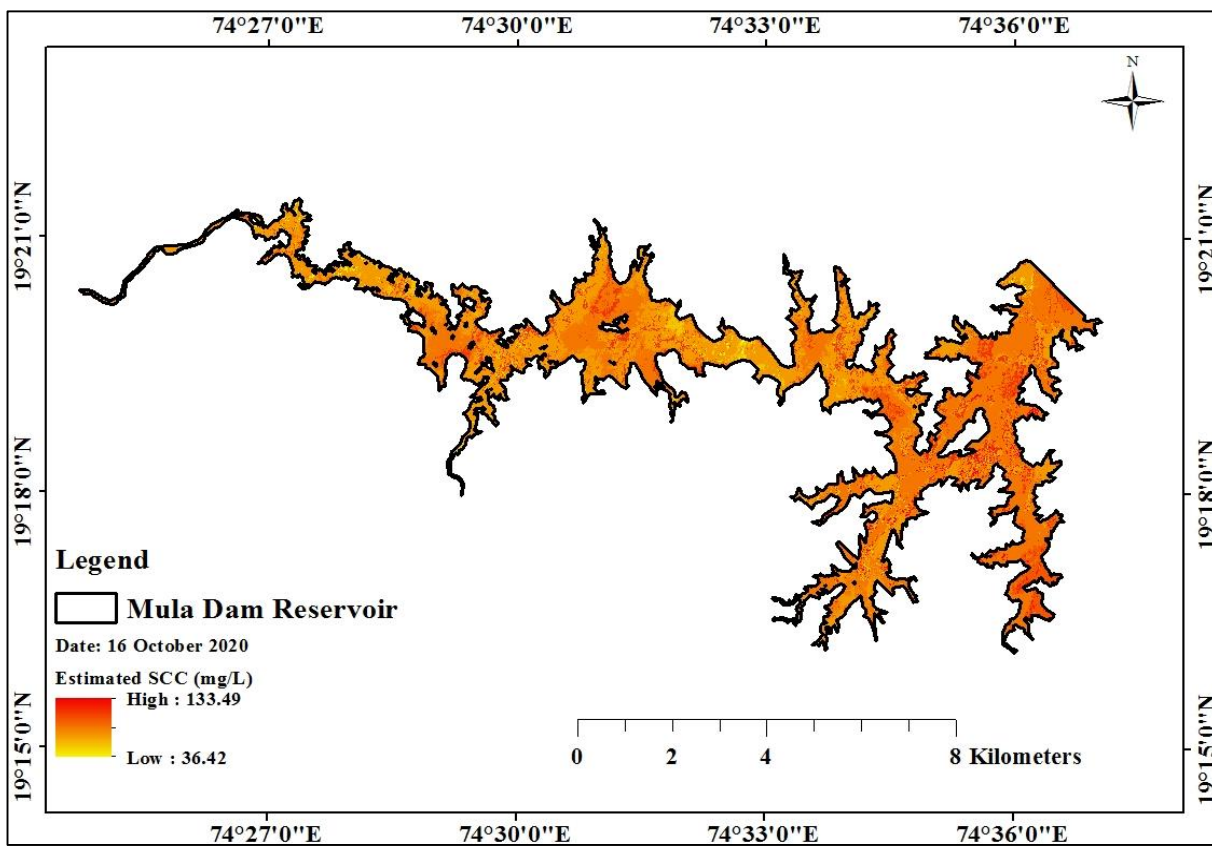
mg/L. It is also observed that, there is comparatively higher SSC in the region where the river enters the reservoir and in the dendritic portions where small streams contribute to the reservoir. This is due to turbulence caused by incoming flow which keeps the incoming sediment in suspended state whereas in central portion, velocity is relatively low which allows the silt to get deposited.

The observed and estimated data for Suspended Sediment Concentration (SSC) in the surface waters of Mula Dam reservoir consistently reveal lower concentrations. This indicates that the reservoir maintains relatively low levels of suspended sediments. World Health Organization, Environment Protection Agency, and the European Union have not provided a standard for Total Suspended Matter in drinking or domestic water.

However, it's important to continue monitoring SSC levels, as they can change due to seasonal variations, weather patterns, land use, and other factors. Consistent monitoring can help ensuring the long-term sustainability and water quality of the reservoir. These findings underline the seasonal dynamics of sediment in the reservoir and emphasize the need for continuous monitoring and adaptive management, especially during peak rainy seasons, to maintain water quality and preserve the reservoir's ecological balance.

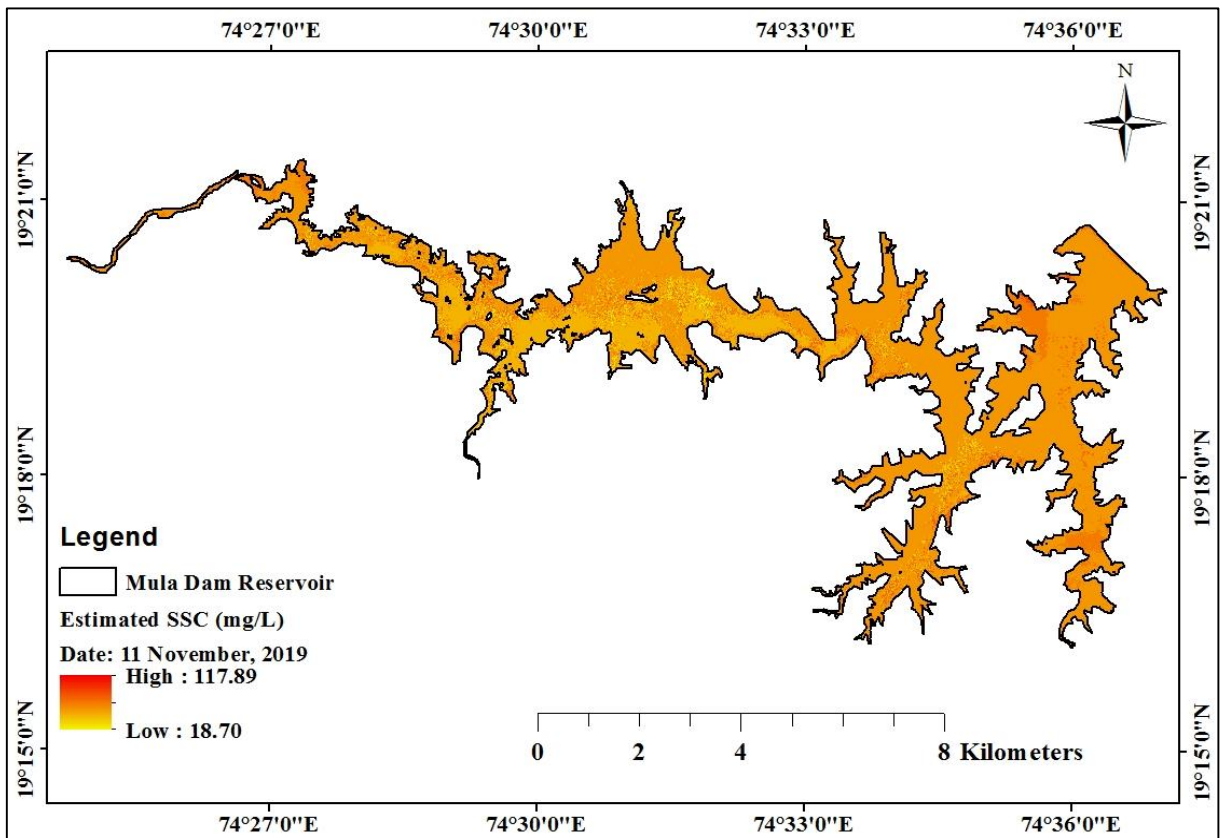


(a)

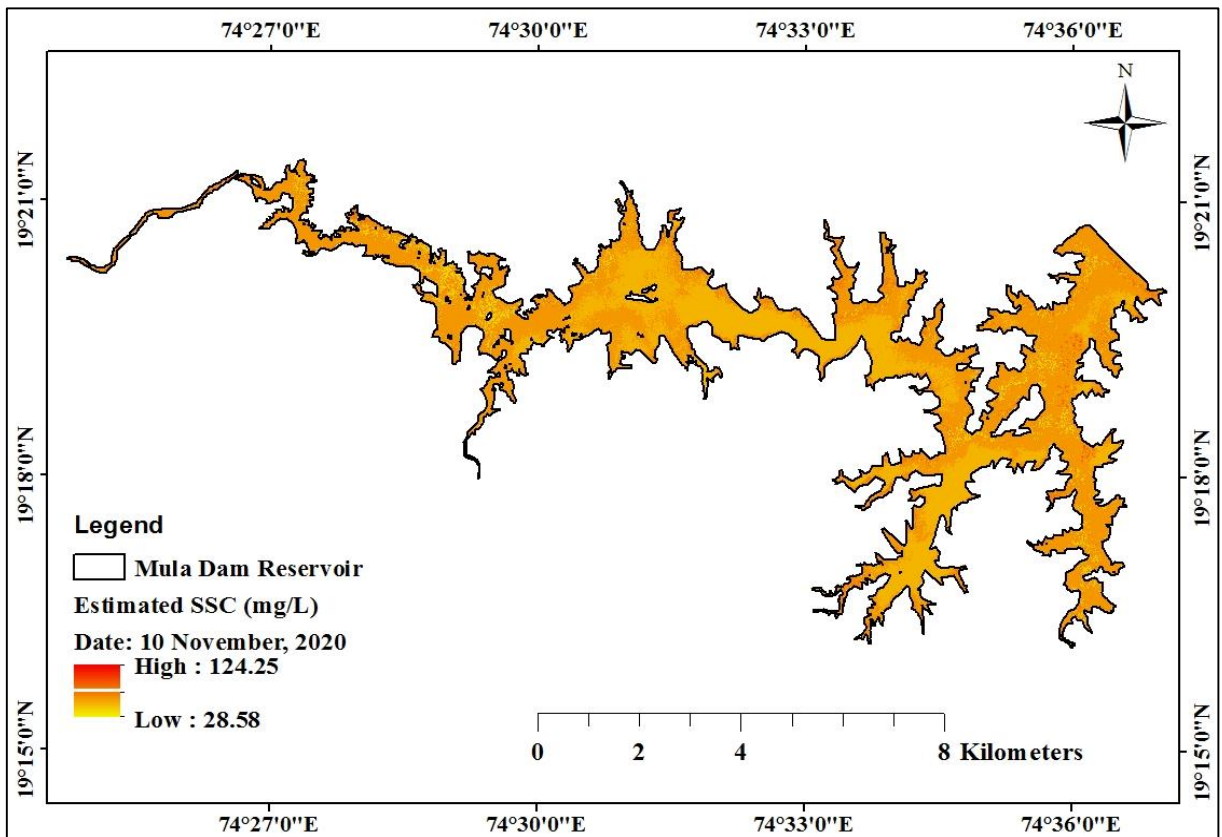


(b)

**Figure 4.28: Distribution of SSC in surface waters of Mula dam reservoir on a) 17<sup>th</sup> October, 2019 and b) 16<sup>th</sup> October, 2020**

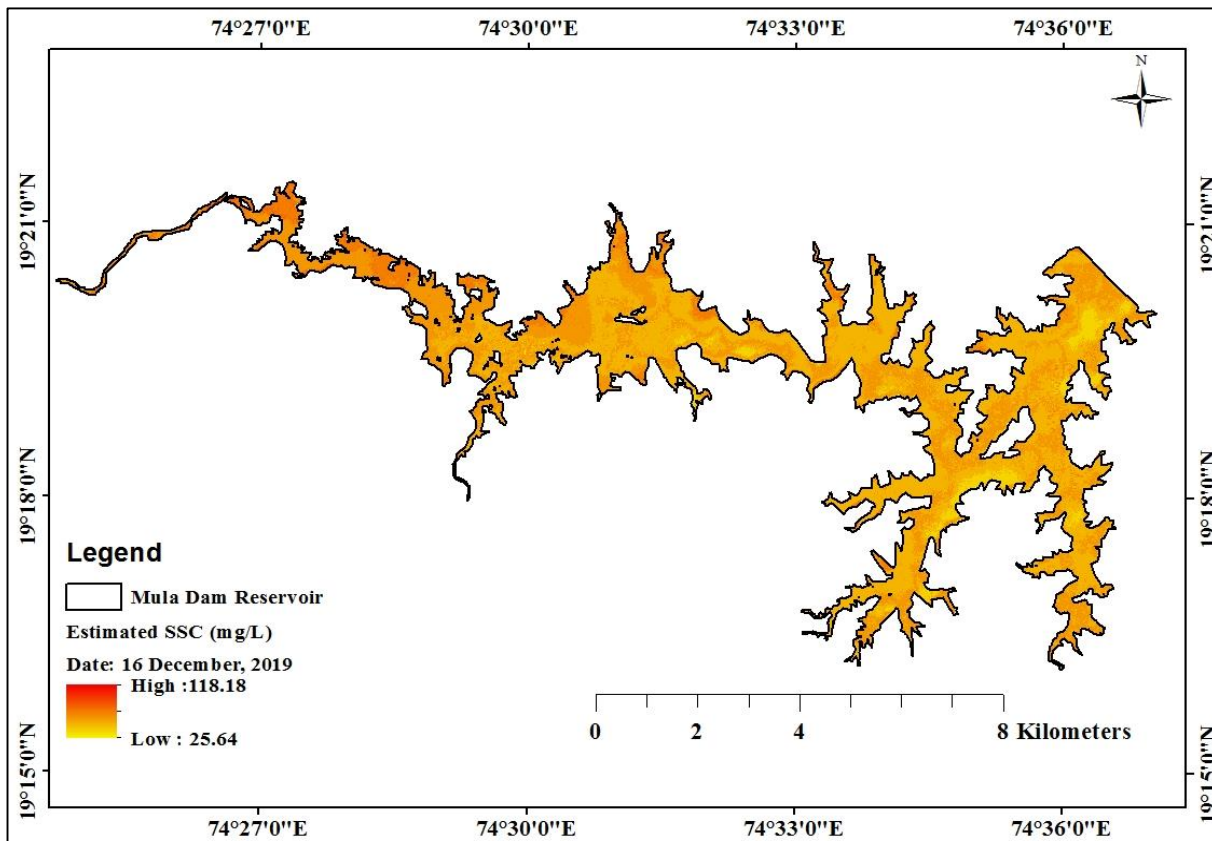


(a)

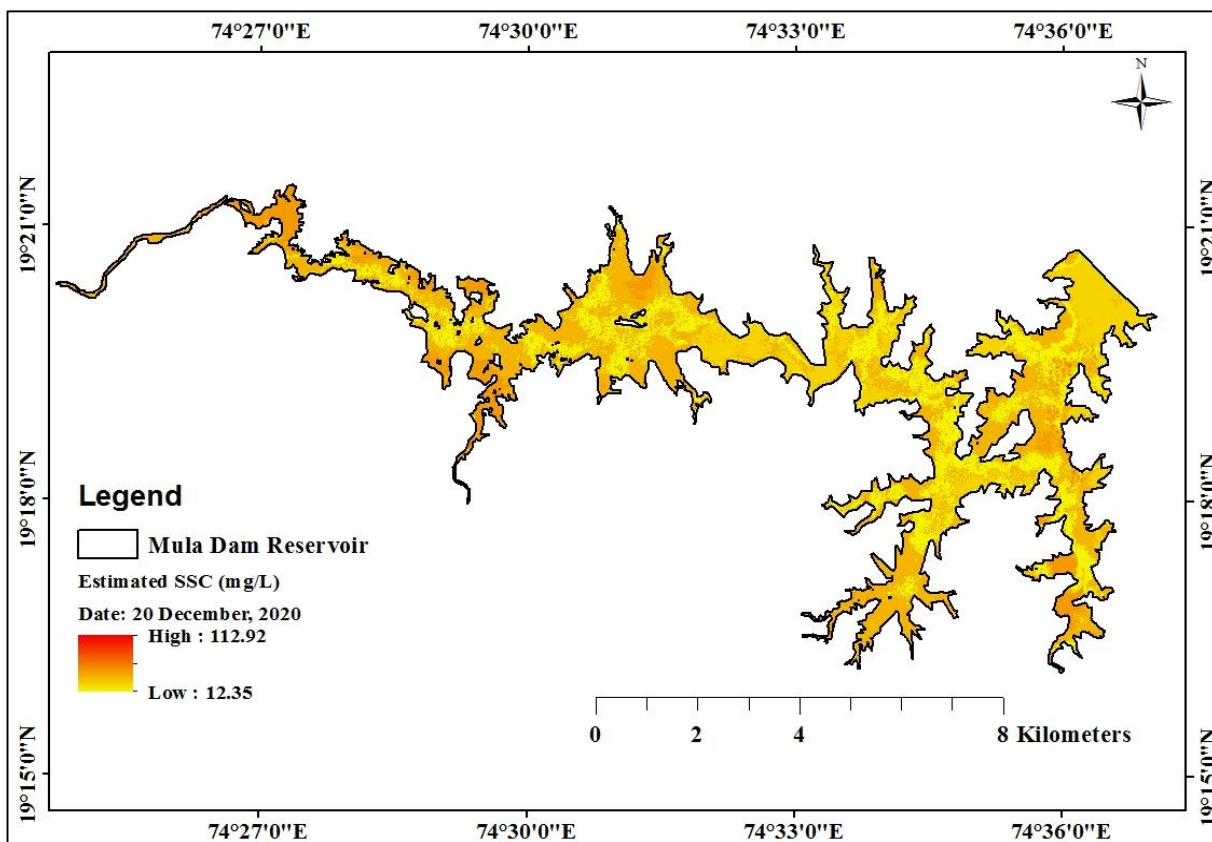


(b)

**Figure 4.29: Distribution of SSC in surface waters of Mula dam reservoir on a) 11<sup>th</sup> November, 2019 and b) 10<sup>th</sup> November, 2020**

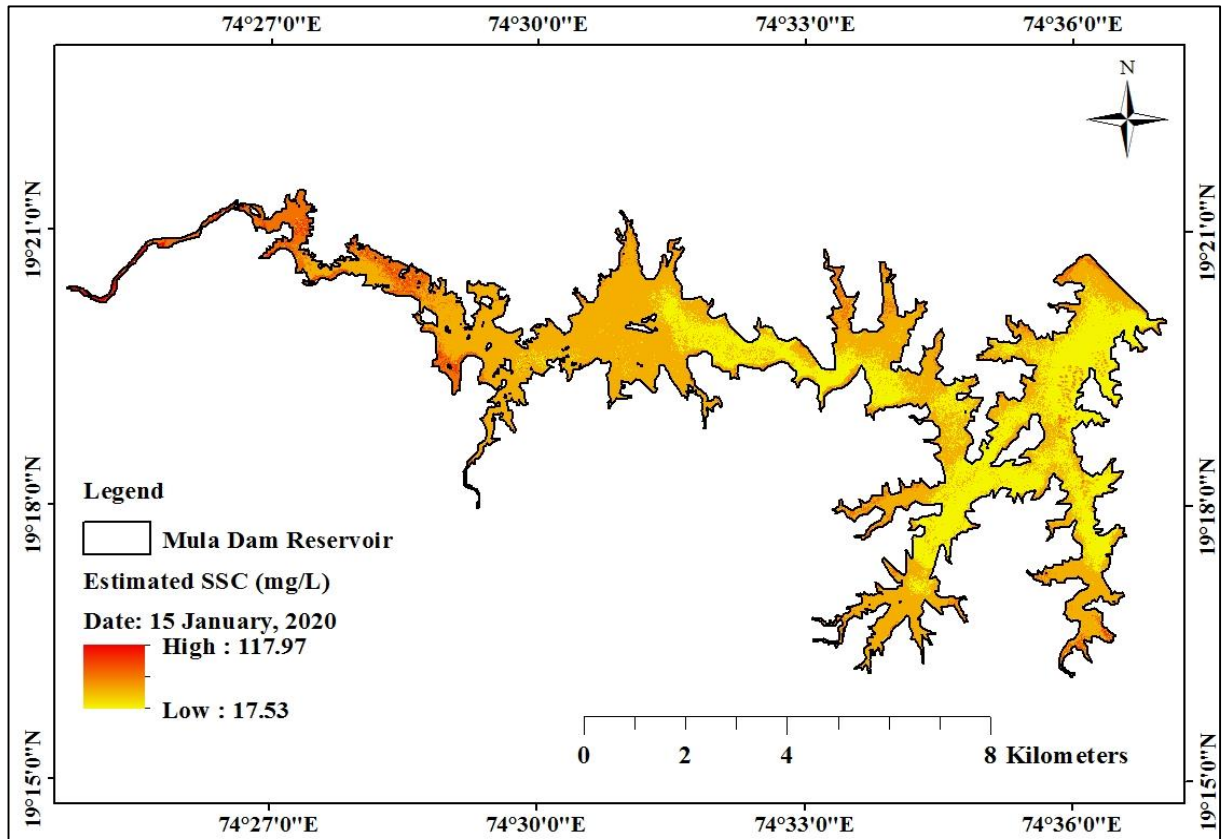


(a)

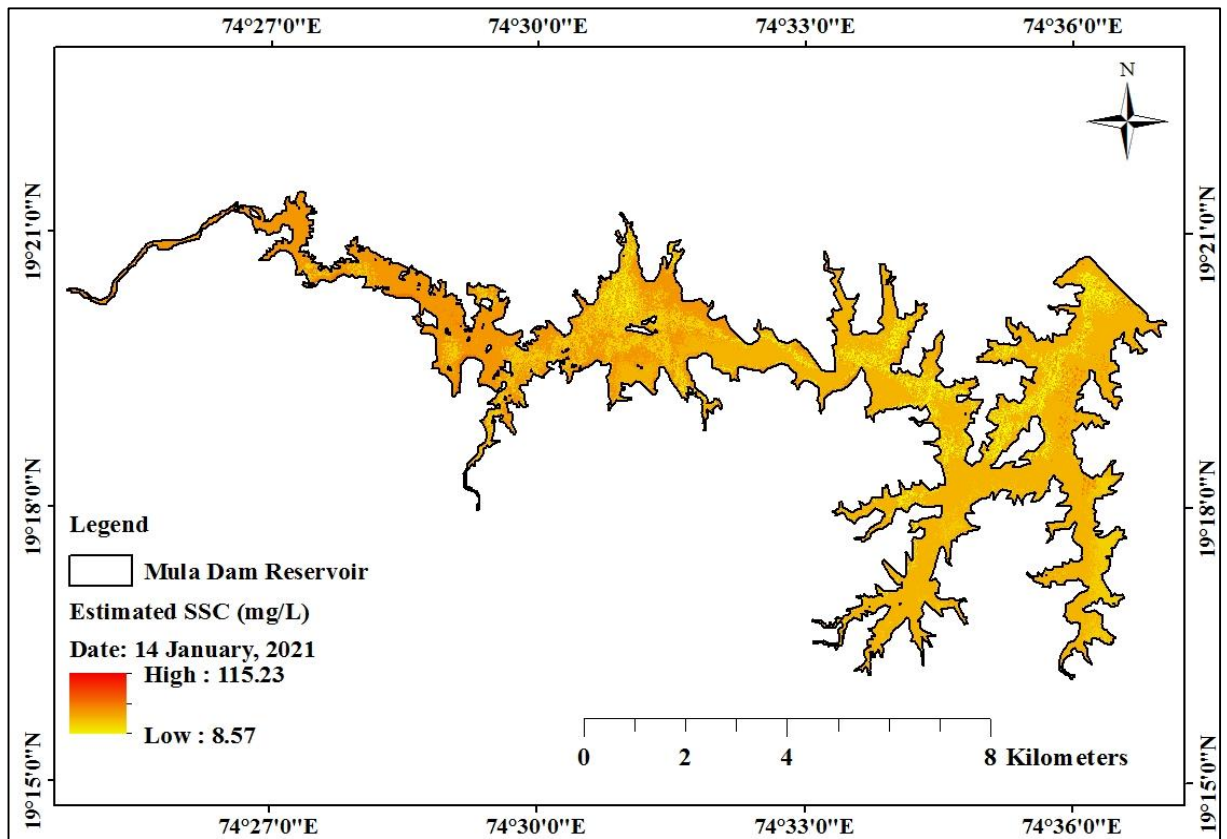


(b)

Figure 4.30: Distribution of SSC in surface waters of Mula dam reservoir on a) 16<sup>th</sup> December, 2019 and b) 20<sup>th</sup> December, 2020.

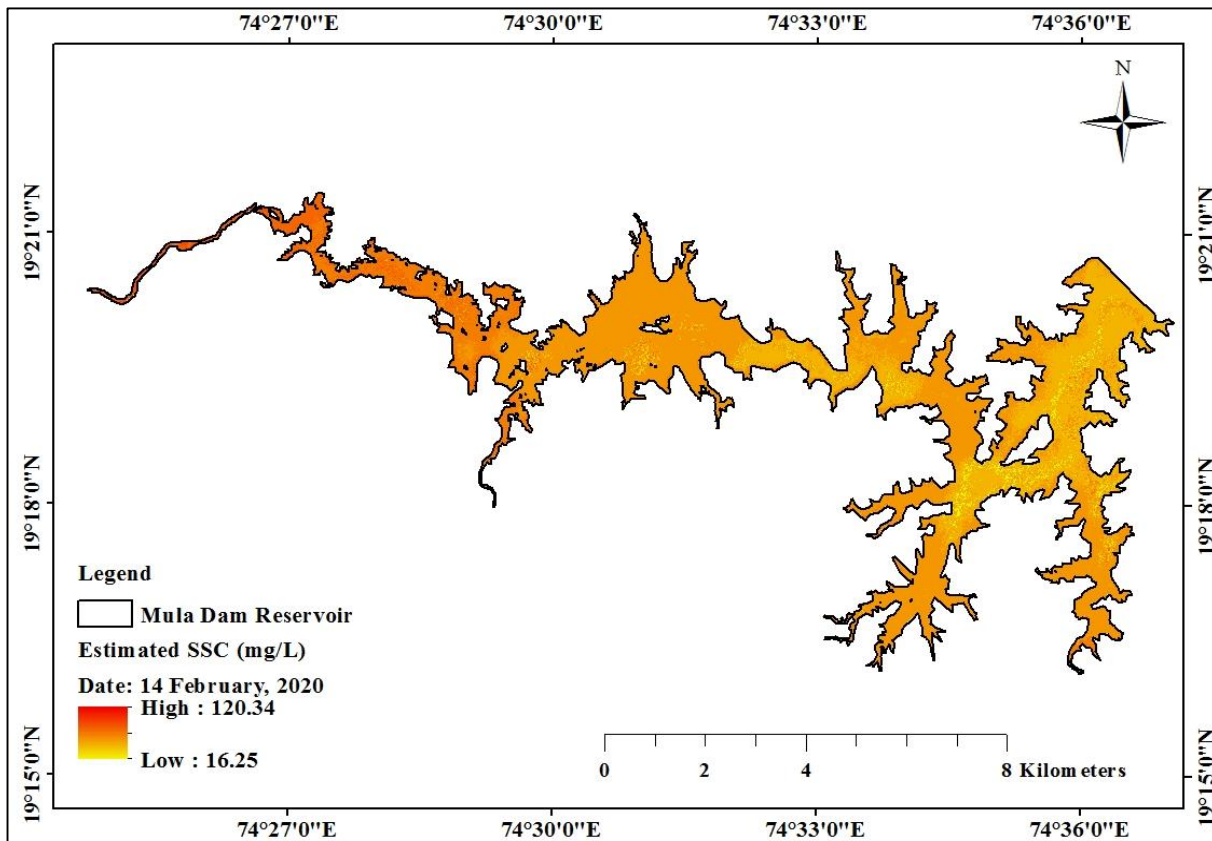


(a)

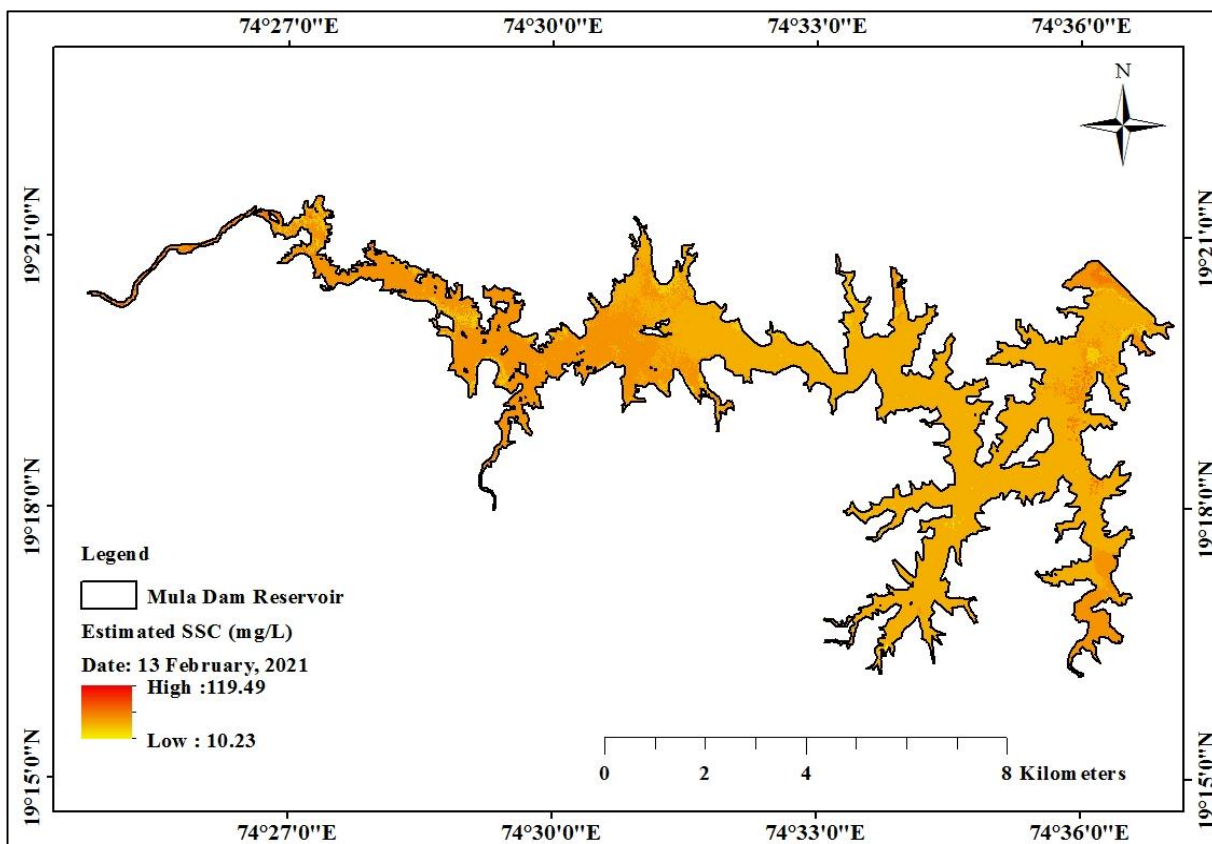


(b)

Figure 4.31: Distribution of SSC in surface waters of Mula dam reservoir on a) 15<sup>th</sup> January, 2020 and b) 14<sup>th</sup> January, 2021.



(a)



(b)

Figure 4.32: Distribution of SSC in surface waters of Mula dam reservoir on a) 14<sup>th</sup> February, 2020 and b) 13<sup>th</sup> February, 2021.

## V. SUMMARY AND CONCLUSIONS

Sediment plays a crucial role in aquatic ecosystems, but when it becomes excessive or poorly managed, it can lead to a range of environmental and engineering challenges. Sediment particles, carried by water or air, can be broadly categorized into suspended sediment, consisting of fine inorganic particles like clay and silt, and bed load sediment, comprising coarser materials like gravel. Suspended sediment is of particular concern, as it makes up a significant portion of the annual sediment transported in river systems, affecting downstream areas. Excessive sediment inflow into reservoirs, driven by factors like rainfall, wind, and slope, can lead to reservoir sedimentation, causing a host of problems such as storage loss, navigational issues, and ecological disruptions. High concentrations of suspended sediment pose environmental risks, including benthic smothering, altered water chemistry, and reduced light penetration, impacting aquatic life and biodiversity. Furthermore, sediment can carry pollutants like phosphorus and pesticides, further endangering ecosystems.

To address these challenges, researchers have explored remote sensing techniques to efficiently estimate suspended sediment concentration over large water bodies. Remote sensing, offers a cost-effective and widespread approach to monitor sediment dynamics by analysing the spectral reflectance of water affected by suspended sediment, these techniques provide valuable data for sediment management. The reviewed literature offers a comprehensive overview of diverse methodologies for assessing Suspended Sediment Concentration (SSC) in aquatic environments using remote sensing techniques. These methods range from handheld Spectroradiometers to satellite-based systems like Sentinel-2, emphasizing the importance of integrating field spectrometry with satellite imagery to bridge ground-based measurements and remote observations. The literature has highlighted that, the ground-based Spectroradiometer can be used validate and refine remote sensing data, improving monitoring precision. To advance water resource management, there is a growing need for refined methodologies and rigorous validation, as well as the exploration of integrated approaches and diverse methods to improve SSC estimation techniques.

This study, conducted at the Mula Dam reservoir near M. P. K. V., Rahuri, focuses on estimating suspended sediment concentration using integrated spectroscopy. It aims to capture spectral responses from both Spectroradiometer and satellite imagery, establish relationships between surface reflectance and sediment concentration, develop integrated surface reflectance functions and methodology, and validate the accuracy of these methods. Figure 5.1 outlines the methodology used in the research.

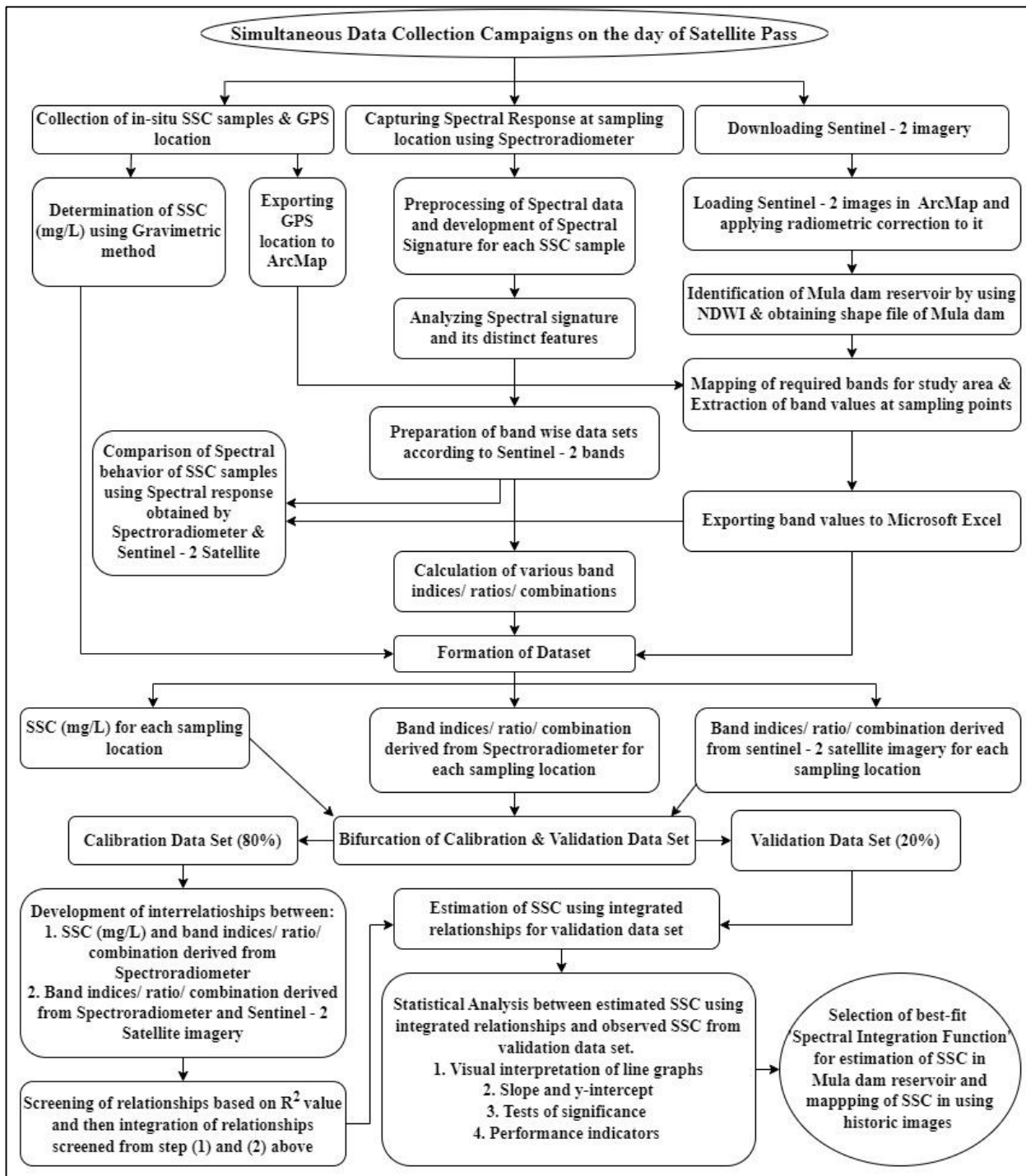


**Figure 5.1: Flowchart of methodology used in the research.**

## 5.1 Summary of Results

The study was started with collecting suspended sediment samples and capturing spectral signatures at sampling locations using a Spectroradiometer. Simultaneously, the GPS was used to record the precise locations of the sampling sites, synchronized with the Sentinel-2 satellite passes over the Mula dam reservoir during five different campaigns during October 2021 to February 2022.

It was observed that, SSC in the Mula dam reservoir ranged from 15.62 to 137.65 mg/L, with an average SSC of 61.43 mg/L. During the study, 85% of the data points showed SSC values below 100 mg/L, while 15% has values exceeding 100 mg/L, mainly in the Mula river stretch.

This implies that the Mula dam reservoir generally experienced lower suspended sediment concentrations during the research, consistent with most data points being below the 100 mg/L.

At all the sampling locations, spectral response was captured using Spectroradiometer to analyse the spectral behaviour of SSC present in the surface water (0 to 20 cm) of Mula dam reservoir. It was observed that, the in-situ surface reflectance spectra consistently exhibit distinct patterns, showing a parallel increase in surface reflectance with rising suspended sediment concentrations. Significantly, distinct peaks are observed in the Red region (650 to 680 nm), with a small or minor peak in the Red Edge 1 region (698 to 713 nm) and a flat peak in the Green region (543 to 578 nm). To confirm the suitability of these bands, average band values for all the bands *viz.*, Blue, Green, Red, Red Edge 1, 2 3 and 4 and NIR bands were correlated with corresponding value of SSC (mg/L). The findings revealed that, there is a strong positive correlation between Suspended Sediment Concentration (SSC) and Green band reflectance, followed by Red Edge 1, Red band, and Blue band. Weaker correlations are seen with Red Edge 2, 3, and 4 bands, as well as the NIR band. The next step involved a comparison between the spectral responses obtained from a ground-based Spectroradiometer and Sentinel-2 satellite imagery. The spectral signatures derived from both sources exhibited parallel nature in their patterns of spectral behavior. However, the Sentinel-2 spectral signature consistently displayed greater reflectance values across the entire range of wavelengths, spanning from 400 to 900 nm. These results pave the way for exploring various band ratios, combinations, or indices utilizing the Green, Red, and Red Edge 1 bands, as recommended in existing literature, or devising new ratios, combinations, or indices involving these bands for precise SSC estimation.

Various indices *viz.*, NDSSI, NSMI, M-NDSSI and R-NDSSI derived using Spectroradiometer were correlated by means of regression equations with observed SSC from calibration data set. NDSSI demonstrated a weak correlation with SSC, indicating limited precision. Positive correlations were found between SSC and NSMI, and strong negative correlations with SSC were observed for both M-NDSSI and R-NDSSI, particularly the second-order polynomial equation, showing  $R^2$  values exceeding 0.7, signifying their accuracy in estimating SSC. Different band ratio/ combinations  $(Red + Green)/2$ ,  $(Red + Green + Red\ Edge\ 1)/2$ ,  $(Green - Red\ Edge\ 1)$  and  $(Green \times Red\ Edge\ 1)/Red$  were also correlated with observed SSC and it was observed that, in all the cases second-order polynomial equation best fits the calibration data having  $R^2$  values equal to 0.67, 0.82, 0.71 and 0.86 respectively.

Following the establishment of relationships between different band indices, ratios, and combinations with observed SSC (mg/L), an effort was made to establish a relation between these spectral parameters derived from the Spectroradiometer and those obtained from Sentinel-2 satellite imagery. It was observed that, for M-NDSSI and the combination  $(Green - Red\ Edge\ 1)$  there exists a weaker correlation with  $R^2$  values of 0.57 and 0.67, as compared to other indices,

ratios or combinations. Spectral parameters derived from the Spectroradiometer and Sentinel-2 satellite imagery correlated well with  $R^2$  values greater than 0.70. Higher degree of correlation was observed in case of the ratio  $(\text{Red} + \text{Green} + \text{Red Edge } 1)/3$ , followed by  $R\text{-NDSSI}$ ,  $(\text{Red} + \text{Green})/2$ ,  $\text{NSMI}$  and  $(\text{Green} \times \text{Red Edge } 1)/\text{Red}$ . There is variability in the goodness of fit, as reflected in the  $R^2$  values, the established relationships were further subjected to validation through the estimation of SSC after integrating corresponding developed equations also termed as spectral integration functions.

Estimation of SSC using spectral integration functions, first involved estimation of band indices, ratios, and combinations for Spectroradiometer by using the same obtained from Sentinel-2 satellite imagery from validation data set and then using these estimated values of band indices, ratios, and combinations for estimation of SSC. Estimated SSC and observed SSC from validation data set were then subjected to statistical analysis for the selection of most suitable spectral integration function for estimation of SSC in Mula dam reservoir.

Visual assessments of line graphs revealed that specific spectral integration functions, including  $(\text{Red} + \text{Green})/2$ ,  $(\text{Red} + \text{Green} + \text{Red Edge } 1)/3$ , and  $(\text{Green} \times \text{Red Edge } 1)/\text{Red}$ , exhibited a close agreement between observed and estimated SSC. This suggests the potential of these functions for accurate estimations. On the other hand, functions like  $\text{NSMI}$ ,  $M\text{-NDSSI}$ ,  $R\text{-NDSSI}$ , and  $(\text{Green} - \text{Red Edge } 1)$  showed differences in magnitude and intricate patterns, indicating less reliable SSC estimations. Among these,  $M\text{-NDSSI}$  displayed a relatively better association with observed SSC.

Effectiveness of various spectral integration functions in estimating SSC was assessed based on their  $R^2$  values.  $\text{NSMI}$  and  $M\text{-NDSSI}$  exhibited weak linear relationships and were statistically insignificant. These functions were rejected.  $R\text{-NDSSI}$  and  $(\text{Green} - \text{Red Edge } 1)$  performed slightly better but still fell short. In contrast,  $(\text{Red} + \text{Green})/2$ ,  $(\text{Red} + \text{Green} + \text{Red Edge } 1)/3$ , and  $(\text{Green} \times \text{Red Edge } 1)/\text{Red}$  showed strong and reliable linear relationships. However, in subsequent Student t-tests for testing the significance of difference between means of observed and estimated SSC,  $(\text{Red} + \text{Green})/2$  and  $(\text{Green} - \text{Red Edge } 1)$  significantly overestimated SSC compared to observed values.  $R\text{-NDSSI}$ ,  $(\text{Red} + \text{Green} + \text{Red Edge } 1)/3$ , and  $(\text{Green} \times \text{Red Edge } 1)/\text{Red}$  yielded statistically insignificant difference between means of observed and estimated SSC.

In the final stage of the study, three spectral integration functions for estimating Suspended Sediment Concentration (SSC) were evaluated using various performance criteria, including  $R^2$ , RMSE, MAPE, NSE, and the Index of Agreement. "Spectral Integration of  $(\text{Green} \times \text{Red Edge } 1)/\text{Red}$ " emerged as the most accurate and reliable estimator, with the highest  $R^2$  at 0.80 and the lowest RMSE at 8.58 mg/L, indicating the best fit and smallest deviation from observed SSC values. Additionally, it had the lowest MAPE at 19.41%, reflecting the closest percentage

difference. "Spectral Integration of (Red + Green + Red Edge 1)/3" also performed well with high NSE and d values but slightly higher errors. In contrast, "Spectral Integration of R-NDSSI" lagged behind with lower R<sup>2</sup>, higher RMSE, and MAPE, confirming the superior performance of the former two functions in accurately estimating SSC in large reservoirs using remote sensing.

The study utilized "Spectral Integration of (Green × Red Edge 1)/Red" as the most accurate estimator for Suspended Sediment Concentration (SSC) and applied it to create spatio-temporal maps of SSC in the Mula Dam reservoir. Historical Sentinel-2 (BOA) satellite imagery were used to assess SSC variations from October 2019 to February 2020 and from October 2020 to February 2021, providing insights into sediment dynamics and seasonal changes, if any.

The analysis revealed a consistent seasonal pattern, with higher SSC levels in October and November, indicating intensified sediment runoff. Conversely, January and February displayed lower SSC values due to reduced sediment transport in drier periods. Year-on-year comparisons showed increased sediment concentrations in 2020, particularly in October and November. Additionally, areas near river inflows and smaller streams exhibited higher SSC, while the central portion had lower SSC, suggesting sediment deposition due to reduced flow velocity. Overall, the study found that the Mula Dam reservoir maintains relatively low SSC levels, below 150 mg/L, indicating good water quality for various uses. However, continuous monitoring is essential to account for seasonal variations and environmental factors, ensuring long-term water quality and maintaining ecological balance. These findings emphasize the need for ongoing monitoring and adaptive management, particularly during peak rainy seasons, to safeguard the reservoir's water quality and ecosystem.

## 5.2 Conclusions

In the study, "Estimation of Suspended Sediment Concentration by Developing Integrated Surface Reflectance Function", an attempt was made to develop a methodology for assessment and monitoring of SSC in Mula dam reservoir.

Following are the conclusions drawn from this study:

1. In-situ reflectance spectra obtained from the Spectroradiometer is homogeneous in shape showing narrow peaks in Red (650-680 nm) and Red Edge 1 (698-713 nm) and flat peak in Green (543-578 nm) region of electromagnetic spectrum indicated the presence of lower concentration of suspended sediment concentration in surface waters of Mula dam reservoir.
2. Among various band indices/ combinations selected from literature, band indices/ combinations obtained from both Spectroradiometer and Sentinel – 2 image having Green, Red and Red Edge 1 band confirmed good correlation with SSC during calibration and validation.

3. Among all the developed functions, ‘Spectral Integration Function of Green  $\times$  Red Edge 1)/Red’ performed significantly well in estimating SSC in Mula dam reservoir in terms of different statistical indicators followed by ‘Spectral Integration Function of (Red + Green + Red Edge 1)/3’ and ‘Spectral Integration function of R-NDSSI’.
4. Applicability of this Spectral Integration Methodology for synoptic retrieval of spatially variable SSC using Sentinel-2 (BOA) L2A imagery with high spatial and frequent temporal resolution is a great promise as a source of information for managers, researchers, or other stakeholders involved in the assessment and sustainable use of surface water resources or large water bodies.

### 5.3 Suggestions for Future work

1. Investigations Saturation Effects at Higher Concentrations:

At a higher concentration, above 100 mg/L, reflectance in green and red bands saturated and the concentration tends to be underestimated probably as a result of a small fraction of data with higher SSC values and large variation of maximum and minimum SSC value. Increase in number of samples in wet season may help to overcome this limitation.

2. Long term Monitoring and Validation:

To assess the methodology's reliability over time, long-term monitoring and validation efforts are recommended. Seasonal variations may influence the behaviour of suspended sediment, and conducting the study during different seasons could provide insights into the dynamics and help refine the methodology for accurate SSC estimation.

3. Application the Methodology to Other Large Water Bodies:

To validate and generalize the proposed methodology, future work should consider applying the developed techniques to other large water bodies. Different environmental conditions, geographic features, and sediment characteristics may influence the performance of the methodology. Conducting similar studies in diverse settings will enhance the robustness of the methodology and provide valuable insights into its applicability across various water bodies.

## VI. REFERENCES

- Agrawal, K. C., and Pottsmith, H. C. (1996). Measurement of Particle Size and Volume Fraction by Laser Backscatter. *Measurement Science and Technology*, 7(7), 1012-1024.
- Aher, M. S., and Sonawane, P. A. (2015). Fish Fauna of Mula River at Mula Dam Reservoir, Rahuri (M.S.), India. *Journal of Basic Sciences*, Special Issue on BioIPPF, 41-44.
- Anonymous, (2020). The Status Report: Capacity Assessment of Reservoirs in Maharashtra, Survey from 1974 to 2020. (2020). Resources Engineering Centre, Maharashtra Engineering Research Institute (M.E.R.I.), Nashik-04.
- Anonymous, Ahmednagar Gazetteers, Government of India. (1976).
- Anonymous, Dams of India, National Register of Large Dams, (2009).
- Arisanty, D., and Saputra, A. N. (2017). Remote Sensing Studies of Suspended Sediment Concentration Variation in Barito Delta. IOP Conference Series: *Earth and Environmental Science*, 98.
- Arstila, V. (2012). Why the transitivity of perceptual simultaneity should be taken seriously. *Frontiers in Integrative Neuroscience*, 6(3).
- ASCE. (1993). Criteria for evaluation of watershed models. *J. Irrigation Drainage Eng.*, 119(3), 429-442.
- Badgley, B. D., Thomas, F. I., and Harwood, V. J. (2011). Zebra Mussel (*Dreissena polymorpha*) Density and Distribution as a Potential Surrogate for Dreissenid Spore Viability in the Detroit River. *Journal of Great Lakes Research*, 37(2), 361-366.
- Baker, E. T., and Lavelle, J. (1984). The effect of particle size on the light attenuation coefficient of natural suspensions. *Journal of Geophysical Research*, 89(C5), 8197-8203.
- Bejestan, M. S., and Rezaia, S. (2010). An Assessment of Suspended Sediment Distribution in Riverine Systems. *Environmental Geology*, 60(6), 1305-1311.
- Bhatti, A. M., Nasu, S., Takagi, M., and Nojiri, Y. (2008). Assessing the potential of remotely sensed data for water quality monitoring of coastal and inland waters. *Research Bulletin of the Kochi University of Technology*, 5, 201-207.
- Bhatti, A., Nasu, S., and Takagi, M. (2007). Effect of Suspended Sediment Concentration on Remote Sensing Reflectance and Light Penetration Depth. *Proceedings of the Symposium on Global Environment*, 15, (7).
- Bhatti, A., Rundquist, D., Schalles, J., and Ramirez, L. (2010). Application of Hyperspectral Remotely Sensed Data for Water Quality Monitoring: Accuracy and Limitation. *In Proceedings of the Accuracy Symposium*, Leicester, UK, 20-23.

- Bhatti, M. A., Mori, T., Nakamura, N., and Ahmed, S. (2011). Monitoring spatial and temporal variability of suspended sediment in Indus River by means of remotely sensed data. *Journal of Environmental Monitoring*, 13(8), 2276-2287.
- Bhatti, S. A. (2006). A remote sensing approach for monitoring suspended sediment concentration in the Indus River, Pakistan. *Remote Sensing of Environment*, 104(1), 130-139.
- Black, K. S., and Rosenberg, R. (1994). Use of an Optical Backscatter Technique to Measure Temporal and Spatial Variation in Suspended Sediment Concentrations in a Shallow-Water Environment. *Estuarine, Coastal and Shelf Science*, 39(4), 367-378.
- Branigan, M. (2013). Understanding the Impacts of Suspended Sediment on Estuarine Productivity. Final Report. NSW Office of Environment and Heritage.
- Chen, J. M., Curran, P. J., and Hansom, J. D. (1992). Comparing Neural Network and Linear Spectral Mixture Models to Estimate Leaf Area Index of Boreal Forest. *Remote Sensing of Environment*, 41(3), 209-222.
- Chen, Z., Hanson, J. D., and Curran, P. J. (1991). The Form of the Relationship between Suspended Sediment Concentration and the Spectral Reflectance: It's Implications for the Use of Daedalus Data. *International Journal of Remote Sensing*, 12(1), 215-222.
- Dehkordi, A. T., Ghasemi, H., and Valadan Zoej, M. J. (2021). Machine Learning-Based Estimation of Suspended Sediment Concentration along Missouri River using Remote Sensing Imageries in Google Earth Engine. In 7th International Conference on Signal Processing and Intelligent Systems (ICSPIS).
- Doxaran, D., Cherukuru, R. C. N., and Lavender, S. J. (2005). Use of Reflectance Band Ratios to Estimate Suspended and Dissolved Matter Concentrations in Estuarine Waters. *International Journal of Remote Sensing*, 26(8), 1763–1769.
- Doxaran, D., Froidefond, J. M., Lavender, S., and Castaing, P. (2002). Spectral signature of highly turbid waters: Application with SPOT data to quantify suspended particulate matter concentrations. *Remote Sensing of Environment*, 81, 149-161.
- Edwards, T. K., and Glysson, G. D. (1988). Field Methods for Measurement of Fluvial Sediment. U.S. Geological Survey, Techniques of Water-Resources Investigations, Book 3, Chapter 2.
- Gare A., Wondwosen S., William P., and Catherine O. (2021). Spatiotemporal Analysis of Water Quality Indicators in Small Lakes Using Sentinel-2 Satellite Data: Lake Bloomington and Evergreen Lake, Central Illinois, USA. *Environmental Processes*, 8, 637–660.

- Garg V., Aggarwal S. P., and Chauhan P. (2020). Changes in turbidity along Ganga River using Sentinel-2 satellite data during lockdown associated with COVID-19. *Geomatics, Natural Hazards and Risk*, 11(1), 1175-1195.
- Gartner, J. W., Cheng, R. T., Wang, P.-F., and Richter, K. (2001). Laboratory and field evaluations of the LISST-100 instrument for suspended particle size determinations. *Marine Geology*, 175(1), 199-219.
- Gholizadeh, A., Keesstra, S., Ghodousi, J., and Ahmadi, H. (2016). Water Quality and Quantity Monitoring in Large River Basins with Limited Data Availability: Review of Current and Future Satellite and UAV-Based Sensors for Monitoring Nutrients and Sediments. *International Journal of Applied Earth Observation and Geoinformation*, 47, 48-64.
- Green, D. E., and Boon, J. D. (1993). Optical Backscatterance Sediment Analyzer for Real-Time Measurement of Sediment Concentration and Particle Size in Flowing Waters. *Limnology and Oceanography*, 38(8), 1664-1672.
- Gruber, M., Schmid, F., and Aydin, G. (2016). Field Study on Suspended Sediment Measurement with Single-Frequency Acoustic Methods. *Journal of Hydraulic Engineering*, 142(6).
- Gupta, M. (2015). Modeling and remote sensing of suspended sediments in the Gulf of Kachchh, India. *European Journal of Remote Sensing*, 48, 201-221.
- Guy, H. P. (1965). Laboratory Theory and Methods for Sediment Analysis. *Techniques of Water-Resources Investigations of the United States Geological Survey*, Book 5, Chapter 1.
- Han, L. (1997). Spectral Reflectance with Varying Suspended Sediment Concentrations in Clear and Algae-Laden Waters. *Photogrammetric Engineering and Remote Sensing*, 63(6), 701-705.
- Hossain, A. A., Jia, Y., and Chao, X. (2010). Development of Remote Sensing Based Index for Estimating/Mapping Suspended Sediment Concentration in River and Lake Environments. *In Proceedings of the 8<sup>th</sup> International Symposium on ECOHYDRAULICS*, Paper No. 0435: 578-585.
- House, W. A., Warwick, M. S., Greenwood, R., Bowes, M. J., and Hodgkinson, R. (1998). Use of Settling Particles to Remove Phosphorus from Wastewater. *Environmental Technology*, 19(5), 455-464.
- Interagency Committee. (1963). Sedimentation Investigation Methods. United States Government Printing Office.
- Joshi, J., Atre., A., Nandgude, S., Shinde, M., Durgude A., Gorantiwar S., Patil M., (2023), Estimation Of Suspended Sediment Concentration Using Sentinel-2 Band Functions In

- Mula Reservoir, Rahuri, India. *Environmental Engineering and Management Journal*, 22 (2): 375-387.
- Kadam S. A. (2014). Spatial Decision Support System Based on Remote Sensing Approach for Irrigation Water Management. A Ph.D. Thesis submitted to Department of Irrigation and Drainage Engineering, Mahatma Phule Krishi Vidyapeeth Rahuri, pp. 110-111.
- Kavan, J., Wieczorek, I., Tallentire, G., and Demidionov, M. (2022). Estimating Suspended Sediment Fluxes from the Largest Glacial Lake in Svalbard to Fjord System Using Sentinel-2 Data: Trebrevatnet Case Study. *Water*, 14(12).
- Kazemzadeh, M. B., Ayyoubzadeh, S. A., and Moridnezhad, A. (2013). Remote Sensing of Temporal and Spatial Variations of Suspended Sediment Concentration in Bahmanshir Estuary, Iran. *Indian Journal of Science and Technology*, 6(8):1-10.
- Khair, A. W., Salim, N., Rahman, N. S. A., Alias, N. A., and Shabri, A. (2017). Application of fuzzy time series and neural network model for time series forecasting. *Applied Mathematical Sciences*, 11(43):2141-2156.
- Khair P. B. (2019). Estimation of Suspended Sediment Concentration in Small Reservoir using Drone Survey. An M.Tech Thesis submitted to Department of Soil and Water Conservation Engineering, Mahatma Phule Krishi Vidyapeeth Rahuri, pp. 28.
- Kineke, G. C., and Sternberg, R. W. (1992). Effects of Particle Characteristics on the Measurement of Suspended Sediment Concentration with an Optical Backscatterance Sensor. *Marine Geology*, 108(3):257-265.
- Kwon, S., Shin, J., Seo, I. W., and Noh, H. (2021). Measurement of Suspended Sediment Concentration in Open Channel Flows Based on Hyperspectral Imagery from UAVs. *Advances in Water Resources*, 159, 104076.
- Larson, M. D., Milas Anita, S., Vincent, R. K., and Evans, J. (2018). Multi-depth suspended sediment estimation using high-resolution remote-sensing UAV in Maumee River, Ohio. *International Journal of Remote Sensing*, 39(3), 1-18.
- Law, D. J., Bale, A. J., and Jones, S. E. (1997). Adaptation of focused beam reflectance measurement to in-situ particle sizing in estuaries and coastal waters. *Marine Geology*, 140(1-2), 47-59.
- Legates, D. R., and McCabe, G. J. (1999). Evaluating the use of 'goodness-of-fit' measures in hydrologic and hydro climatic model validation. *Water Resources Research*, 35(1), 233-241.
- Li, Y., Chen, J., Ma, Q., and Zhang, H. K. (2018). Evaluation of Sentinel-2A Surface Reflectance Derived Using Sen2Cor in North America. *IEEE Journal of Selected Topics in Applied Earth Observations and Remote Sensing*, 99, 1-25.

- Liew, M. W., Veith, T. L., and Bosch, D. D. (2003). Design, evaluation, and application of a database for model parameter estimation. *Journal of the American Water Resources Association*, 39(5), 1209-1223.
- Liu, H., Li, Q., Shi, T., Hu, S., Wu, G., and Zhou, Q. (2017). Application of Sentinel 2 MSI Images to Retrieve Suspended Particulate Matter Concentrations in Poyang Lake. *Remote Sensing*, 9, 761.
- Lodhi, M. A. K., Simonovic, S. P., and Adamowski, J. (1998). Environmental Impacts of Reservoir Sedimentation and Sediment Management Strategies. *Environmental Management*, 22(2), 259-269.
- Lodhi, M., Rundquist, D., Han, L., and Kuzila, M. (2007). The potential for remote sensing of loess soils suspended in surface waters. *Journal of the American Water Resources Association*, 33, 111-117.
- Long, C., and Pavelsky, T. (2013). Remote sensing of suspended sediment concentration and hydrologic connectivity in a complex wetland environment. *Remote Sensing of Environment*, 129, 197-209.
- Margareta, N., and Ulf, H. (2000). Sediment Delivery from Forested and Non-Forested Catchments in Central Sweden during the 20th Century. *Hydrological Processes*, 14(16-17), 3033-3047.
- Marinho, M. M. R., Gomes, V. V., Cunha, A. C. C., Lima, F. P. A., Correia, A. T., Soares, C. P., and Oliveira, E. R. (2021). Remote Sensing for Monitoring the Water Quality of a Tropical Reservoir. *Frontiers in Environmental Science*, 9, 667146.
- McFeeters, S. K. (1996). The use of the Normalized Difference Water Index (NDWI) in the delineation of open water features. *International Journal of Remote Sensing*, 17(7), 1425-1432.
- McHenry, J. R., Siddiqi, N. A., and Kennedy, V. C. (1967). A Nuclear Technique for Measuring Sediment Concentration in Streams. *Water Resources Research*, 3(3), 705-713.
- Meral, R., Smerdon, A., Merdun, H., and Demirkiran, A. (2010). Estimation of suspended sediment concentration by acoustic equations for soil sediment. *African Journal of Biotechnology*, 9, 170-177.
- Miller, R. L., and McKee, B. A. (2004). Using MODIS Terra 250 m imagery to map concentrations of total suspended matter in coastal waters. *Remote Sensing of Environment*, 93, 259-266.
- Milton, E. J. (1987). Review Article: Principles of Field Spectroscopy. *International Journal of Remote Sensing*, 8(12), 1807-1827.

- Milton, E. J., Fox, N. P., and Schaepman, M. E. (2006). Progress in Field Spectroscopy. In Proceedings of the IEEE International Geoscience and Remote Sensing Symposium.
- Montanher, O. C., Novo, E. M. L. M., Barbosa, C. C. F., Rennó, C. D., and Silva, T. S. F. (2014). Empirical models for estimating the suspended sediment concentration in Amazonian white water rivers using Landsat 5/TM. *International Journal of Applied Earth Observation and Geoinformation*, 29, 67-77.
- Moriasi, D. N., Arnold, J. G., Van Liew, M. W., Bingner, R. L., Harmel, R. D., and Veith, T. L. (2007). Model Evaluation Guidelines for Systematic Quantification of Accuracy in Watershed Simulations. *Transactions of the ASABE*, 50(3), 885-900.
- Muller W., Richter R., Gascon F., Jerome L., and Mark N. (2013). Sentinel-2 Level-2A Prototype Processor: Architecture, Algorithms and First Results. *ESA Living Planet Symposium, Edinburgh, Volume: ESA SP-722*.
- Munir M., Ramadhan A. F., Nastiti A., Putri A. A., Bawono M. R. K. S., Afifah Z. N., and Wicaksono P. (2019). Utilization of Sentinel-2A imagery for mapping the dynamics of Total Suspended Sediment at The River Mouth of The Padang City. 5<sup>th</sup> International Conference on Science and Technology (ICST), Yogyakarta, Indonesia.
- Myint, S. W., and Walker, N. D. (2002). Quantification of surface suspended sediments along a river-dominated coast with NOAA AVHRR and SeaWiFS measurements: Louisiana, USA. *International Journal of Remote Sensing*, 23(16), 3229–3249.
- Nash, J. E., and Sutcliffe, J. V. (1970). River flow forecasting through conceptual models part I - A discussion of principles. *Journal of Hydrology*, 10(3), 282-290.
- Novoa S., Doxaran D., Ody A., Vanhellemont Q., Lafon V., Lubac B., and Gernez P. (2017). Atmospheric corrections and multi-conditional algorithm for multi-sensor remote sensing of suspended particulate matter in low-to-high turbidity levels coastal waters. *Remote Sensing*, 9.
- Oliveira, P. A., Blanco, C. J. C., and Mesquita, A. L. A. (2021). Estimation of suspended sediment concentration in Guamá River in the Amazon region. *Environmental Monitoring and Assessment*, 193(79).
- Paulista, R. S. D., de Almeida, F. T., de Souza, A. P., Hoshide, A. K., de Abreu, D. C., da Silva Araujo, J. W. and Martim, C. C. (2023). Estimating Suspended Sediment Concentration Using Remote Sensing for the Teles Pires River, Brazil. *Sustainability*, 15, 7049. <https://doi.org/10.3390/su15097049>
- Pereira L. F., es L. C., Cox A. L., and Ghulam A. (2018). Measuring Suspended-Sediment Concentration and Turbidity in The Middle Mississippi and Lower Missouri Rivers

- using Land sat Data. *Journal of the American Water Resources Association*, 54(2):440-450.
- Phillips, J. M., and Walling, D. E. (1995). An assessment of the effect of sample collection, storage and resuspension on the representativeness of measurements of the effective particle size distribution of fluvial suspended sediment. *Water Research*, 29(11):298–2508.
- Pinet, S., Martinez, J. M. M., Ouillon, S., Lartiges, B., and Villar, R. E. (2017). Variability of apparent and inherent optical properties of sediment-laden waters in large river basins—lessons from in situ measurements and bio-optical modelling. *Opt. Express*, 25, A283.
- Pitchaikani, J. S., Ramakrishnan, R., Bhaskaran, P. K., Ilangoan, D., and Rajawat, A. S. (2019). Development of Regional Algorithm to Estimate Suspended Sediment Concentration (SSC) Based on the Remotely Sensed Reflectance and Field Observations for the Hooghly Estuary and West Bengal Coastal Waters. *Journal of the Indian Society of Remote Sensing*, 47(1):177–183.
- Premkumar, R., Venkatachalapathy, R., and Visweswaran, S. (2021). Mapping of Total Suspended Matter based on Sentinel-2 data on the Hooghly River, India. *Indian Journal of Ecology*, 48(1):159-165.
- Que, L. (2014). Transport and Deposition of Suspended Sediment. *Water Encyclopedia: Surface and Agricultural Water*, 6, 661-665.
- Ramakrishnan, D., Bharti, R., and Das, M. (2013). A technique for estimation of suspended sediment concentration in very high turbid coastal waters: An investigation from Gulf of Cambay, India. *Marine Geology*, 346, 256-261.
- Raut, S.S., and Gavit, B.K. (2015). Development of spectral signature curve for the suspended sediment using Spectroradiometer. *Engg. and Tech. in India*, 6(1):19-24.
- Reddy, M. A. (1993). Remote sensing for mapping of suspended sediments in Krishna Bay Estuary, Andhra Pradesh, India. *International Journal of Remote Sensing*, 14(11):2215-2221.
- Ritchie, J. C., and Cooper, C. M. (2003). Remote Sensing of Suspended Sediment Concentrations in the Suwannee River Estuary. *Remote Sensing of Environment*, 84(4), 554-566.
- Ritchie, J. C., Schiebe, F. R. (1987). Remote Sensing for Identification of Watersheds with Sediment Problems. *Photogrammetric Engineering and Remote Sensing*, 53(10):1369-1373.

- Ritchie, J. C., Schiebe, F. R. (2000). Remote Sensing of Suspended Sediments: The New Moderate-Resolution Imaging Spectrometer (MODIS) and Beyond. *Remote Sensing of Environment*, 74(2):172-185.
- Ritchie, J. C., Schiebe, F. R., and McHenry, J. R. (1976). Remote Sensing of Suspended Sediments in Surface Waters. *Photogrammetric Engineering and Remote Sensing*, 42(12):1539-1545.
- Robert, E., Grippa, M., Kergoat, L., Pinet, S., Gal, L., Cochonneau, G., and Martine, J.-M. (2016). Monitoring water turbidity and surface suspended sediment concentration of the Bagre Reservoir (Burkina Faso) using MODIS and field reflectance data. *International Journal of Applied Earth Observation and Geoinformation*, 52:243–251.
- Saenz, N., Paez, D. E., and Arango, C. (August 2015). Local Algorithm for Monitoring Total Suspended Sediments in Micro-Watersheds Using Drones and Remote Sensing Applications. Case Study: Teusacá River, La Calera, Colombia. *The International Archives of the Photogrammetry, Remote Sensing and Spatial Information Sciences*, XL-1/W4:159-165.
- Santhi, C., Arnold, J. G., Williams, J. R., Dugas, W. A., and Srinivasan, R. (2001). A modeling approach to evaluate the impacts of water quality management plans implemented in a watershed in Texas. *Journal of Environmental Quality*, 30(6), 1944-1957.
- Schiebe, F. R., Harrington Jr., J. A., and Ritchie, J. C. (1992). Remote sensing of suspended sediments: the Lake Chicot, Arkansas project, *International Journal of Remote Sensing*, 13(8):1487-1509.
- Shahzad, M. I., Meraj, M., Nazeer, M., and Zia, I. (2018). Empirical estimation of suspended solids concentration in the Indus Delta Region using Land sat-7 ETM+ imagery. *Journal of Environmental Management*, 209:254-261.
- Sheela, A. M., Singh, J. G., and Dhakate, R. (2014). Effect of Suspended Sediments on Aquatic Life: A Review. *International Journal of Environmental Sciences*, 5(4):697-709.
- Sibanda, M., Mutanga, O., Chimonyo, V. G. P., Clulow, A. D., Shoko, C., Mazvimavi, D., Dube, T., and Mabhaudhi, T. (2021). Application of Drone Technologies in Surface Water Resources Monitoring and Assessment: A Systematic Review of Progress, Challenges, and Opportunities in the Global South. *Drones*, 5, 84.
- Singh, R., Mujumdar, P., and Kumar, D. N. (2004). Regional flood frequency analysis using L-moments. *Journal of Hydrology*, 285(1-4):96-113.
- Sokoletsky, L., Shen, F., Xianping, Y., and Wei, X. (2016). Evaluation of Empirical and Semi analytical Spectral Reflectance Models for Surface Suspended Sediment Concentration

- in the Highly Variable Estuarine and Coastal Waters of East China. *IEEE Journal of Selected Topics in Applied Earth Observations and Remote Sensing*, 9(11): 1-11.
- Sravanthi, N., Ramana, I. V., Yunus Ali, P., Ashraf, M., Ali, M. M., and Narayana, A. C. (Autumn 2013). An Algorithm for Estimating Suspended Sediment Concentrations in the Coastal Waters of India using Remotely Sensed Reflectance and its Application to Coastal Environments. *International Journal of Environmental Research*, 7(4):841-850.
- Stow, C. A., Jorgenson, Z. G., and Hrenchuk, L. (2015). Suspended sediment and turbidity dynamics in a large river: Fraser River, British Columbia, Canada. *Water Resources Research*, 51(12):9579-9597.
- Stumph, C. L. (1989). An Assessment of Remote Sensing Applications to Water Resources in Texas. *Remote Sensing Applications in Water Resources*, 149-168.
- Sutari, C. A. T., van der Perk, M., and Middelkoop, H. (March 2020). Estimation of suspended sediment concentrations in the Rhine River using Landsat Satellite Images. *IOP Conference Series Earth and Environmental Science*, 451(1).
- Titkare, T. L. (2009), Stochastic Modelling of Streamflow of Mula River for Generation and Forecasting. M.Tech Thesis submitted to the Department of Irrigation and Drainage Engineering, Dr. ASCAET, MPKV, Rahuri.
- Vanoni, V. A. (2006). "Sedimentation Engineering". ASCE Manuals and Reports on Engineering Practice No. 54.
- Vercruyssen, K., Wei, Y., and Meire, P. (2017). Sediment and nutrient budgets for the entire Seine estuary: Considering the sediment bed as an integral part of the budget. *Estuarine, Coastal and Shelf Science*, 188:137-147.
- Wang, F., Zhou, B., Xu, J., Song, L., and Wang, X. (2009). Application of neural network and MODIS 250 m imagery for estimating suspended sediments concentration in Hangzhou Bay, China. *Environmental Geology*, 56:1093–1101.
- Wang, J. J., and Lu, X.X. (2010). Estimation of suspended sediment concentrations using Terra MODIS: An example from the Lower Yangtze River, China. *Science of the Total Environment*, 408:1131–1138.
- Wang, M., and Lu, A. (2005). Estimating suspended sediment concentration in Erhai Lake from MODIS imagery. *Remote Sensing of Environment*, 95(1), 158-167.
- Wang, X., Xu, J., Wang, S., and Zhang, M. (2018). Temporal-Spatial Variation of Suspended Sediment in the Yarlung Zangbo River Basin Based on Landsat Data (1987–2016). *Remote Sensing*, 10(2), 311.
- Willmott, C. J. (1981). On the validation of models. *Physical Geography*, 2:184-194.

- Womber, Z. R., Zimale, F. A., Kebedew, M. G., Asers, B. W., DeLuca, N. M., Guzman, C. D., Tilahun, S. A., and Zaitchik, B. F. (2021). Estimation of Suspended Sediment Concentration from Remote Sensing and In Situ Measurement over Lake Tana, Ethiopia. *Advances in Civil Engineering*, Volume 2021.
- Wren, D. G., Barkdoll, B. D., Kuhnle, R. A., and Derrow, R. W. (2000). Field Techniques for Suspended-Sediment Measurement. *Journal of Hydraulic Engineering*, 126:97-104.
- Wright, D. (2018). Sentinel-2 as a tool for quantifying suspended particulate matter in the Tamar Estuary, UK. *The Plymouth Student Scientist*, 11(2):3-33.
- Xavier, B. C., Silva, I. O., Guimaraes, L. G., Gallo, M. N., Ribeiro, C. P., and Figueiredo, A. G., Jr. (2014). Estimation of Suspended Sediment Concentration by Acoustic Scattering: An Experimental and Theoretical Analysis for Spherical Particles. *Journal of Soils and Sediments*, 14:1325–1333.
- Yong, K. H., Gutierrez, B., Nelson, T., Dumars, A., Maza, M., Perales, H., and Voulgaris, G. (2004). Study on Acoustics for SSC Measurements: Using the Acoustic Doppler Current Profiler (ADCP) to Estimate Suspended Sediment Concentration. Technical Report CPSD: 04-01, Coastal Processes Sediment Dynamics Laboratory, Department of Geological Sciences, University of South Carolina, Columbia, SC.
- Yu Z., Wang J., Li Y., Shum C. K., Wang B., He X., Xu H., Xu Y. and Zhou B. (2022). Remote sensing of suspended sediment in high turbid estuary from sentinel-3A/OLCI: A case study of Hangzhou Bay. *Front. Mar. Sci.* 9:1008070. doi: 10.3389/fmars.2022.1008070
- Zhan, C., Yu, J., Wang, Q., Li, Y., Zhou, D., Xing, Q., and Chu, X. (2017). Remote Sensing Retrieval of Surface Suspended Sediment Concentration in the Yellow River Estuary. *Chinese Geographical Science*, 27:934-947.
- Zhang, C.; Liu, Y.; Chen, X.; Gao, Y. (2022) Estimation of Suspended Sediment Concentration in the Yangtze Main Stream Based on Sentinel-2 MSI Data. *Remote Sens*, 14:4446.
- Zhang, Y., and Wang, H. (2015). Remote Sensing Retrieval of Suspended Sediment Concentration in the Changjiang Estuary, China. *Remote Sensing*, 7(9):12089–12109.

## VII. APPENDICES

### Appendix – A

---

#### Procedure for Determination of Suspended Sediment Concentration and Observations

---

$$SSC = \frac{X_2 - X_1}{Y} \times 10^6$$

Where,

SSC = Suspended Sediment Concentration (mg/L)

X<sub>2</sub> = Mass of sample paper and filter paper after oven drying (g)

X<sub>1</sub> = Dry weight of blank filter (g)

Y = Volume of water sample (ml)



Date 31/10/21	Depth (m)	Weight of filter paper (g)	Lid box number	Weight of empty lid box (g)	Sample Volume (L)	Weight of oven dried sediment sample + Filter paper + Lid box (g)	Weight of Suspended Sediment (g)	Observed SSC (mg/L or PPM)
1	30.94	1.559	1(JJ)	31.921	0.93	33.501	0.021	22.581
2	30.94	1.528	2(JJ)	35.722	0.94	37.269	0.019	20.213
3	31.94	1.525	3(JJ)	40.404	0.91	41.956	0.027	29.508
4	21.50	1.472	4(JJ)	35.945	0.91	37.442	0.025	27.473
5	26.00	1.513	5(JJ)	32.468	0.95	33.998	0.017	17.895
6	34.88	1.615	6(JJ)	33.605	0.94	35.235	0.015	15.957
7	33.88	1.552	7(JJ)	33.684	0.93	35.258	0.022	23.529
8	32.01	1.547	8(JJ)	31.845	0.95	33.408	0.016	16.842
9	26.50	1.543	9(JJ)	33.647	0.93	35.213	0.023	24.731
10	12.60	1.449	1(JJ)	31.921	0.93	33.397	0.027	28.877
11	25.02	1.484	2(JJ)	35.722	0.93	37.222	0.016	17.204
12	31.90	1.609	3(JJ)	40.404	0.88	42.027	0.014	15.909
13	29.85	1.584	4(JJ)	35.945	0.95	37.548	0.019	20.000
14	23.62	1.539	5(JJ)	32.468	0.95	34.023	0.016	16.842
15	26.08	1.572	6(JJ)	33.605	0.94	35.195	0.018	19.149
16	29.18	1.526	7(JJ)	33.684	0.94	35.226	0.016	16.931
17	22.01	1.554	8(JJ)	31.845	0.95	33.424	0.025	26.316
18	22.08	1.619	9(JJ)	33.647	0.95	35.29	0.024	25.131
19	16.38	1.502	1(JJ)	31.921	0.92	33.439	0.016	17.391
20	15.52	1.631	2(JJ)	35.722	0.93	37.375	0.022	23.656
21	13.56	1.499	3(JJ)	40.404	0.96	41.918	0.015	15.625
22	1.20	1.524	4(JJ)	35.945	0.92	37.541	0.072	78.261
23	14.72	1.623	5(JJ)	32.468	0.93	34.106	0.015	16.043
24	16.32	1.503	6(JJ)	33.605	0.95	35.128	0.02	20.942
25	30.94	1.616	7(JJ)	33.684	0.96	35.323	0.023	23.834

Date 20/12/21	Depth (m)	Weight of filter paper (g)	Lid box number	Weight of empty lid box (g)	Sample Volume (L)	Weight of oven dried sediment sample + Filter paper + Lid box (g)	Weight of Suspended Sediment (g)	Observed SSC (mg/L or PPM)
26	1.65	1.629	1(JJ)	31.921	1.02	33.597	0.047	45.854
27	17.20	1.459	2(JJ)	35.722	1.03	37.235	0.054	52.326
28	5.50	1.594	3(JJ)	40.404	1.03	42.047	0.049	47.435
29	8.00	1.475	4(JJ)	35.945	1.00	37.476	0.056	55.611
30	3.74	1.476	5(JJ)	32.468	1.00	33.998	0.054	52.838
31	4.00	1.587	6(JJ)	33.605	0.99	35.241	0.049	49.495
32	3.00	1.586	7(JJ)	33.684	1.02	35.32	0.05	48.685
33	7.04	1.563	8(JJ)	31.845	1.02	33.465	0.057	55.828
34	6.42	1.553	9(JJ)	33.647	1.02	35.252	0.052	50.682
35	4.00	1.539	10 (JJ)	36.066	1.01	37.658	0.053	52.475
36	7.20	1.559	11 (JJ)	36.946	1.00	38.56	0.055	55.000
37	3.00	1.513	12 (JJ)	33.283	1.01	34.85	0.054	53.045
38	2.00	1.559	13 (JJ)	28.965	0.97	30.575	0.051	52.308
39	4.24	1.499	14 (JJ)	34.855	0.95	36.407	0.053	55.789
40	3.00	1.53	15 (JJ)	34.178	0.97	35.763	0.055	56.701
41	4.96	1.59	16 (JJ)	39.276	1.02	40.917	0.051	49.756
42	2.20	1.516	17 (JJ)	33.638	0.96	35.2	0.046	47.668
43	2.52	1.593	18 (JJ)	33.476	0.95	35.119	0.05	52.632
44	6.00	1.518	19 (JJ)	31.98	0.93	33.556	0.058	62.366
45	2.38	1.552	20 (JJ)	34.703	0.99	36.306	0.051	51.515
46	2.35	1.535	21 (JJ)	37.073	0.97	38.669	0.061	62.887
47	5.20	1.518	22 (JJ)	28.868	0.99	30.451	0.065	65.657
48	3.40	1.563	23 (JJ)	36.273	0.93	37.886	0.05	53.763
49	4.75	1.545	24 (JJ)	33.885	0.97	35.485	0.055	56.701
50	9.20	1.531	25 (JJ)	33.348	0.99	34.933	0.054	54.271
51	10.96	1.52	26 (JJ)	38.791	0.99	40.375	0.064	64.646
52	12.80	1.495	27 (JJ)	32.786	0.99	34.337	0.056	56.566
53	5.48	1.516	28 (JJ)	35.603	0.98	37.172	0.053	54.082
54	35.72	1.579	29 (JJ)	35.998	1.00	37.624	0.047	47.000
55	5.00	1.589	30 (JJ)	36.079	0.95	37.716	0.048	50.526

<b>Date 04/01/22</b>	<b>Depth (m)</b>	<b>Weight of filter paper (g)</b>	<b>Lid box number</b>	<b>Weight of empty lid box (g)</b>	<b>Sample Volume (L)</b>	<b>Weight of oven dried sediment sample + Filter paper + Lid box (g)</b>	<b>Weight of Suspended Sediment (g)</b>	<b>Observed SSC (mg/L or PPM)</b>
56	18.26	1.588	1(JJ)	31.921	1.02	33.567	0.058	56.863
57	9.80	1.591	2(JJ)	35.722	1.02	37.359	0.046	44.747
58	4.70	1.589	3(JJ)	40.404	1.02	42.037	0.044	42.927
59	4.74	1.58	4(JJ)	35.945	0.98	37.576	0.051	52.041
60	4.60	3.21	5(JJ)	32.468	1.01	35.718	0.04	39.604
61	1.80	1.581	6(JJ)	33.605	1.00	35.25	0.064	64.000
62	1.92	1.597	7(JJ)	33.684	1.00	35.32	0.039	39.000
63	15.80	1.54	8(JJ)	31.845	1.03	33.445	0.06	58.252
64	5.85	1.617	9(JJ)	33.647	1.02	35.312	0.048	47.059
65	2.12	1.591	10 (JJ)	36.066	0.96	37.718	0.061	63.542
66	5.62	1.611	11 (JJ)	36.946	1.00	38.616	0.059	59.000
67	4.40	1.567	12 (JJ)	33.283	1.00	34.895	0.045	44.643
68	6.50	1.608	13 (JJ)	28.965	0.99	30.615	0.042	42.424
69	2.00	1.569	14 (JJ)	34.855	1.00	36.457	0.033	33.000
70	3.60	1.585	15 (JJ)	34.178	0.97	35.819	0.056	57.732
71	7.00	3.171	16 (JJ)	39.276	1.00	42.517	0.07	70.000
72	7.70	1.568	17 (JJ)	33.638	0.99	35.258	0.052	52.525
73	5.80	1.592	18 (JJ)	33.476	1.00	35.109	0.041	41.000
74	5.22	1.593	19 (JJ)	31.98	0.97	33.628	0.055	56.701
75	2.10	1.608	20 (JJ)	34.703	0.95	36.356	0.045	47.368
76	14.05	1.574	21 (JJ)	37.073	0.99	38.689	0.042	42.424
77	10.45	3.226	22 (JJ)	28.868	0.96	32.151	0.057	59.375
78	18.15	1.622	23 (JJ)	36.273	0.94	37.943	0.048	51.064
79	2.20	1.59	24 (JJ)	33.885	0.98	35.528	0.053	54.082
80	1.90	1.612	25 (JJ)	33.348	1.02	35.003	0.043	42.157
81	5.20	3.239	26 (JJ)	38.791	0.98	42.077	0.047	47.959

<b>Date 03/02/22</b>	<b>Depth (m)</b>	<b>Weight of filter paper (g)</b>	<b>Lid box number</b>	<b>Weight of empty lid box (g)</b>	<b>Sample Volume (L)</b>	<b>Weight of oven dried sediment sample + Filter paper + Lid box (g)</b>	<b>Weight of Suspended Sediment (g)</b>	<b>Observed SSC (mg/L or PPM)</b>
82	11.90	1.567	1(JJ)	31.921	0.99	33.548	0.06	60.606
83	10.45	1.572	2(JJ)	35.722	0.98	37.361	0.067	68.367
84	11.37	1.577	3(JJ)	40.404	0.97	42.044	0.063	64.948
85	8.21	1.589	4(JJ)	35.945	1.00	37.596	0.062	62.000
86	6.60	1.551	5(JJ)	32.468	1.02	34.077	0.058	56.863
87	10.65	1.552	6(JJ)	33.605	0.96	35.216	0.059	61.458
88	13.62	1.585	7(JJ)	33.684	0.95	35.331	0.062	65.263
89	13.60	1.578	8(JJ)	31.845	0.95	33.484	0.061	64.211
90	7.28	1.562	9(JJ)	33.647	0.97	35.281	0.072	74.227
91	6.06	1.537	10 (JJ)	36.066	0.94	37.677	0.074	78.723
92	7.75	1.59	11 (JJ)	36.946	1.01	38.608	0.072	71.287
93	2.92	1.568	12 (JJ)	33.283	0.91	34.921	0.07	76.923
94	7.24	1.593	13 (JJ)	28.965	1.04	30.634	0.076	73.077
95	4.44	3.166	14 (JJ)	34.855	0.98	38.097	0.076	77.551
96	5.42	3.158	15 (JJ)	34.178	1.03	37.431	0.095	92.233
97	8.04	1.573	16 (JJ)	39.276	1.00	40.912	0.063	63.000
98	6.00	1.678	17 (JJ)	33.638	0.91	35.4	0.084	92.308
99	8.90	1.573	18 (JJ)	33.476	1.03	35.113	0.064	62.136
100	16.35	1.587	19 (JJ)	31.98	0.90	33.639	0.072	80.000

<b>Date 18/02/2 2</b>	<b>Depth (m)</b>	<b>Weight of filter paper (g)</b>	<b>Lid box number</b>	<b>Weight of empty lid box (g)</b>	<b>Sample Volume (L)</b>	<b>Weight of oven dried sediment sample + Filter paper + Lid box (g)</b>	<b>Weight of Suspended Sediment (g)</b>	<b>Observed (mg/L or PPM)</b>
101	9.72	1.584	1(JJ)	31.921	0.95	33.618	0.113	118.947
102	10.75	1.553	2(JJ)	35.722	0.97	37.389	0.114	117.526
103	8.28	1.554	3(JJ)	40.404	0.98	42.071	0.113	115.306
104	8.66	1.553	4(JJ)	35.945	0.99	37.622	0.124	125.253
105	9.12	1.581	5(JJ)	32.468	0.98	34.168	0.119	121.429
106	6.80	1.553	6(JJ)	33.605	0.9	35.273	0.115	127.778
107	5.20	1.579	7(JJ)	33.684	0.85	35.38	0.117	137.647
108	5.15	1.57	8(JJ)	31.845	0.95	33.527	0.112	117.895
109	6.46	1.588	9(JJ)	33.647	0.94	35.349	0.114	121.277
110	5.90	1.58	10 (JJ)	36.066	1.00	37.764	0.118	118.000
111	4.75	1.597	11 (JJ)	36.946	0.99	38.657	0.114	115.152
112	0.39	1.553	13 (JJ)	28.965	1.03	30.631	0.113	109.709
113	4.18	1.596	14 (JJ)	34.855	1.07	36.565	0.114	106.542
114	1.76	1.594	15 (JJ)	34.178	1.00	35.885	0.113	113.000
115	4.33	1.578	16 (JJ)	39.276	1.06	40.971	0.117	110.377
116	3.56	1.562	17 (JJ)	33.638	0.95	35.316	0.116	122.105
117	6.60	1.552	18 (JJ)	33.476	1.05	35.146	0.118	112.381
118	8.04	1.57	19 (JJ)	31.98	1.02	33.66	0.11	107.843
119	7.72	1.607	20 (JJ)	34.703	1.00	36.429	0.119	119.000
120	2.32	1.577	21 (JJ)	37.073	1.04	38.767	0.117	112.500
121	9.20	1.56	22 (JJ)	28.868	1.03	30.55	0.122	118.447



## Appendix – B

### Operating procedure for Capturing Spectral Response using Spectroradiometer SVC HR - 1024i and Data Processing

This section describes the details of HR 1024i Spectroradiometer including operating procedure and data processing.

#### 1. Spectroradiometer SVC HR 1024i

The instrument includes memory and a display for stand-alone operation as well as capability for personal computer (PC) and personal data assistant (PDA) assisted operation. PC communications to the instrument are available through its USB client port, a Bluetooth wireless connection, or via RS-232. A PDA may control the instrument via a Bluetooth connection or via RS-232. When operated in stand-alone mode, up to 1000 spectral readings can be stored within the instrument for subsequent down loading and analysis using a PC. All Spectroradiometer identification and calibration information is stored on board, so there are no external files to manage.

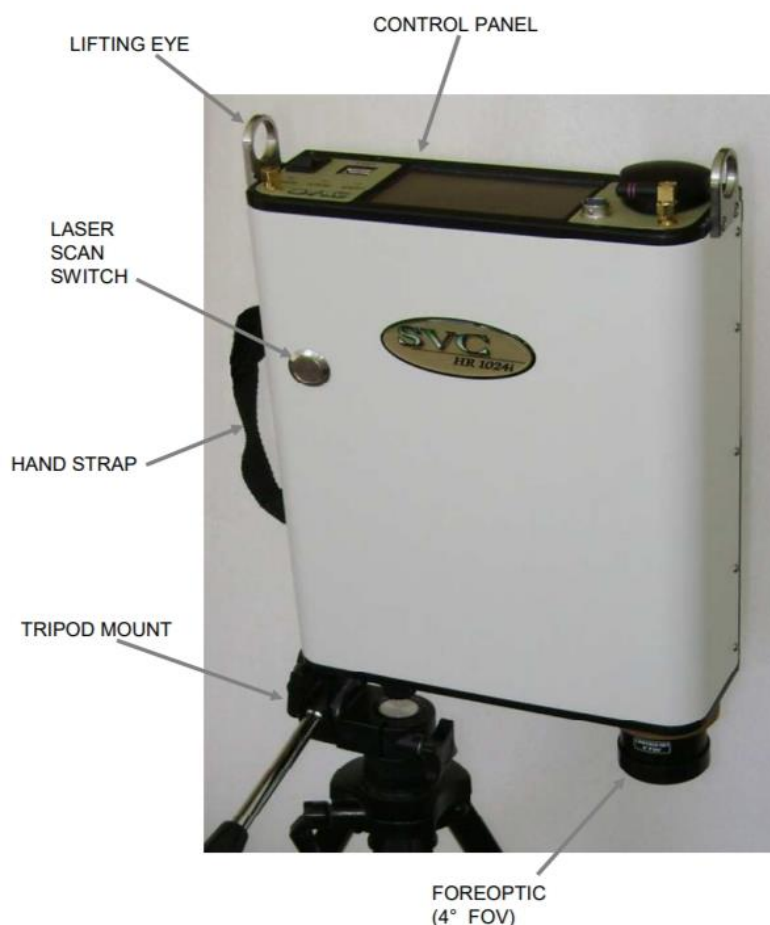


Fig 1. Spectroradiometer

The instrument contains an internal GPS device to record the latitude, longitude, and time of each spectral reading. This instrument is self-contained and incorporates an easily replaceable

battery called a SMARTPACK. The battery chargers supplied with the instrument have the capability to charge the LI-Ion batteries from line voltage with the AC adapter.

The computer based operation allows for real time data display and data analysis. Radiance and percent reflectance are provided within the acquisition software. A full range of options are available. These options include alternate foreoptics, fiber optic light guides, irradiance spheres, cosine diffusers, Reflectance Probe, back packs, white reference panels, tripods and other custom engineered field devices.

Spectral Range	350 nm to 2500 nm
Number of Channels	1024 (including overlapped channels)
Type of Sensors	512 Channel Silicon Array 256 Channel InGaAs array 256 Channel Extended InGaAs array
Resolution	$\leq 3.5$ nm FWHM @ 700 nm $\leq 9.5$ nm FWHM @ 1500 nm $\leq 6.5$ nm FWHM @ 2100 nm
Unit Weight	3.8 kg
Internal Memory	1000 scans maximum
Standard Foreoptics	4° Nominal FOV
Optional Foreoptics	8° Nominal FOV 14° Nominal FOV 25° Fiber Optic Light guide, various lengths Irradiance Spheres and Diffusers
Power	Li-Ion Battery operated, 6.5 – 8.0 VDC @ 2.5A
Environmental	Temperature: -10°C to +40°C Humidity: <90%, non-condensing
Cleaning	Wipe down exterior with soft, dry cloth only.

## 2. Operating procedure

- 1) Install fully charged battery into the Spectroradiometer and attach Bluetooth antenna. If connection is to be made by cable then cable need to be plugged to Spectroradiometer as well as PDA.
- 2) For optimal performance, switch on the instrument for a period of approximately 15 minutes (warm-up time) prior to first use.

- 3) Start PDA data acquisition software and go to 'File' menu and check the 'AutoSave' option. This causes measurements to automatically be saved to file after each target acquisition.
- 4) Select radiance graph type from the 'Graph' menu.
- 5) Then in 'Instrument' menu, go to the 'Connect'. A list of COM ports is displayed that is used for connecting PDA to the Spectroradiometer. Select 'COM8' which is for connection using Bluetooth.
- 6) Then in 'Settings' menu, select optic to Lens 4 for four optic drum is in use. Usually keep the integration settings to factory default.
- 7) Now focus the Spectroradiometer on white spectralon panel and click on the 'Reference' button in software to initiate the reference scan. For all the next readings up to next reference scan, this reading will be used as reference.
- 8) Once the reference scan is complete, just go on clicking on the 'Target' button for every next scan.
- 9) After the completion of experiment, disconnect the device from PDA.

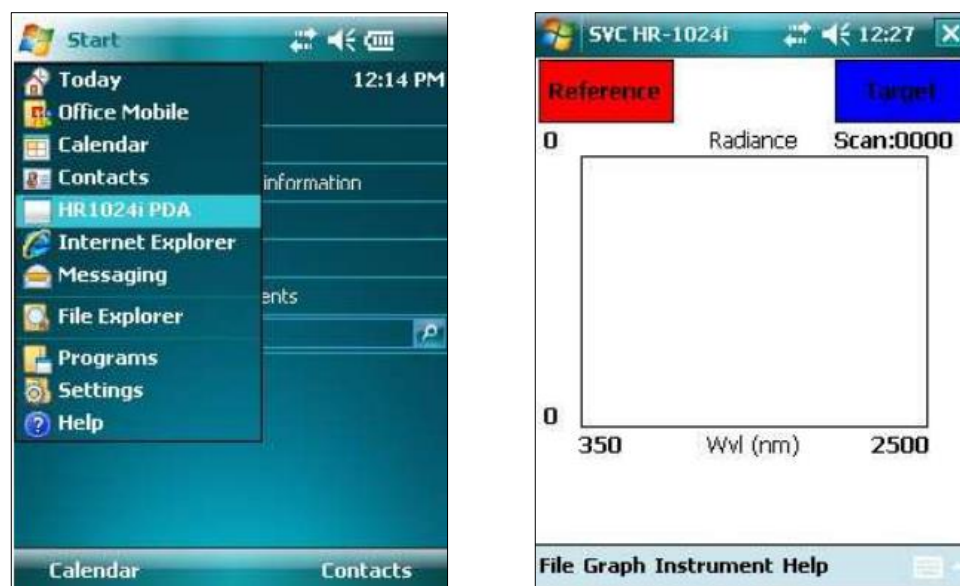


Fig. 2 Starting the PDA data acquisition software

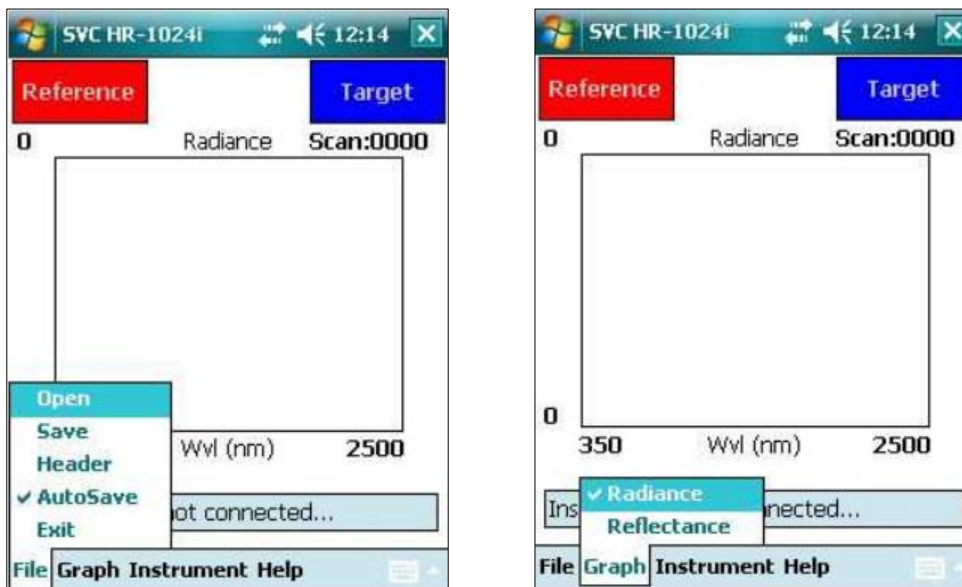


Fig. 3 Selection of Autosave option and graph type

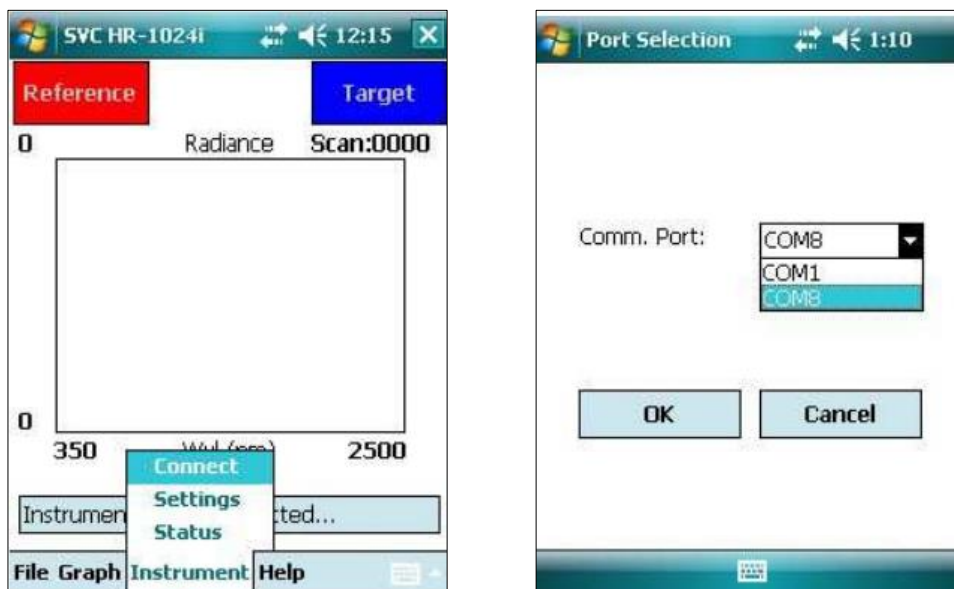


Fig. 4 Selection of the COM port

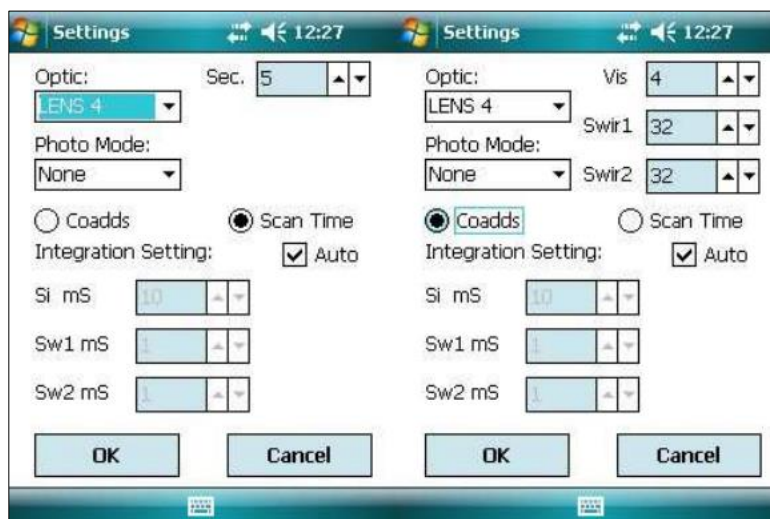
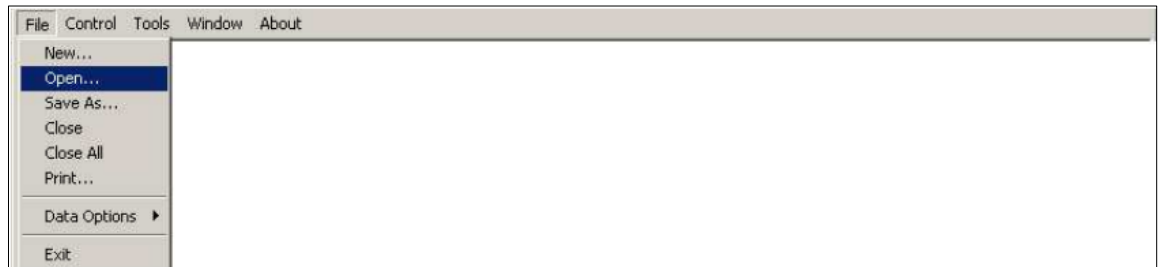


Fig. 5 Other settings of software

### 3. Processing of Data

- 1) Start the SVC HR-1024i software. Go to the 'File' and select 'Open' menu to open the desired .sig format files which are obtained from spectroradiometer observations.

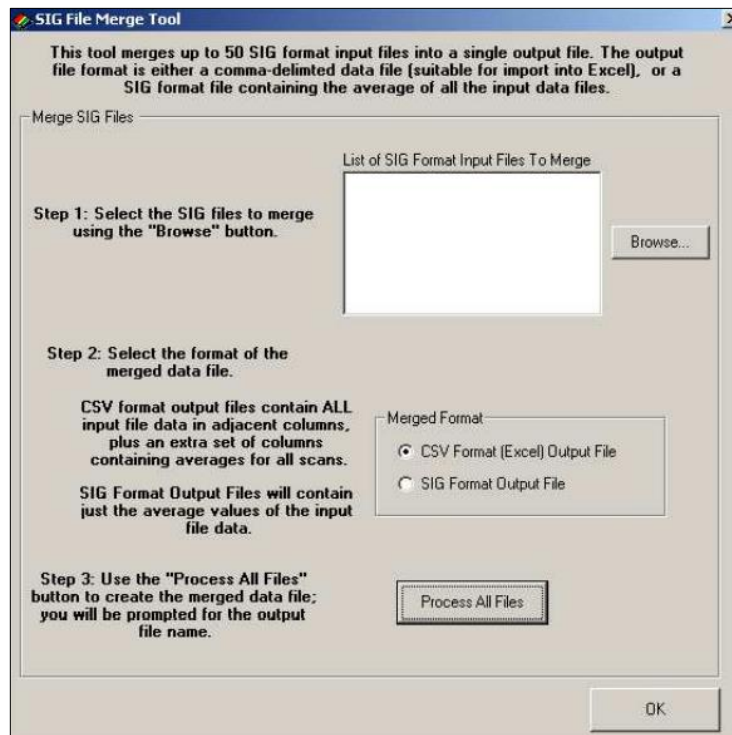


- 2) SIG File Merge:

In the 'Tool' menu, select 'SIG File Merge' to merge multiple SIG files into a single comma-delimited text data file.



In the dialog box, use 'Browse' button to select SIG format files of interest to merge. Select merged format as 'SIG Format Output File' and then click on 'Process All Files'.



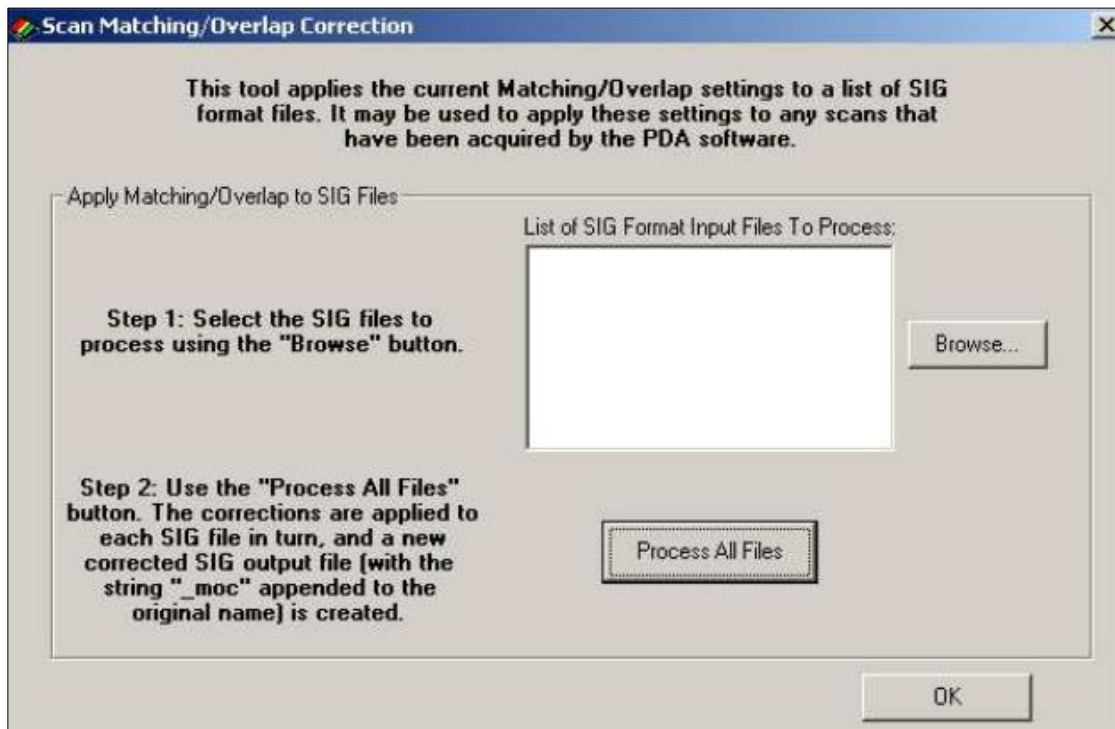
- 3) SIG Files Overlap / Matching:

In the 'Tool' menu, select 'SIG Files Overlap / Matching' which applies the current overlap and matching settings to a set of input SIG format files. SIG data files that are acquired by the PDA Software do not have overlapping data removed, and have not had any matching

algorithm applied. Use this tool to remove overlap and possibly apply detector matching algorithms.



In the dialog box, use the 'Browse' button to select the SIG format input files to process. Begin processing the SIG files; each SIG file in turn is read and processed, and the modified data is written to an output file with the string "\_moc" (Matching Overlay Correction) appended to the original name. For example, if the input SIG file name is: "cn2103003\_001.sig", then the output SIG file name is: "cn2103003\_001\_moc..sig"



#### 4) Resample spectral data:

In the 'Tool' menu, select 'Resample Spectral Data' and resample the input SIG format data files, and write the resampled data to new output SIG format data files.



In the dialog box, select wavelength range between 350 nm to 2500 nm. Select resampling interval (the interval used to perform the resample process) as 1 nm and use the 'Browse' button to select the SIG format input files to process. Begin processing the SIG files; each SIG file in turn is read and is linearly resampled at the specified Resampling Interval, and

the modified data is written to an output file with the string “\_resamp” appended to the original name. For example, if the input SIG file name is: “cn2103003\_001.sig”, then the output SIG file name is: “cn2103003\_001\_resamp.sig”



- 5) Open these resample files in notepad format from where they are then copied to excel sheet. It gives reflectance readings of observations.



## Appendix – C

### False Colour Composite of Sentinel-2 (BOA) Satellite Imageries

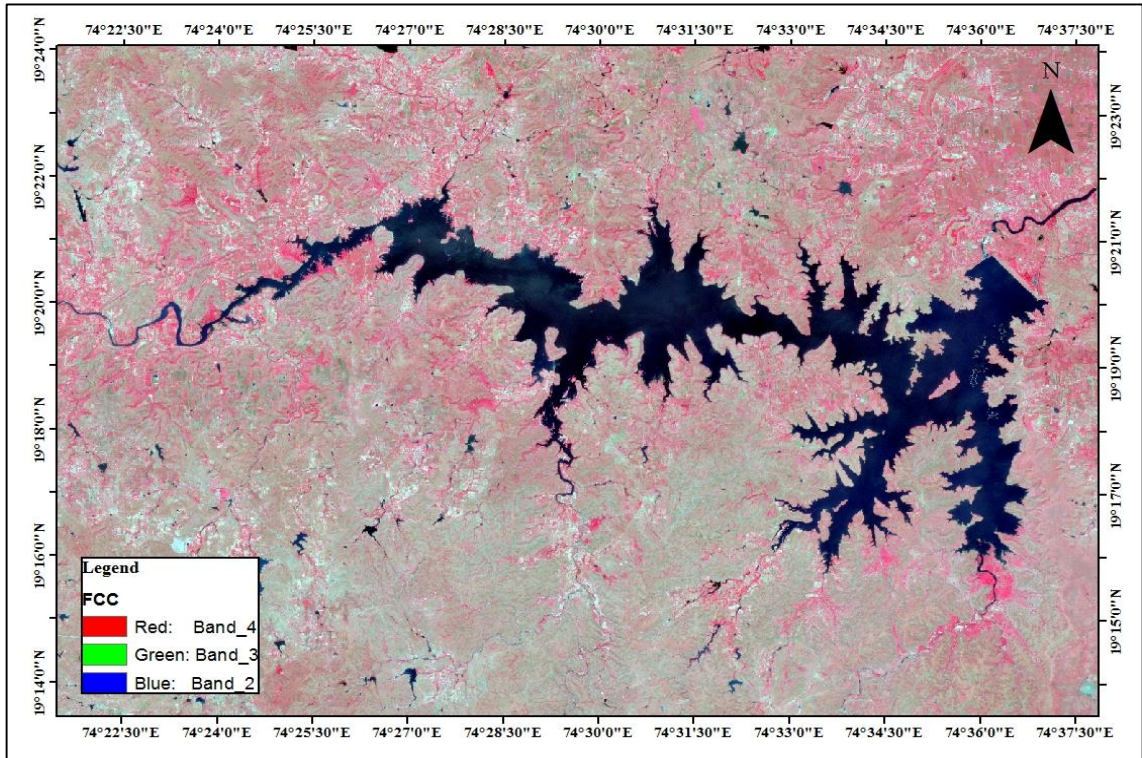


**Figure D-1: False Colour Composite (FCC) of study area on 31<sup>st</sup> October, 2021**

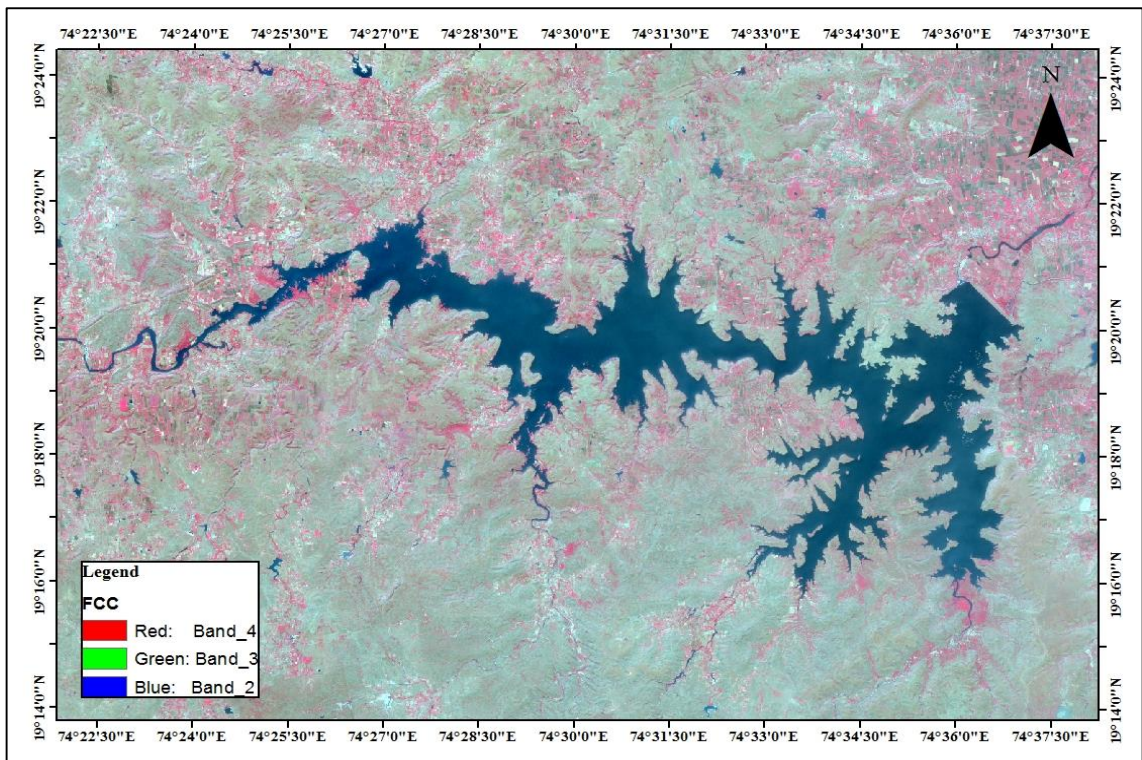


**Figure D-2: False Colour Composite (FCC) of study area on 20<sup>th</sup>, December 2021**

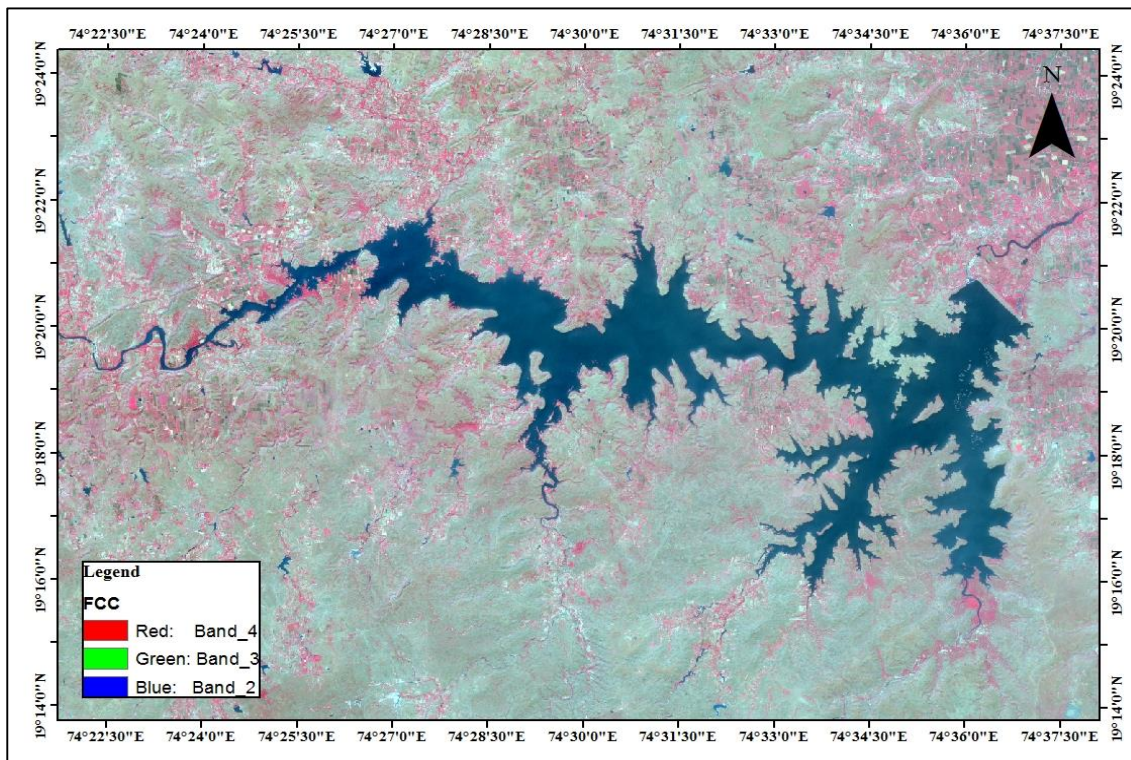


**Figure D-3: False Colour Composite (FCC) of study area on 04<sup>th</sup>, January, 2022**

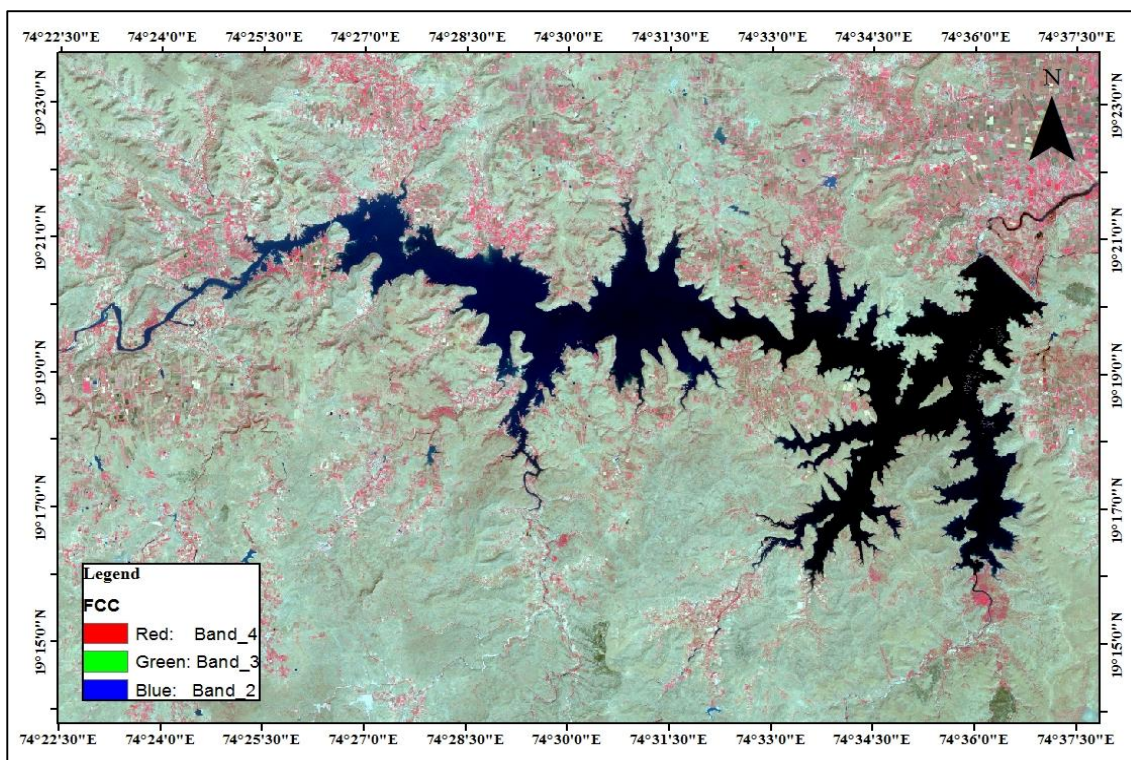
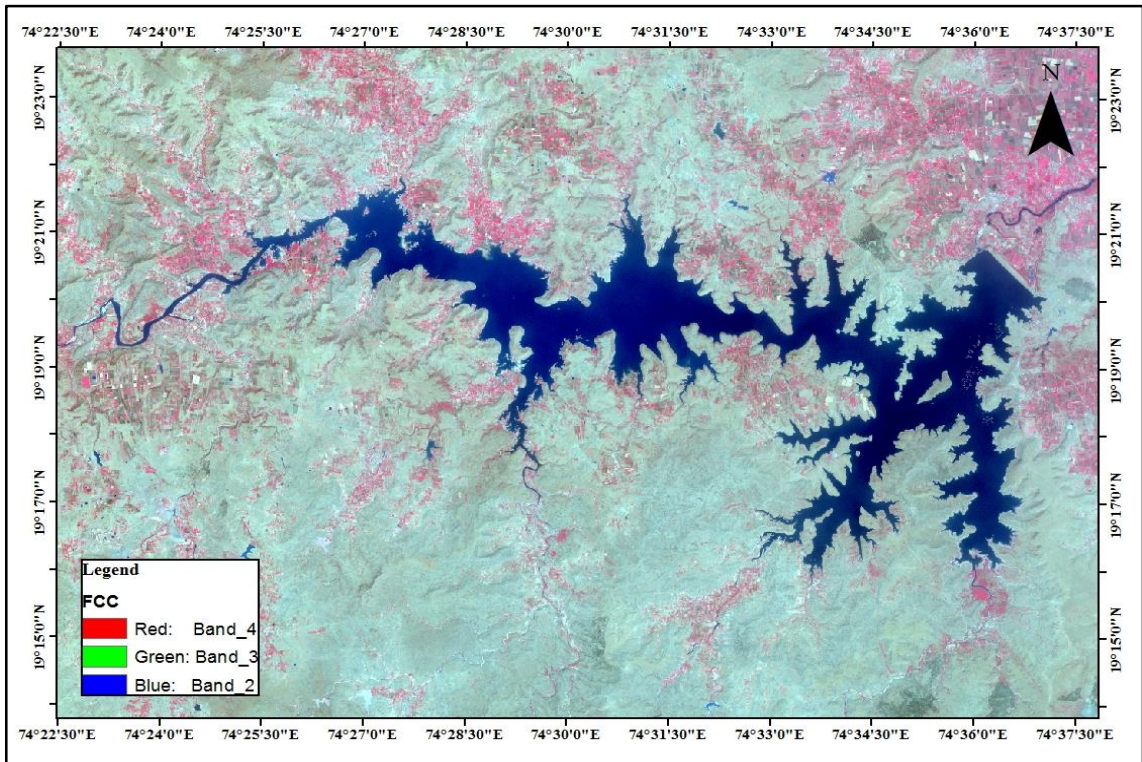


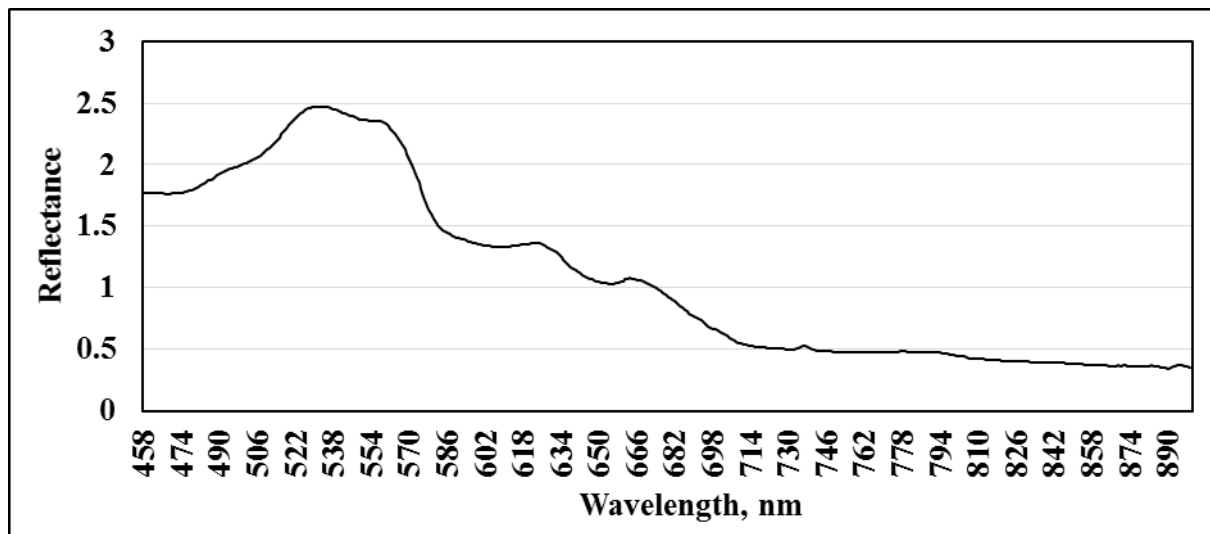
**Figure D-4: False Colour Composite (FCC) of study area on 03<sup>rd</sup>, February 2022**



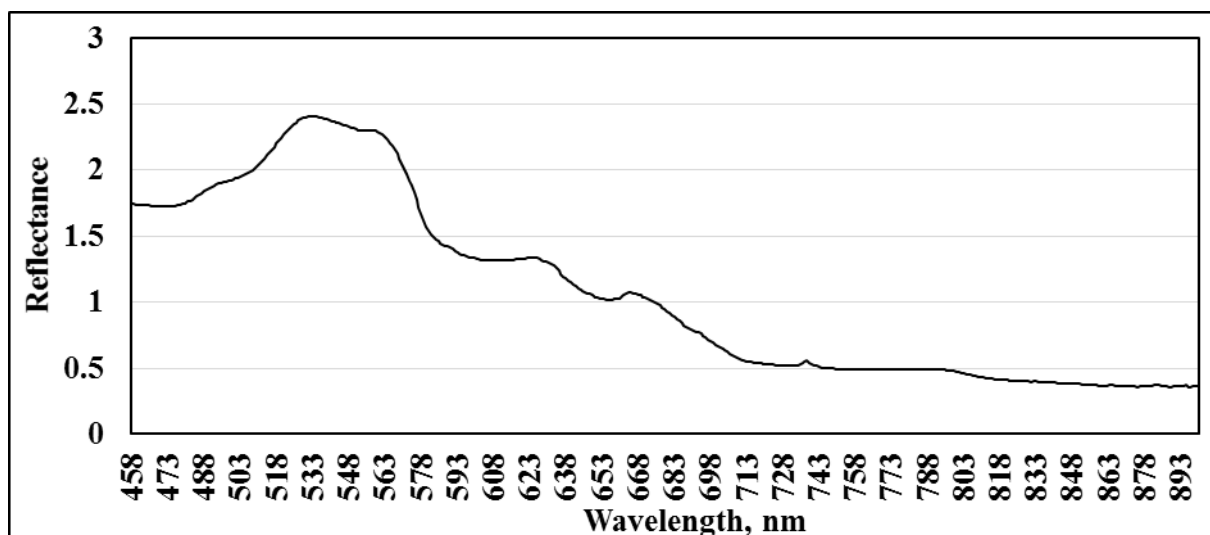


## Appendix – D

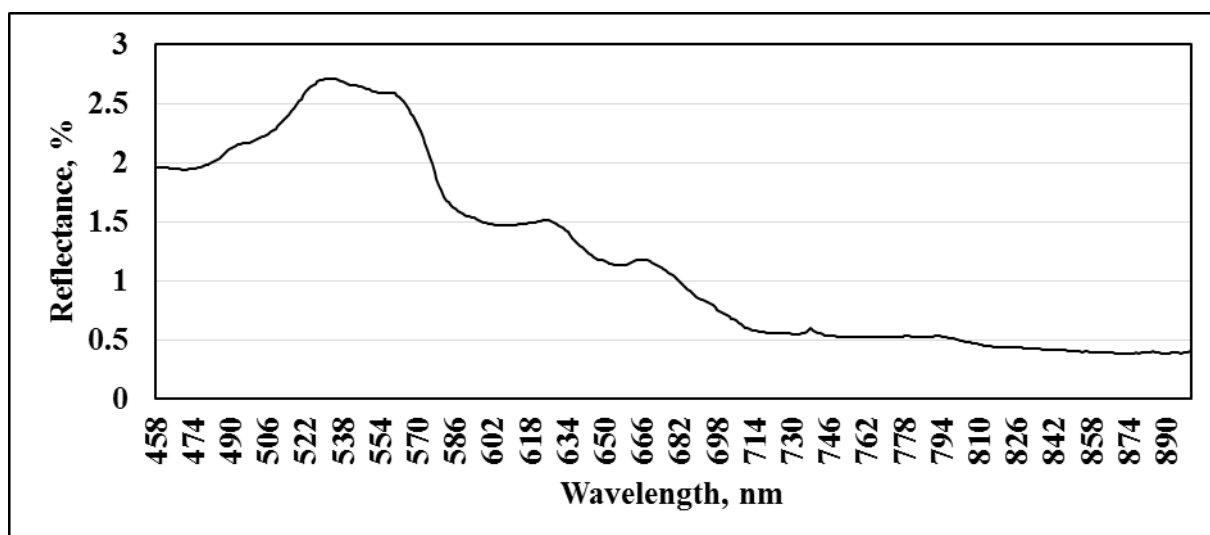
Spectral signatures captured by using Spectroradiometer SVC HR - 1024i



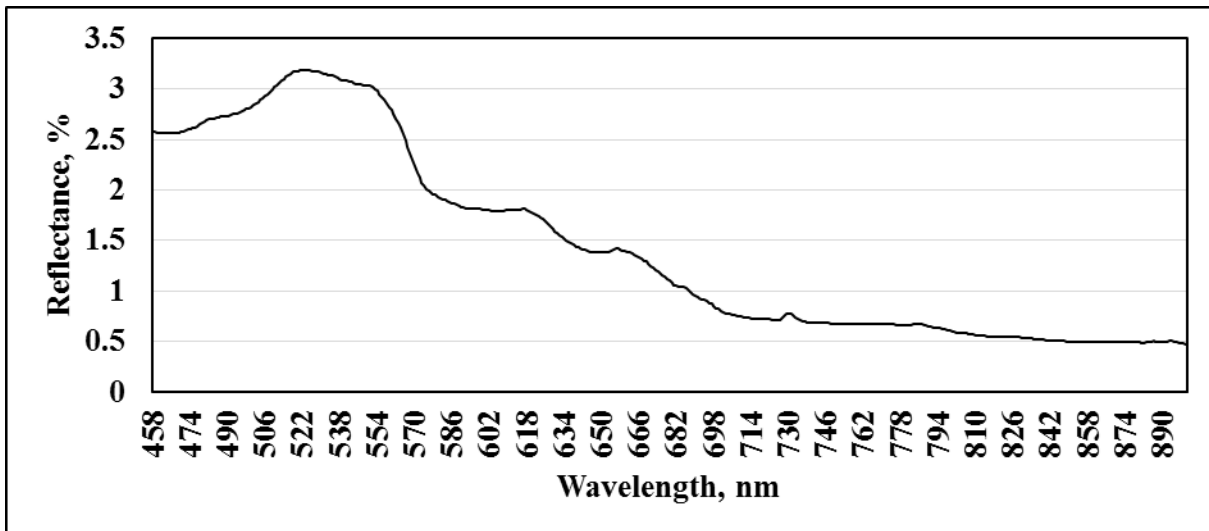
Sample 1



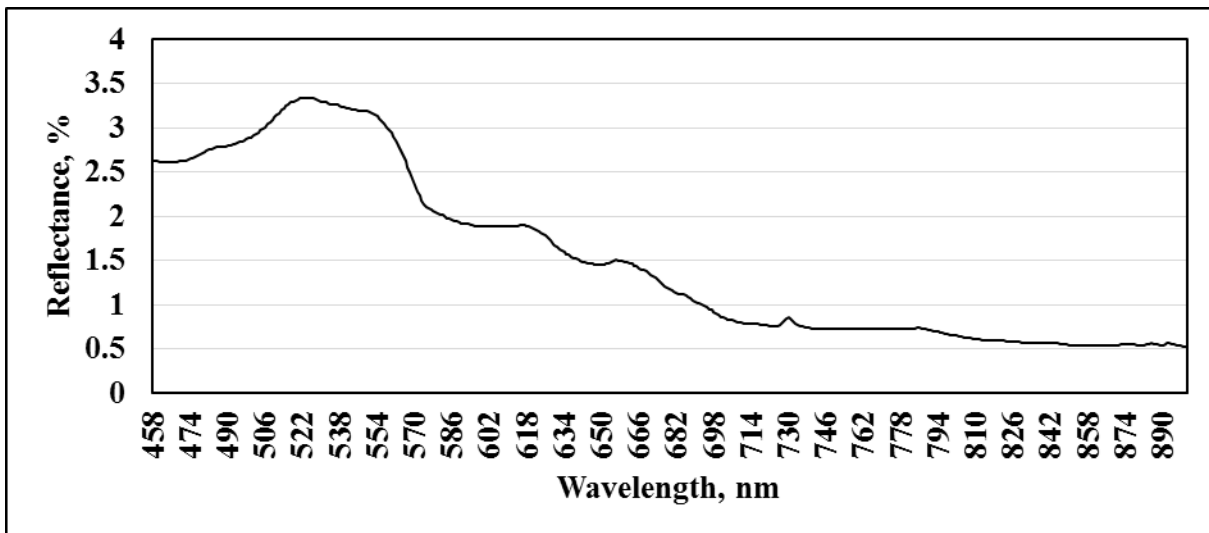
Sample 2



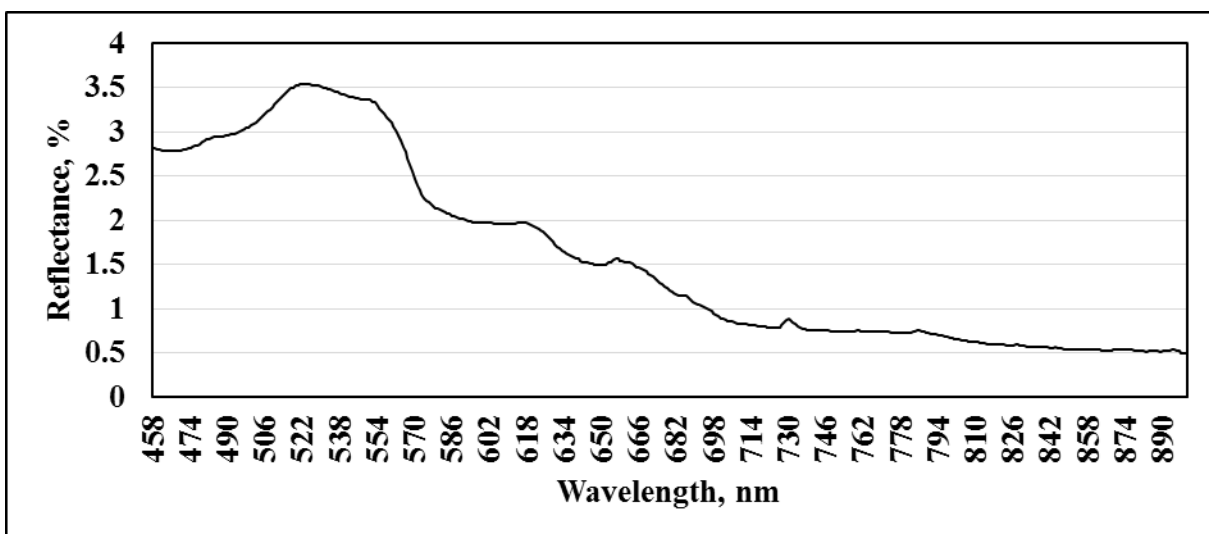
Sample 3



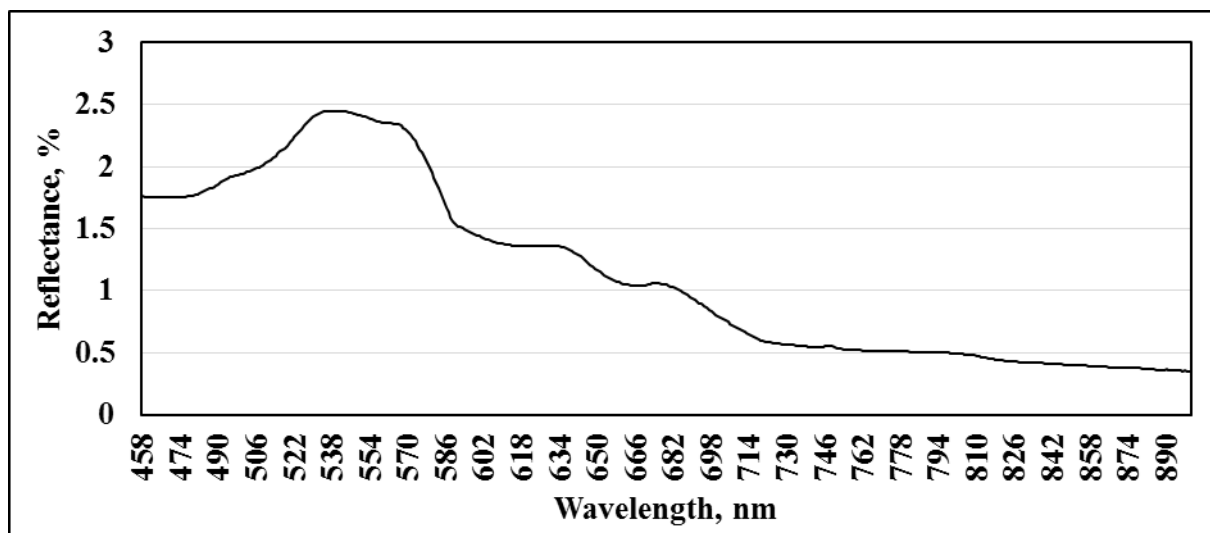
Sample 4



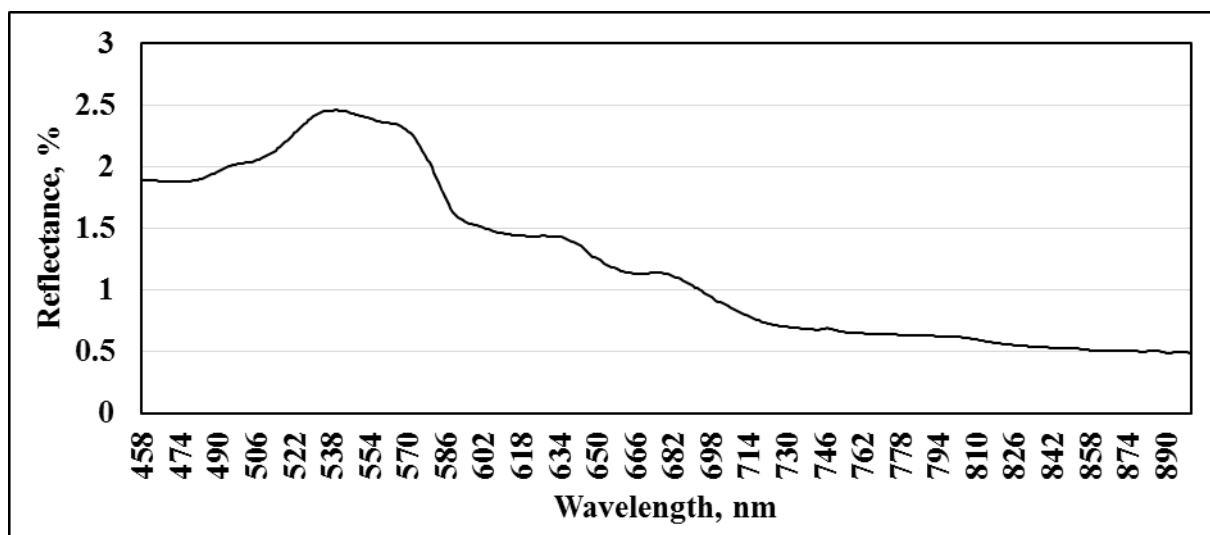
Sample 5



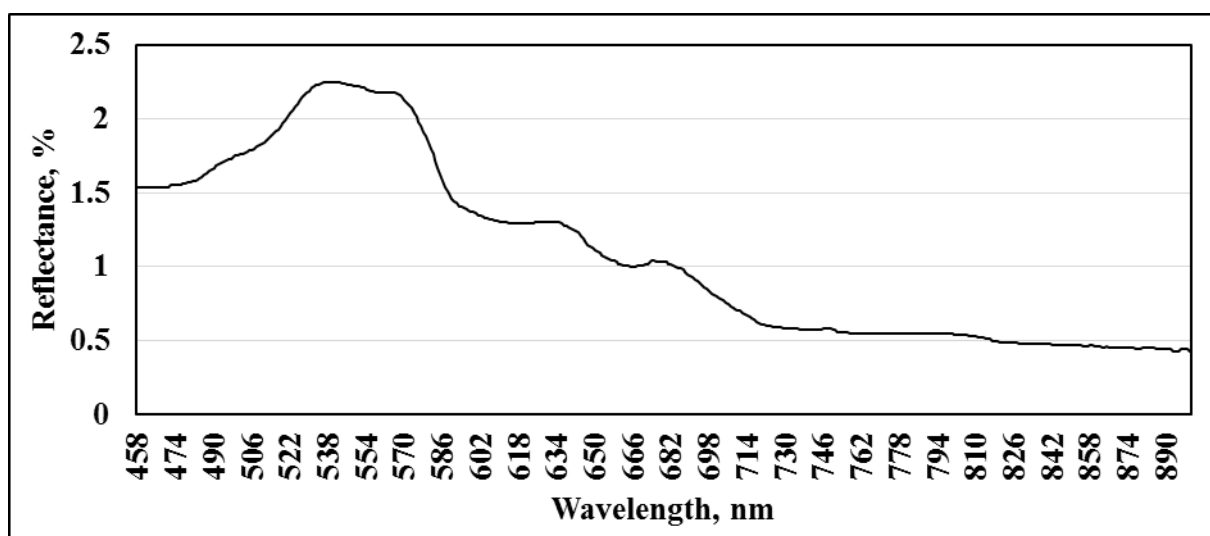
Sample 6



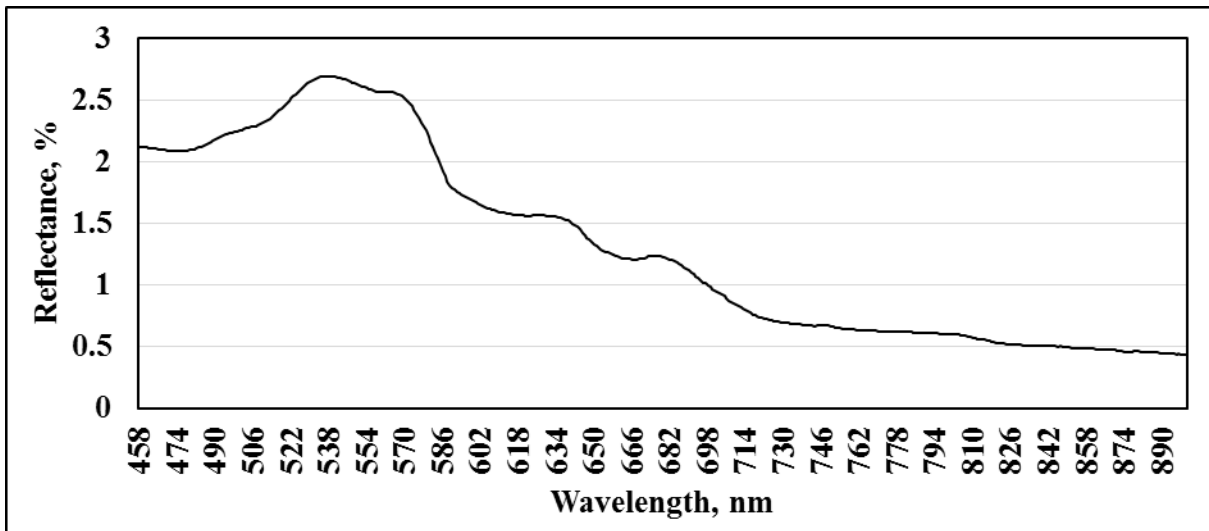
Sample 7



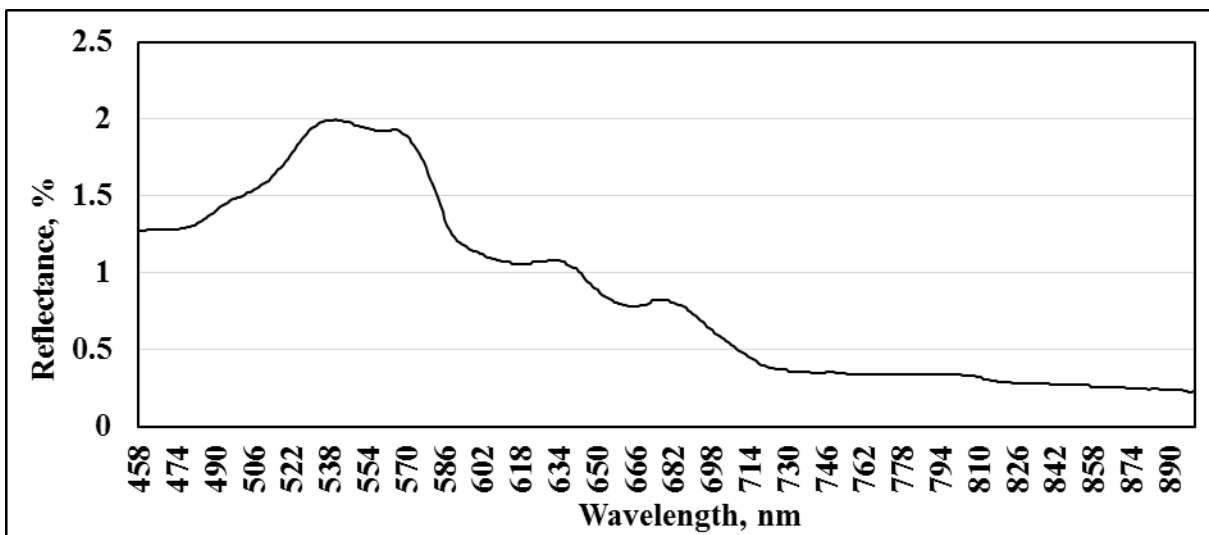
Sample 8



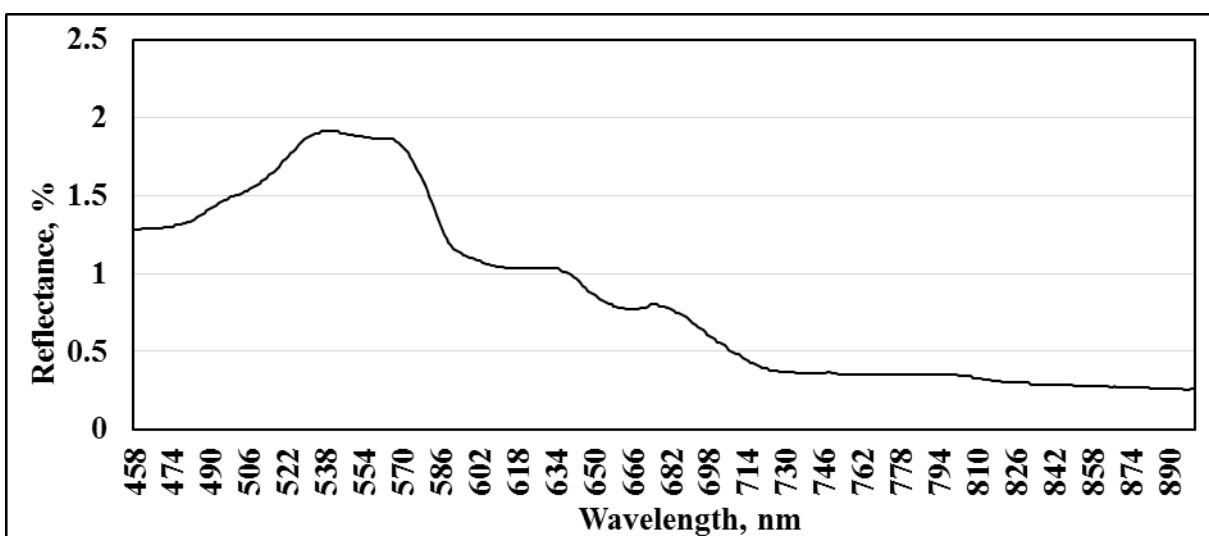
Sample 9



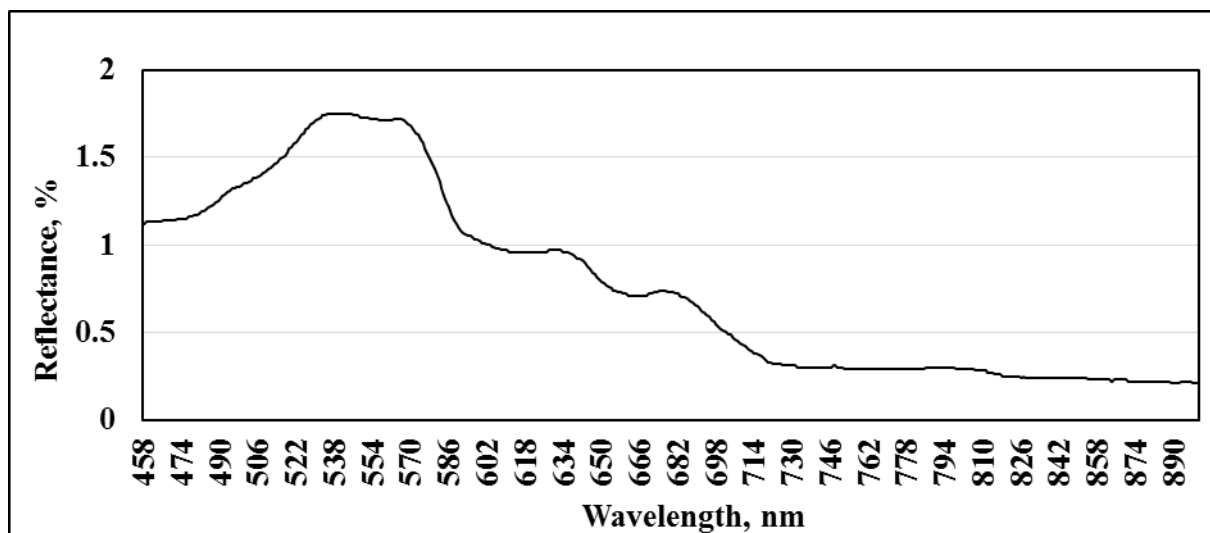
Sample 10



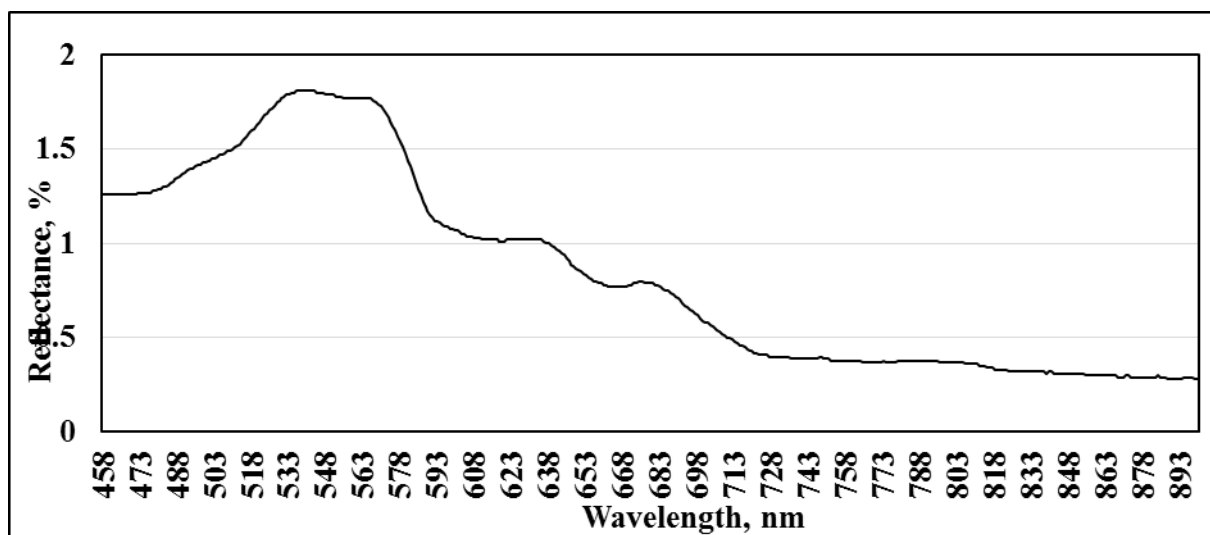
Sample 11



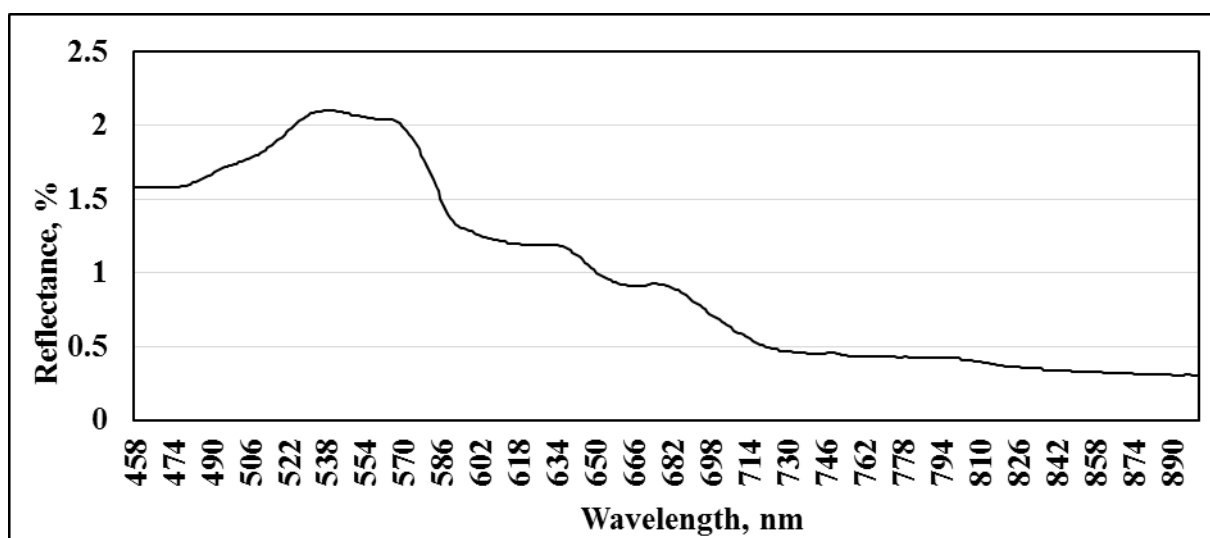
Sample 12



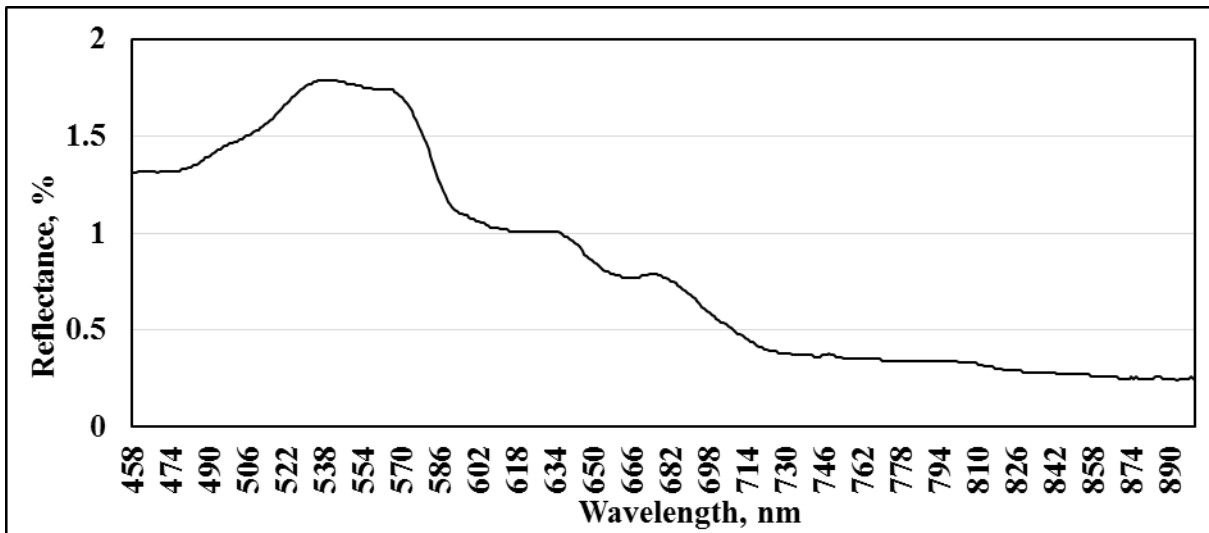
Sample 13



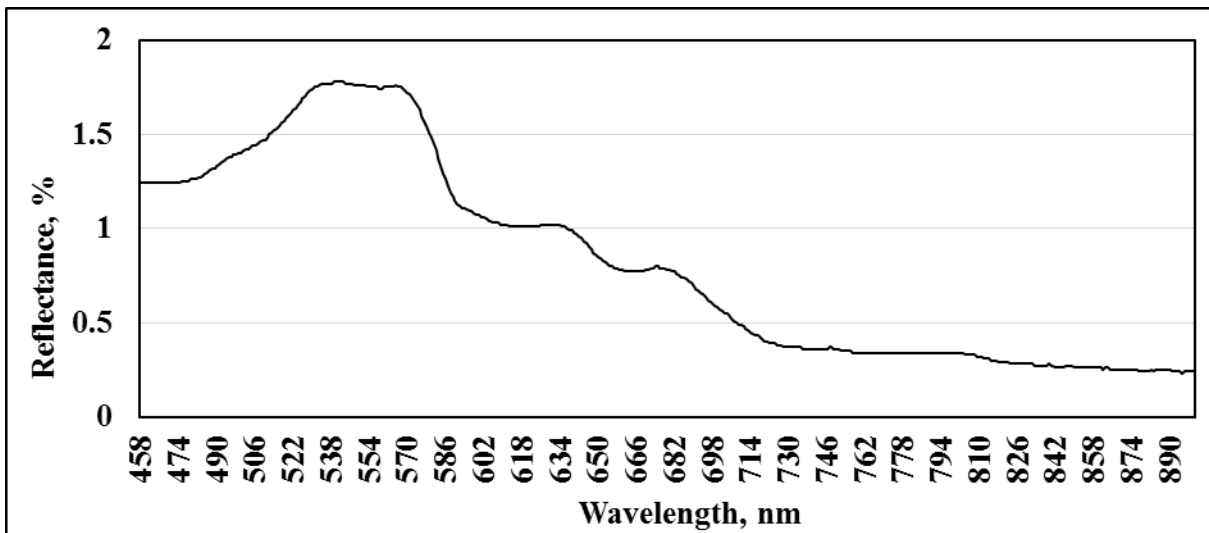
Sample 14



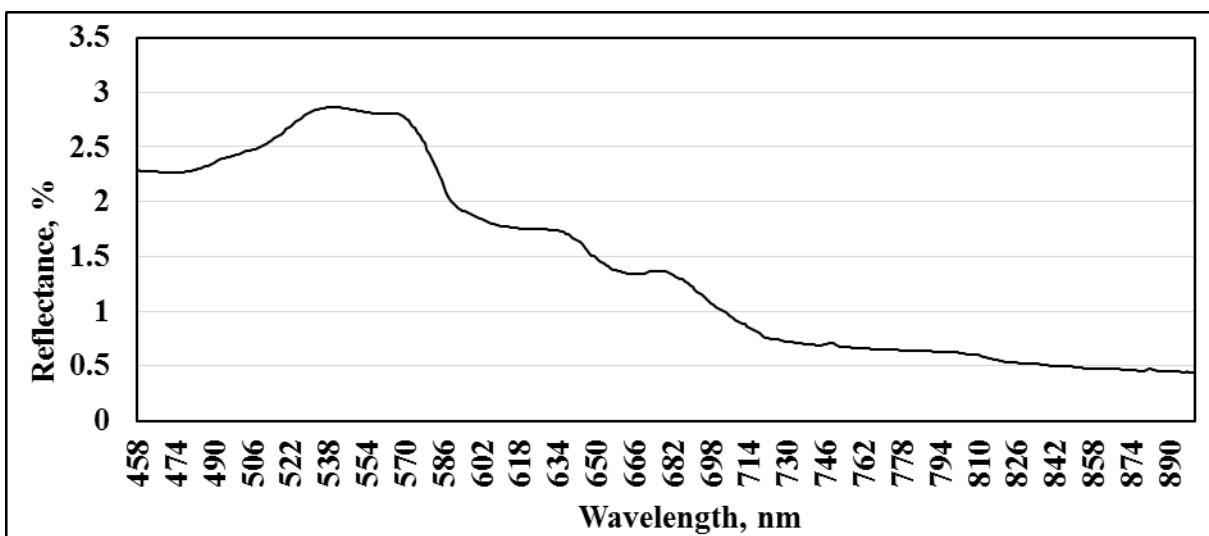
Sample 15



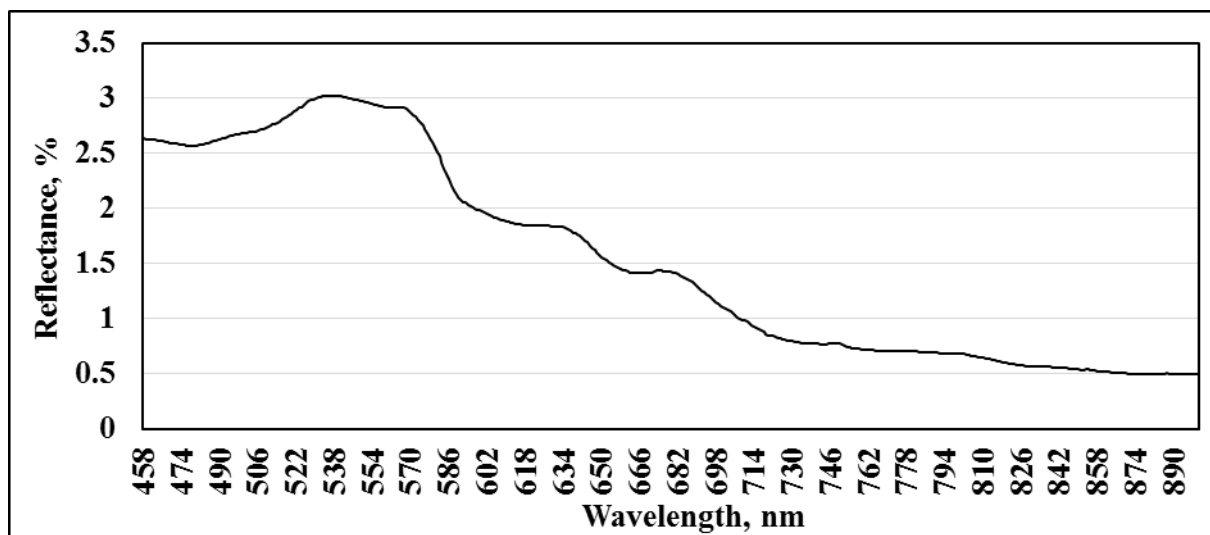
Sample 16



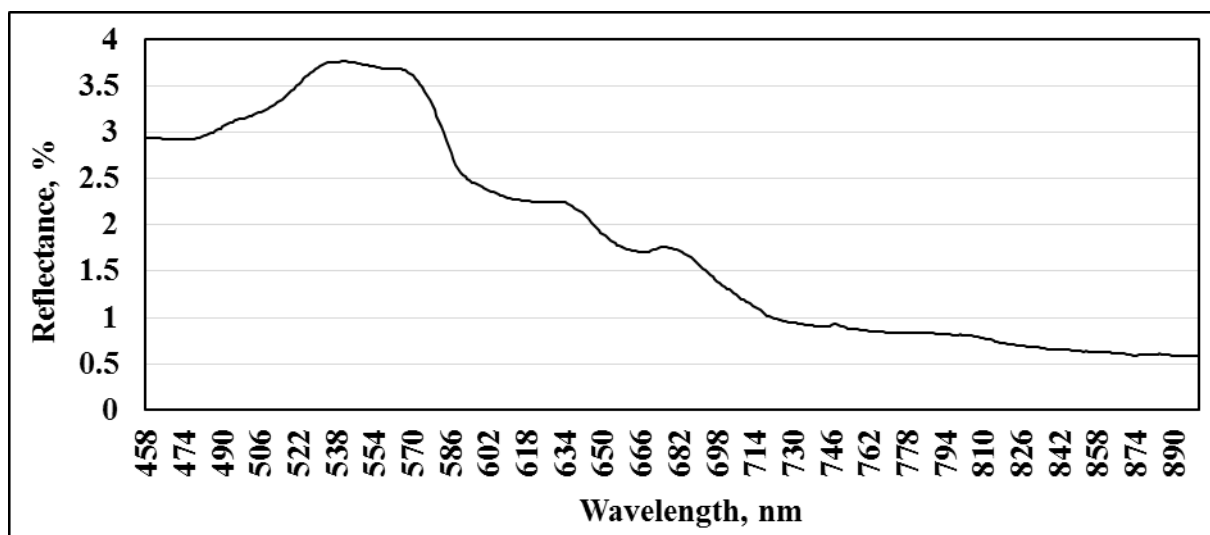
Sample 17



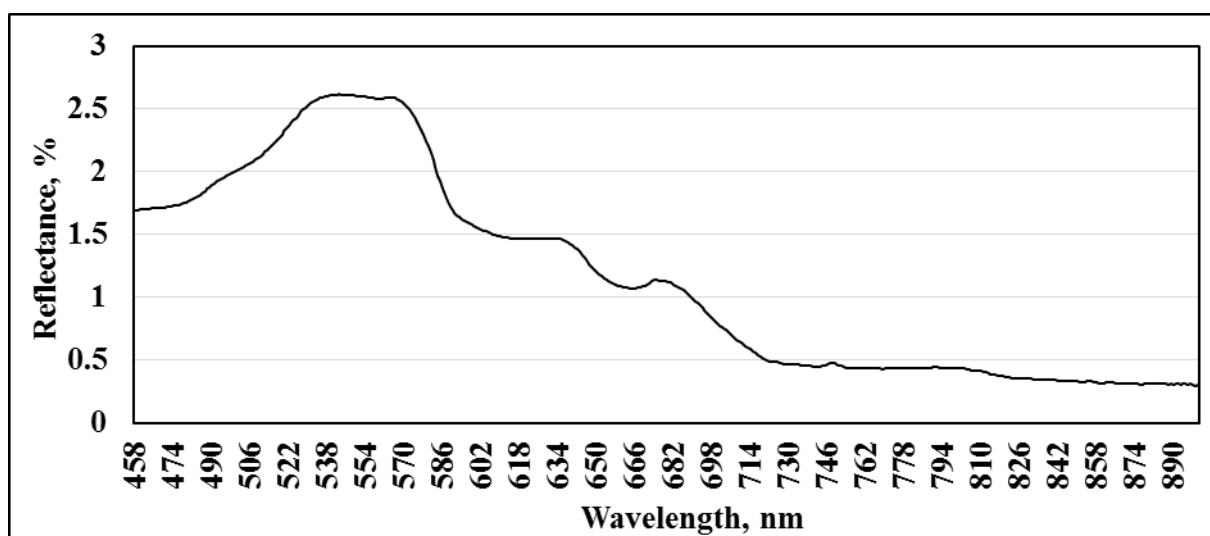
Sample 18



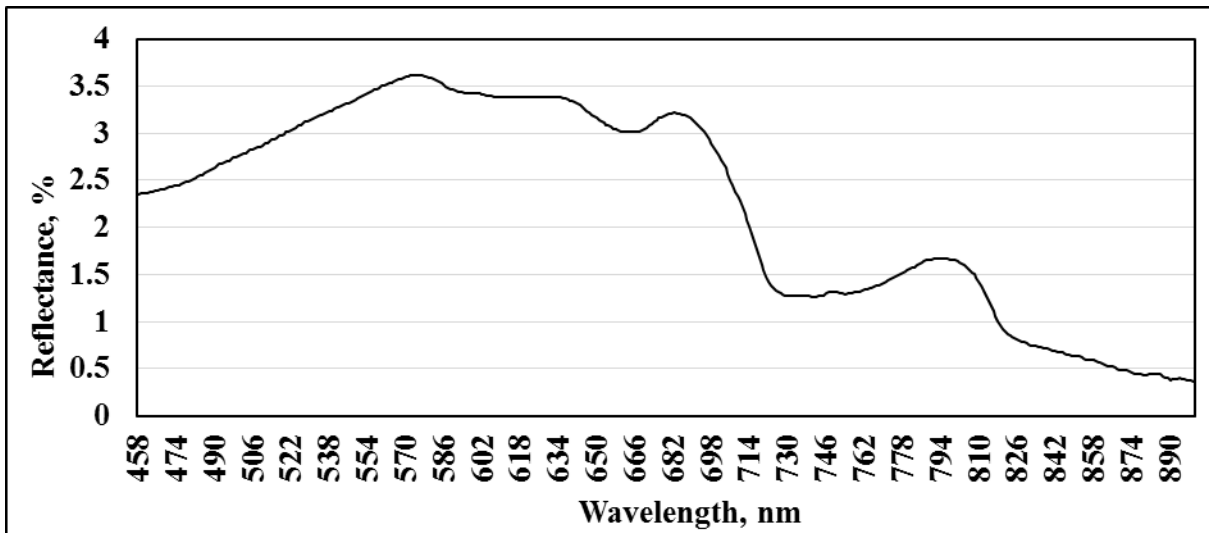
Sample 19



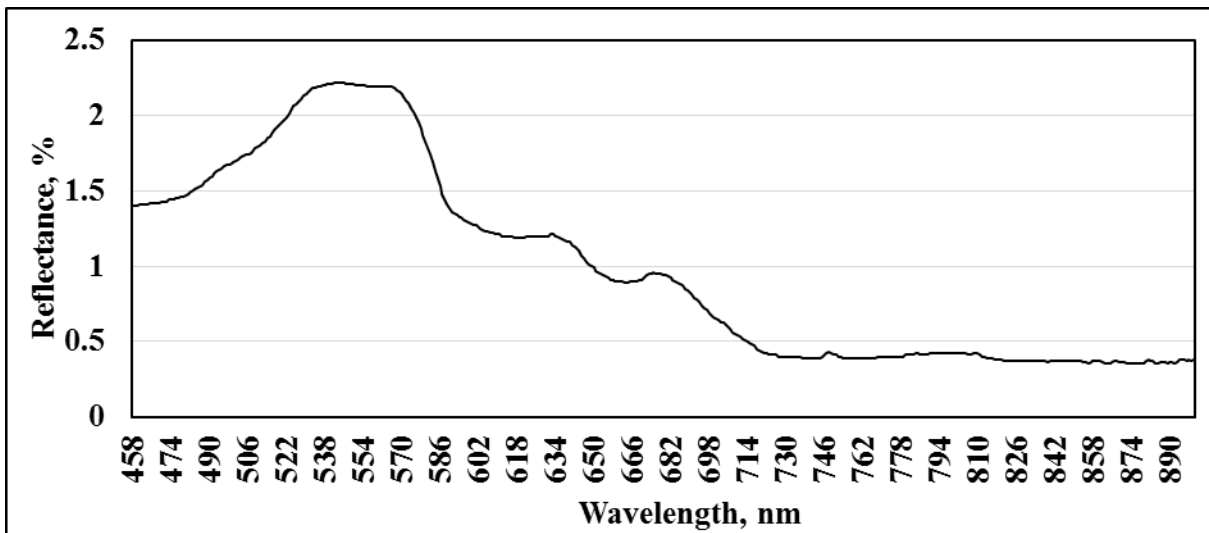
Sample 20



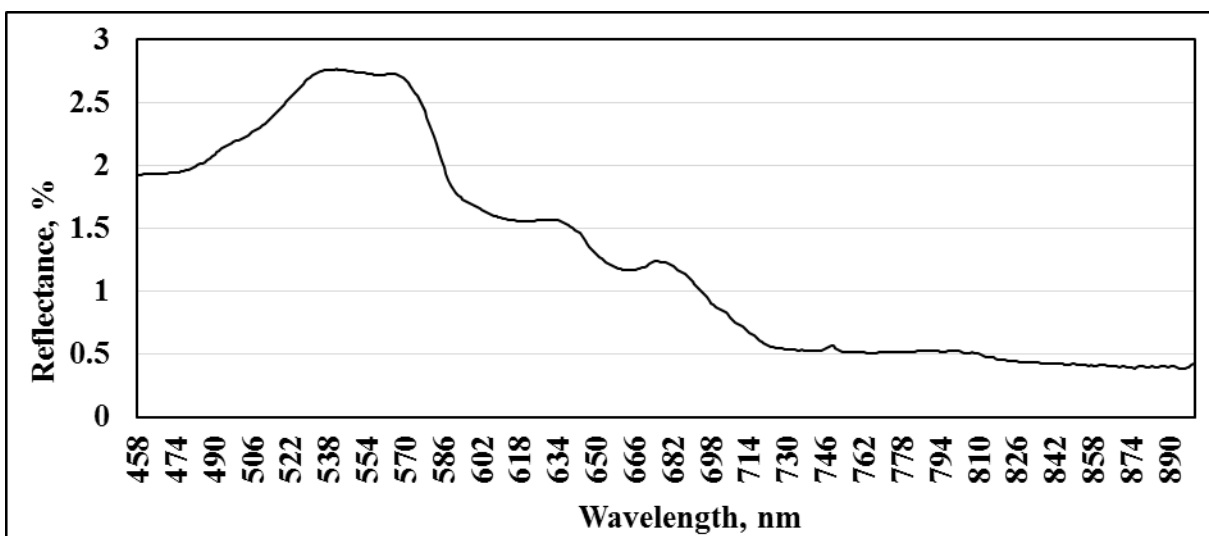
Sample 21



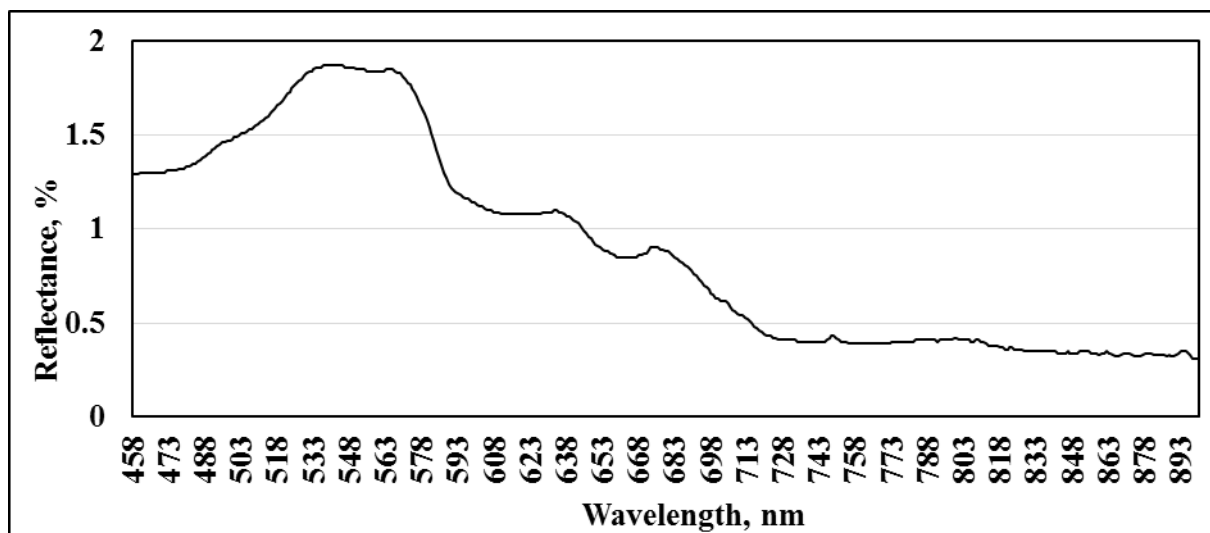
Sample 22



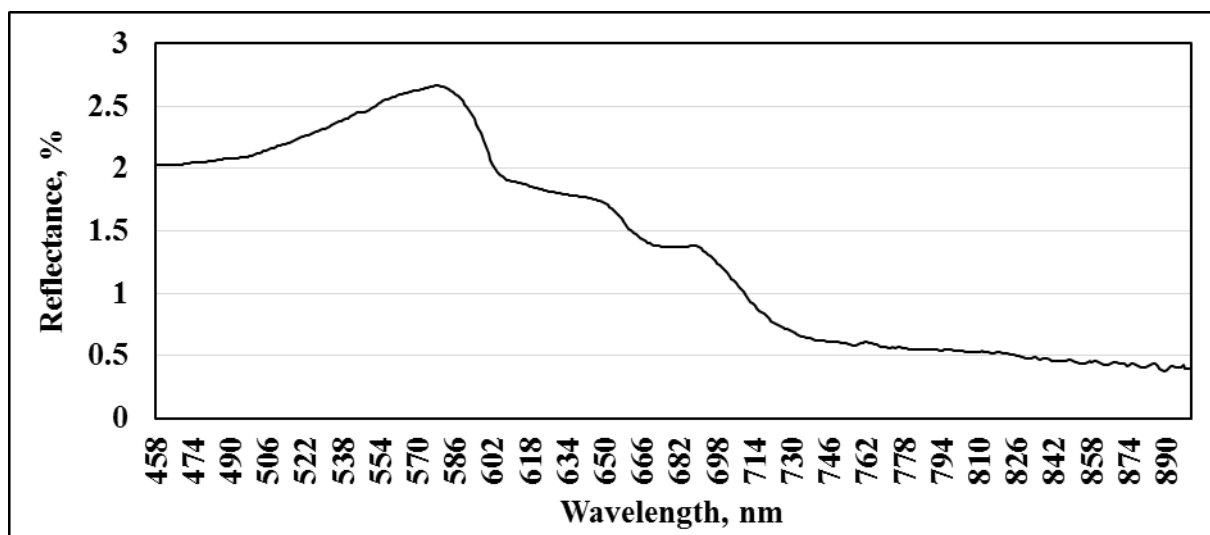
Sample 23



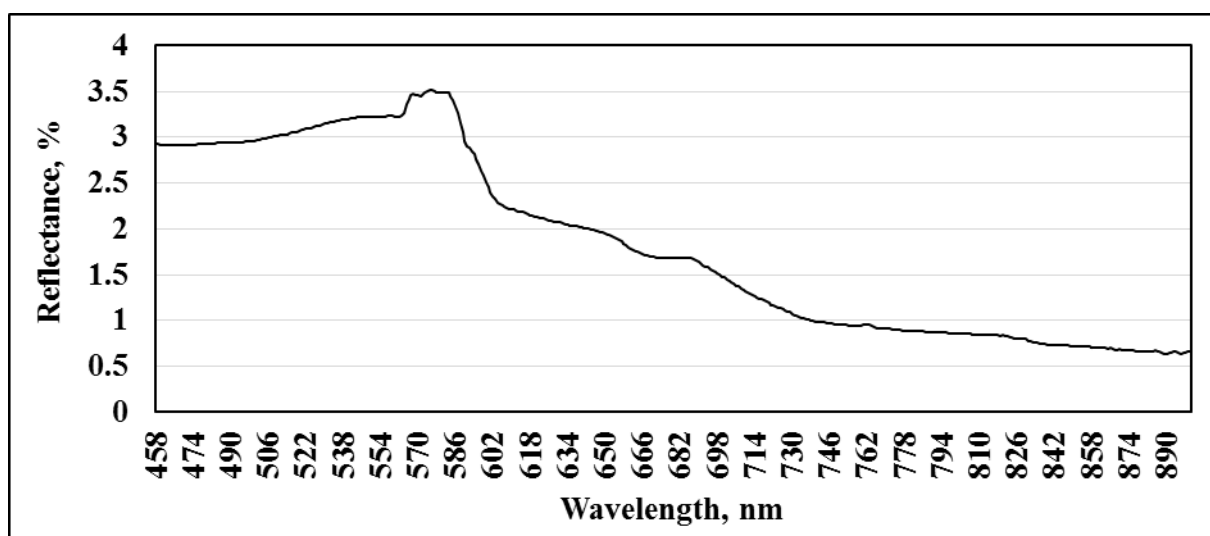
Sample 24



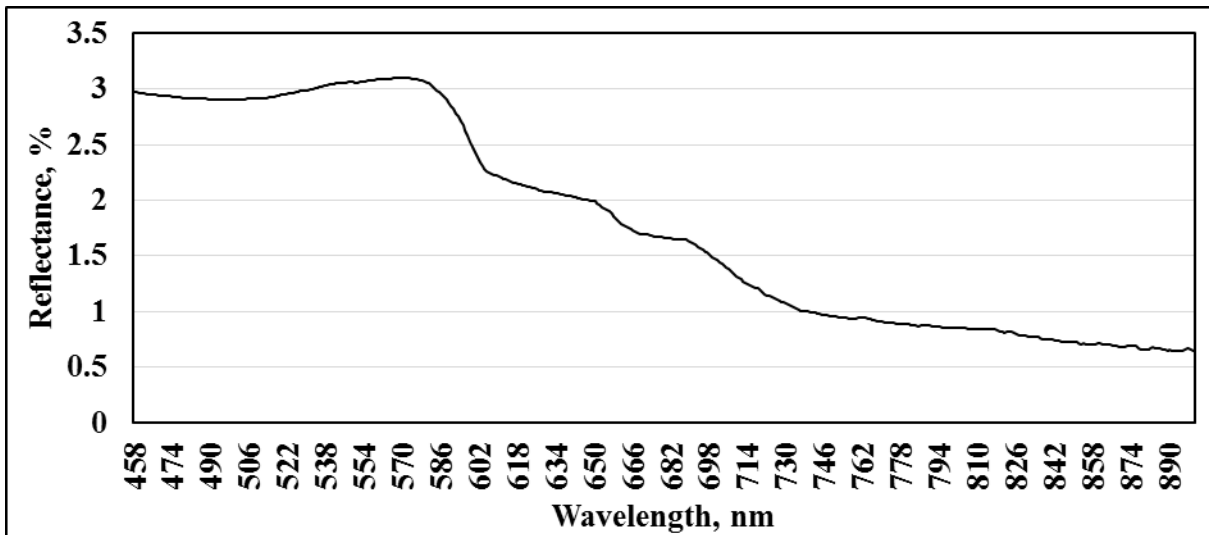
Sample 25



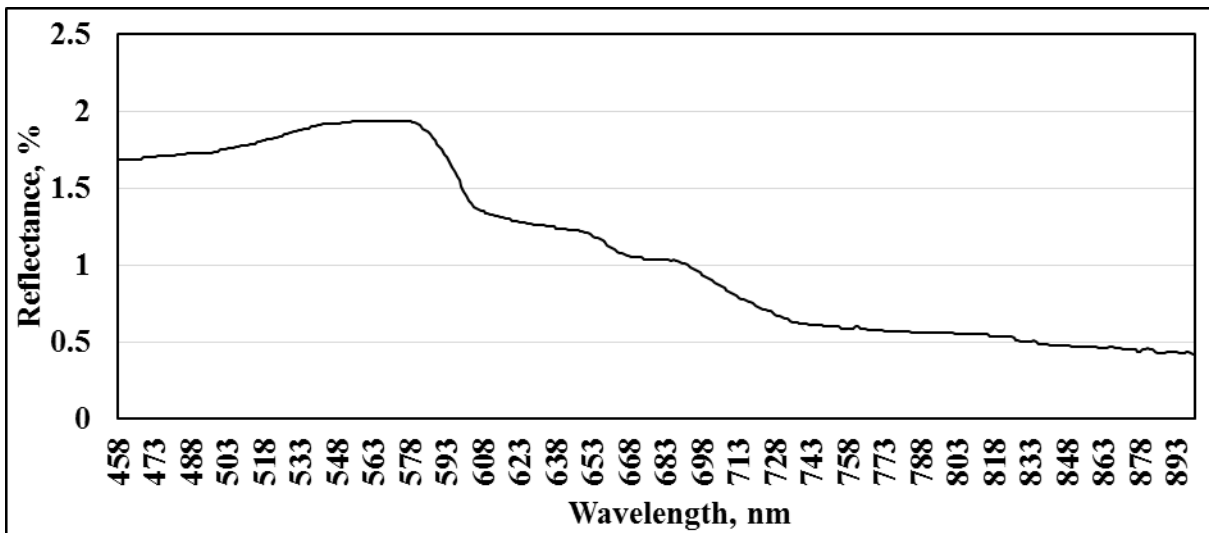
Sample 26



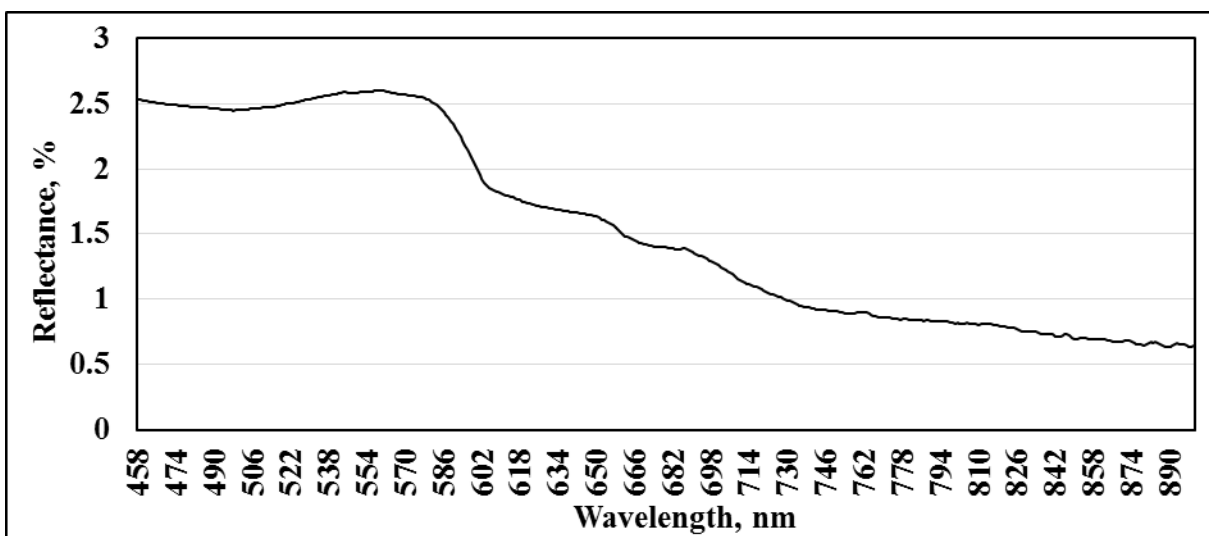
Sample 27



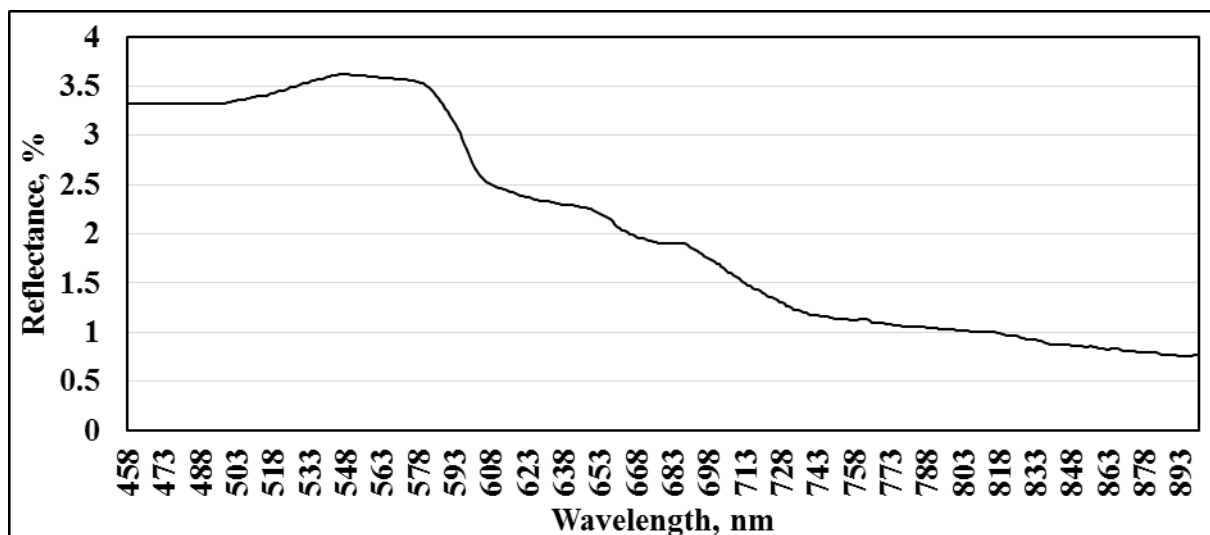
Sample 28



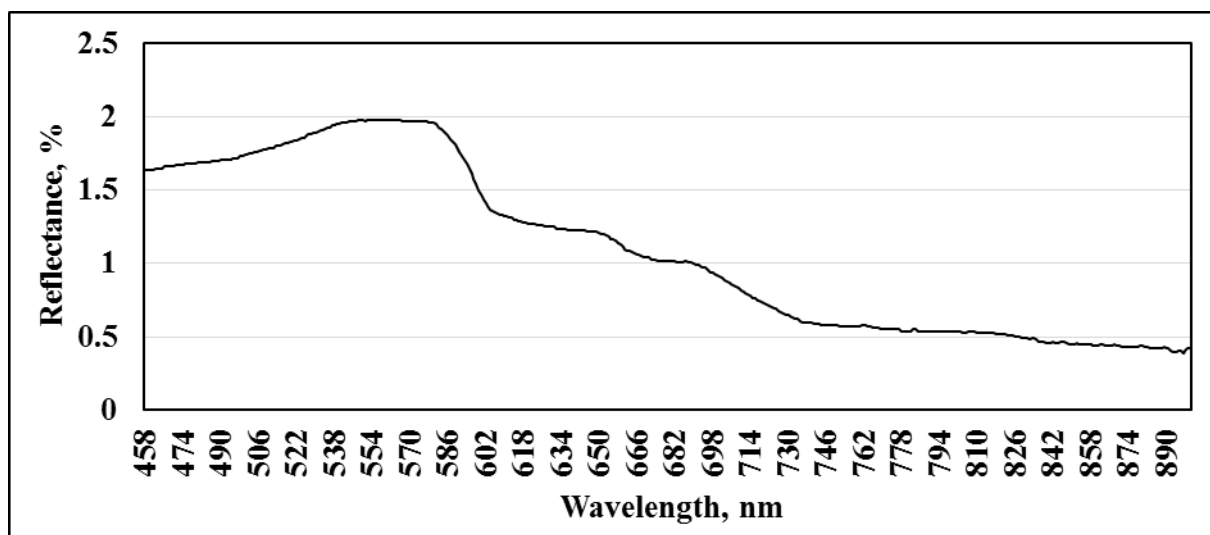
Sample 29



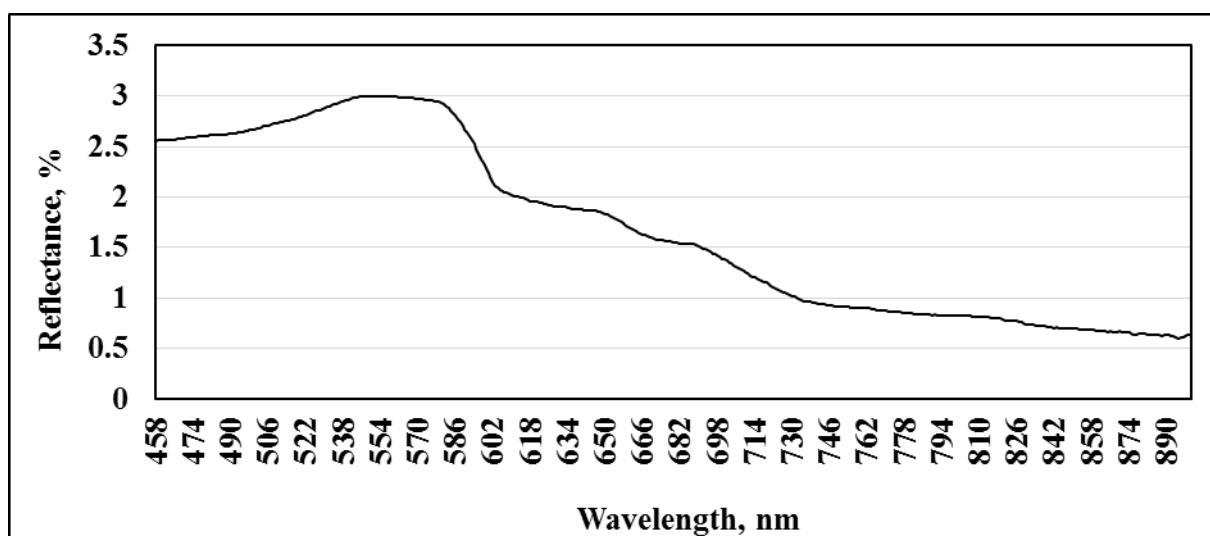
Sample 30



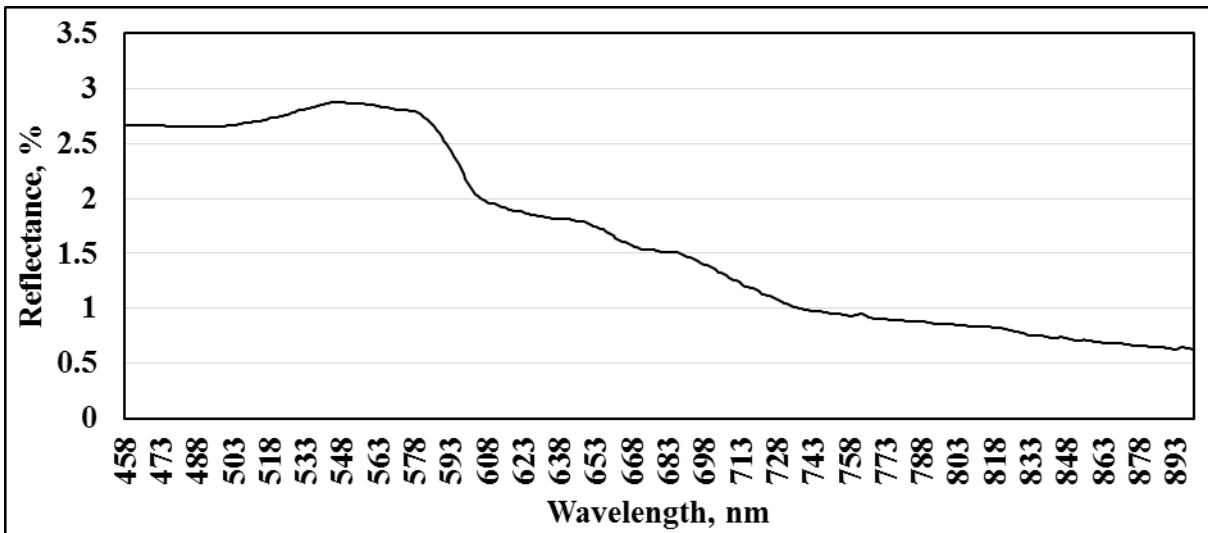
Sample 31



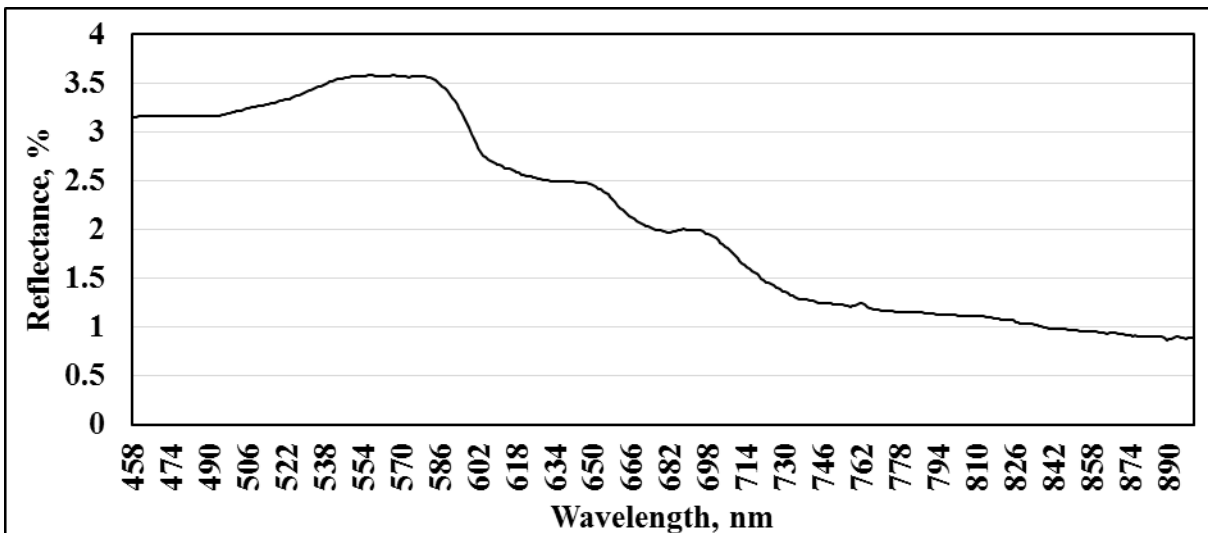
Sample 32



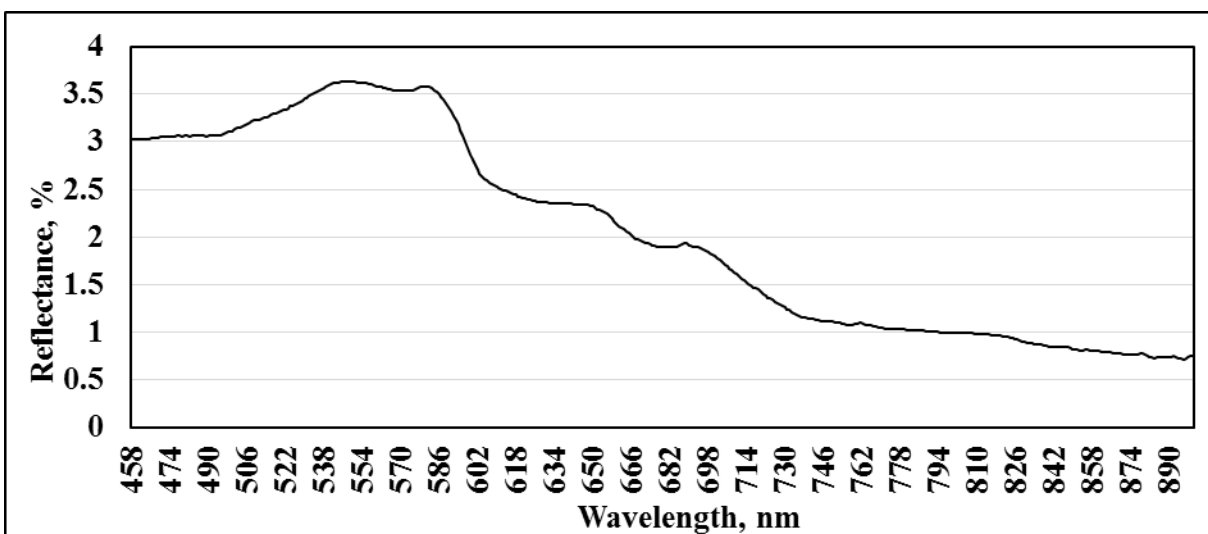
Sample 33



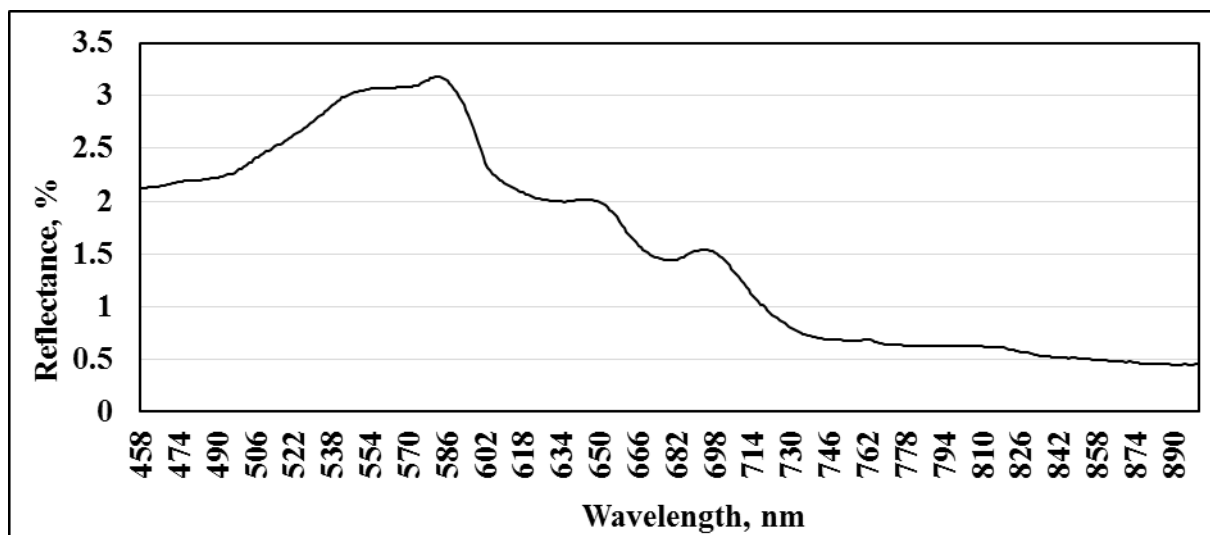
Sample 34



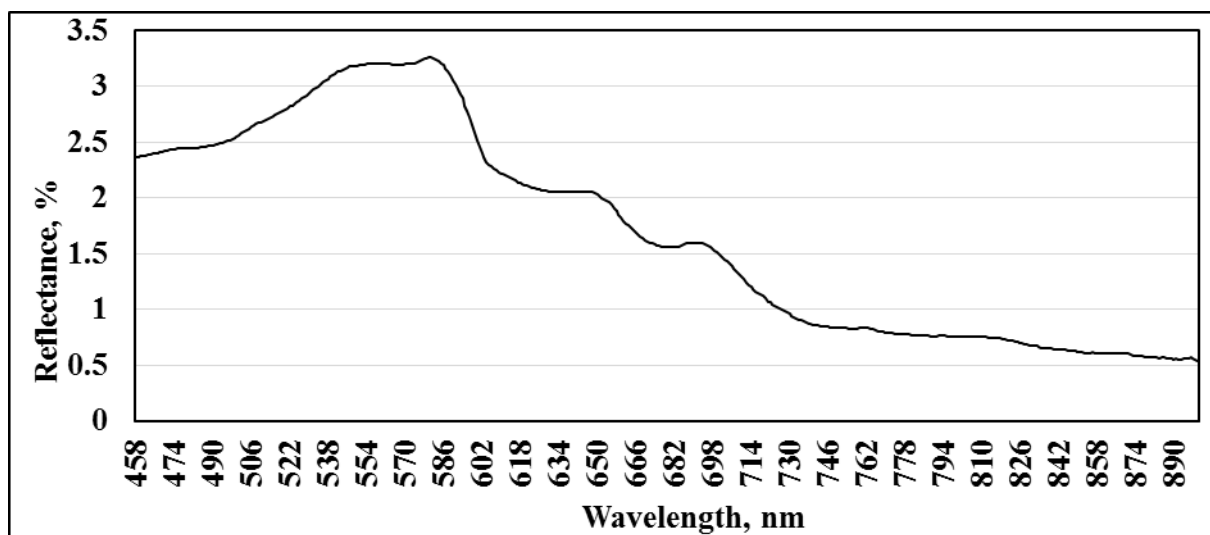
Sample 35



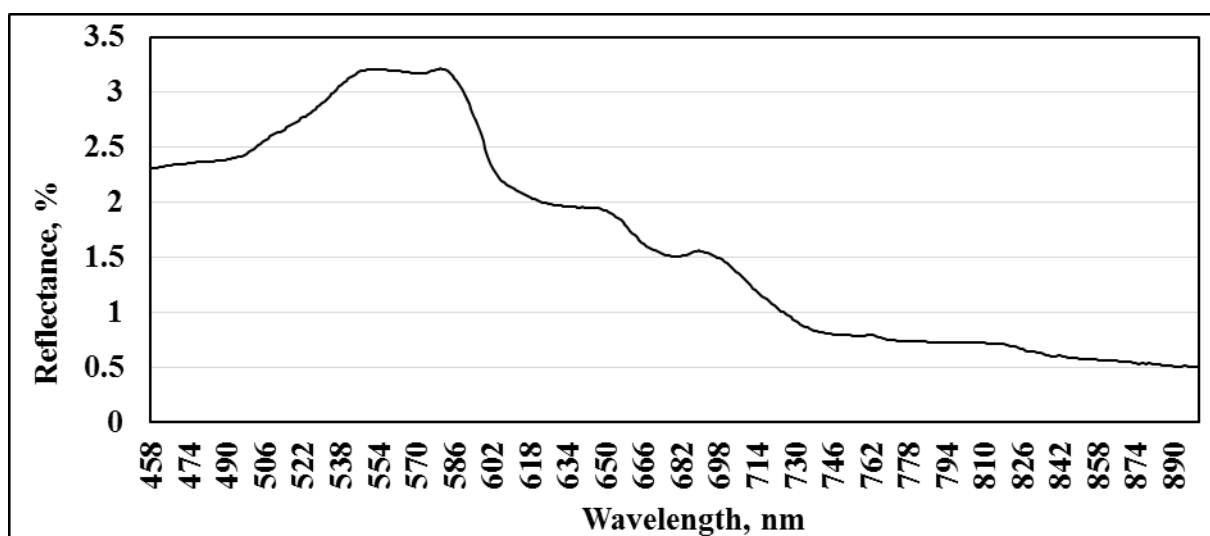
Sample 36



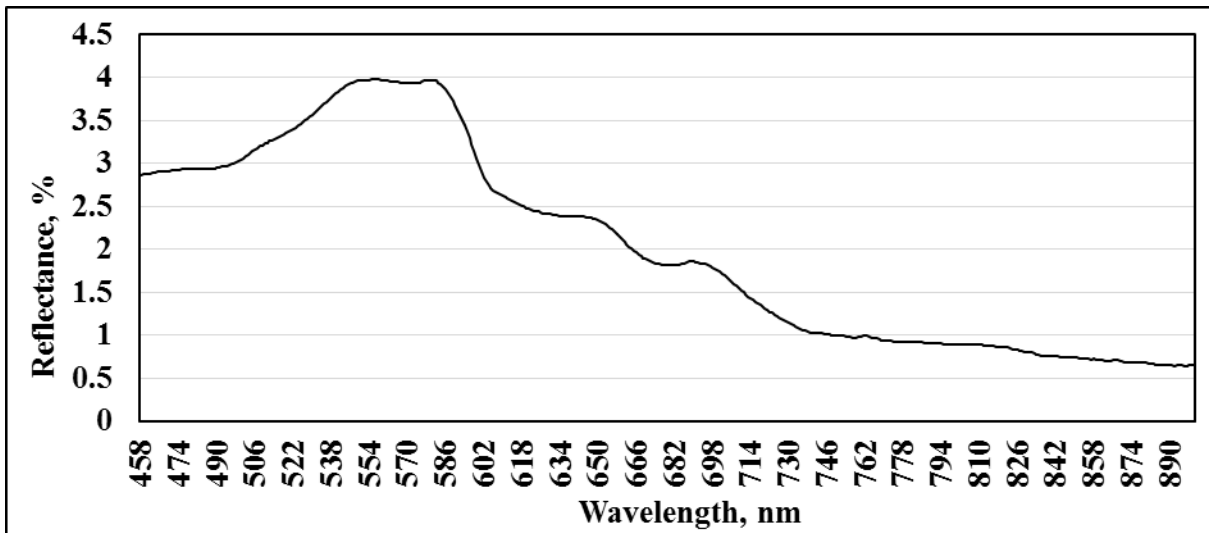
Sample 37



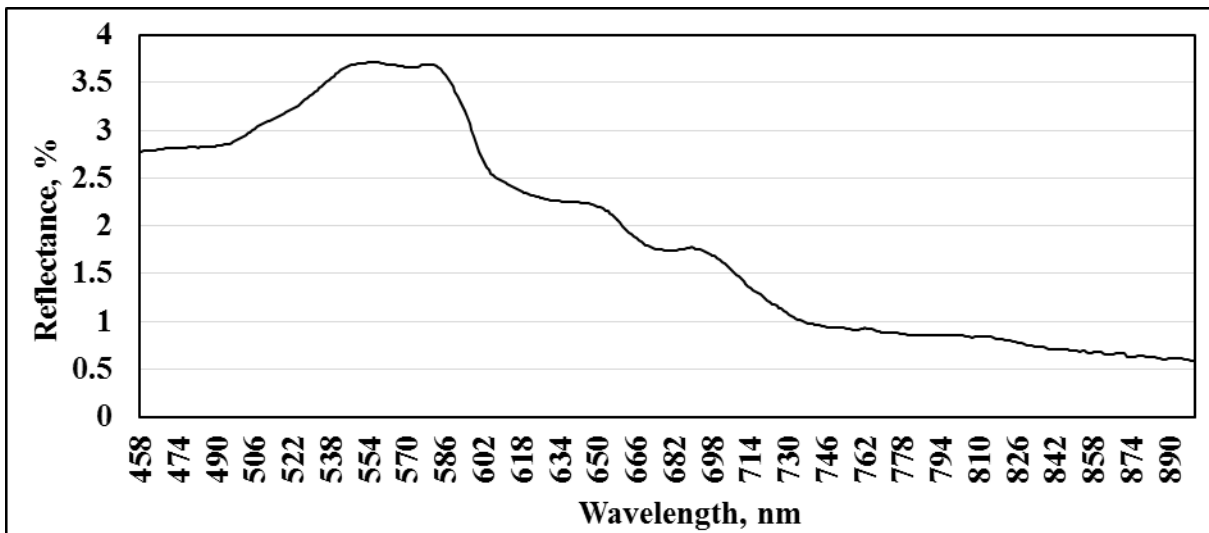
Sample 38



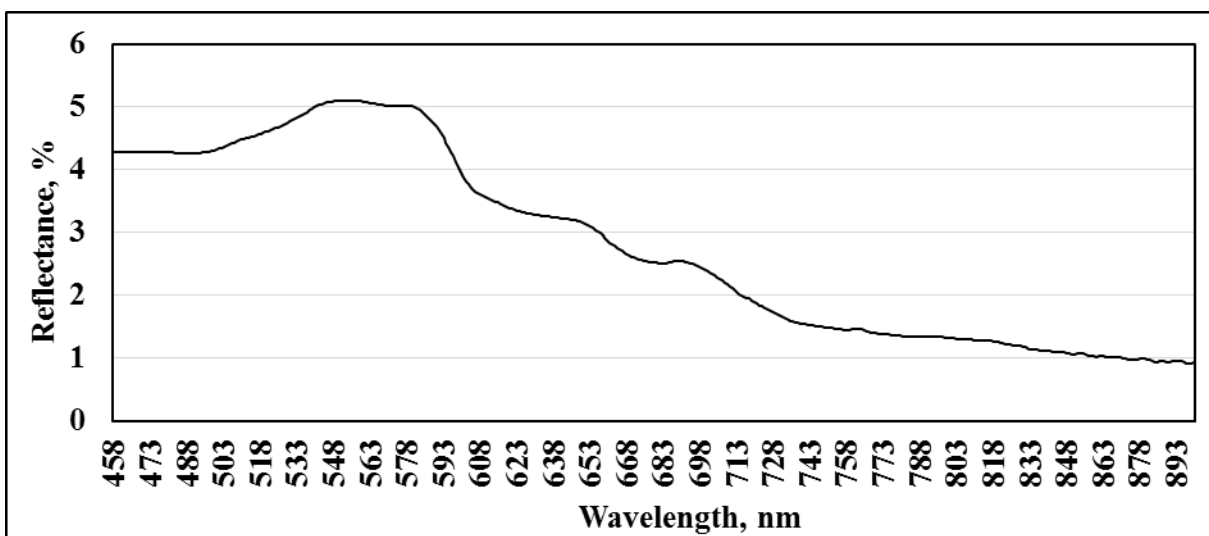
Sample 39



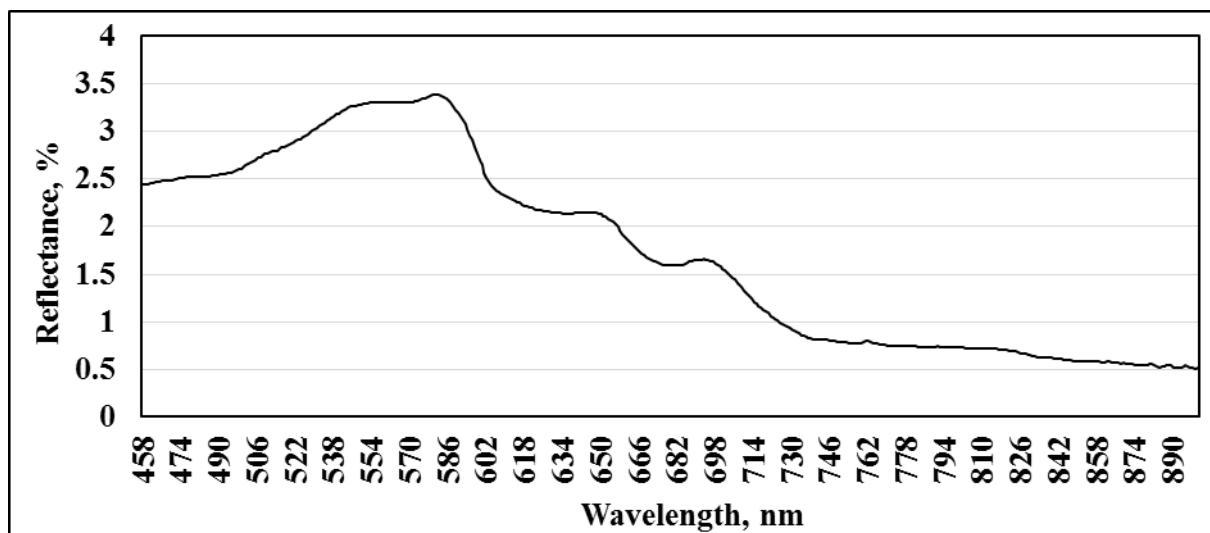
Sample 40



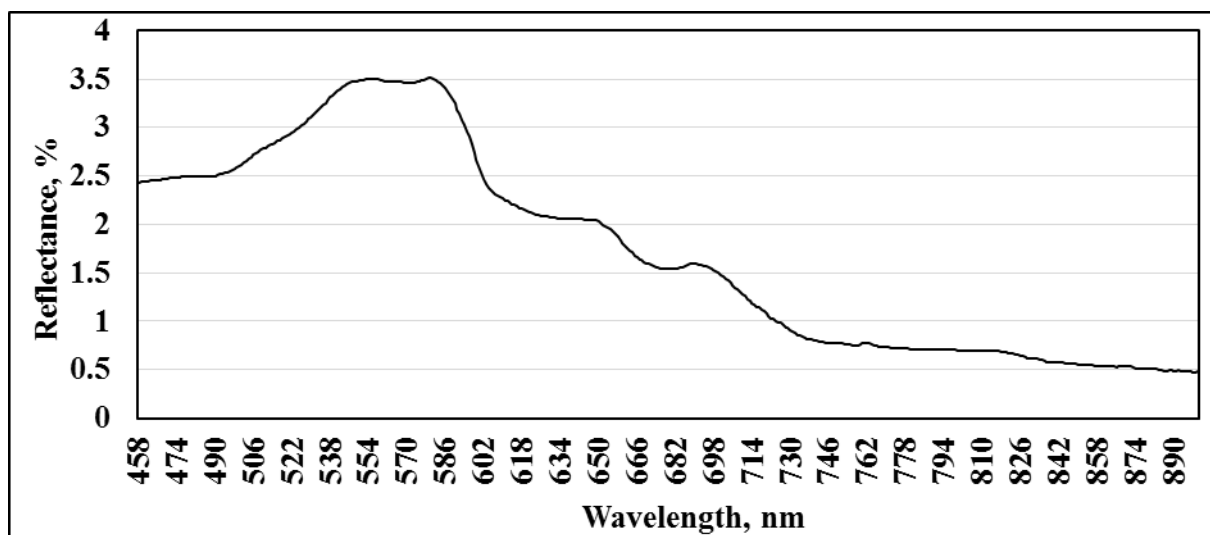
Sample 41



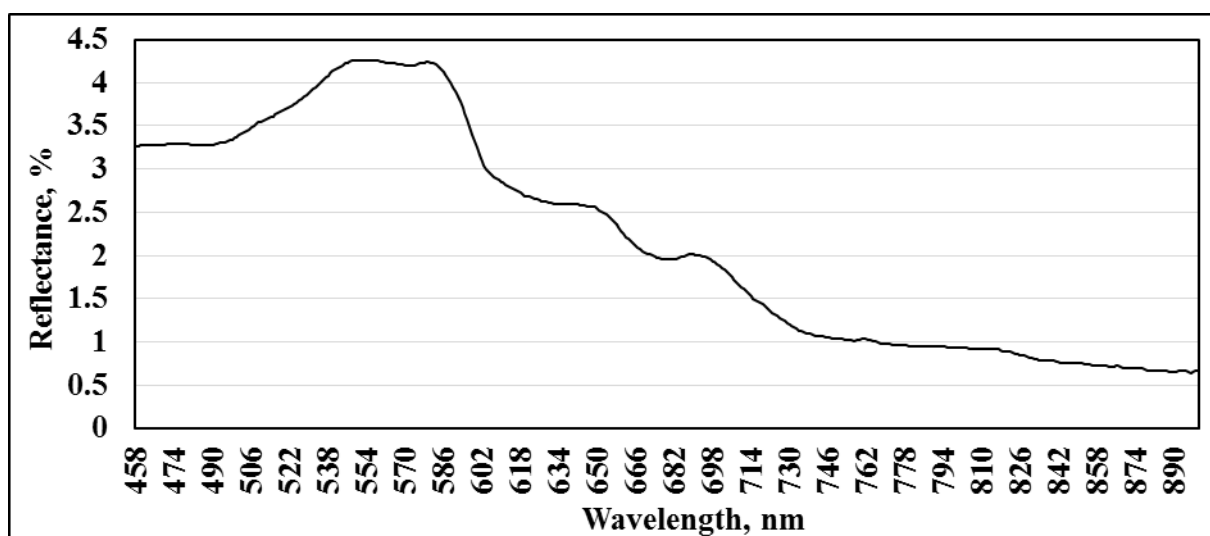
Sample 42



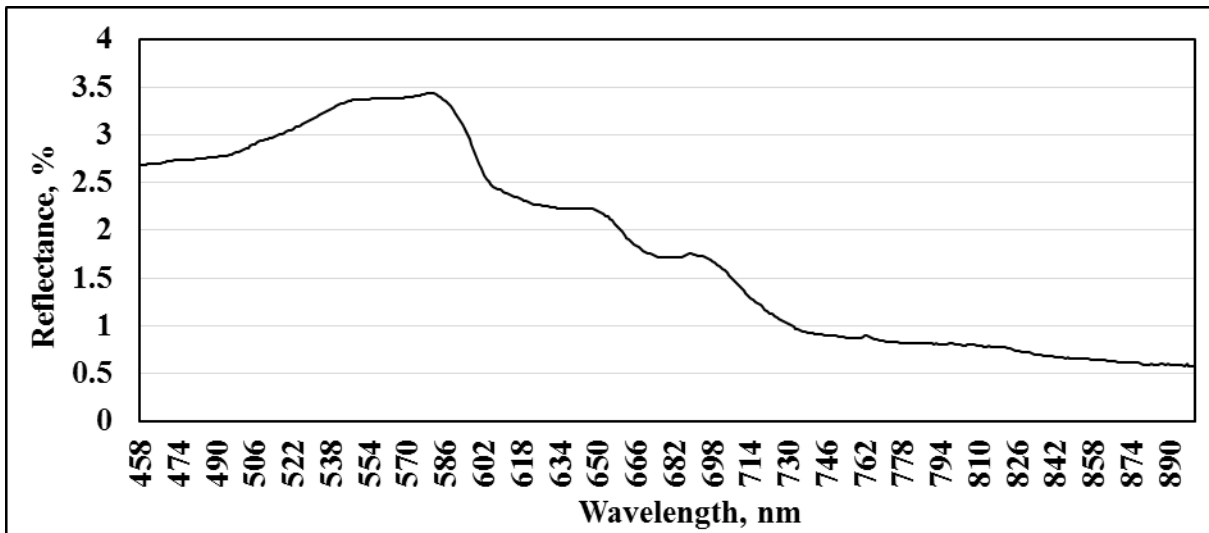
Sample 43



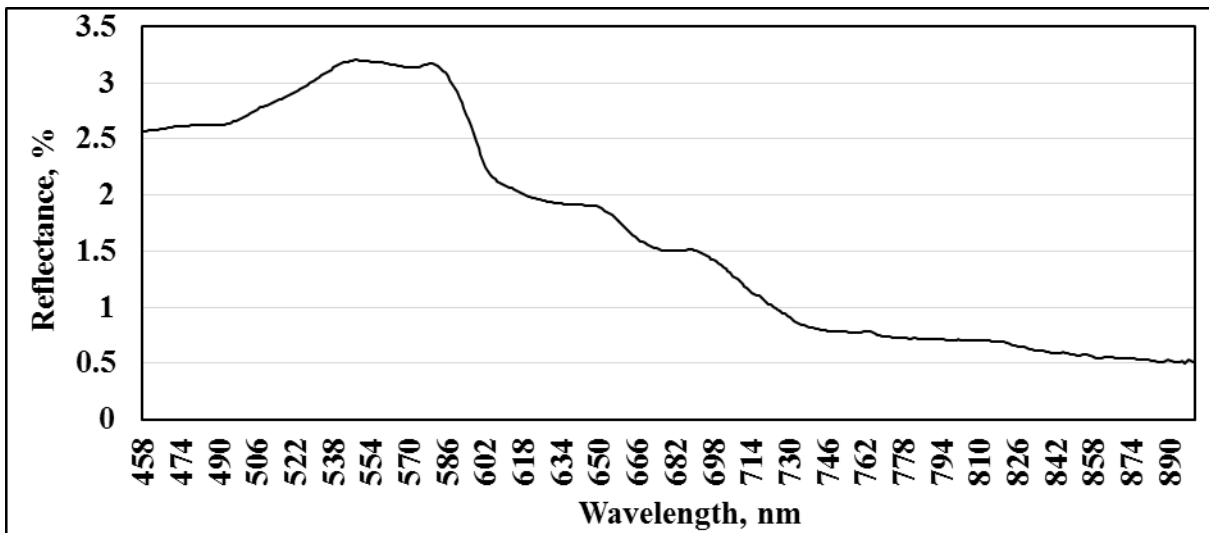
Sample 44



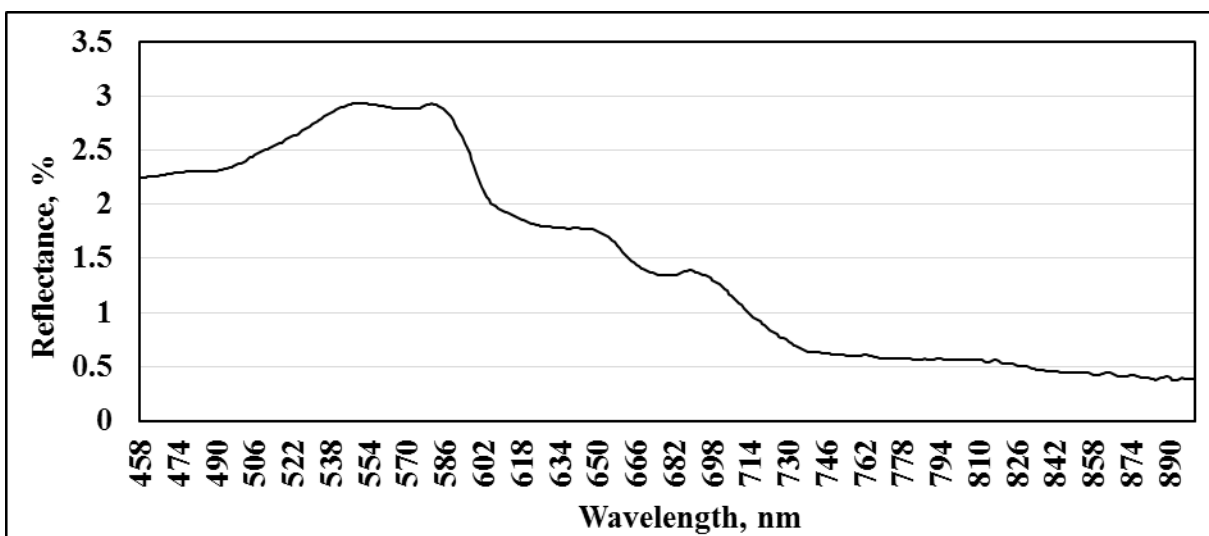
Sample 45



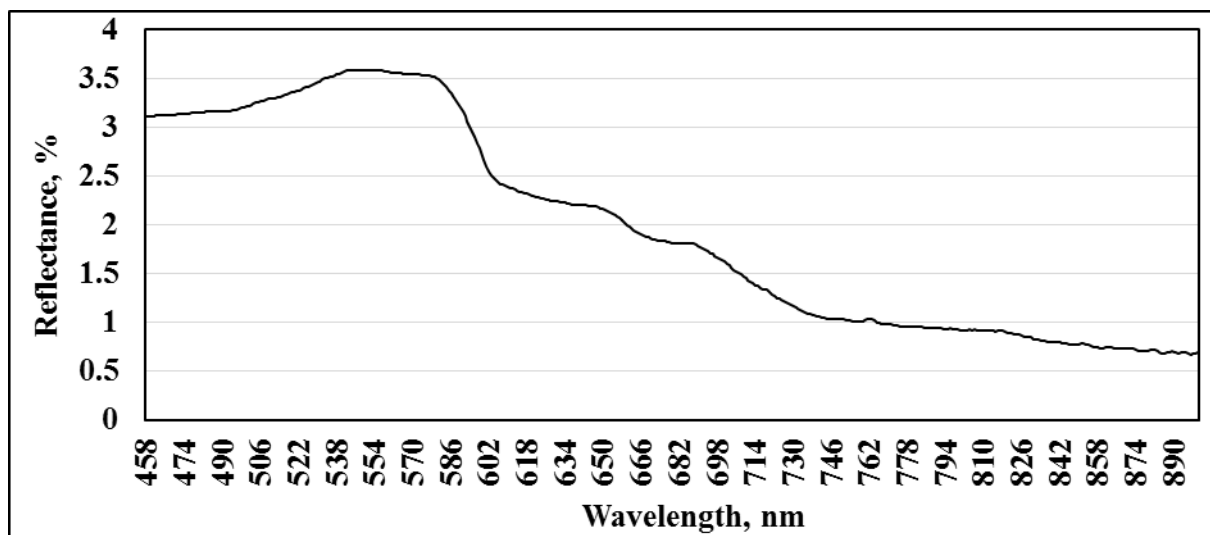
Sample 46



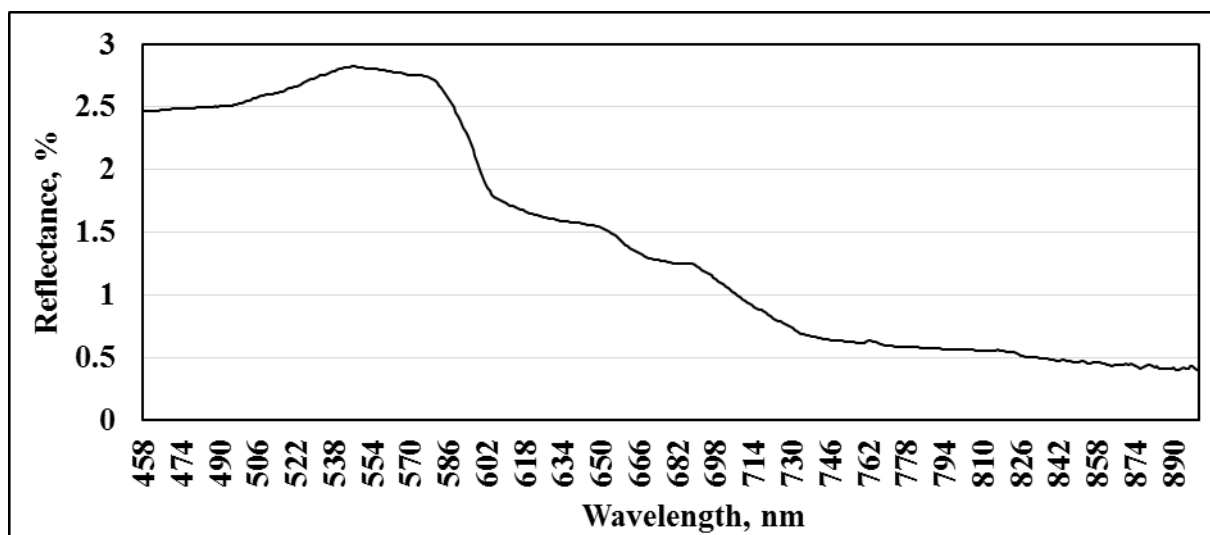
Sample 47



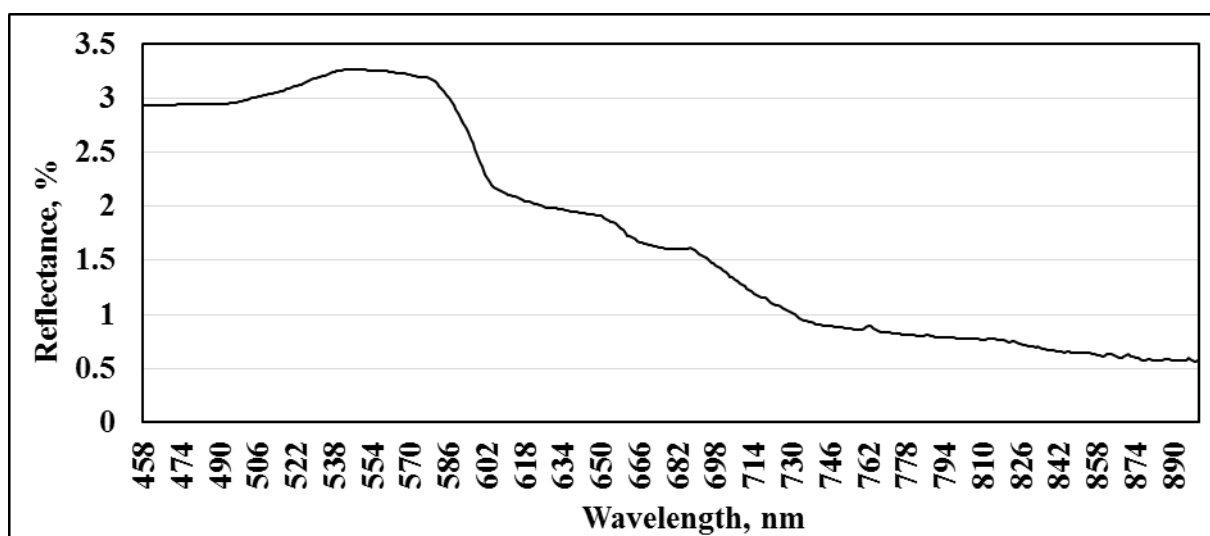
Sample 48



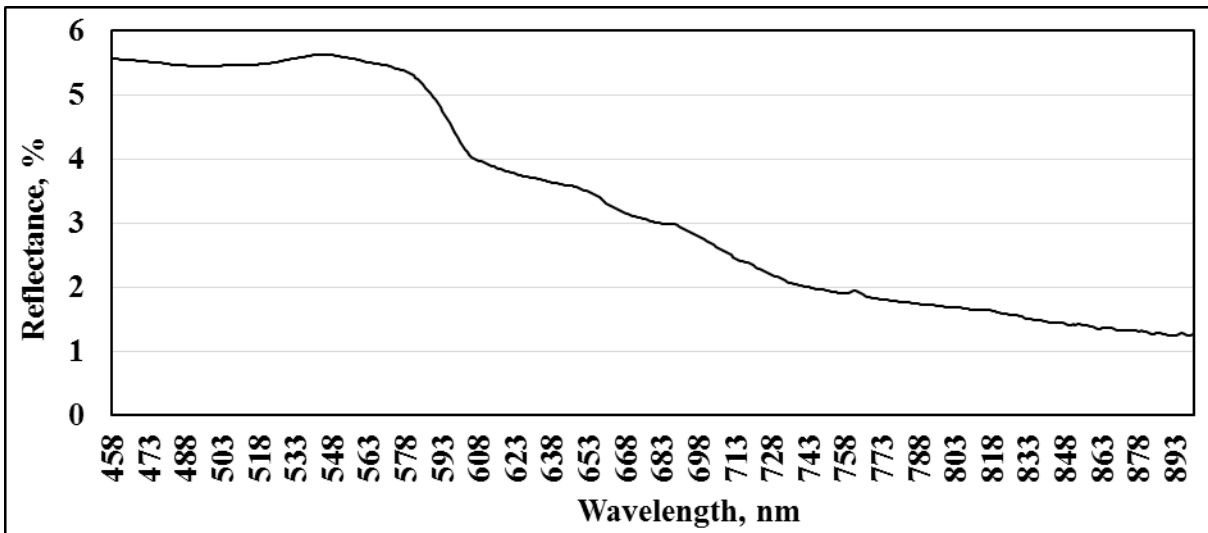
Sample 49



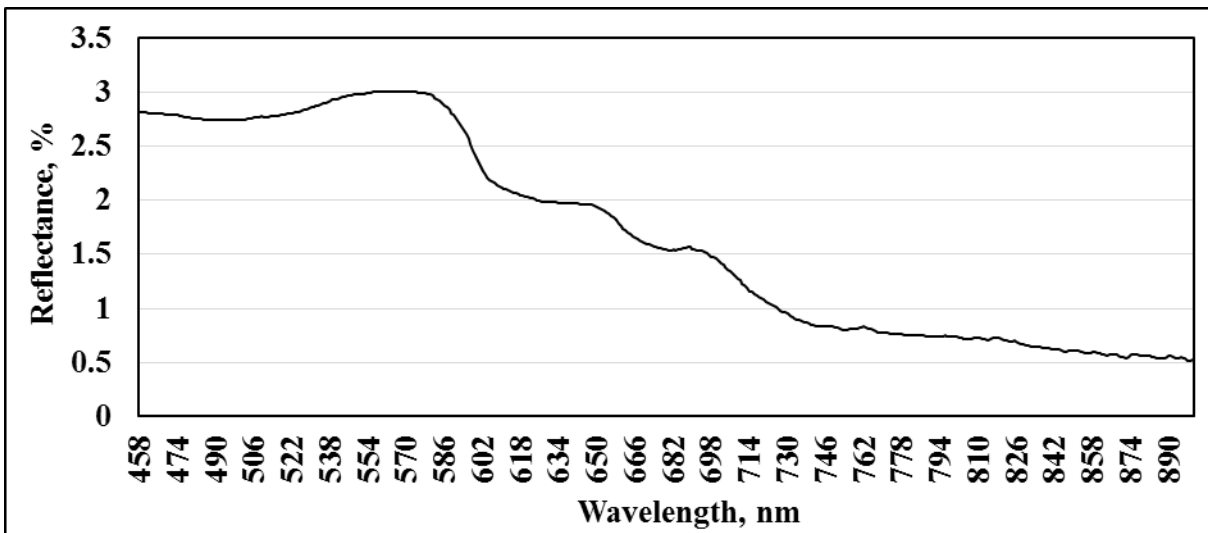
Sample 50



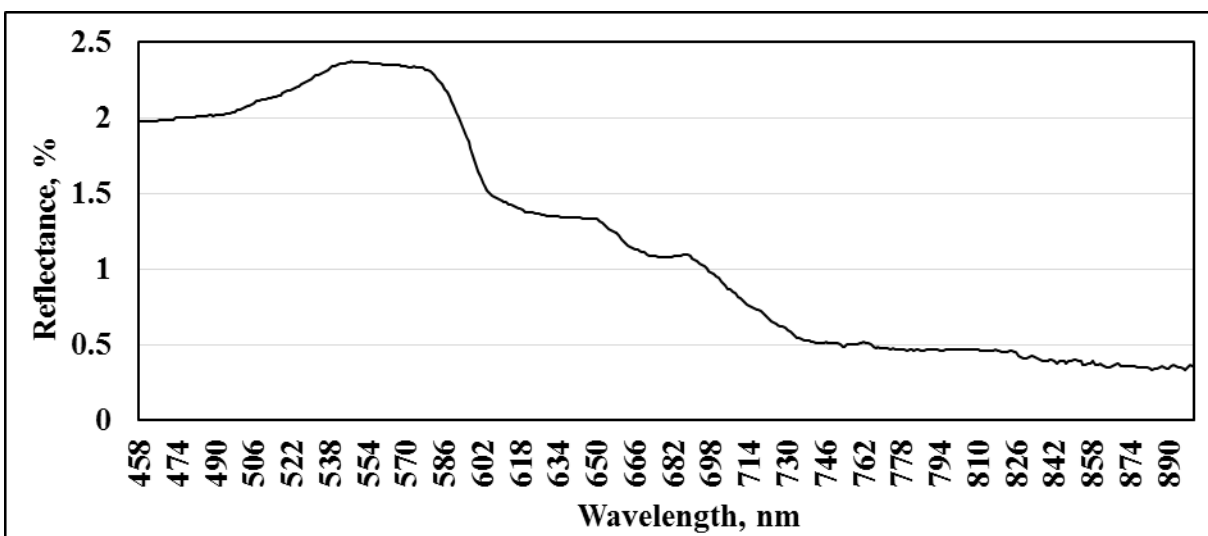
Sample 51



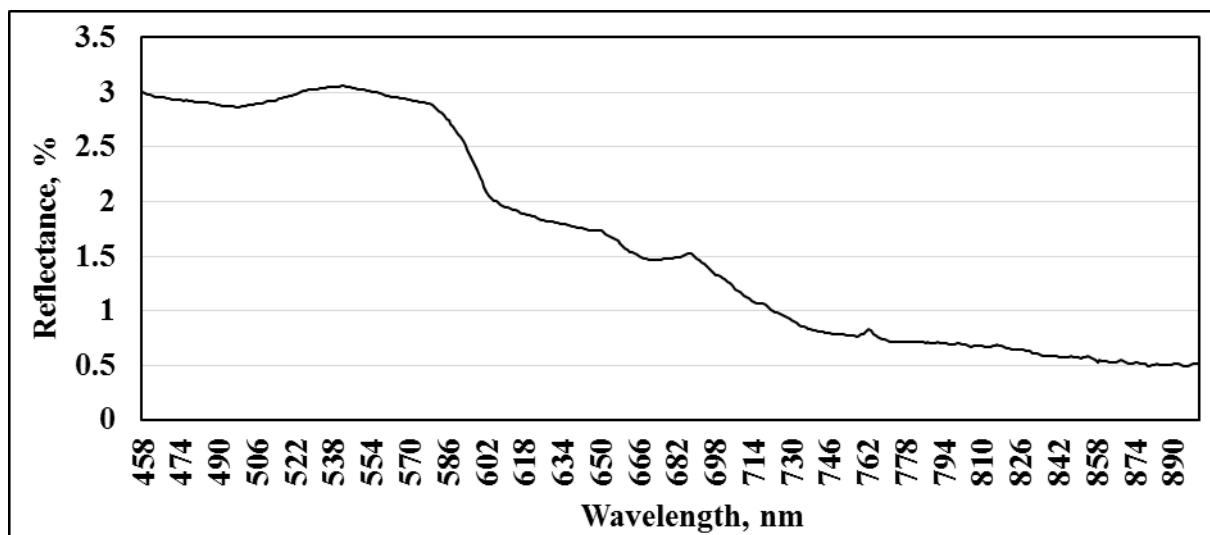
Sample 52



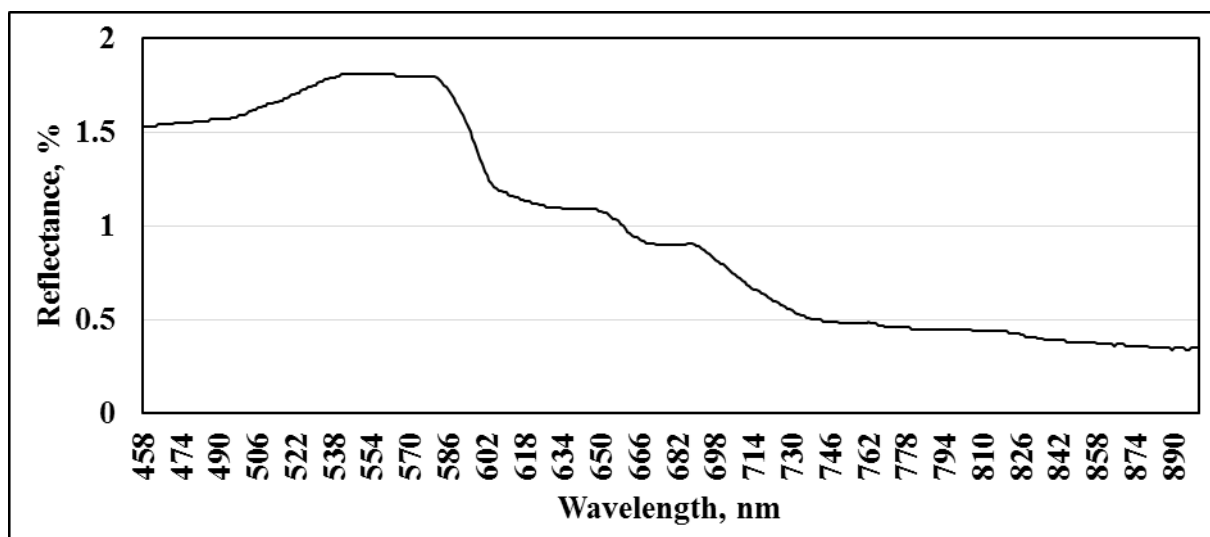
Sample 53



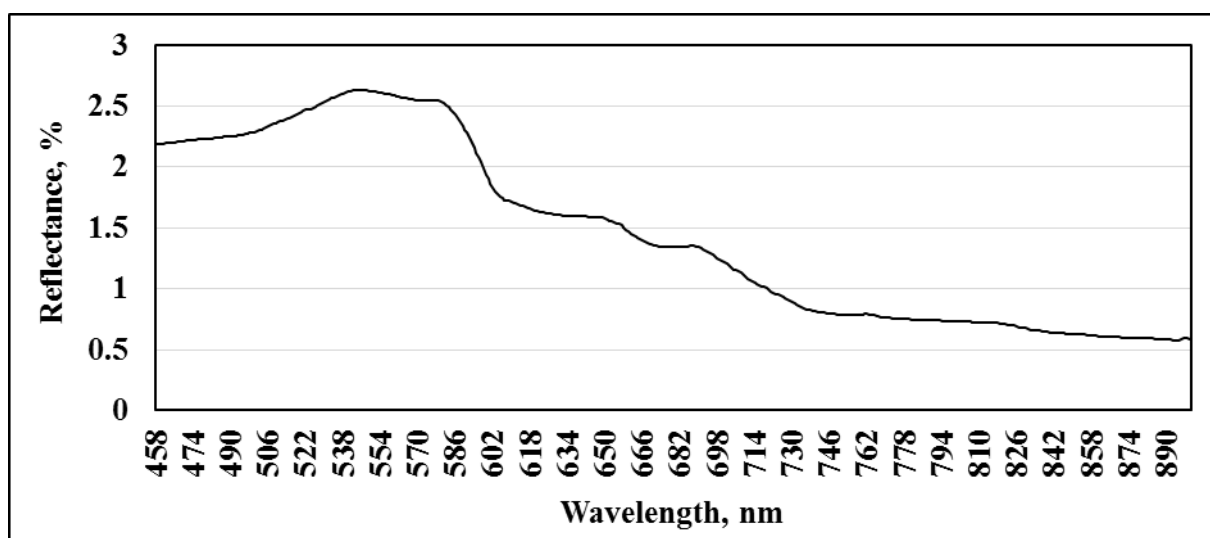
Sample 54



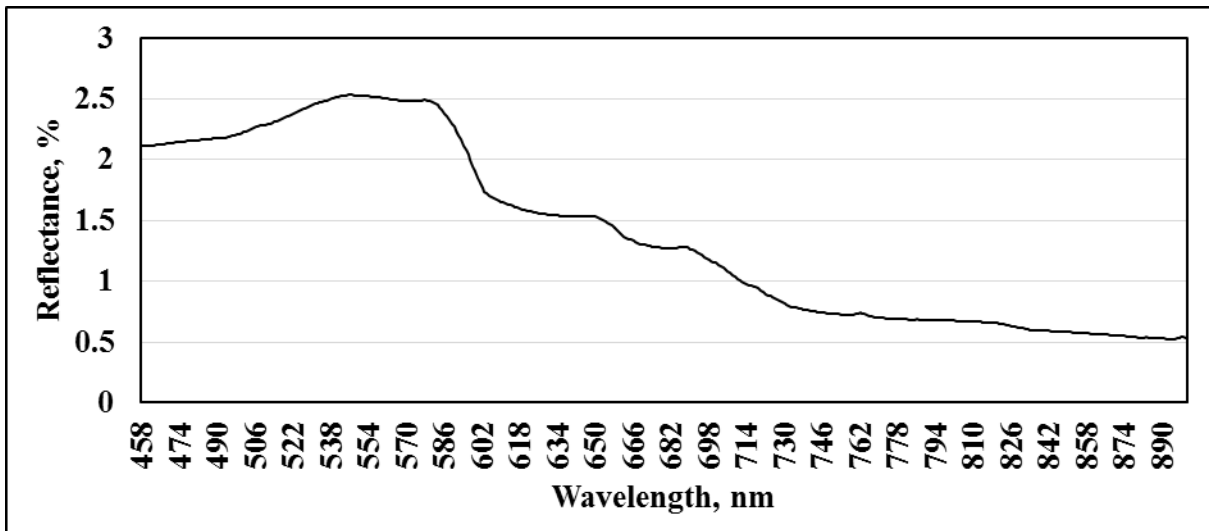
Sample 55



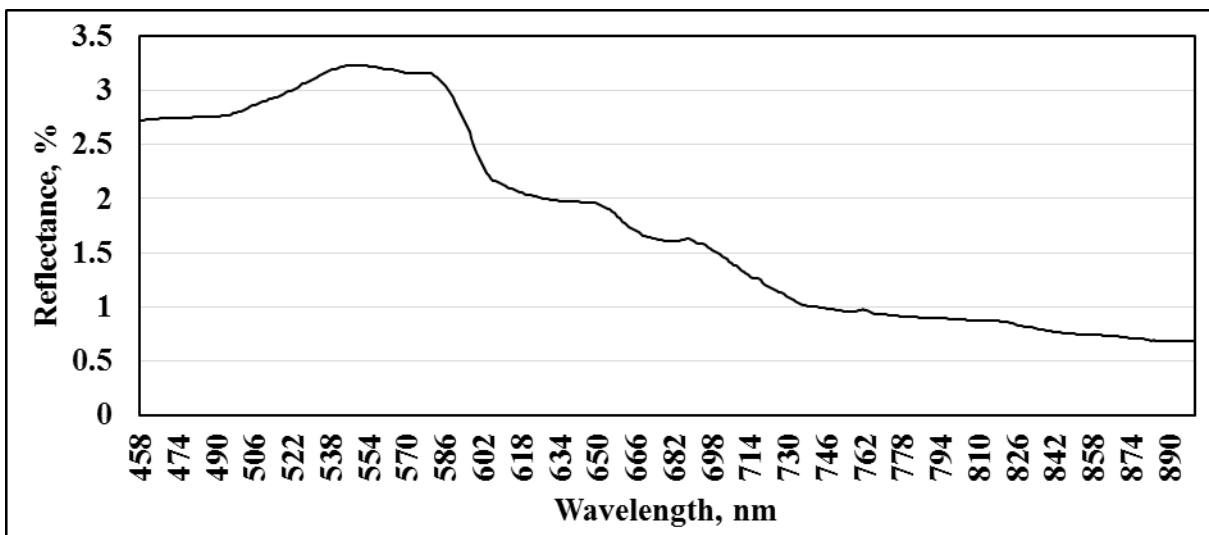
Sample 56



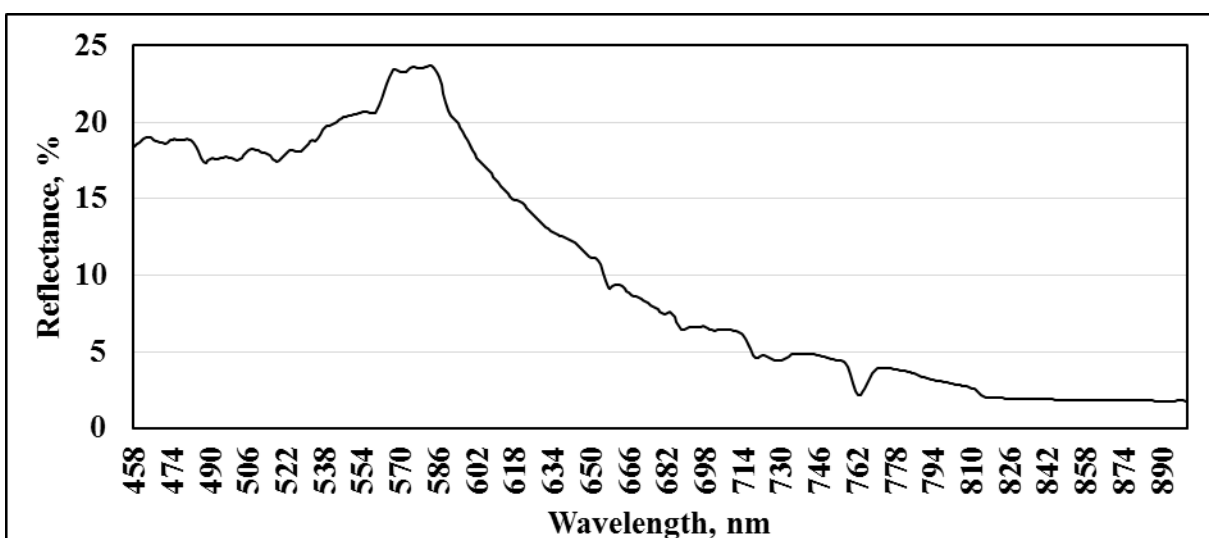
Sample 57



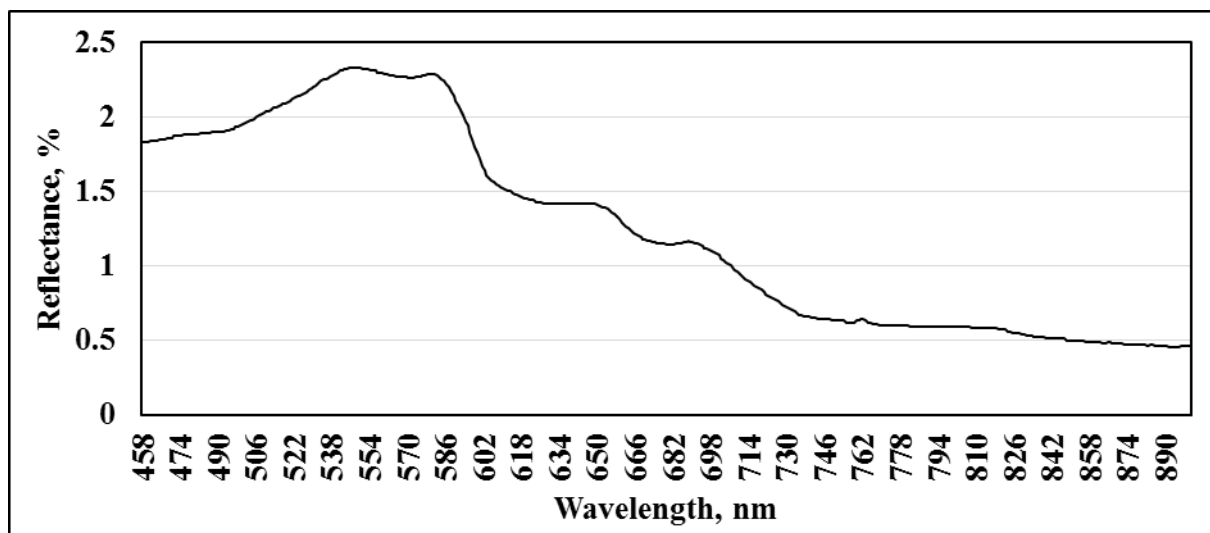
Sample 58



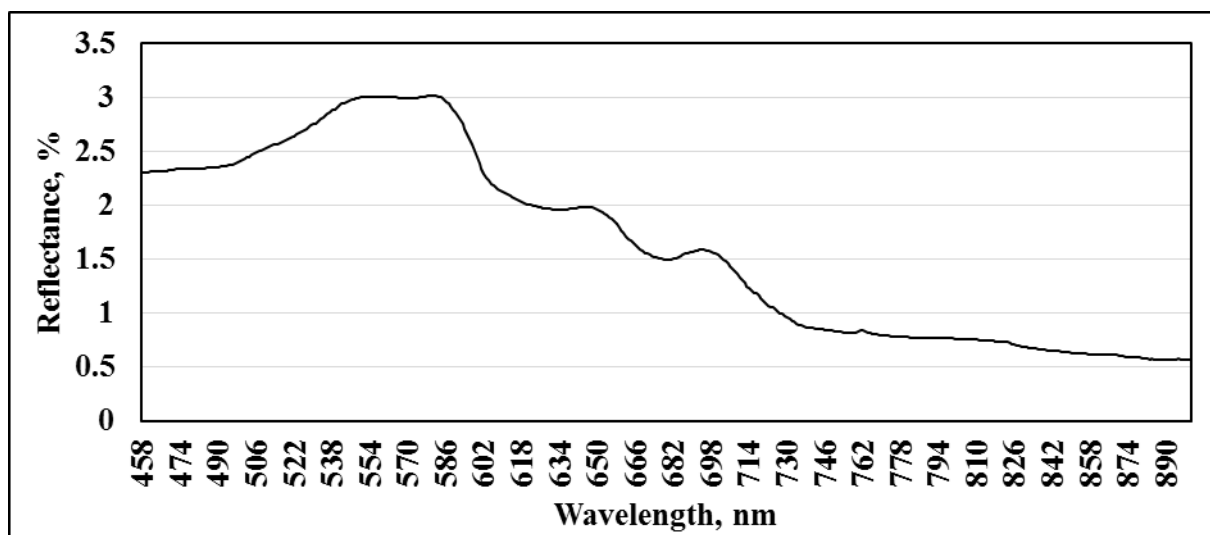
Sample 59



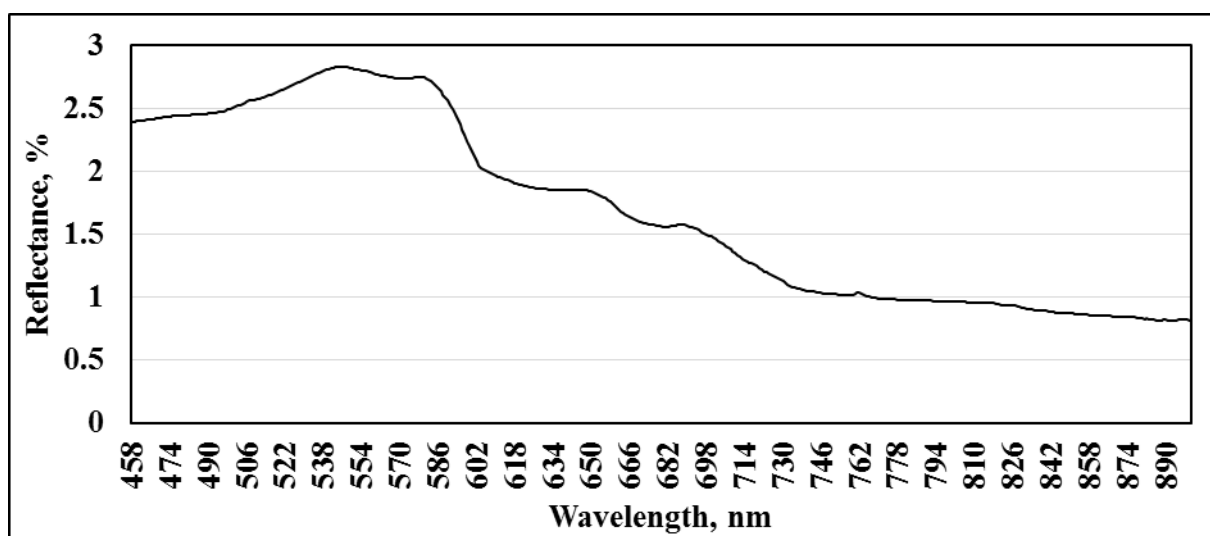
Sample 60



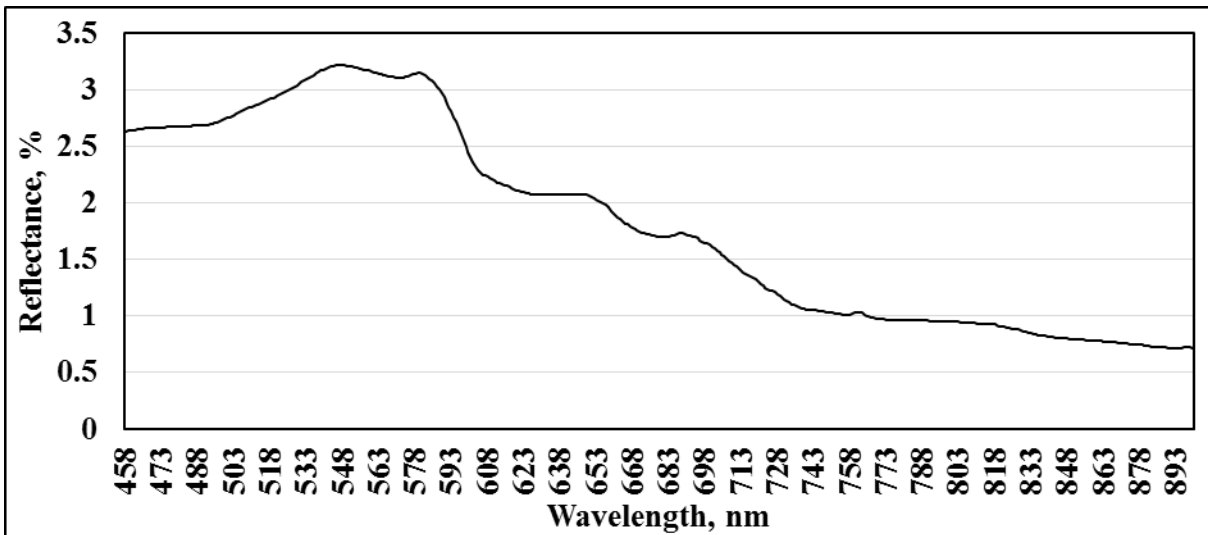
Sample 61



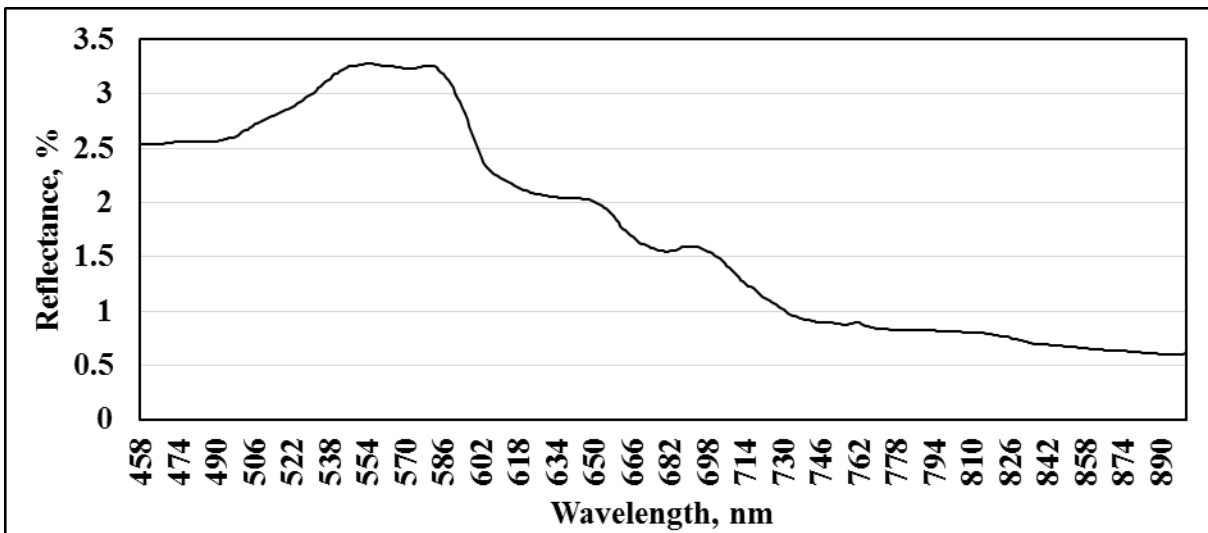
Sample 62



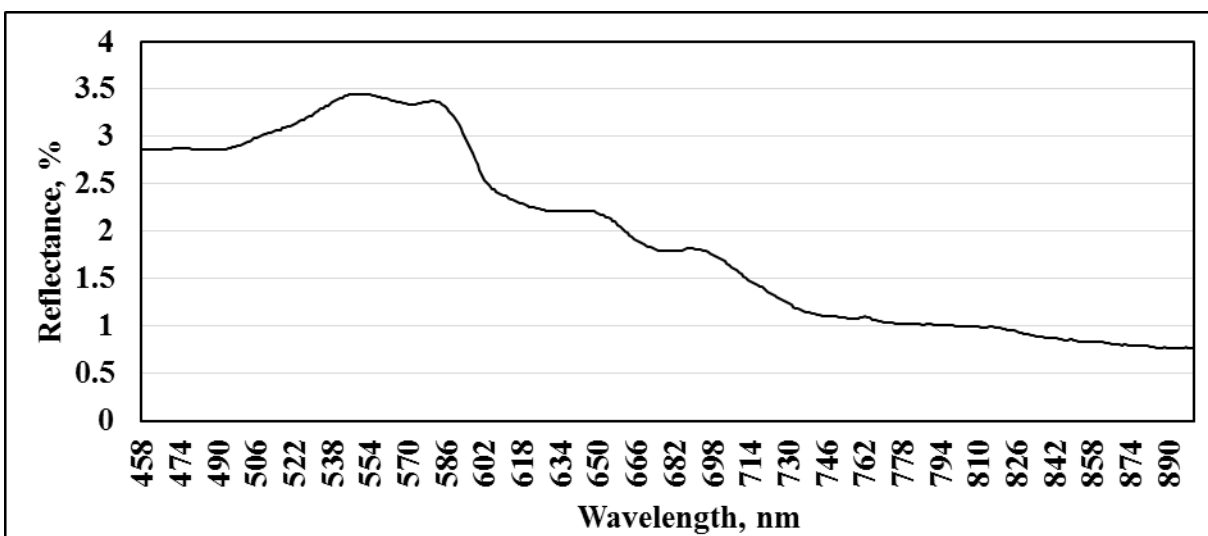
Sample 63



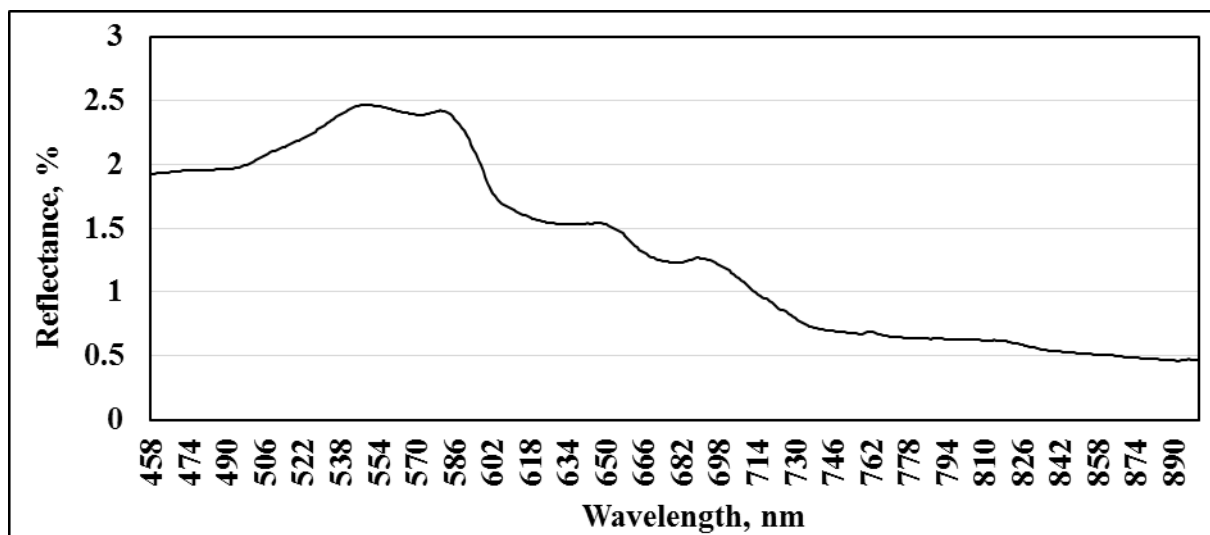
Sample 64



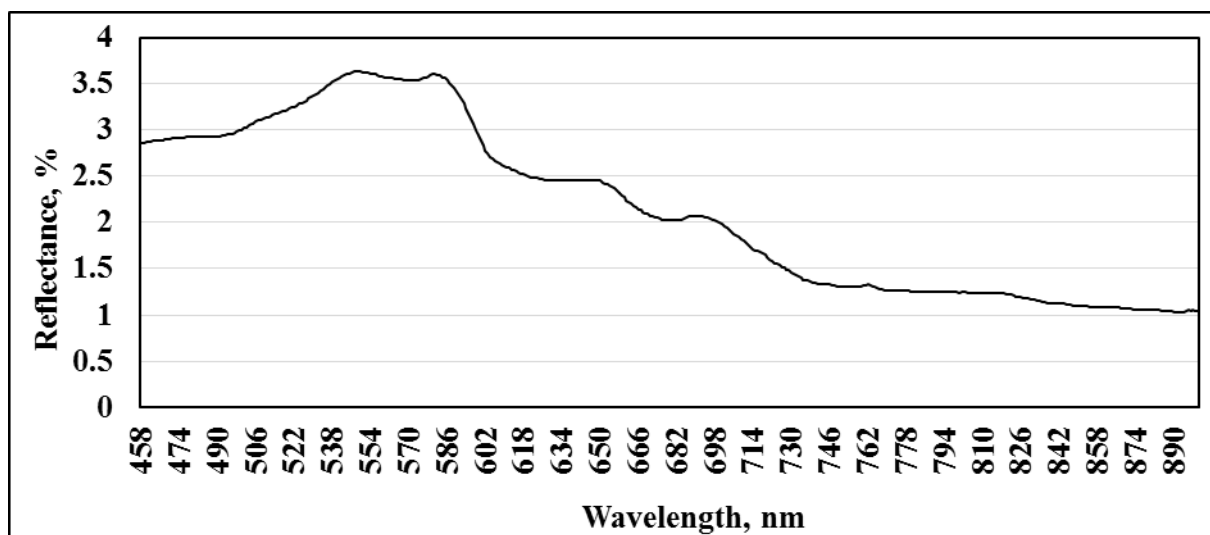
Sample 65



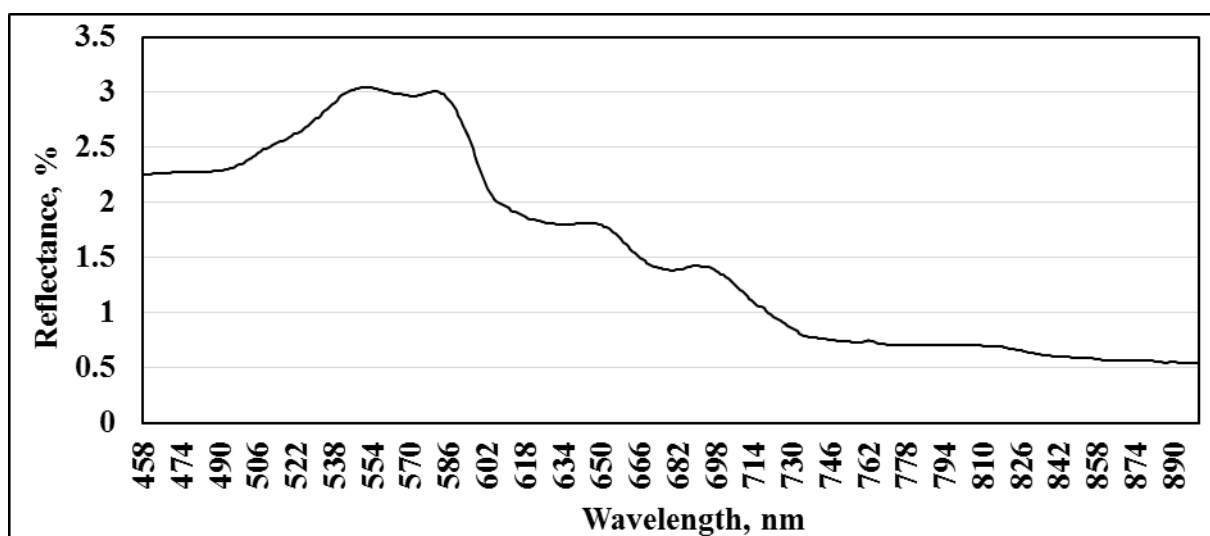
Sample 66



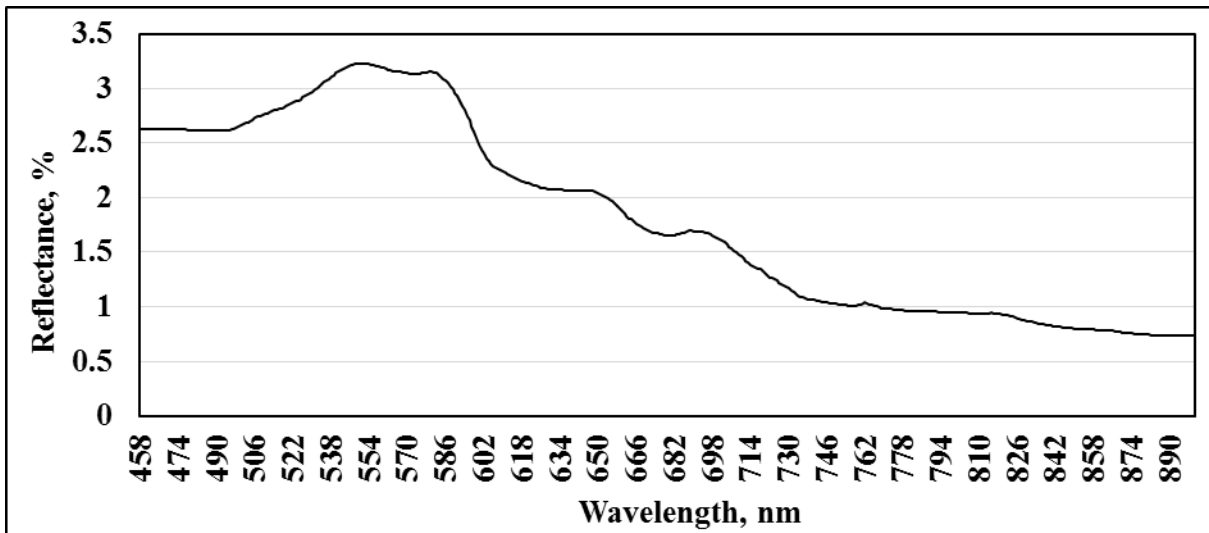
Sample 67



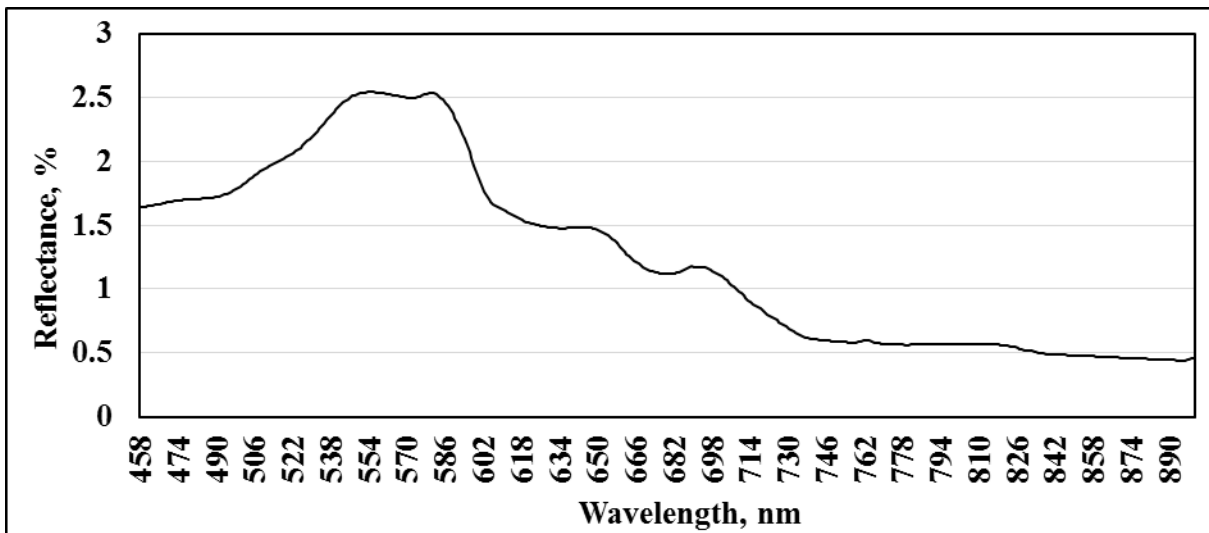
Sample 68



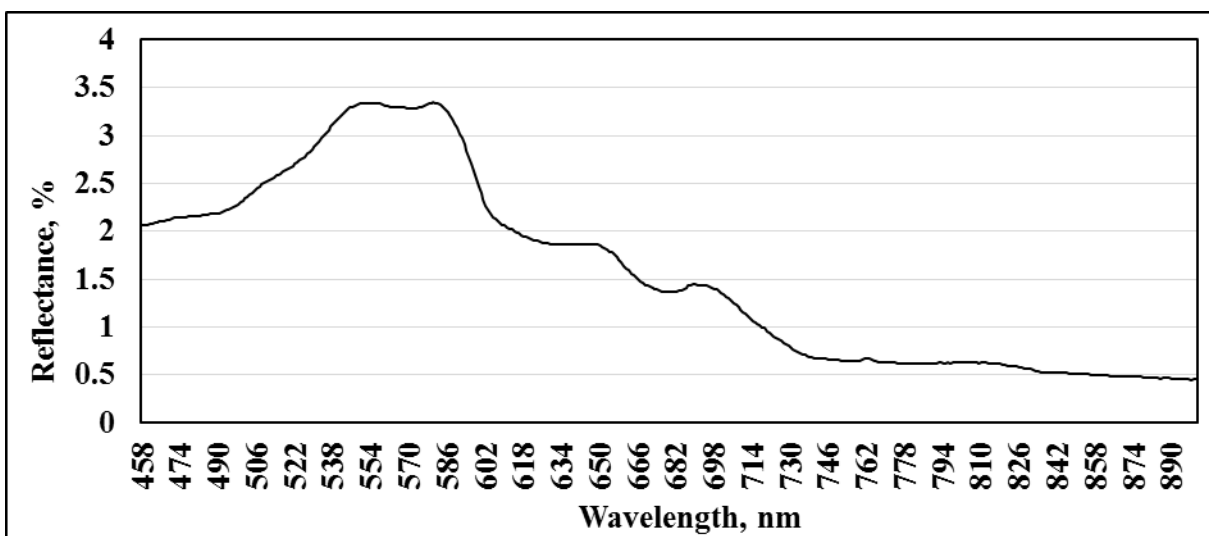
Sample 69



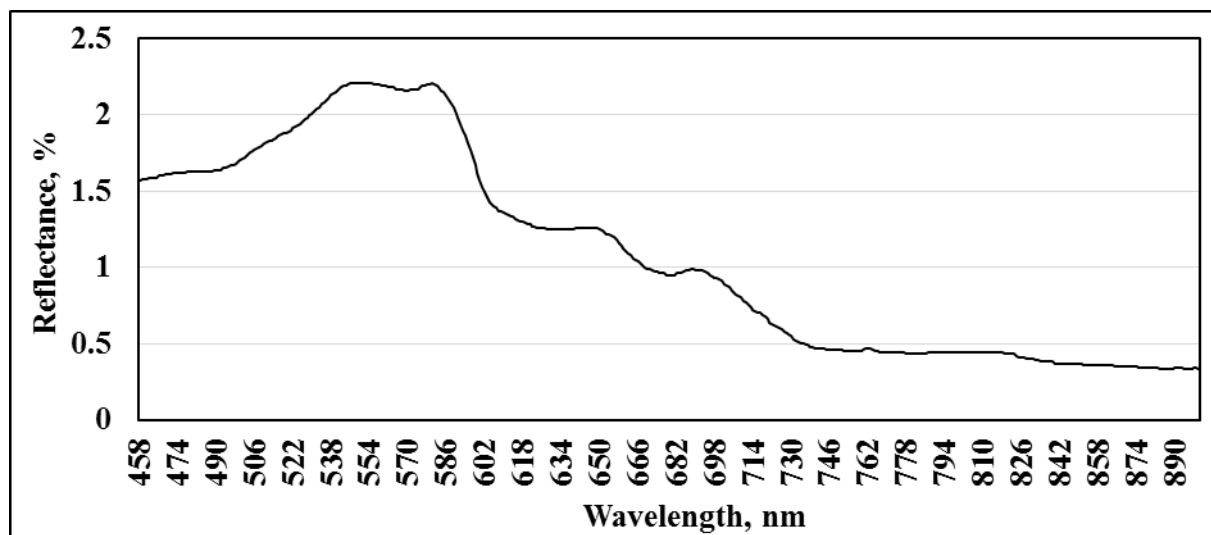
Sample 70



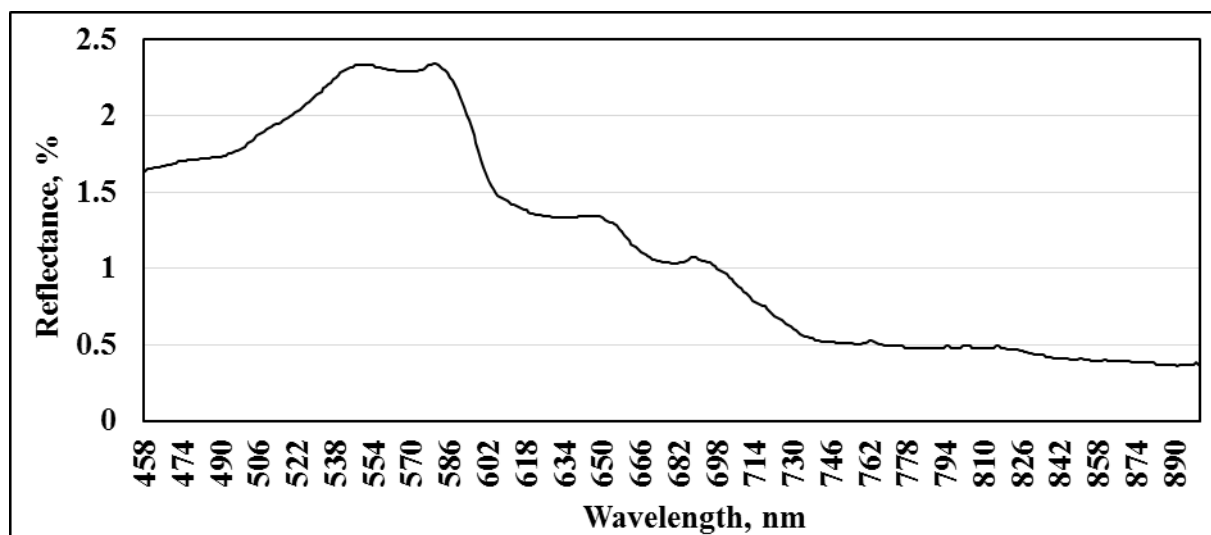
Sample 71



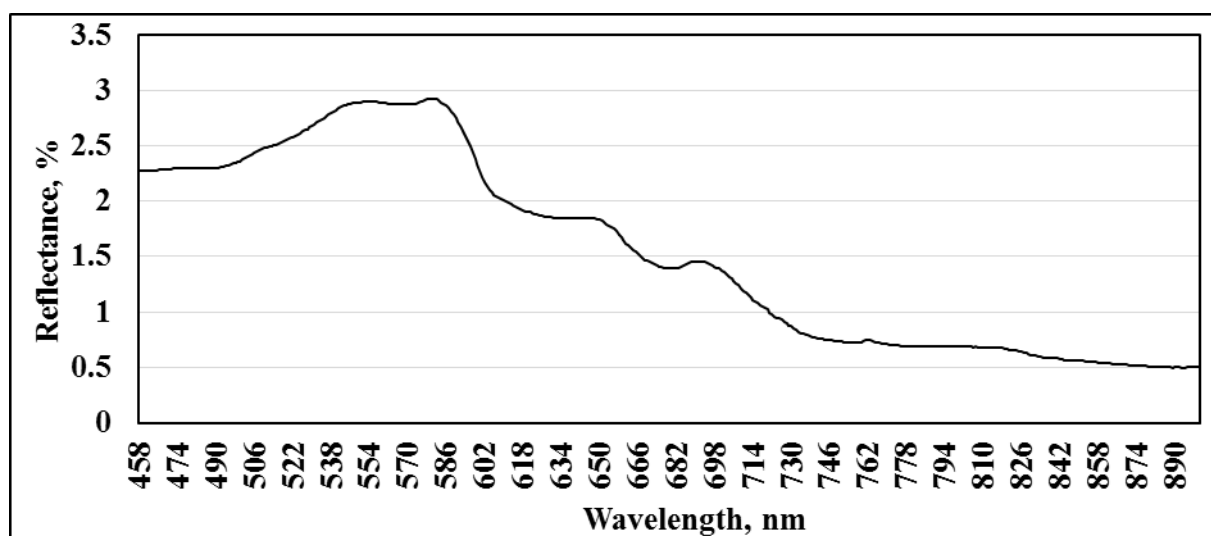
Sample 72



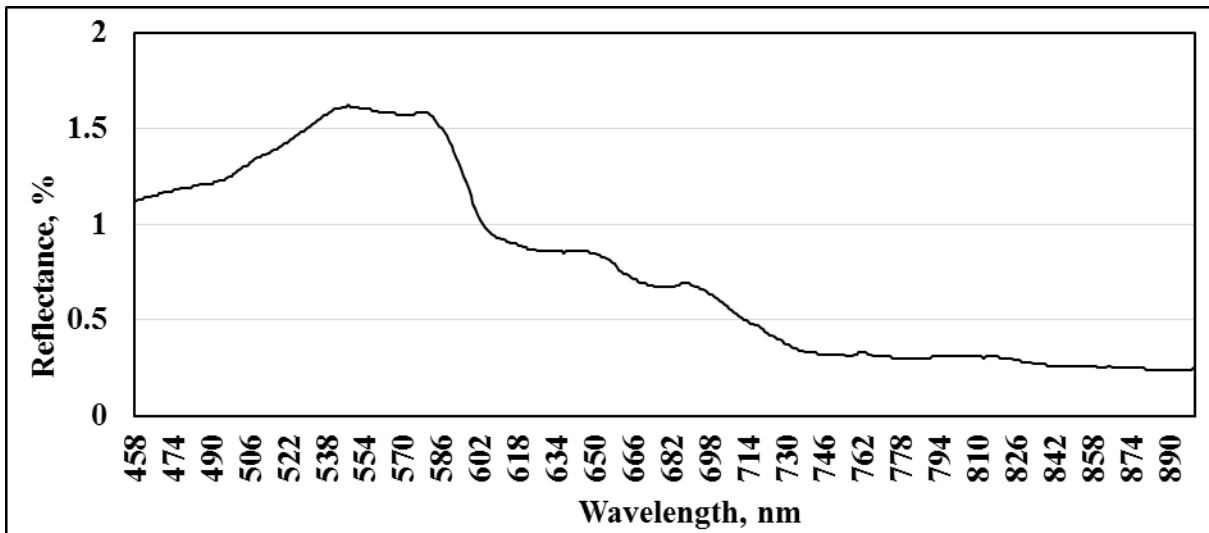
Sample 73



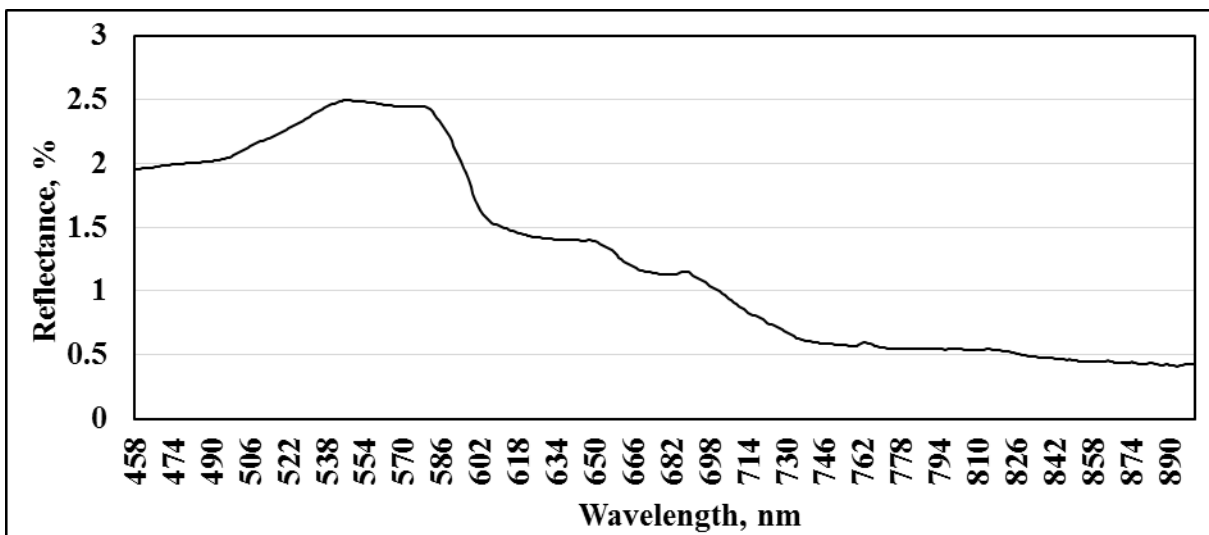
Sample 74



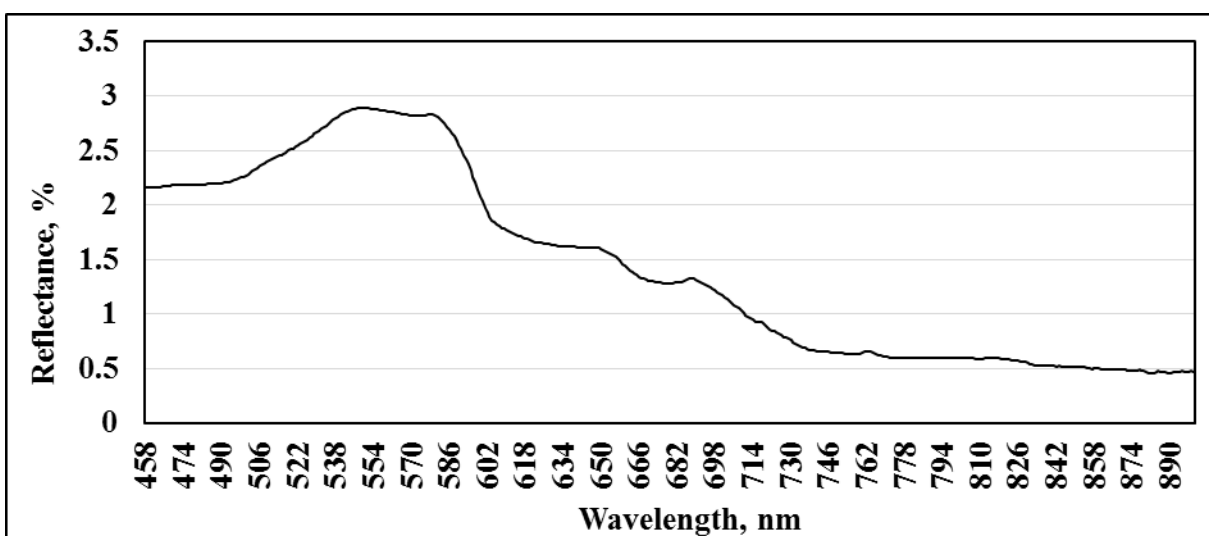
Sample 75



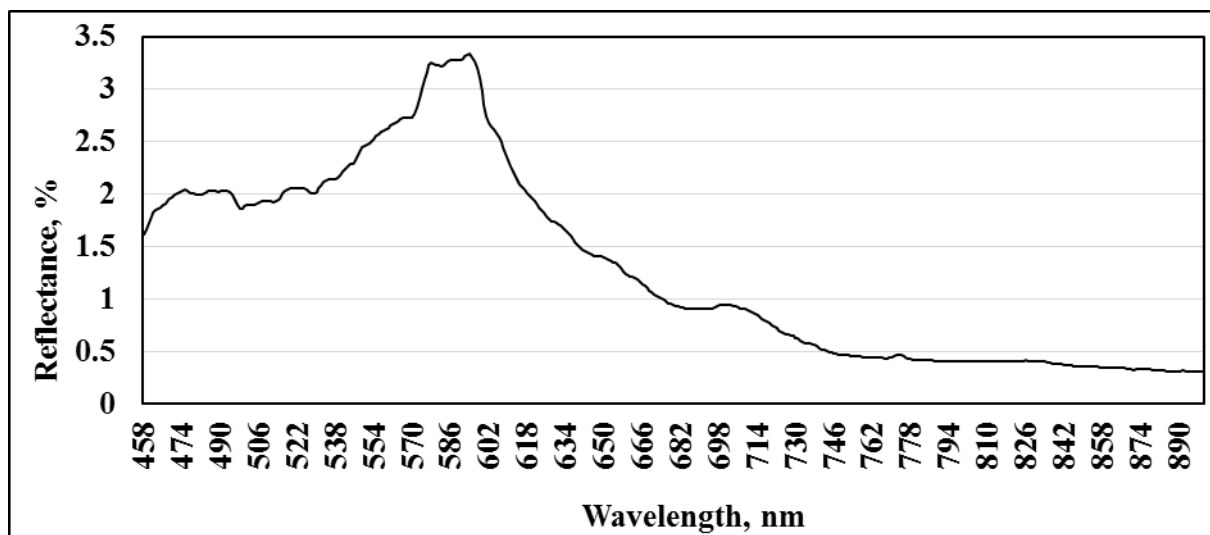
Sample 76



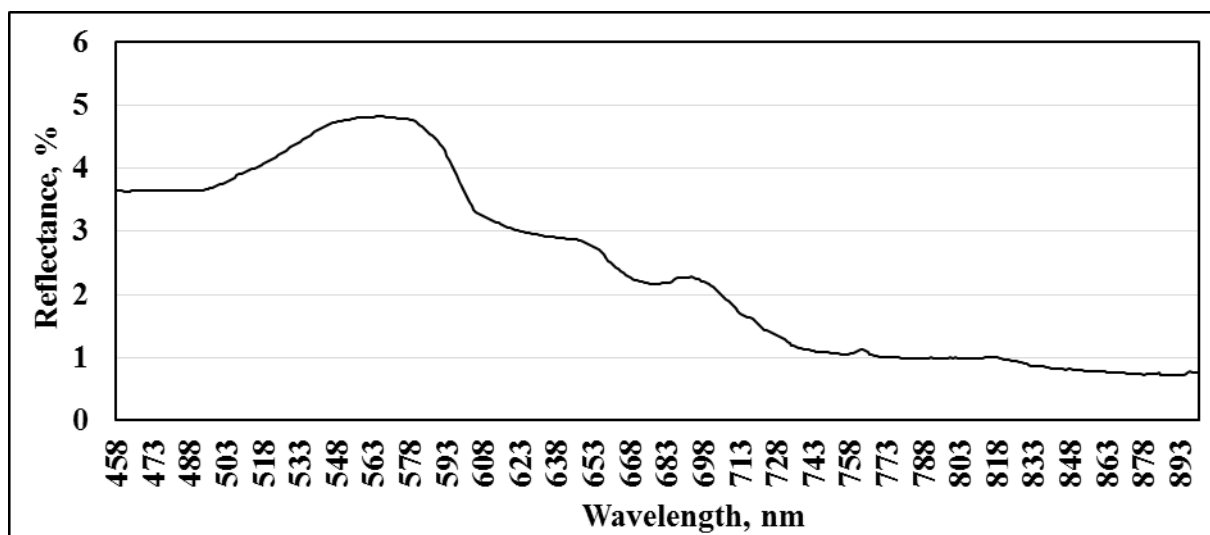
Sample 77



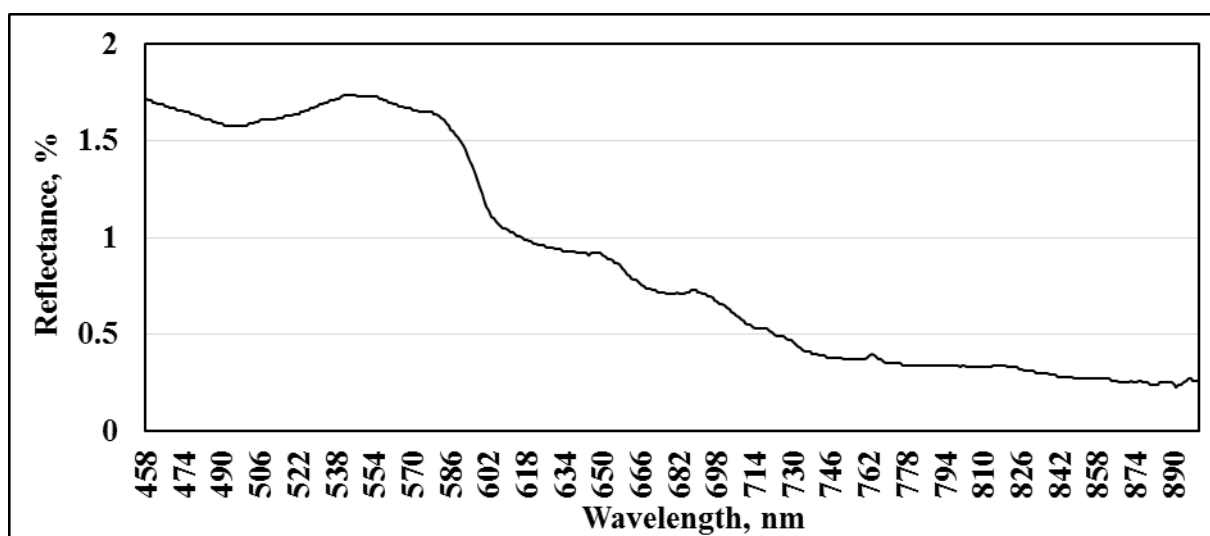
Sample 78



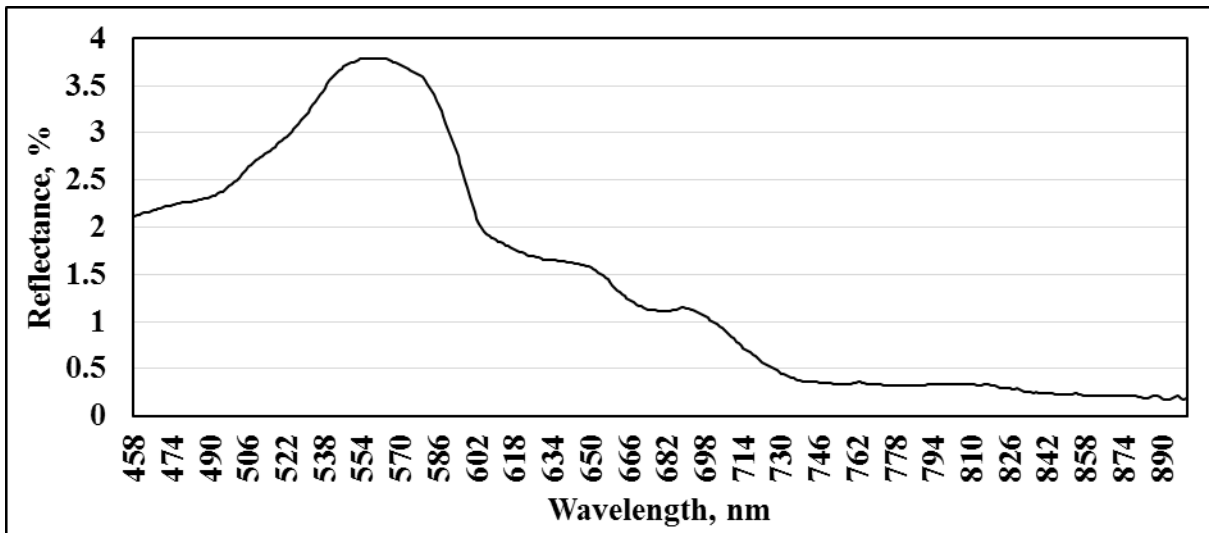
Sample 79



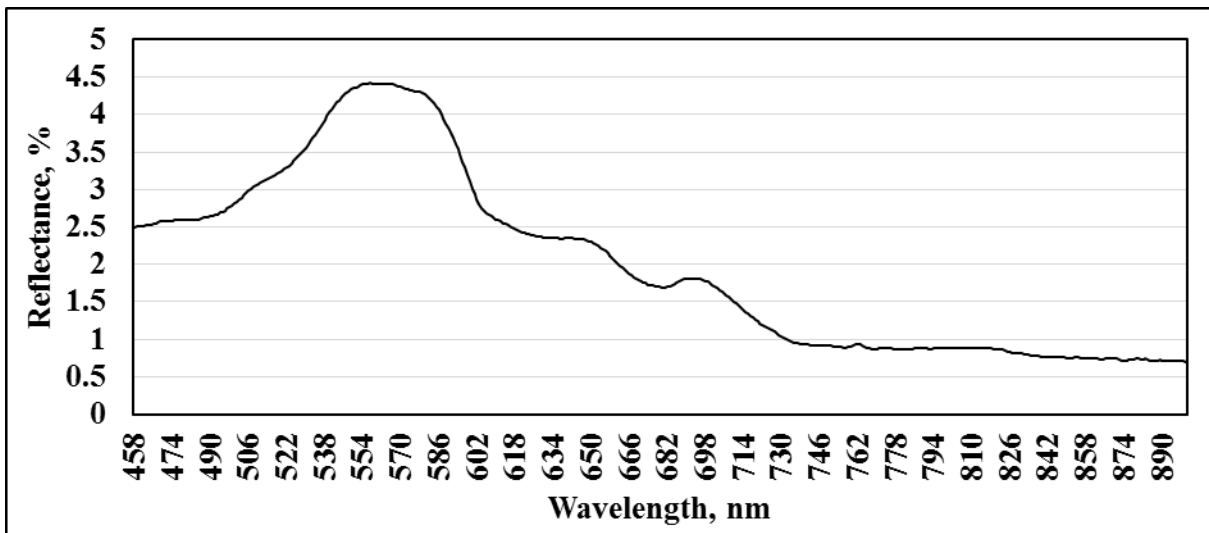
Sample 80



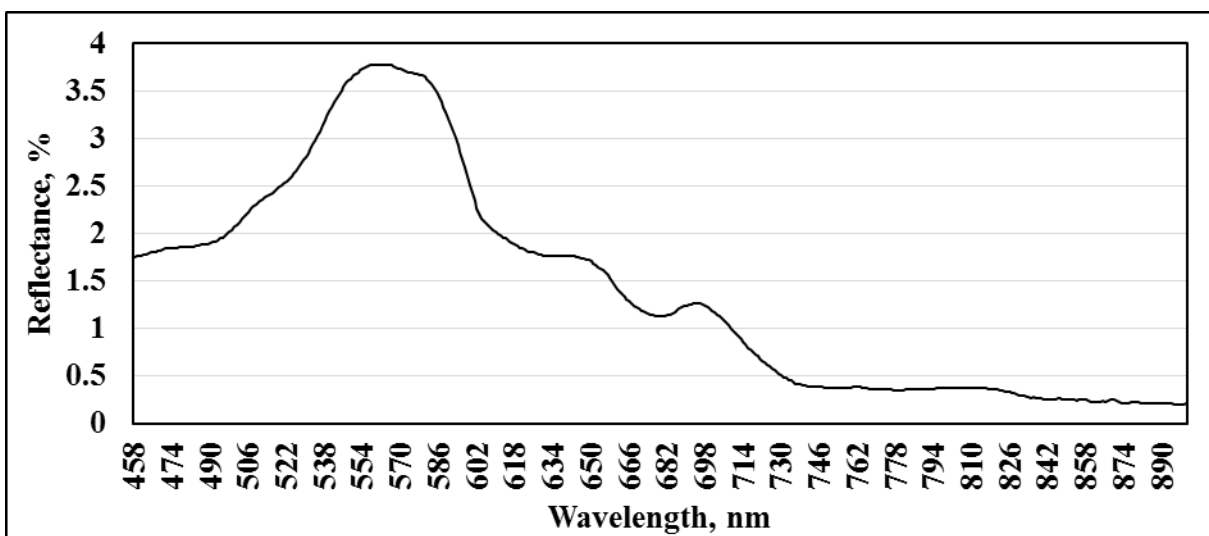
Sample 81



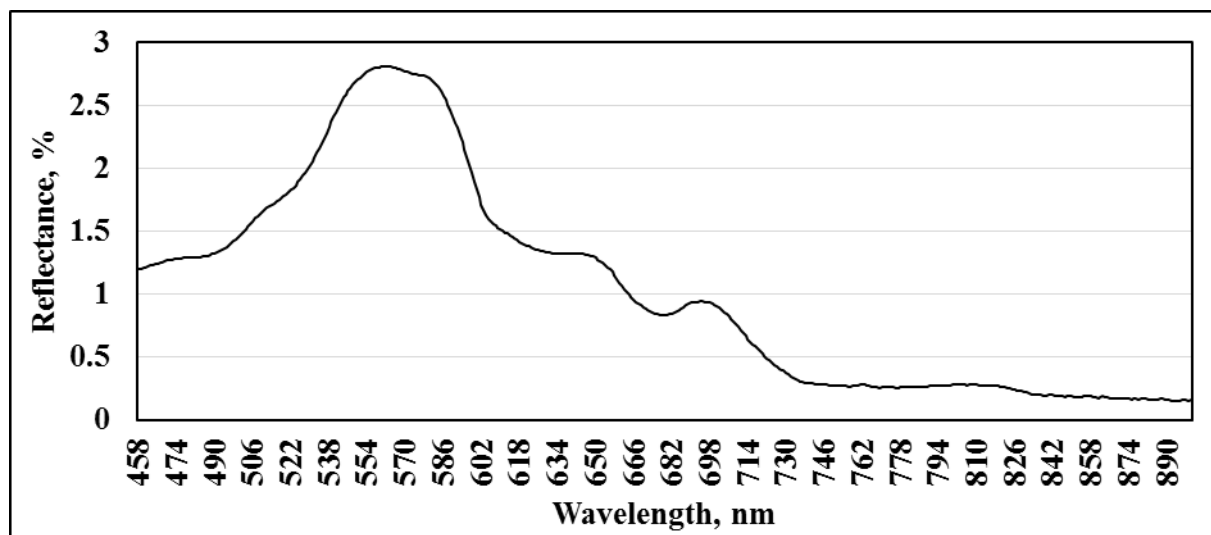
Sample 82



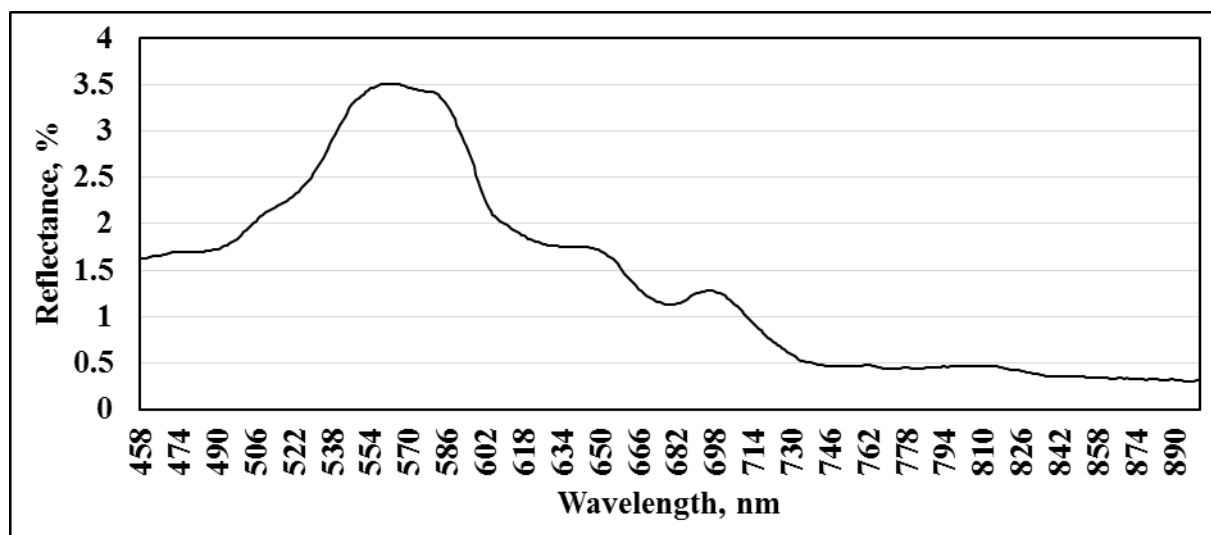
Sample 83



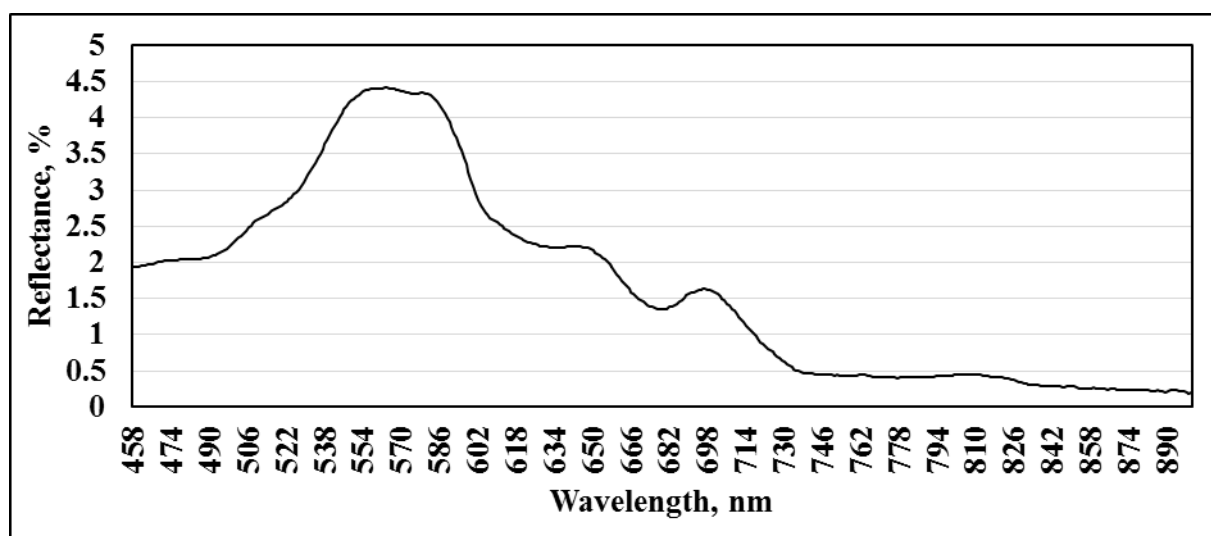
Sample 84



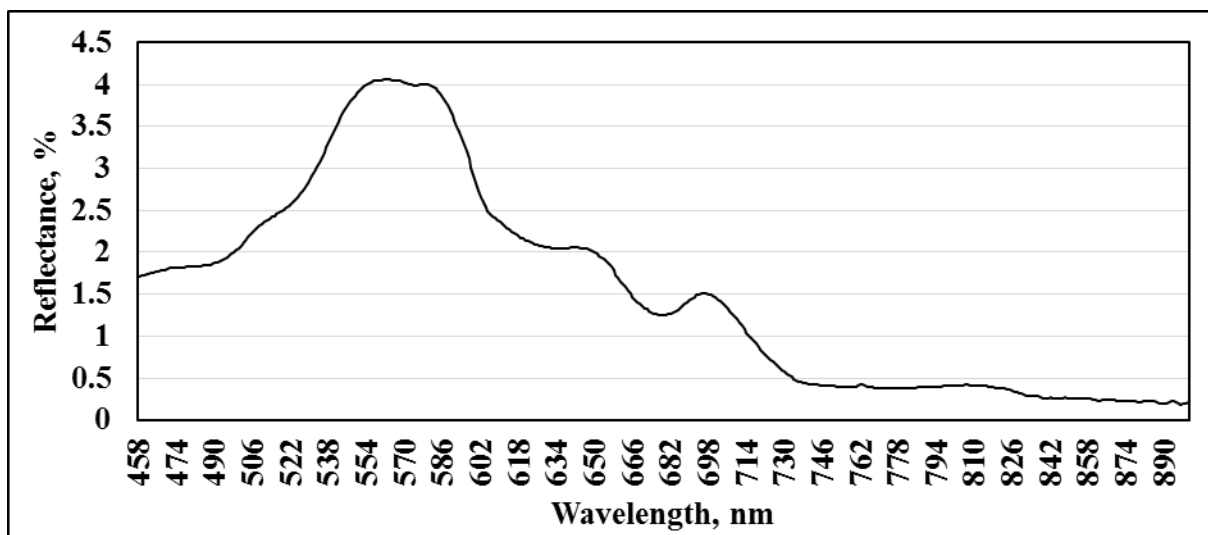
Sample 85



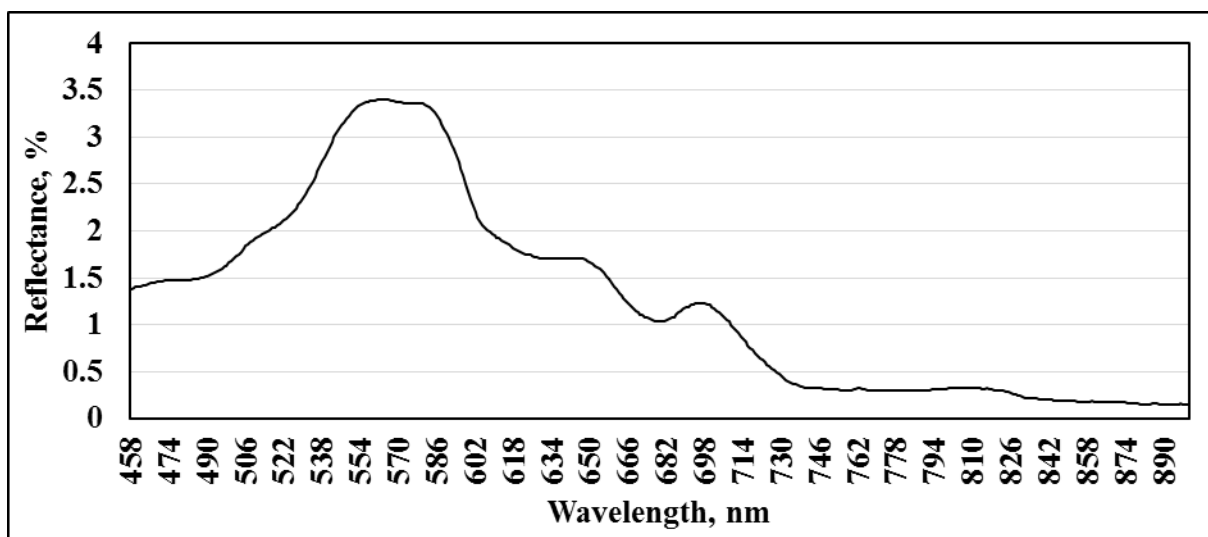
Sample 86



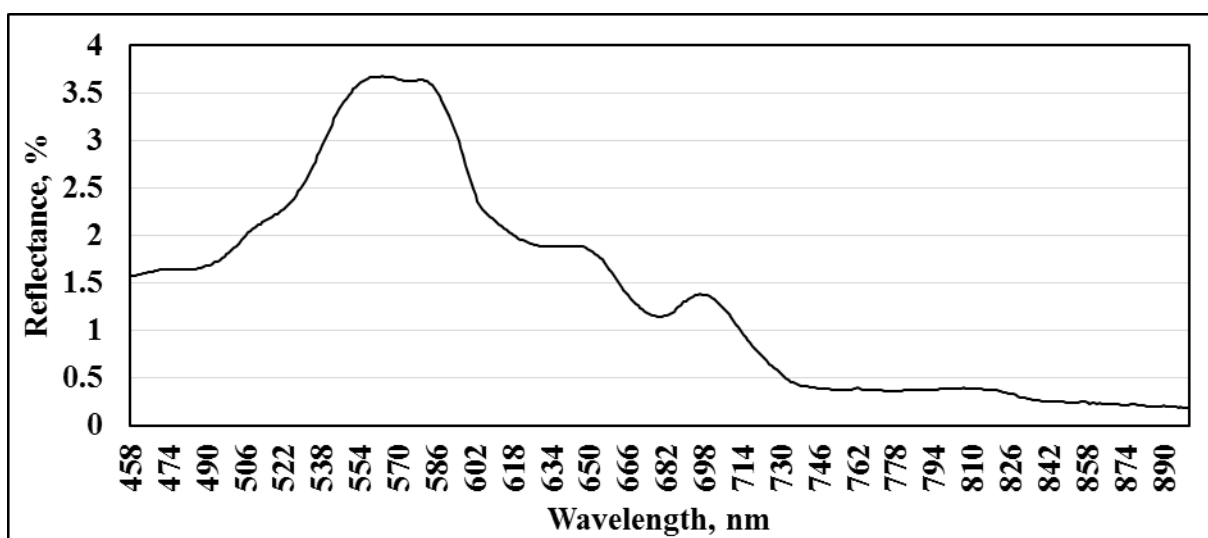
Sample 87



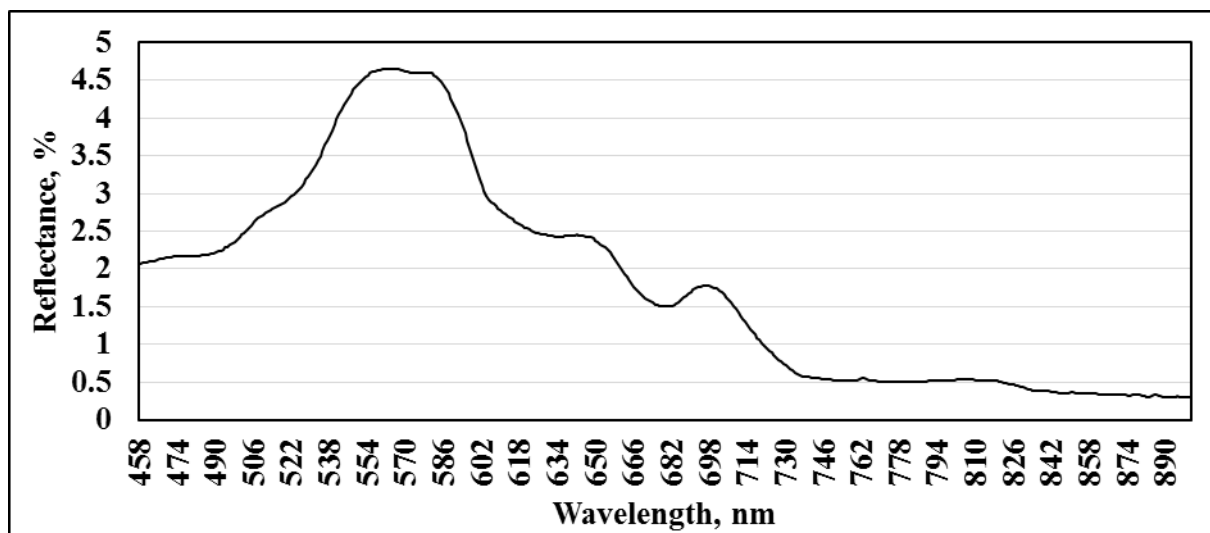
Sample 88



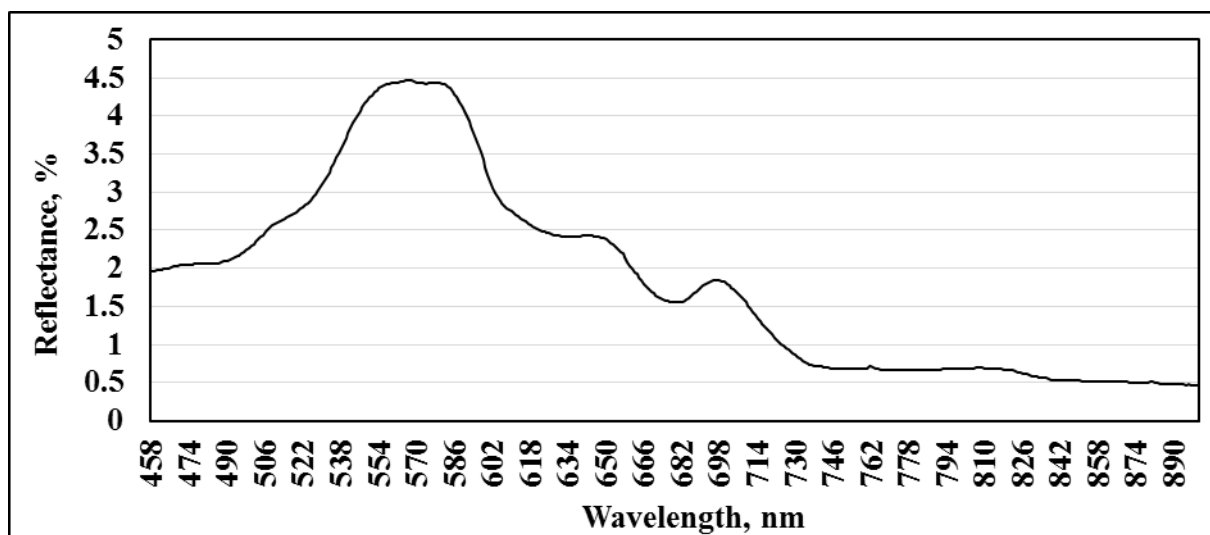
Sample 89



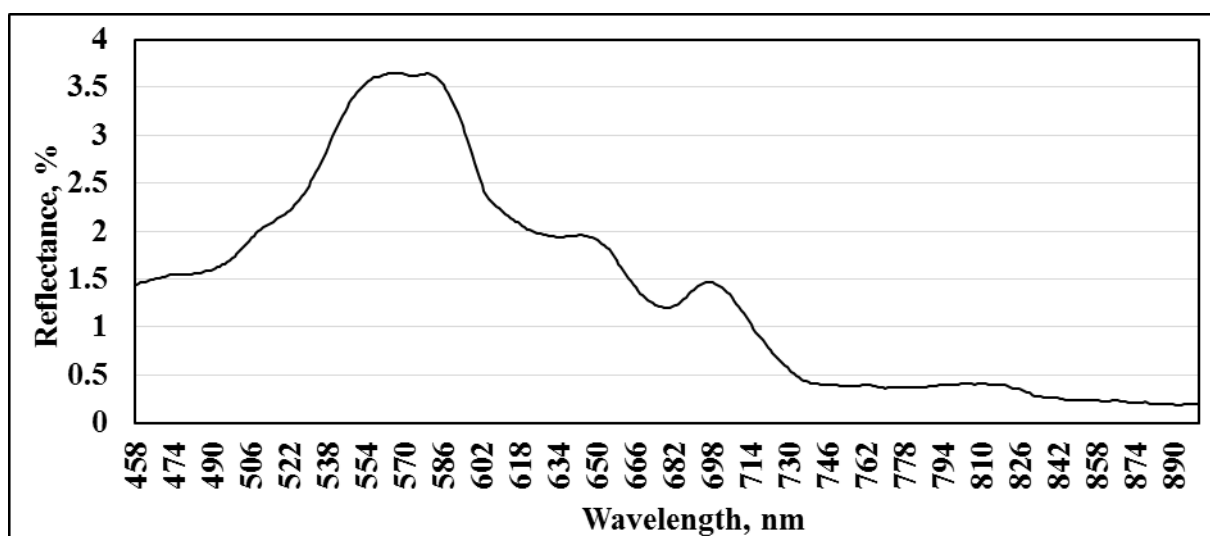
Sample 90



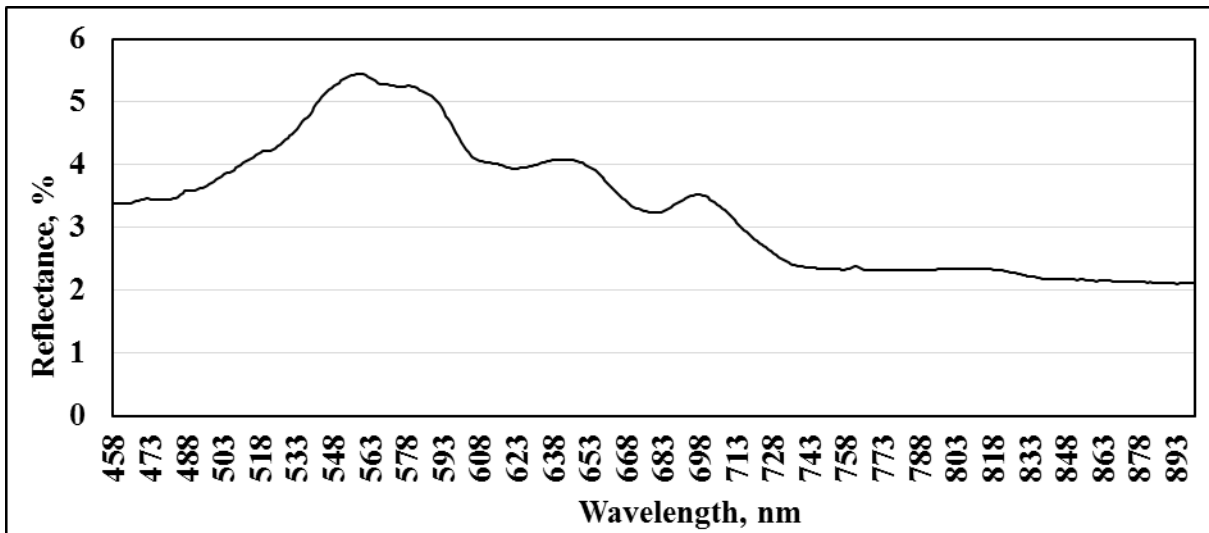
Sample 91



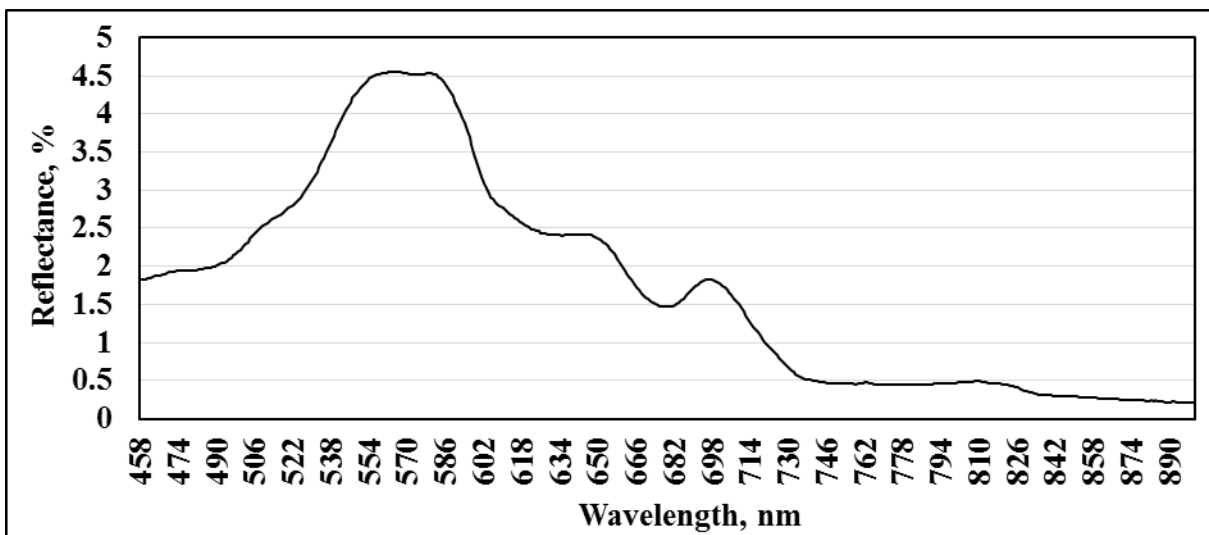
Sample 92



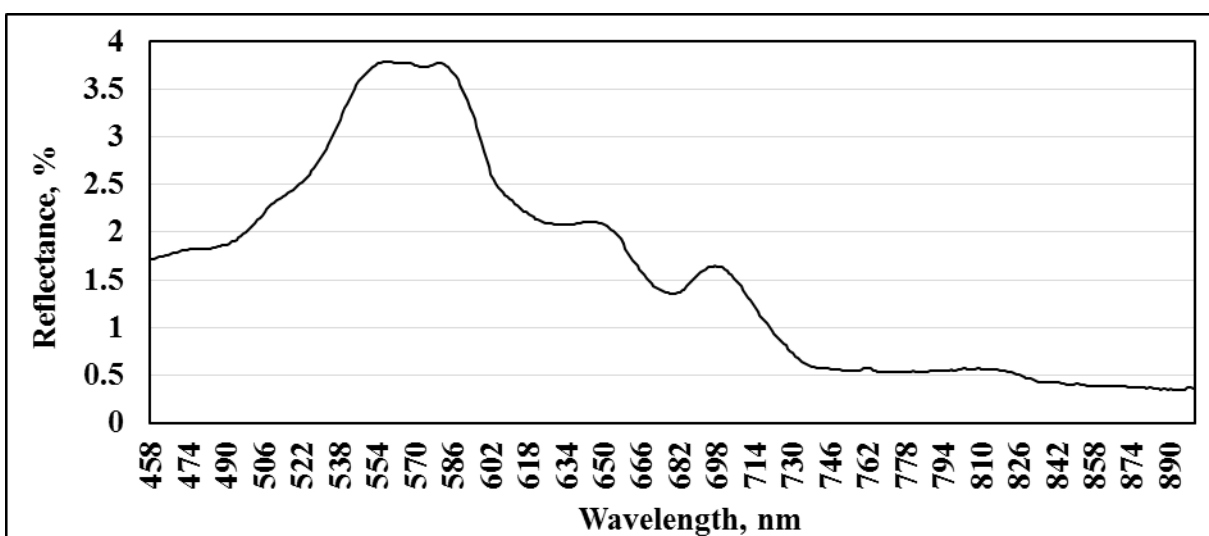
Sample 93



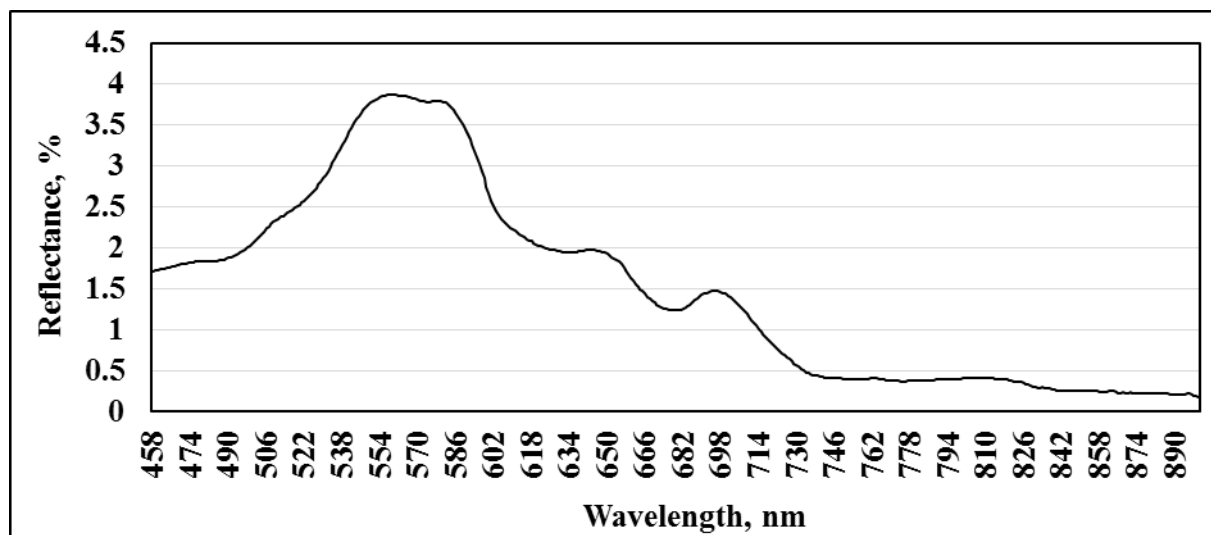
Sample 94



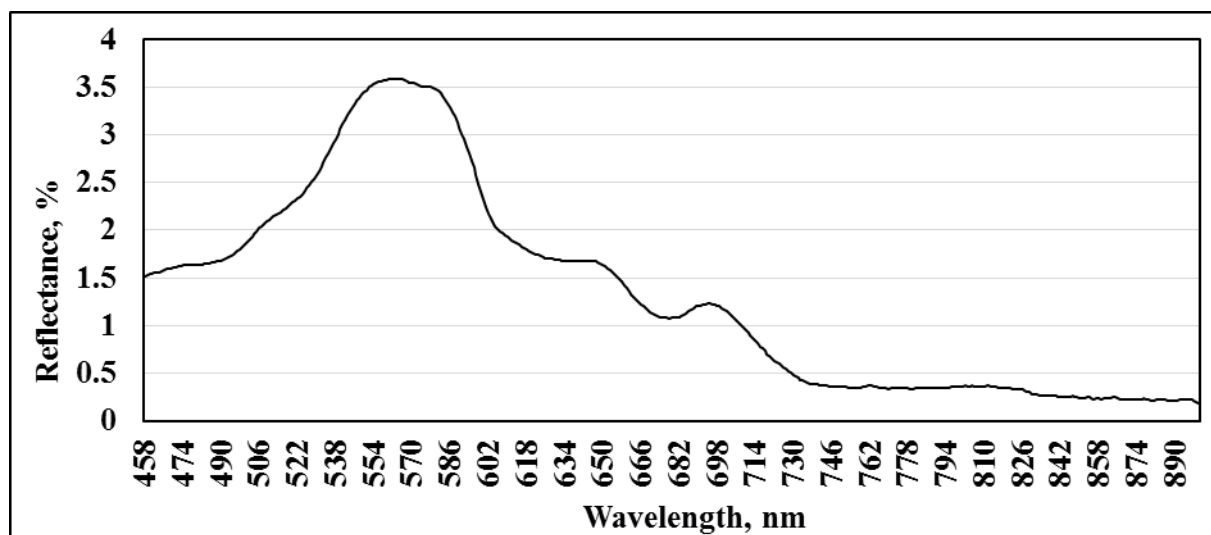
Sample 95



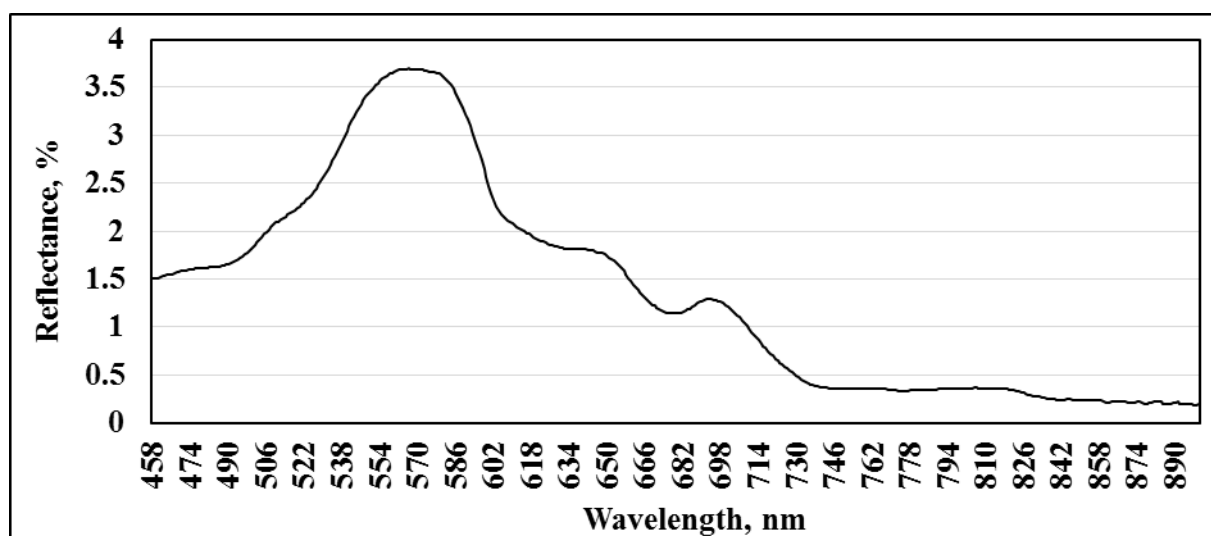
Sample 96



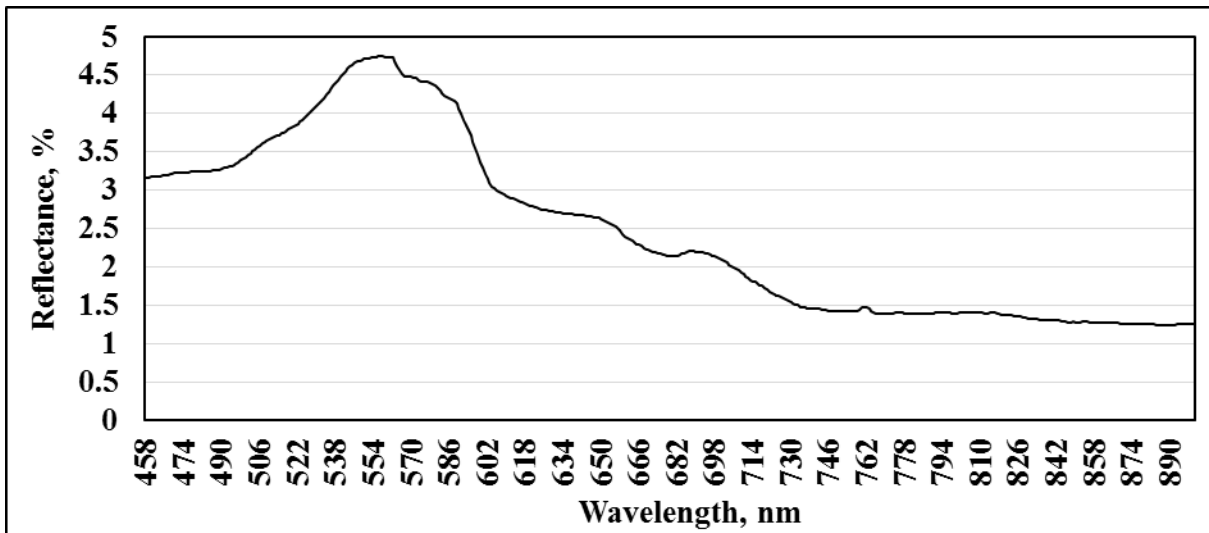
Sample 97



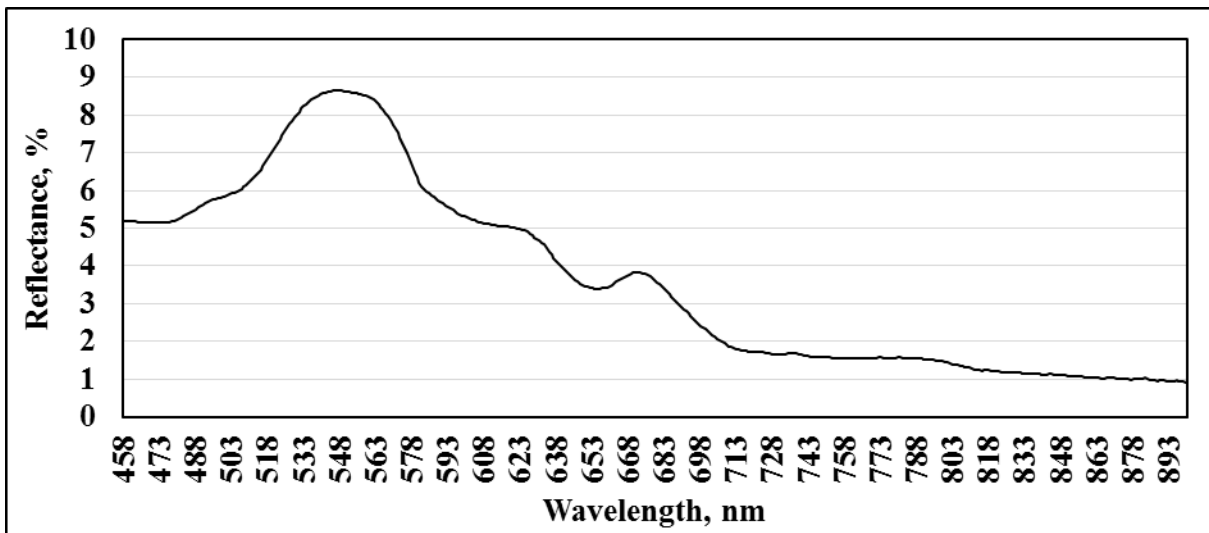
Sample 98



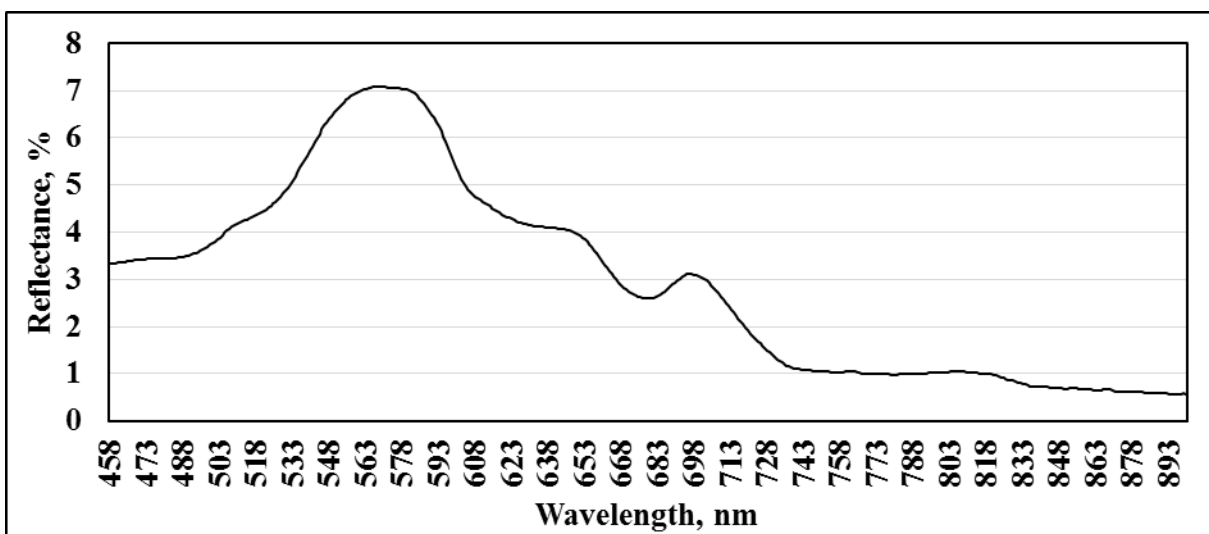
Sample 99



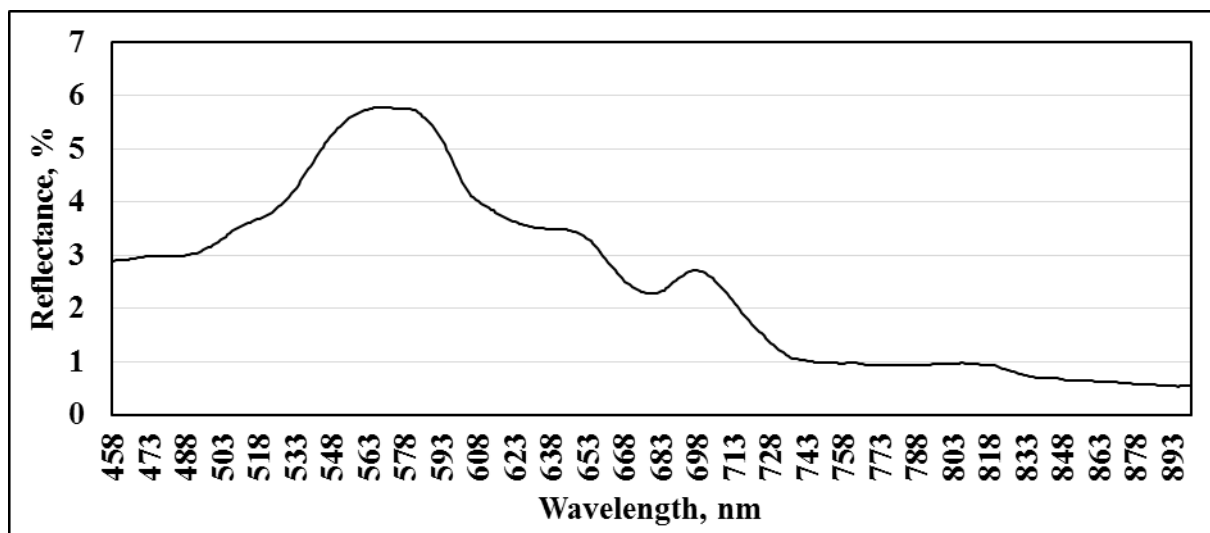
Sample 100



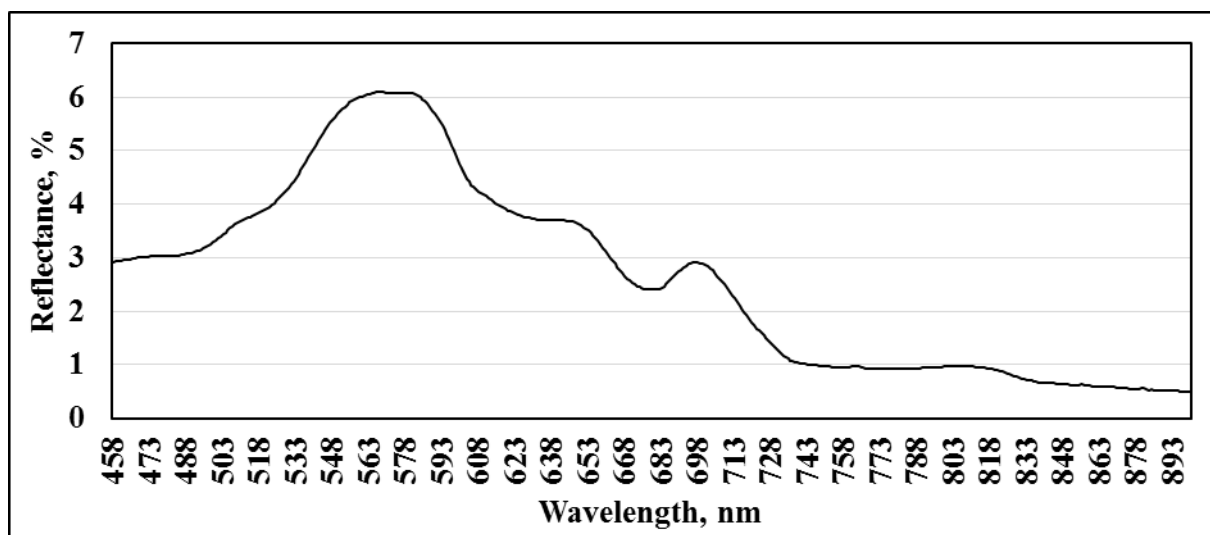
Sample 101



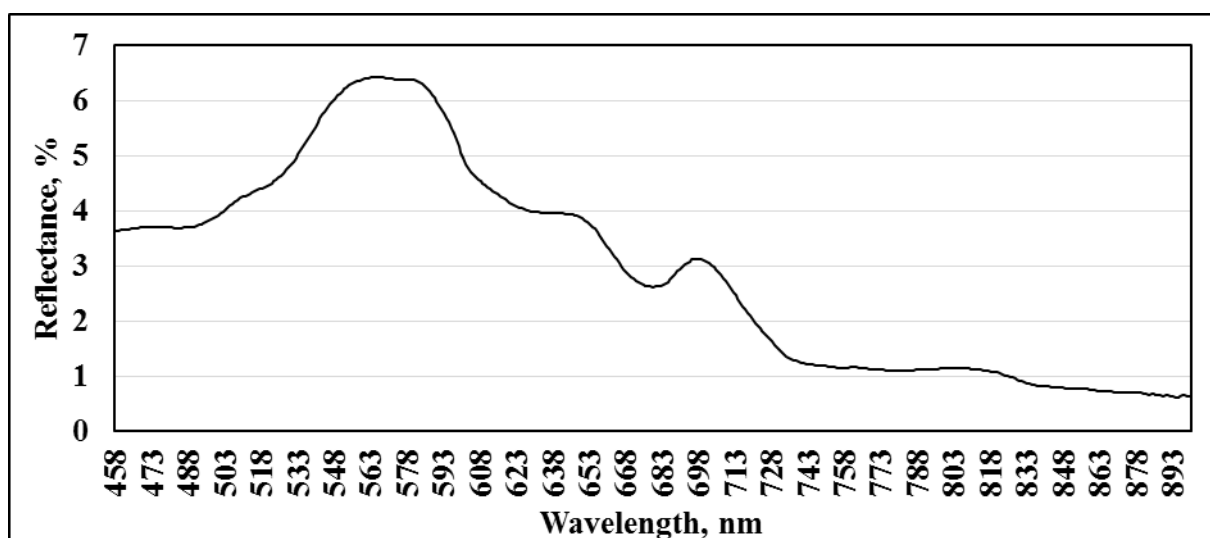
Sample 102



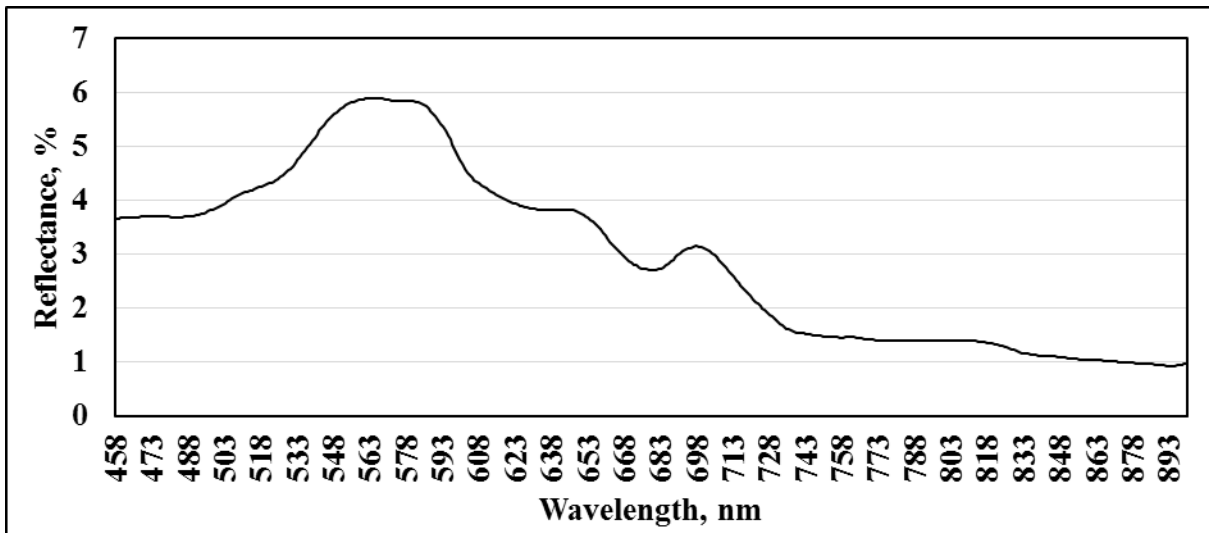
Sample 103



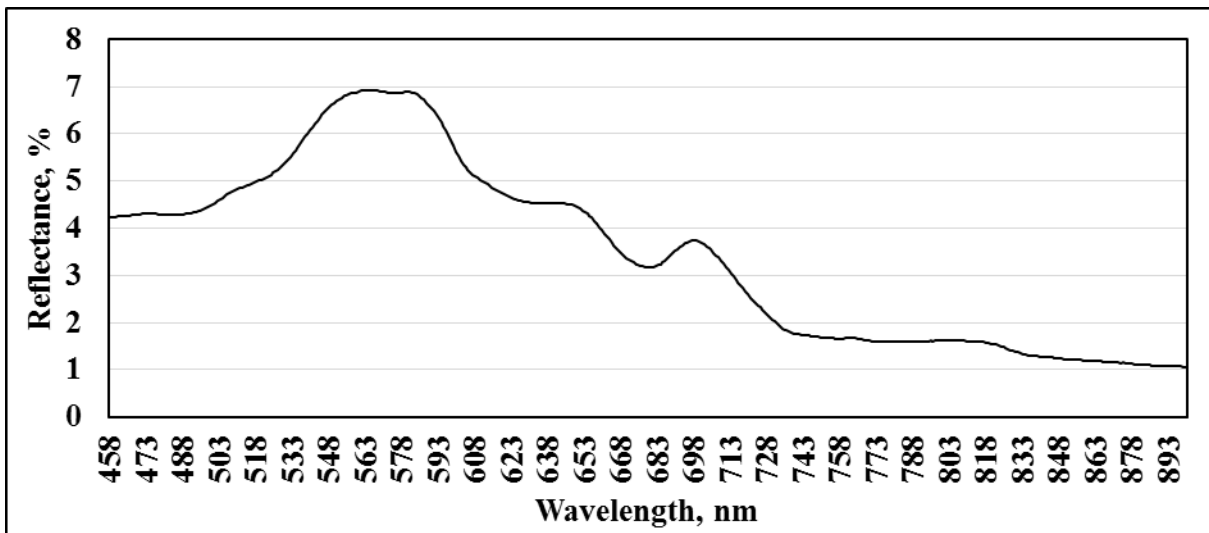
Sample 104



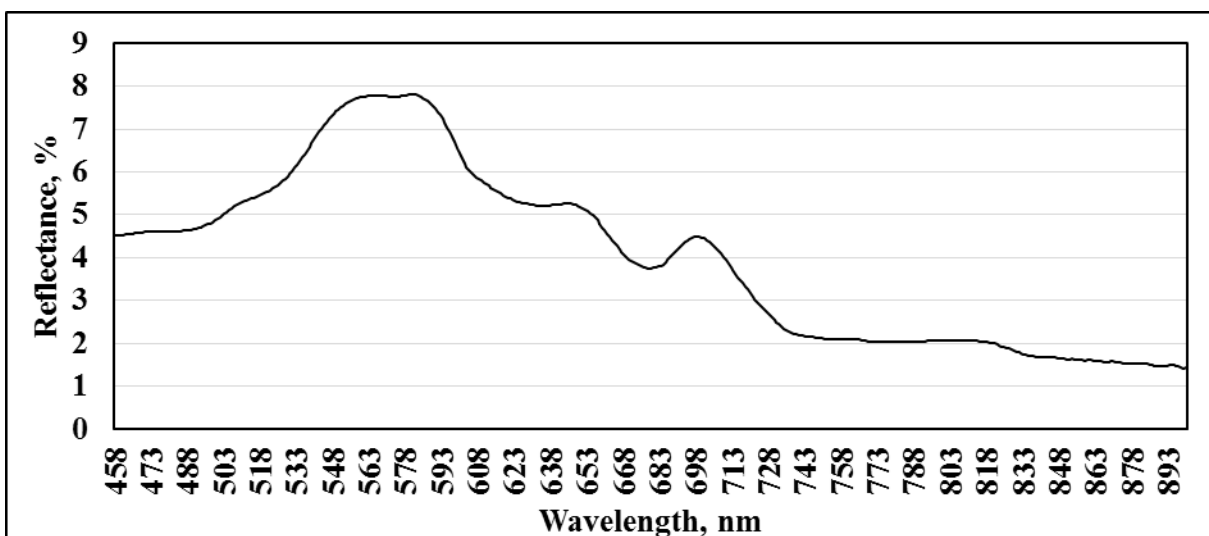
Sample 105



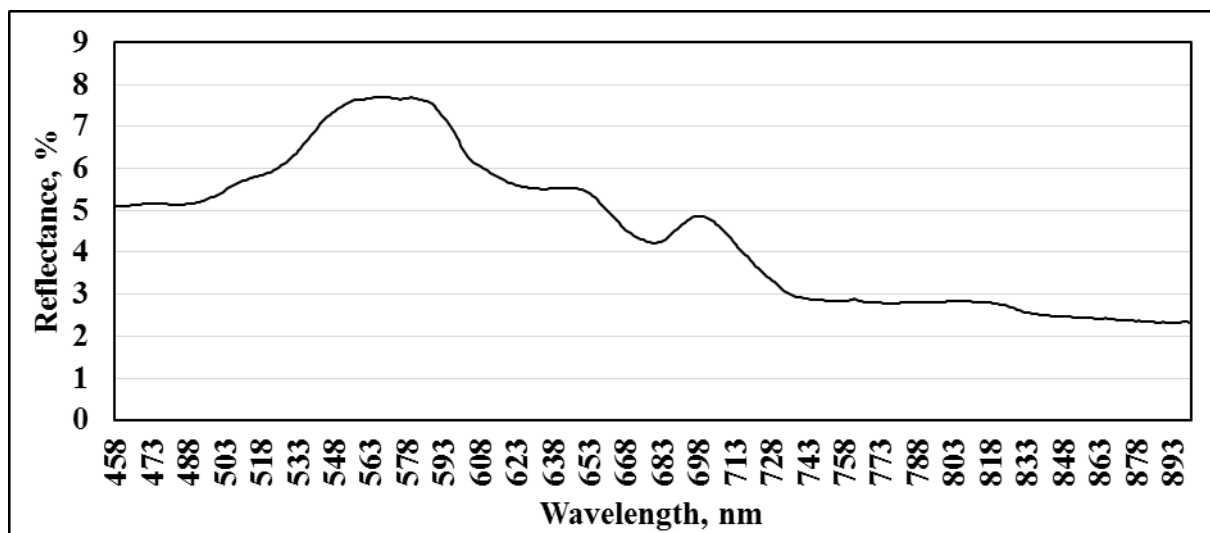
Sample 106



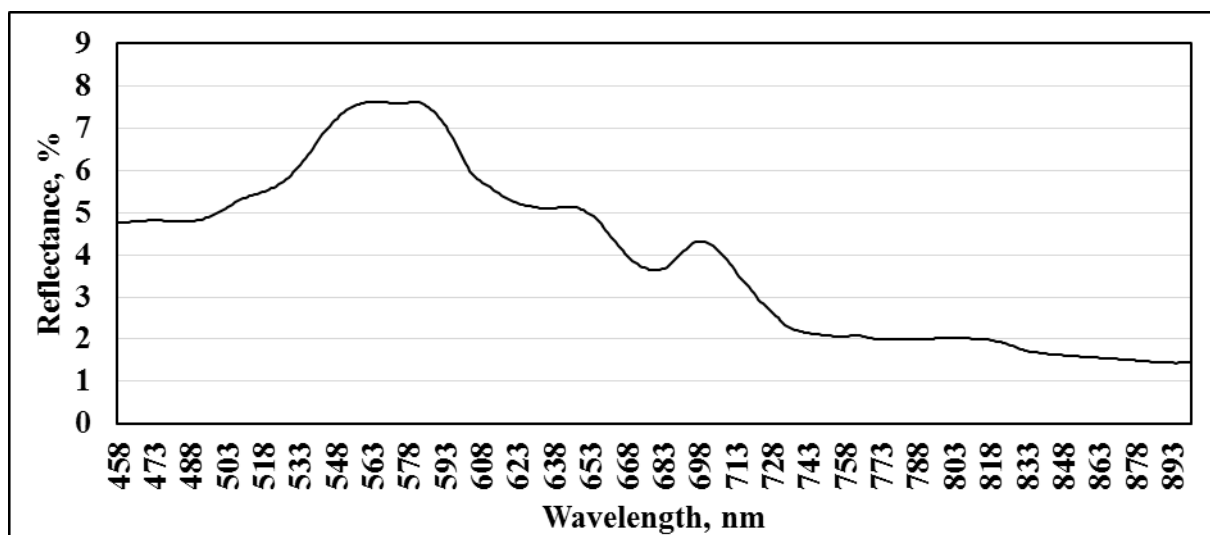
Sample 107



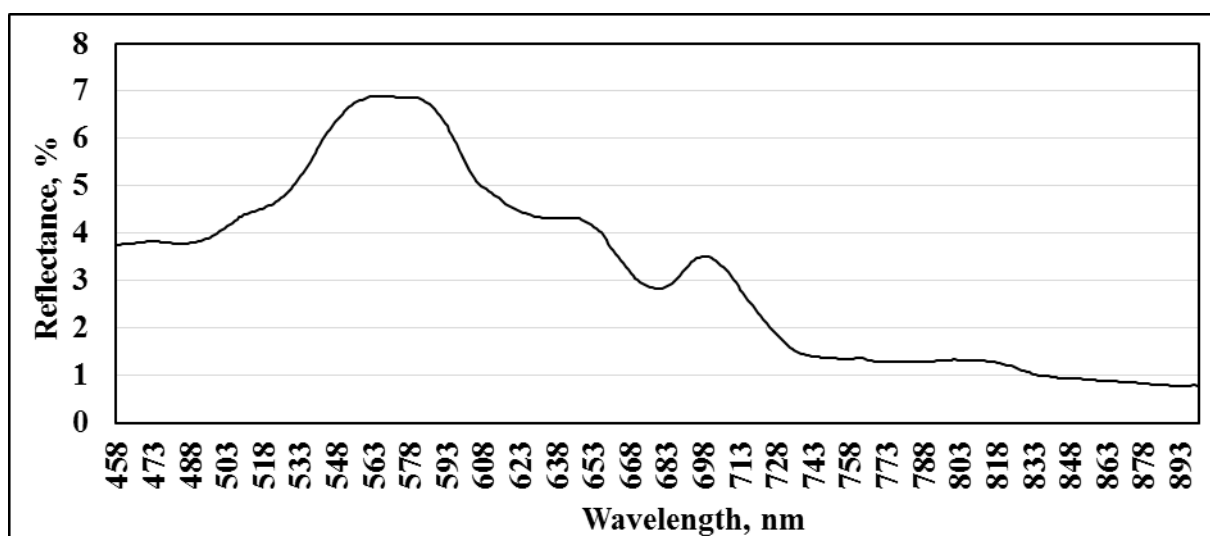
Sample 108



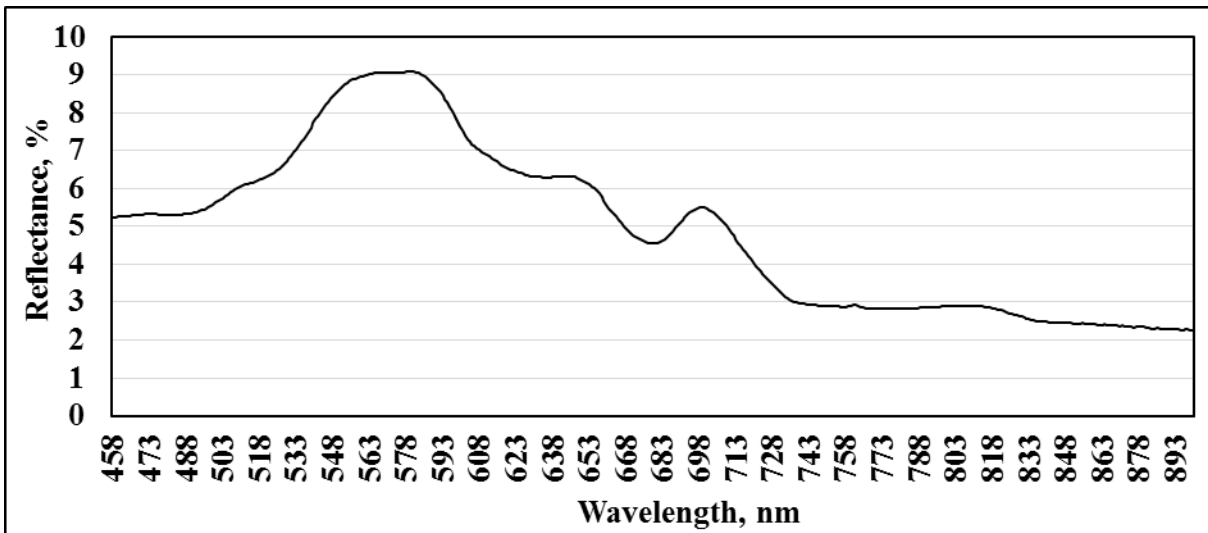
Sample 109



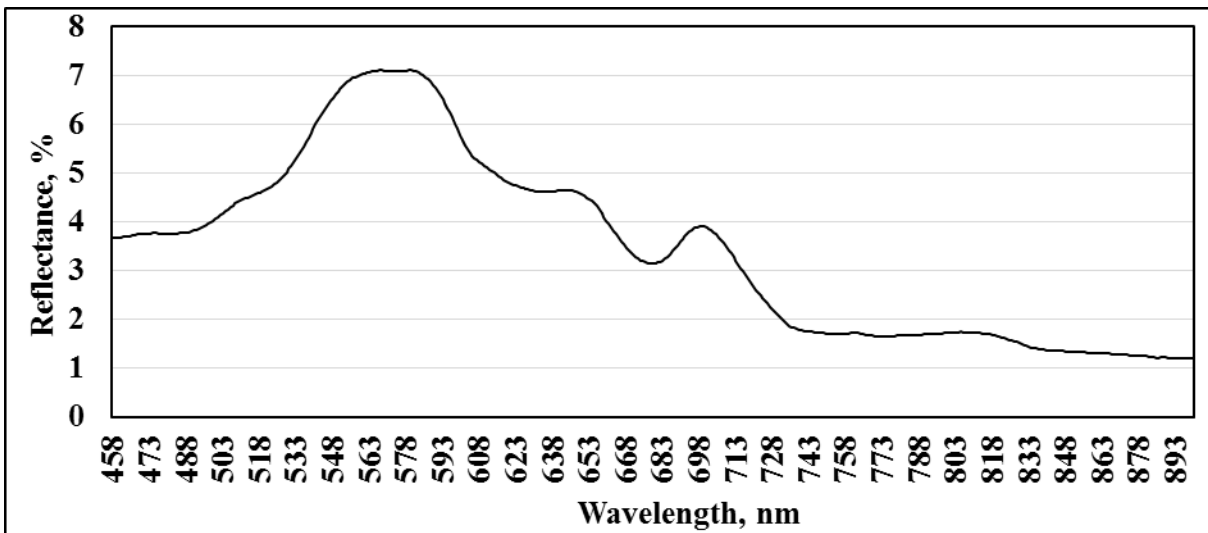
Sample 110



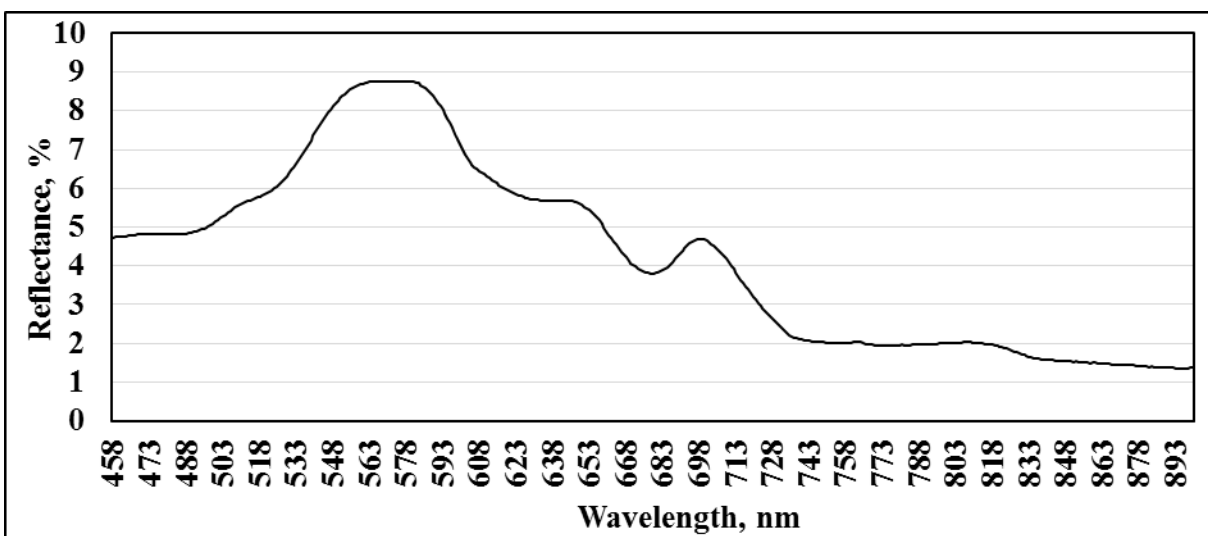
Sample 111



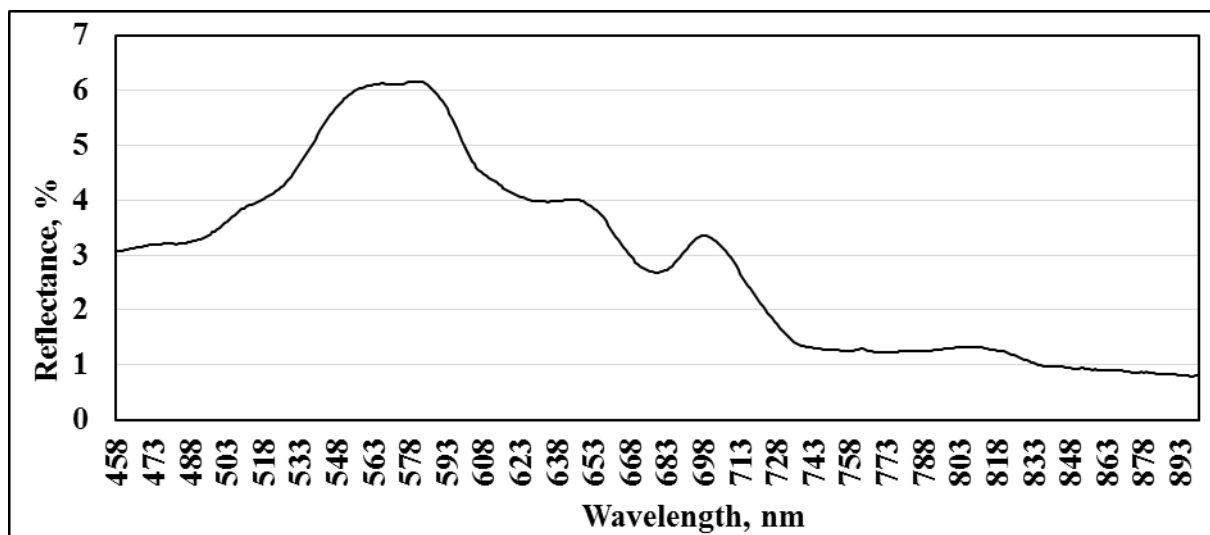
Sample 112



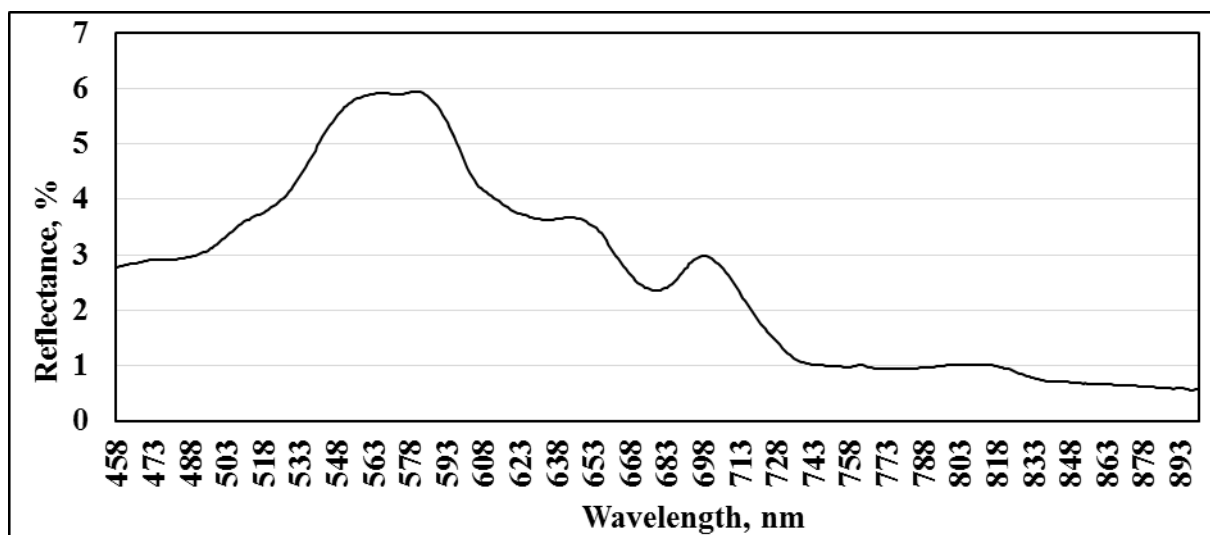
Sample 113



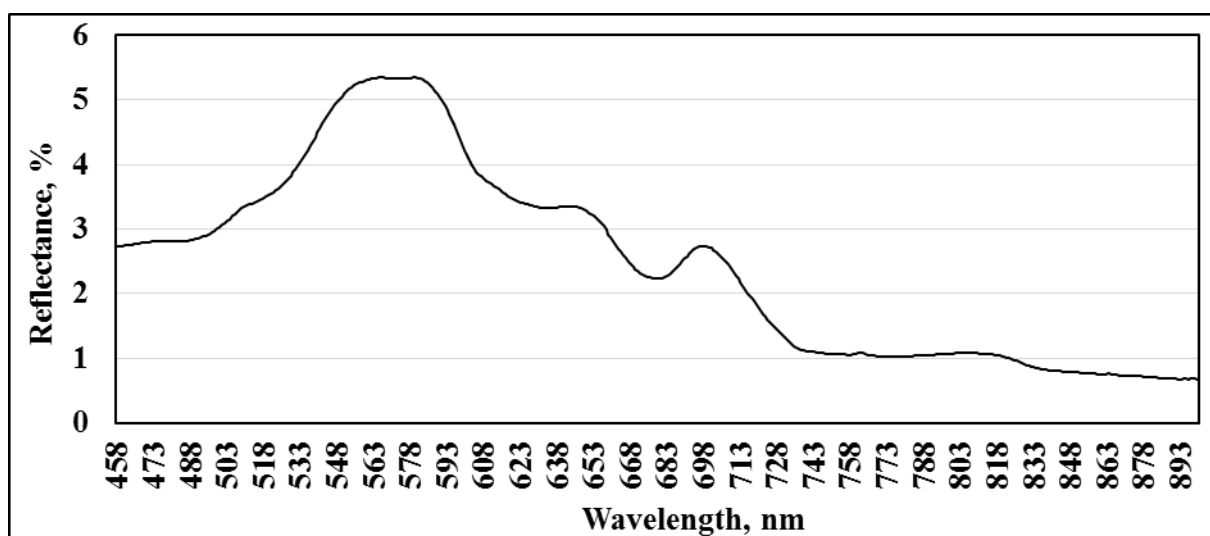
Sample 114



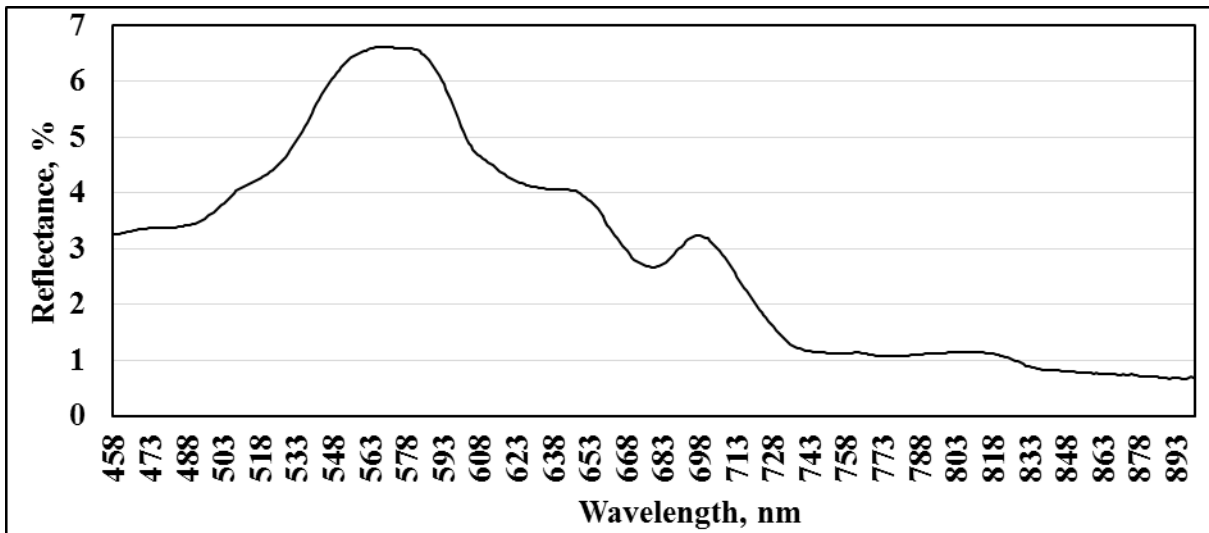
Sample 115



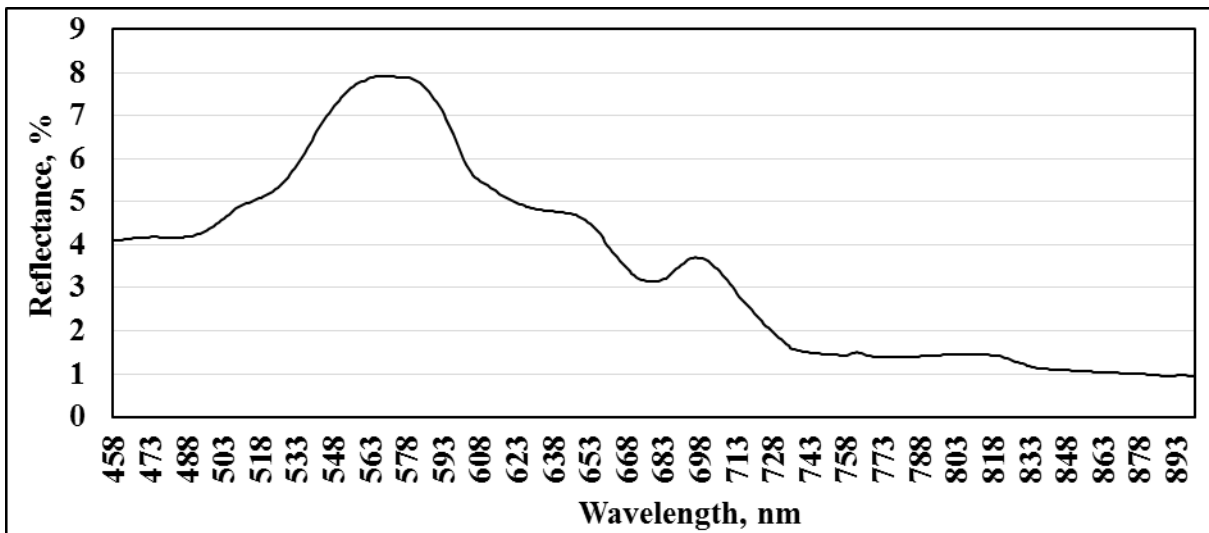
Sample 116



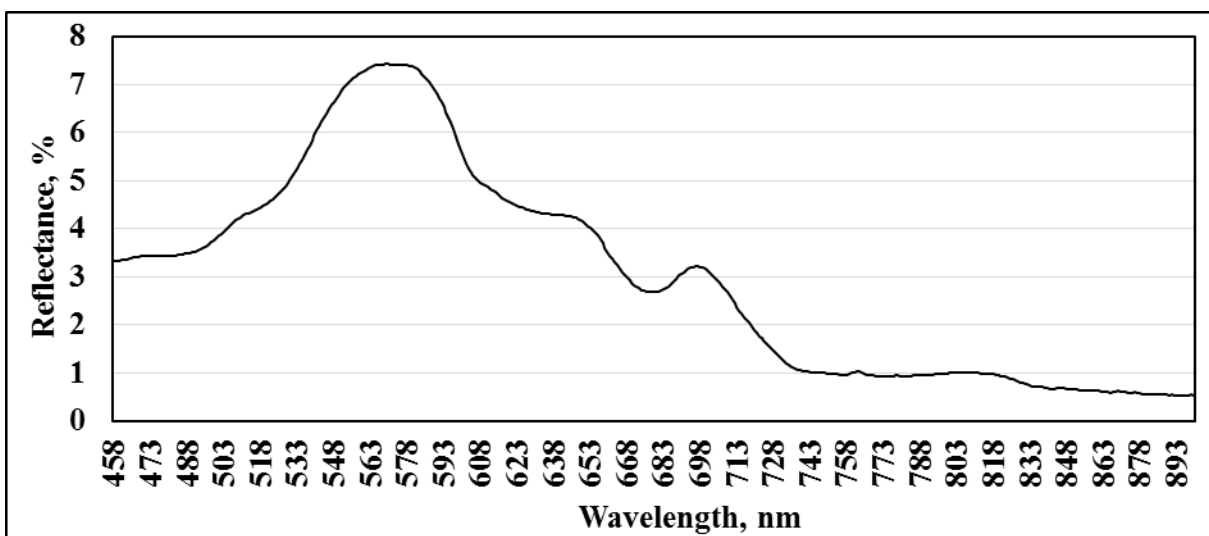
Sample 117



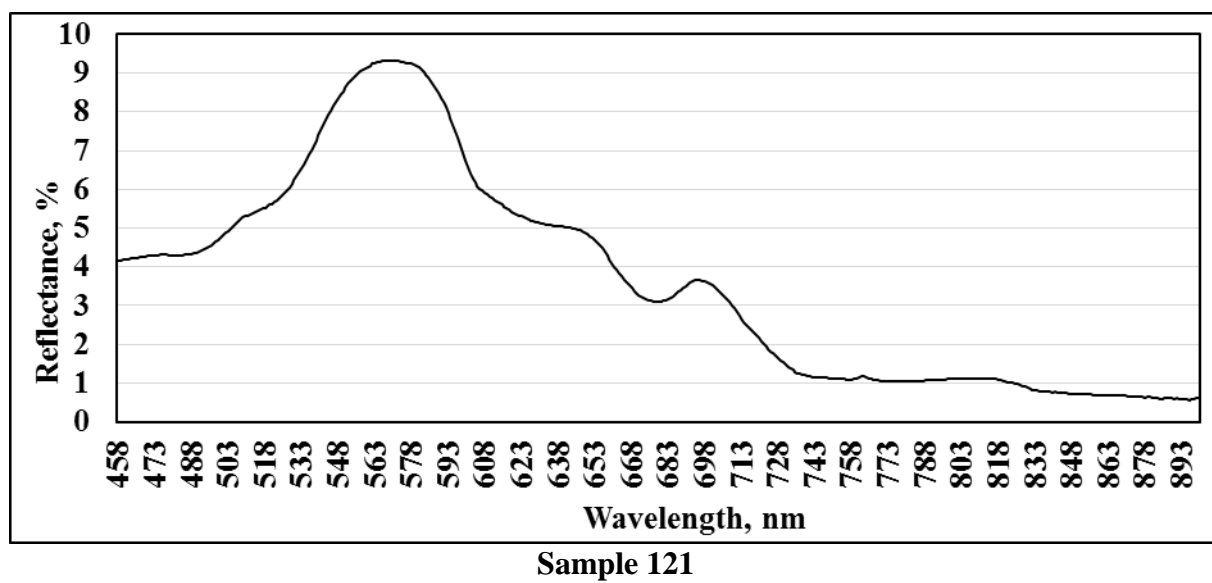
Sample 118



Sample 119



Sample 120





## Appendix - E

### Band Values Obtained from Spectroradiometer SVC – 1024i & Sentinel – 2 Satellite Imagery

Appendix - E(a): Band Values Obtained From Spectroradiometer SVC – 1024i for Calibration Data Set

Observed SSC (mg/Litre)	Sample No.	Spectroradiometer Band Values for Calibration Data Set							
		Blue	Green	Red	Red Edge 1	Red Edge 2	Red Edge 3	NIR	Red Edge 4
22.581	1	1.95	2.22	1.03	0.60	0.50	0.48	0.40	0.37
20.213	2	1.90	2.18	1.03	0.62	0.52	0.49	0.40	0.36
29.508	3	2.15	2.45	1.13	0.66	0.55	0.52	0.43	0.39
27.473	4	2.80	2.64	1.30	0.78	0.69	0.66	0.53	0.49
17.895	5	2.87	2.78	1.39	0.83	0.74	0.72	0.58	0.54
16.842	8	1.99	2.33	1.16	0.86	0.68	0.63	0.55	0.51
24.731	9	1.70	2.16	1.03	0.75	0.57	0.55	0.48	0.46
28.877	10	2.22	2.55	1.24	0.90	0.67	0.62	0.51	0.47
17.204	11	1.44	1.90	0.81	0.54	0.36	0.34	0.28	0.26
15.909	12	1.45	1.83	0.79	0.52	0.36	0.35	0.30	0.28
20.000	13	1.29	1.69	0.73	0.47	0.30	0.29	0.25	0.23
16.842	14	1.39	1.74	0.79	0.55	0.39	0.38	0.32	0.30
19.149	15	1.70	2.01	0.93	0.63	0.46	0.42	0.35	0.32
16.931	16	1.43	1.72	0.79	0.52	0.37	0.34	0.28	0.26
26.316	17	1.36	1.73	0.79	0.53	0.36	0.34	0.28	0.25
25.131	18	2.40	2.78	1.37	0.96	0.70	0.64	0.52	0.47
16.043	23	1.62	2.16	0.93	0.60	0.40	0.41	0.38	0.36
20.942	24	2.13	2.69	1.21	0.80	0.54	0.52	0.45	0.41
23.834	25	1.44	1.82	0.87	0.59	0.40	0.40	0.36	0.34
45.854	26	2.10	2.56	1.49	1.09	0.63	0.55	0.48	0.44
52.326	27	2.97	3.32	1.77	1.39	0.99	0.88	0.76	0.70
47.435	28	2.93	3.08	1.78	1.38	0.99	0.88	0.76	0.70
48.685	32	1.72	1.97	1.09	0.87	0.60	0.54	0.48	0.44
50.682	34	2.67	2.84	1.62	1.31	0.99	0.88	0.75	0.69
52.475	35	3.21	3.57	2.18	1.81	1.27	1.15	1.01	0.94
55.000	36	3.12	3.58	2.07	1.70	1.15	1.02	0.87	0.79
53.045	37	2.30	3.07	1.65	1.34	0.71	0.63	0.53	0.48
52.308	38	2.53	3.20	1.75	1.39	0.87	0.77	0.66	0.60
55.789	39	2.46	3.19	1.68	1.36	0.83	0.74	0.62	0.56
47.668	42	4.35	5.06	2.77	2.26	1.55	1.35	1.13	1.02
52.632	43	2.61	3.30	1.81	1.44	0.83	0.74	0.63	0.57
65.657	47	2.69	3.17	1.66	1.29	0.82	0.72	0.61	0.55
54.271	50	2.53	2.79	1.37	1.02	0.67	0.58	0.49	0.44
64.646	51	2.98	3.24	1.72	1.33	0.92	0.80	0.68	0.62
54.082	53	2.77	2.99	1.71	1.35	0.86	0.75	0.64	0.57
47.000	54	2.05	2.35	1.17	0.87	0.53	0.47	0.41	0.37
56.863	56	1.59	1.81	0.96	0.75	0.50	0.45	0.40	0.37
52.041	59	2.81	3.20	1.74	1.42	1.01	0.91	0.79	0.73
58.252	63	2.49	2.78	1.67	1.41	1.06	0.98	0.89	0.85
63.542	65	2.64	3.25	1.74	1.42	0.92	0.83	0.71	0.64

Observed SSC (mg/Litre)	Sample No.	Spectroradiometer Band Values for Calibration Data Set							
		Blue	Green	Red	Red Edge 1	Red Edge 2	Red Edge 3	NIR	Red Edge 4
42.424	68	3.00	3.58	2.20	1.89	1.35	1.25	1.14	1.08
33.000	69	2.37	3.00	1.55	1.25	0.77	0.70	0.62	0.57
57.732	70	2.68	3.18	1.81	1.54	1.06	0.96	0.84	0.77
70.000	71	1.79	2.51	1.25	1.04	0.62	0.57	0.51	0.47
52.525	72	2.29	3.31	1.56	1.26	0.69	0.62	0.54	0.49
42.424	76	1.25	1.59	0.74	0.57	0.33	0.30	0.27	0.25
59.375	77	2.06	2.46	1.23	0.95	0.61	0.55	0.48	0.45
51.064	78	2.27	2.85	1.40	1.09	0.67	0.60	0.53	0.49
54.082	79	1.95	2.65	1.15	0.92	0.53	0.42	0.37	0.34
47.959	81	1.63	1.70	0.79	0.61	0.40	0.34	0.29	0.26
60.606	82	2.44	3.73	1.29	0.91	0.37	0.32	0.26	0.21
68.367	83	2.78	4.35	1.95	1.62	0.93	0.87	0.80	0.74
64.948	84	2.04	3.70	1.36	1.08	0.41	0.36	0.29	0.24
56.863	86	1.86	3.43	1.37	1.13	0.49	0.45	0.38	0.33
61.458	87	2.25	4.32	1.69	1.43	0.47	0.41	0.32	0.25
65.263	88	2.02	3.96	1.56	1.33	0.44	0.38	0.30	0.24
64.211	89	1.65	3.32	1.30	1.08	0.34	0.30	0.23	0.18
74.227	90	1.82	3.58	1.44	1.22	0.42	0.37	0.29	0.23
78.723	91	2.38	4.54	1.87	1.58	0.57	0.51	0.41	0.34
71.287	92	2.26	4.34	1.89	1.65	0.72	0.66	0.58	0.51
76.923	93	1.73	3.54	1.49	1.30	0.42	0.37	0.29	0.22
77.551	95	2.18	4.44	1.83	1.61	0.51	0.45	0.34	0.26
63.000	97	2.02	3.79	1.52	1.29	0.44	0.38	0.30	0.24
92.308	98	1.82	3.50	1.29	1.06	0.38	0.34	0.28	0.24
62.136	99	1.79	3.58	1.38	1.10	0.38	0.34	0.27	0.22
80.000	100	3.40	4.61	2.34	2.00	1.45	1.39	1.32	1.27
118.947	101	5.74	8.16	3.61	2.08	1.64	1.56	1.17	1.04
117.526	102	3.72	6.82	3.15	2.81	1.12	0.99	0.79	0.65
125.253	104	3.28	5.89	2.90	2.65	1.04	0.93	0.73	0.59
121.429	105	3.91	6.27	3.13	2.86	1.25	1.10	0.87	0.73
127.778	106	3.87	5.77	3.15	2.93	1.56	1.40	1.16	1.03
137.647	107	4.50	6.78	3.71	3.47	1.78	1.60	1.34	1.18
117.895	108	4.87	7.62	4.36	4.19	2.22	2.04	1.76	1.59
121.277	109	5.36	7.57	4.77	4.60	2.93	2.79	2.57	2.41
118.000	110	5.01	7.47	4.24	4.04	2.18	2.00	1.72	1.55
111.385	111	4.03	6.71	3.44	3.26	1.45	1.29	1.04	0.88
109.709	112	5.59	8.83	5.26	5.20	2.98	2.84	2.57	2.39
106.542	113	4.02	6.90	3.75	3.65	1.79	1.67	1.45	1.29
110.377	115	3.45	5.96	3.22	3.09	1.34	1.25	1.04	0.90
122.105	116	3.18	5.77	2.88	2.72	1.05	0.95	0.78	0.65
112.381	117	3.01	5.21	2.67	2.52	1.13	1.04	0.87	0.75
119.000	119	4.45	7.64	3.73	3.36	1.53	1.40	1.18	1.03
112.500	120	3.75	7.11	3.26	2.85	1.05	0.94	0.75	0.61
118.447	121	4.68	8.95	3.80	3.22	1.20	1.06	0.83	0.68

**Appendix - E(b): Band Values Obtained From Spectroradiometer SVC – 1024i for Validation Data Set**

Observed SSC (mg/Litre)	Sample No.	Spectroradiometer Band Values for Validation Data Set							
		Blue	Green	Red	Red Edge 1	Red Edge 2	Red Edge 3	NIR	Red Edge 4
15.957	6	2.87	2.78	1.39	0.83	0.74	0.72	0.58	0.54
23.529	7	1.90	2.32	1.07	0.74	0.55	0.50	0.42	0.39
17.391	19	2.67	2.90	1.45	1.04	0.77	0.69	0.57	0.51
23.656	20	3.11	3.65	1.76	1.25	0.92	0.83	0.68	0.61
15.625	21	1.93	2.55	1.11	0.71	0.45	0.43	0.35	0.31
52.838	30	2.48	2.58	1.48	1.20	0.93	0.84	0.73	0.68
55.828	33	2.65	2.98	1.66	1.32	0.95	0.84	0.73	0.67
56.701	40	3.04	3.95	2.03	1.63	1.04	0.92	0.78	0.70
49.756	41	2.92	3.68	1.93	1.54	0.97	0.86	0.73	0.66
62.366	44	2.60	3.48	1.73	1.38	0.81	0.71	0.60	0.53
62.887	46	2.82	3.38	1.90	1.51	0.92	0.82	0.69	0.63
56.701	49	3.20	3.56	1.95	1.53	1.07	0.95	0.81	0.73
42.927	58	2.21	2.51	1.37	1.09	0.76	0.69	0.60	0.56
64.000	61	1.94	2.30	1.25	1.00	0.66	0.59	0.52	0.48
44.643	67	2.01	2.42	1.35	1.11	0.72	0.64	0.55	0.50
41.000	73	1.69	2.19	1.07	0.84	0.48	0.44	0.39	0.35
62.000	85	1.43	2.74	1.01	0.82	0.29	0.26	0.21	0.18
73.077	94	3.69	5.31	3.56	3.33	2.39	2.32	2.22	2.14
92.233	96	2.01	3.72	1.66	1.48	0.59	0.53	0.45	0.38
115.306	103	3.19	5.58	2.73	2.46	1.04	0.93	0.74	0.62
107.843	118	3.65	6.42	3.20	2.94	1.20	1.09	0.89	0.75

## Appendix - E(c): Band Values Obtained From Sentinel 2 – BOA Satellite Imagery for Calibration Data Set

Observed SSC (mg/Litre)	Sample No.	Sentinel-2 Band Values for Calibration Data Set							
		Blue	Green	Red	Red Edge 1	Red Edge 2	Red Edge 3	NIR	Red Edge 4
22.581	1	4.11	5.03	2.67	2.76	2.49	2.60	2.18	2.06
20.213	2	4.38	4.21	2.98	3.06	2.72	2.89	2.52	2.45
29.508	3	4.68	4.23	3.23	3.41	3.19	3.28	2.74	2.65
27.473	4	4.31	4.70	3.34	3.46	3.49	3.62	3.02	2.95
17.895	5	4.72	4.53	3.26	3.29	3.09	3.00	2.69	2.75
16.842	8	4.81	4.78	3.15	3.21	3.11	3.05	2.55	2.59
24.731	9	4.65	4.69	3.05	3.30	3.20	3.06	2.63	2.60
28.877	10	4.76	4.91	3.12	3.28	2.89	2.75	2.34	2.54
17.204	11	4.55	4.64	3.20	3.28	2.87	2.85	2.47	2.47
15.909	12	4.24	4.27	2.85	2.90	2.62	2.71	2.25	2.24
20.000	13	4.12	4.39	2.90	2.98	2.65	2.71	2.17	2.24
16.842	14	4.23	4.40	2.89	2.96	2.76	2.83	2.43	2.27
19.149	15	4.56	4.22	3.14	3.06	2.79	3.00	2.57	2.51
16.931	16	3.83	3.91	2.96	2.69	2.65	2.64	2.29	2.31
26.316	17	3.82	4.09	2.67	2.74	2.37	2.44	1.98	1.96
25.131	18	3.87	3.98	2.89	2.95	2.69	2.88	2.33	2.35
16.043	23	4.77	4.71	3.41	3.43	2.99	2.93	2.65	2.59
20.942	24	4.57	4.75	3.32	3.56	3.26	3.08	2.56	2.76
23.834	25	4.40	4.62	3.24	3.18	2.79	2.88	2.39	2.50
45.854	26	9.93	10.46	11.34	11.73	13.08	14.13	14.84	14.84
52.326	27	7.97	7.42	5.91	5.86	5.79	5.64	5.07	4.93
47.435	28	7.94	7.56	6.01	6.08	5.75	5.74	5.22	4.77
48.685	32	7.65	7.69	6.71	6.74	6.84	7.01	6.95	6.17
50.682	34	7.77	7.74	5.97	5.99	5.57	5.40	4.85	4.58
52.475	35	7.79	7.84	5.97	6.07	5.92	5.75	4.94	5.00
55.000	36	6.77	6.32	4.82	4.98	4.46	4.46	3.80	3.68
53.045	37	6.92	7.21	5.40	6.09	5.83	5.65	4.52	4.86
52.308	38	7.22	7.04	5.46	5.66	5.62	5.55	5.12	4.88
55.789	39	6.98	7.03	5.11	5.31	4.99	4.90	4.52	4.38
47.668	42	7.41	7.54	6.02	6.32	6.39	6.21	5.83	5.62
52.632	43	7.41	6.92	5.32	5.25	4.92	4.88	4.21	3.99
65.657	47	7.72	7.77	6.00	6.33	6.19	5.85	5.82	5.22
54.271	50	7.77	7.38	6.18	6.15	6.15	6.37	6.12	6.15
64.646	51	7.52	7.14	5.42	5.17	4.62	4.71	4.14	4.01
54.082	53	8.23	7.75	6.39	6.47	7.01	6.80	6.45	5.89
47.000	54	7.73	6.63	5.34	4.93	4.52	4.45	3.87	3.63
56.863	56	5.76	5.95	4.58	4.90	4.22	4.48	3.85	3.69
52.041	59	5.29	5.64	4.41	4.61	4.47	4.10	3.69	3.93
58.252	63	5.96	6.21	4.86	4.73	4.53	4.16	3.89	3.66
63.542	65	5.99	6.20	4.70	5.22	5.32	5.13	4.63	4.68
42.424	68	5.83	6.15	4.48	4.57	4.08	3.98	3.57	3.61
33.000	69	6.50	6.82	5.12	5.13	4.61	4.53	4.07	3.98
57.732	70	6.06	6.92	5.21	5.68	5.53	5.60	4.70	5.12
70.000	71	6.28	7.00	5.37	5.49	4.94	5.06	4.53	4.64

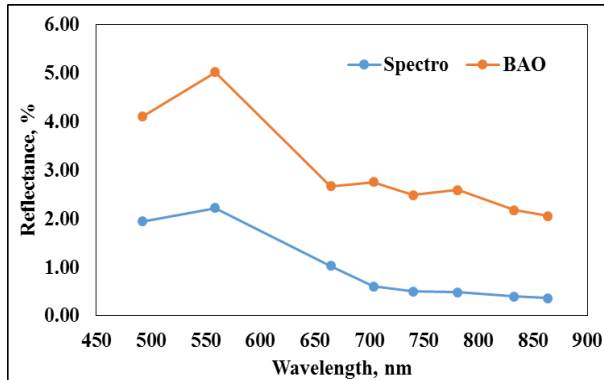
Observed SSC (mg/Litre)	Sample No.	Sentinel-2 Band Values for Calibration Data Set							
		Blue	Green	Red	Red Edge 1	Red Edge 2	Red Edge 3	NIR	Red Edge 4
52.525	72	5.85	6.47	4.92	5.03	4.59	4.34	4.05	4.07
42.424	76	5.50	5.83	4.63	4.43	4.29	4.07	3.77	3.62
59.375	77	5.44	5.24	4.25	3.94	3.82	3.60	3.09	3.15
51.064	78	6.10	6.38	5.15	4.91	4.88	4.66	4.23	4.18
54.082	79	6.66	6.91	5.67	5.99	5.54	5.60	5.76	5.17
47.959	81	5.38	6.09	5.21	4.71	4.68	4.25	6.08	4.55
60.606	82	11.80	12.82	11.13	10.88	10.35	10.55	10.41	10.30
68.367	83	11.23	12.91	11.06	10.83	10.31	10.31	10.31	10.16
64.948	84	11.48	13.04	11.11	10.86	10.32	10.34	10.32	10.37
56.863	86	11.48	13.20	11.23	11.05	10.35	10.38	10.34	10.29
61.458	87	11.50	13.21	11.43	11.17	10.38	10.31	10.42	10.35
65.263	88	11.50	13.45	11.17	11.20	10.29	10.26	10.28	10.17
64.211	89	11.39	13.51	11.41	11.40	10.53	10.58	10.34	10.36
74.227	90	11.29	13.40	11.36	11.22	10.16	10.46	10.36	10.25
78.723	91	11.92	14.01	11.59	11.64	10.58	10.67	10.50	10.48
71.287	92	11.96	13.82	11.60	11.54	10.53	10.50	10.43	10.40
76.923	93	11.63	13.82	11.61	11.66	10.48	10.51	10.52	10.46
77.551	95	11.33	13.10	11.39	11.29	10.27	10.50	10.32	10.12
63.000	97	11.67	13.19	11.40	11.06	10.35	10.33	10.38	10.41
92.308	98	11.23	12.95	11.14	10.98	10.27	10.36	10.28	10.26
62.136	99	11.52	13.13	11.29	10.99	10.19	10.26	10.30	10.16
80.000	100	11.40	12.73	11.00	10.86	10.40	10.44	10.39	10.29
118.947	101	12.64	15.38	12.44	12.36	10.73	10.53	10.53	10.04
117.526	102	12.43	15.21	12.45	12.43	10.46	10.31	9.97	9.81
125.253	104	11.79	14.48	12.15	12.41	9.87	10.12	9.51	9.29
121.429	105	11.06	13.66	11.63	12.19	9.88	10.05	9.70	9.21
127.778	106	11.86	13.70	11.75	11.86	9.65	9.93	9.61	9.29
137.647	107	12.24	14.43	12.41	12.96	10.79	10.75	10.26	10.12
117.895	108	11.79	13.96	11.86	11.94	9.77	9.86	9.39	9.54
121.277	109	11.19	13.20	11.28	11.93	10.06	10.15	9.97	10.07
118.000	110	11.40	14.38	12.45	12.92	10.54	10.57	10.59	10.68
111.385	111	11.77	14.50	11.46	12.78	10.33	10.10	9.77	9.85
109.709	112	12.11	15.11	11.92	11.62	10.22	10.46	10.87	9.34
106.542	113	11.74	14.46	11.62	12.43	9.26	9.82	9.64	9.31
110.377	115	11.26	13.44	11.55	11.93	9.88	9.63	9.61	9.21
122.105	116	11.38	14.00	11.53	11.71	10.12	10.34	9.41	9.16
112.381	117	11.28	13.93	11.96	12.13	9.98	9.98	9.54	9.12
119.000	119	11.44	14.50	11.86	11.73	9.42	9.00	8.93	8.72
112.500	120	12.41	15.06	12.53	12.38	9.73	10.48	10.17	9.61
118.447	121	13.27	15.79	13.33	13.24	11.59	11.38	11.14	11.11

**Appendix - E(d): Band Values Obtained From Sentinel 2 – BOA Satellite Imagery for Validation Data Set**

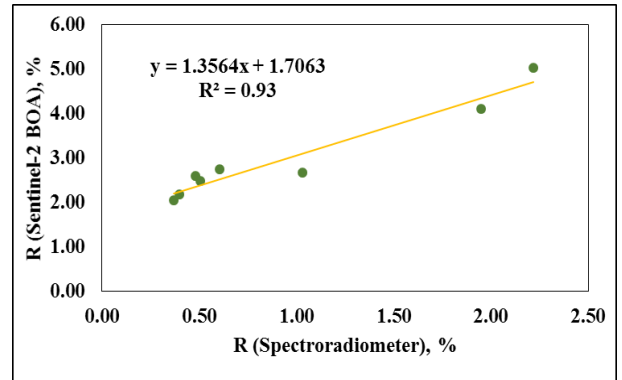
<b>Observed SSC (mg/Litre)</b>	<b>Sample No.</b>	<b>Blue</b>	<b>Green</b>	<b>Red</b>	<b>Red Edge 1</b>	<b>Red Edge 2</b>	<b>Red Edge 3</b>	<b>NIR</b>	<b>Red Edge 4</b>
15.957	6	4.72	4.53	3.26	3.29	3.09	3.00	2.69	2.75
23.529	7	4.44	4.83	3.14	3.20	2.83	2.89	2.44	2.43
17.391	19	4.00	4.11	2.73	2.79	2.41	2.51	2.02	2.08
23.656	20	4.13	4.34	3.07	3.02	2.63	2.83	2.11	2.40
15.625	21	4.28	4.30	3.09	2.98	2.52	2.55	2.03	2.05
52.838	30	7.87	7.29	5.84	5.78	5.52	5.55	4.77	4.72
55.828	33	8.83	8.52	6.68	6.77	6.80	6.83	6.22	5.95
56.701	40	6.49	6.79	5.04	5.26	4.93	4.94	4.52	4.36
49.756	41	6.91	6.89	4.96	5.22	4.85	4.58	4.23	4.15
62.366	44	7.57	7.72	5.91	5.87	5.54	5.53	4.91	4.55
62.887	46	7.56	7.16	5.33	5.28	4.61	4.56	4.03	3.88
56.701	49	7.09	6.62	5.36	5.34	4.63	4.77	4.33	4.38
42.927	58	6.02	5.99	4.77	4.76	4.79	4.46	4.20	4.38
64.000	61	5.64	5.95	4.70	4.74	4.65	4.46	4.19	4.17
44.643	67	5.89	6.09	4.56	4.38	4.20	4.02	3.75	3.36
41.000	73	5.99	6.37	5.54	6.14	6.83	6.85	5.73	6.86
62.000	85	11.41	13.16	11.22	10.98	10.31	10.43	10.33	10.25
73.077	94	11.85	14.07	11.81	11.67	10.68	10.91	10.92	10.57
92.233	96	11.84	13.04	11.37	11.34	10.56	10.44	10.61	10.44
115.306	103	12.71	15.06	12.20	12.48	9.98	10.32	9.65	9.44
107.843	118	11.60	13.74	11.67	11.90	9.77	9.69	9.55	9.31

Appendix - F

Comparison of Spectral Signatures obtained by Spectroradiometer SVC HR – 1024i and Sentinel - 2 Satellite data

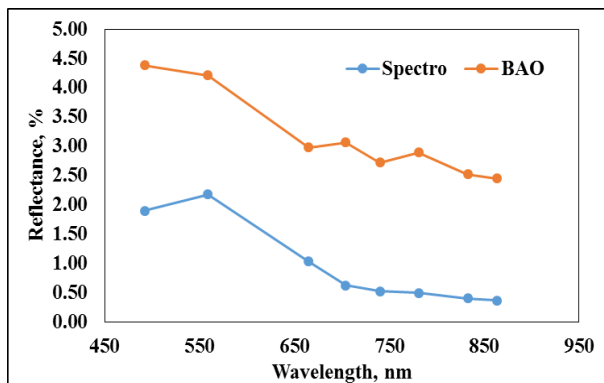


a)

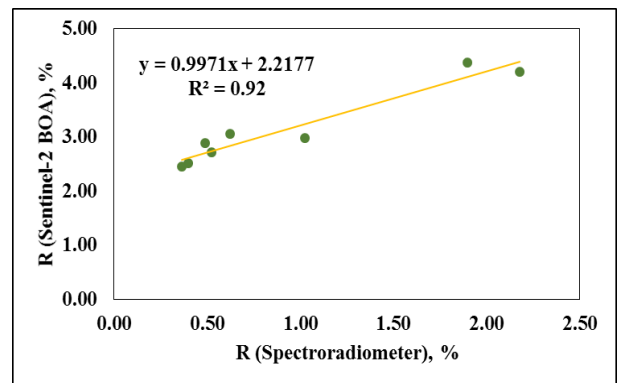


b)

Fig. F-1: a) Spectral Signatures Obtained from Spectroradiometer SVC-1024i & Sentinel-2 BOA Image and b) linear relation between band values for sample 1 having SSC

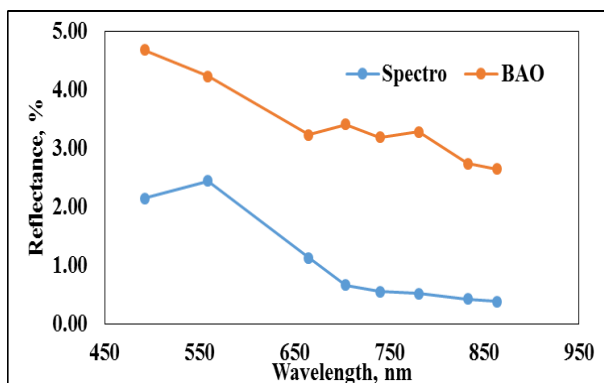


a)

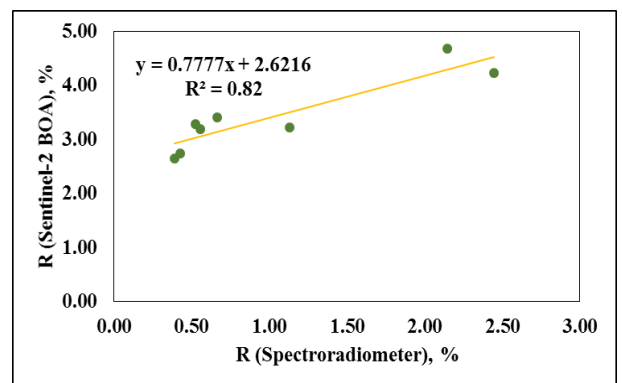


b)

Fig. F -2: a) Spectral Signatures Obtained from Spectroradiometer SVC-1024i & Sentinel-2 BOA Image and b) linear relation between band values for sample 2 having SSC



a)



b)

Fig. F -3: a) Spectral Signatures Obtained from Spectroradiometer SVC-1024i & Sentinel-2 BOA Image and b) linear relation between band values for sample 3 having SSC

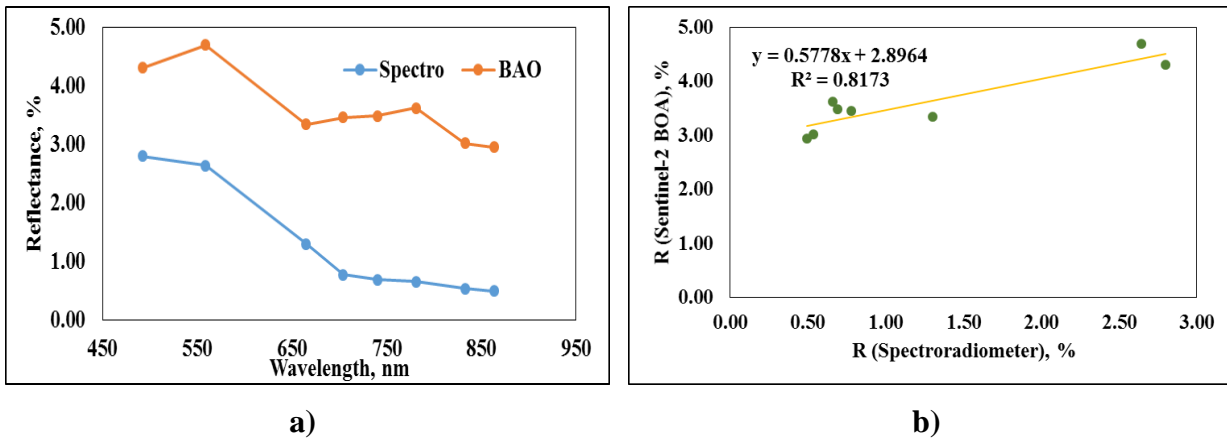


**Fig. F-4: a) Spectral Signatures Obtained from Spectroradiometer SVC-1024i & Sentinel-2 BOA Image and b) linear relation between band values for sample 4 having SSC**

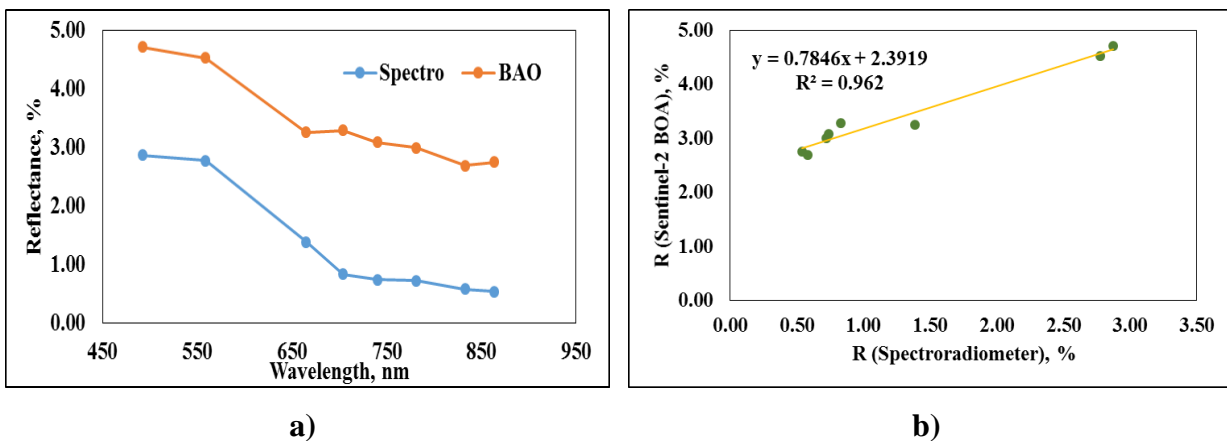


**Fig. F-5: a) Spectral Signatures Obtained from Spectroradiometer SVC-1024i & Sentinel-2 BOA Image and b) linear relation between band values for sample 5 having SSC**

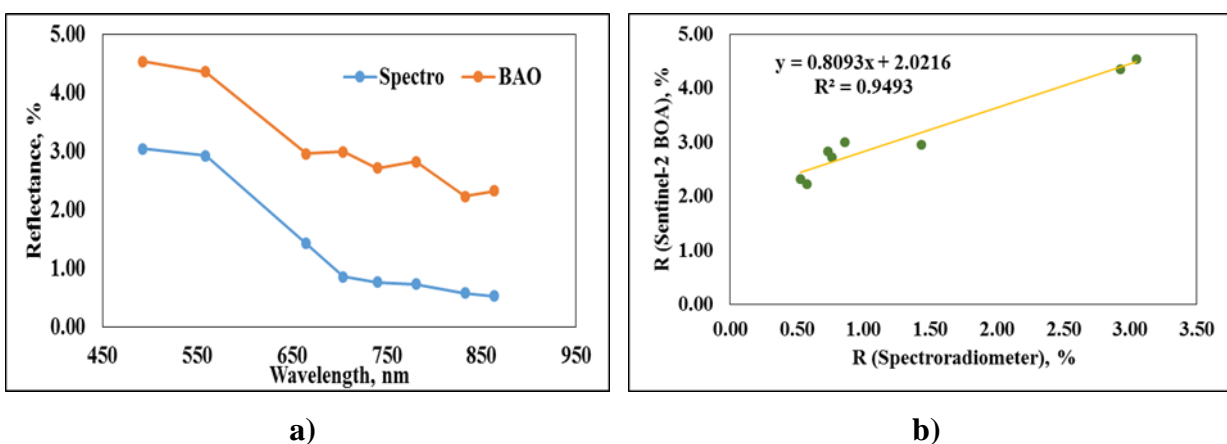
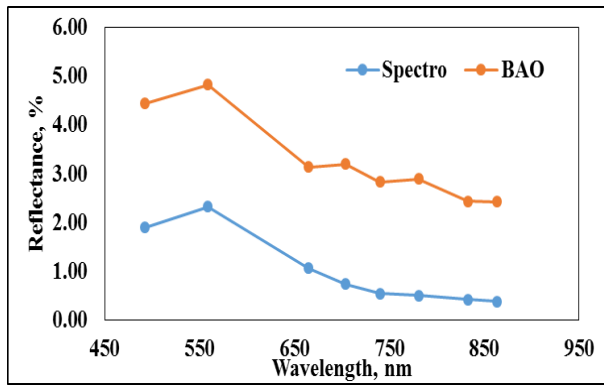
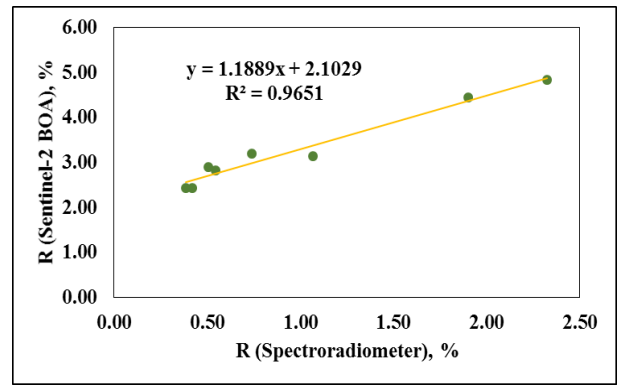


**Fig. F-6: a) Spectral Signatures Obtained from Spectroradiometer SVC-1024i & Sentinel-2 BOA Image and b) linear relation between band values for sample 6 having SSC**

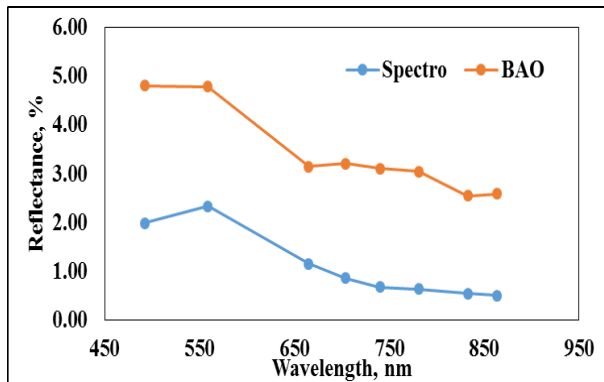


0a)

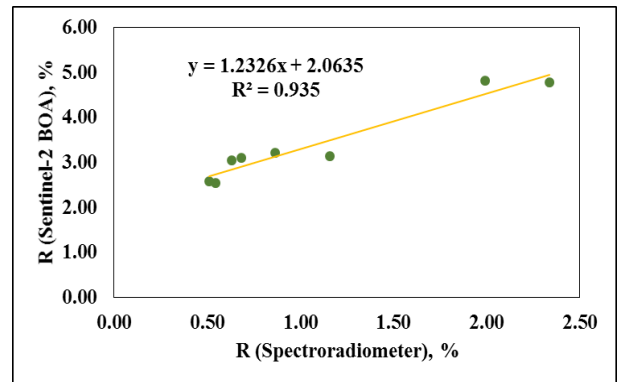


b)

**Fig. F -7: a) Spectral Signatures Obtained from Spectroradiometer SVC-1024i & Sentinel-2 BOA Image and b) linear relation between band values for sample 7 having SSC**

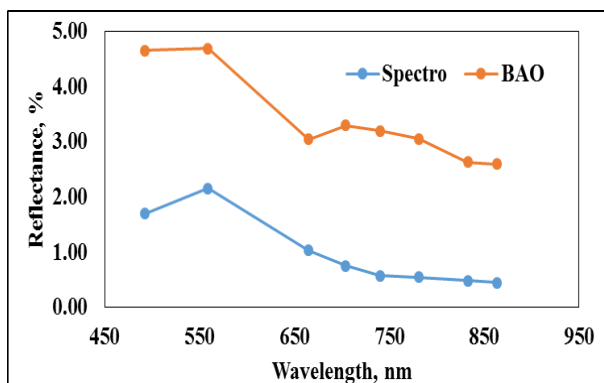


a)

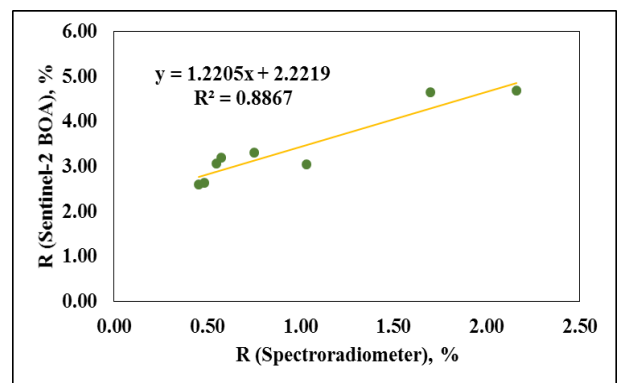


b)

**Fig. F -8: a) Spectral Signatures Obtained from Spectroradiometer SVC-1024i & Sentinel-2 BOA Image and b) linear relation between band values for sample 8 having SSC**



a)



b)

**Fig. F -9: a) Spectral Signatures Obtained from Spectroradiometer SVC-1024i & Sentinel-2 BOA Image and b) linear relation between band values for sample 9 having SSC**

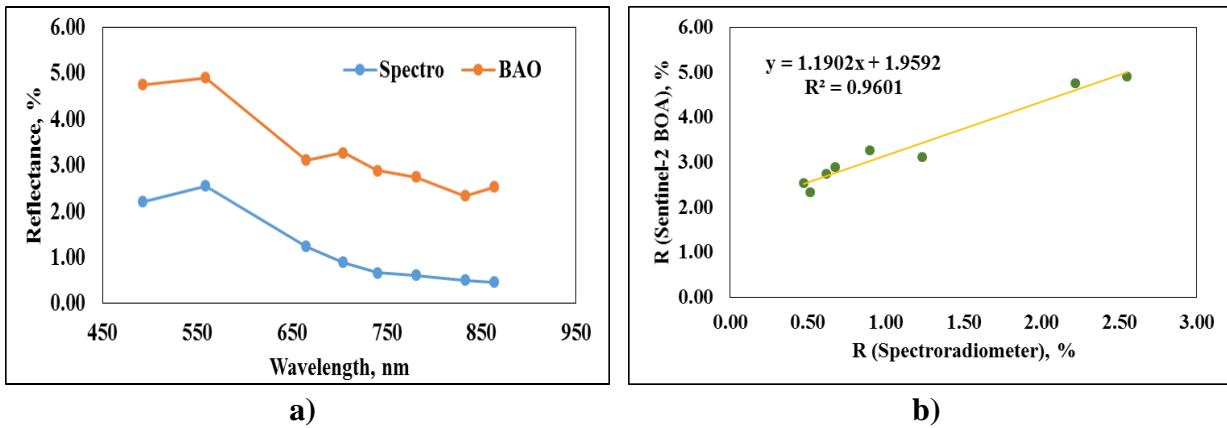


**Fig. F-10: a) Spectral Signatures Obtained from Spectroradiometer SVC-1024i & Sentinel-2 BOA Image and b) linear relation between band values for sample 10 having SSC**

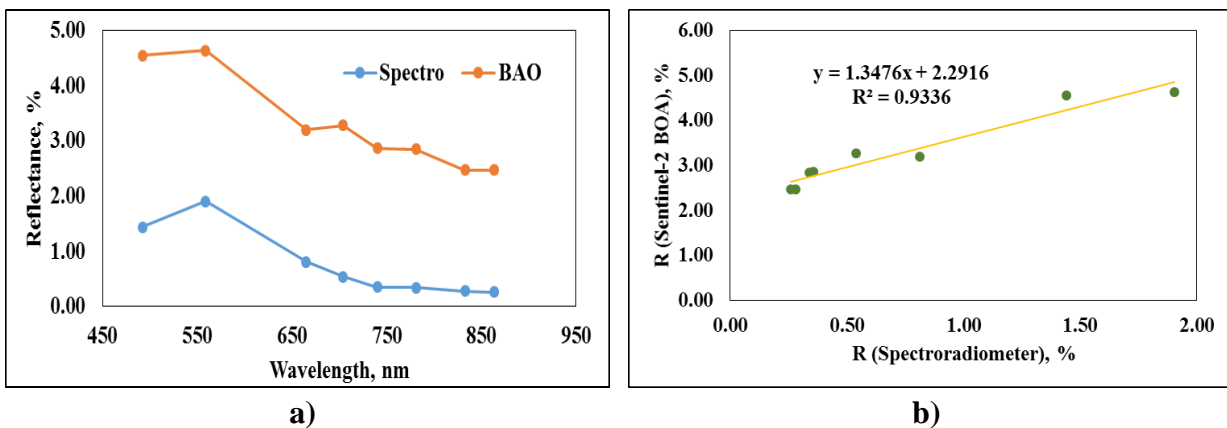


**Fig. F-11: a) Spectral Signatures Obtained from Spectroradiometer SVC-1024i & Sentinel-2 BOA Image and b) linear relation between band values for sample 11 having SSC**

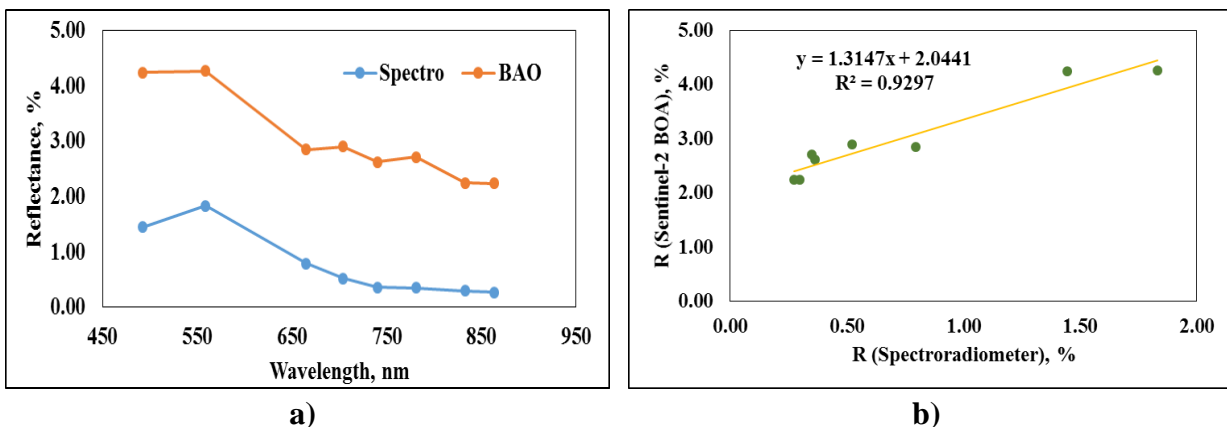


**Fig. F-12: a) Spectral Signatures Obtained from Spectroradiometer SVC-1024i & Sentinel-2 BOA Image and b) linear relation between band values for sample 12 having SSC**

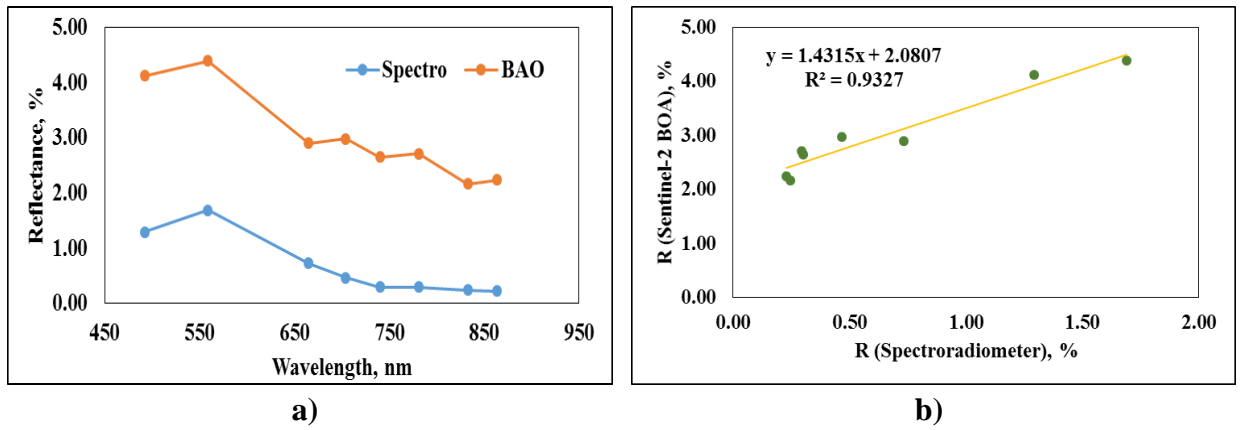


**Fig. F-13: a) Spectral Signatures Obtained from Spectroradiometer SVC-1024i & Sentinel-2 BOA Image and b) linear relation between band values for sample 13 having SSC**

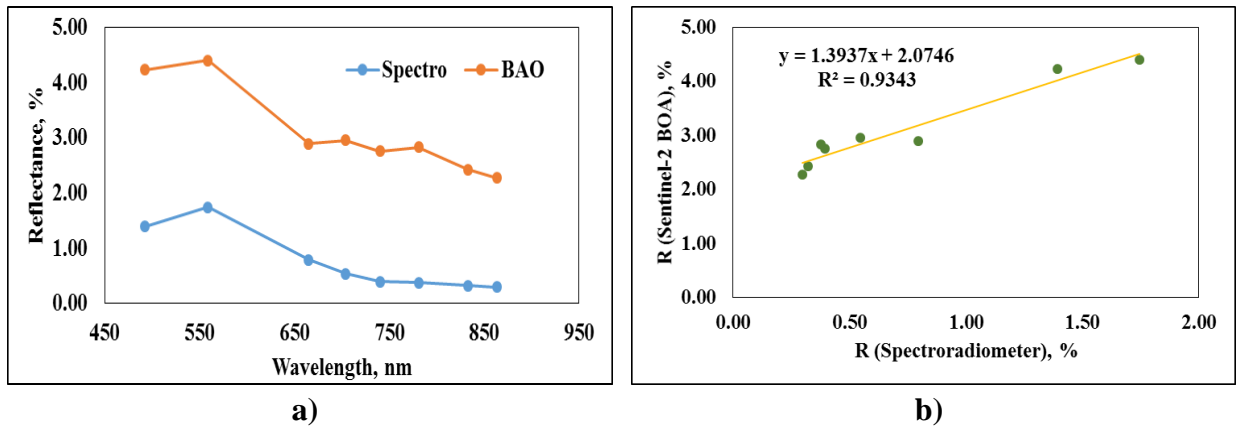


**Fig. F-14: a) Spectral Signatures Obtained from Spectroradiometer SVC-1024i & Sentinel-2 BOA Image and b) linear relation between band values for sample 14 having SSC**

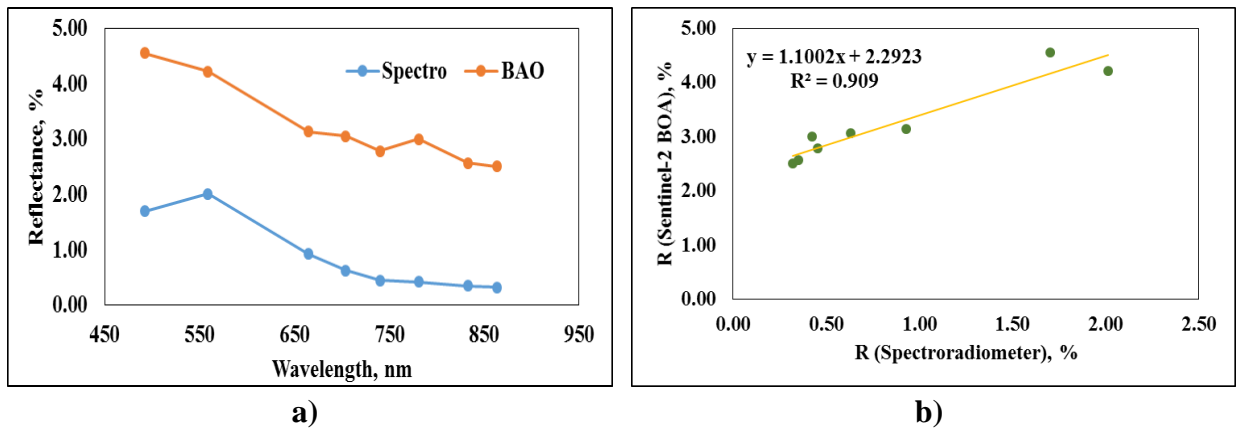


**Fig. F-15: a) Spectral Signatures Obtained from Spectroradiometer SVC-1024i & Sentinel-2 BOA Image and b) linear relation between band values for sample 15 having SSC**

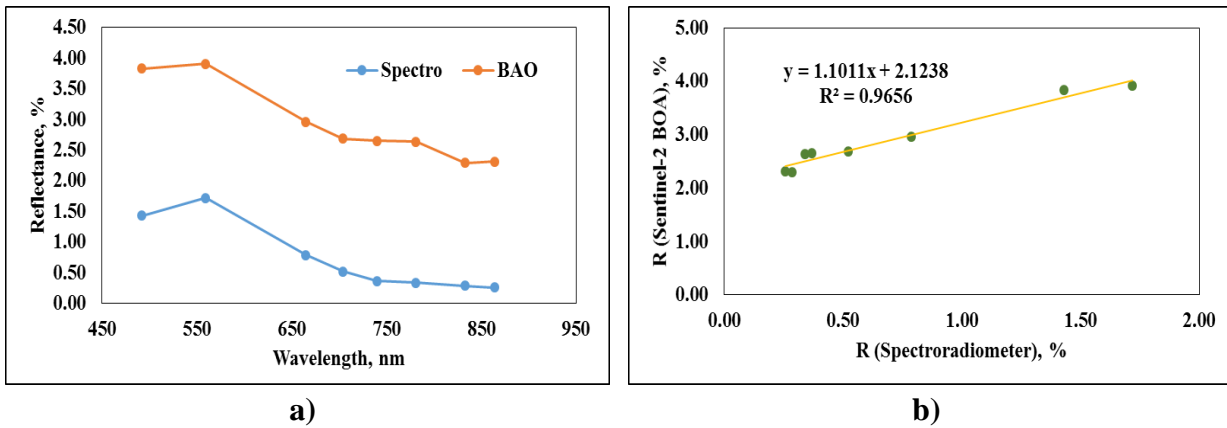


**Fig. F-16: a) Spectral Signatures Obtained from Spectroradiometer SVC-1024i & Sentinel-2 BOA Image and b) linear relation between band values for sample 16 having SSC**

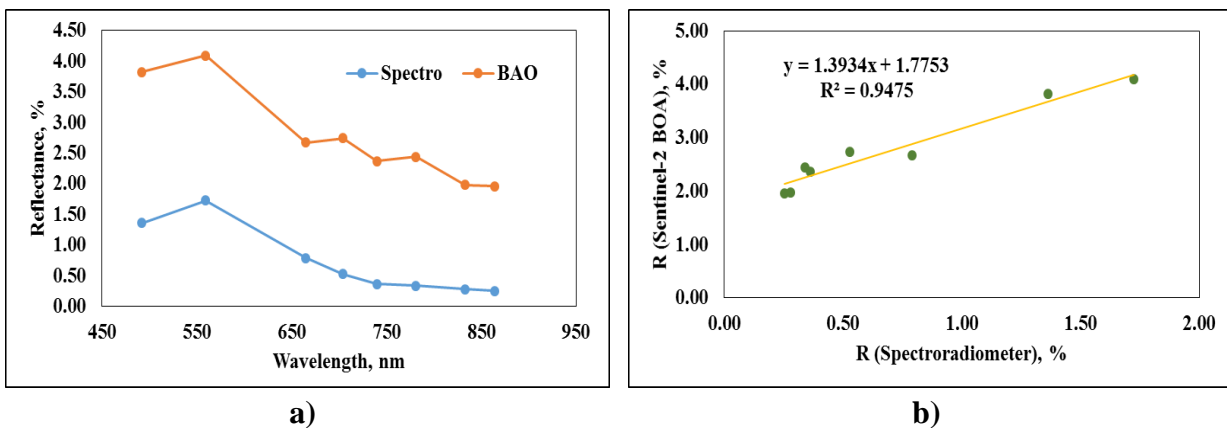


**Fig. F-17: a) Spectral Signatures Obtained from Spectroradiometer SVC-1024i & Sentinel-2 BOA Image and b) linear relation between band values for sample 17 having SSC**

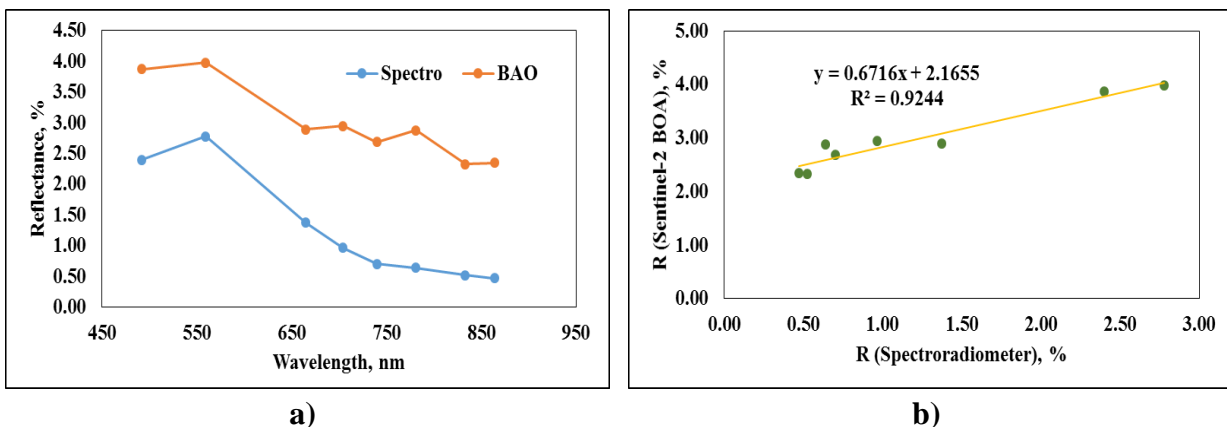
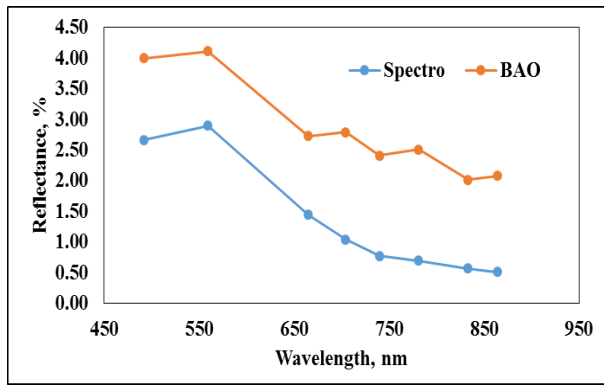
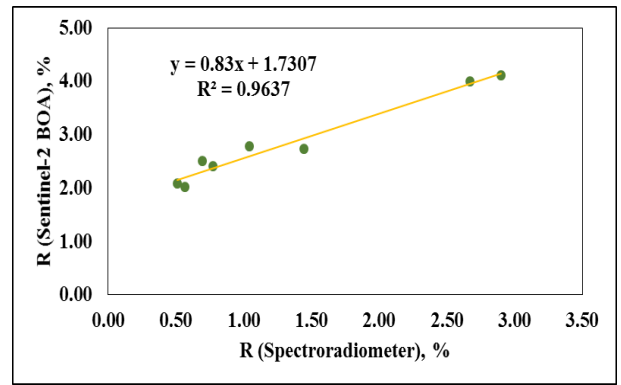


**Fig. F-18: a) Spectral Signatures Obtained from Spectroradiometer SVC-1024i & Sentinel-2 BOA Image and b) linear relation between band values for sample 18 having SSC**

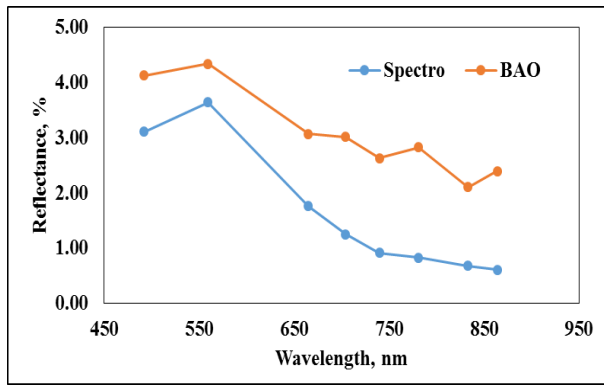


a)

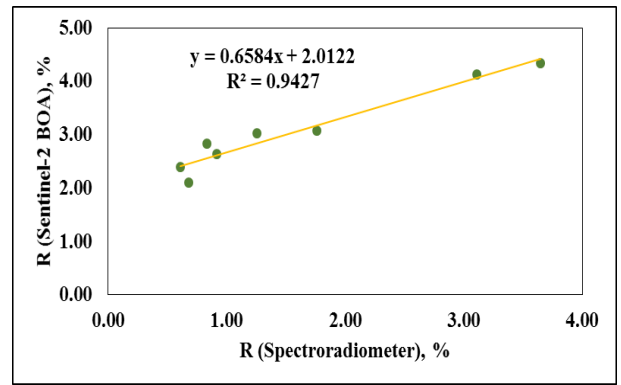


b)

**Fig. F-19: a) Spectral Signatures Obtained from Spectroradiometer SVC-1024i & Sentinel-2 BOA Image and b) linear relation between band values for sample 19 having SSC**

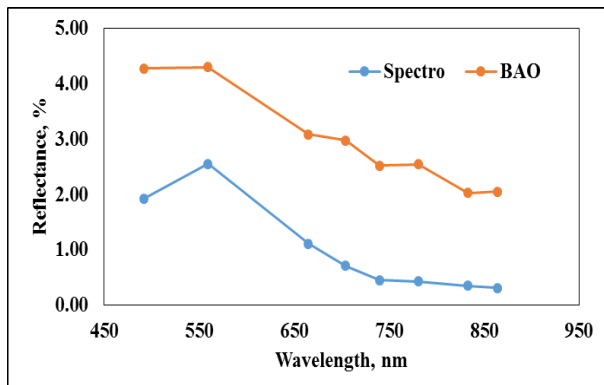


a)

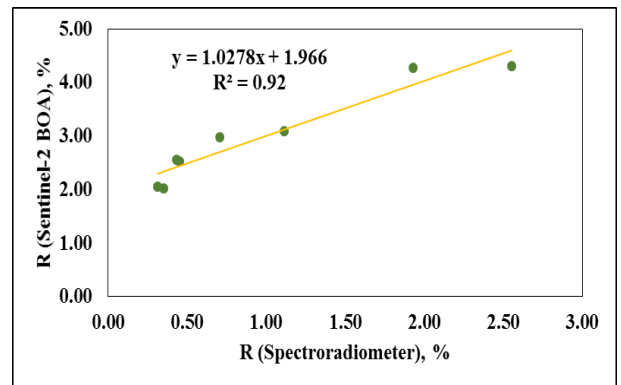


b)

**Fig. F-20: a) Spectral Signatures Obtained from Spectroradiometer SVC-1024i & Sentinel-2 BOA Image and b) linear relation between band values for sample 20 having SSC**



a)



b)

**Fig. F-21: a) Spectral Signatures Obtained from Spectroradiometer SVC-1024i & Sentinel-2 BOA Image and b) linear relation between band values for sample 21 having SSC**

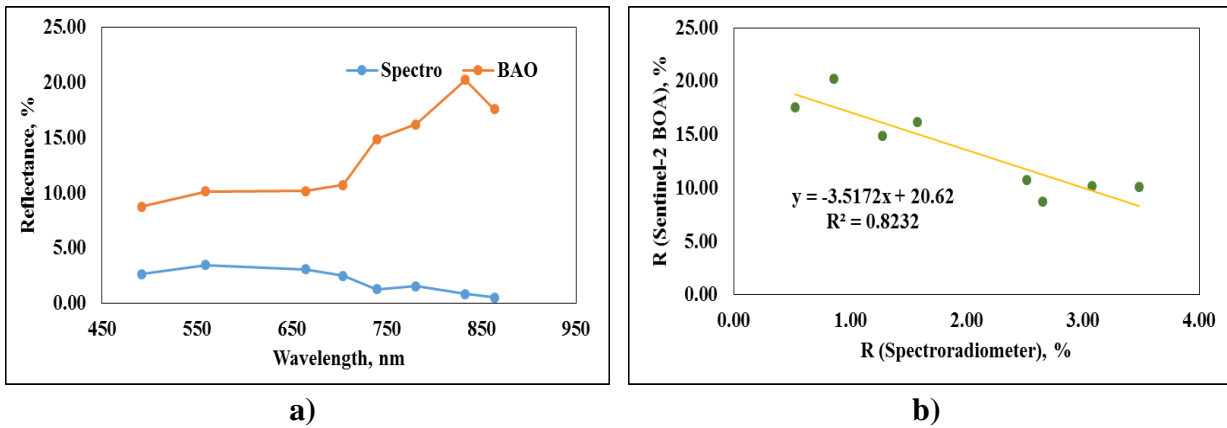


**Fig. F-22: a) Spectral Signatures Obtained from Spectroradiometer SVC-1024i & Sentinel-2 BOA Image and b) linear relation between band values for sample 22 having SSC**

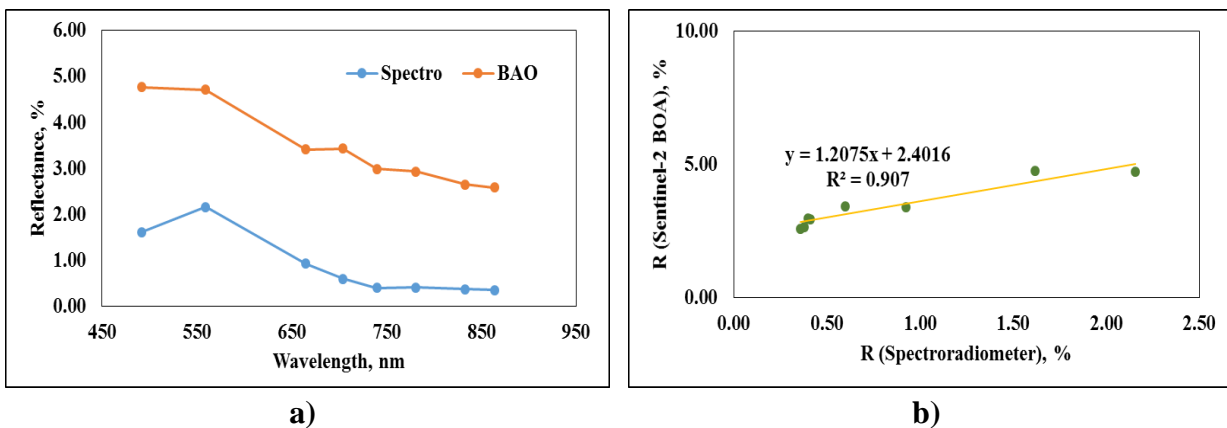


**Fig. F-23: a) Spectral Signatures Obtained from Spectroradiometer SVC-1024i & Sentinel-2 BOA Image and b) linear relation between band values for sample 23 having SSC**

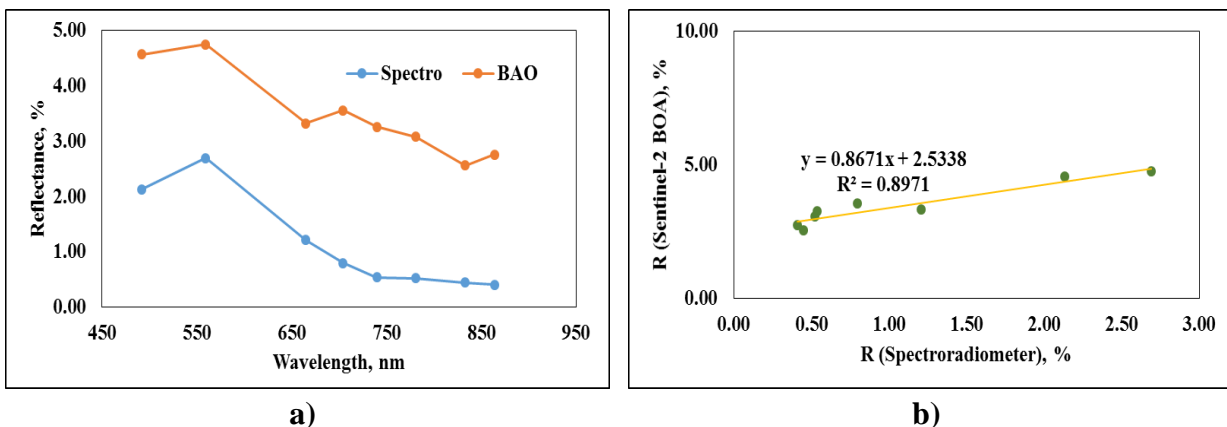
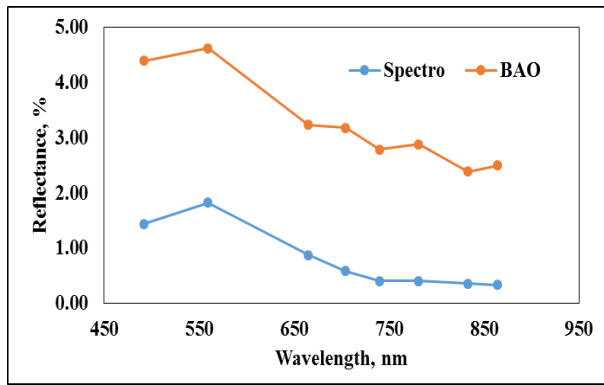
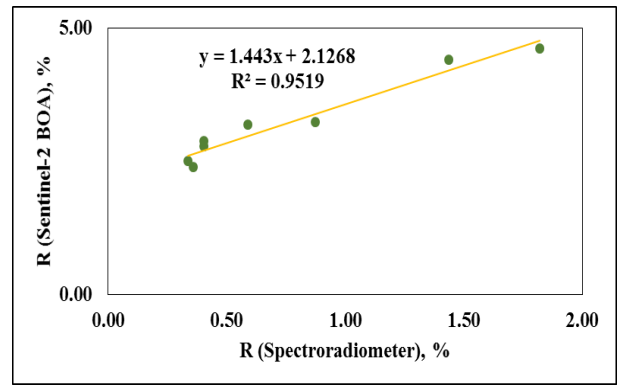


**Fig. F-24: a) Spectral Signatures Obtained from Spectroradiometer SVC-1024i & Sentinel-2 BOA Image and b) linear relation between band values for sample 24 having SSC**

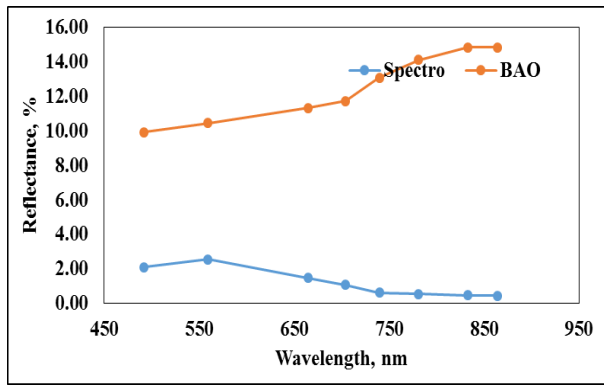


a)

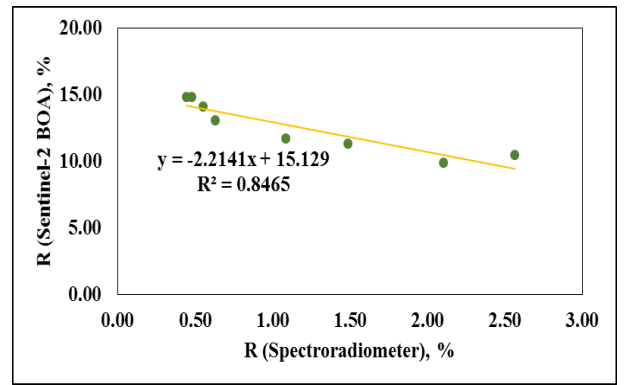


b)

**Fig. F-25: a) Spectral Signatures Obtained from Spectroradiometer SVC-1024i & Sentinel-2 BOA Image and b) linear relation between band values for sample 25 having SSC**

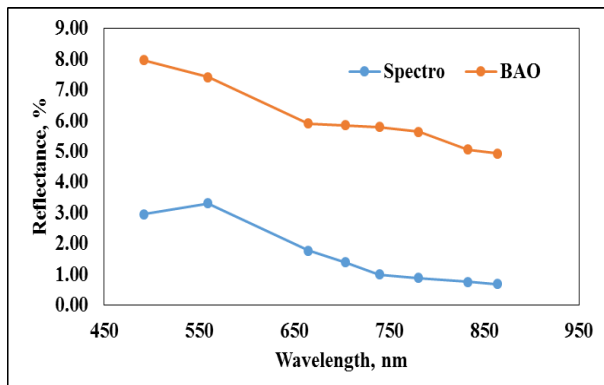


a)

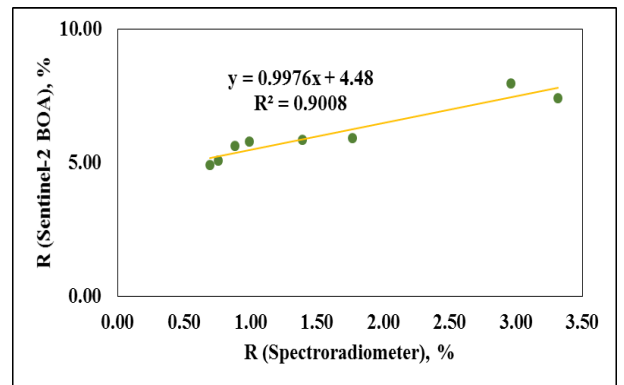


b)

**Fig. F-26: a) Spectral Signatures Obtained from Spectroradiometer SVC-1024i & Sentinel-2 BOA Image and b) linear relation between band values for sample 26 having SSC**



a)



b)

**Fig. F-27: a) Spectral Signatures Obtained from Spectroradiometer SVC-1024i & Sentinel-2 BOA Image and b) linear relation between band values for sample 27 having SSC**

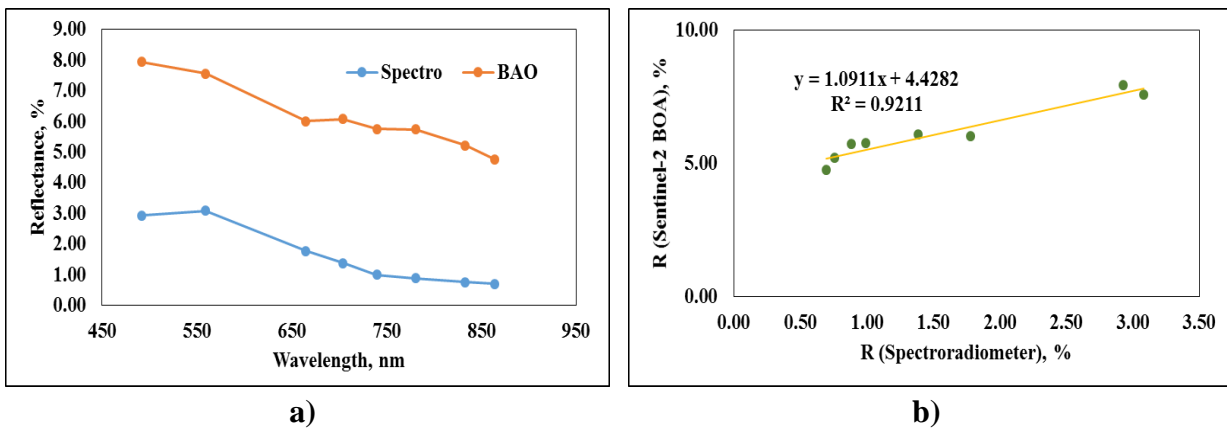


**Fig. F-28: a) Spectral Signatures Obtained from Spectroradiometer SVC-1024i & Sentinel-2 BOA Image and b) linear relation between band values for sample 28 having SSC**

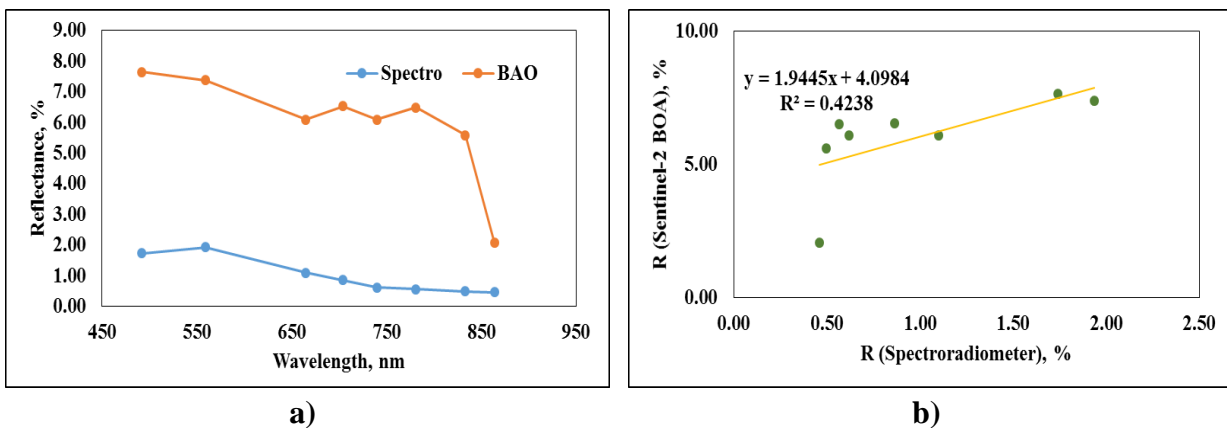


**Fig. F-29: a) Spectral Signatures Obtained from Spectroradiometer SVC-1024i & Sentinel-2 BOA Image and b) linear relation between band values for sample 29 having SSC**

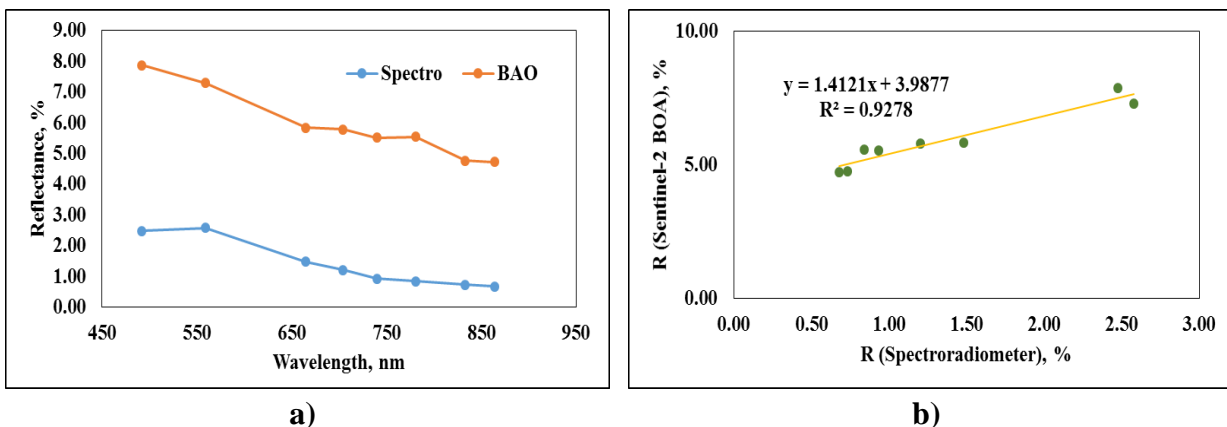
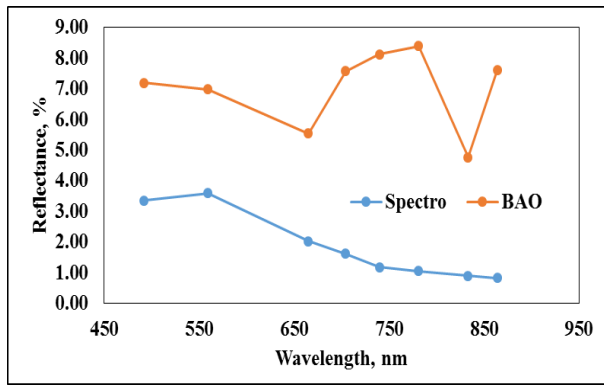
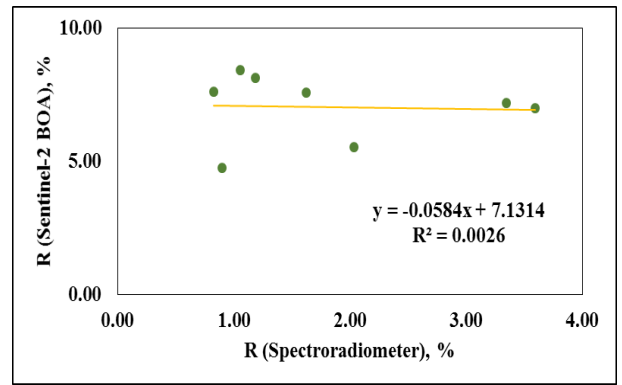


**Fig. F-30: a) Spectral Signatures Obtained from Spectroradiometer SVC-1024i & Sentinel-2 BOA Image and b) linear relation between band values for sample 30 having SSC**

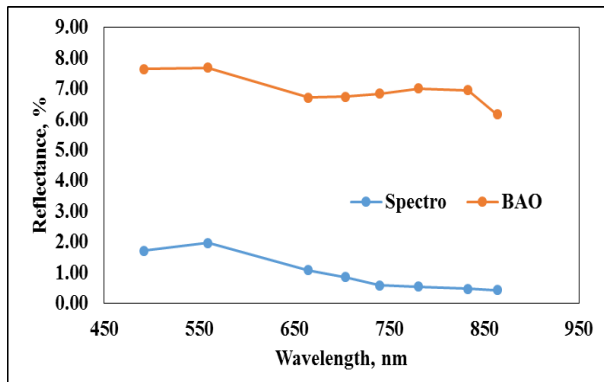


a)

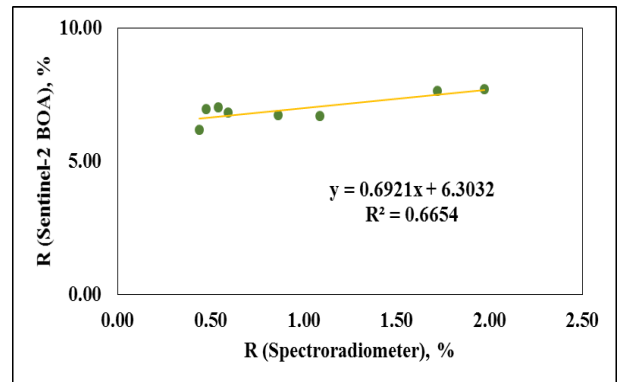


b)

**Fig. F-31: a) Spectral Signatures Obtained from Spectroradiometer SVC-1024i & Sentinel-2 BOA Image and b) linear relation between band values for sample 31 having SSC**

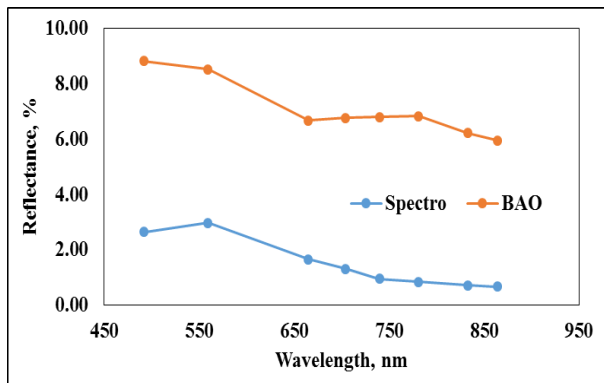


a)

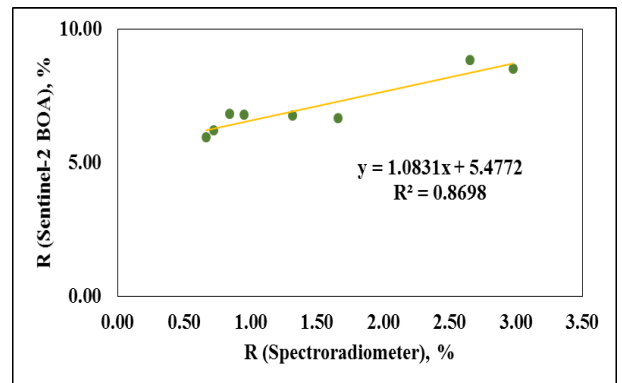


b)

**Fig. F-32: a) Spectral Signatures Obtained from Spectroradiometer SVC-1024i & Sentinel-2 BOA Image and b) linear relation between band values for sample 32 having SSC**



a)



b)

**Fig. F-33: a) Spectral Signatures Obtained from Spectroradiometer SVC-1024i & Sentinel-2 BOA Image and b) linear relation between band values for sample 33 having SSC**

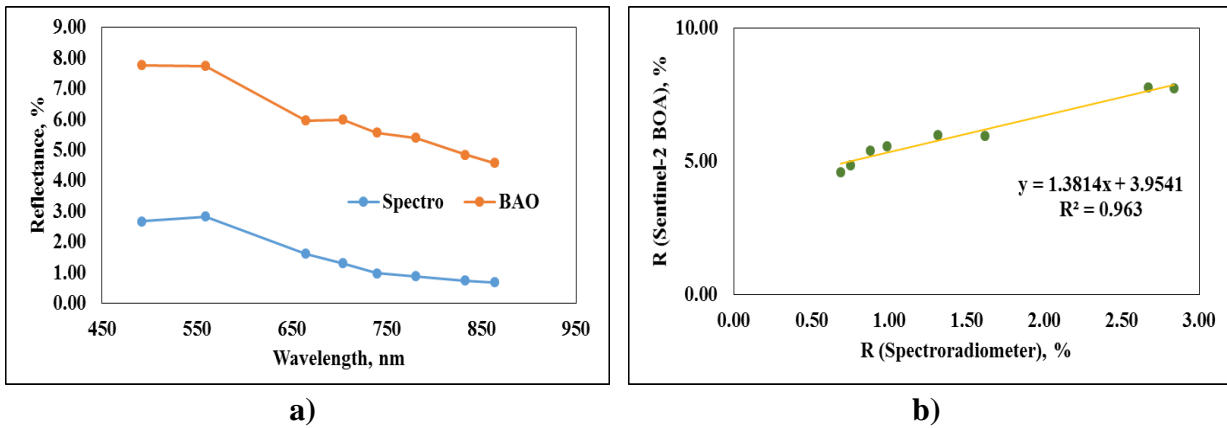


**Fig. F-34: a) Spectral Signatures Obtained from Spectroradiometer SVC-1024i & Sentinel-2 BOA Image and b) linear relation between band values for sample 34 having SSC**

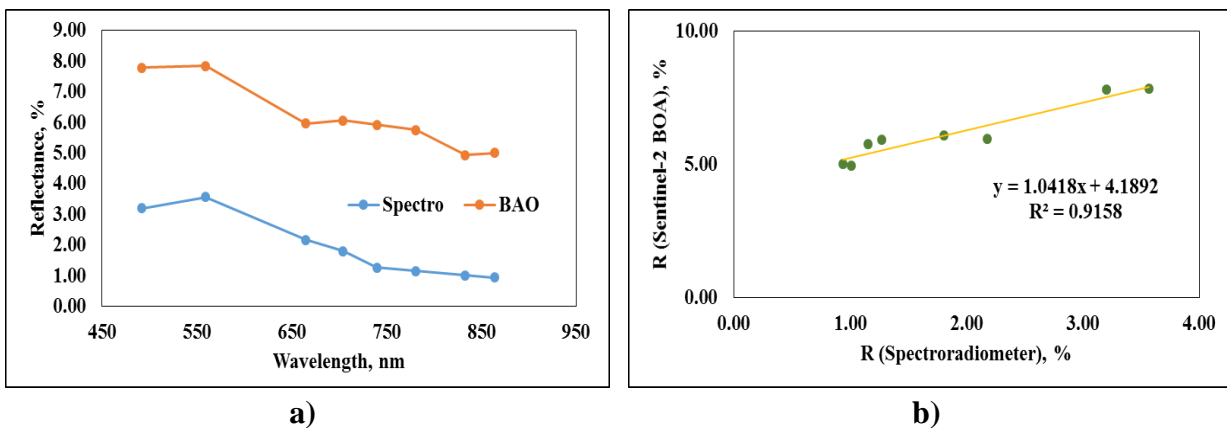


**Fig. F-35: a) Spectral Signatures Obtained from Spectroradiometer SVC-1024i & Sentinel-2 BOA Image and b) linear relation between band values for sample 35 having SSC**

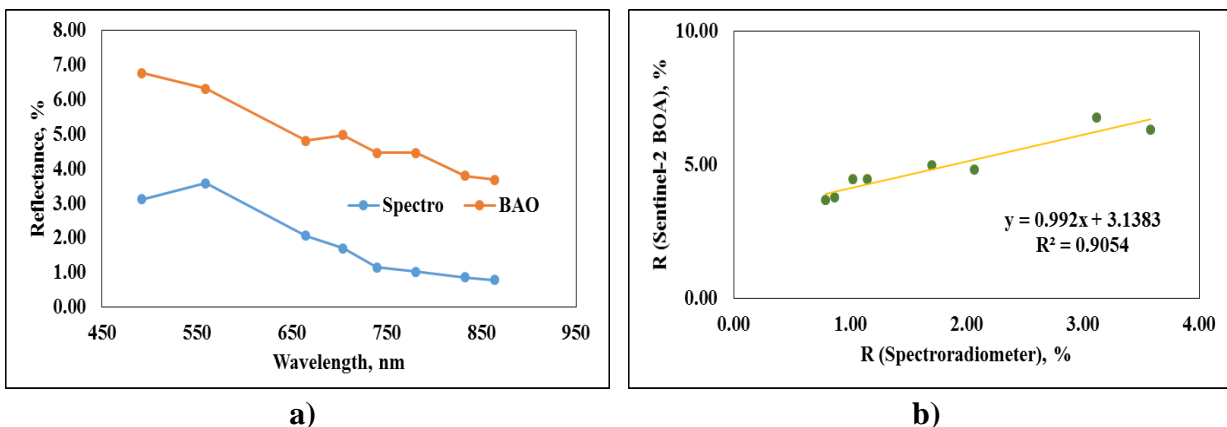


**Fig. F-36: a) Spectral Signatures Obtained from Spectroradiometer SVC-1024i & Sentinel-2 BOA Image and b) linear relation between band values for sample 36 having SSC**

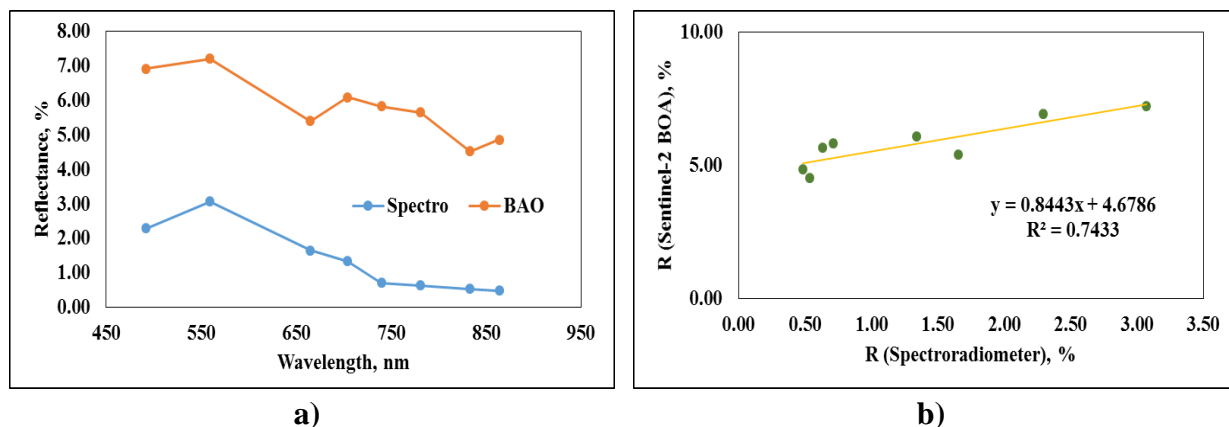


**Fig. F-37: a) Spectral Signatures Obtained from Spectroradiometer SVC-1024i & Sentinel-2 BOA Image and b) linear relation between band values for sample 37 having SSC**

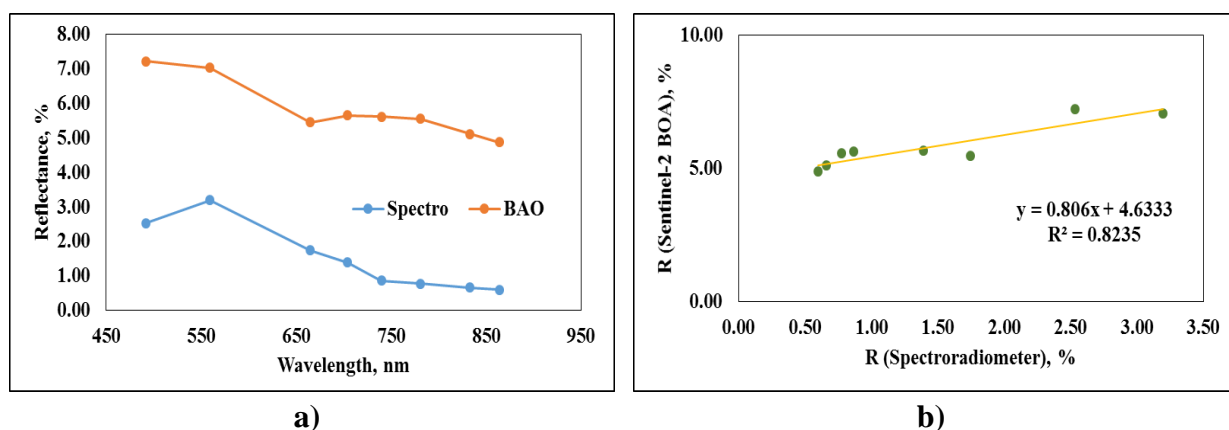


**Fig. F-38: a) Spectral Signatures Obtained from Spectroradiometer SVC-1024i & Sentinel-2 BOA Image and b) linear relation between band values for sample 38 having SSC**

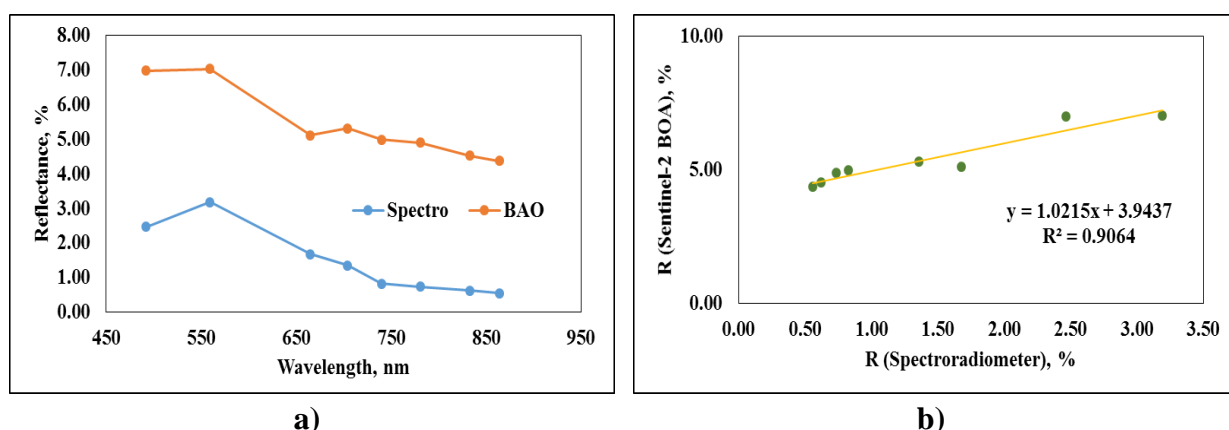


**Fig. F-39: a) Spectral Signatures Obtained from Spectroradiometer SVC-1024i & Sentinel-2 BOA Image and b) linear relation between band values for sample 39 having SSC**

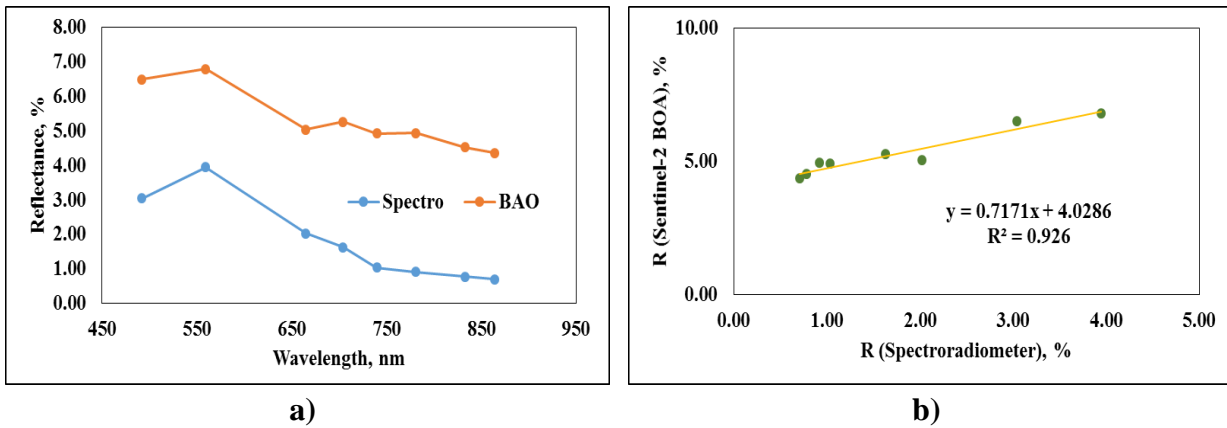


**Fig. F-40: a) Spectral Signatures Obtained from Spectroradiometer SVC-1024i & Sentinel-2 BOA Image and b) linear relation between band values for sample 40 having SSC**

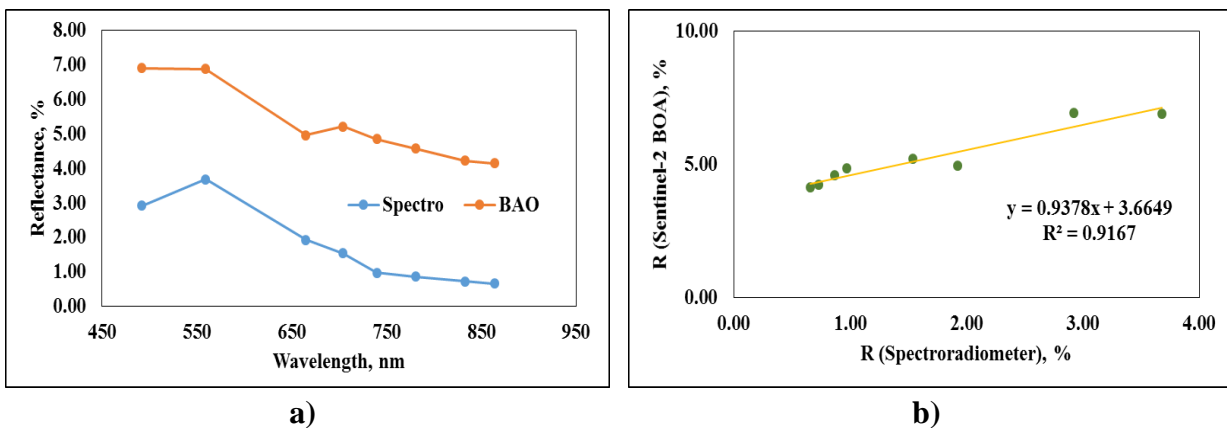


**Fig. F-41: a) Spectral Signatures Obtained from Spectroradiometer SVC-1024i & Sentinel-2 BOA Image and b) linear relation between band values for sample 41 having SSC**

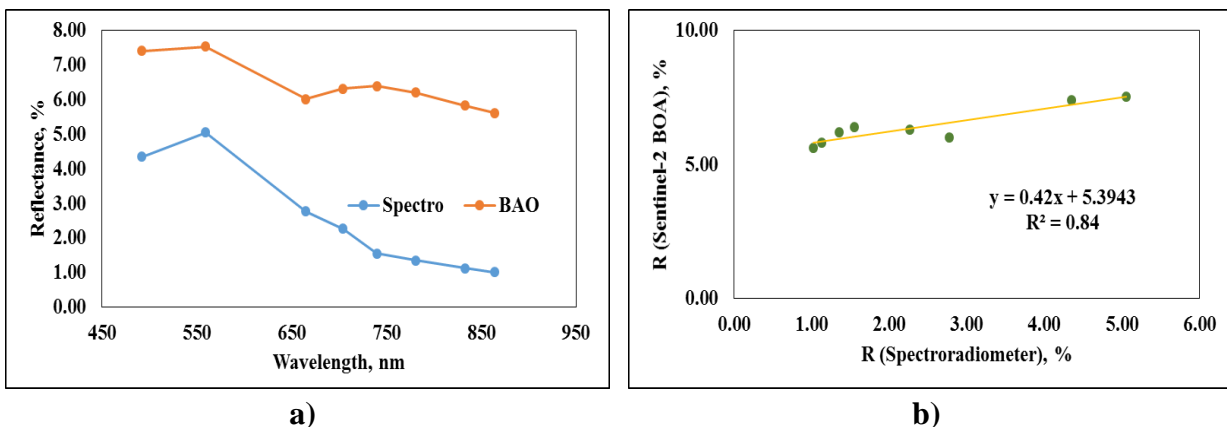
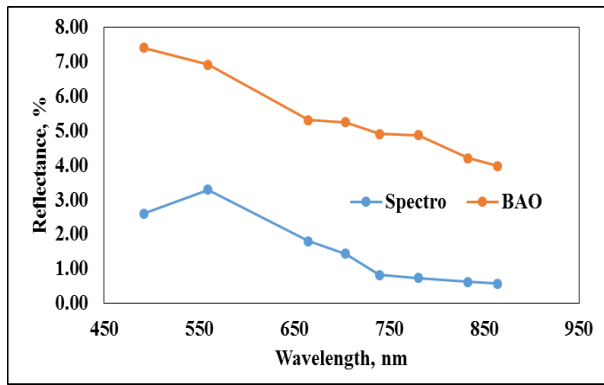
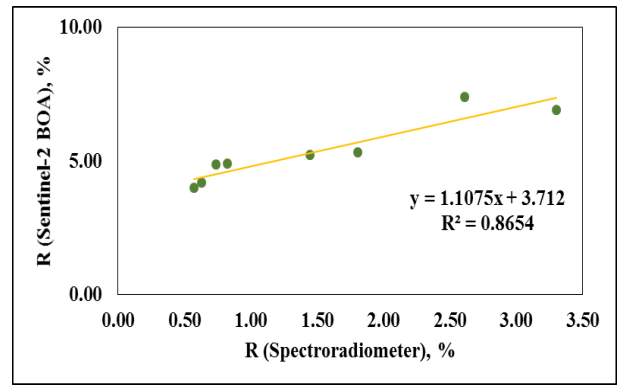


**Fig. F-42: a) Spectral Signatures Obtained from Spectroradiometer SVC-1024i & Sentinel-2 BOA Image and b) linear relation between band values for sample 42 having SSC**

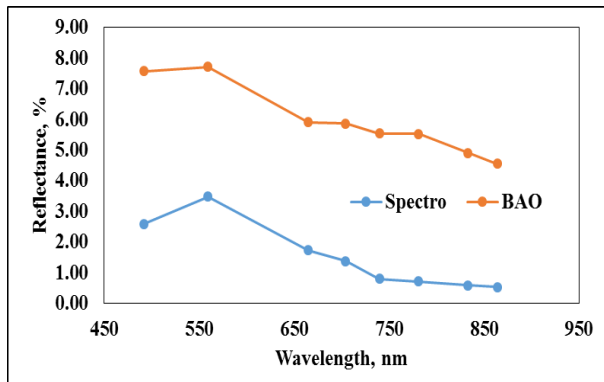


a)

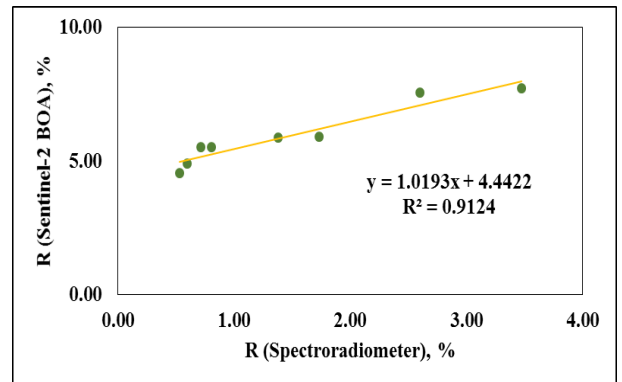


b)

**Fig. F-43: a) Spectral Signatures Obtained from Spectroradiometer SVC-1024i & Sentinel-2 BOA Image and b) linear relation between band values for sample 43 having SSC**

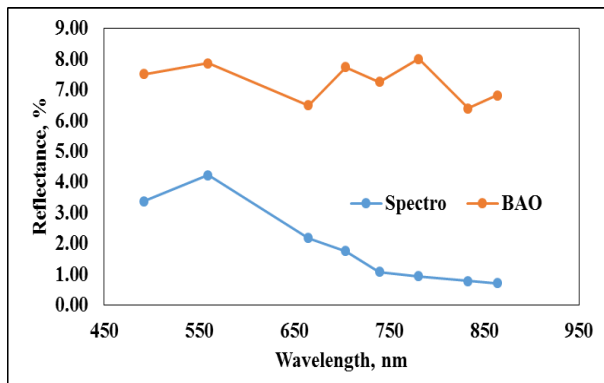


a)

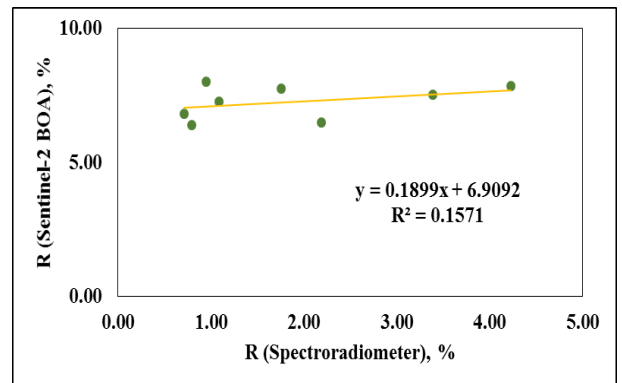


b)

**Fig. F-44: a) Spectral Signatures Obtained from Spectroradiometer SVC-1024i & Sentinel-2 BOA Image and b) linear relation between band values for sample 44 having SSC**



a)



b)

**Fig. F-45: a) Spectral Signatures Obtained from Spectroradiometer SVC-1024i & Sentinel-2 BOA Image and b) linear relation between band values for sample 45 having SSC**

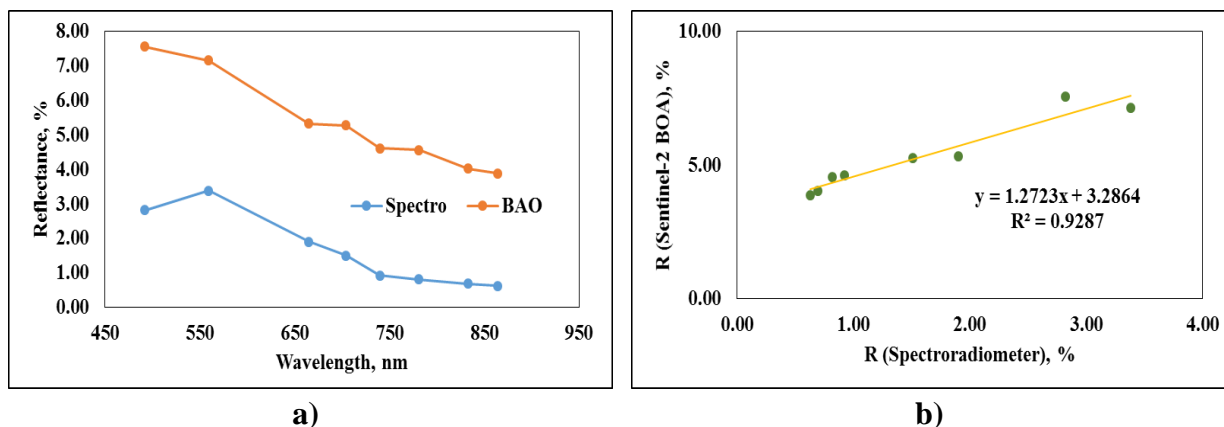


**Fig. F-46: a) Spectral Signatures Obtained from Spectroradiometer SVC-1024i & Sentinel-2 BOA Image and b) linear relation between band values for sample 46 having SSC**

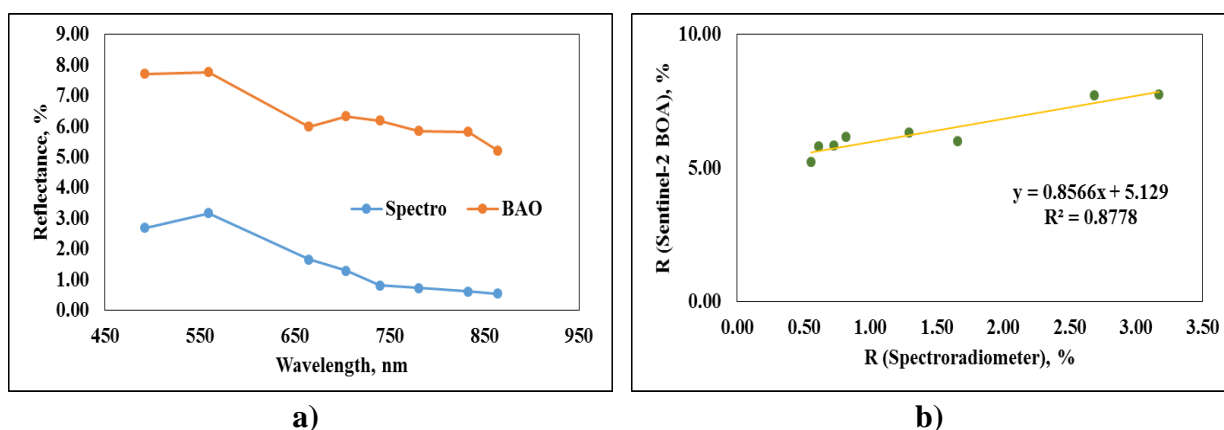


**Fig. F-47: a) Spectral Signatures Obtained from Spectroradiometer SVC-1024i & Sentinel-2 BOA Image and b) linear relation between band values for sample 47 having SSC**

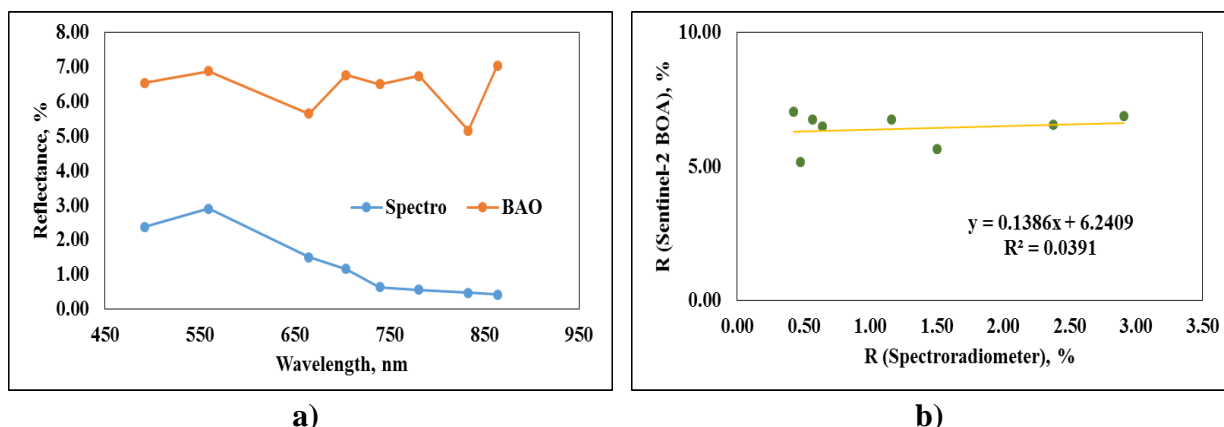
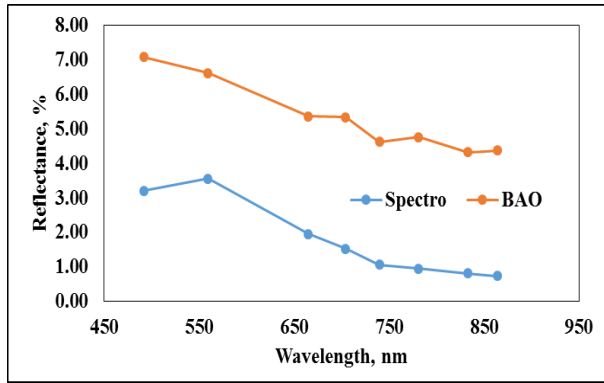
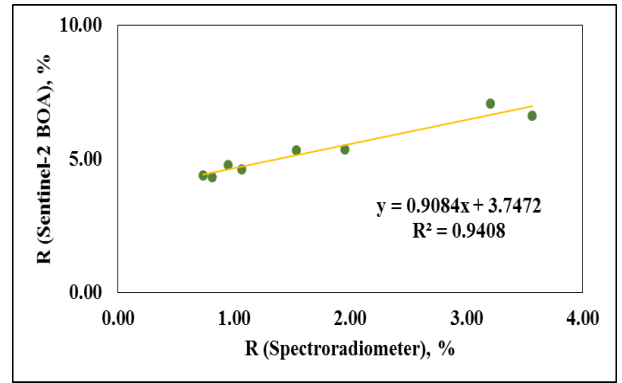


**Fig. F-48: a) Spectral Signatures Obtained from Spectroradiometer SVC-1024i & Sentinel-2 BOA Image and b) linear relation between band values for sample 48 having SSC**

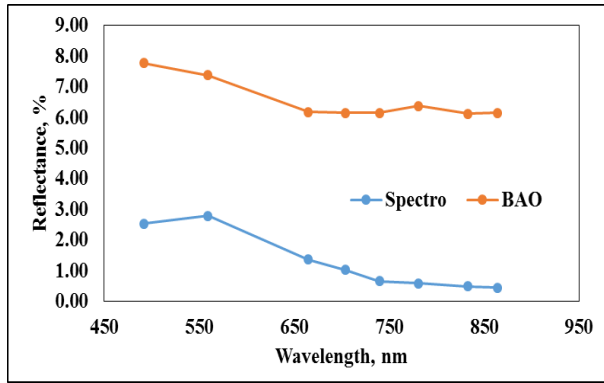


a)

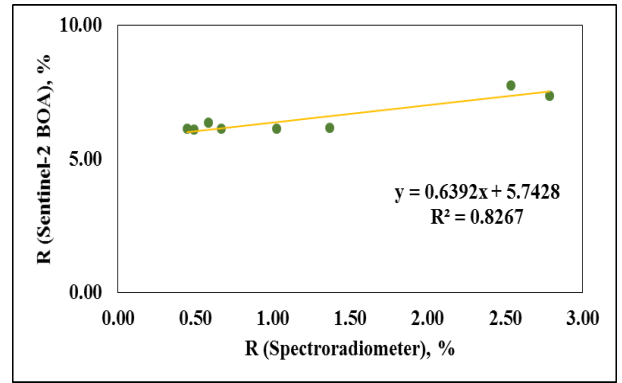


b)

**Fig. F-49: a) Spectral Signatures Obtained from Spectroradiometer SVC-1024i & Sentinel-2 BOA Image and b) linear relation between band values for sample 49 having SSC**

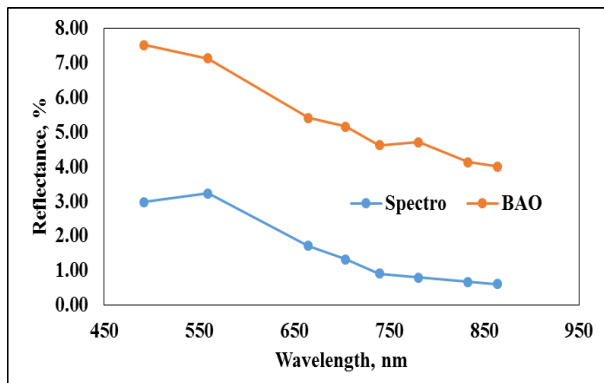


a)

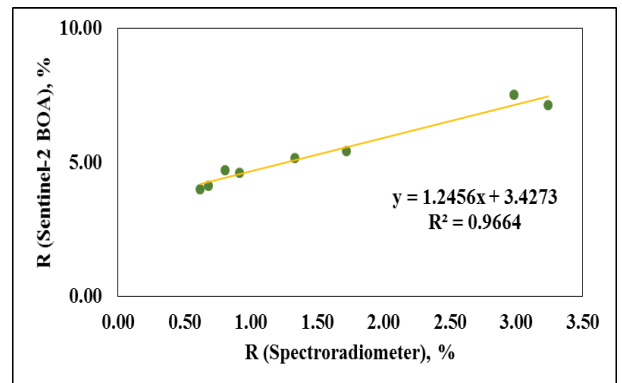


b)

**Fig. F-50: a) Spectral Signatures Obtained from Spectroradiometer SVC-1024i & Sentinel-2 BOA Image and b) linear relation between band values for sample 50 having SSC**



a)



b)

**Fig. F-51: a) Spectral Signatures Obtained from Spectroradiometer SVC-1024i & Sentinel-2 BOA Image and b) linear relation between band values for sample 51 having SSC**

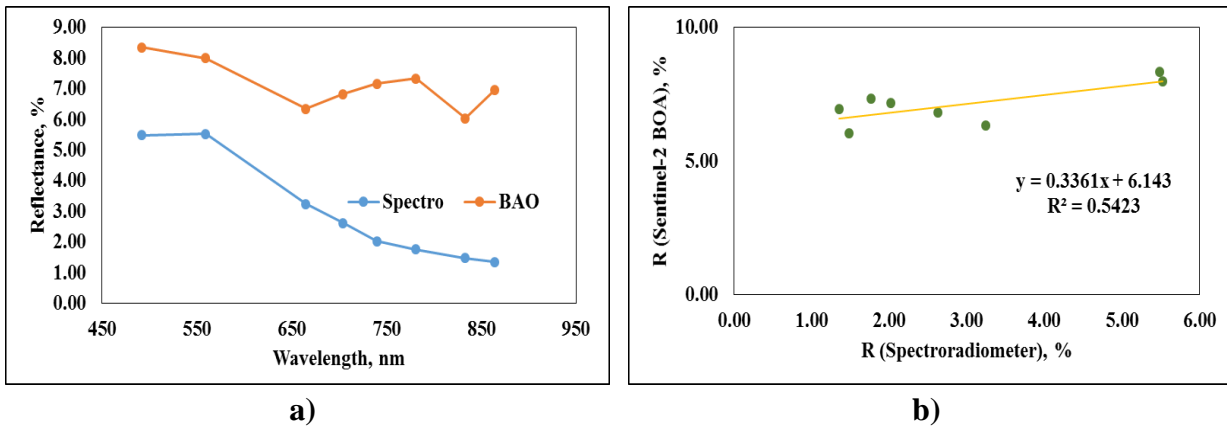


**Fig. F-52: a) Spectral Signatures Obtained from Spectroradiometer SVC-1024i & Sentinel-2 BOA Image and b) linear relation between band values for sample 52 having SSC**

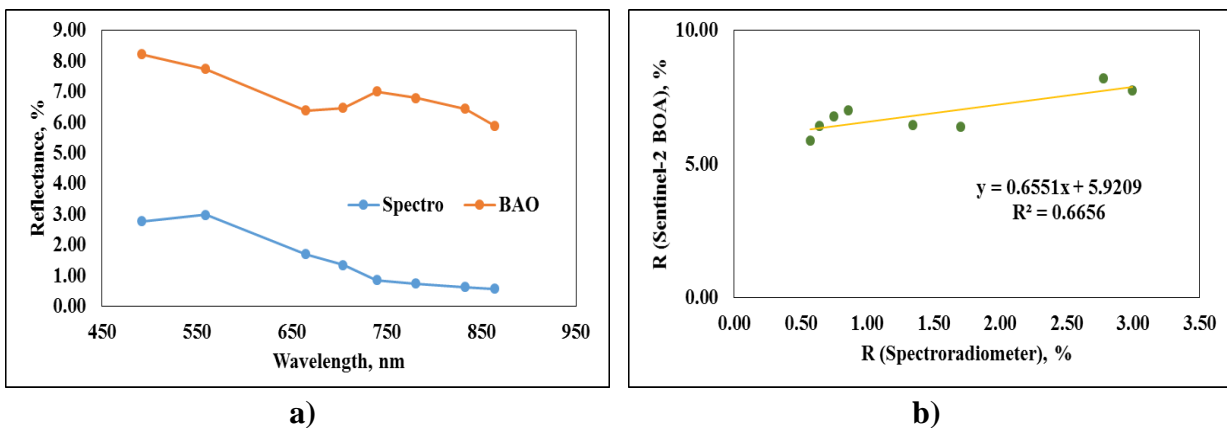


**Fig. F-53: a) Spectral Signatures Obtained from Spectroradiometer SVC-1024i & Sentinel-2 BOA Image and b) linear relation between band values for sample 53 having SSC**

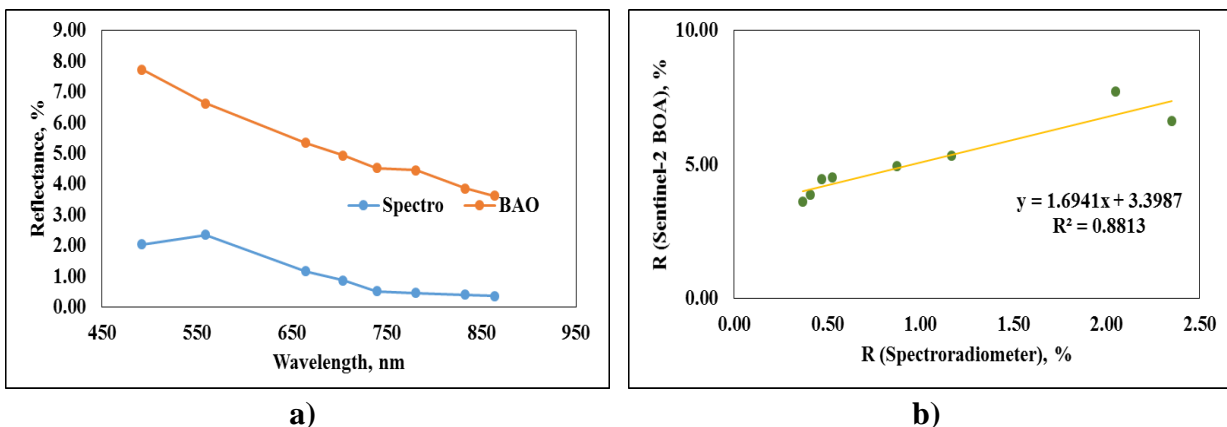
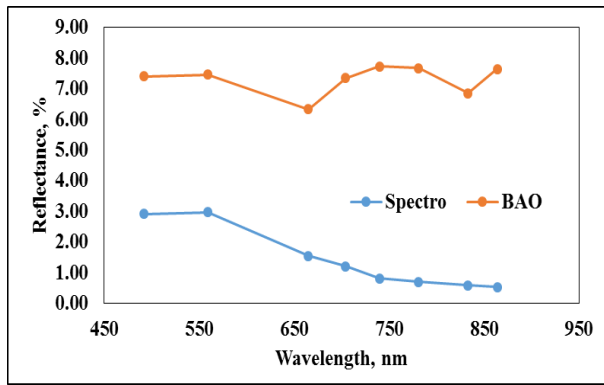
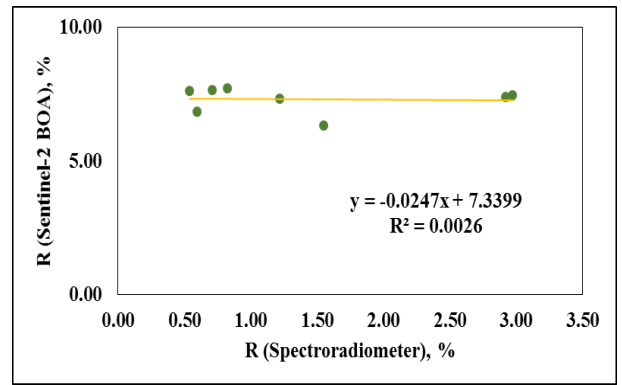


**Fig. F-54: a) Spectral Signatures Obtained from Spectroradiometer SVC-1024i & Sentinel-2 BOA Image and b) linear relation between band values for sample 54 having SSC**

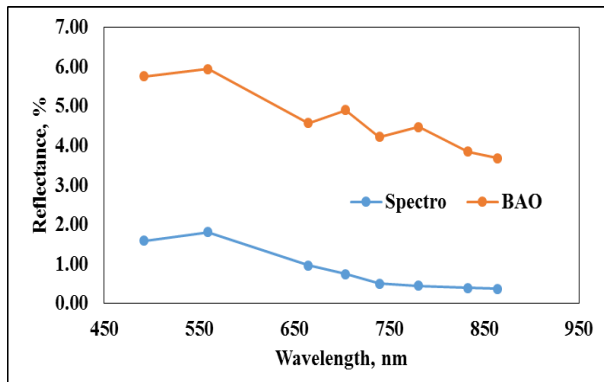


a)

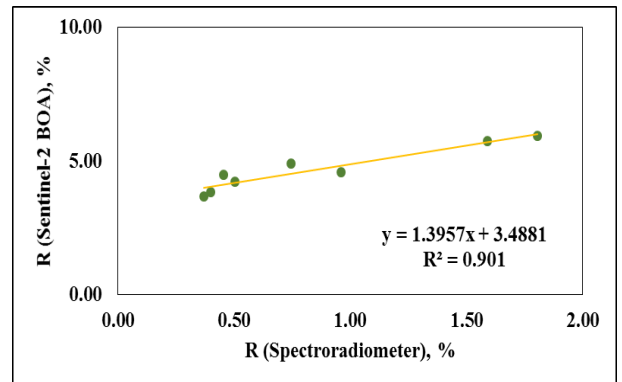


b)

**Fig. F-55: a) Spectral Signatures Obtained from Spectroradiometer SVC-1024i & Sentinel-2 BOA Image and b) linear relation between band values for sample 55 having SSC**

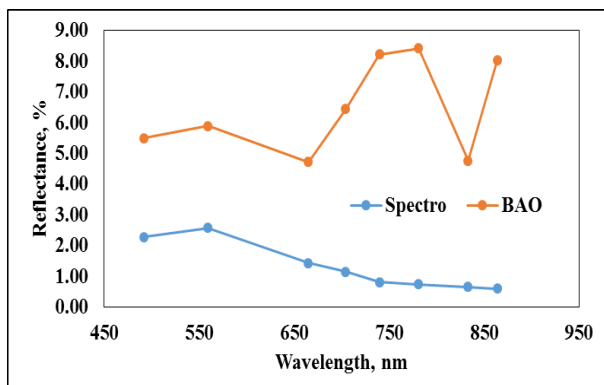


a)

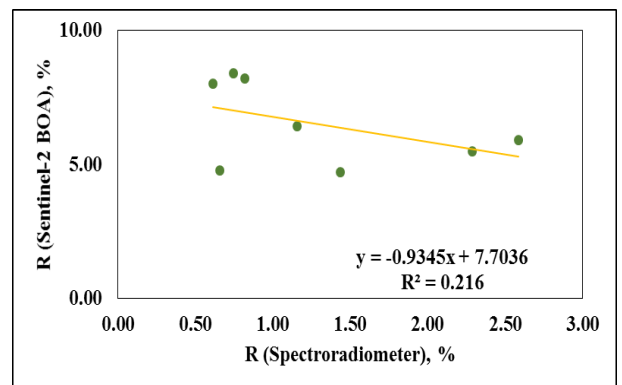


b)

**Fig. F-56: a) Spectral Signatures Obtained from Spectroradiometer SVC-1024i & Sentinel-2 BOA Image and b) linear relation between band values for sample 56 having SSC**



a)



b)

**Fig. F-57: a) Spectral Signatures Obtained from Spectroradiometer SVC-1024i & Sentinel-2 BOA Image and b) linear relation between band values for sample 57 having SSC**

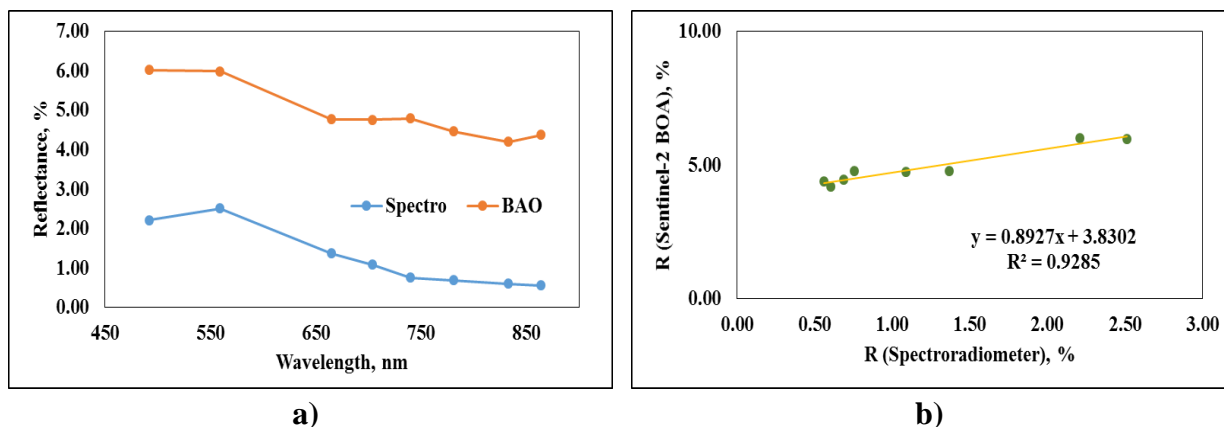


**Fig. F-58: a) Spectral Signatures Obtained from Spectroradiometer SVC-1024i & Sentinel-2 BOA Image and b) linear relation between band values for sample 58 having SSC**

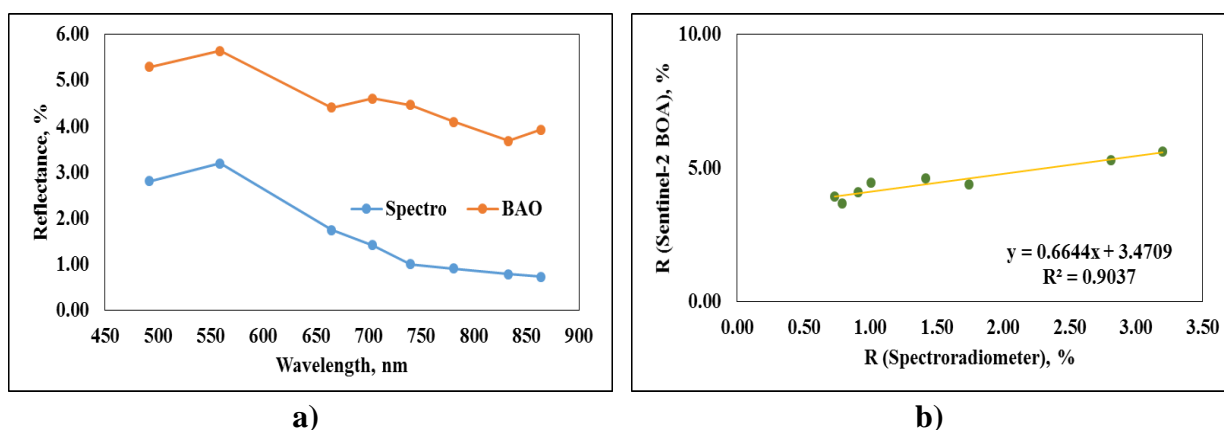


**Fig. F-59: a) Spectral Signatures Obtained from Spectroradiometer SVC-1024i & Sentinel-2 BOA Image and b) linear relation between band values for sample 59 having SSC**

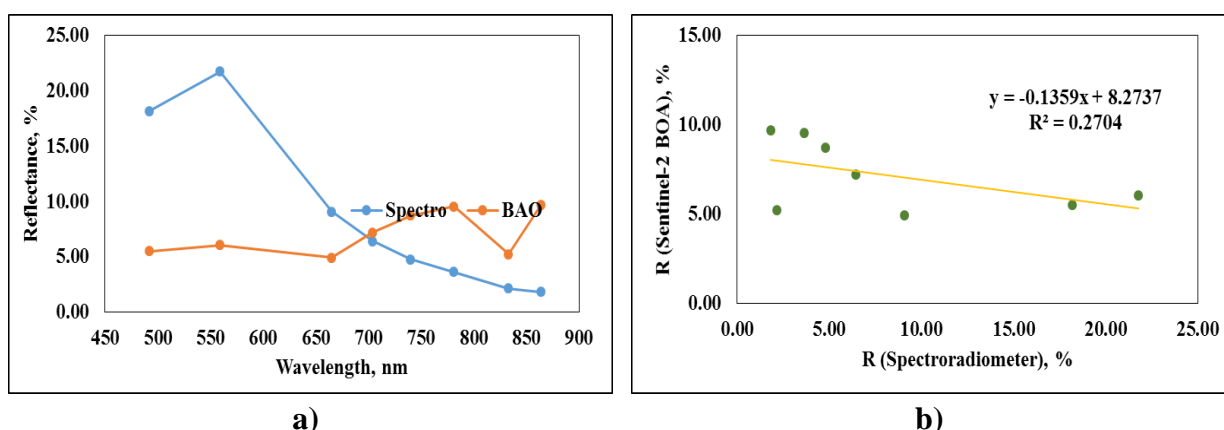
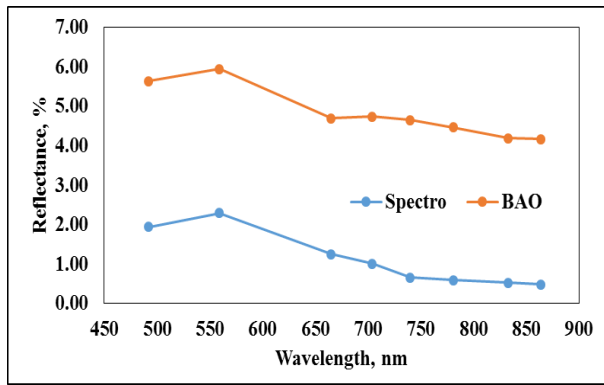
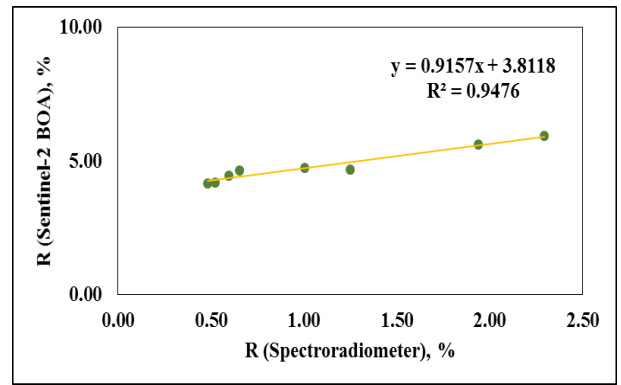


**Fig. F-60: a) Spectral Signatures Obtained from Spectroradiometer SVC-1024i & Sentinel-2 BOA Image and b) linear relation between band values for sample 60 having SSC**

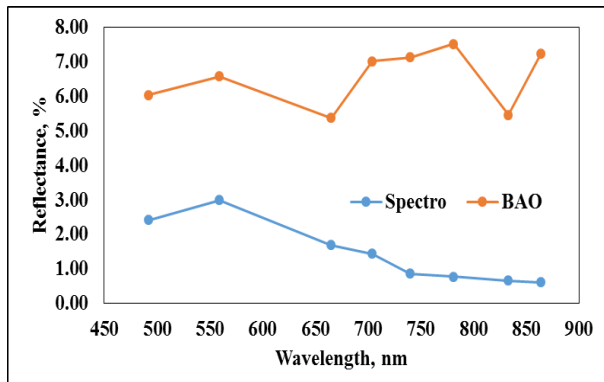


a)

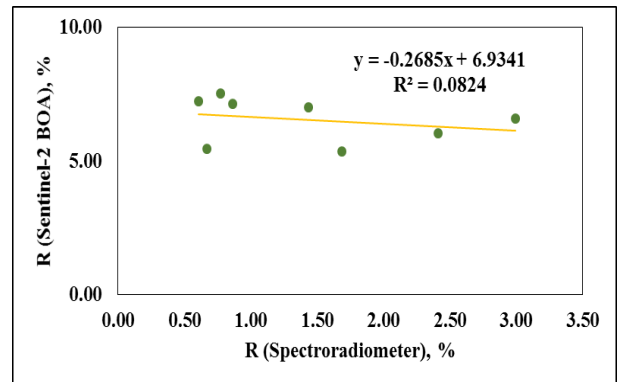


b)

**Fig. F-61: a) Spectral Signatures Obtained from Spectroradiometer SVC-1024i & Sentinel-2 BOA Image and b) linear relation between band values for sample 61 having SSC**

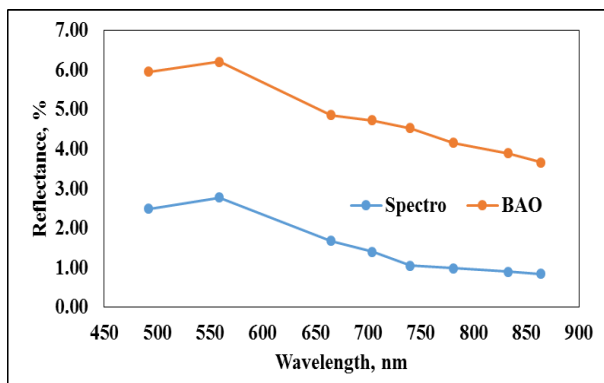


a)

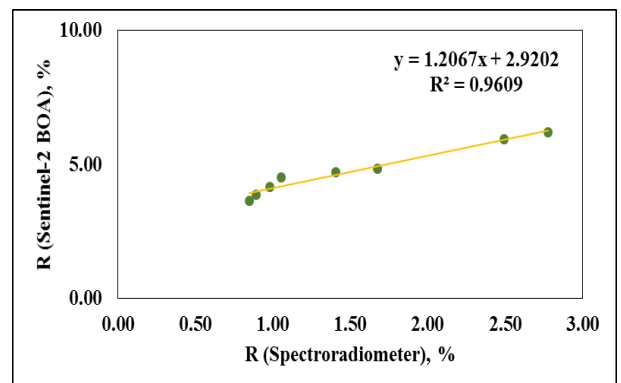


b)

**Fig. F-62: a) Spectral Signatures Obtained from Spectroradiometer SVC-1024i & Sentinel-2 BOA Image and b) linear relation between band values for sample 62 having SSC**



a)



b)

**Fig. F-63: a) Spectral Signatures Obtained from Spectroradiometer SVC-1024i & Sentinel-2 BOA Image and b) linear relation between band values for sample 63 having SSC**

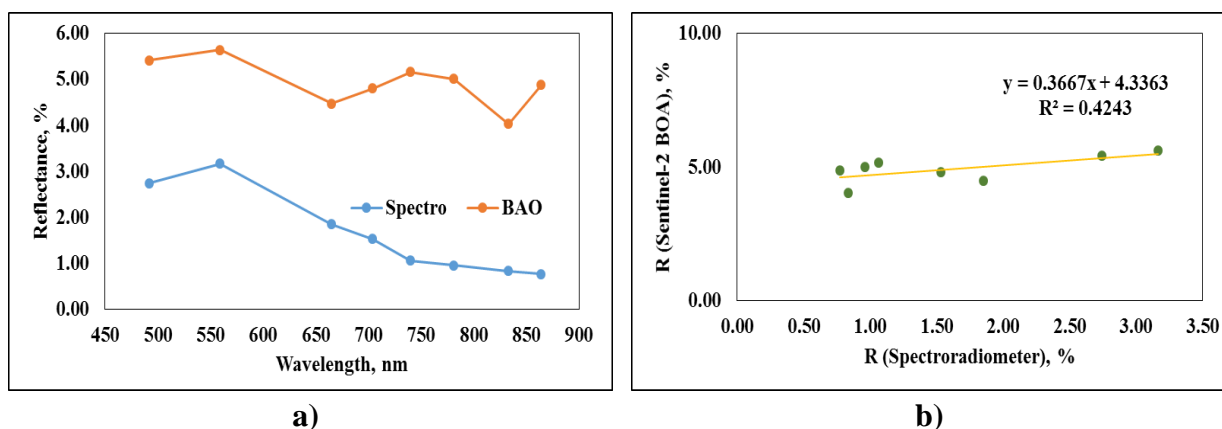


**Fig. F-64: a) Spectral Signatures Obtained from Spectroradiometer SVC-1024i & Sentinel-2 BOA Image and b) linear relation between band values for sample 64 having SSC**

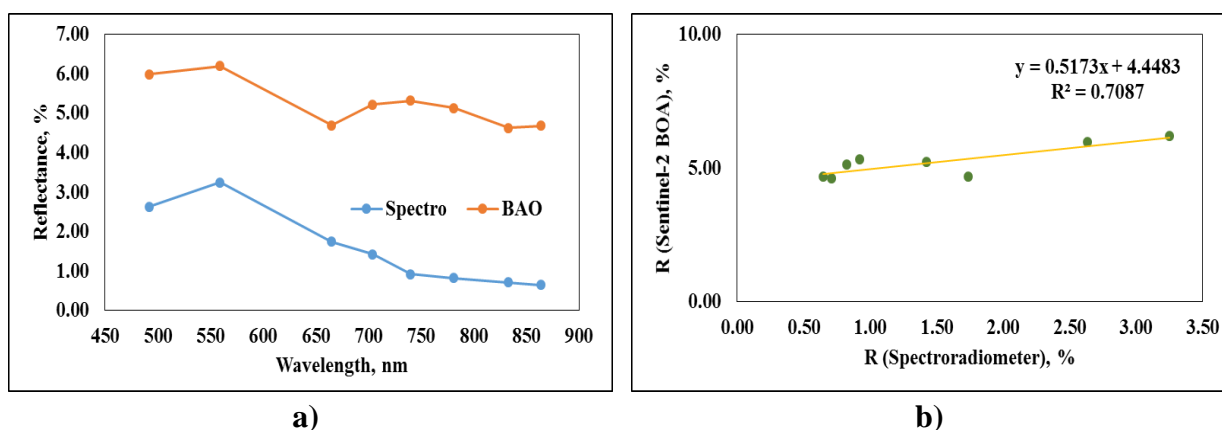


**Fig. F-65: a) Spectral Signatures Obtained from Spectroradiometer SVC-1024i & Sentinel-2 BOA Image and b) linear relation between band values for sample 65 having SSC**

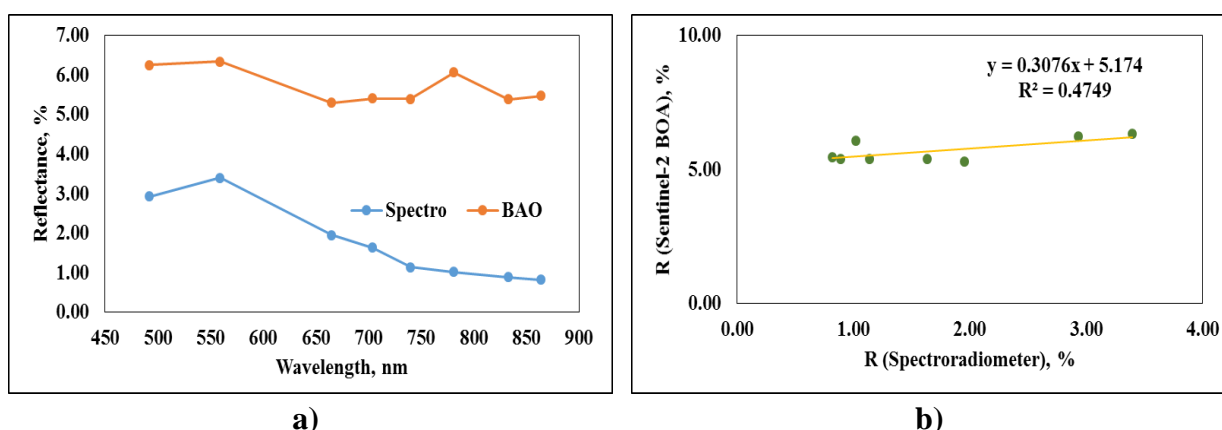


**Fig. F-66: a) Spectral Signatures Obtained from Spectroradiometer SVC-1024i & Sentinel-2 BOA Image and b) linear relation between band values for sample 66 having SSC**

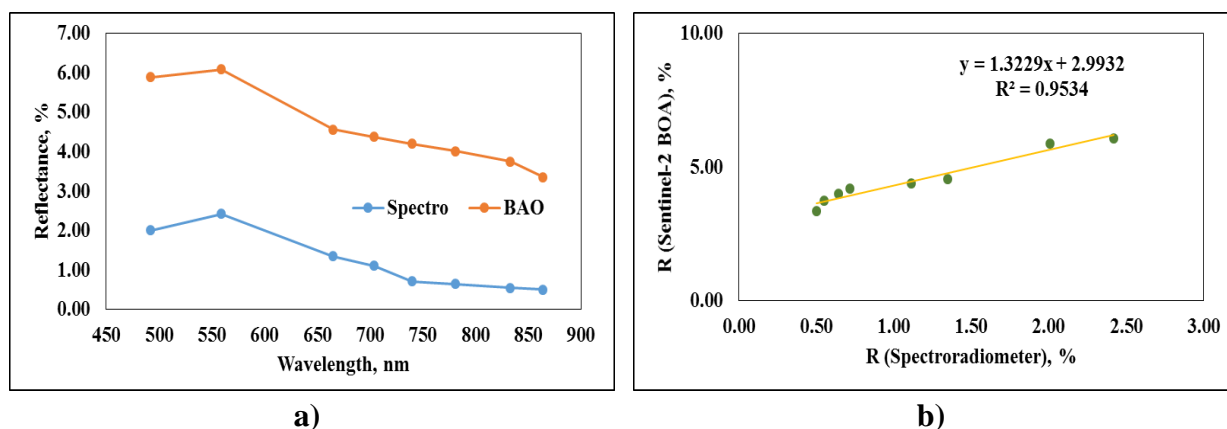


**Fig. F-67: a) Spectral Signatures Obtained from Spectroradiometer SVC-1024i & Sentinel-2 BOA Image and b) linear relation between band values for sample 67 having SSC**

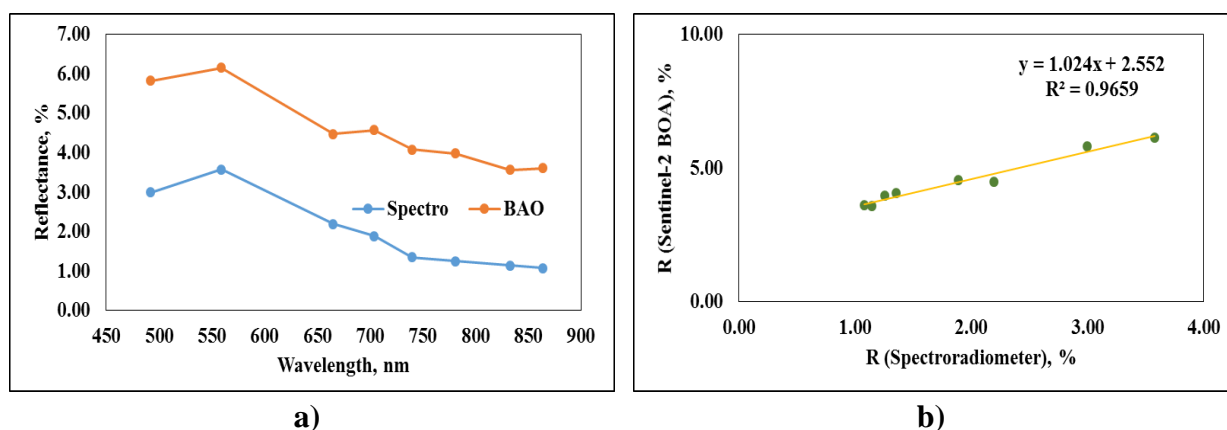


**Fig. F-68: a) Spectral Signatures Obtained from Spectroradiometer SVC-1024i & Sentinel-2 BOA Image and b) linear relation between band values for sample 68 having SSC**

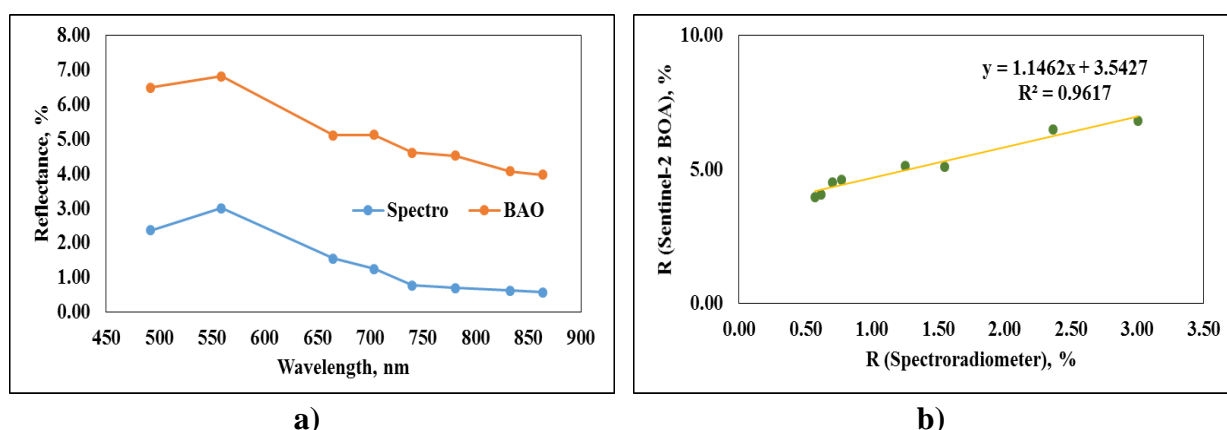


**Fig. F-69: a) Spectral Signatures Obtained from Spectroradiometer SVC-1024i & Sentinel-2 BOA Image and b) linear relation between band values for sample 69 having SSC**

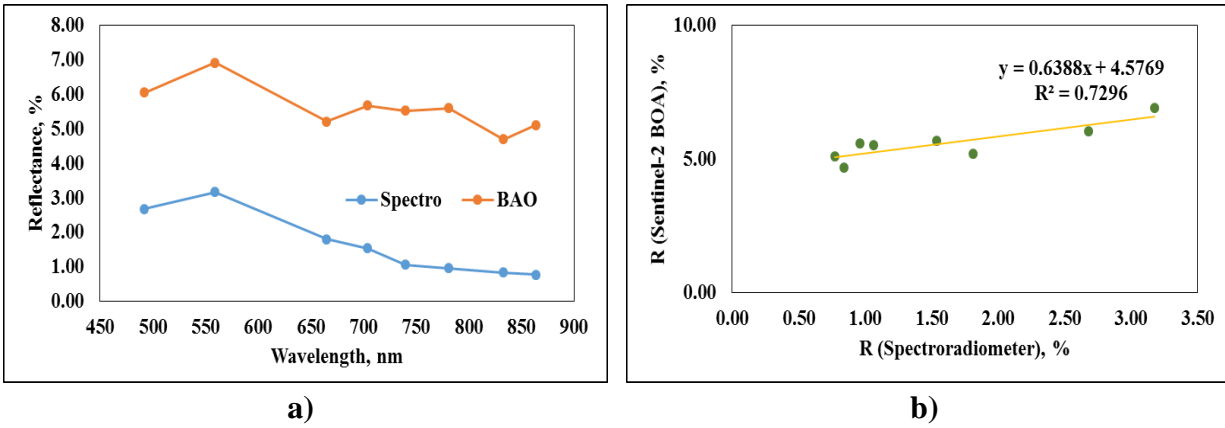


**Fig. F-70: a) Spectral Signatures Obtained from Spectroradiometer SVC-1024i & Sentinel-2 BOA Image and b) linear relation between band values for sample 70 having SSC**

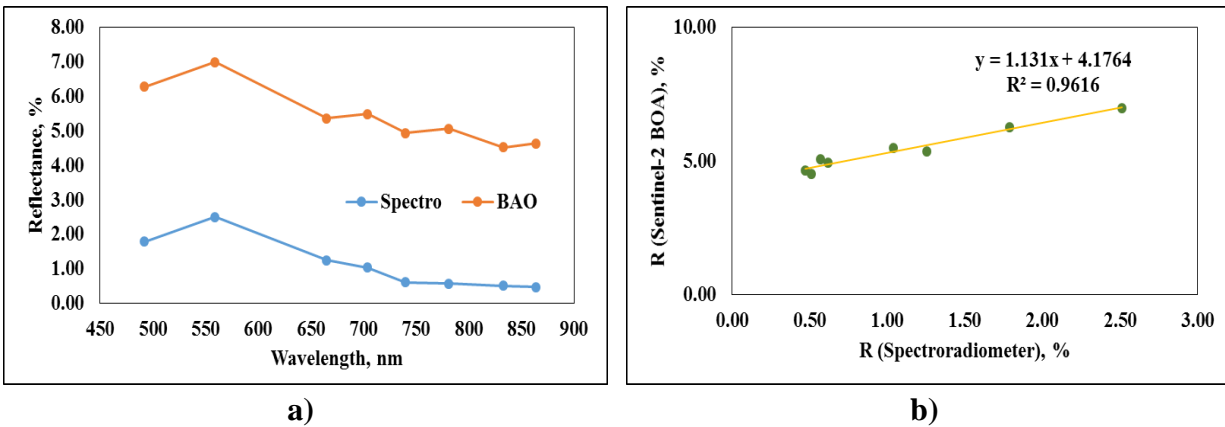


**Fig. F-71: a) Spectral Signatures Obtained from Spectroradiometer SVC-1024i & Sentinel-2 BOA Image and b) linear relation between band values for sample 71 having SSC**

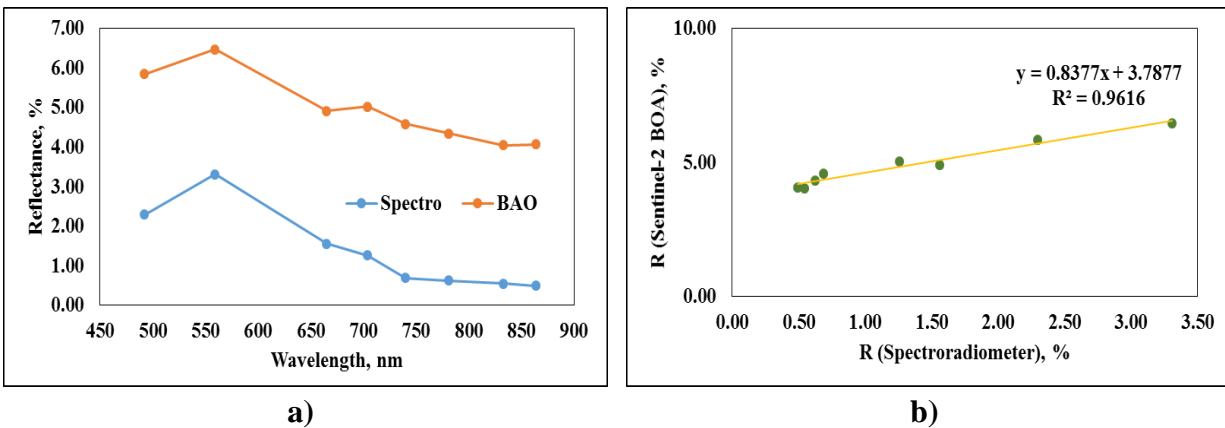


**Fig. F-72: a) Spectral Signatures Obtained from Spectroradiometer SVC-1024i & Sentinel-2 BOA Image and b) linear relation between band values for sample 72 having SSC**

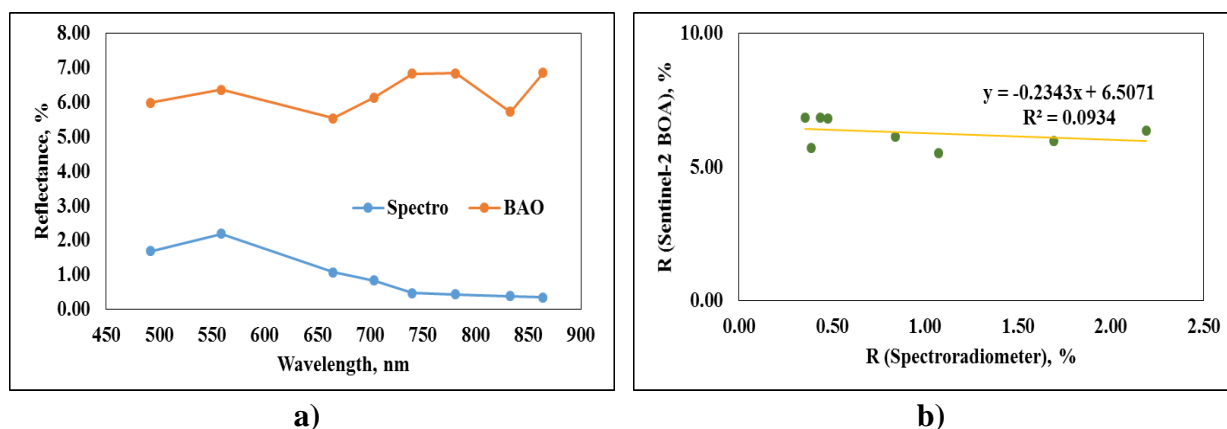


**Fig. F-73: a) Spectral Signatures Obtained from Spectroradiometer SVC-1024i & Sentinel-2 BOA Image and b) linear relation between band values for sample 73 having SSC**

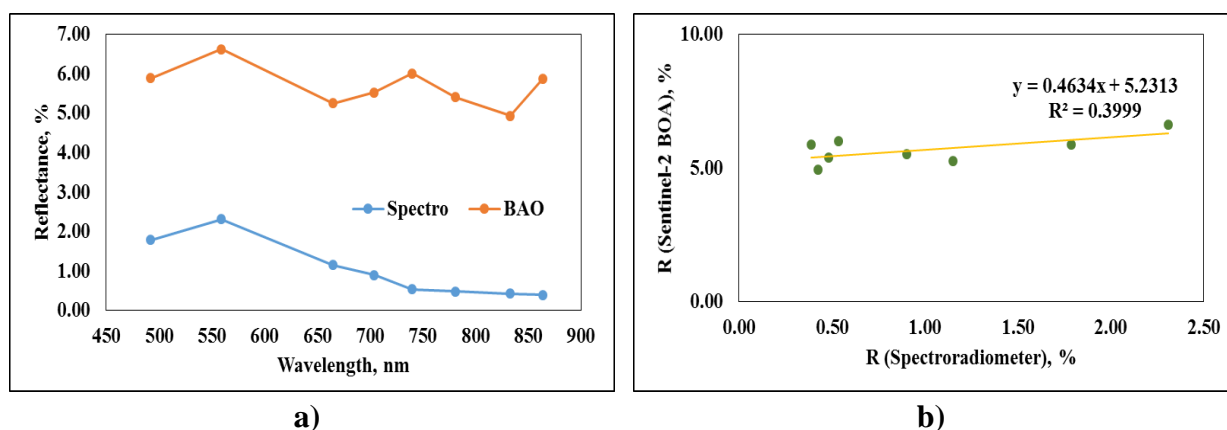


**Fig. F-74: a) Spectral Signatures Obtained from Spectroradiometer SVC-1024i & Sentinel-2 BOA Image and b) linear relation between band values for sample 74 having SSC**

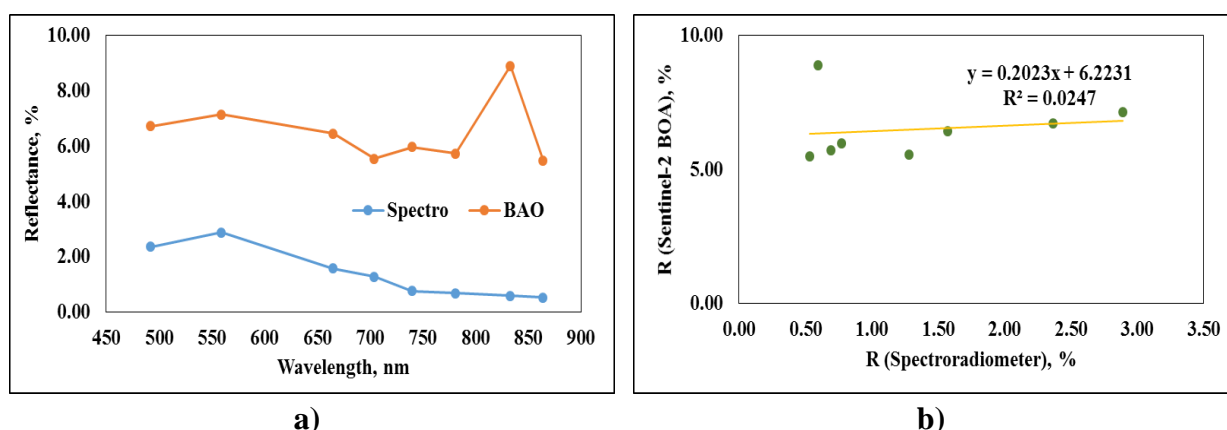


**Fig. F-75: a) Spectral Signatures Obtained from Spectroradiometer SVC-1024i & Sentinel-2 BOA Image and b) linear relation between band values for sample 75 having SSC**

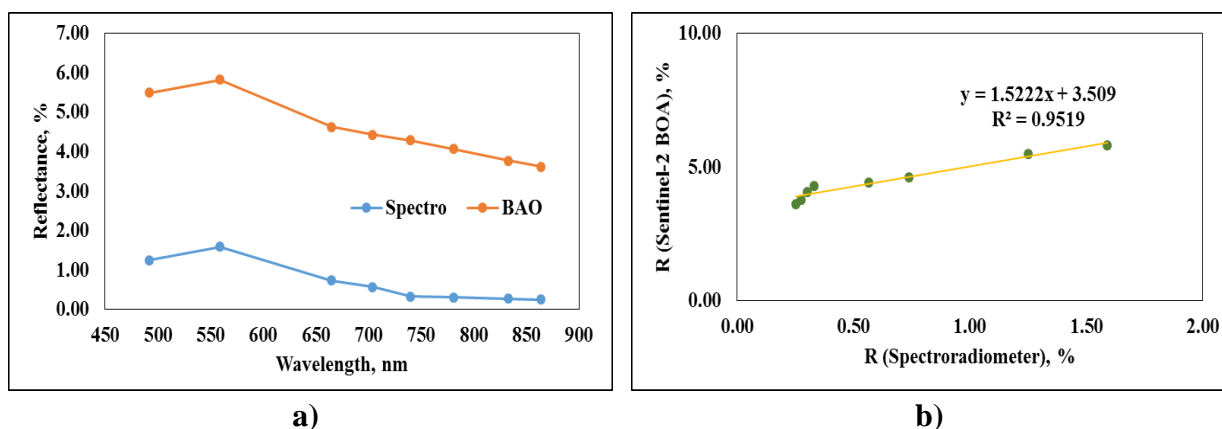


**Fig. F-76: a) Spectral Signatures Obtained from Spectroradiometer SVC-1024i & Sentinel-2 BOA Image and b) linear relation between band values for sample 76 having SSC**

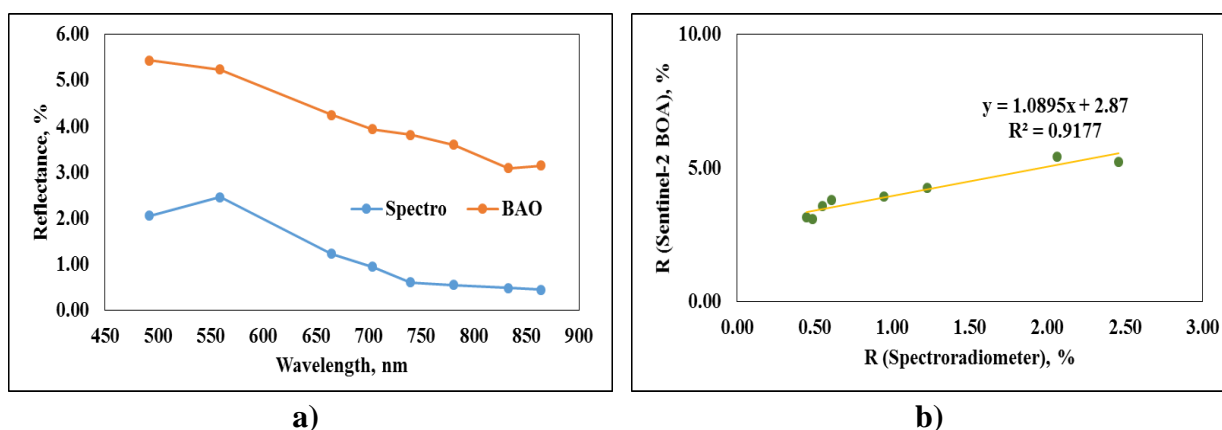


**Fig. F-77: a) Spectral Signatures Obtained from Spectroradiometer SVC-1024i & Sentinel-2 BOA Image and b) linear relation between band values for sample 77 having SSC**

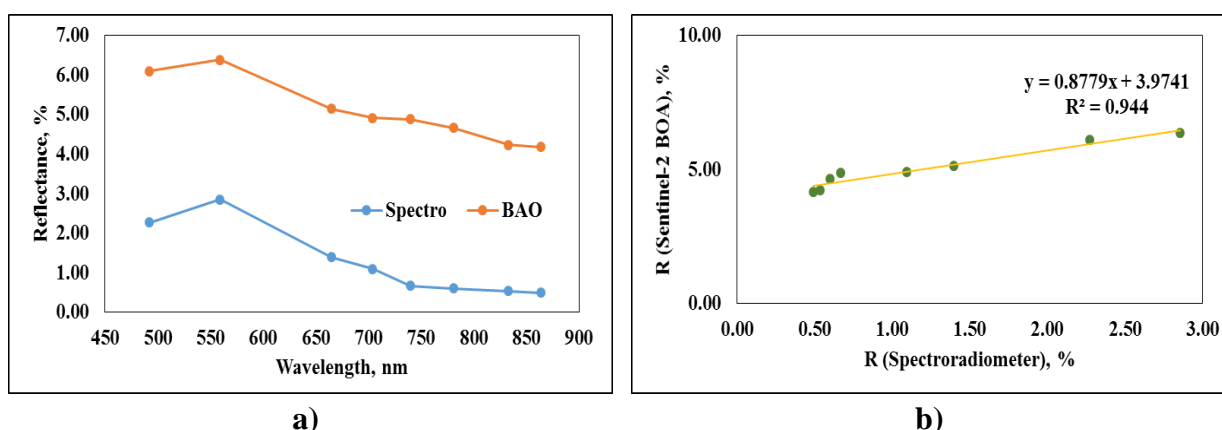


**Fig. F-78: a) Spectral Signatures Obtained from Spectroradiometer SVC-1024i & Sentinel-2 BOA Image and b) linear relation between band values for sample 78 having SSC**

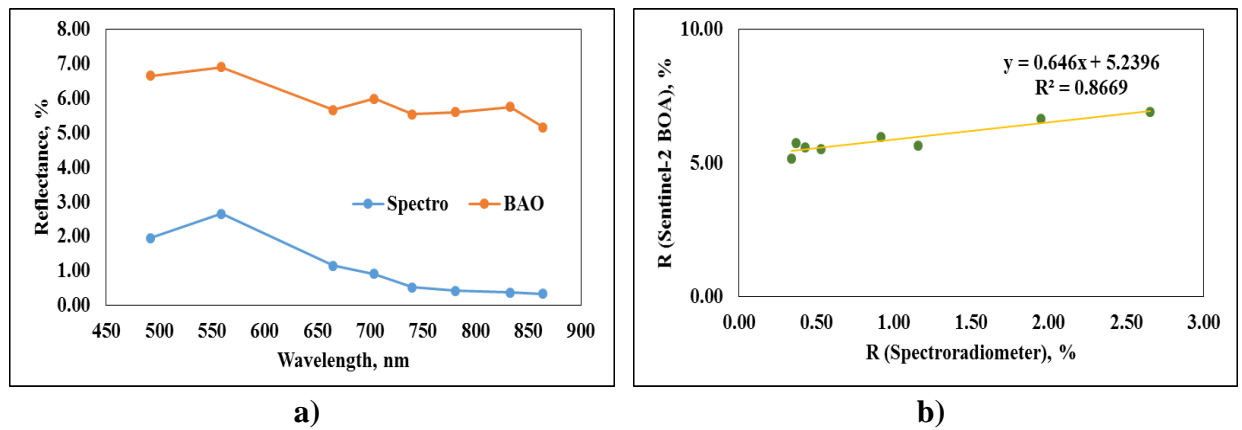


**Fig. F-79: a) Spectral Signatures Obtained from Spectroradiometer SVC-1024i & Sentinel-2 BOA Image and b) linear relation between band values for sample 79 having SSC**

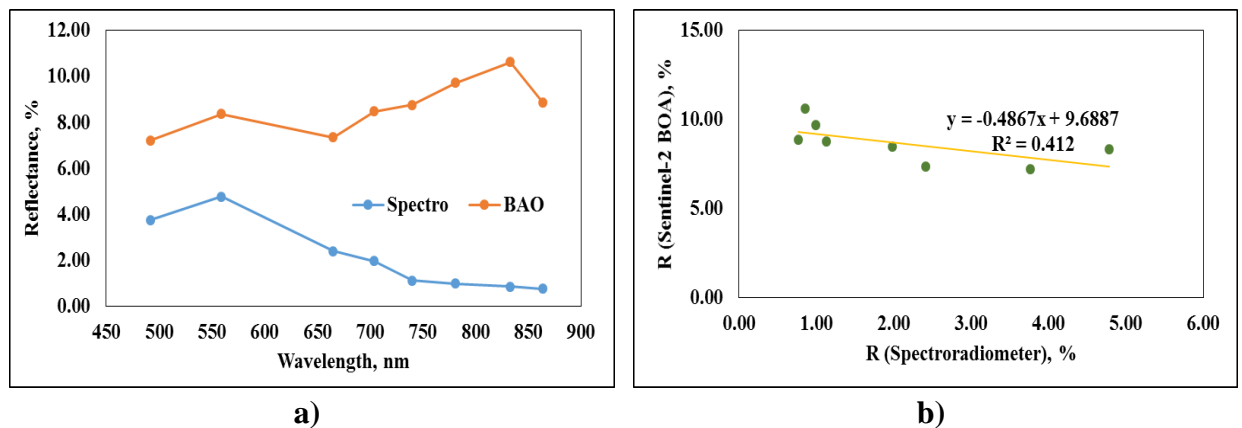


**Fig. F-80: a) Spectral Signatures Obtained from Spectroradiometer SVC-1024i & Sentinel-2 BOA Image and b) linear relation between band values for sample 80 having SSC**

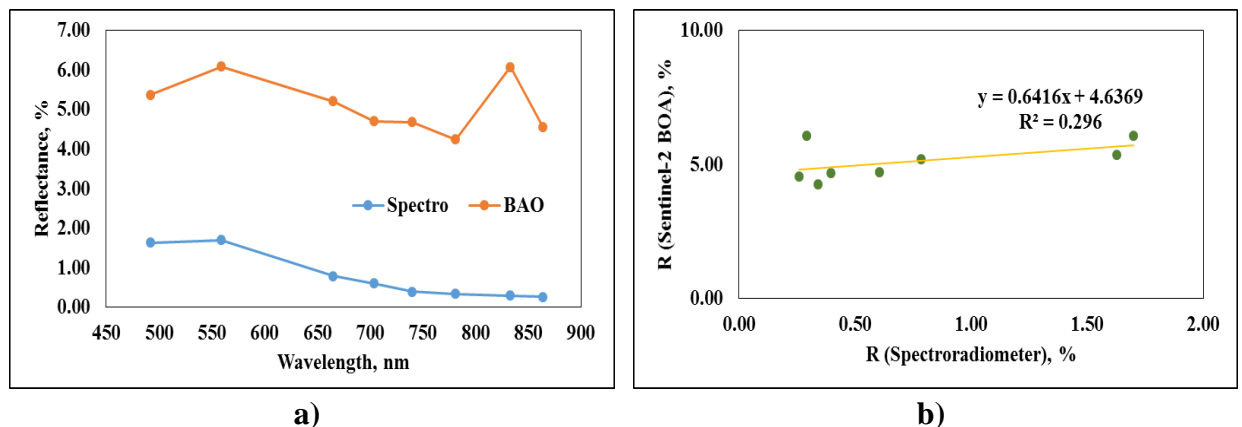


**Fig. F-81: a) Spectral Signatures Obtained from Spectroradiometer SVC-1024i & Sentinel-2 BOA Image and b) linear relation between band values for sample 81 having SSC**

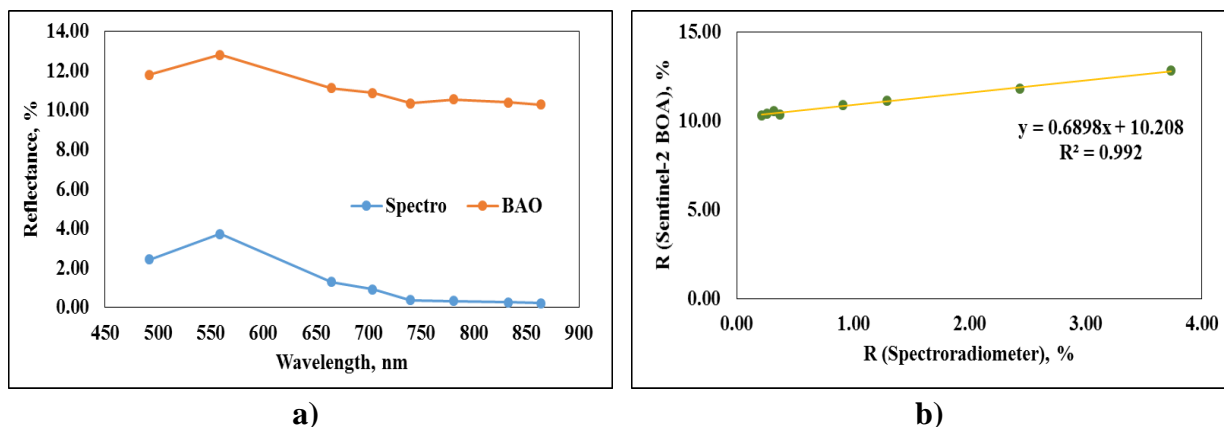


**Fig. F-82: a) Spectral Signatures Obtained from Spectroradiometer SVC-1024i & Sentinel-2 BOA Image and b) linear relation between band values for sample 82 having SSC**

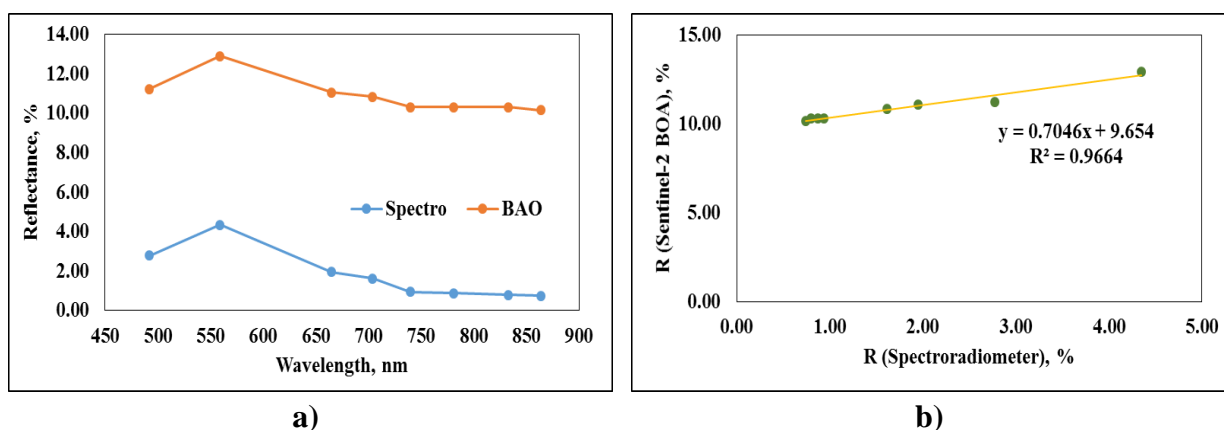


**Fig. F-83: a) Spectral Signatures Obtained from Spectroradiometer SVC-1024i & Sentinel-2 BOA Image and b) linear relation between band values for sample 83 having SSC**

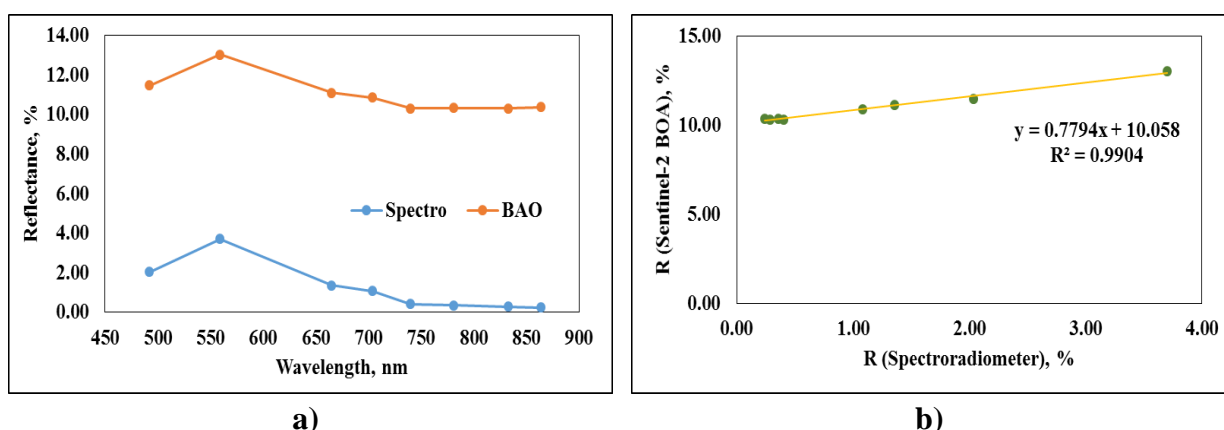
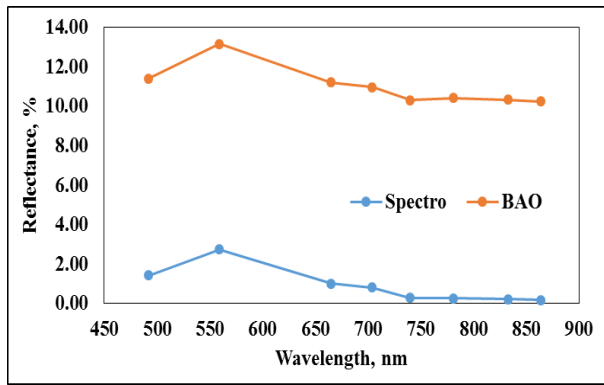
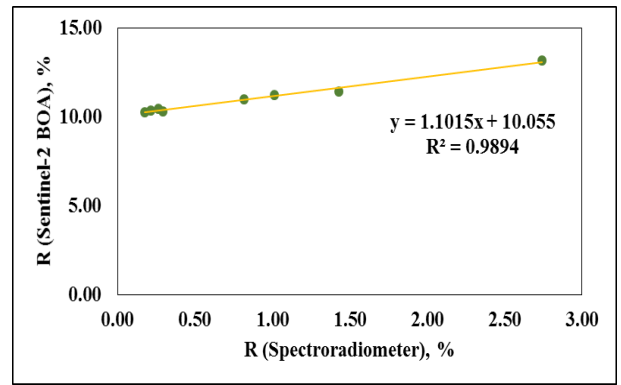


**Fig. F-84: a) Spectral Signatures Obtained from Spectroradiometer SVC-1024i & Sentinel-2 BOA Image and b) linear relation between band values for sample 84 having SSC**

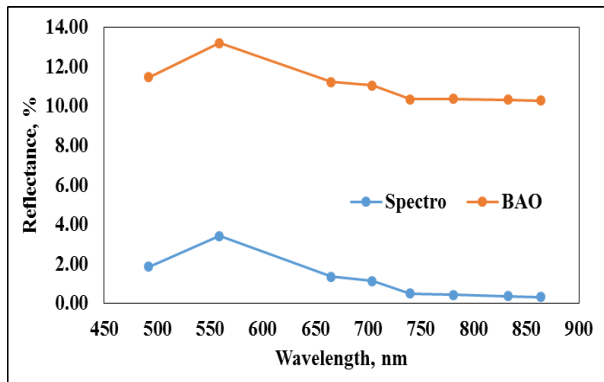


a)

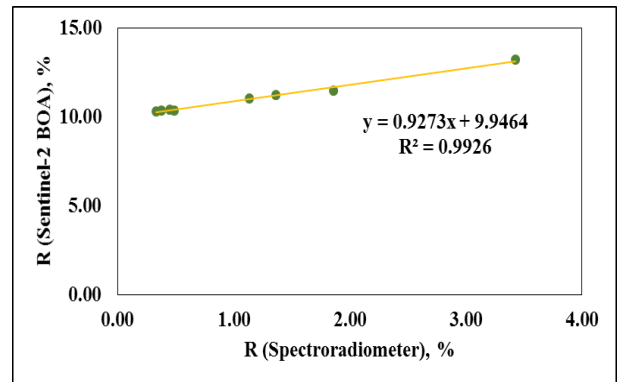


b)

**Fig. F-85: a) Spectral Signatures Obtained from Spectroradiometer SVC-1024i & Sentinel-2 BOA Image and b) linear relation between band values for sample 85 having SSC**

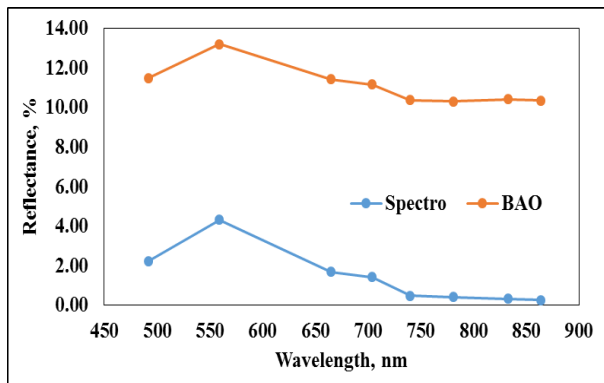


a)

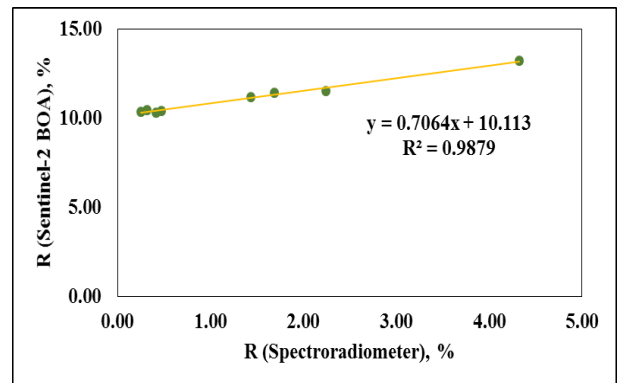


b)

**Fig. F-86: a) Spectral Signatures Obtained from Spectroradiometer SVC-1024i & Sentinel-2 BOA Image and b) linear relation between band values for sample 86 having SSC**



a)



b)

**Fig. F-87: a) Spectral Signatures Obtained from Spectroradiometer SVC-1024i & Sentinel-2 BOA Image and b) linear relation between band values for sample 88 having SSC**

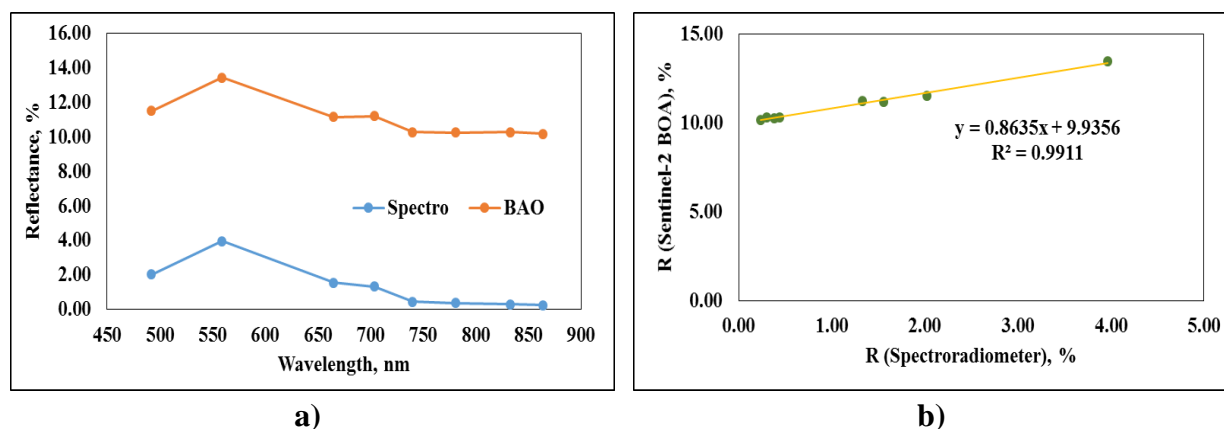


**Fig. F-88: a) Spectral Signatures Obtained from Spectroradiometer SVC-1024i & Sentinel-2 BOA Image and b) linear relation between band values for sample 88 having SSC**

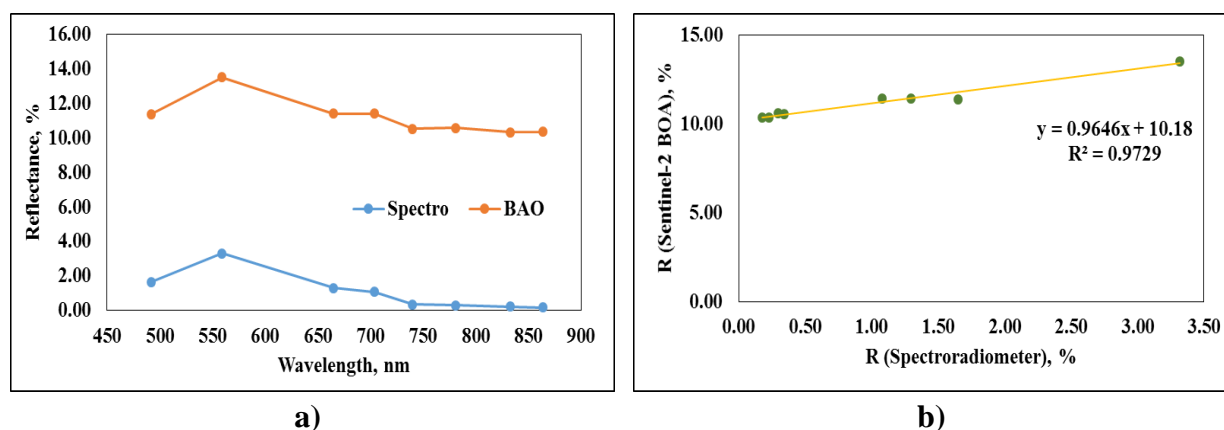


**Fig. F-89: a) Spectral Signatures Obtained from Spectroradiometer SVC-1024i & Sentinel-2 BOA Image and b) linear relation between band values for sample 89 having SSC**

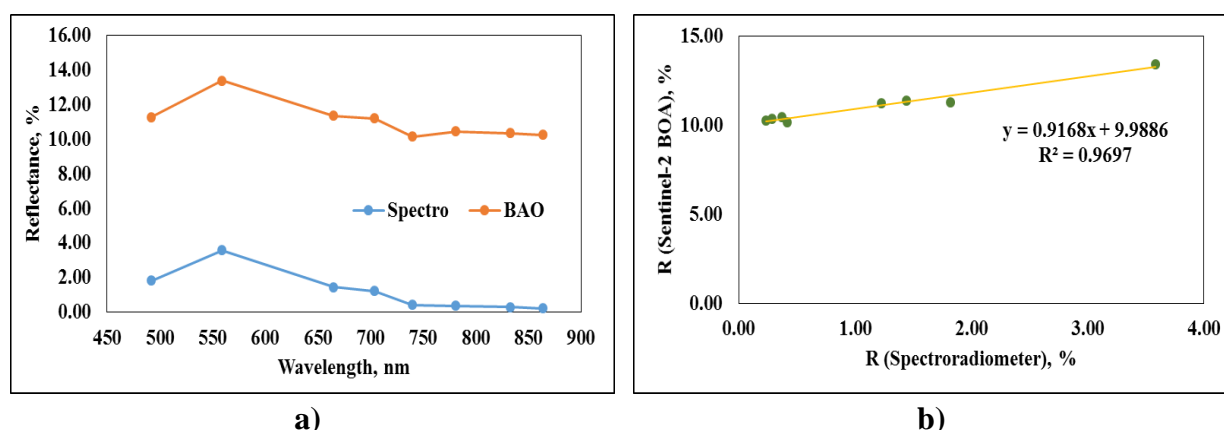
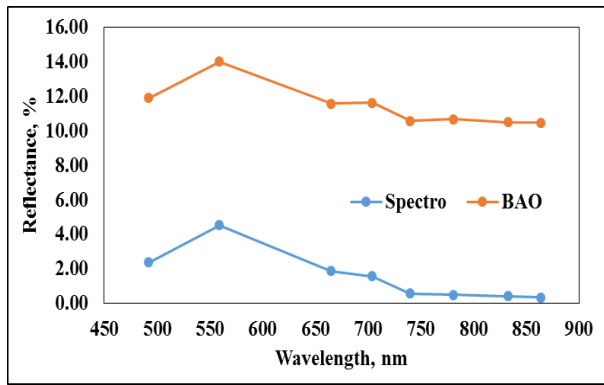
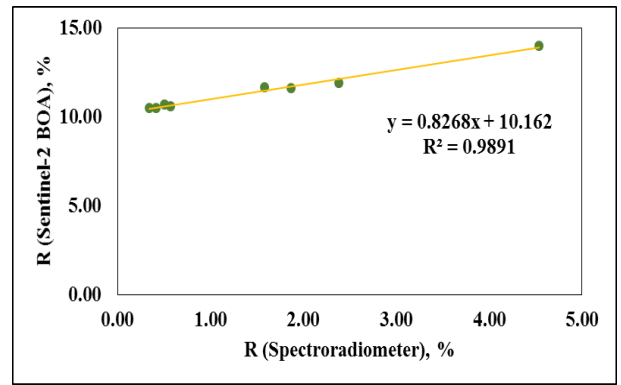


**Fig. F-90: a) Spectral Signatures Obtained from Spectroradiometer SVC-1024i & Sentinel-2 BOA Image and b) linear relation between band values for sample 90 having SSC**

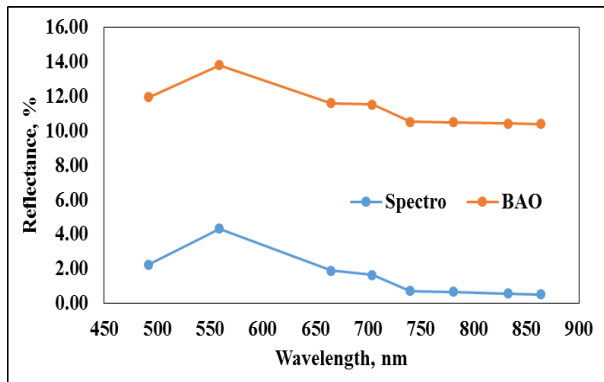


a)

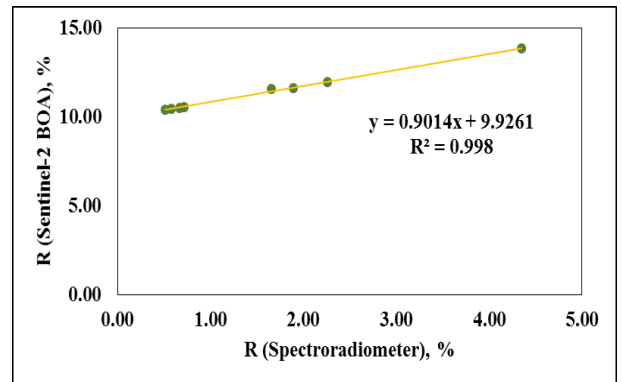


b)

**Fig. F-91: a) Spectral Signatures Obtained from Spectroradiometer SVC-1024i & Sentinel-2 BOA Image and b) linear relation between band values for sample 91 having SSC**

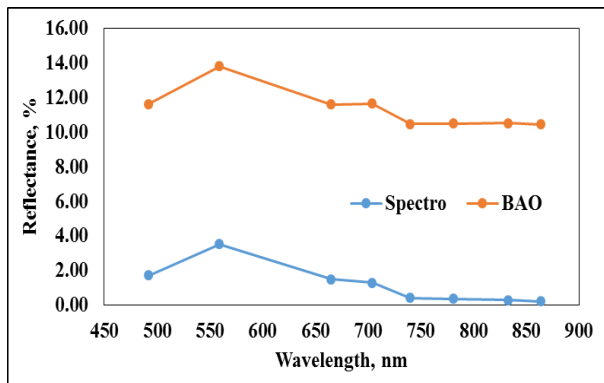


a)

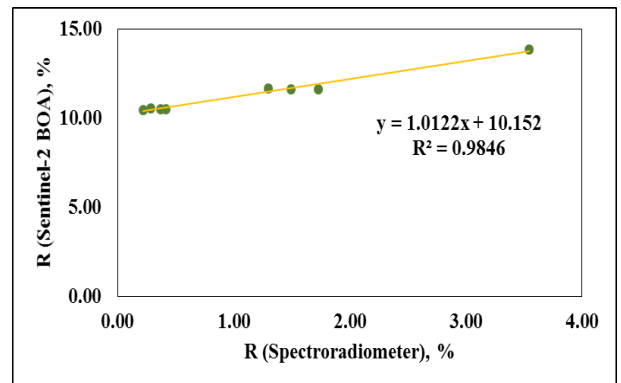


b)

**Fig. F-92: a) Spectral Signatures Obtained from Spectroradiometer SVC-1024i & Sentinel-2 BOA Image and b) linear relation between band values for sample 92 having SSC**



a)



b)

**Fig. F-93: a) Spectral Signatures Obtained from Spectroradiometer SVC-1024i & Sentinel-2 BOA Image and b) linear relation between band values for sample 93 having SSC**

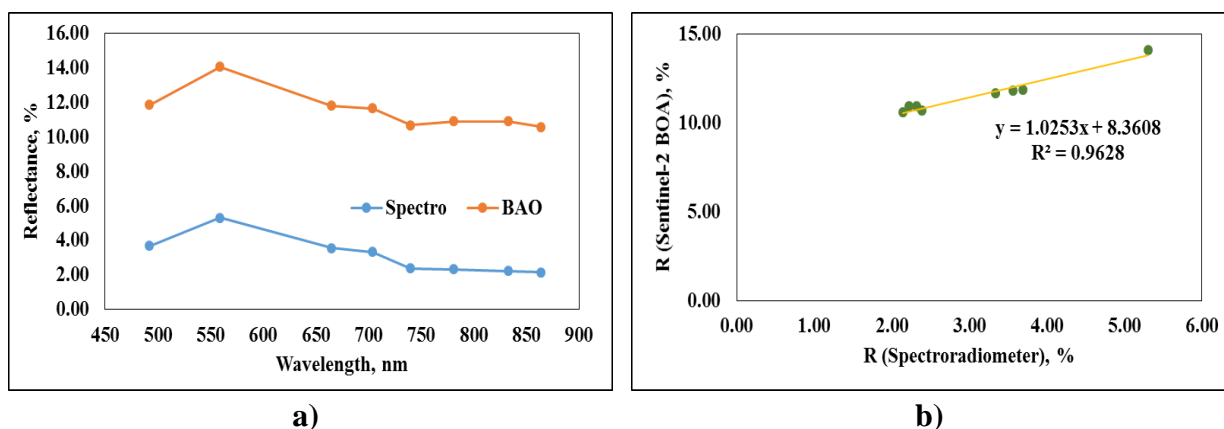


**Fig. F-94: a) Spectral Signatures Obtained from Spectroradiometer SVC-1024i & Sentinel-2 BOA Image and b) linear relation between band values for sample 94 having SSC**

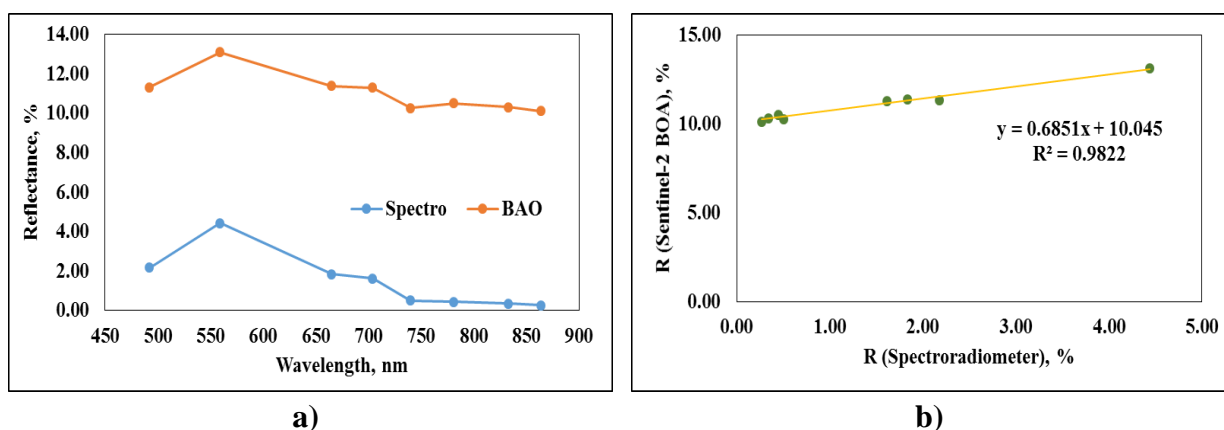


**Fig. F-95: a) Spectral Signatures Obtained from Spectroradiometer SVC-1024i & Sentinel-2 BOA Image and b) linear relation between band values for sample 95 having SSC**

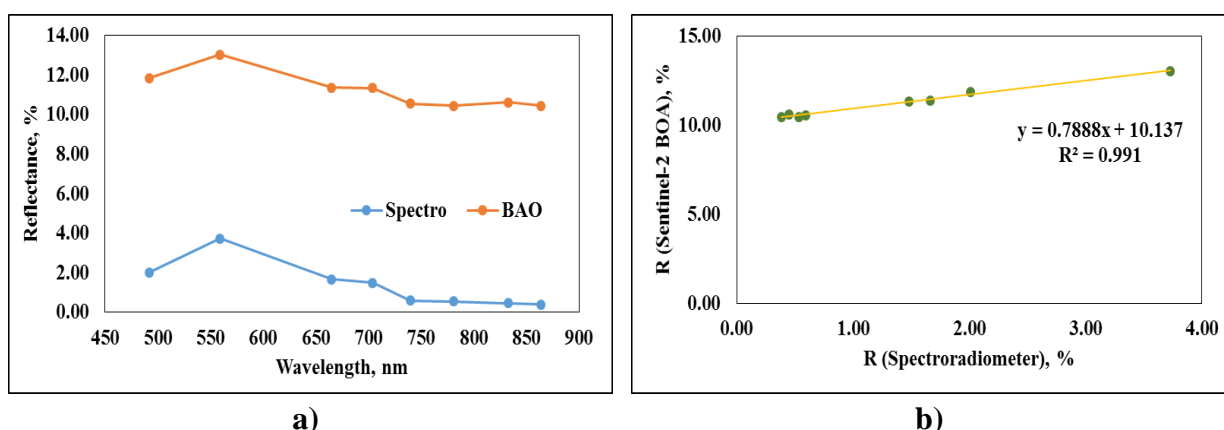


**Fig. F-96: a) Spectral Signatures Obtained from Spectroradiometer SVC-1024i & Sentinel-2 BOA Image and b) linear relation between band values for sample 96 having SSC**

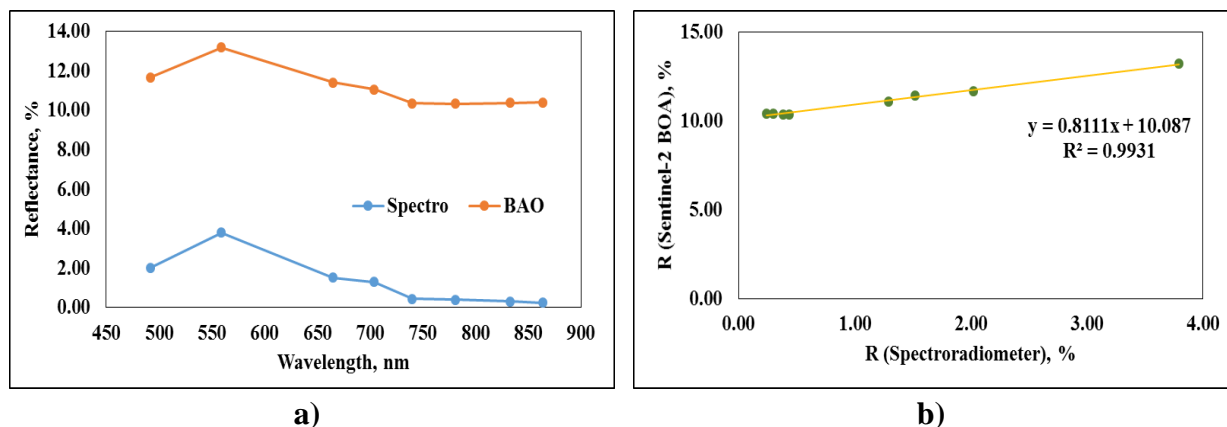


**Fig. F-97: a) Spectral Signatures Obtained from Spectroradiometer SVC-1024i & Sentinel-2 BOA Image and b) linear relation between band values for sample 97 having SSC**

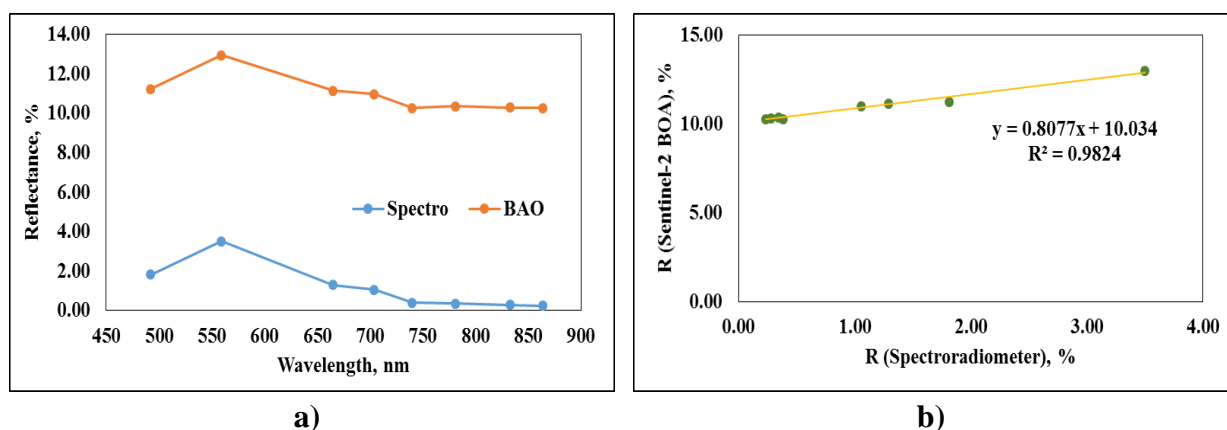


**Fig. F-98: a) Spectral Signatures Obtained from Spectroradiometer SVC-1024i & Sentinel-2 BOA Image and b) linear relation between band values for sample 98 having SSC**

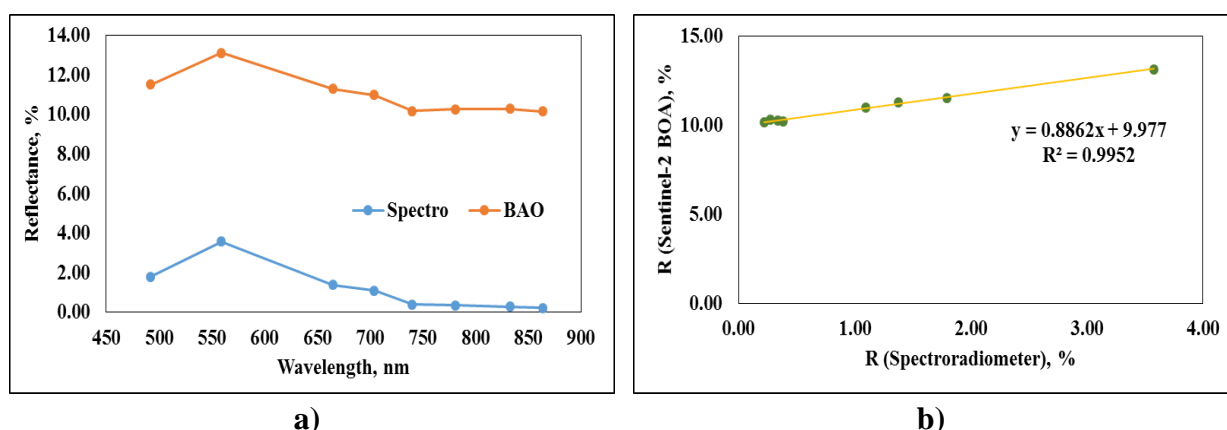


**Fig. F-99: a) Spectral Signatures Obtained from Spectroradiometer SVC-1024i & Sentinel-2 BOA Image and b) linear relation between band values for sample 99 having SSC**

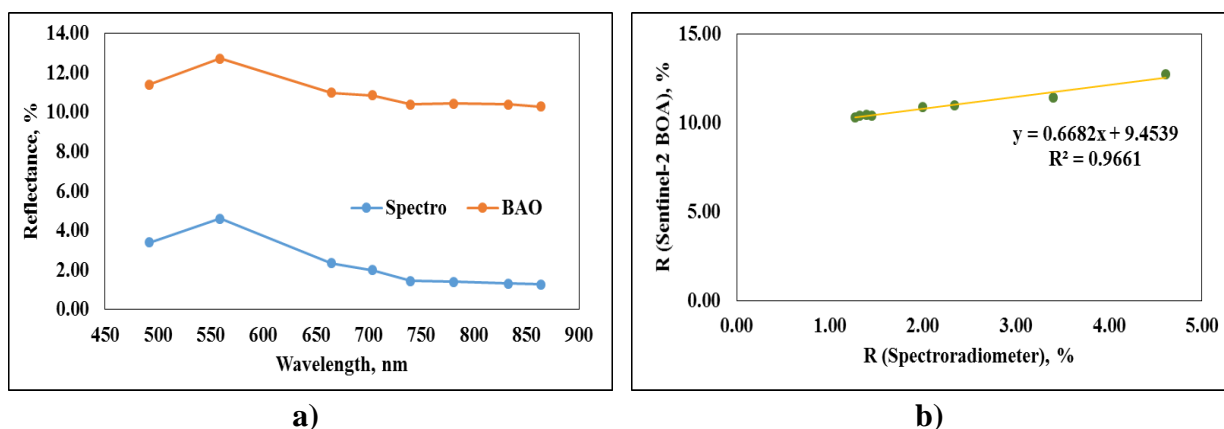


**Fig. F-100: a) Spectral Signatures Obtained from Spectroradiometer SVC-1024i & Sentinel-2 BOA Image and b) linear relation between band values for sample 100 having SSC**

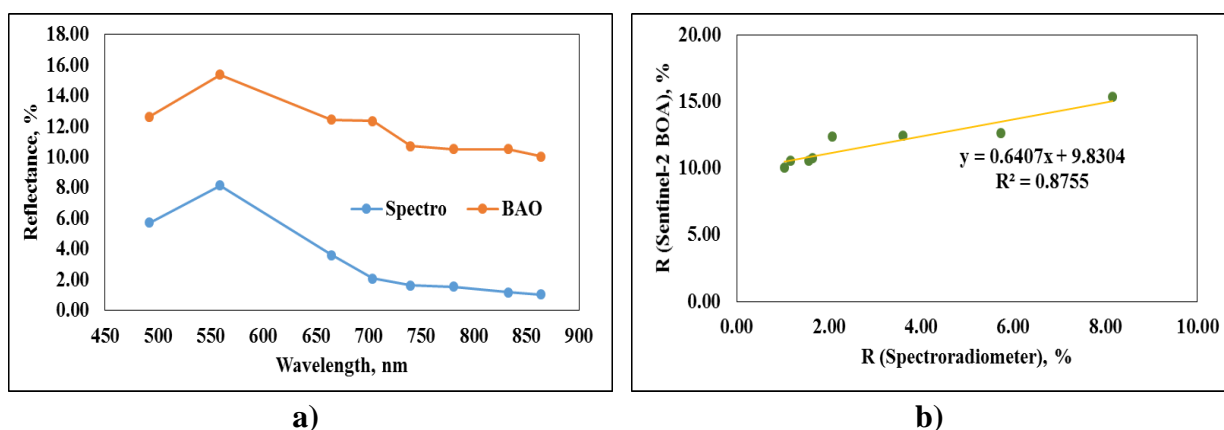


**Fig. F-101: a) Spectral Signatures Obtained from Spectroradiometer SVC-1024i & Sentinel-2 BOA Image and b) linear relation between band values for sample 101 having SSC**

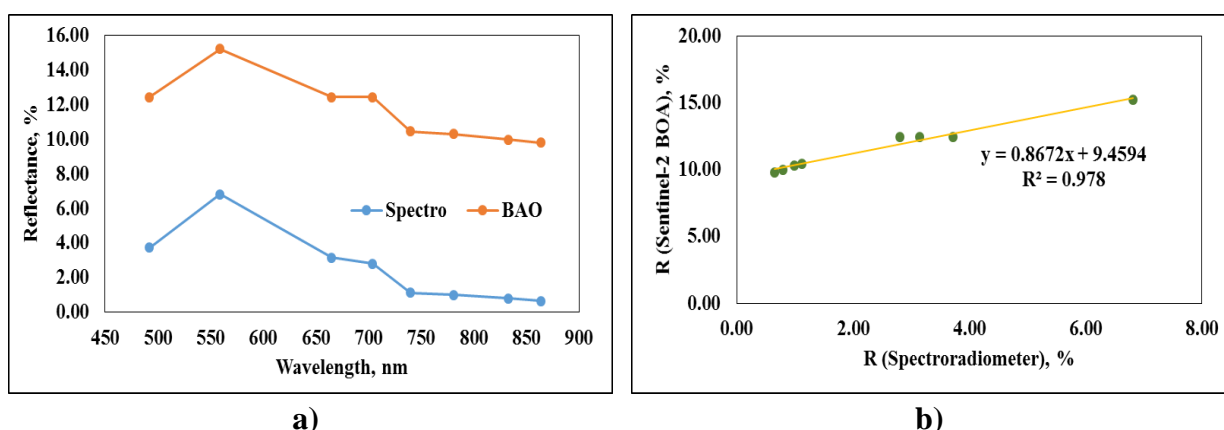
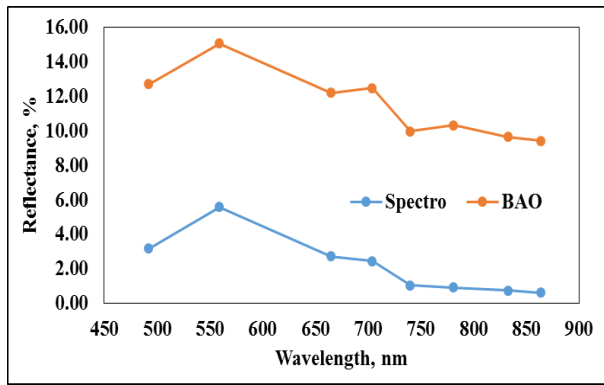
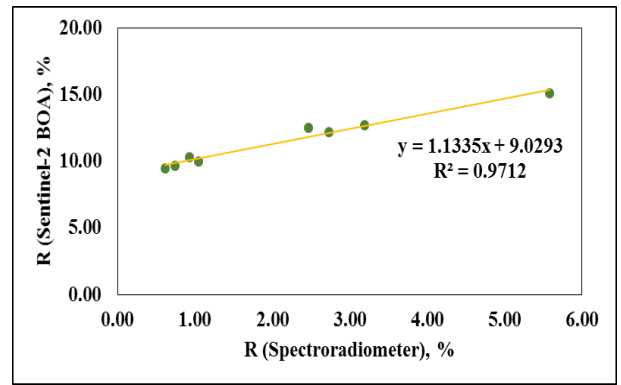


**Fig. F-102: a) Spectral Signatures Obtained from Spectroradiometer SVC-1024i & Sentinel-2 BOA Image and b) linear relation between band values for sample 102 having SSC**

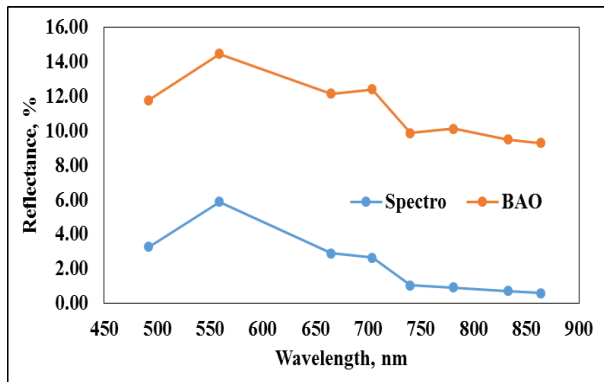


a)

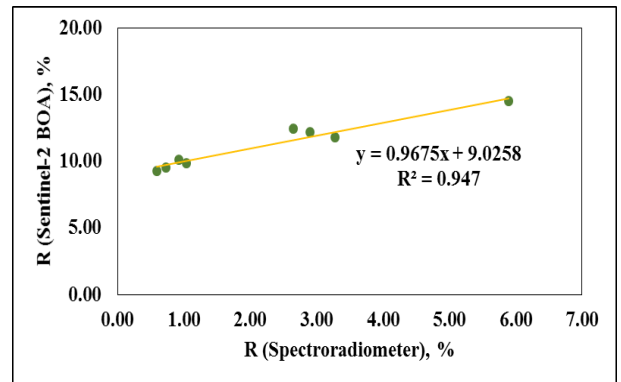


b)

**Fig. F-103: a) Spectral Signatures Obtained from Spectroradiometer SVC-1024i & Sentinel-2 BOA Image and b) linear relation between band values for sample 103 having SSC**

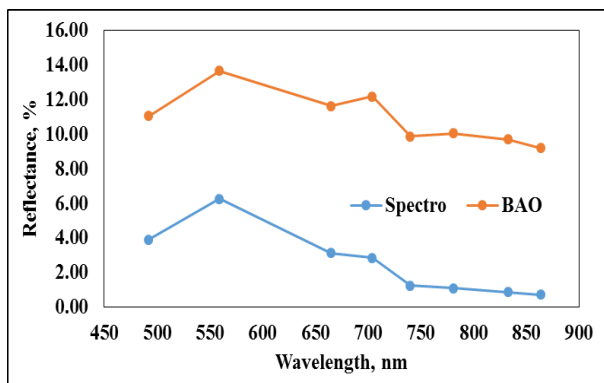


a)

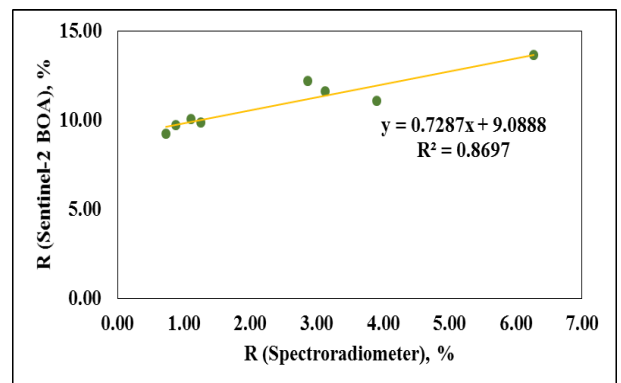


b)

**Fig. F-104: a) Spectral Signatures Obtained from Spectroradiometer SVC-1024i & Sentinel-2 BOA Image and b) linear relation between band values for sample 104 having SSC**



a)



b)

**Fig. F-105: a) Spectral Signatures Obtained from Spectroradiometer SVC-1024i & Sentinel-2 BOA Image and b) linear relation between band values for sample 105 having SSC**

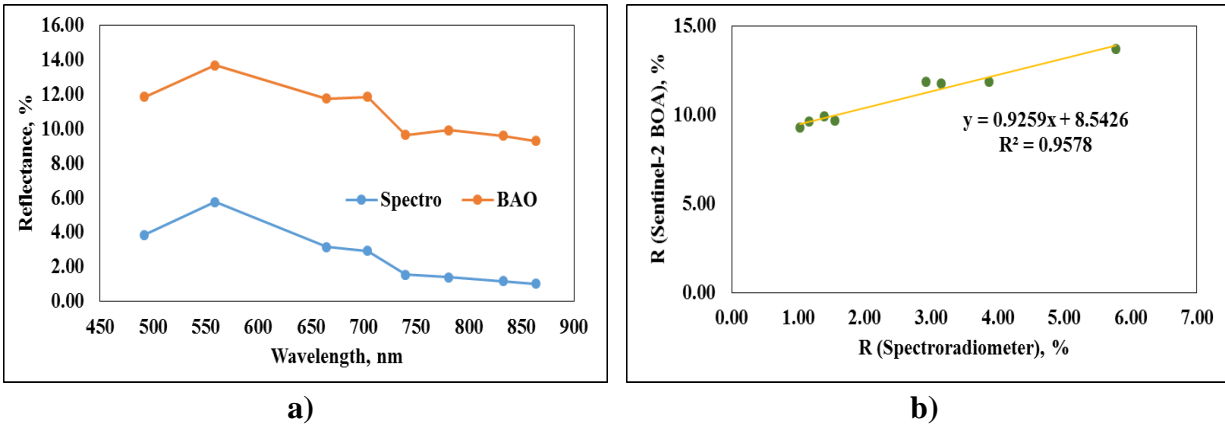


**Fig. F-106: a) Spectral Signatures Obtained from Spectroradiometer SVC-1024i & Sentinel-2 BOA Image and b) linear relation between band values for sample 106 having SSC**

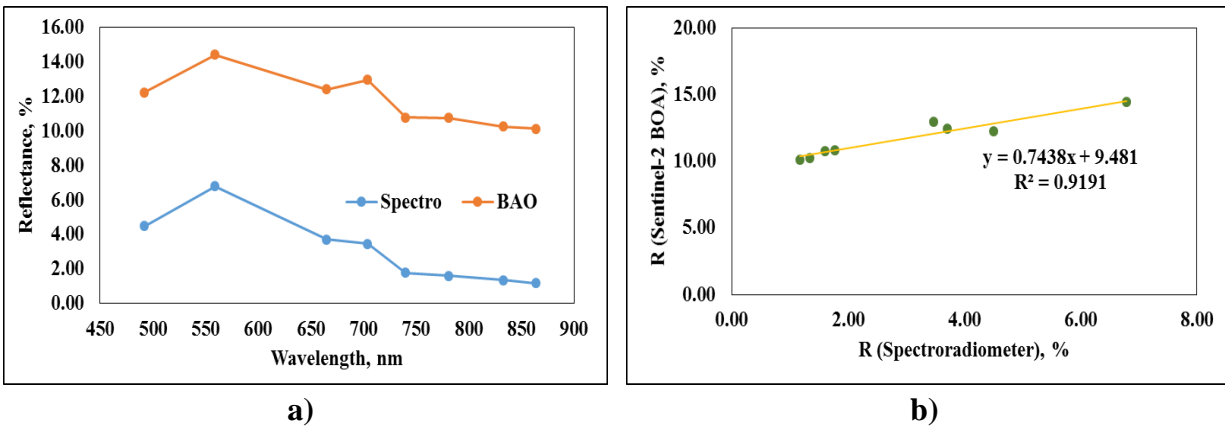


**Fig. F-107: a) Spectral Signatures Obtained from Spectroradiometer SVC-1024i & Sentinel-2 BOA Image and b) linear relation between band values for sample 107 having SSC**

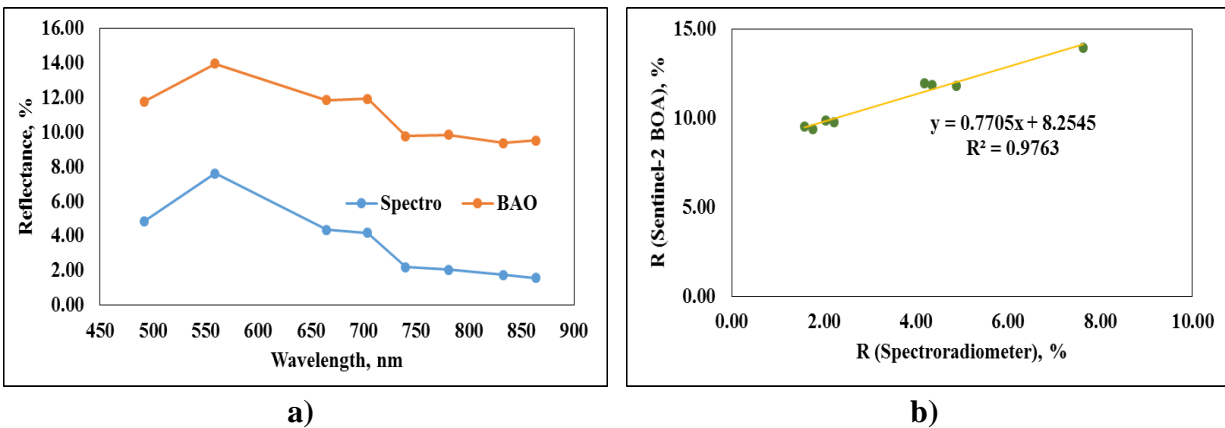
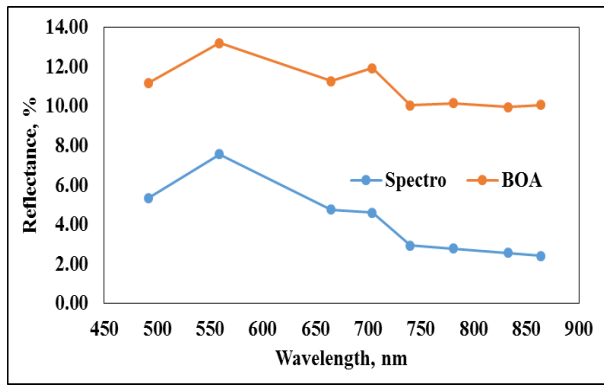
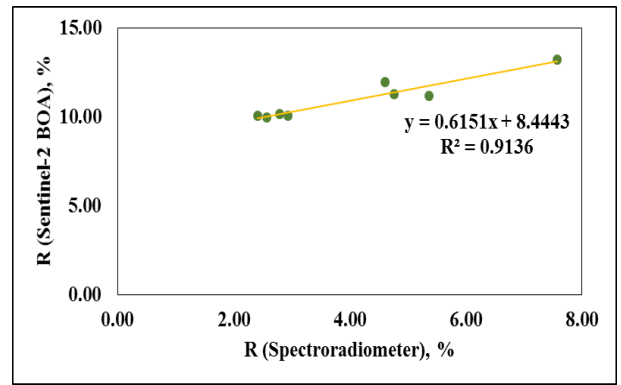


**Fig. F-108: a) Spectral Signatures Obtained from Spectroradiometer SVC-1024i & Sentinel-2 BOA Image and b) linear relation between band values for sample 108 having SSC**

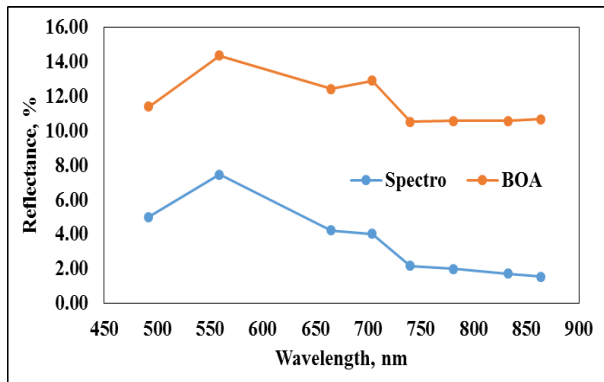


a)

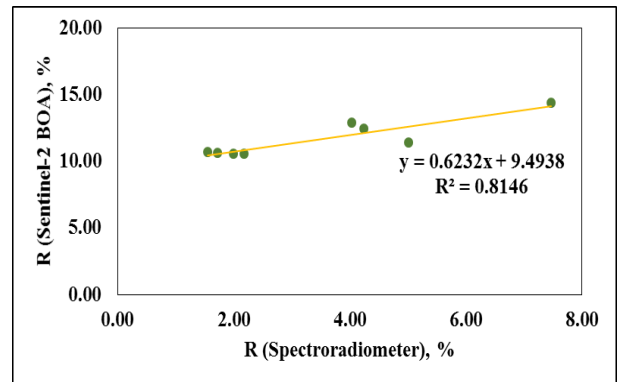


b)

**Fig. F-109: a) Spectral Signatures Obtained from Spectroradiometer SVC-1024i & Sentinel-2 BOA Image and b) linear relation between band values for sample 109 having SSC**

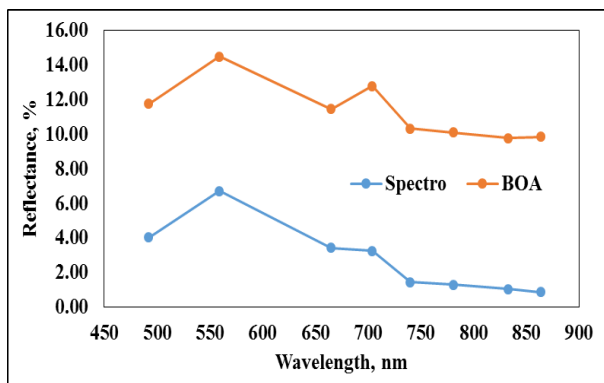


a)

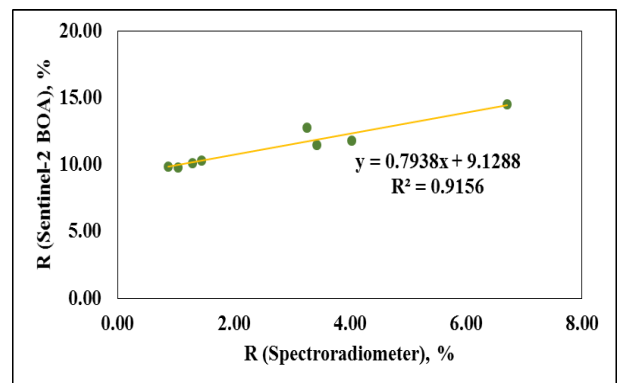


b)

**Fig. F-110: a) Spectral Signatures Obtained from Spectroradiometer SVC-1024i & Sentinel-2 BOA Image and b) linear relation between band values for sample 110 having SSC**



a)



b)

**Fig. F-111: a) Spectral Signatures Obtained from Spectroradiometer SVC-1024i & Sentinel-2 BOA Image and b) linear relation between band values for sample 111 having SSC**

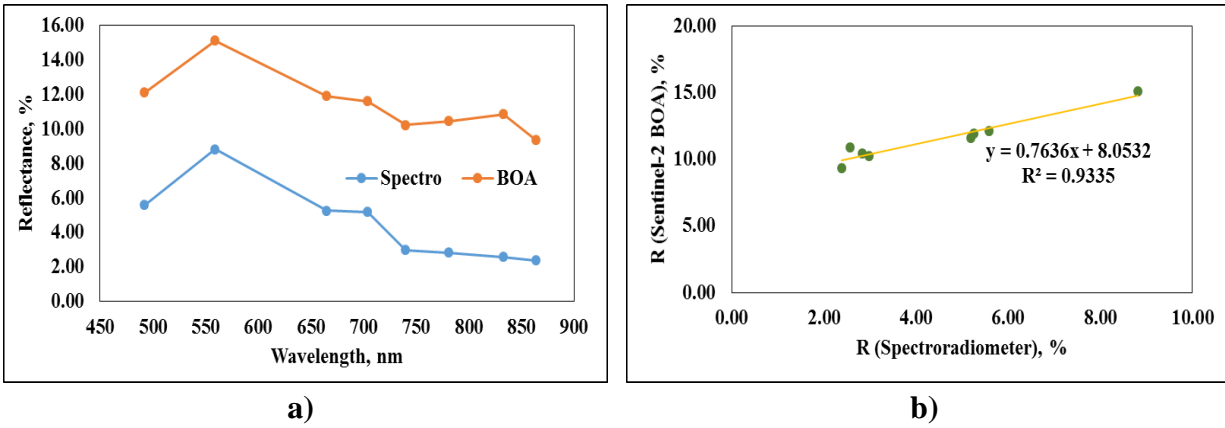


**Fig. F-112: a) Spectral Signatures Obtained from Spectroradiometer SVC-1024i & Sentinel-2 BOA Image and b) linear relation between band values for sample 112 having SSC**

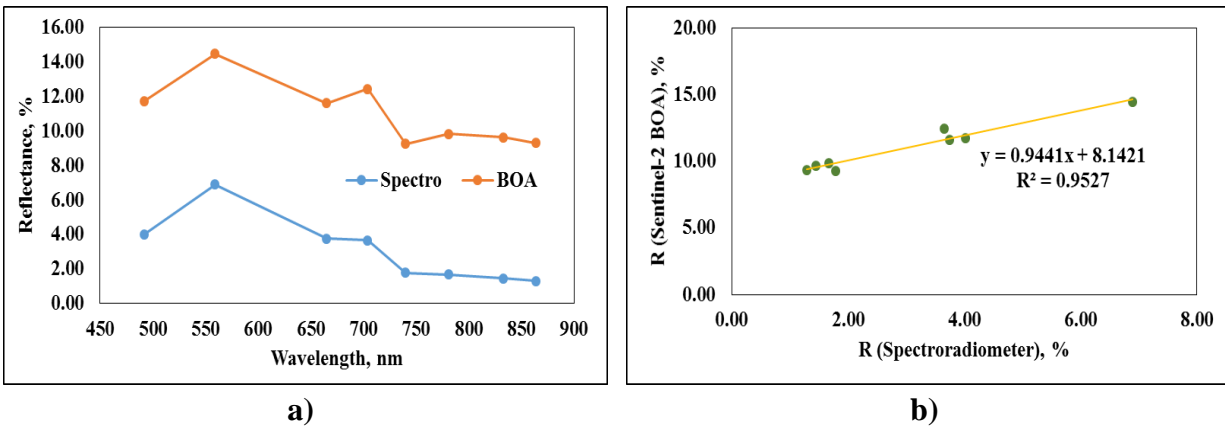


**Fig. F-113: a) Spectral Signatures Obtained from Spectroradiometer SVC-1024i & Sentinel-2 BOA Image and b) linear relation between band values for sample 113 having SSC**

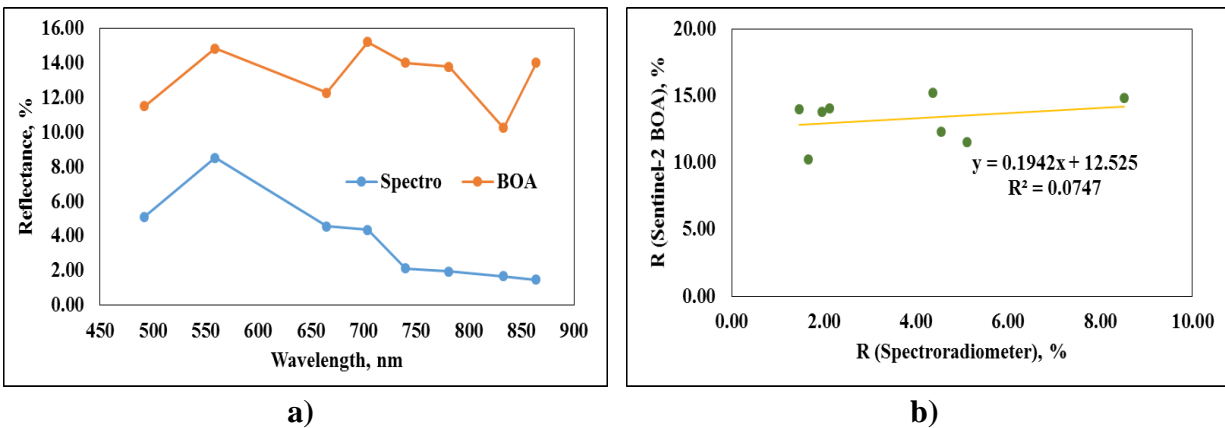


**Fig. F-114: a) Spectral Signatures Obtained from Spectroradiometer SVC-1024i & Sentinel-2 BOA Image and b) linear relation between band values for sample 114 having SSC**

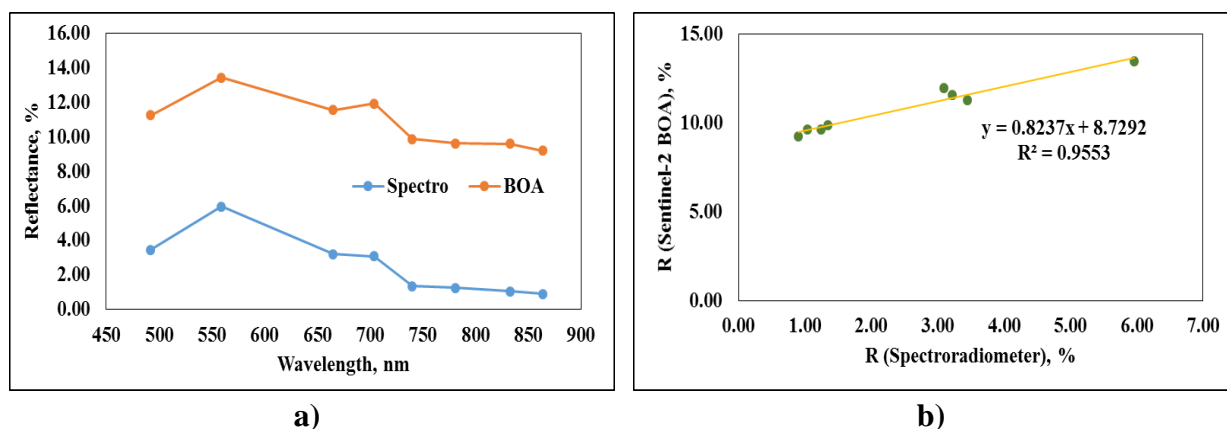


**Fig. F-115: a) Spectral Signatures Obtained from Spectroradiometer SVC-1024i & Sentinel-2 BOA Image and b) linear relation between band values for sample 115 having SSC**

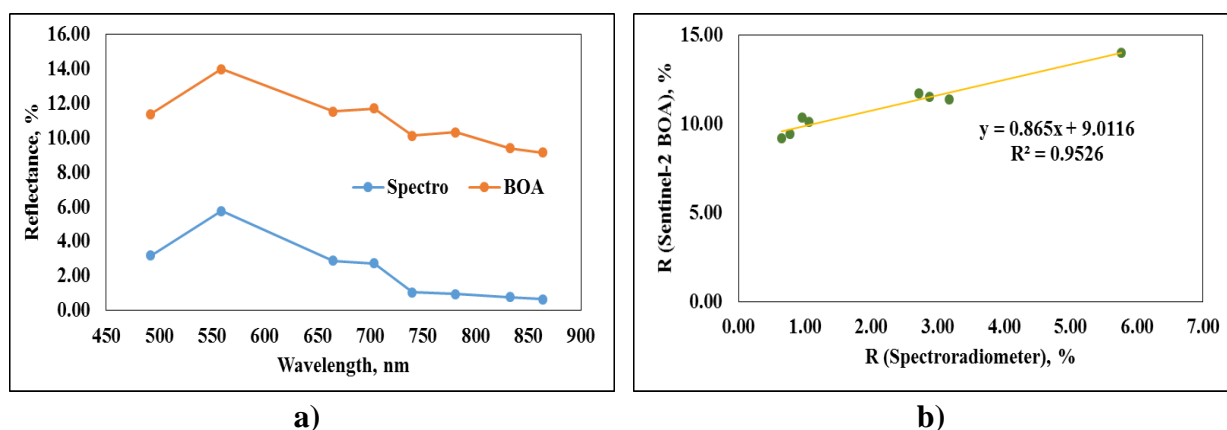


**Fig. F-116: a) Spectral Signatures Obtained from Spectroradiometer SVC-1024i & Sentinel-2 BOA Image and b) linear relation between band values for sample 116 having SSC**

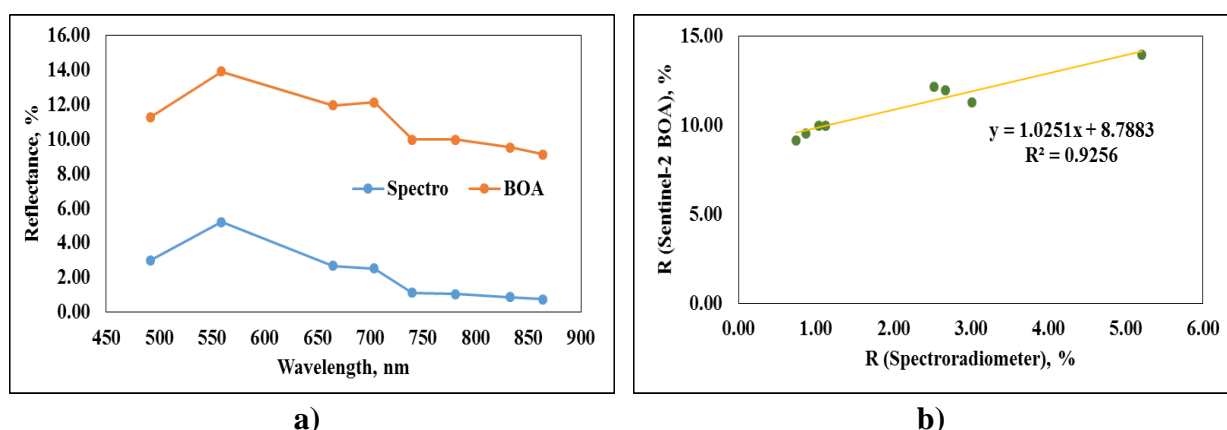


**Fig. F-117: a) Spectral Signatures Obtained from Spectroradiometer SVC-1024i & Sentinel-2 BOA Image and b) linear relation between band values for sample 117 having SSC**

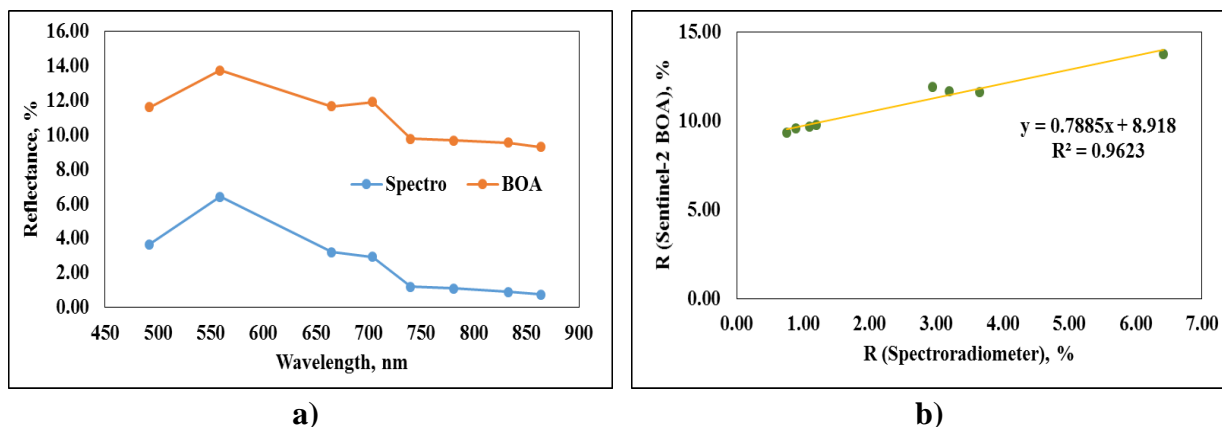


**Fig. F-118: a) Spectral Signatures Obtained from Spectroradiometer SVC-1024i & Sentinel-2 BOA Image and b) linear relation between band values for sample 118 having SSC**

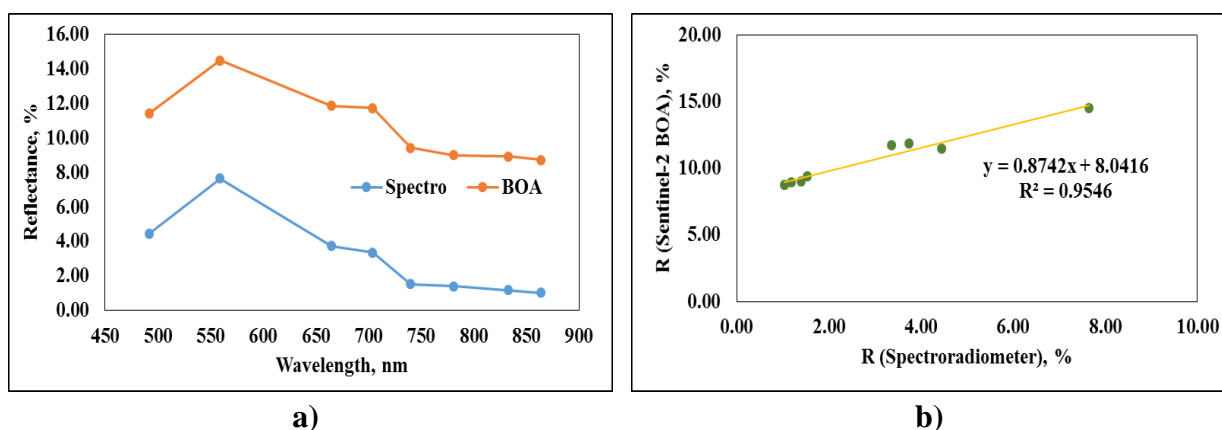


**Fig. F-119: a) Spectral Signatures Obtained from Spectroradiometer SVC-1024i & Sentinel-2 BOA Image and b) linear relation between band values for sample 119 having SSC**

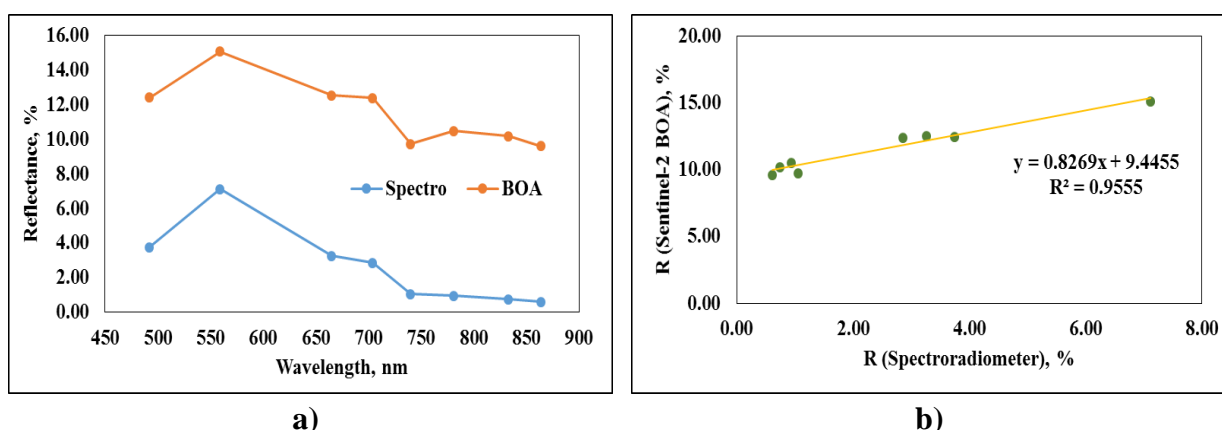
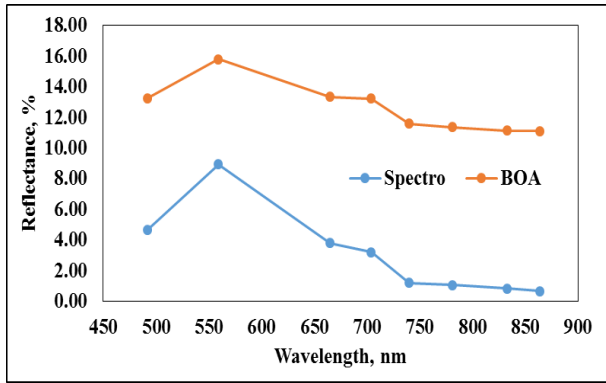
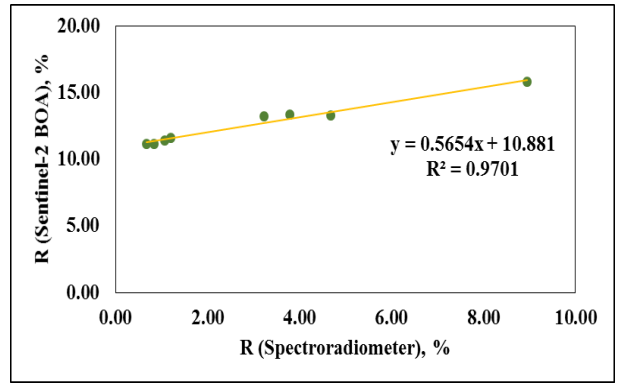


**Fig. F-120: a) Spectral Signatures Obtained from Spectroradiometer SVC-1024i & Sentinel-2 BOA Image and b) linear relation between band values for sample 120 having SSC**



a)



b)

**Fig. F-121: a) Spectral Signatures Obtained from Spectroradiometer SVC-1024i & Sentinel-2 BOA Image and b) linear relation between band values for sample 118 having SSC**



## Appendix – G

### Values of band indices/ ratio/ combinations obtained from Spectroradiometer SVC - HR 1024i and Sentinel 2 Satellite data

**Appendix G(I): Values of Band indices/ ratio/ combination Obtained From Spectroradiometer for calibration data Set**

Sample No.	Indices				Ratios/ Combination			
	NDSSI	NSMI	M-NDSSI	R-NDSSI	(Red + Green) /2	(Red + RE1 + Green)/3	Green-Red edge 1	(Green×Red Edge 1)/ Red
1	0.661	0.250	0.154	0.528	1.491	1.285	1.617	1.296
2	0.652	0.256	0.142	0.506	1.460	1.274	1.554	1.318
3	0.668	0.250	0.159	0.528	1.638	1.414	1.784	1.435
4	0.679	0.170	0.207	0.566	2.050	1.573	1.865	1.572
5	0.663	0.184	0.186	0.551	2.128	1.664	1.944	1.664
8	0.570	0.273	0.079	0.395	1.575	1.452	1.471	1.743
9	0.556	0.305	0.056	0.386	1.366	1.315	1.405	1.569
10	0.624	0.262	0.118	0.424	1.726	1.562	1.655	1.851
11	0.673	0.307	0.136	0.454	1.126	1.086	1.364	1.267
12	0.660	0.290	0.140	0.469	1.120	1.049	1.310	1.203
13	0.679	0.304	0.138	0.470	1.011	0.963	1.224	1.078
14	0.624	0.292	0.110	0.437	1.093	1.028	1.199	1.197
15	0.658	0.267	0.141	0.458	1.317	1.192	1.377	1.367
16	0.668	0.274	0.143	0.464	1.109	1.010	1.196	1.141
17	0.659	0.297	0.121	0.441	1.077	1.015	1.198	1.155
18	0.642	0.268	0.117	0.426	1.886	1.706	1.815	1.952
23	0.620	0.312	0.107	0.460	1.272	1.228	1.560	1.393
24	0.653	0.293	0.126	0.456	1.672	1.567	1.895	1.775
25	0.600	0.304	0.076	0.419	1.156	1.095	1.232	1.227
26	0.630	0.316	0.034	0.319	1.795	1.711	1.476	1.871
27	0.593	0.264	0.079	0.361	2.369	2.161	1.926	2.609
28	0.589	0.248	0.072	0.358	2.353	2.081	1.698	2.398
32	0.566	0.280	0.047	0.331	1.406	1.310	1.109	1.567
34	0.561	0.251	0.060	0.341	2.145	1.924	1.525	2.306
35	0.522	0.284	0.003	0.279	2.692	2.518	1.760	2.964
36	0.565	0.289	0.030	0.295	2.595	2.450	1.883	2.940
37	0.623	0.346	0.024	0.263	1.976	2.021	1.730	2.485
38	0.587	0.322	0.026	0.291	2.140	2.111	1.804	2.545
39	0.598	0.328	0.035	0.290	2.070	2.074	1.833	2.581
42	0.588	0.286	0.054	0.316	3.562	3.365	2.795	4.128
43	0.613	0.323	0.035	0.288	2.209	2.184	1.858	2.639
47	0.629	0.285	0.084	0.351	2.173	2.041	1.880	2.473
50	0.675	0.242	0.154	0.425	1.950	1.726	1.765	2.088
51	0.629	0.249	0.109	0.383	2.351	2.097	1.907	2.513
53	0.626	0.257	0.084	0.347	2.240	2.014	1.646	2.360
54	0.669	0.264	0.130	0.403	1.609	1.465	1.480	1.756
56	0.600	0.270	0.079	0.362	1.276	1.171	1.060	1.401
59	0.561	0.275	0.052	0.330	2.278	2.119	1.781	2.594
63	0.472	0.283	-0.015	0.278	2.083	1.954	1.372	2.336
65	0.577	0.309	0.038	0.299	2.187	2.138	1.829	2.660
68	0.448	0.317	-0.054	0.228	2.597	2.554	1.693	3.075

69	0.585	0.316	0.043	0.307	1.958	1.936	1.749	2.430
70	0.522	0.301	0.005	0.271	2.244	2.174	1.640	2.698
71	0.558	0.356	0.008	0.266	1.522	1.601	1.475	2.077
72	0.618	0.359	0.044	0.292	1.928	2.042	2.049	2.666
76	0.641	0.301	0.105	0.377	0.993	0.964	1.024	1.217
77	0.619	0.283	0.092	0.371	1.644	1.544	1.515	1.896
78	0.620	0.303	0.083	0.352	1.835	1.780	1.764	2.232
79	0.682	0.322	0.123	0.362	1.553	1.574	1.738	2.102
81	0.696	0.208	0.203	0.458	1.207	1.030	1.092	1.306
82	0.808	0.347	0.223	0.456	1.863	1.978	2.820	2.635
83	0.554	0.388	0.006	0.264	2.361	2.638	2.734	3.616
84	0.753	0.426	0.106	0.306	1.698	2.046	2.616	2.941
86	0.661	0.441	0.031	0.243	1.612	1.975	2.295	2.841
87	0.752	0.456	0.056	0.222	1.967	2.480	2.888	3.662
88	0.742	0.464	0.042	0.207	1.789	2.283	2.635	3.382
89	0.759	0.474	0.039	0.209	1.472	1.898	2.241	2.760
90	0.726	0.469	0.025	0.196	1.630	2.082	2.359	3.039
91	0.705	0.458	0.022	0.202	2.125	2.662	2.957	3.840
92	0.593	0.469	-0.045	0.154	2.074	2.630	2.690	3.797
93	0.714	0.489	-0.015	0.142	1.610	2.111	2.241	3.084
95	0.729	0.485	0.000	0.149	2.006	2.628	2.823	3.898
97	0.742	0.448	0.053	0.222	1.770	2.199	2.503	3.217
98	0.732	0.450	0.071	0.264	1.555	1.950	2.440	2.862
99	0.736	0.469	0.041	0.241	1.584	2.017	2.481	2.847
100	0.442	0.342	-0.036	0.261	2.871	2.980	2.611	3.928
101	0.661	0.344	0.091	0.468	4.674	4.614	6.078	4.694
102	0.649	0.456	-0.029	0.140	3.436	4.258	4.012	6.072
104	0.637	0.457	-0.050	0.106	3.087	3.812	3.244	5.386
105	0.634	0.413	-0.012	0.154	3.518	4.089	3.410	5.738
106	0.537	0.395	-0.055	0.138	3.507	3.949	2.848	5.365
107	0.541	0.400	-0.058	0.130	4.103	4.652	3.318	6.337
108	0.469	0.422	-0.113	0.075	4.615	5.390	3.433	7.333
109	0.353	0.394	-0.156	0.076	5.063	5.646	2.961	7.307
110	0.488	0.401	-0.087	0.107	4.623	5.248	3.434	7.121
111	0.590	0.432	-0.053	0.106	3.731	4.468	3.458	6.359
112	0.371	0.432	-0.167	0.037	5.427	6.428	3.630	8.714
113	0.470	0.452	-0.128	0.048	3.884	4.766	3.243	6.715
115	0.535	0.454	-0.106	0.054	3.332	4.091	2.873	5.731
116	0.606	0.463	-0.070	0.078	3.028	3.789	3.054	5.450
117	0.554	0.447	-0.080	0.089	2.840	3.465	2.686	4.919
119	0.580	0.438	-0.050	0.140	4.090	4.910	4.289	6.873
120	0.667	0.469	-0.034	0.136	3.506	4.409	4.260	6.217
121	0.697	0.463	0.006	0.185	4.238	5.320	5.726	7.590

**Appendix G(II): Values of Band indices/ ratio/ combination Obtained From Spectroradiometer for validation data Set**

Sample No.	Indices				Ratios/ Combination			
	NDSSI	NSMI	M-NDSSI	R-NDSSI	(Red + Green)/2	(Red + RE1 + Green)/3	Green-Red edge 1	Green*Red Edge 1 / Red
6	0.663	0.184	0.186	0.551	2.081	1.664	1.944	1.402
7	0.637	0.282	0.121	0.439	1.696	1.377	1.583	1.483
19	0.649	0.239	0.140	0.439	2.174	1.796	1.860	1.286
20	0.641	0.270	0.120	0.425	2.703	2.220	2.391	1.359
21	0.692	0.310	0.137	0.463	1.833	1.458	1.844	1.656
30	0.543	0.242	0.055	0.346	2.031	1.756	1.374	0.926
33	0.571	0.273	0.052	0.337	2.321	1.987	1.663	1.000
40	0.593	0.325	0.041	0.302	2.987	2.535	2.319	1.145
41	0.600	0.315	0.048	0.309	2.804	2.383	2.142	1.112
44	0.627	0.334	0.056	0.307	2.603	2.195	2.097	1.213
46	0.605	0.304	0.041	0.303	2.641	2.263	1.872	0.985
49	0.597	0.265	0.075	0.353	2.757	2.349	2.030	1.041
58	0.572	0.274	0.058	0.341	1.940	1.655	1.426	1.043
61	0.575	0.293	0.045	0.318	1.772	1.516	1.292	1.034
67	0.570	0.304	0.029	0.288	1.885	1.627	1.310	0.972
73	0.629	0.317	0.074	0.335	1.631	1.369	1.347	1.255
85	0.741	0.449	0.076	0.271	1.878	1.525	1.925	1.898
94	0.249	0.412	-0.221	0.051	4.433	4.067	1.972	0.554
96	0.635	0.456	-0.024	0.151	2.692	2.289	2.242	1.350
103	0.623	0.445	-0.042	0.129	4.158	3.593	3.122	1.143
118	0.607	0.450	-0.057	0.108	4.810	4.187	3.479	1.087

**Appendix G(III): Values of Band indices/ ratio/ combination Obtained from Sentinel 2 satellite data for calibration data Set**

Sample No.	Indices				Ratios/ Combination			
	NDSSI	NSMI	M-NDSSI	R-NDSSI	Red + Green /2	(Red + RE1 + Green)/3	Green-Red edge 1	Green*Red Edge 1 / Red
1	0.307	0.304	-0.083	0.197	3.39	3.49	2.27	5.20
2	0.270	0.243	-0.113	0.177	3.68	3.42	1.15	4.32
3	0.261	0.229	-0.121	0.157	3.96	3.62	0.82	4.47
4	0.176	0.302	-0.192	0.109	3.83	3.83	1.24	4.87
5	0.274	0.245	-0.115	0.179	3.99	3.69	1.24	4.57
8	0.307	0.245	-0.085	0.200	3.98	3.71	1.57	4.87
9	0.277	0.249	-0.100	0.170	3.85	3.68	1.39	5.07
10	0.341	0.256	-0.068	0.184	3.94	3.77	1.63	5.16
11	0.296	0.266	-0.110	0.162	3.88	3.71	1.36	4.76
12	0.307	0.254	-0.092	0.188	3.55	3.34	1.37	4.34
13	0.310	0.278	-0.103	0.161	3.51	3.42	1.41	4.51
14	0.270	0.266	-0.114	0.177	3.56	3.42	1.44	4.51
15	0.279	0.235	-0.112	0.197	3.85	3.47	1.16	4.11
16	0.252	0.284	-0.156	0.175	3.40	3.19	1.22	3.55
17	0.317	0.278	-0.098	0.165	3.25	3.17	1.35	4.20
18	0.248	0.279	-0.149	0.135	3.38	3.27	1.03	4.06
23	0.286	0.260	-0.119	0.163	4.09	3.85	1.28	4.74
24	0.282	0.277	-0.125	0.124	3.95	3.88	1.19	5.09
25	0.296	0.282	-0.123	0.161	3.82	3.68	1.44	4.53
26	-0.198	0.374	-0.450	-0.083	10.64	11.18	-1.27	10.82
27	0.222	0.252	-0.159	0.153	6.94	6.40	1.56	7.36
28	0.207	0.262	-0.172	0.133	6.98	6.55	1.48	7.65
32	0.048	0.306	-0.282	0.063	7.18	7.05	0.95	7.72
34	0.231	0.277	-0.164	0.129	6.87	6.57	1.75	7.77
35	0.224	0.279	-0.167	0.124	6.88	6.63	1.77	7.97
36	0.281	0.244	-0.120	0.152	5.80	5.37	1.34	6.53
37	0.210	0.291	-0.178	0.064	6.16	6.23	1.12	8.13
38	0.170	0.268	-0.189	0.121	6.34	6.05	1.38	7.30
39	0.214	0.270	-0.160	0.136	6.05	5.82	1.72	7.31
42	0.119	0.293	-0.231	0.079	6.72	6.63	1.22	7.92
43	0.275	0.246	-0.125	0.171	6.37	5.83	1.67	6.83
47	0.140	0.282	-0.210	0.099	6.86	6.70	1.44	8.20
50	0.119	0.271	-0.226	0.116	6.98	6.57	1.23	7.34
51	0.290	0.251	-0.119	0.185	6.47	5.91	1.97	6.81
53	0.121	0.264	-0.219	0.120	7.31	6.87	1.28	7.85
54	0.333	0.215	-0.087	0.221	6.54	5.63	1.70	6.12
56	0.199	0.293	-0.188	0.081	5.17	5.14	1.05	6.37
59	0.178	0.310	-0.210	0.069	4.85	4.89	1.03	5.90
63	0.210	0.300	-0.190	0.115	5.41	5.27	1.48	6.04
65	0.128	0.291	-0.218	0.069	5.35	5.37	0.98	6.89
68	0.240	0.292	-0.160	0.121	5.16	5.07	1.58	6.27
69	0.230	0.295	-0.171	0.118	5.81	5.69	1.69	6.83
70	0.126	0.334	-0.241	0.032	5.64	5.94	1.24	7.54
71	0.162	0.327	-0.224	0.067	5.83	5.95	1.51	7.16
72	0.182	0.321	-0.211	0.075	5.39	5.47	1.44	6.61
76	0.187	0.311	-0.209	0.108	5.07	4.96	1.40	5.58

7	0.275	0.271	-0.149	0.160	4.85	4.48	1.30	4.86
78	0.181	0.308	-0.212	0.108	5.63	5.48	1.47	6.08
79	0.072	0.308	-0.264	0.053	6.17	6.19	0.92	7.30
81	-0.061	0.355	-0.355	0.066	5.30	5.34	1.38	5.51
82	0.063	0.340	-0.292	0.041	11.47	11.61	1.94	12.53
83	0.043	0.362	-0.311	0.018	11.15	11.60	2.08	12.64
84	0.053	0.356	-0.302	0.028	11.30	11.67	2.18	12.75
86	0.052	0.361	-0.305	0.019	11.36	11.83	2.15	12.99
87	0.049	0.364	-0.310	0.015	11.47	11.94	2.04	12.91
88	0.056	0.363	-0.302	0.013	11.34	11.94	2.25	13.49
89	0.048	0.373	-0.313	0.000	11.40	12.11	2.11	13.50
90	0.043	0.374	-0.316	0.003	11.33	11.99	2.18	13.23
91	0.063	0.365	-0.299	0.012	11.76	12.41	2.37	14.07
92	0.068	0.360	-0.296	0.018	11.78	12.32	2.28	13.75
93	0.050	0.372	-0.311	-0.001	11.62	12.36	2.16	13.88
95	0.047	0.367	-0.314	0.002	11.36	11.93	1.81	12.98
97	0.059	0.356	-0.302	0.027	11.54	11.88	2.13	12.80
98	0.044	0.364	-0.312	0.011	11.19	11.69	1.97	12.76
99	0.056	0.359	-0.304	0.024	11.41	11.80	2.14	12.78
100	0.046	0.351	-0.305	0.024	11.20	11.53	1.87	12.57
101	0.091	0.375	-0.290	0.011	12.54	13.39	3.02	15.28
102	0.110	0.380	-0.287	0.000	12.44	13.36	2.78	15.19
104	0.107	0.386	-0.295	-0.026	11.97	13.01	2.07	14.79
105	0.066	0.391	-0.317	-0.049	11.35	12.49	1.47	14.32
106	0.105	0.364	-0.286	0.000	11.81	12.44	1.84	13.83
107	0.088	0.374	-0.299	-0.029	12.33	13.27	1.47	15.07
108	0.113	0.373	-0.286	-0.006	11.83	12.59	2.02	14.05
109	0.058	0.373	-0.310	-0.032	11.24	12.14	1.27	13.96
110	0.037	0.404	-0.338	-0.063	11.93	13.25	1.46	14.92
111	0.093	0.376	-0.287	-0.041	11.62	12.91	1.72	16.17
112	0.054	0.381	-0.306	0.021	12.02	12.88	3.49	14.73
113	0.098	0.379	-0.288	-0.029	11.68	12.84	2.03	15.47
115	0.079	0.379	-0.305	-0.029	11.41	12.31	1.51	13.88
116	0.095	0.383	-0.296	-0.014	11.46	12.41	2.29	14.22
117	0.084	0.393	-0.312	-0.036	11.62	12.67	1.80	14.13
119	0.123	0.395	-0.290	-0.013	11.65	12.70	2.77	14.34
120	0.099	0.380	-0.293	0.001	12.47	13.32	2.68	14.88
121	0.087	0.374	-0.297	0.001	13.30	14.12	2.55	15.68

**Appendix G(IV): Values of Band indices/ ratio/ combination Obtained from Sentinel 2 satellite data for validation data Set**

Sample No.	Indices				Ratios/ Combination			
	NDSSI	NSMI	M-NDSSI	R-NDSSI	Red + Green /2	(Red + RE1 + Green)/3	Green-Red edge 1	Green*Red Edge 1 / Red
6	-0.890	-0.455	-0.893	-0.835	3.895	3.693	1.240	0.380
7	-0.894	-0.583	-0.898	-0.876	3.985	3.723	1.630	0.519
19	-0.902	-0.729	-0.906	-0.891	3.420	3.210	1.320	0.484
20	-0.883	-1.755	-0.886	-0.854	3.705	3.477	1.320	0.430
21	-0.898	-0.590	-0.902	-0.884	3.695	3.457	1.320	0.427
30	-0.904	-0.362	-0.908	-0.884	6.565	6.303	1.510	0.259
33	-0.906	-0.561	-0.909	-0.878	7.600	7.323	1.750	0.262
40	-0.906	-0.377	-0.909	-0.878	5.915	5.697	1.530	0.304
41	-0.894	-0.669	-0.898	-0.872	5.925	5.690	1.670	0.337
44	-0.890	-0.452	-0.894	-0.867	6.815	6.500	1.850	0.313
46	-0.884	-0.659	-0.888	-0.853	6.245	5.923	1.880	0.353
49	-0.889	-0.619	-0.893	-0.861	5.990	5.773	1.280	0.239
58	-0.892	-0.469	-0.897	-0.885	5.380	5.173	1.230	0.258
61	-0.852	-0.878	-0.858	-0.846	5.325	5.130	1.210	0.257
67	-0.876	-0.613	-0.880	-0.842	5.325	5.010	1.710	0.375
73	-0.871	-1.102	-0.875	-0.847	5.955	6.017	0.230	0.042
85	-0.896	-0.709	-0.899	-0.881	12.190	11.787	2.180	0.194
94	-0.897	-1.008	-0.899	-0.869	12.940	12.517	2.400	0.203
96	-0.883	-0.761	-0.887	-0.862	12.205	11.917	1.700	0.150
103	-0.933	5.705	-0.933	-0.932	13.630	13.247	2.580	0.211
118	-0.934	-1.051	-0.935	-0.930	12.705	12.437	1.840	0.158

## Appendix – H

### Procedure for Applying t-test for testing linear regression coefficients and Student t-test

#### A. Preliminary evaluation through t-test for testing the linear regression coefficients:

The observed and estimated values of SSC were treated as dependent (y) and independent (x) variables, respectively for linear regression,  $y = a + b x$ .

Null hypothesis,  $H_0$ :  $a = 0$  and  $b = 1$

Alternate hypothesis  $H_1$ :  $a \neq 0$  and  $b \neq 1$

Hypothesis test: t (a) and t (b) for  $(n - 2)$  degrees of freedom at 5 % level of significance.

#### Illustration:

X	Y		
Estimated SSC (mg/L)	Observed SSC (mg/L)		
29.736	17.895	n	= 21
31.222	24.731	$\Sigma X$	= 1260.11
32.580	17.204	$\Sigma Y$	= 1254.97
32.879	20.000	$\bar{X}$	= 57.28
33.872	23.656	$\bar{Y}$	= 57.04
29.647	15.625	$\Sigma XY$	= 86117.62
38.431	47.435	SS(X)	= $\Sigma(X^2) - (\Sigma X)^2/n$
56.666	48.685		= $84957.95 - 72176.24$
34.426	55.000		= 12781.71
39.782	62.366	SS(Y)	= $\Sigma(Y^2) - (\Sigma Y)^2/n$
51.400	56.863		= $92108.63 - 71931.30$
53.943	59.000		= 20177.33
55.449	70.000	SS(P)	= $\Sigma XY - \Sigma X \times \Sigma Y/n$
52.949	52.525		= $86117.60 - (1260.11 \times 1254.97)/22$
86.490	41.000		= 14235.77
72.926	68.367	b	= $SS(P)/SS(X) = 14235.77/12781.71$
74.959	65.263		= 1.113
75.520	78.723	a	= $\bar{Y} - b \times \bar{X} = 57.04 - 1.113 \times 57.28$
79.916	77.551		= - 6.71
105.921	121.429		
96.532	121.277		
94.865	110.377		

$$\text{Reg. (SS)} = b \times \text{SS (P)} = 1.113 \times 14235.77 = 15844.41$$

$$\text{Res. (SS)} = \text{SS(Y)} - b \times \text{SS(P)} = 20177.33 - 1.113 \times 14235.77 = 4332.92$$

$$S^2_{YX} = \text{Res. (SS)} / (n - 2) = 4332.92 / 20 = 216.65$$

$$\text{SE(a)} = S^2_{YX} \times \sqrt{\frac{1}{n} + \bar{X}^2 / \text{SS(X)}} = 216.65 \times 0.55 = 119.15$$

$$SE(b) = \sqrt{S^2_{YX} / SS(X)} = 0.13$$

$$t(a) = |a/SE(a)| = \mathbf{0.056}$$

t(a) is less than t-table value 2.08 for (n – 2) i.e. 20 degrees of freedom at 5 % level of significance. Hence value of 'a' is found insignificant.

$$t(b) = |(b - 1)/SE(b)| = \mathbf{0.8}$$

t(b) is less than t-table value 2.08 for (n – 2) i.e. 20 degrees of freedom at 5 % level of significance. Hence value of 'b' is found insignificant.

### B. Secondary evaluation through student's t-test:

The mean values of observed and estimated SSC are compared using student t-test for  $(n - 2)$  degrees of freedom at 5 per cent level of significance.

Null hypothesis,  $H_0: \bar{X} = \bar{Y}$

Alternate hypothesis  $H_1: \bar{X} \neq \bar{Y}$

$$t_{cal} = \frac{|\bar{X} - \bar{Y}|}{\sqrt{S^2_{YX}/n}}$$

#### Illustration:

$$\bar{X} = 57.28$$

$$\bar{Y} = 57.04$$

$$S^2_{YX} = 216.65$$

$$n = 22$$

$$t_{cal} = \frac{|57.28 - 57.04|}{\sqrt{216.65/22}} = 0.07$$

Value of  $t_{cal}$  is less than t-table value 2.08 for  $(n - 2)$  i.e. 20 degrees of freedom at 5 % level of significance. Hence, the difference between two means is found insignificant. It means that there is no significant difference between the mean of estimated values of SSC and observed values of SSC.



## Appendix – I

### Publications based on this research work

Sr. No	Publication	NAAS Rating
1.	Estimation of Suspended Sediment Concentration Using Sentinel-2 Band Functions in Mula Reservoir, Rahuri (2023), <i>Environmental Engineering and Management Journal</i> , 22(2): 375-387.	7.1
2.	Development and Evaluation of Adjusted – NDSSI using Sentinel – 2 Satellite Data: A Case Study of Mula Dam Reservoir, Maharashtra State India, Technical Bulletin, 38 <sup>th</sup> Indian Engineering Congress, Jabalpur, 245-253.	Conference Proceeding
3.	An Attempt to Develop, Calibrate and Validate Spectral Integration Function for Assessment and Monitoring of Suspended Sediment Concentration in Large Water Body Submitted to the journal – Environmental Engineering Research	9.5

## VIII. VITAE

<b>Title of the Thesis</b>	:	Estimation of Suspended Sediment Concentration by Developing Integrated Surface Reflectance Function
<b>Major Field</b>	:	Soil and Water Conservation Engineering
<b>Biographical Information</b>		
<b>Personal</b>	<b>Date of Birth</b>	: 11 <sup>th</sup> November, 1994
	<b>Place of Birth</b>	: Beed, Maharashtra
	<b>Fathers Name</b>	: Mr. Kishor Narayan Joshi
	<b>Mothers Name</b>	: Mrs. Shubhada Kishor Joshi
<b>Educational</b>	<b>Bachelor Degree Obtained</b>	: B.Tech (Agricultural Engineering)
	<b>Class</b>	: First Class
	<b>Name of University</b>	: Vasantao Naik Marathwada Krishi Vidyapeeth, Parbhani
	<b>Master Degree Obtained</b>	: M.Tech (Agricultural Engineering) in (Soil and Water Conservation Engineering)
	<b>Class</b>	: First Class with Distinction
	<b>Name of University</b>	: Mahatma Phule Krishi Vidyapeeth, Rahuri
<b>Contact Details</b>	<b>Address</b>	: 796, Agasti, At Post – Wargaon, Taluka – Kankavli, District – Sindhudurg. Pin Code – 416801
	<b>Email ID</b>	: <a href="mailto:jkjosh194@gmail.com">jkjosh194@gmail.com</a>
	<b>Contact No.</b>	: 9527827082, 9404396958